Physics of the Solid State, Vol. 46, No. 4, 2004, pp. 595–599. Translated from Fizika Tverdogo Tela, Vol. 46, No. 4, 2004, pp. 581–584.

INTRODUCTION

On the History of the Discovery of Nanodiamond Synthesis

V. V. Danilenko

ZAO ALIT, Kiev, 03067 Ukraine

e-mail: vvdan@list.ru

Abstract—The history of the discovery of nanodiamond synthesis, the investigation of nanodiamond properties, and the application and organization of their production in the second half of the 20th century is expounded. It is noted that this history is unique, since nanodiamond synthesis was discovered in the USSR three times over 19 years: first by K.V. Volkov, V.V. Danilenko, and V.I. Elin at the VNIITF (Snezhinsk) in 1963 and then, in 1982, by A.M. Staver and A.I. Lyamkin at the Institute of Hydrodynamics, Siberian Division, Academy of Sciences of the USSR (Novosibirsk), and by G.I. Savvakin at the Institute of Problems of Materials Science, Academy of Sciences of the UkSSR (Kiev). All of these researchers discovered nanodiamond synthesis accidentally while studying diamond synthesis by shock compression of nondiamond carbon modifications in blast chambers. The priority of work by Russian scientists in this field is demonstrated. © *2004 MAIK "Nauka/Interperiodica".*

About 40 years ago, in July 1963, the detonation synthesis of nanodiamonds was discovered. In the 40-year history of nanodiamonds, the following three periods can be traced.

(i) The discovery of nanodiamond synthesis in 1963–1982, followed by a prolonged suspension of active study.

(ii) Rediscovery of the synthesis in 1982–1993, with intensified study and production of nanodiamonds simultaneously at several research centers in the USSR. In this period, production potential exceeded the scale of application.

(iii) Unprofitable production of small batches of nanodiamonds in 1993–2003, leading to the closure of a number of research centers and the termination of production.

However, some enthusiasts, who believe that nanodiamonds will find wide application in industry, continue to work hard on this area. The interest in nanodiamonds is being gradually revived, which was demonstrated by the organization of the International Symposium in St. Petersburg.

In analyzing the history of the discovery of the synthesis of nanodiamonds or ultrafine-dispersed diamonds (UDDs), it is necessary to take proper account of the following facts.

(1) The history of the discovery of UDDs is part of the general history of the development of explosive technologies in the synthesis of superhard materials, and this discovery is a natural result of the development of previous studies.

(2) The history of the discovery of UDD synthesis is simultaneously the history of many years of studies of carbon condensation in a detonation wave, the properties and application of UDDs, and the organization of the commercial production of UDDs.

(3) In the history of any discovery, what is important is the priorities. Pioneers always use the experience gained by their predecessors, who are often little known. This should be borne in mind.

The discovery of diamond synthesis under static pressures at the end of the 1950s stimulated studies aimed at determining the application of explosion energy in diamond synthesis. For the first time, diamond was detected in a preserved shock-compressed graphite sample in the USA in 1961 [1].

In 1960–1980, a sort of "diamond club" of research centers was formed in the USSR, where dynamic methods for producing superhard materials were devised. This club incorporated the following institutes:

All-Union Research Institute of Technical Physics (VNIITF, Snezhinsk, Chelyabinsk oblast);

Institute of Chemical Physics, Academy of Sciences of the USSR (IKhF, Chernogolovka, Moscow oblast);

Institute of Hydrodynamics, Siberian Division, Academy of Sciences of the USSR (IG, Novosibirsk);

Institute of Superhard Materials, Academy of Sciences of the UkSSR (ISM, Kiev);

Institute of Problems of Materials Science, Academy of Sciences of the UkSSR (IPM, Kiev); and

Dnepropetrovsk Institute of Mines (DGI, Dnepropetrovsk).

Basic information on the history of the development of dynamic methods for diamond synthesis is given in the table. The history of the discovery of UDD synthesis is unique. UDDs were discovered in the USSR three times over 19 years by scientists from different research centers.

1063-7834/04/4604-0595$26.00 © 2004 MAIK "Nauka/Interperiodica"

From the history of dynamic diamond synthesis

Authors	Year	Subject of research
Yu.N. Ryabinin	1956	Unsuccessful attempts at dynamic synthesis
E.I. Zababakhin (VNIITF)	1960	Substantiation of the possibility of diamond synthesis via shock compression of graphite; beginning of experimental research at the VNIITF
B.J. Alder and R.H. Christian	1961	
M.N. Pavlovskiĭ (VNIIÉF), K.K. Krupnikov (VNIITF), A.N. Dremin, and S.V. Pershin (IKhF)	1963 1968	Obtainment of the shock adiabat for graphite and confirmation of its conversion into diamond
P.J. De Carli and A.C.Jamisson	1961	Diamond synthesis with preservation of shock-compressed graphite in a plane ampoule
K.V. Volkov, V.V. Danilenko, and V.I. Elin (VNIITF)	1962	The same, but in spherical and cylindrical ampoules (diamond yield ~2%)
	1963	Diamond synthesis by compression of graphite + *Me* and carbon black + *Me* mixtures (diamond yield ~20%)
	1963	UDD synthesis from carbon of explosion products (diamond yield 8–12% of the TG40 charge mass)
G.A. Adadurov (IKhF)	1965	Diamond synthesis from graphite
Dupon Co.(USA)	1976	Commercial production of diamond micropowder Mypolex by compressing a graphite–copper mixture with a charge mass of 5 t in cylindrical ampoules
G.I. Savvakin (IPM)	1982	UDD synthesis
A.M. Staver and A.I. Lyamkin (IG)	1982	The same
O.N. Breusov, V.N. Drobyshev, G.A. Adadurov, and A.N. Dremin (IKhF)	1983	Pilot-scale production of diamond micropowders DAG and DAS by explosion of pressed 100-g charges of a graphite or carbon black mixture with hexogen in an explosion chamber
G.V. Sakovich and coworkers (NPO “Altaĭ)	1984	Pilot-industrial production of UDDs
	1985	Application of wear-resistive chromium + UDD composite coating for instruments and accessories, production of antiwear additive with UDDs for motor oils
Collaborators of the VNIITF and FGUP Industrial Complex “Élektrokhimpribor” (Lesnoĭ)	1990	Pilot-scale production of UDDs
V.V. Danilenko and V.I. Padalko (ZAO “ALIT,” Zhitomir)	1992	The same (TG40 charges of a mass of 10 kg, water cooling of DPs in a 100-m^3 chamber)
V.V. Danilenko and I.A. Petrusha (ISM)	1994	Beginning of studies on UDD sintering under static conditions
V.V. Danilenko (ZAO “ALIT”)	1994	Ampoule-free sintering of high-density UDD grains by explosion, obtainment of diamond single crystals
V.V. Danilenko, P.P. Tolochko, B.A. Vyskubenko, and É.É. Lin (ZAO “ALIT,” VNIIÉF)	1986–1992	Experiments on UDD synthesis by explosion of large-mass charges (10–140 kg)

Specialists from the VNIITF, a research institute where nuclear armaments were developed, were the first in the USSR to launch studies on diamond synthesis in 1960. The merit of these studies is due to Academician E.I. Zababakhin, an outstanding scientist who headed the VNIITF (the institute was named after him). Owing to his initiative and support, a group of scientists in gas dynamics, including K.V. Volkov, V.V. Danilenko, and V.I. Elin, carried out the following pioneering works in diamond synthesis in 1960–1965:

(i) for the first time, diamonds were obtained by shock compression of graphite and carbon black in spherical and cylindrical storage ampoules (1962);

(ii) for the first time, compression of a graphite–metallic coolant mixture was used, which made it possible to increase the diamond yield by an order of magnitude (1963);

(iii) for the first time, the superhard wurtzite modification of boron nitride was obtained using explosion (1963); and

(iv) for the first time, detonation synthesis of diamonds from carbon molecules of explosives was discovered and investigated (1963) [2–4].

To simplify the diamond synthesis, the author proposed and implemented (in 1962) ampoule-free synthesis with explosions in the explosion chamber instead of ampoule synthesis. Graphite was placed directly into a cylindrical charge consisting of a trotyl–hexogen mixture TG40; the charge was enveloped in a water jacket to suppress graphitization and reduce the unloading rate of the synthesized diamond.

Even the first experiment with such a setup resulted in a sharp increase in the diamond yield. A control experiment, carried out with a graphite-free charge in July, 1963, confirmed the hypothesis that diamond was synthesized from the carbon contained in the detonation products (DPs).

Simultaneously, a comparison of the phase diagram for carbon and the parameters at the Jouguet point for the detonation of high-density charges of powerful explosives (the values of pressure and temperature obtained in DPs as a result of detonation-induced decomposition of explosive molecules) proved that the free carbon of DPs must condense in the form of diamond (see figure). It can also be seen that, in order to obtain free carbon in DPs, an explosive with a negative oxygen balance should be used. Such explosive compounds simultaneously serve as sources of energy and carbon. As compared to diamond synthesis from graphite, the advantage of condensation of atomic carbon of DPs into diamond is that neither energy nor time expenditures are required for the destruction or rearrangement of the initial crystal lattice of graphite. Thus, the main problem lies not in the formation of UDD but in its storage (i.e., in creating conditions that prevent oxidation and graphitization of the UDDs obtained).

Despite convincing theoretical premises, only the experiment carried out in 1963 proved for the first time

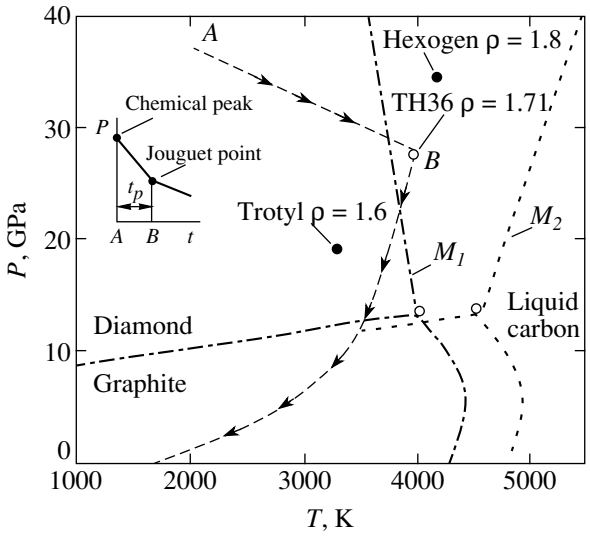

Phase diagram of carbon and the detonation parameters. The inset shows the pressure profile in a detonation wave: *A* corresponds to the shock compression of the explosive (chemical peak), *AB* corresponds to the decomposition of explosive molecules with the formation of DPs and condensation of the free carbon (for an explosive with a negative oxygen balance) to UDDs at pressures higher than 20 GPa, *B* is the termination of the decomposition (the Jouguet point), and t_p is the duration of the decomposition. In the diagram, points *A* and *B* are indicated for the trotyl–hexogen mixture TH36, M_1 and M_2 are possible melting lines of carbon, and ρ is the density (in g/cm^3).

that diamond is indeed formed in a detonation wave and that the obtained substance can be preserved.

In 1963–1965, about 100 successful experiments were carried out to analyze the effect of explosion conditions, as well as the composition and configuration of charges, on the UDD synthesis and the properties of the UDDs produced [2–4]. It was shown that DP cooling as a result of conversion of the potential energy of DPs into kinetic energy of the envelope surrounding the charge plays a decisive role in the UDD synthesis. It was found that an elongated cylinder is the best shape for TG40 charges; the explosion of such a charge in a water jacket gives a UDD yield of 8–12% of the charge mass for a UDD concentration in the batch mixture of up to 75%.

At that time, experiments aimed at developing methods for diamond synthesis were absolutely classified; for security reasons, the results were initially contained only in secret reports from the VNIITF. In 1987, part of those reports were forwarded to the other members of the diamond club.

The UDD synthesis was analogously rediscovered by A.M. Staver, E.A. Petrov, and A.I. Lyamkin under the guidance of Academician V.M. Titov at the Institute of Hydrodynamics, Siberian Division, Academy of Sciences of the USSR (Novosibirsk) [5, 6], and by G.I. Savvakin under the guidance of Academician V.I. Trefilov at the Institute of Problems of Materials

Science, Academy of Sciences of the UkSSR (Kiev) [7], who investigated ampoule-free diamond synthesis through shock compression of graphitized carbon and hydrocarbon materials (but without a water jacket).

In those experiments, the DP cooling required for UDD storage was attained by shock compression of a noble gas in an explosion chamber. The UDD yield was 4–6% for a UDD concentration in the charge of 40–60%.

In the USA, UDD synthesis was reported for the first time only in 1988 [8].

The development of this interesting trend in science and technology was hampered by the following circumstances:

(i) security measures existing in the USSR and extending to any research work on diamond synthesis;

(ii) the decision of the Soviet government regarding the inexpediency of developing simultaneously explosive methods and intense research work aimed at the production of diamonds by catalytic synthesis;

(iii) the discovery of UDD synthesis at the VNIITF, which specialized in fields far removed from diamond production;

(iv) the lack of preparedness in the industry in general in the 1960s to develop nanoscale materials and nanotechnologies.

In 1984, a pilot-scale production of UDDs was organized for the first time at the Research-and-Production Association (NPO) "Altaĭ" headed by Academician G.V. Sakovich; subsequently, a number of new fields of application of UDDs that are not traditional for diamonds were proposed and investigated [4, 9]. It has been proved that small UDD admixtures in various materials noticeably improve the properties of these materials and of coating. In all cases, UDD plays the role of a powerful builder.

The First Interbranch Scientific Conference on UDDs held at the NPO "Altaĭ" in 1986 demonstrated full agreement between the UDD data obtained at the VNIITF in 1963–1964 and at the IG in 1982–1986.

At the end of the 1980s, the technology for UDD purification by using nitric acid alone under pressure was developed at the Special Technical Design Office (SKTB) "Tekhnolog" (St. Petersburg), where a continuous-operation unit was constructed. As a result of the graphitization of UDDs, peculiar bulb-shaped graphite with closed carbon bonds was obtained at the IG in 1993 [10].

Detailed studies of the properties and possible areas of application of UDDs have been carried out at the ISM and IPM (Kiev), NPO "Sinta" (Minsk), ZAO "Almaznyĭ Tsentr" (St. Petersburg), and VNIITF (Snezhinsk). To ensure a preset level of controllable parameters for various UDD powders and suspensions, standard-engineering specifications (TU of Russia, VNIITF, 1994; TU of Ukraine, ISM, 2001) were developed.

In 1988–1998, extensive studies of the regularities of carbon condensation in the form of UDDs during detonation were performed by A.I. Lyamkin, A.M. Staver, V.F. Anisichkin, I.Yu. Mal'kov, E.A. Petrov, A.P. Ershov, and V.M. Titov at the IG [5, 6].

The effect of UDD formation on the detonation parameters was demonstrated in [11–13].

In 1986–1988, the present author investigated UDD synthesis for the first time through the explosion of heavy charges (with a mass of up to 20 kg) of various explosives in large explosion chambers with a view to organize large-scale production of inexpensive, high-quality UDDs, which is essential for UDD application on the industrial scale. It was shown that an increase in the mass of TG40 charges does not change the UDD yield but UDD grains become coarser (the specific surface of UDD grains is reduced by half) and macroscopic lonsdaleite crystals form [4]. In 1991, a unique experiment on UDD synthesis by exploding a TG40 charge with a mass of 140 kg in a water jacket was carried out in a chamber 300 m^3 in volume [14].

In 1992, the present author developed a technology for producing UDDs and implemented it at the commercial plant of the "ALIT" company (Zhitomir). The main part of the plant was an explosion chamber 100 m^3 in volume (designed by the present author [15]) with water cooling of the UDDs.

In 1994, successful experiments on obtaining diamond single crystals by sintering high-density UDD grains were carried out in this chamber [4].

Even now, the UDD-manufacturing facilities created in the USSR considerably exceed the current demand in UDDs. In view of the absence of large-scale application of UDDs in industry, the laboratory and plant at the VNIITF and at the Krasnoyarsk Technical University were closed and production at the NPO "Altaĭ" and at the industrial complex "*Élektrokhimpribor*" was suspended.

At the beginning of the current century, the interest in UDDs, which combine high values of dispersity, chemical resistance, and adsorption activity, has increased in connection with the intense development of nanotechnologies round the world.

Detailed information on the synthesis, properties, and applications of UDDs can be found in [4, 9, 16, 17].

REFERENCES

1. P. J. De Carli and A. C. Jamisson, Science **113**, 3467 (1961).
2. K. V. Volkov, V. V. Danilenko, V. I. Elin, *et al.*, *Explosion, Shock, Protection* (Inst. Geofiz. Sib. Otd. Akad. Nauk SSSR, Novosibirsk, 1987), Inf. Byull., No. 17.
3. K. V. Volkov, V. V. Danilenko, and V. I. Elin, Fiz. Goreniya Vzryva, No. 3, 123 (1990).
4. V. V. Danilenko, *Synthesis and Sintering of Diamonds by Explosion* (Énergoatomizdat, Moscow, 2003).

5. A. M. Staver and A. I. Lyamkin, in *Ultradisperse Materials. Production and Properties* (Krasnoyarsk, 1990), p. 3.
6. V. M. Titov, V. F. Anisichkin, and I. Yu. Mal'kov, Fiz. Goreniya Vzryva, No. 3, 117 (1989).
7. V. F. Petrunin, V. A. Pogonin, G. I. Savvakin, and V. I. Trefilov, Poroshk. Metall. (Kiev), No. 2, 20 (1984).
8. N. Roy Greiner, P. S. Philips, and J. D. Johnson, Nature **333**, 6172 (1988).
9. G. V. Sakovich, V. F. Komarov, E. A. Petrov, *et al.*, in *Proceedings of V All-Union Workshop on Detonation* (Krasnoyarsk, 1991), Vol. 2, p. 272.
10. I. Yu. Mal'kov, V. M. Titov, V. D. Kuznetsov, and A. L. Chuvilin, Fiz. Goreniya Vzryva, No. 1, 130 (1994); Chem. Phys. Lett. **222**, 343 (1994).
11. L. N. Akimova, S. A. Gubin, V. D. Odintsov, and V. I. Pepekin, in *Proceedings of V All-Union Workshop on Detonation* (Krasnoyarsk, 1991), Vol. 1, p. 14.
12. C. L. Mader, *Numerical Modeling of Explosives and Propellants*, 2nd ed. (CRC, Boca Raton, FL, 1998).
13. S. V. Pershin and D. N. Tsaplin, in *Proceedings of V All-Union Workshop on Detonation* (Krasnoyarsk, 1991), Vol. 2, p. 237.
14. B. A. Vyskubenko, V. V. Danilenko, É. É. Lin, *et al.*, Fiz. Goreniya Vzryva, No. 2, 108 (1992).
15. V. V. Danilenko, V. I. Trefilov, and V. N. Danilenko, USSR Patent No. SU 181,329 AZ (May 12, 1991).
16. V. Yu. Dolmatov, Usp. Khim. **70** (7), 607 (2001).
17. *Proceedings of Scientific Seminar on Nanoscale Diamonds* (Kiev, 2002); Sverkhtverd. Mater., No. 6 (2002).

Translated by N. Wadhwa

Physics of the Solid State, Vol. 46, No. 4, 2004, pp. 600–605. Translated from Fizika Tverdogo Tela, Vol. 46, No. 4, 2004, pp. 585–590.

METHODS OF FABRICATION AND PROCESSING OF DETONATION NANODIAMONDS

Detonation Diamonds in Ukraine

N. V. Novikov, G. P. Bogatyreva, and M. N. Voloshin

Bakul Institute for Superhard Materials, National Academy of Sciences of Ukraine, Avtozavodskaya ul. 2, Kiev, 04074 Ukraine

e-mail: bogatyreva@ism.kiev.ua

Abstract—Some information on the history of dynamic synthesis of diamond in Ukraine is considered. Basic characteristics of ASM5 0.1/0 and ASM1 0.1/0 nanodiamond powders produced by static synthesis are described. The characteristics and surface properties of nanodiamond powders produced by detonation synthesis in Ukraine are presented. It is shown that the chemical activity of the particle surface can be controlled. Applications of nanopowders produced by detonation synthesis in various technologies are considered. © *2004 MAIK "Nauka/Interperiodica".*

1. DIAMOND NANOPOWDERS PRODUCED BY STATIC SYNTHESIS

Diamond nanopowders (with grains smaller than 100 nm in size) have been produced by static synthesis, studied, and applied in the Institute for Superhard Materials (ISHM) for more than three decades.

Diamond nanopowders produced from static-synthesis diamond are classified as submicropowders (with grains smaller than 1 μm in size) with a narrow range of grain size. They are produced in Ukraine according to the DSTU 3992-95 state standard as nanopowders of grades ASM5 0.1/0 and ASM1 0.1/0. This standard allows up to 5% of particles 0.3–0.1 μm in size in the ASM5 0.1/0 powder composition; the remaining particles should be 0.1 μm in size and finer. ASM1 0.1/0 powders can contain no more than 1% coarse fraction (0.3–0.1 μm), and the major fraction (0.1 μm and finer) is 99%. The grain composition of powders is measured using a transmission electron microscope. Submicropowders in the as-delivered condition are also regulated in moisture content (less than 1%) and impurity mass fraction (less than 2%). This is the cubic-structure diamond containing no graphite, which is fully removed by chemical cleaning. The specific surface of nanometer powders is 40–45 $m^2 g^{-1}$ (as determined from nitrogen adsorption); 60 and 40% of the particle surface are associated with hydrophilic and hydrophobic centers, respectively [1].

Figure 1 shows electron-microscopic images of an ASM5 0.1/0 powder containing ~20% of the 100-nm fraction; the other particles are finer. Submicropowders, as well as most of the available grades of micropowders, are produced by crushing of larger diamond particles, which has an effect on the particle shape. This powder mostly contains thin (≤50-nm-thick) platelike particles with polyhedral facets and smooth or rough surfaces. There are aggregates of platelike particles (2–3 particles) contacting by edge surfaces and aggregates of platelike particles layered against each other, as well as flaky structures, such as strongly deformed films 10–30 nm in size.

The technology of submicropowders is very laborious and requires certain clean conditions. Such powders, in particular, the finest ones, aggregate into strong

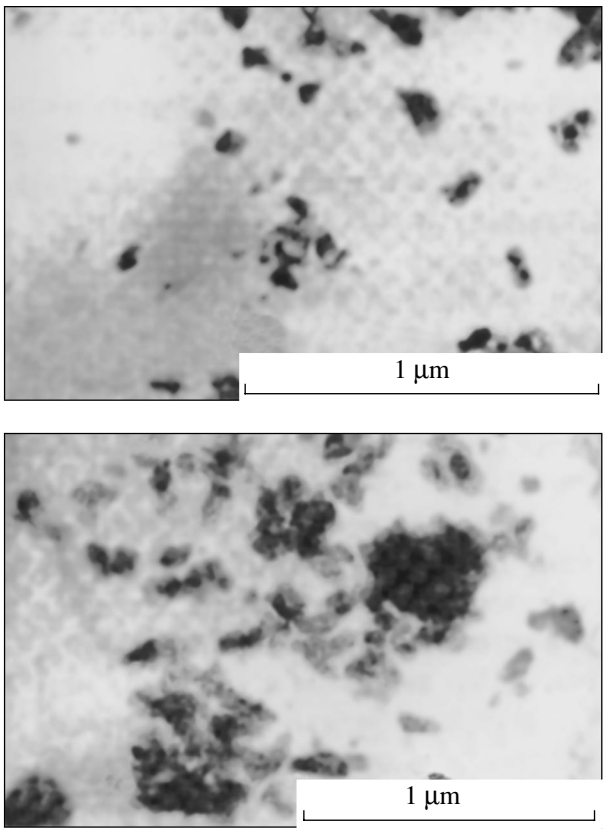

Fig. 1. ASM5 0.1/0 powder synthesized under static conditions.

1063-7834/04/4604-0600$26.00 © 2004 MAIK "Nauka/Interperiodica"

structures upon drying and require additional preparation of a dry product when producing pastes. For this reason, it is a better practice to keep them as suspensions.

Powders of granularity 0.1/0 in the form of pastes with a diamond concentration of 2, 5, and 10 wt % are most efficient in superfine lapping and polishing of semiconductor objects. This is the main field of application of such powders.

2. DYNAMIC SYNTHESIS OF DIAMOND

Diamonds have been synthesized using detonation energy since 1961, when the first reports on initiating the direct graphite–diamond phase transition were made by the Du Pont Company (USA). In the following years, various methods and schemes of the dynamic impact on pure carbon and carbon-containing mixtures were developed and tested in many countries. Ukrainian scientists also developed unique methods and equipment for such synthesis. The ISHM, Frantsevich Institute of Materials Science Problems (IMSP), Dnepropetrovsk Mining Academy, and other institutions carried out experimental and theoretical studies of the dynamic synthesis of diamond in metal–graphite (carbon black) compositions using plane and cylindrical loading. As reagents, both cast iron and Fe–C, Ni–C, and Cu–C pressed mixtures were used. Experimental studies in the ISHM were performed using cylindrical loading of reaction mixtures in large-scale cells in collaboration with a research group from the Lavrent'ev Institute of Hydrodynamics (Novosibirsk) headed by A.A. Deribas and S.M. Staver.

The first diamonds were synthesized in the ISHM using plane loading of cast iron by a research group headed by Andreev in 1975 [2]. By initiating the direct graphite–diamond phase transition, flaky structures were obtained that reproduced the particle shape of the initial graphite used and a 100-μm powder was produced. Figure 2 shows particles of this diamond, whose crystal structure represents the cubic and hexagonal (lonsdaleite) carbon modifications. The lonsdaleite content in fine-grained diamond fractions reached 50%. Electron microscopy and selected-area diffraction studies of powders detected individual lonsdaleite particles [3]. These diamonds attracted particular interest due to both their specific structure and morphology. Diamond particles produced by dynamic synthesis were characterized by a significantly developed surface, which opened up new opportunities for their application [4]. Despite the mostly flat shape of the particles, these powders could be classified, which made it possible to carry out comparative tests with powders of static synthesis and to specify their fields of application. The new powders were especially efficient as components of synthetic-fiber raising tools (texturing disks), as well as in ARS3 polycrystals. However, this synthesis method has not found commercial application because of the laborious and expensive operation of chemical dissolution of metal components of reaction mixtures and high cost of disposable metal tooling (retaining devices), as well as due to increased prices of explosive materials.

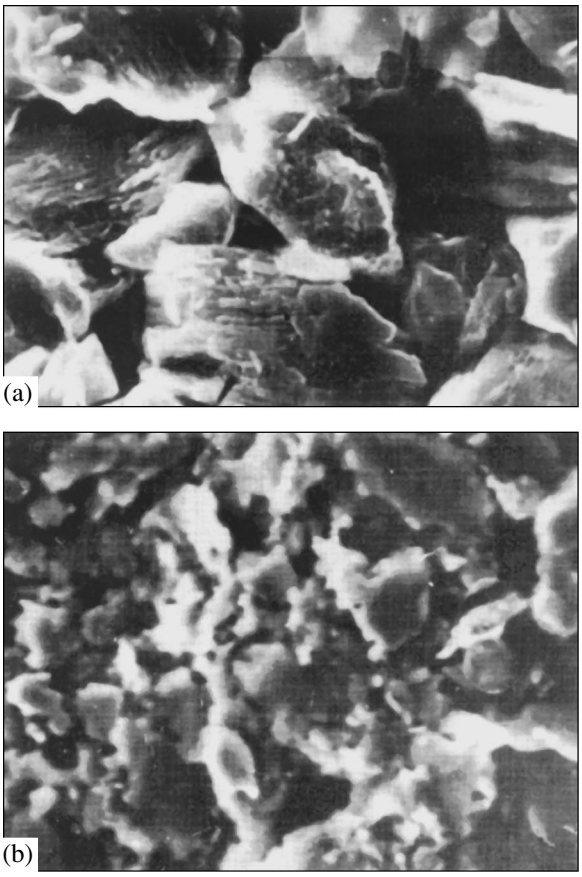

Fig. 2. Diamond powders of grades (a) AV 7/5 and (b) AV 2/1 produced by shock-wave loading of cast iron.

Simultaneously with the studies of the shock-wave synthesis in metal–carbon powder systems, G.I. Savvakin (IMSP) studied diamond synthesis using explosive detonation with a negative oxygen balance, as well as with admixtures of carbon materials (graphite and carbon black). Results of successful experiments have been published since 1978 [5, 6].

Under high-temperature compression for over 5×10^{-6} s, transformations of noncrystalline carbon (lamp black and detonation carbon black) were observed and diamonds with average sizes of 10–20 nm were produced.

Diamond synthesis under detonation of explosives with a negative oxygen balance, carried out by K.V. Volkov, V.V. Danilenko, and V.I. Elin in Chelyabinsk in the early 1960s [7], was commonly accepted as a priority area of study in the former USSR. Later, V.V. Danilenko continued his studies in Ukraine (IMSP); in 1991, he established the ALIT Company in Zhitomir. The ALIT has a blast chamber with a volume of 100 m^3 and is the largest manufacturer of nanodia-

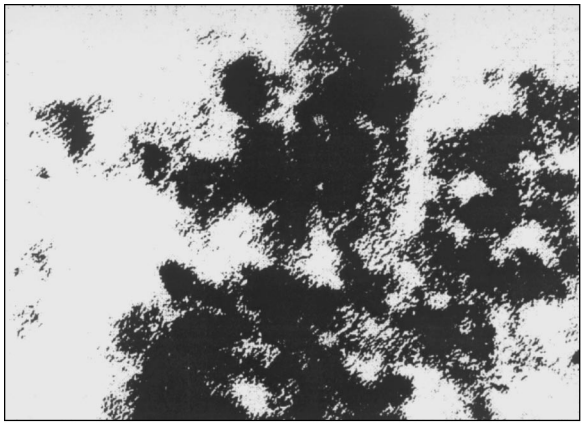

Fig. 3. Nanodiamond powder synthesized under detonation conditions (400000 ×).

monds. The ISHM develops technologies for the chemical cleaning and production of nanodiamond powders.

3. STUDIES OF THE CHARACTERISTICS AND PROPERTIES OF DIAMOND NANOPOWDERS SYNTHESIZED UNDER DETONATION CONDITIONS

Currently, ASUDO- and ASUDCh-grade diamond nanopowders of detonation synthesis that differ in purity are produced according to the TU 28.5-05417377-094-2003 specification, and diamond–graphite mixtures containing 35–60 wt % diamond phase are produced according to the TU U 88.090.053-01specification.

Diamond produced under detonation conditions following the ALIT technology is a single-phase material with a cubic crystal lattice with parameter $a = 0.357$ nm. According to x-ray diffraction data, coherent-scattering regions (subgrains) are 4 nm in size. The Raman spectrum of diamond contains a weak broad asymmetric peak at 1325.4–1325.8 cm^{-1} with a halfwidth of ~30 cm^{-1}. A comparison of this spectrum with the standard spectrum shows a line shift of 6 cm^{-1} to lower wave numbers, which can be explained by tensile stresses [8].

Powders in the as-delivered condition consist of agglomerates 0.5–50 μm in size, composed (according to data from electron microscopy) mostly of spherical particles 15–20 nm in size (Fig. 3).

The powder specific surface measured using the low-temperature adsorption method is ~200 $m^2\ g^{-1}$, and the pycnometric density is 3.3 $g\ cm^{-3}$. The heuristic relation $d = 6/\rho S_{spec}$ between the specific surface S_{spec}, density ρ, and average particle size d yields the average size of diamond particles to be ~8 nm. Thus, the comparison of various methods shows that individual particles of detonation diamond are polycrystals.

The x-ray diffraction and coordination-shell diffractometry methods showed that the average size of coherent-scattering regions of nanodiamond is 4.2 ± 2 nm [9]. These regions contain an insignificant number of dispersed carbon atoms that do not enter the diamond lattice. Those studies confirmed the polycrystalline structure of the particles and demonstrated that the shape of the interatomic-distance distribution in grain boundaries is close to Gaussian, which suggests that grain boundaries are amorphous.

Electron spin resonance studies of diamond samples of various origin [10] showed that the effect of the surface on the properties of diamond particles increases as their size decreases.

The long-term studies performed at the ISHM have shown that the most significant features of nanodiamond produced by detonation synthesis are associated with its surface properties.

Currently, it is known that nanodiamond particles are characterized by a supermolecular structure of variable activity depending on the nature and number of adsorbed functional groups.

Infrared spectroscopy of nanodiamonds shows that an increased content (in comparison with that in micropowders of static synthesis) of moisture in the form of bound –OH groups and free water molecules, as well as the presence of carbonyl and carboxyl groups, is observed on the particle surface in as-delivered powders. The content of $–CH_2$ and $–CH_3$ groups in powders is insignificant [11]. Auger spectroscopy showed that the initial powders contain 0.5% nitrogen and 5.4% or 6.0% oxygen (in ultrafine-dispersed diamonds UDD_1 and UDD_2, respectively) and that the balance is carbon. As for the incombustible residue (whose quantity is less than 2%), the predominant impurities are chromates, Ca and Al sulfates, and complex compounds with silicon. It should be noted that the composition of the particle surface somewhat changes even under the standard conditions and can be significantly affected by thermal or physicochemical treatment. For example [11], thermal treatment of powders in argon results in substantial loss of OH groups (Fig. 4a), which is confirmed by the change in IR absorption near 1640 cm^{-1} and the rupture of hydrogen bonds. The latter is illustrated by the change in the shape of the spectral curve near 3580 cm^{-1} (Fig. 4b).

The electrophoretic charge of the particle surface (ξ potential) is negative and exceeds that of static-synthesis powders by an order of magnitude, which is obviously caused by an increase in the content of ionogenic oxygen-containing groups.

Diamond nanopowders feature a significant hydrophily, which can be characterized by the water-vapor saturation free energy ΔG_s per unit powder mass

$$\Delta G_s = RTn \log P/P_s \ [\text{mJ/mol g}],$$

where R is the gas constant, T is the temperature, n is the quantity of water (in moles), and P and P_s are the partial pressure and the saturated vapor pressure of water, respectively. We estimated the nanopowder hydrophily degree as approximately –3000 mJ $mol^{-1}\ g^{-1}$,

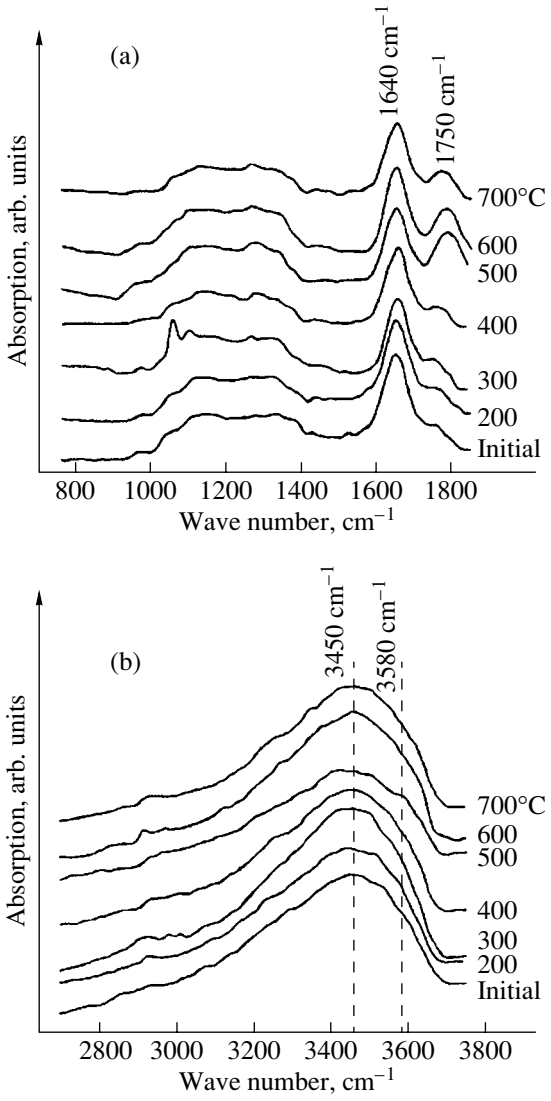

Fig. 4. Infrared absorption spectra of nanodiamond samples after thermal treatment.

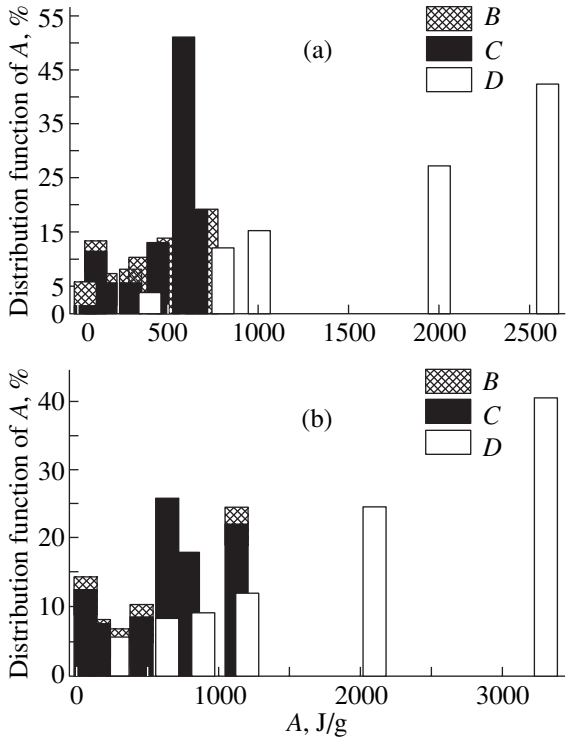

Fig. 5. Distribution functions of the adsorption potential of powders of grades (a) UDD_1 and (b) UDD_2 for (*B*) the initial powders and powders after thermal treatment at (*C*) 200 and (*D*) 700°C.

which is two times larger in magnitude than that for diamonds produced by static synthesis.

Among currently known types of diamond, detonation-synthesis powders are distinguished by an extremely large number of uncompensated surface bonds and by high adsorption activity due to small particle sizes and the specific features of the powder production. By using the Brunauer–Emmet–Teller method of low-temperature nitrogen adsorption at a temperature of 200°C and a pressure of 1×10^{-4} Torr, we determined the adsorption potential of nanodiamond powders from adsorption isotherms; this potential takes into account both the activity of surface centers and their quantity.

The studies carried out by us have shown that the chemical activity of the diamond particle surface causing ion-exchange processes of adsorption and desorption can be varied without changing the inherent chemical inertness of diamond. It was established that the adsorption potential of nanoparticles depends on the chemical cleaning method applied and can be significantly increased using thermal treatment or modification (see table, Fig. 5). Figure 5 shows the distribution function of the adsorption potential for two grades of powder (differing in the initial surface characteristics) after thermal treatment in argon at 200 and 700°C. The thermal treatment is seen to affect the particle surface activity significantly; the activity increases by a factor of 3.5–4 after treatment at 700°C.

The studies have shown that this material is unique, but its production poses severe problems, because it is difficult to produce powders with strictly preset surface properties and to preserve them.

4. APPLICATION OF DIAMOND NANOPOWDERS SYNTHESIZED UNDER DETONATION CONDITIONS

The unique surface properties of nanopowders determine their application in electrochemical and chemical coatings, pastes, and suspensions; as additives in polymeric, ceramic, and industrial rubber goods and glues; as adsorbents and catalysts, in filters and membranes; etc.

Control of the chemical activity of the diamond particle surface

Treatment of powders	Powder grade	Adsorption potential (for nitrogen adsorption) A, J g^{-1}
Chemical cleaning:		
treatment with a solution of NaOH and KOH	UDD_1	419
sintering with a mixture of NaOH and KOH	UDD_2	595
Thermal treatment in argon		
at 200°C	UDD_1	498
	UDD_2	634
at 700°C	UDD_1	1892
	UDD_2	2143
Modification by boric anhydride	Initial	506
	UDD-20V	902

In the ISHM, nanodiamond powders of detonation synthesis are applied in technologies of hard electrochemical composite coatings of diamond tools. In particular, a nanodiamond additive changes the structure of nickel coatings with the formation of nickel dendrites radiating outward from dispersed particles and increases the microhardness of coatings by a factor of 1.9 and their wear resistance by 3–4 times. Such composite coatings significantly improve the quality of galvanic tools with various types of dimension and functions (grinding wheels, core drills, faceplates, etc.) and harden the work surfaces of flying grippers for printing machines, sleeves of internal-combustion engines, etc.

Techniques have been developed for metallizing static-synthesis diamond powders by composite chemical coatings with nanodiamond additives and for metallizing nanodiamond itself by nickel to produce diamond-containing cells 0.35–1.8 μm in size [12, 13]. The application of composites based on metallized nanodiamond to produce faceting disks for processing jewels at the Izumrud State Company increased the wear resistance, elasticity, rollability, and cutting ability of the disks by a factor of 1.5–1.8.

Studies of the catalytic and adsorption properties of nanodiamond have shown that adsorption centers on the particle surface are simultaneously catalytic centers. It was shown that electrochemical treatment of the particle surface makes it possible to saturate it with atomic oxygen, thereby significantly enhancing catalytic oxidation of carbon monoxide into dioxide [14]. Since nanodiamonds have proved to be promising catalysts of oxygen electrodes in fuel cells [15], those studies were further developed.

Techniques are being developed for sintering nanopowders and for applying them as structuring additives in the production of dense polycrystals from static-synthesis diamonds [16].

One of the most interesting results is the technology of polycrystalline micropowders whose porous particles have different nanostructures [17]. Such powders are produced by crushing diamond nanopowder sinters obtained under static conditions in the region of stability of the diamond phase. The minimum pore size in powder particles, estimated from the characteristics of nitrogen adsorption, is 1.2 nm. In particles of a powder of granularity 1/0, pores range in size from 1.2 to 2.5 nm. As the granularity increases, the largest pore size increases to ~10 nm [18]. The important advantages of polycrystalline powders are their large specific surface area (~140 $m^2 g^{-1}$), which is close to that of the initial nanopowder (~170 $m^2 g^{-1}$), and their high adsorption activity (above 250 J g^{-1}). These characteristics make it possible to use polycrystalline powders as adsorbents and catalysts; therefore, the search for their most efficient fields of application is carried out in this direction. As for the polishing ability of powders, they can be used for the processing of both hard and soft materials. Unconventional fields of application of nanopowders and polycrystalline micropowders produced from them are also being searched for.

5. CONCLUSIONS

(I) The output of nanodiamond powders synthesized under detonation conditions in Ukraine is ~100 kg per month.

(II) Technologies of nanodiamond powders with controlled properties have been developed. Problems are experienced in connection with (a) instrumental estimation of the powder quality under production conditions and (b) conservation of the achieved surface properties over a long period of time.

(III) In view of the significantly increased interest in nanotechnology and the availability of a large variety of nanopowders of different nature, the following promising nanodiamond applications can be given.

(i) Development of hardening and structurization technologies for various materials, including coatings. The problems arising in this case are associated with (a) the introduction of nanoparticles in a dispersed form into a material and (b) the achievement of a uniform distribution of particles in a material.

(ii) Applications of nanodiamonds as sorbents, catalysts, and fuel cells of current sources. In this case, the regeneration of objects presents technological difficulties.

(iii) Production of diamond and composite polycrystals with a nanostructure intended for use in construction and as tools and for producing powders, including porous ones. Problems are associated with the presence of functional groups on the diamond particle surface and with the necessity of removing them to produce dense sinters.

REFERENCES

1. Yu. I. Nikitin, S. M. Uman, L. V. Kobernichenko, and L. M. Martynova, *Powders and Pastes Based on Synthetic Diamonds* (Naukova Dumka, Kiev, 1992).
2. V. N. Bakul' and V. D. Andreev, *Synthetic Diamonds* (Naukova Dumka, Kiev, 1975), No. 5, p. 3.
3. V. D. Andreev, M. N. Voloshin, V. A. Lukash, *et al.*, Sverkhtverd. Mater., No. 5, 25 (1984).
4. V. D. Andreev, A. S. Vishnevskiĭ, M. N. Voloshin, *et al.*, Sverkhtverd. Mater., No. 3, 8 (1980).
5. V. I. Trefilov, G. I. Savvakin, V. V. Skorokhod, *et al.*, Dokl. Akad. Nauk SSSR **239** (4), 838 (1978) [Sov. Phys. Dokl. **23**, 269 (1978)].
6. V. I. Trefilov, G. I. Savvakin, V. V. Skorokhod, *et al.*, Poroshk. Metall. (Kiev), No. 1, 32 (1979).
7. K. V. Volkov, V. V. Danilenko, and V. I. Elin, Fiz. Goreniya Vzryva **26** (3), 123 (1990).
8. V. I. Padalko, G. P. Bogatyreva, and M. N. Voloshin, Instrum. Svit, Nos. 4–5, 39 (1999).
9. V. D. Andreev and Yu. I. Sozin, Fiz. Tverd. Tela (St. Petersburg) **41** (10), 1890 (1999) [Phys. Solid State **41**, 1736 (1999)].
10. V. M. Maevskiĭ, E. V. Mozdor, and V. I. Padalko, Sverkhtverd. Mater., No. 6, 43 (2002).
11. G. P. Bogatyreva, M. N. Voloshin, V. G. Malogolovets, *et al.*, J. Optoelectron. Adv. Mater. **2** (5), 469 (2000).
12. T. M. Duda, Yu. I. Nikitin, V. G. Poltoratskiĭ, *et al.*, Sverkhtverd. Mater., No. 5, 88 (2002).
13. T. M. Duda, Instrum. Svit, No. 1 (13), 16 (2002).
14. G. P. Bogatyreva, M. A. Marinich, V. L. Ishchenko, *et al.*, Sverkhtverd. Mater., No. 6, 11 (2002).
15. G. V. Zhutaeva, M. A. Marinich, G. P. Bogatyreva, *et al.*, Sverkhtverd. Mater., No. 6, 55 (2002).
16. A. A. Shul'zhenko, V. G. Gargin, A. A. Bochechka, *et al.*, Sverkhtverd. Mater., No. 3, 3 (2000).
17. K. V. Kirilin and V. V. Padalko, WO 02/078871 A2 IPK[7] BO1J 3/00 (21 July 2000).
18. N. V. Novikov, G. P. Bogatyreva, M. N. Voloshin, *et al.*, Sverkhtverd. Mater., No. 6, 4 (2002).

Translated by A. Kazantsev

Physics of the Solid State, Vol. 46, No. 4, 2004, pp. 606–610. Translated from Fizika Tverdogo Tela, Vol. 46, No. 4, 2004, pp. 591–595.

METHODS OF FABRICATION AND PROCESSING OF DETONATION NANODIAMONDS

The State of the Art and Prospects of Detonation-Synthesis Nanodiamond Applications in Belarus

P. A. Vityaz

National Academy of Sciences of Belarus, Minsk, Belarus

e-mail: vitiaz@presidium.bas-net.by

Abstract—Technological features of the commercial production of detonation-synthesis nanodiamonds at the SINTA Joint-Stock Company and the characteristics of the nanodiamonds and diamond-containing mixtures produced are considered. Nanodiamond applications in the production of composite electrolytic coatings that are based on chromium, nickel, gold, and silver, exhibit good service properties, and save on the use of noble metals and electric power are exemplified. Nanodiamond applications for the modification of plastics, antifriction lubricants, and oxide coatings grown by microarc oxidation of aluminum alloys are also considered. The prospective application of nanodiamonds as a raw material in the synthesis of diamond powders and superhard composites by static and shock-wave loading is demonstrated. © *2004 MAIK "Nauka/Interperiodica"*.

1. INTRODUCTION

We consider the state of the art and prospects of application of detonation-synthesis nanodiamonds in Belarus. The commercial production of detonation-synthesis nanodiamonds in Belarus developed thanks to the developed infrastructure and highly skilled specialists in the country in the field of experimental-industrial production of composite materials and wares using high explosives. This industry was organized in the Sinta Joint-Stock Company in 1993–1996 within the "Diamonds" state scientific and technical program and supported by leading Russian scientists and specialists in the field. The nanodiamond production capacity of the Sinta Company is 10^7 carats per year.

2. COMMERCIAL PRODUCTION OF NANODIAMONDS

In the process of establishing and developing nanodiamond production, the main problems encountered were the application of explosives and "melanzh" rocket oxidizer for the synthesis and chemical purification of detonation products, the development of nonpolluting closed methods of separating nanoparticles from liquid reactive media and the synthesis technology, etc. Specialists from the Institute of Pulsed Technological Processes, the Institute of Powder Metallurgy, "Akademicheskoe" Central Design Office (Sosny), and others were brought in to solve these problems. A unique industrial system successfully designed on the basis of the Sinta Company (Fig. 1) is currently in operation, which employs original engineering solutions and produces high-quality products. National standards on diamond powders have been developed, and the products have been state certified. The products are delivered to more than thirty Belarus enterprises and are exported to Russia, Ukraine, Taiwan, India, Germany, the USA, the Czech Republic, the Republic of Korea, and other countries. It should be noted that the technological aspects of nanodiamond production are of particular interest to Belarus, in particular, for practical recycling of certain types of ammunition and the "melanzh" liquid rocket oxidizer. Synthesis methods using "supernumerary" explosives produced in ammunition recycling were developed in the Sinta Company in collaboration with the Institute of Pulsed Processes. The urgent problem of recycling melanzh rocket oxidizer was solved with the help of the "Akademicheskoe" Central Design Office. This made it possible to reduce the cost of nanodiamond, to enhance

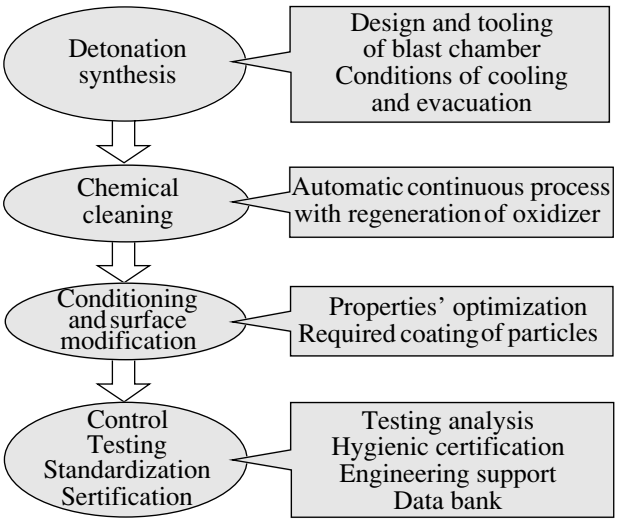

Fig. 1. Functional diagram of the automated technological system of the SINTA Company.

1063-7834/04/4604-0606$26.00 © 2004 MAIK "Nauka/Interperiodica"

Table 1. Characteristics of diamond mixtures from the SINTA Company (standardized according to the TU RB 28619110.003-03 specification)

Grade	Specifications						Destination
	total carbon quantity, no less than, wt %	diamond carbon, wt %	oxidized carbon, no more than, wt %	ash content, wt %	dry-powder moisture, %	pH of aqueous suspensions and pastes	
ASh-A	87	32–55	55	3	2	7.5–9	Production of antifriction lubricant and polymer–diamond composites and modified ultrafine-dispersed diamonds (UDDs)
ASh-B	85	30–75	55	7	5	7.5–9	Production of basic-grade and modified UDDs and polymer–diamond composites
ASh-V	80	25–75	55	10	2–5	8–10	Production of basic-grade UDDs

acid recycling in chemical cleaning, and to improve product quality.

A distinctive feature of the technology implemented in the Sinta Company is dry detonation synthesis, in which explosive charge detonation and collection and evacuation of detonation products are carried out without using water or other liquid media. This technology provides an optimum functional coating of the surface of nanodiamonds, which promotes their efficient use in lubricant and polymer composites.

Variations of the detonation conditions in the available blast chambers, with a volume of 100 and 20 m^3, and of the temperature and velocity parameters of detonation product evacuation makes it possible to produce three types of diamond-containing mixtures; the parameters of these mixtures are listed in Table 1.

The production of nanodiamonds has been developed simultaneously with the study of their structure, properties, and potential fields of commercial application in collaboration with scientific and education centers and a number of industrial enterprises. Methods were developed for intentionally changing the properties of the functional coating of nanodiamonds and for their doping with various elements in the form of adsorbates, mobile ions, metal-oxide and other surface structures. These methods significantly extend the range of properties and structural characteristics of nanodiamonds. The main characteristics of modified nanodiamond powders are listed in Table 2.

3. COMPOSITE ELECTROLYTIC COATINGS (CECs)

It is known that the use of nanodiamonds in galvanic coatings makes it possible to grow composite layers with optimum diamond contents, ≤1 wt %. The distinctive features of such coatings are an increased microhardness, the absence of microporosity (and, hence, pitting corrosion), increased wear resistance, and a decreased coefficient of friction. The most significant results have been achieved for medical, processing, and measuring tools and for pressing tooling with nickel–diamond coatings. In these cases, the tool lifetime was increased by a factor of 1.5–2.0 [1, 2].

Since gold and silver coatings are the most attractive commercially, the influence of nanodiamonds on the coating mechanism and on the properties of such coatings has been studied in detail.

These studies were coordinated by the Belarussian State University of Informatics and Radioelectronics. A series of studies carried out in 1997–2003 showed that the deposition of CECs with nanodiamonds offers the following advantages.

(i) An increase in the reaction rate on electrodes, above all, in the coating deposition rate, which can be

Table 2. Characteristics of modified nanodiamond powders from the SINTA Company (powders are standardized according to the TU RB 28619110.001-95 and TU RB 28619110.003-03 specifications)

Characteristic	
Diamond phase content, wt %	40–99
Total carbon content, wt %	65–95
Content of non-carbon (ash) components, wt %	0.1–10
Specific surface,* $m^2\ g^{-1}$	130–470
Adsorption capacity (for electrolyte ions), mg-equiv g^{-1}	0.1–3.5 0.5–25
Electrokinetic potential, mV	From –100 to +100
Thermal stability in air, K	423–1573
Resistivity, $\Omega\ cm^{-1}$	10^2–10^{14}

* The specific surface is determined using the Brunauer–Emmet–Teller method.

explained by the activation influence of nanoparticles on the electrode surface.

(ii) The diffusion layer thickness and concentration polarization decrease and the physical–mechanical properties are improved because of a decrease in the hydrogen content and an increase in the internal stresses, which changes the coating composition and structure.

(iii) The relative wear resistance of coatings increases with the nanodiamond content, which, in turn, depends on the cathode current density.

The features of the formation of CECs based on noble metals and nanodiamonds were ascertained, which made it possible to relate the kinetic conditions of deposition and the parameters of periodic currents with the coating structure and properties. This, in turn, allows one to optimize the deposition conditions and develop a coating technology with an increased wear resistance and a low and stable electrical contact resistance. In particular, in the case of deposition of CECs based on silver and nanodiamonds, the particle content in the matrix increases from 0.1 to 0.6 wt % as the current density increases from 1 to 3 A dm^{-2}. In this case, the introduction of nanodiamonds into an electrolyte changes not only the electrolysis parameters (viscosity, conductivity, pH, electrode polarization) but also the crystallization mechanism itself. Nanoparticles dispersed in an electrolyte and contacting with electrodes have a depolarizing effect, eliminate hydrogen bubbles and surfactant films from the cathode, make the surface smooth, and steadily refresh the electrolyte in the cathode region. As a result, the degree of texturization and the average size of coating grains decrease, while the internal stresses, microhardness, and wear resistance increase. In this case, the use of periodic currents and programmed electrolysis conditions makes it possible to optimize the deposition rate and physical–mechanical properties and to obtain a microhardness of 1500–1680 MPa, a contact resistance of 1.43–1.48 $\mu\Omega\ m^{-1}$, and an increased wear resistance, by a factor of 2.6–3.2. The deposition rate was increased by a factor of 2.5–5, and the coating thickness was diminished by 2–3 times without deterioration in the electrophysical and protective properties.

As a result of the studies carried out, three modifications of the "Kompozit" automated system were developed for the deposition of gold- and silver-based CECs using unsteady electrolysis methods. Implementation of the technology and equipment for producing contacts with nanodiamonds using these methods in the "Integral" Scientific Production Association made it possible to significantly save on the use of electric power and noble metals and reduce the coating cost by 15–20%. The equipment and technology were sold to the Chinese People's Republic and are successfully employed for the production of contacts with gold and silver galvanic coatings.

The studies carried out at the Institute of Powder Metallurgy (National Academy of Sciences of Belarus, NASB) have shown that chromium–nanodiamond coatings grown by ion-plasma sputtering of a Cr + 5 wt % nanodiamond composite target are characterized by a subgrain size of 30–70 nm and that nanodiamond particles form a network over the subgrain boundaries [3].

A series of studies carried out at the Institute of Mechanics and Reliability of Machines (NASB) showed that modification with nanodiamonds during microarc oxidation of AK5M2 aluminum alloys significantly increases the coating–substrate bond strength, decreases the inhomogeneity of coating, and doubles the rate of its formation. In the case of microoxidation, the predominant phase of the oxide layer is high-temperature α-Al_2O_3 and the microhardness and wear resistance of the oxide layers increase by a factor of 1.5–2.0 due to the introduction of nanodiamond [4]. This method makes it possible to solve the known problem of growth of dense oxide coatings strongly bound to a substrate for aluminum–silicon alloys.

4. ANTIFRICTION LUBRICANTS

Nanodiamonds synthesized under highly nonequilibrium conditions have no distinct crystalline faceting; their round shape and high affinity for a carbon base of oils and lubricants, strengthened by surface modification, provides their efficient application as constituents of liquid, consistent, and solid lubricants. The introduction of isometric nanodiamond particles and graphite–diamond conglomerates up to 10 nm in size into lubricants makes it possible to change the mechanism of the contact interactions of a friction pair, to increase the surface layer microhardness, and to prevent metal–metal contact at the friction surface. The self-accommodation time is significantly shortened, after which the wear intensity sharply decreases (by a factor of 2–4). The friction surface takes on a characteristic high luster caused by an appreciable decrease in roughness, and the friction coefficient decreases by 15–20%. Diamond and diamond–carbon clusters increase the lubricant viscosity in thin films, and their dynamic strength and durability increase appreciably, which, in turn, reduces leakages through clearances and gaskets in internal-combustion engines (ICEs) and diminishes friction loss, thereby increasing the compression and service life of carburetor and diesel ICEs and fuel economy.

Nanodiamond additives in solid lubricants allowed no-wear operation of sliding bearings of vapor boilers and turbine units in the power-supply system in Belarus. The great potential of a new antifriction heterogeneous material consisting of Sn–Zn–Pb bronze and cast iron granules was applied in practice using a special consistent lubricant with a nanodiamond additive. Only the application of the consistent lubricant modified by nanodiamonds provided no-wear operation of journal bearings, the absence of seizure, and a decrease in the friction coefficient paired with steel from f = 0.12–0.18 to 0.08–0.10 at specific loads of up to 300 MPa [5].

5. MODIFICATION OF PLASTICS

Studies carried out at the Institute of Mechanics of Metal–Polymer Systems, Institute of Physical and Organic Chemistry (NASB), Research Institute of Powder Metallurgy, Grodno State University, and other institutions show the efficiency of introducing nanodiamonds and diamond–graphite clusters into polymeric composites and films based on polyamides, polyolefins, fluoroplastics, etc.

Modification improves the mechanical characteristics and, in many cases, provides unique tribo-technical properties due to the formation of a space network of physical bonds at the interface between the polymer matrix and nanoparticles having enhanced adsorption properties.

A technology for gas-flame deposition of single- and multilayer polymer coatings with dispersed nanodiamonds has been developed at the Institute of Powder Metallurgy (NASB). In the case of single-layer sputtering, the deposited material is a mechanical mixture of a polyamide powder with ultrafine-dispersed diamonds (UDDs) and also with metal and ceramic components. The technology developed makes it possible to deposit coatings of various thicknesses onto friction units with various shapes and sizes.

Two-layer metal–polymer coatings with 0.5 wt % UDDs produced by gas-flame deposition reliably protect bearings and rotors of immersed pumps and other units against the joint influence of corrosion and wear, which makes it possible to maintain good operating characteristics over a long period of time [6].

Ultrafine-dispersed diamonds increase the density, coating–substrate cohesion, and lubricant adhesion to the friction surface, which increases the service life by a factor of 1.5–2. Polymer coatings modified by nanodiamonds are characterized by good antifriction properties, mechanical strength, non-toxicity, noiselessness, good machinability by cutting tools, as well as high resistance to liquid fuel, mineral oils and fats, organic solvents, alkalis, and acids.

We also note the high efficiency of modifying plastics with nanodiamonds at minimum cost. This line of inquiry is treated independently in the fundamentally oriented study program “NANOTECHNOLOGY” of NASB for 2003–2005.

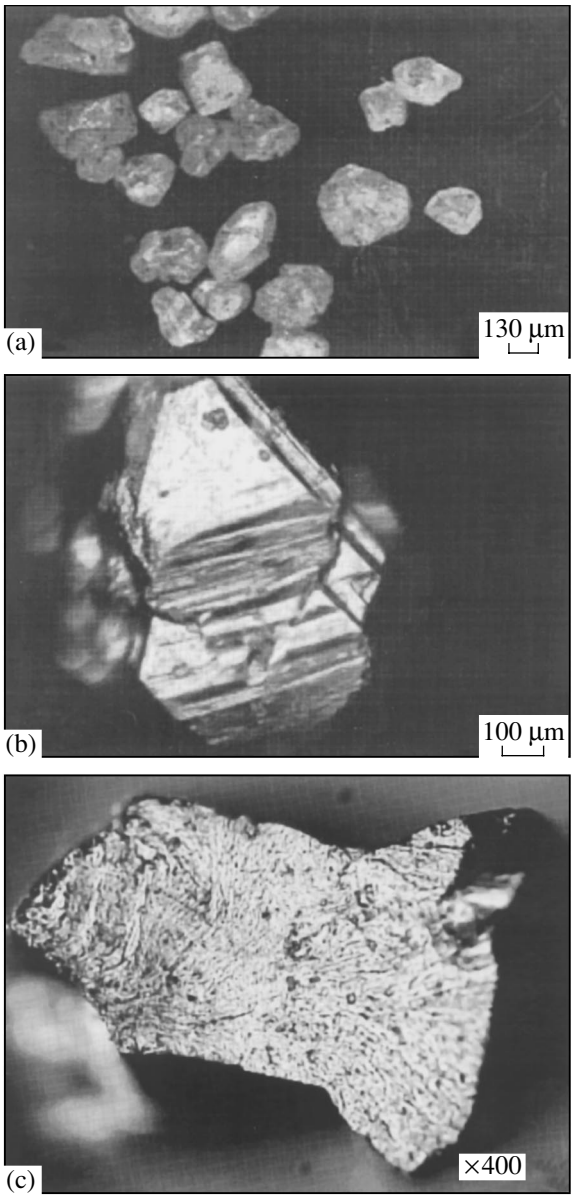

Fig. 2. Polycrystalline diamond powders synthesized from detonation-synthesis nanodiamonds: (a, b) powders produced using vacuum thermal treatment of nanodiamonds and (c) a polycrystal cleaved surface obtained by crushing of a compact after shock-wave consolidation of nanodiamonds.

6. POLYCRYSTALLINE DIAMOND POWDERS

Continuous studies on cost reduction and improvement of the physical–mechanical properties of detonation-synthesis nanodiamonds makes the methods for producing polycrystalline powders and compacts using available and inexpensive nanodiamond powders as initial mixtures competitive. These studies are carried out at the Concern of Powder Metallurgy of the Republic of Belarus and at the Institute of Mechanics and Reliability of Machines (NASB) using the shock-wave and static consolidation methods, respectively.

Among all the promising methods for producing superhard composites containing nanodiamonds fabricated by static thermobaric synthesis that are currently being studied in the NASB [7], we briefly consider the methods for producing nanostructural diamond polycrystals.

It has been ascertained that transparent diamond polycrystals 100–750 μm in size can be formed by processing a nanodiamond mixture in vacuum at moderate temperatures (T = 100–1200°C; Fig. 2). The formation of such particles can be caused both by the excess sur-

face energy of the initial diamond-containing mixture and by a widening of the region of diamond thermodynamic stability for nanoparticles. X-ray diffraction studies did not detect graphite in such powders with a microhardness H_V = 15–40 GPa at a load of 200 g; for the largest particle (the sizes along the major and minor diagonals are 750 and 300 μm, respectively), H_V exceeded 100 GPa [8, 9]. It seems that these synthesized structures are nanodiamond-based colloid crystals, which, depending on the treatment conditions, can contain non-diamond carbon forms.

Let us consider the application of shock-wave consolidation for producing diamond polycrystalline compacts from detonation-synthesis nanodiamonds.

Nanodiamond powders from the Sinta Company, after cleaning and prepressing up to a density $\rho \sim 1.23$ g m^{-3} in a stainless steel cell and 30-min vacuum refinement at 700 K, underwent shock-wave treatment using high explosives (trotyl–hexogen mixture or PVV-4 plastit) to produce polycrystalline compacts without cracks. The first commercial applications of tools made from such polycrystals for processing granites of high and medium hardness permitted one to lower the specific consumption of diamonds by a factor of 2 and 3, respectively. The diamond polycrystal cleaved surface obtained by the crushing of compacts after shock-wave consolidation is shown in Fig. 2.

7. FINISHING

Nanodiamond-based polishing pastes are efficiently employed for superfine finishing with roughness $R_a < 0.01$ μm, the polishing of diamond and precious stones, Si and Ge semiconductor wafers, the production of optical units, etc. The molecular level of interaction provides the formation of a perfect mirrorlike surface without a defect layer. Suspensions and pastes based on water, water–polymer, and oil are produced on a commercial scale at the Sinta Company and the Institute of Powder Metallurgy (NASB).

Further studies on nanodiamond applications in Belarus are associated with the establishment of the National Center of Nanomaterials, in which high technology materials and technologies will be developed for key areas of the Belarussian economy: mechanical engineering, electronic engineering, and petrochemistry.

It should be noted that the new century is proving to be the century of nanoscale materials and nanotechnologies that are dissimilar to the technological practice of the past and are likely to become the basis of a new global technological level. It would be good to see detonation-synthesis nanodiamonds occupy a worthy niche in this nanoworld.

8. CONCLUSIONS

In closing, we point out that detonation-synthesis nanodiamonds are produced on a commercial scale with a capacity of 10^7 carats per year at the Sinta Company, Belarus. Nine types of nanodiamonds and diamond-containing mixtures for protective coatings, lubricant additives, modification of plastics, finishing, etc., are produced.

REFERENCES

1. Yu. V. Timoshkov, T. M. Gubarevich, T. I. Orekhovskaya, *et al.*, Gal'vanotekh. Obrab. Poverkhn. **7** (1), 20 (2000).
2. P. A. Vityaz, *Nanostructural Materials-2000* (Minsk, 2000), p. 8.
3. M. A. Andreev, V. A. Chekan, L. V. Markova, and T. A. Kuznetsova, in *Proceedings of 4th Belarussian Seminar on Scanning Sound Microscopy* (Nats. Akad. Nauk Belorus., Gomel, 2000), p. 60.
4. P. A. Vityaz, V. I. Zhornik, A. I. Komarov, and V. I. Komarova, *Physics and Chemistry of Ultrafine-Dispersed (Nano-) Systems* (Mosk. Inzh.–Fiz. Inst., Moscow, 2002), p. 393.
5. P. A. Vityaz, V. I. Zhornik, V. A. Kukarenko, and A. S. Kalinichenko, Trenie Iznos **21** (5), 527 (2000).
6. E. D. Manoĭlo, É. N. Tolstik, D. G. Kobyak, and A. A. Osipov, *Welding and Related Technologies* (Belaruskaya Navuka, Minsk, 1999), p. 124.
7. *Production, Properties, and Application of Powders of Diamond and Cubic Boron Nitride*, Ed. by P. A. Vityaz (Belaruskaya Navuka, Minsk, 2003).
8. V. T. Senyut, Sverkhtverd. Mater., No. 6, 68 (2002).
9. V. N. Senyut, in *Proceedings of International Conference on Science for Materials in the Frontier of Centuries: Advantages and Challenges* (Kiev, 2002), p. 485.

Translated by A. Kazantsev

Physics of the Solid State, Vol. 46, No. 4, 2004, pp. 611–615. Translated from Fizika Tverdogo Tela, Vol. 46, No. 4, 2004, pp. 596–600.

METHODS OF FABRICATION AND PROCESSING OF DETONATION NANODIAMONDS

Currently Available Methods of Industrial Nanodiamond Synthesis

V. Yu. Dolmatov, M. V. Veretennikova, V. A. Marchukov, and V. G. Sushchev

"Almaznyĭ tsentr" Joint-Stock Company, St. Petersburg, 192076 Russia

e-mail: alcen@comset.net

Abstract—The main theoretical aspects of detonation decomposition of powerful mixed explosives with a negative oxygen balance accompanied by the formation of nanodiamonds (ultrafine-dispersed diamonds, UDDs) are described. The basic UDD synthesis parameters are considered, and the expediency of using trotyl–hexogen alloys is shown. The conditions of diamond phase conservation in the detonation products are specified. Various versions of industrial detonation synthesis of UDDs are considered. The most efficient technology of chemical cleaning of UDDs (with nitric acid at high temperatures and pressures) for producing UDDs with the highest purity is described. © *2004 MAIK "Nauka/Interperiodica".*

By comparing the explosive detonation parameters with the carbon phase diagram and performing thermodynamic calculations, it has been shown empirically and then theoretically that free carbon in detonation products (DPs) of powerful condensed carbon-containing individual explosives with a negative oxygen balance should condense in a diamond or liquid phase.

Thermodynamic calculations of the detonation and subsequent adiabatic expansion of products have shown that the conditions of diamond stability in expanding DPs are conserved for a very short time. At a DP density close to the initial explosive density, the diamond stability conditions are followed by the graphite stability conditions [1]. Since the relative drop in the DP pressure during the adiabatic expansion significantly exceeds the relative decrease in temperature, the thermodynamic state of the carbon component falls in the region of graphite stability at high temperatures, which facilitates the diamond-to-graphite phase transition and prevents diamond conservation.

The diamond graphitization rate heavily depends on temperature. At a certain temperature, the graphitization rate decreases to the point where the amount of carbon undergoing the transition from the diamond to the graphite phase becomes negligible at later stages of DP expansion; i.e., the graphitization is "frozen." This temperature can be referred to as the temperature of graphitization or diamond phase freezing. In the case where the temperature for the onset of graphitization is higher than the temperature for its freezing, the diamond-to-graphite phase transition takes place. If the temperature for the onset of graphitization is much higher than the freezing temperature, the entire diamond has time to transform into graphite and ultrafine-dispersed diamond (UDD) is not detected in the cooled DPs.

The rate of decrease in the DP temperature during expansion in the rarefaction wave is controlled by the gas dynamics of this process, which in many respects depends on the geometric configuration and size of the explosive charge.

The general conclusion is that the optimum conditions for the UDD formation in a detonation wave and UDD conservation in the rarefaction wave are a relatively high pressure and a low temperature of DPs at the Chapman–Jouguet point.

Calculations using the standard values of the thermodynamic functions of graphite and diamond yielded an abrupt change in the dependence of the detonation rate on the initial density of carbon-rich explosives near 1250–1300 kg m^{-3} [2]. This feature was explained by the fact that the phase state of the free carbon in DPs changes with an increase in the initial explosive density, which increases the detonation pressure.

A detailed mechanism explaining all the stages of UDD synthesis has not yet been proposed. Three stages can be distinguished in the detonation synthesis. The first stage is the transformation of the explosive under conditions of a high pressure and temperature. Due to the detonation, free carbon must appear in DPs. The pressure and temperature in the detonation wave should provide the thermodynamic conditions necessary for conservation of the produced diamond phase and for preventing the diamond-to-graphite transition. For a 50/50 trotyl/hexogen (TH) mixture, these conditions take place at 22 GPa and 3200 K. At the second stage, the DPs expand rapidly and diamond particles are cooled to a temperature lower than the graphitization temperature. The third stage is characterized by intense heat and mass exchange between the DPs and the medium surrounding the explosive. The main parameters determining the final temperature and the time after

1063-7834/04/4604-0611$26.00 © 2004 MAIK "Nauka/Interperiodica"

DB and UDD yields depending on the synthesis conditions

No.	Quality parameters of end product	Synthesis conditions		
		inert gas medium	aqueous medium	ice armor of a charge
1	DB yield, wt %	3–8	6–12	8–18
2	UDD content in DB, wt %	20–40	40–63	55–75
3	UDD yield per unit explosive mass, wt %	0.6–3.2	2.4–7.6	4.4–13.5
4	Content of incombustible impurities in DB, wt %	3–5	1.5–3.0	1–2

which this temperature sets in are the specific heat, amount, and chemical activity of the medium.

Analysis of the experimental data on the detonation synthesis of diamond allows us to draw conclusions about the most important factors controlling the UDD yield per explosive unit mass. These factors can be conventionally classified into external factors (associated with the detonation-synthesis conditions in the volume bounded by the blast chamber walls) and internal factors related to the explosive parameters (mass, shape, density, and chemical composition).

Experiments on UDD synthesis in various media have shown that the diamond yield depends on the gaseous medium in which the explosive detonates; the yield increases in the series vacuum–hydrogen–argon–nitrogen–carbon dioxide. Moreover, the diamond yield increases with the initial pressure of the gas filling the blast chamber. This dependence is caused by the conditions and the possibility of DPs cooling during and after their expansion; i.e., the controlling factor in this case is the amount of inert medium (coolant) per explosive unit mass. Another important characteristic is the specific heat of the coolant; the yield becomes higher as this parameter increases. Water, water-based foams, and ice can be efficiently used as cooling media. The use of metal cases does not affect the UDD yield appreciably in comparison with water and ice jackets. Air in the chamber causes full oxidation of carbon and the absence of condensed products.

Among the wide variety of explosives, trotyl (TNT), hexogen, octogen, and their mixtures are most appropriate for UDD synthesis. The characteristics of these materials have been studied in sufficient detail, and they are produced on a commercial scale. Processing of these explosives does not pose any difficulties; explosive charges with any shape can be produced by pressing and casting. The intensive formation of the diamond phase occurs in the 70/30 TH mixture, which is more powerful than pure TNT. The pressure in the initiating shock wave in such a mixture, as measured by a manganin sensor, is higher than 25 GPa; the pressure calculated at an initial mixture density of 1650 kg m^{-3} is 31 GPa. As the density of a charge of the same composition decreases, the diamond yield is lowered down to complete disappearance. The time of formation of the diamond phase is several tenths of a microsecond, which corresponds to the chemical-reaction duration in TH alloys. Hence, diamonds arise in the region of chemical transformations up to the Chapman–Jouguet plane under conditions of a high rate of change in the pressure and temperature.

As a rule, explosive mixtures (TH) are used in industrial diamond synthesis. The diamond yield from individual trotyl and hexogen is very low. Thermodynamic calculations have shown that the temperature of hexogen DPs is lower than that of trotyl DPs at the same expansion stages. For this reason, hexogen in TH alloys is a coolant for trotyl DPs. Hence, hexogen is a source of increased pressure and is a coolant. Diamonds are mostly formed from trotyl carbon. As the DPs expand in the gas filling the blast chamber, strong overheating (the formation of a hot core) in circulating shock waves takes place in the central region of the chamber; the temperature depends on the molecular mass of the gas and the adiabatic exponent $\gamma = C_p/C_v$. In the case of initial CO_2, the core is less pronounced due to the high gas density and the small value of γ (good compressibility). To conserve the diamond phase, the DP cooling rate should be within 3000–4000 K min^{-1} [3], which can be provided by choosing an appropriate heat capacity of the gas or water–gas medium in the blast chamber.

The diamond production includes the following: detonation synthesis, UDD chemical cleaning and washing from acid, product conditioning, and diamond modification. The production technique also includes systems for entrapping and recycling acid vapors and gases, preparation and recycling of nitric acid, and water preparation.

The detonation synthesis is carried out in special blast chambers, typically 1–20 m^3 in volume. The chambers are made from low- or high-alloy steels. The optimum choice is a chamber made from high-alloy steels (e.g., boiler steel) plated on the inside with a corrosion- and shockproof alloy. Chambers are equipped with gas-transport lines and a system for evacuating and entrapping condensed DPs. The detonated (cast or pressed) charge, as a rule, is a TH mixture with a ratio from 40/60 to 70/30. The charge weight varies from 0.5 to 2.0 kg. The typical detonation conditions are listed in the table. The largest mass of detonated charges is dictated by the conditions of DP cooling, namely, by the

volume, pressure, and composition of the gases and by the strength characteristics and volume of the chamber. For example, for chambers 11 and 100 m^3 in volume, explosive charges can reach 5 and 10 kg, respectively.

The non-carbon impurity content in the condensed carbon (or else the so-called diamond blend, DB) for any detonation type is substantially controlled by the wall material of the blast chamber and the optimum ratio between the chamber and charge volumes.

The use of a foam or water drops increases the heat capacity of the medium in which the structure of carbon particles forms during their condensation (in some form) from the plasma, in comparison with the heat capacity of a gas medium. The UDD yield increases in comparison with the case of detonation in a gas medium, because the cooling of the explosion products is more intense and, hence, the UDD fraction that transforms into graphite decreases. Charge detonation in water or ice (in the case of the optimized gas medium in the blast chamber) increases not only the quantity of DB and the UDD yield per initial explosive amount but also significantly changes the hydrophilic–hydrophobic balance of surface-active centers. In this case, we recommend an ice-to-explosive ratio of (4–9) : 1.

The highest DB and UDD yield is observed for mixtures of octogen or hexogen with trotyl in which the content of the latter is 60 to 70 wt % and the density is ≥ 1630 kg m^{-3}.

Condensed carbon represents a complex physicochemical system containing diamond carbon and various graphite-like structures [4–6]. Diamond crystals are rather small (~4 nm) and are incorporated in various aggregated particles. It is more correct to characterize the UDD synthesis product as a cluster material with a complex hierarchy of levels of aggregation of diamond and non-diamond forms of carbon with specific relaxation of the energy-saturated surfaces. The excess surface energy is compensated by chemically bound molecular fragments containing heteroatoms (N, H, O). The excess surface energy is compensated by the formation of more or less stable absorbate and/or solvate shells, whose composition depends primarily on the medium in which the UDDs are synthesized. The specific features of the DB are a high dispersity, an imperfect carbon structure, a developed active surface, and, hence, increased reactivity. Thus, the following basic conclusions can be drawn that need to be taken into account when solving the problem of purifying UDDs.

(i) Sufficiently pure UDD particles can be produced using only intense influences capable of supplying enough energy to rupture chemical bonds.

(ii) Chemical cleaning yields a material with an outer shell structure depending on the applied method; this structure can have a strong effect on the consumer properties of the material.

(iii) Due to the highly developed surface, high rates of chemical transformations can be expected.

It is important that chemical cleaning is the most expensive and complex stage in the UDD technology. The developed methods of liquid-phase cleaning of UDDs conserve the free-state dispersity of a carbon material at all stages of its treatment. Reactive blend suspensions in liquid oxidizing mixtures are homogeneous, colloidally stable, high-disperse, and low-viscous. Free access of an oxidizer to solid-phase particles is provided during the reaction, and the diffusion limitation on the rate of the process is practically removed.

Oxidizing systems based on nitric acid (with a balanced ratio of components and under the corresponding operating conditions) efficiently oxidize as much as 99% of non-diamond carbon and transfer up to 90% of non-carbon impurities into a soluble state. The oxidation reaction products are mostly gaseous [7].

According to modern concepts, cleaned UDD is a material consisting of ultrafine particles, each having a diamond core coated by an outer peripheral stabilizing shell of carbon–oxygen functional groups and a very complex surface structure [8]. Chemical treatments almost do not touch the diamond core structure, which is a distinctive feature of this material; furthermore, an outer boundary layer of UDD particles is formed anew and controls the behavior of nanodiamond when it is a component of a highly disperse system. Therefore, the cleaning stage controls the formation of UDD consumer properties and allows the production of various modified types of the product. The method (recommending itself well in industrial practice) based on high-temperature liquid-phase oxidation of a diamond-containing blend by aqueous solutions of nitric acid under pressure makes it possible to solve all cleaning problems within a single technological process and to produce various commercial types of UDDs [9, 10] with small amounts of ecologically dangerous wastes. All the problems associated with the development, organization, and safe operation of an autoclave reactor unit continuously functioning under pressure are efficiently solved.

The initial raw material for producing UDDs is a diamond-containing blend prepared using any of the available detonation synthesis methods (explosive detonation in a gas phase, water, or ice).

Apart from DB, the raw materials used in the technological process are technical nitric acid (50–98%), air, and demineralized water. From the chemical viewpoint, nitric acid is an oxygen carrier and provides intense processes of oxidation. Simultaneously, an aqueous solution of nitric acid is both a reaction medium and a transporting agent. In this case, oxidation is combined with acid dissolution of metal-containing impurities and their transition to water-soluble products.

The UDD cleaning process runs as follows: active carbon begins to oxidize even at rather low temperatures (80–180°C) under the action of a strong (50–99%) nitric acid; the initial oxidizing processes take place

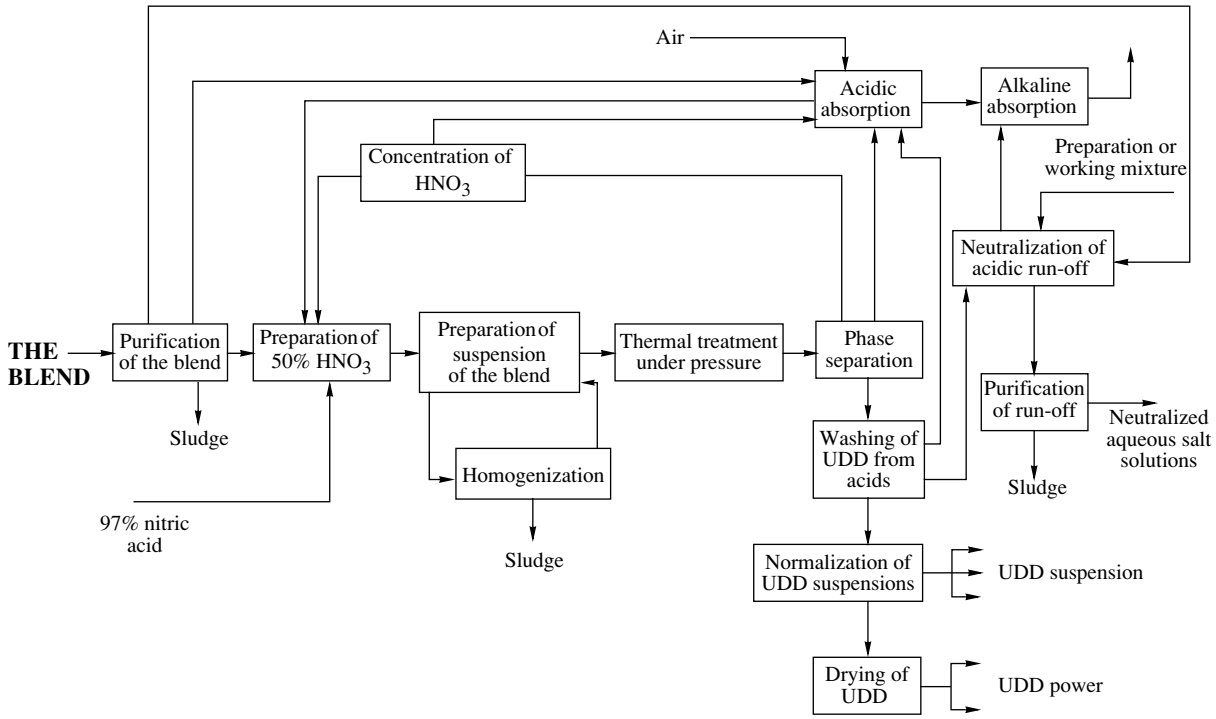

Block diagram of UDD cleaning.

even at atmospheric pressure with the release of carbon dioxide and nitrogen oxides.

After the transition of the active component of nanodiamond carbon to the gaseous state and incomplete dissolution of the accompanying metal oxides, the temperature should be increased to 220–280°C in order for further oxidation of the residual non-diamond passive carbon and practically total dissolution of metal oxides to occur. Experiments have shown that weak (10–40%) nitric acid is sufficient for this purpose and the higher the temperature, the weaker the acid that can be used.

The block diagram showing the main stages of the cleaning process and the flow structure is shown in the figure.

In general, the UDD cleaning technology includes the following.

(1) Preliminary preparation of DB (grinding, averaging, removal of mechanical impurities, magnetic separation, fractionation, and drying to a certain moisture).

(2) Preparation of aqueous solutions of nitric acid.

(3) Preparation of mobile homogenized DB suspensions in aqueous solutions of nitric acid.

(4) Continuous thermal-oxidation treatment of blend suspensions in pressure devices. To this end, special equipment and techniques for starts, tests, operation, and emergency and scheduled stops have been developed. The process runs at the equilibrium pressure in a cascade of flow-type devices under profiled temperature conditions. The pressure is 8–10 MPa, and the temperature is up to 240°C.

(5) Separation of the products of thermal-oxidation treatments. At this stage, operation in the pressure equipment changes to operation in devices without pressure. The thickened acid suspension is directed to UDD washing from acids and water-soluble impurities.

(6) Organization of nitric-acid recycling.

(7) UDD washing from acids.

(8) Waste treatment.

(9) Production of normalized, stabilized UDD suspensions in distilled water.

(10) Production of UDD in the form of a dry homogeneous powder.

Currently, the UDD cleaning technology employing the thermal-oxidation method with liquid-phase high-temperature oxidation in a nitric-acid medium provides the highest and most stable cleaning characteristics; this technology can be readily scaled and is the most developed.

REFERENCES

1. L. N. Akimova, S. A. Gubin, V. V. Odintsov, and V. I. Pepekin, in *Proceedings of V All-Union Workshop on Detonation* (Krasnoyarsk, 1991), Vol. 1, p. 14.
2. S. A. Gubin, V. V. Odintsov, and V. I. Pepekin, Khim. Fiz. **5** (1), 111 (1986).

3. A. L. Vereshchagin, E. A. Petrov, G. V. Sakovich, *et al.*, U.S. Patent No. 591,655 (29 June 1999).
4. V. Yu. Dolmatov and T. Fujimura, Sverkhtverd. Mater., No. 6, 34 (2001).
5. T. M. Gubarevich, V. Yu. Dolmatov, Yu. V. Kulagina, and L. I. Poleva, Zh. Prikl. Khim. (St. Petersburg) **66** (8), 1882 (1993).
6. V. Yu. Dolmatov, *Ultrafine-Dispersed Diamonds of Detonation Synthesis: Production, Properties, Application* (SPbGPU, St. Petersburg, 2003).
7. V. Yu. Dolmatov, V. G. Sushchev, V. A. Marchukov, *et al.*, RF Patent No. 2,109,683, Byull. Izobret., No. 12 (1998).
8. A. E. Aleksenskiĭ, M. V. Baĭdakova, A. Ya. Vul', and V. I. Siklitskiĭ, Fiz. Tverd. Tela (St. Petersburg) **41** (4), 740 (1999) [Phys. Solid State **41**, 668 (1999)].
9. V. Yu. Dolmatov, V. G. Sushchev, and E. N. Vishnevskiĭ, USSR Inventor's Certificate No. 1,828,067 (25 March 1986).
10. T. M. Gubarevich, R. R. Sataev, and V. Yu. Dolmatov, in *Proceedings of V All-Union Workshop on Detonation* (Krasnoyarsk, 1991), Vol. 1, p. 135.

Translated by A. Kazantsev

Physics of the Solid State, Vol. 46, No. 4, 2004, pp. 616–619. From Fizika Tverdogo Tela, Vol. 46, No. 4, 2004, pp. 601–604.

METHODS OF FABRICATION AND PROCESSING OF DETONATION NANODIAMONDS

Synthesis Mechanism and Technology of Ultrafine Diamond from Detonation[1]

Huang Fenglei, Tong Yi, and Yun Shourong

National Key Laboratory of Explosion and Safety Science, Beijing Institute of Technology, Beijing, 100081 China

Abstract—Ultrafine diamond (UFD) is a hybrid product of explosion mechanics and material science. In this paper, we established the synthesis mechanism of UFD, built the direct-simulation Monte Carlo computing method for the generation of liquid drops from free carbon through coagulation during detonation, and constructed the computing programs for explosion thermodynamics conditions and phase-transition dynamics. The synthesis and purification technology were studied systemically. *© 2004 MAIK "Nauka/Interperiodica".*

1. INTRODUCTION

Ultrafine diamond (UFD) is formed from unoxidized carbon in a negative oxygen balance explosive at high pressure and high temperature produced during detonation. Analysis by SAXS and TEM has shown that the particle size distribution is mainly 1–60 nm and the median size (D_{50}) is 9–11 nm. It possesses some properties of natural diamond and simultaneously some properties of nanometric particles. This perfect combination is a special quality of UFD that differentiates it from traditional manmade diamond and natural diamond. Its excellent potential was predicted in the field of material science, the improvement of material surface, and even in medicine [1]. A lot of research work on it has been performed in several countries, including Russia [2], Japan, and the USA. Some research results have already been put into commercial use. In China, several institutes and universities are conducting related research. The Beijing Institute of Technology is one of them. A research group at this institute began systematic research in 1990. Here, we give part of our research work.

2. SYNTHESIS MECHANISM OF UFD

In the detonation process of a negative oxygen balance explosive, free carbon is released and then turns into UFD. There are differing viewpoints on the mechanism of this process. It could not be decided in which in which section of the detonation process UFD was formed, in that involving the leading shock wave (von Neumann peak), the chemical reaction zone (ending at the point *CJ*), or the Taylor zone (Fig. 1). Most scholars put their mechanism forward only through theoretical analysis or experiment and neglected necessary calculation [3]. In our research, we managed to find the forming mechanism of UFD through quantitative calculation.

2.1. The Leading Shock Wave

Molecular calculation shows that the wave-front energy can focus several electronvolts of energy on the bands of the explosive molecule in 10^{-10} s and the energy is sufficient to break the molecular bonds. This splitting only occurs at the local "hot spots." The explosive molecule at first absorbs the energy from the splitting and then breaks into individual atoms, free radicals, and fragments of molecules, in which the free carbon is included.

2.2. The Chemical Reaction

At the hot spots, the decomposed components of the explosive are reunited and release chemical energy, which makes the temperature rise and leads to decom-

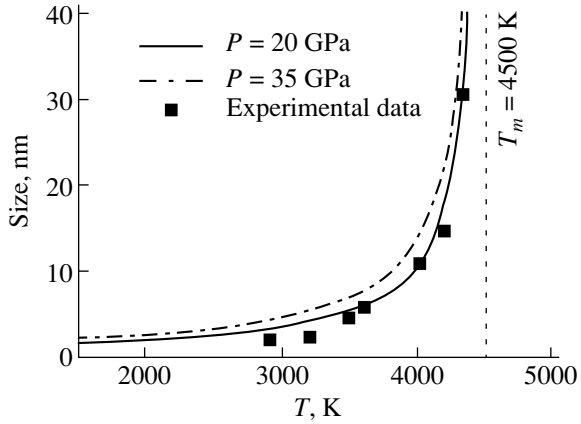

Fig. 1. Relation between the melting points and size (r_s) of UFD.

[1] This article was submitted by the authors in English.

position and reaction of the explosive. Consequently, the chemical energy impels the leading shock wave to move forward continually. As there is an oxygen deficiency, part of the carbon in the explosive is left and becomes free carbon after the detonation reaction. When the free carbon collide with each other in the reaction zone, the liquid state carbon will coagulate into a bigger drop and the solid state carbon will again leave after the collision. In a traditional carbon-phase plot, the temperature and pressure of detonation should sit in the solid zone. We found that the melting point of carbon particles is related to the particle size; for instance, the melting point of nanometer-sized metal particles is lower than that of the block metal. On the basis of former researcher work and by means of thermodynamics relations, we obtained the following relation between the melting point (T) and the ultrafine particle size (r_s):

$$1 - \theta = \frac{2}{\rho_s \Delta H_m r_s}\left[\gamma_s - \gamma_l\left(\frac{\rho_s}{\rho_l}\right)^{\frac{2}{3}}\right], \qquad (1)$$

where $\theta = T/T_m$, T_m is the melting point of the block material, ΔH_m is the melt enthalpy of the solid, ρ is the density, γ is the surface tension, subscribe s indicates solid phase, and subscribe l indicates liquid phase. The above formula is the one order Tailor formula. By substituting the related parameters of diamond into formula (1), we find that pressure has only a little influence on the melt point, but the influence of the particle size is greater (shown in Fig. 1). When the size is less than 10 nm, the melting point decreases rapidly. This can be explained as follows: when the free carbon collide and coagulate to make the drop bigger, the melting point becomes higher until it reaches the detonation temperature (T_{CJ}). In Fig. 2, the *CJ* locations of five explosives are given. It is clear that the *CJ* location of the TNT60/RDX40 explosive is situated in the liquid-phase zone, which indicates that the free carbon from this explosive could coagulate into bigger drops.

The collision and coagulation of the free carbon can be described by the Smoluchowski equation [4], which can be solved by direct Monte Carlo simulation. For this purpose, we worked out a computing program by the C language and passed the test of analytic solution of the Smoluchowski equation.

The results calculated using the DSMC program are as follows.

(1) The number of atoms in the original cluster has little influence on the coagulation.

(2) The results of numerical calculation are shown as a solid line in Fig. 3. It shows that, when the coagulation time is 1.18×10^{-9} s, the particle size (r_s) is concentrated at 2 nm and located at the lower limit in comparison with the experiment data (2–4 nm). Here, the distribution function of the coagulating particles is logarithmic. The distribution plotted from the calculation is shown as a dotted line in Fig. 3. The above results

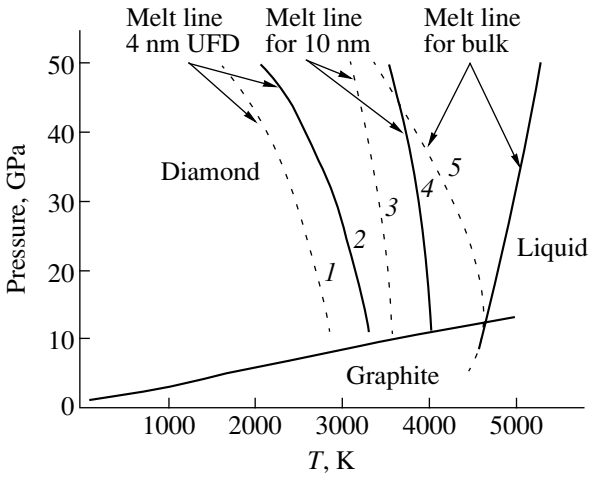

Fig. 2. Phase graph of block diamond and UFD (4 nm, 10 nm). Explosives: (*1*) TNT, (*2*) TNT/RDX 60/40, (*3*) RDX, (*4*) PETN, (*5*) BTF.

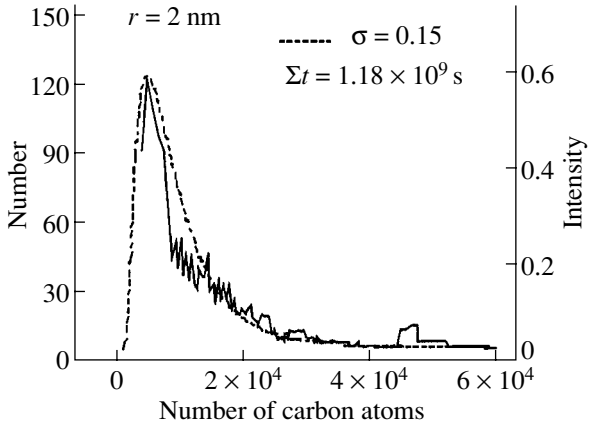

Fig. 3. Distribution of particle size at 1.18×10^{-9} s.

illustrate that it is enough for the UFD to be coagulated in the reaction zone (less than 10^{-9} s).

(3) The "melting point-size" effect. The calculation of the coagulation is performed without any conditions. Actually, when the particles become big enough, the melting point will go up. In the calculated pressure and temperature, the situation is already in the solid state. Therefore, the particles cannot be coagulated after colliding. When this limiting condition is added to the process, the time it takes for the particle size to be coagulated to 5 nm increases to the 10^{-7} s range, which is almost the same range as the detonation reaction time. It is deduced that a limitation on the particle size would come from a limitation on the coagulating process.

In the reaction zone, the explosive decomposes continuously and, correspondingly, free carbon is produced. Along with the growth, the carbon drop began to crystallize into a solid. The following calculation will

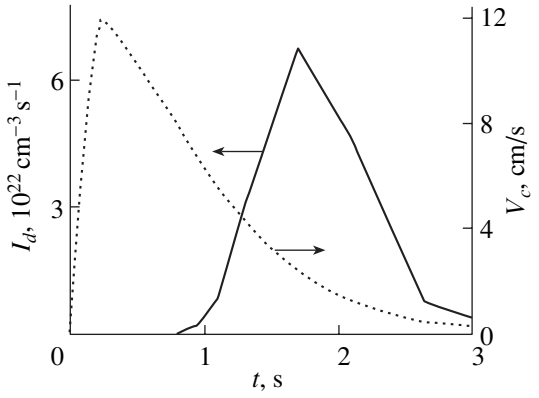

Fig. 4. The nucleation rate and the growing velocity of UFD.

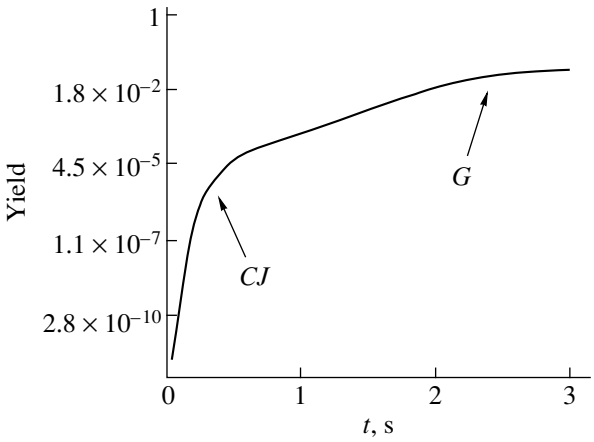

Fig. 5. Yield of UFD. (*CJ*) End of chemical reaction zone and beginning of Taylor zone and (*G*) graphitization point.

prove that the crystallizing process in this zone is very slight.

2.3. The Tailor Expansion

In this section, the decomposition of the explosive is completed. Although there is chemical reaction, the effective heat is no longer able to support the leading shock wave. The Tailor wave will make the temperature and pressure decrease sharply. In this thermodynamic situation, the crystallizing process starts. If the state is located in the diamond stabilization zone, the diamond will be turned out, and if the state is located in the graphite zone, the crystallized diamond will be turned into graphite (called graphitization). At the same time, another kind of solid carbon will be formed. As the temperature drops, the graphitization process of the diamond will stop and the diamond will exist in a metastable state; this is the UFD we want to obtain.

Table 1. Purifying results of UFD by different technologies (from XPS)

Purification technology	Perchloric acid	Nitric acid	Permanganate kalium
C (diamond), %	89–92	86–92	90–94

Table 2. Further purifying results of UFD (from XRF)

Element	C	Fe	Cr	Ti	Ba
content, %	98.591	0.303	0.219	0.200	0.042
Element	Cl	S	P	Si	Al
content, %	0.025	0.025	0.001	0.021	0.032
Element	Cu	Ca	K	Mg	Na
content, %	0.316	0.025	0.030	0.042	0.128

As the effective heat of the phase transition and the volume effect are relatively small, the process can be divided into two steps. In the first step, the mechanics and the chemical reaction are considered and we can find rules for the temperature, pressure, specific volume, and quantity of free carbon along with time. In the second step, the crystal dynamics is considered on the basis of the conditions gained in the first step.

2.4. Calculation of the Crystal Dynamics of UFD Formation

In detonation, the crystallizing process of the liquid carbon is carried out under the condition of supercooling, which can be described by using the spontaneous crystallization theory according to the processes of nucleation and growth of the crystal nucleus.

From the von Neumann peak to the Tailor expansion zone, a special computing program was worked out. The yield (per explosive mass) of UFD was calculated. The $I_d(t)$, $V_c(t)$, and $Y_{ie}(t)$ relations are shown in Figs. 4 and 5 (where I_d is the nucleation rate of diamond, V_c is the growth velocity of UFD, and Y_{ie} is the yield of UFD). It can be seen from Fig. 5 that the yield of UFD is only 1.1×10^{-6} up to the *CJ* point. This means that the UFD was formed mainly in the Tailor expansion zone.

3. SYNTHESIS AND PURIFICATION TECHNOLOGY OF UFD

3.1. Detonation Synthesis

The raw materials used in our the synthesis of UFD are a type of mixed explosive, TNT/RDX. The detonation of the explosive provides not only a source of carbon but also the high pressure and high temperature conditions needed to form UFD, which makes the method of synthesis relatively simple. In order to gather the detonation products (detonation soot) and to fill the protective media, a pressurized metal vessel was used

Table 3. Particle size distribution of UFD purified by different technologies (from SAXS)

Technology	Perchloric acid			Nitric acid			Permanganate kalium		
size interval, nm	$f(D)$, % nm	mass fraction, %	cumulative, %	$f(D)$, % nm	mass fraction, %	cumulative, %	$f(D)$, % nm	mass fraction, %	cumulative, %
1–5	100	34.9	34.9	66.2	23.9	23.9	79.2	27.1	27.1
5–10	95.1	41.4	76.3	100	45.2	69.1	100	42.8	69.9
10–18	23.1	16.1	92.4	28.6	20.6	89.8	30.3	20.8	90.7
18–36	2.2	3.5	95.9	4.3	6.9	96.7	1.8	2.8	93.6
36–60	2.0	4.1	100	1.5	3.3	100	3.1	6.4	100
Median size D_{50}, nm		9.3			10.5			10.8	

in the experiment as the explosion tank. It is clear that the amount of explosives, the kind of protective media, and the charge structure are key factors for determining the synthesis rate of UFD.

3.2. Chemical Purification

The purification technology plays a very important role in the production of UFD as it is the main factor in production cost and affects product quality to a certain extent. By means of XRD, TES, and laser Raman spectroscopy, it was found that the main impurity of the detonation soot is nanometric graphite and amorphous carbon, which can be cleaned away using oxidation technology. Normal-pressure perchloric acid technology (as perchloric acid technology), high-pressure dilute nitric acid technology (as nitric acid technology), and permanganate kalium and sulfuric acid technology (as permanganate kalium technology) are three of the practical methods used in our study.

The perchloric acid technology was used earlier. It has the advantages of employing simple equipment and having a good purification efficiency, but has the disadvantage that chlorine gas and other harmful gases, as well as waste acid, are produced in the reaction process, which can result in serious pollution of the environment. It is limited in performing experiments. The nitric acid technology from Russia is relatively advanced and has a high level of automatic control. However, at high pressure and high temperature, dilute nitric acid requires expensive titanium as the reaction vessel to prevent corrosion; thus, great expenditure is inevitable for the use of this technology. However, a medium production line with a yield of UFD 10^7 carat/year has already been set up in the experimental area of our university. In comparing the above two technologies, we see the permanganate kalium technology can make up for some of their disadvantages. It is efficient, economical, safe, less polluting, and is easy to put into commercial use. Most importantly, this method can get better purification results than the others discussed above. At present, this technology is suitably applied in 10^5 carat/year scale production.

The purifying results of UFD tested by means of XPS are listed in Table 1, from which it can be seen that the purity of UFD obtained from the permanganate kalium technology is superior to that obtained from the perchloric acid technology and the nitric acid technology. If we perform further treatment, the purity of the products can be improved even more. An example is given in Table 2, which shows data from XRF.

Furthermore, there are some differences in the particle sizes of UFD purified through different technologies. Table 3 shows the test results by SAXS. It can be seen that, of the three test sets of data, the particle size distribution from the nitric acid technology is closer to that from the permanganate kalium technology.

4. CONCLUSIONS AND PROSPECTS

(1) The synthesis mechanism of UFD was established by qualitative analysis and quantitative calculations, including explosion thermodynamics, the coagulating dynamics of a carbon drop, and the phase transition. The results show that the calculation can be used to predict the formation process and the yield of UFD.

(2) The synthesis and purification technology of UFD were studied systematically. The characteristics of three purification technologies suitable for different scales of production were discussed.

(3) It is believed that UFD that possesses some of the properties of both diamond and nanometer particles has great future potential.

REFERENCES

1. S. R. Yun, F. L. Huang, F. Ma, *et al.*, Study Dev. World Sci. Technol. **22** (1), 39 (2000).
2. A. M. Staver, A. I. Lyamkin, N. A. Gubarev, and E. A. Petrov, Fiz. Goreniya Vzryva **20** (5), 100 (1984).
3. K. Yamada and A. B. Sawaoka, Carbon **32** (4), 665 (1994).
4. K. Liffman, J. Comput. Phys. **100**, 116 (1992).

Physics of the Solid State, Vol. 46, No. 4, 2004, pp. 620–621. Translated from Fizika Tverdogo Tela, Vol. 46, No. 4, 2004, pp. 605–606.

METHODS OF FABRICATION AND PROCESSING OF DETONATION NANODIAMONDS

Selective Inhibition of the Oxidation of Nanodiamonds for Their Cleaning

A. S. Chiganov

Department of the Physics of Nanophase Materials, Krasnoyarsk Scientific Center, Siberian Division, Russian Academy of Sciences, Krasnoyarsk, 660036 Russia

Abstract—The effect of selective inhibition of nanodiamond oxidation upon heating of detonation carbon in air is used to extract nanodiamonds from the detonation products. The methods for cleaning nanodiamonds from nondiamond carbon modifications are described depending on the synthesis conditions. © *2004 MAIK "Nauka/Interperiodica".*

One of the most important problems in cleaning synthetic diamonds is to remove them from carbon that did not transform into the diamond phase. In the chemical methods of cleaning, conditions are chosen under which nondiamond carbon (graphite or soot) is more reactive. Different reaction rates, e.g., oxidation rates, are explained by the different reaction mechanisms (formation of layered graphite compounds), by the effect of graphite porosity or of the large surface of soot, and by the significantly different oxidation activation energies (including oxidation in glow-discharge plasmas). The carbon that condenses upon the detonation of explosives is extremely dispersed and possesses an imperfect structure; therefore, it is highly improbable that the mechanisms of oxidation of different modifications of detonation carbon differ radically. The specific oxidation behavior of detonation carbon was confirmed in experiments on the oxidation of the products of detonation of a trinitrotoluene–hexogen mixture in an air glow-discharge plasma.

Glow discharge was initiated in a quartz tube 50 mm in diameter and 600 mm long. The interelectrode distance was varied from 200 to 400 mm, and the discharge current, from 0.1 to 2 A. The device was placed in a volume pumped out to 10^{-2} mmHg. A system of inlet valves and differential pressure gages allowed us to maintain a controlled atmosphere of various gases in the range 1–100 mmHg. To remove the diffusion restrictions, samples to be studied were arranged as a thin layer on the bottom of a flat alundum crucible in the zone of the positive column of the glow discharge. The oxidation products were examined by using x-ray diffraction, standard techniques of chemical analysis, and back chromatometric titration.

The kinetic-oxidation data for the detonation carbon and the oxidation products show that the majority of nondiamond carbon (more than 60% of its total content under the experimental conditions) oxidizes at a high rate. The rest of the carbon oxidizes at a rate that is close to the oxidation rate of diamonds. The imperfection of the nondiamond carbon, of course, has an effect on the different oxidation rates, but it cannot completely explain this nonuniform reactivity. The oxidation rate of diamonds increases with the content of metallic impurities in the initial powders (originating from the explosion chamber and detonator), which indicates the necessity of taking their catalytic influence into account.

To study the kinetics of the isothermal oxidation of various detonation-carbon modifications by atmospheric oxygen, we took nanodiamonds (extracted from the detonation products by boiling in a mixture of sulphuric and nitric acids) and nondiamond carbon synthesized under conditions unfavorable for the formation of the diamond phase. To remove metallic impurities, the powders were boiled in dilute acids. After having been washed in water and dried, the powders had almost equal specific surfaces (about 270 m^2/g) and contents of metal-containing impurities (less than 0.5%). Upon heat treatment in air, the diffusion restrictions were absent, which was indicated by the relative powder mass loss being independent of the sample weight. The experiments showed that, up to a certain degree of transformation ($\alpha \le 0.3$), the oxidation of all samples proceeded as in a reaction in which all particles retain their shape; as a result, we could use the Roginskiĭ– Schulz equation to calculate the reaction rate. The diamond powder mass loss after the time τ of isothermal oxidation is given by [1]

$$(m/m_0)^{1/3} = 1 - A\sigma_0\tau\exp(-E/RT)/3,$$

where m_0 is the initial powder mass, m is the powder mass at the instant of time τ, A is a constant, σ_0 is the initial specific surface of the powder, and E is the oxidation activation energy [1].

Using the temperature dependences of the reaction rates, we calculated the oxidation activation energy for nanodiamonds (about 180 kJ/mol) and the average oxi-

1063-7834/04/4604-0620$26.00 © 2004 MAIK "Nauka/Interperiodica"

dation activation energy for nondiamond carbon (~160 kJ/mol). These results explain why it is difficult to retain diamonds during the gasification of nondiamond carbon by heat treatment in air. Catalysts are traditionally applied to selectively oxidize untransformed carbon for cleaning synthetic diamonds. The relatively low oxidation temperatures of detonation carbon allow us to apply another method, namely, selective inhibition of diamond oxidation. A study of the effect of boron-containing compounds on the oxidation of detonation carbon showed that the oxidation rate decreases significantly. When using boric anhydride, we chose conditions for which diamonds were completely retained with a residual nondiamond carbon content of less than a fraction of a percent. To reveal the mechanism of the effect of the boron-containing compounds, we studied the kinetics of oxidation of nanodiamonds and nondiamond carbon in the presence of boric anhydride at various temperatures. The results show that the activation energy of oxidation remains almost unchanged for nondiamond carbon and increases substantially for diamonds (to 250 kJ/mol). The selectivity of oxidation inhibition makes it possible to separate the diamond and nondiamond modifications of detonation carbon. This finding was applied to develop a method for cleaning nanodiamonds [2]. The optimum cleaning conditions, including the temperature and the amount of boric anhydride, depend on the characteristics of the detonation carbon, such as the ratio of the quantities of the diamond and nondiamond modifications and the fraction of more ordered graphite-like carbon. The table gives the conditions for removing nondiamond carbon that make it possible to retain the maximum amount of nanodiamonds depending on various parameters of their synthesis.

The extraction of nanodiamonds by using this method of removing nondiamond carbon was performed at the pilot bay of the Department of the Physics of Nanophase Materials (Krasnoyarsk Scientific Center) and of the Krasnoyarsk State Technical University. The products made at the pilot bay are certified. Nanodiamonds produced using this method and diamonds produced by other manufacturers were compared by us and other researchers. Chiganova *et al.* [3] showed that, as compared to diamonds from acid cleaning, the oxidation rate of the nanodiamonds thus produced is significantly lower and the sedimentation stability of suspensions fabricated through ultrasonic dispersion of powders in water is higher. Our technology provides the minimum size of particle aggregates among the powders studied in [4]. According to [5, 6], our technology provides a significant output of individual diamond particles about 4 nm in size, which was used to produce two-dimensional diamond crystals.

Techniques of cleaning nanodiamonds depending on the synthesis conditions

Charge composition	Conservation medium	Average temperature, K	Treatment time, h
Trinitrotoluene/hexogen	CO_2	770	2.5
40/60	N_2	740	3.0
Trinitrotoluene/hexogen	CO_2	770	3.0
60/40	H_2O	800	3.0
	Ice (shell)	820	2.0
Graphite	N_2	920	4.0

Thus, the surface modification of nanodiamonds upon cleaning by the method proposed in [2] can be useful in a number of technical applications of nanodiamonds.

REFERENCES

1. O. N. Breusov, V. M. Volkov, V. N. Drobyshev, and V. F. Tatsiĭ, *Interaction of Diamonds to Liquid and Gas Media* (Naukova Dumka, Kiev, 1984), p. 23.
2. RF Patent No. 2,004,491, Byull. Izobret., Nos. 45–46, 85 (1993).
3. G. A. Chiganova, A. S. Chiganov, and Yu. V. Tushko, Neorg. Mater. **30** (1), 56 (1994).
4. A. Ya. Korets, E. V. Mironov, V. P. Malyĭ, and E. A. Petrov, in *Proceedings of II Interregional Conference on Ultrafine-Dispersed Powders, Nanostructures, and Materials* (Krasnoyarsk, 1999).
5. S. V. Kukhtetskiĭ and L. P. Mikhaĭlenko, Kolloidn. Zh. **58** (1), 137 (1996).
6. S. V. Kukhtetskiĭ and L. P. Mikhaĭlenko, Dokl. Akad. Nauk **357** (5), 616 (1997) [Phys.–Dokl. **42**, 661 (1997)].

Translated by K. Shakhlevich

Physics of the Solid State, Vol. 46, No. 4, 2004, pp. 622–624. Translated from Fizika Tverdogo Tela, Vol. 46, No. 4, 2004, pp. 607–609.

METHODS OF FABRICATION AND PROCESSING OF DETONATION NANODIAMONDS

Thermal Oxidation Initiated in Explosive Detonation Products by Exothermal Pyrolysis of Metal Acetylacetonates

V. G. Isakova and V. P. Isakov

Krasnoyarsk State University, Krasnoyarsk 660041 Russia

e-mail: isakov@siberianet.ru

Abstract—Thermal interactions between solid-phase mixtures of metal acetylacetonates with ultradispersed diamond and explosive detonation products are investigated. It is shown that these processes occur through combustion. The behavior of ultradispersed diamond and carbon (not transformed into the diamond phase) during thermal oxidation initiated in air due to exothermal pyrolysis of metal acetylacetonates is examined. The combustion reactions of solid-phase mixtures of this type can find application in the synthesis of new diamond-containing materials. © *2004 MAIK "Nauka/Interperiodica".*

1. INTRODUCTION

Improvement in the technical and economic characteristics of the processes of synthesis of ultradispersed diamond (UDD) through explosive detonation is determined primarily by the optimization of the technological parameters of the extraction of UDD from the diamond–carbon blend (DCB). Ultradispersed diamond has been produced using different techniques of eliminating graphite from the blend (for example, boiling in hydrochloric and sulfuric acids, oleum–nitric purification, reactions with boron oxide and chromic mixtures in sulfuric acid, heating in the presence of a catalyst, etc.). Initially, the blend contains no less than 85% carbon, of which diamond accounts for 5–15%. The content of incombustible impurities is approximately equal to 10%, and the content of gaseous products and moisture is no more than 5%. The bulk density of the blend falls in the range 0.02–0.20 g/cm^3.

The choice of the purification method depends on many factors, including the technique of synthesizing the diamonds, the content of concomitant impurities, and the specification and function of the diamonds. Apart from the UDD and nondiamond carbon phases, the blend contains specific impurities, such as iron oxides and carbides, metallic iron, and other species (up to 20 wt %). Moreover, proper allowance must be made for the very high specific surface of detonation diamonds and large amounts of surface functional (predominantly, carboxyl) groups and adsorbed gases in UDD with ultrasmall particles. For these reasons, extraction of the diamond phase is a complex problem.

The purification conditions are also determined by the reactivity of the diamonds involved. The main objective of the process is to extract a desired product of specified purity with minimum loss. This process can be rather efficient due to the relatively high chemical stability of diamonds.

In this work, we demonstrated that thermal interaction between solid-phase mixtures of metal acetylacetonates with UDD and the explosive detonation products proceeds through combustion.

Earlier [1], it was established that reactions involving fullerenes and fullerene black proceed through the same mechanism. With the aim of searching for new activators of burning graphite out of the diamond-containing blend, we investigated the behavior of the UDD phase and carbon (not transformed into the diamond phase) during thermal oxidation initiated in air due to exothermal pyrolysis of metal acetylacetonates ($Me(acac)_n$, where *acac* = $CH_3COCHCOCH_3$; *Me* is Na, Mg, Cr, Cu, Fe, or a platinum metal; and *n* is the oxidation number of metals).

2. EXPERIMENTAL TECHNIQUE

The reactants were heated in air to the temperature of the onset of pyrolysis of $Me(acac)_n$ (300–350°C). This led to glowing of the reaction mixture, and further reaction proceeded spontaneously. Upon heating in the absence of UDD, volatile acetylacetonates $Me(acac)_n$ almost completely sublimated without combustion. In the absence of $Me(acac)_n$, UDD did not undergo transformation. It is possible that the oxygen chemisorbed by the UDD surface initiates exothermal decomposition of $Me(acac)_n$, which, in turn, activates gasification of the UDD. The degree of gasification of UDD in the thermal reactions under investigation is governed by the type of metal ion in the acetylacetonate complexes. The largest losses of diamond (more than 70%) were observed during combustion of UDD in a mixture with $Cu(acac)_2$. The combustion of UDD in the presence of acetylacetonates of platinum metals proceeded at a high intensity. This can be associated with intensive heat release, which is characteristic of thermal decomposition of acetylacetonate complexes of platinum met-

1063-7834/04/4604-0622$26.00 © 2004 MAIK "Nauka/Interperiodica"

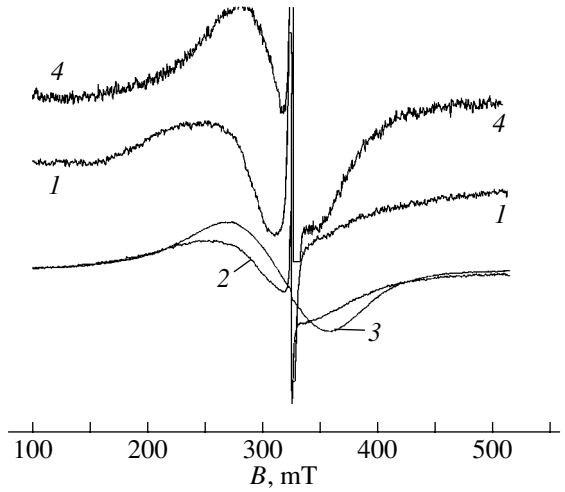

Fig. 1. Electron magnetic resonance spectra of (*1*) the UDD/Fe(*acac*)$_3$ initial mixture, (*2*) the products of thermal oxidation of the UDD/Fe(*acac*)$_3$ mixture upon heating without combustion (heating of the reactants at a temperature corresponding to thermal decomposition of the metal acetylacetonate under conditions of restricted access to air), (*3*) the products of thermal oxidation of the UDD/Fe(*acac*)$_3$ mixture through combustion, and (*4*) the products of combustion of the UDD/Cu(*acac*)$_2$ mixture.

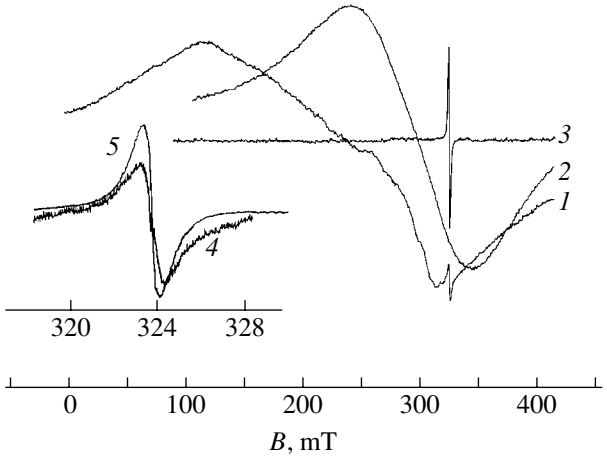

Fig. 2. Electron magnetic resonance spectra of (*1*) the DCB/Fe(*acac*)$_3$ initial mixture, (*2*) the products of thermal oxidation of the DCB/Fe(*acac*)$_3$ mixture through combustion, (*3*) the products of thermal oxidation of the DCB/Fe(*acac*)$_3$ mixture through combustion with subsequent acid treatment, (*4*) the UDD radical in the initial DCB, and (*5*) the UDD radical in the products of combustion of the DCB/Fe(*acac*)$_3$ mixture after acid treatment.

als in air. However, the degree of gasification of UDD was considerably less than that in the case of Cu(*acac*)$_2$. Note that UDD was oxidized to a lesser extent (~20–30%) during thermal reactions in a mixture of UDD with acetylacetonates of Na, Mg, Cr, and Fe.

The combustion of the diamond–graphite blend with an additive of *Me*(*acac*)$_n$ rapidly (for 3–5 min) spread over the entire bulk of the material and led to a substantial decrease in the weight of the reaction mixture. It should be noted that all the acetylacetonates studied in this work activated primarily the combustion of nondiamond carbon.

Taking into account that the main metal contaminating the detonation diamond–carbon blend is iron (the material of the explosion chamber), it is convenient to use iron acetylacetonate as an activator of the combustion of nondiamond carbon. Iron acetylacetonate can be synthesized immediately in the blend through its treatment with acetylacetonate.

3. RESULTS AND DISCUSSION

The products of the combustion of the UDD/Fe(*acac*)$_3$ and DCB/Fe(*acac*)$_3$ mixtures are black magnetic powders. In the first case, the *g* factor of the line attributed to the metal in the electron magnetic resonance spectrum is close to the *g* factor of magnetite (Fig. 1, line *3*). Since the spectra of the iron-containing products under investigation are not typical electron paramagnetic resonance (EPR) spectra and differ from the ferromagnetic resonance spectra of bulk materials, we use the term "electron magnetic resonance." The EPR spectrum of the diamond radical is similar to the spectrum observed for the initial UDD. In the second case, the line assigned to iron is broadened (Fig. 2, line *2*). The x-ray powder diffraction analysis of the sample revealed that iron is present in the form of Fe_2O_3. The line of the diamond radical is not observed. Apparently, this line is screened by strong resonance from the metal. After the residual black and metal-containing components were removed from the combustion product through acid treatment and subsequent washing with water, the spectrum of the final product exhibited electron paramagnetic resonance of the radical of free UDD, whereas resonance from the metal was not observed (Fig. 2, line *3*). According to the x-ray powder diffraction data, the material synthesized is ultradispersed diamond; no graphite fractions and metal-containing impurities were identified by electron paramagnetic resonance and x-ray powder diffraction. The yield was 75% with respect to the UDD produced from an identical amount of DCB through traditional acid treatment. However, preliminary burning of the bulk of nondiamond carbon leads not only to a substantial decrease in the amount of acids used in treatment but also to an acceleration of the UDD extraction from DCB. The duration of the process is 30–35 min. The UDD powder thus obtained has the following characteristics: the particle size is 20–120 Å, the specific surface is 200–400 m^2/g, the moisture content is no higher than 5%, and the metal impurity content is no higher than 1.5%.

The combustion reactions of UDD/*Me*(*acac*)$_n$ solid-phase mixtures can find application in the synthesis of new diamond-containing materials. The products

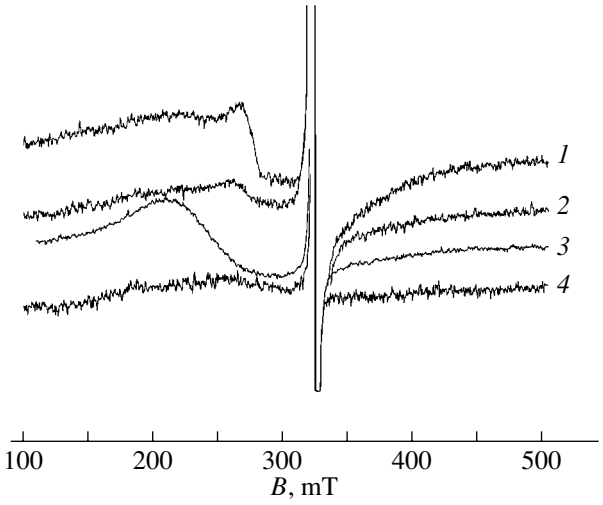

Fig. 3. Electron magnetic resonance spectra of the products of combustion of (*1*) the UDD/Pd(*acac*)$_2$ mixture, (*2*) the UDD/Ir(*acac*)$_3$ mixture, (*3*) the UDD/Ir(*acac*)$_3$ mixture heated without combustion under the same conditions as those used for recording curve *2* in Fig. 1, and (*4*) the UDD/Pt(*acac*)$_2$ mixture.

formed during thermal decomposition of *Me*(*acac*)$_n$ depend on the metal type, the reaction medium, and the temperature conditions of the process. Diamond either can be an inert diluent or can interact with the products of thermal decomposition of the metal complexes. The thermal decomposition of acetylacetonates of 3*d* transition metals in air brings about the formation of oxides, whereas the processes involving platinum metal compounds produces the free metal [2]. In the EPR spectra of the products of combustion of UDD/*Me*(*acac*)$_n$ (*Me* = Pt, Ir, Pd) (Fig. 3), the resonance lines of metals are observed at room temperature. We assume that these lines are associated with dispersed metal particles, which is confirmed by the x-ray powder diffraction data. The lines attributed to the radicals in the products of combustion of UDD/*Me*(*acac*)$_n$ are somewhat broadened compared to the lines assigned to free UDD. This is most pronounced for the products of combustion of UDD/Fe(*acac*)$_3$, which can be explained by the stronger magnetic properties of iron oxides.

ACKNOWLEDGMENTS

We would like to thank É.A. Petrakovskaya for performing the EPR measurements of the products obtained in our experiments.

REFERENCES

1. V. G. Isakova, É. A. Petrakovskaya, A. D. Balaev, and T. A. Kolpakova, Zh. Prikl. Khim. (St. Petersburg) **76** (4), 597 (2003).
2. V. N. Mitkin and V. G. Isakova, in *Proceedings of the International Symposium on Iridium, TMS-2000*, Ed. by Evan K. Ohriner, Richard D. Lanam, Peter Panfilov, and Hiroshi Harada (Nashville, Tennessee, 2000), p. 377.

Translated by N. Korovin

Physics of the Solid State, Vol. 46, No. 4, 2004, pp. 625–628. Translated from Fizika Tverdogo Tela, Vol. 46, No. 4, 2004, pp. 610–613.

METHODS OF FABRICATION AND PROCESSING OF DETONATION NANODIAMONDS

Synthesis, Properties, and Applications of Fractionated Nanodiamonds

S. I. Chukhaeva

Zababakhin All-Russia Research Institute of Technical Physics, Russian Federal Nuclear Center, Snezhinsk, Chelyabinsk oblast, 456770 Russia

e-mail: Chukhaeva@mail.snz.ru

Abstract—The methods for dispersing nanodiamond powders of different purity grades and preparing nanodiamond powder suspensions suitable for fractionation are analyzed. The main physicochemical properties of fractions separated from the synthesis products (blends) and purified nanodiamonds are investigated. It is found that the size distribution of nanodiamonds in the blend is inhomogeneous: an increase in the particle size leads to a decrease in the fraction of these particles. The advantages of nanodiamonds fractionated in size are demonstrated for different applications. © *2004 MAIK "Nauka/Interperiodica".*

1. INTRODUCTION

At present, nanodiamonds have found extensive application in many industrial processes. In this respect, particular research attention has been concentrated on the problems regarding the dispersion of the grain-size composition and its constancy in different media. However, there are only a few works concerned with the investigation into the influence of the particle size on the physicochemical and operational properties of nanodiamonds. The formation of stable nanodiamond particles occurs through a complex multistage mechanism [1, 2]. Since the particle surface is characterized by a high activity, the grain-size composition of the same nanodiamonds in various media can differ substantially [3]. The removal of water from these particles leads to the formation of stable aggregates that are difficult to disperse. In this work, I analyzed the methods for dispersing nanodiamond powders of different purity grades with the aim of preparing suspensions suitable for fractionation and investigated the properties of separated nanodiamond fractions and the synthesis products (blends).

2. ANALYSIS OF THE METHODS FOR DISPERSING NANODIAMOND POWDERS

One of the most universally employed methods for dispersing nanodiamond powders is ultrasonic treatment [4]. It has been found that the treatment of nanodiamond powders with a cation-exchange resin leads not only to a decrease in the amount of an incombustible residue (as was noted earlier in [5]) but also to the formation of sedimentation-resistant suspensions of treated nanodiamonds due to a deeper purification from cation impurities. A similar situation takes place upon treatment of nanodiamond powders with an anion-exchange resin. As is known, these effects are not observed upon simple washing of nanodiamond powders with distilled water at different temperatures (except for powders purified by gas-phase oxidation).

The nanodiamond powders studied in this work were prepared at the Zababakhin All-Russia Research Institute of Technical Physics, Russian Federal Nuclear Center [6]. The nanodiamond powders were processed using several methods, such as treatment with an AV-17P anion-exchange resin, treatment with a KU 8-2 cation-exchange resin, ultrasonic treatment on an UZG 3-10 setup, and combinations of these treatments. The efficiency of each technique of producing sedimentation-resistant suspensions was evaluated from the accumulation of nanodiamond sediments in a centrifugal force field of an OS-6M centrifuge (Russia). The particle sizes were calculated from the data obtained and relationship (1) (see below). Immediately prior to sedimentation measurements, all the studied suspensions were diluted with distilled water to a nanodiamond concentration of 5–10 g/dm^3. The electrical conductivity of these suspensions was equal to 4–8 μS/cm.

According to microscopic investigations of nanodiamond powders prepared at the Zababakhin All-Russia Research Institute of Technical Physics, Russian Federal Nuclear Center, nanodiamond crystallites are approximately spherical in shape. On this basis and taking into account the data obtained in [7, 8], the particle size (or, more precisely, the equivalent radius) was calculated from the Talbot–Svedberg equation for spherical particles:

$$r = \sqrt{\frac{9\eta}{2(\rho - \rho_0)\omega^2}\frac{\ln(h_2/h_1)}{t}}. \quad (1)$$

1063-7834/04/4604-0625$26.00 © 2004 MAIK "Nauka/Interperiodica"

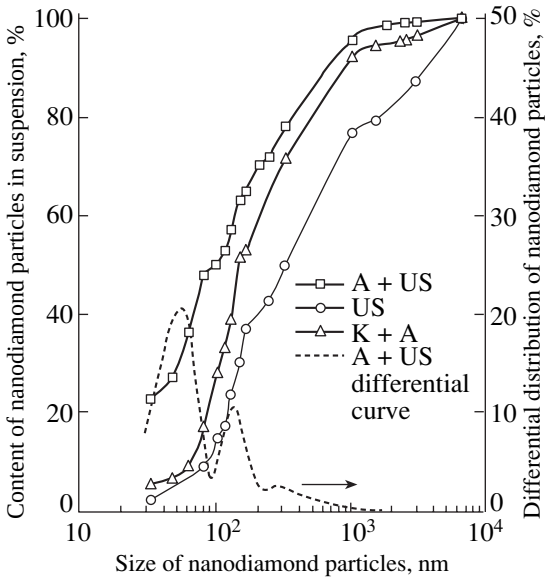

Fig. 1. Size distributions of nanodiamond particles prepared by different dispersion methods. Designations of the methods for processing nanodiamond powders: A + US = treatment with an anion-exchange resin and subsequent ultrasonic treatment, US = ultrasonic treatment, and K + A = treatment first with a cation-exchange resin and then with an anion-exchange resin.

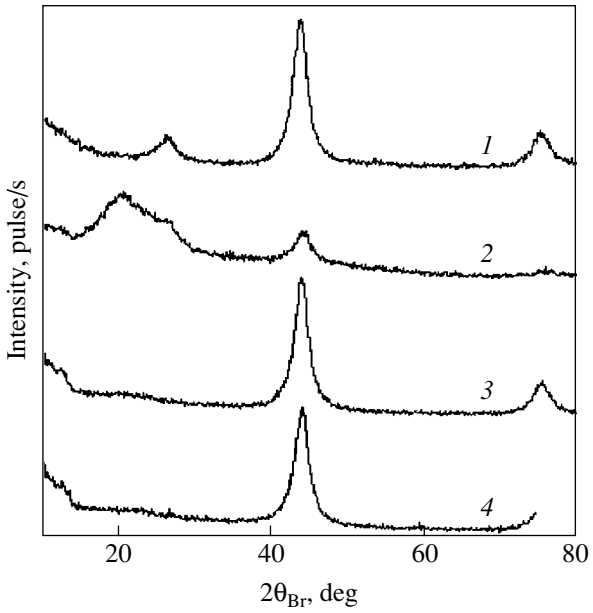

Fig. 2. X-ray diffraction patterns of blend fractions and separated nanodiamonds: (*1*, *3*) fraction **3** and (*2*, *4*) fraction **1**.

Here, r is the radius of the spherical particle [m]; η is the viscosity of the dispersive medium [Pa s]; ρ and ρ_0 are the densities of the nanodiamond and dispersive medium [kg/dm^3], respectively; $\omega = 2\pi n$ is the rotational speed of the centrifuge rotor (n is the number of revolutions per second); $(h_2 - h_1)$ is the distance passed by the particle in the centrifugal force field [m]; and t is the time of sedimentation of the particle from the level h_1 to the level h_2 [s].

Figure 1 shows the size distributions of nanodiamond particles in the sample prepared by mixing equal amounts of seven commercial batches stored for four and six years.

Table 1. Physicochemical properties of fractions separated from commercial nanodiamonds (prepared at the Zababakhin All-Russia Research Institute of Technical Physics, Russian Federal Nuclear Center)

Parameter	Fraction **1**	Fraction **2**	Fraction **3**
Size range, nm	250–7000	100–250	5–100
external appearance	light gray readily free-flowing powder	gray powder	black crystalline aggregates
Pycnometric density, g/cm^3	3.2	3.25	3.3
Incombustible residue, %	1.6	1.3	0.9
Oxidizable carbon, %	1.0	1.5	1.9
Viscosity of aqueous suspension (nanodiamond concentration, 10 g/l; temperature, 20°C), mPa s	1.04	1.07	1.12
Electrokinetic potential ξ, mV	+16	+32	+41
Specific surface*, m^2/g	170	Not determined	48
Sorption capacity with respect to benzene, mmol/g	17–18	15–16	12–13

* Determined by the Brunauer–Emmett–Teller method (nitrogen) at the Bakul' Institute for Superhard Materials of the National Academy of Sciences of Ukraine. The specific surface of an unfractionated powder is equal to 227 m^2/g.

Table 2. Physicochemical properties of fractions of the blend for the preparation of commercial nanodiamonds

Parameter	Fraction **1**	Fraction **2**	Fraction **3**
external appearance	black readily free-flowing powder	dark gray free-flowing powder	black crystalline aggregates
Pycnometric density, g/cm^3	2.6–2.7	2.9	3.1
Incombustible residue*, %	2–3	0.4–1.0	0.1–0.5
Nondiamond carbon**, %	40–50	25	5–10
Activation energy for oxidation of nondiamond carbon, kJ/mol	55–60	70–75	90–95
Thermal stability, °C	160–165	200–210	>450
Sorption capacity with respect to benzene (20°C), mmol/g	24–26	22–24	18–20

* After acid treatment, the value depends on the initial content in the blend.

** The content of nondiamond carbon in the initial unfractionated blend amounts to 76%.

The analysis of the experimental data obtained allows us to draw the following inferences.

(1) The most finely dispersed suspensions of nanodiamonds can be prepared only by combining the ultrasonic and ion-exchange resin treatments.

(2) The treatment with only ion-exchange resins is more efficient than the ultrasonic treatment under the operational conditions provided by the generator.

Moreover, prior to sedimentation measurements, it is necessary to carry out additional purification of aqueous phases of suspensions from ion impurities precipitated upon ultrasonic dispersion.

3. SEPARATION OF FRACTIONS FROM NANODIAMONDS OF DIFFERENT PURITY GRADES

Reasoning from the analysis of the particle size distributions of nanodiamonds, the nanodiamond particles were conventionally divided into three fractions. The results of this fractionation were considered in [6]. By analogy, fractions of the blend were separated from the synthesis products of nanodiamonds. The main physicochemical characteristics of the fractions separated from commercial nanodiamonds and fractions of the blend are presented in Tables 1 and 2, respectively.

As can be seen from the x-ray diffraction patterns (Fig. 2), the fractions of the blend are characterized not only by different contents of nanodiamonds but also by differences in the structure of nondiamond carbon. In particular, the x-ray diffraction pattern of fraction **3** exhibits a weak peak that corresponds to $d = 3.376$ Å (curve *1*) and is assigned to the 2*H* crystalline modification of graphite in the hexagonal crystal system. In the diffraction pattern of fraction **1**, this peak overlaps with a diffuse halo in the angle range $2\theta_{Br} = 18°–26°$ (curve *2*), which corresponds to the amorphous phase. It was revealed that the amounts of the oxidizing agent used for separating diamonds from the blend fractions differed by a factor of 1.5. This fact and the experimental activation energies for the oxidation of nondiamond carbon indicate that the chemical compositions of the nondiamond components differ significantly.

4. PROSPECTS OF APPLYING FRACTIONATED NANODIAMONDS

In a number of cases, the fractionation of nanodiamonds increases the efficiency of their application. For example, the use of fraction **3** in gold electroplating leads to an increase in the microhardness of the coating by a factor of approximately 1.5 [9]. In the case of nickel coatings on different metal matrices and in galvanic cells of different designs, the use of fraction **3** ensures an increase in the microhardness as compared to unfractionated nanodiamonds (Table 3).

According to the data obtained at the Bakul' Institute for Superhard Materials of the National Academy of Sciences of Ukraine, the abrasive capacity of pastes prepared with fractions **3** and **1** of commercial nanodiamonds was higher than that of pastes prepared with unfractionated nanodiamonds. The rate of stock removal from a silicon sample at ASM 0.1/0 was equal

Table 3. Microhardnesses $HV_{0.05}$ of nickel coatings with commercial nanodiamonds (kg/mm^2)

Sample no.	Type of nanodiamonds in coatings	Data taken from [10]	After using an electrolyte for two years
1	Without nanodiamonds	370	348
2	Fraction **1**	370–420	384
3	Fraction **2**	360	379
4	Fraction **3**	540–560	420
5	Unfractionated	470	365

to 0.26–0.28 μm/min, and the roughness of the treated silicon surface was $R_a \approx 0.03$–0.1. For comparison, the rate of stock removal from a silicon sample with the use of a paste produced from unfractionated nanodiamonds was equal to 0.05 μm/min.

Upon the addition of blend fraction **1** (0.3–1.0%) to a VELS-2 engine oil, the friction coefficient for bronze friction pairs decreased by a factor of no less than two, whereas the unfractionated blend exhibited abrasive properties.

5. CONCLUSIONS

Thus, it was demonstrated that the described methods of dispersing nanodiamond powders make it possible to prepare sedimentation-resistant suspensions and to enhance the nanodiamond activity lost upon drying. It was established that the size distributions of nanodiamonds and nondiamond carbon species are inhomogeneous and the physicochemical properties of nanodiamonds differ from those of blends. This offers new possibilities for expanding the field of application of nanocarbon materials and improving technological processes: nondiamond carbon should be removed not from a synthesis product but only from fractions whose operational characteristics deteriorate in the presence of nondiamond carbon.

ACKNOWLEDGMENTS

The author would like to thank G.P. Bogatyreva and Yu.I. Nikitin for performing measurements at the Bakul' Institute for Superhard Materials of the National Academy of Sciences of Ukraine and I.V. Novikova for conducting x-ray diffraction investigations.

REFERENCES

1. A. L. Kupershtokh, A. P. Ershov, and D. A. Medvedev, Fiz. Goreniya Vzryva **34** (4), 102 (1998).
2. M. V. Baĭdakova, A. Ya. Vul', V. I. Siklitskiĭ, and N. N. Faleev, Fiz. Tverd. Tela (St. Petersburg) **40** (4), 776 (1998) [Phys. Solid State **40**, 715 (1998)].
3. L. V. Agibalova, A. P. Voznyakovskiĭ, V. Yu. Dolmatov, and V. V. Klyubin, Sverkhtverd. Mater., No. 4, 87 (1998).
4. E. M. Oparin, RF Patent No. 2,088,689.
5. T. M. Gubarevich, N. M. Kostyukova, R. R. Sataev, and L. V. Fomina, Sverkhtverd. Mater., No. 5, 31 (1991).
6. S. I. Chukhaeva, P. Ya. Detkov, A. P. Tkachenko, and A. D. Toropov, Sverkhtverd. Mater., No. 4, 29 (1998).
7. A. E. Aleksenskiĭ, M. V. Baĭdakova, A. Ya. Vul', *et al.*, Fiz. Tverd. Tela (St. Petersburg) **42** (8), 1531 (2000) [Phys. Solid State **42**, 1575 (2000)].
8. P. W. Chen, Y. S. Ding, Q. Chen, *et al.*, Diamond Relat. Mater. **9**, 1722 (2000).
9. E. N. Loubnin, S. M. Pimenov, A. Blatter, *et al.*, New Diamond Frontier Carbon Technol. **9** (4), 273 (1999).
10. A. D. Toropov, P. Ya. Detkov, and S. I. Chukhaeva, Gal'vanotekh. Obrab. Poverkhn., No. 3, 14 (1999).

Translated by O. Borovik-Romanova

Physics of the Solid State, Vol. 46, No. 4, 2004, pp. 629–635. Translated from Fizika Tverdogo Tela, Vol. 46, No. 4, 2004, pp. 614–620.

METHODS OF FABRICATION AND PROCESSING OF DETONATION NANODIAMONDS

Macrokinetics of the Retention of Condensed Carbon and Detonation Diamond in a Hermetic Explosion Chamber

V. A. Mazanov

All-Russia Research Institute of Experimental Physics, Russian Federal Nuclear Center, Sarov, Nizhni Novgorod oblast, 607190 Russia

e-mail: Mazanov@otd13.vniief.ru

Abstract—The effect of the thermophysical parameters of a cooling medium on the macrokinetics of secondary physicochemical processes that occur in a hermetic chamber after the explosion of a solid explosive charge is studied. The yields of condensed carbon and the content of the diamond phase in it are mainly determined by the temperature of the medium in the chamber after explosion. The maximum yield of detonation diamond synthesized from a trinitrotoluene–hexogen TG50/50 alloy is equal to ~10% of the initial explosive mass and is achieved when the steady-state temperature of the medium in the chamber does not exceed $T_m = 550 \pm 50$ K. As this temperature increases, the yield of detonation diamond decreases approximately in inverse proportion to the temperature, and, at $T_m > 2800$ K, there is virtually no diamond phase in the explosion products. The conversion of condensed carbon due to the presence of the oxygen-containing components of the explosion products (CO_2, H_2O) begins at a temperature of the medium of above 1550 ± 150 K. The decrease in the final energy release that is experimentally detected in calorimetric studies in the case of an explosion of solid explosives with a negative oxygen balance in an inert gaseous medium or in the case where explosives are surrounded by massive shells results from the endothermic conversion of condensed carbon, which absorbs a significant portion of the explosion energy. *© 2004 MAIK "Nauka/Interperiodica".*

1. INTRODUCTION

The diamond phase of carbon detected in the products of explosion of solid explosives with a negative oxygen balance and the detonation synthesis of nanodiamonds developed using explosion chambers aroused interest in the physicochemical processes that occur in closed explosion chambers after detonation [1–7].

2. EXPERIMENTAL

To study the effect of the inert-gas mass and thermophysical processes on the yield of condensed carbon (CC) and the content of ultrafine-dispersed diamonds (UDDs), we used spherical explosion chambers 0.65–1.2 m in diameter (space volume 0.14–800 m^3). Charges of a trinitrotoluene–hexogen TG50/50 alloy 0.05–140 kg in weight were exploded in vacuum, a nitrogen or a helium atmosphere, the atmosphere of explosion products (EPs), atmospheric air, and water shells. The mass of a cooling gaseous or water medium was varied from 10^4 to 20 times the explosive mass. The experimental results are published in part in [3, 4, 7]. To determine the parameters of the medium, we recorded the pulse and quasi-static pressures with pressure transducers. Calorimetric measurements of explosions were carried out using thermocouples placed on an explosion chamber.

After each experiment, we collected a diamond-containing mixture from the chamber, screened it through a vibrosieve with a cell size of ~0.3 mm to remove mechanical impurities, and dried it at a temperature of ~80°C in order to completely remove moisture. The dried mixture was weighed to find the final CC yield $\beta_{cc} = m_{cc}/m$ and then was chemically cleaned with an acid (for details, see [4]). After each experiment, using the results of chemical cleaning, we determined the yield of UDDs (the ratio of the UDD mass to the explosive mass $\beta_d = m_d/m$) and the UDD content in the mixture (the ratio of the UDD mass to the mixture mass m_d/m_{cc}).

3. SPECIFIC FEATURES OF EXPLOSION OF AN EXPLOSIVE CHARGE IN A CLOSED CHAMBER

Analysis of the motion of a shock wave after the detonation of an explosive charge and the pressure profile at the chamber wall allows us to arbitrarily divide the explosion of the explosive charge in a chamber into four qualitatively different stages [6–8] (Fig. 1): the detonation of the explosive charge (stage I); the flight of the EPs into the undisturbed gas medium (stage II); the circulation of the shock wave and the turbulent motion of the EPs with the medium in the space (stage III); and the attainment of a quasi-static state and radiative–convective cooling of the EPs–gas mixture (stage IV). For explosive charges weighing up to 100 kg, the duration of stage I is 10–20 μs. Stage II lasts from the instant the

1063-7834/04/4604-0629$26.00 © 2004 MAIK "Nauka/Interperiodica"

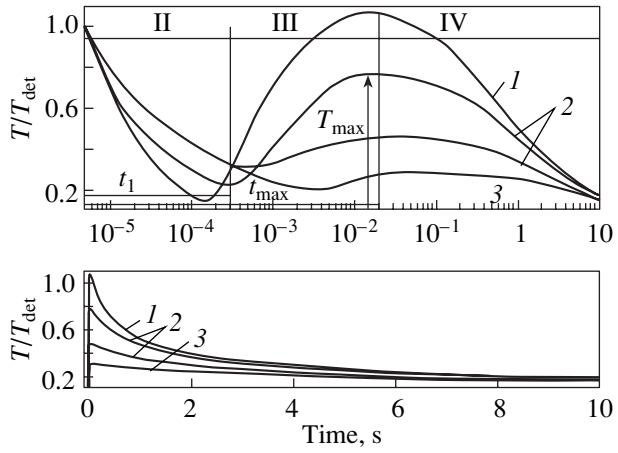

Fig. 1. Average EP temperature in a chamber 2 m in diameter: (*1*) explosion of an explosive charge in vacuum, (*2*) explosion in a gaseous medium, and (*3*) explosion of an explosive charge surrounded by a water shell (m_w/m = 10). T_{det} = 3270 K is the temperature of TG50/50 detonation; T_{max} is the maximum steady-state temperature of a mixture of the EPs and the environment; and t_1 and t_{max} are the times of arrival of the first shock wave to the shell and of the establishment of a quasi-static regime, respectively.

detonation wave reaches the outer boundary of the explosive charge until the first shock wave reaches the chamber wall. For chambers 2–3 m in diameter, this time is equal to 200–800 μs. In the course of stage III, shock waves gradually transform into acoustic pulsations with amplitudes of several atmospheres and periods specified by the medium temperature and the chamber space size. For the chambers noted above, this time is 25–100 ms. Stage IV (cooling of the EPs–gas mixture) lasts several tens of seconds.

In the theoretical work [9], where turbulent mixing was not taken into account, a strongly nonuniform radial temperature distribution was found to occur in the space after damping of the gas-dynamic processes. These nonuniformities level off only after convective mixing, which takes a long time. However, as shown in [3, 10, 11], the low-density core that forms upon the first flight of the EPs exists only until the second or third wave circulation. The development of gas-dynamic instabilities (the Rayleigh–Taylor and Richtmyer–Meshkov instabilities) results in turbulent mixing of the medium components on the molecular level. After 7–15 passes of the shock wave, a multicomponent medium consisting of the EPs and the ambient gas forms, in which the spatial distribution of parameters can be assumed to be virtually uniform. This assumption is supported by the dynamics of after burning of the EPs in atmospheric oxygen, which was studied experimentally and theoretically in [3, 7, 11, 12].

Figure 1 shows (on a semilogarithmic scale) the average EP temperature in the space of the chamber filled with various media, beginning from the instant of detonation to complete cooling. In stages II and III, the temperature was determined from the EP internal energy, which is equal to the total explosion energy release less the kinetic energy of the moving EPs. In stage IV, the temperature was determined from the gas-medium pressure experimentally measured in the chamber space.

As is seen from Fig. 1, the most rapid and strongest gas-dynamic cooling of the EPs with a cooling flow density of up to ~10^3 MW/m^2 is detected for the explosion in vacuum because of the high flight velocities. However, very high temperatures are achieved when the EPs impinge on the chamber wall [9]; after all shock waves have been damped, the temperature in the space is ~3500 K, which is close to the detonation temperature. Therefore, detonation diamond and CC cannot survive after explosion in vacuum [4, 6].

The slowest gas-dynamic cooling is observed for the flight of the EPs surrounded by massive water shells (m_w/m = 10–20), and the maximum temperature of the EPs in this case does not exceed 500–800 K because of efficient energy removal by the water shells [4, 6]. The explosion in an inert atmosphere is intermediate between the explosion in vacuum and the explosion in a water shell (in terms of the intensity of gas-dynamic cooling), since the flight velocity of the EPs in the gas atmosphere is lower than that in vacuum and greater than that in the presence of a water shell. The maximum temperature of the medium depends on the ratio of the EP mass to gas mass; in particular, at m_c/m = 10–20, we have $T_m = T_0 + mQ_{ex}/C_v(m_c + m) \sim (2–3)T_0 \sim$ 600–900 K, where Q_{ex} is the specific energy released upon the explosion of the explosive charge (calorific value of the explosive), C_v is the specific heat of the atmosphere, and T_0 is the initial temperature.

4. COOLING OF THE HEATED MIXTURE OF THE EXPLOSION PRODUCTS AND THE AMBIENT GAS

As is seen from Fig. 1, the detonation products, including CC and its diamond phase, are exposed to high temperatures mainly during the longest stage (stage IV); here, due to the relatively slow reaction of CC gasification, the transformations can be highly profound [13]. The medium heated by explosion and restricted by a cold shell is intensely cooled (Fig. 1, stage IV). Thermodynamic calculations [14] and experimental data on the composition of the gas medium show that, after the explosion of a solid explosive charge, a significant amount of molecules of triatomic gases (CO_2, H_2O) and highly dispersed carbon particles are present in the chamber. According to [15, 16], these molecules and particles have high radiant emittance. Therefore, the cooling of this medium is characterized by heat transfer by convection and radiation [15].

Based on an analysis of numerous experimental data, it was shown in [7, 8] that the dependence of the

heat flow density $q(T)$ on the volume-averaged gas temperature T follows a power law,

$$q(T) = kT^n. \quad (1)$$

The empirical parameters k and n depend mainly on the dimensions of the chamber. For example, for chambers 2–12 m in diameter, n = 3–4.

The authors of [7, 14] solved the non-steady-state heat balance equation for a gas in the closed space of an explosion chamber and found that $C_v\rho dT/dt = -Fq(T)/V$. Using the empirical dependence of the heat flow density of a mixture of the EPs and gas on the temperature given above, we obtain the dependence of the average temperature T of the medium on time t: $1/T^{n-1} = 1/T_m^{n-1} + Bt$. Here, C_v is the volume-averaged specific heat of the medium in the chamber; F and V are the surface and volume of the chamber space, respectively; $T_m = T_0 + mQ_{ex}/C_v(m + m_0)$ is the maximum temperature of the medium in the chamber after explosion; $\rho = (m + m_0)/V$ is the average medium density in the chamber; and $B = (n - 1)Fk/(VC_v\rho)$.

5. RETENTION OF CONDENSED CARBON IN THE EXPLOSION PRODUCTS AND ITS DIAMOND PHASE

In [1, 2, 6], optimum conditions for the retention of CC and detonation diamond were determined using the generalized empirical criterion based on the "specific heat of the medium" $\mu = (C_{v0}\rho_0 Vp)/(p_0 mQ_{ex}) = (C_{v0}M_{0x})/(mQ_{ex})$. Here, p and p_0 are the working and normal initial pressures in the chamber, respectively; ρ_0 and C_{v0} are the density and the specific heat of the gas under normal conditions, respectively; and m and Q_{ex} are the explosive mass and its calorific value, respectively. In [6], this approach was extended to two-phase systems of cooling diamond-containing EPs, in particular, to the case of explosive charges in water shells. This approximate engineering–physical approach made it possible to describe the yields of CC and UDDs as a function of the explosive mass, chamber volume, and cooling conditions using the experimental results. Note that the reciprocal to the generalized variable μ, which was used in the papers mentioned above, is equal to the maximum chamber volume–averaged excess temperature ($\Delta T' = T_{m'} - T_0$) of the cooling medium heated by the explosion of an explosive charge and is calculated without regard for the EP mass at a constant specific heat of the gaseous medium in the space: $\mu^{-1} = mQ_{ex}/C_v m_{0x} = \Delta T_{m'}$. The maximum excess temperature of the medium in the chamber is equal to $\Delta T_{max} = mQ_{ex}/C_v(T)(m + m_{0x})$.

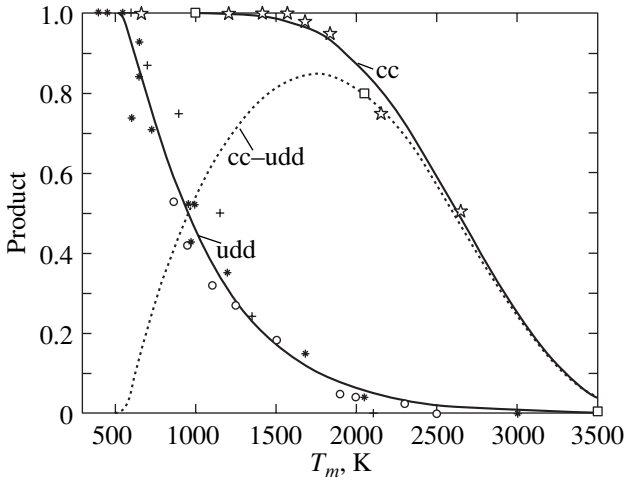

Fig. 2. Final yields of CC and its diamond phase as functions of the maximum medium temperature T_m in the chamber. The curves of retained CC and UDDs (cc and udd, respectively) are calculated using Eqs. (2) and (3), respectively. The cc–udd curve shows the accumulation of nondiamond carbon modifications, and points represent the experimental data.

6. ANISOTHERMIC MACROKINETICS OF THE GASIFICATION OF CONDENSED CARBON IN THE EXPLOSION CHAMBER

In Fig. 2, the CC yield versus the maximum temperature of the gaseous mixture in the chamber is plotted for chambers 0.65, 2.0, 3.2, and 12 m in diameter (obtained in this work) and for explosion chambers having a volume of 0.18 and 3 m^3 (borrowed from [2, 6, 17, 18]). The maximum medium temperature for chambers 0.14, 4.2, 17, and 805 m^3 in volume was determined from the experimentally measured pressures, whereas for the data from [2, 6, 17, 18] the maximum temperature was calculated using the relations given in [7]. It is seen that, at $T_m < 1550 \pm 150$ K, the CC yield is maximum and, for TG50/50, is equal to $\beta_{cc} = m_{cc}/m$ = 12–14%. As T_m increases to 3000–3500 K, the CC yield decreases virtually to zero ($\beta_{cc} < 0.5\%$) upon the explosion of the TG50/50 charges in vacuum at $m/m_c > 5$. After the explosion of charges in vacuum in the chambers 0.65–2 m in diameter, a high content of carbon oxide is detected and the thermal effect of explosion is smaller than Q_{ex} by 100–200 kcal/mol [3, 19].

According to [14, 19], the retention of CC in the EPs is determined by the heterophase endothermic reactions of gasification of CC with (a) carbon dioxide and (b) steam, which can be represented by general formula (c):

$$C + CO_2 \longrightarrow 2CO - Q_1, \quad (a)$$

$$C + H_2O \longrightarrow CO + H_2 - Q_2, \quad (b)$$

$$C + CO_2 + H_2O \longrightarrow 3CO + H_2 - Q, \quad (c)$$

where Q_1 = 41.2 kcal/mol, Q_2 = 31.1 kcal/mol, and $Q = (Q_1 + Q_2)/2$.

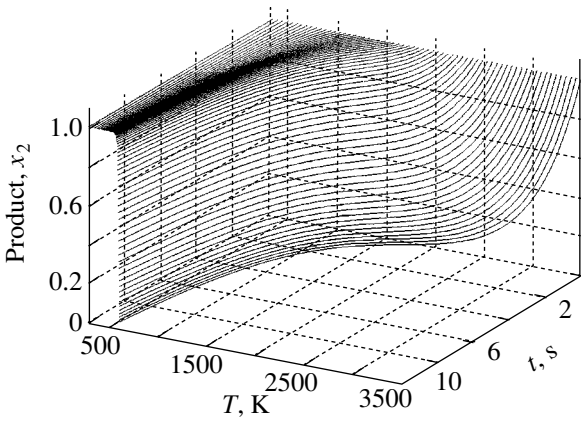

Fig. 3. Trajectory of the retention of CC in the coordinates $\{x_2, T, t\}$ in the anisothermic periodic reactor of ideal mixing in which the medium temperature varies according to the law $1/T^2(t) = 1/T_m^2 + B_1 t$. The set of equations (2) and (3) is solved numerically with the MatLab 5.3 software package.

We assume that, in the stage of cooling of the medium heated by explosion, there are no gradients of the state variables (pressure, temperature, density, concentration) of the medium in the chamber because of intense turbulent mixing of the components, which were initially spaced. Therefore, we can apply the ideal-mixing model and consider that the partial derivatives of these parameters with respect to a spatial variable are equal to zero. On the other hand, the EP temperature, which strongly affects the chemical reaction rates, varies from the detonation temperature $T_{det} \sim$ 3500–4500 K to T_m and, during cooling, to T_0 (Fig. 1). We also assume that a considerable amount of the material does not have time to react in stages II and III because of their short duration and that the controlling step of the secondary, relatively slow chemical reactions of CC gasification is the longest stage (cooling). This assumption allows us to apply the anisothermic model of an ideal-mixing periodic reactor for momentary explosion, which describes chemical reactions in the reactor in terms of a set of ordinary differential equations. This approach significantly simplifies the kinetic study and makes it possible to obtain quantitative relations for the yield of the final product [20].

The dependences obtained in the context of the diffusion-kinetic theory of heterogeneous combustion and gasification of solid carbon fuel [21, 22] are inadequate for describing the processes that occur in the space of an explosion chamber after the explosion of an explosive charge, since these dependences have been derived and experimentally checked for constant values of the medium temperature and CO_2 concentration. As noted above, the gasification of carbon in the EPs in explosion chambers is a non-steady-state process due to the decrease in the temperature of the medium caused by its cooling and the decrease in the concentration of reagents (carbon dioxide, steam, and CC). Since clusters are sufficiently small (a detonation diamond cluster contains ~10^3–10^4 atoms), we consider them as large molecules [16] and apply the equations of the kinetics of a homogeneous system to the gas–cluster heterogeneous system.

For the gasification of CC clusters, we use the macrokinetic equation of a formally simple chemical reaction [20]

$$dx_1/dt = k_0 \exp(-E_a/RT)(a - x_1)^\nu, \qquad (2)$$

and write the heat balance equation making allowance for a small endothermic effect for the CC conversion (the thermal effect Q of the chemical reaction is nonzero) in the form [14, 23]

$$C_\nu \rho dT/dt = -Fq(T)/V + Qk_0 \exp(-F_a/RT)(a - x_1)^\nu \qquad (3)$$

for $0 < t < \infty$, $0 < x < a$, and the initial conditions $T(0) = T_m$ and $x_1(0) = 0$.

Here, a is the initial CC mass in moles; x_1 is the current mass of gasified CC in moles; T is the current medium temperature; t is the time; ρ is the medium density in the reactor; k_0 is the preexponential factor; E_a is the activation energy; ν is the formal chemical reaction order; T_m is the initial medium temperature in the reactor after heating; T_0 is the temperature of the reactor walls ($T_m \gg T_0$); F and V are the reactor surface and volume, respectively; q is the density of the heat flow from the reacting medium to the cold wall; and C_ν is the average specific heat of the medium.

The set of equations (2) and (3) gives the solution of the kinetic problem of transformation of reagents in the chemical reaction proceeding in an ideal-mixing periodic reactor at a variable temperature obeying the power-law dependence $1/T^{n-1} = 1/T_m^{n-1} + Bt$ characteristic of the radiative heat transfer for triatomic molecules of gases (CO_2, H_2O) and clusters [see Eq. (1)]. Obviously, the degree of transformation $x_2 = (a - x_1)/a$ is a single-valued function of the kinetic (E_a, k_0, ν) and thermophysical (B, n, T_m) parameters of the medium in the reactor.

In Fig. 2, the results of simulation of CC gasification [17, 23] are compared with the experimental data. The calculation is seen to agree satisfactorily with the experimental data on the retention of CC in explosion chambers at E_a = 125 kJ/mol and ν = 0.7. In particular, there is virtually no CC in the explosion chamber at temperatures above 3500 K due to complete gasification and CC is completely retained at temperatures below 1550 K.

Figure 3 shows the phase surface of the ideal-mixing periodic reactor with kinetic curves of CC retention $x_2 = (a - x_1)/a$ obtained by solving the set of equations (2) and (3) numerically; these curves specify the dependence of the amount of retained CC x_2 on the time t

and maximum temperature T_m upon cooling the medium in the chamber to the initial temperature T_0. The computation was performed with the MatLab 5.3 software package.

It is seen from Fig. 3 that, as the temperature drops, the reaction "freezes" (is retarded) and the CC (product) concentration levels off (reaches a plateau). At constant values of the kinetic parameters (E_a, k_0, ν) and the cooling rate (B, n), the height of this plateau is a single-valued function of the maximum temperature of the medium; the higher the temperature, the higher the degree of the chemical reaction and the lower the concentration of the initial reagent. The faster the decrease in the temperature (the increase in the cooling parameter B in the cooling zone), the faster the decrease in the reaction rate and the higher the degree of retention of the initial material. The dependence of the yield of the product on T_m (Fig. 3) has a specific shape: there is a maximum temperature at which the yield of the final product becomes virtually zero and a temperature below which the yield is always equal to unity. As the activation energy increases, the curve of the product retention shifts toward higher temperatures.

7. MACROKINETICS OF THE DESTRUCTION OF THE DIAMOND PHASE IN THE CONDENSED EXPLOSION PRODUCTS

Natural and synthetic diamond crystals have a rather high thermal stability. For example, according to [18], the reverse transition of single-crystal tool diamond to graphite (graphitization) at an initial pressure of 1 atm or in vacuum proceeds at 1400–1700 K over a period of several minutes. The diamond–graphite phase transition upon annealing of cleaned clusters of detonation diamond in an inert gaseous atmosphere begins at a temperature higher than 1000–1300 K [24].

Crude clusters of condensed EPs consist of a mixture of the diamond and nondiamond carbon modifications [25]. Because of the presence of an outer closed shell (onion-like carbon) and a "gas fur," the CC clusters differ significantly from pure UDD clusters in terms of their structural and physicochemical properties and are close to nongraphitizing carbon black [26]. Therefore, the thermal–kinetic parameters (activation energy, graphitization temperature, etc.) of the retention of a diamond mixture and pure UDDs can differ significantly [24, 26] and the thermal resistance of the diamond phase in crude condensed EPs is lower than that of cleaned UDD clusters. The temperature of the onset of oxidation of crude condensed EPs is 650 ± 50 K [26, 27], and the oxidation is a two-stage process with maxima at 670 and 770 K. These results of laboratory thermal analysis agree well with the boundary temperature of the onset of graphitization of a diamond mixture determined from the experimental explosion data on detonation synthesis of diamond, which is equal to 550 K (Fig. 2).

Assuming that the transformation of the crystal lattice of a detonation-diamond cluster into a nondiamond phase, because of temperature fluctuations of carbon atoms at lattice sites, obeys the Arrhenius law, we can use formal kinetic equation (2) to describe graphitization. The activation energy E_a for the diamond–graphite transition in a CC cluster (which depends on its structure and size and the presence of functional chemical groups on its surface) and the effective graphitization reaction order ν_a are also unknown in general. Therefore, they were also chosen to fit the experimental data using mathematical simulation. The macrokinetics of the retention of the diamond phase in the CC of explosion products can be described sufficiently accurately if we assume that the graphitization of the diamond phase in the detonation carbon proceeds with an activation energy of ~11.5 kJ/mol and has an order $\nu_a = 0.6$.

Figure 2 generalizes the experimental data on the yield of CC β_{cc} and detonation diamond β_d obtained in chambers ranging in volume from 0.1 to 20 m^3 upon the explosion of TG50/50 explosive charges in various cooling media (vacuum, inert gases, water shells, etc.) [2, 4, 6, 28, 29]. Note that, since the explosive composition and detonation parameters (detonation rate, pressure, temperature) did not change, the variation of the yields of CC and UDDs is unambiguously caused by different conditions of cooling of the detonation products.

A comparison of the calculated and experimental data (Fig. 2), which were obtained by various authors and are in good agreement, shows that the degree of retention of both CC and detonation diamond decreases with increasing maximum temperature of the medium, T_m. As T_m increases, the rate of decreasing the fraction of the diamond phase is maximal in the solid EPs. The experiments indicate that, at a temperature of the medium of below 450–600 K, the yield of UDDs is maximal ($\beta_d \sim 10\%$ for TG50/50). As the temperature increases, the yield of detonation diamond decreases virtually in inverse proportion to T_m, and, at $T_m = 2000$ K, we have $\beta_d = 1\%$. This dependence of the UDD yield on the maximum temperature of the medium in the chamber after explosion is described well by the simple empirical formula $\beta_d = \text{const}/T_m - 0.2$.

Subtracting the fraction of retained diamond $h_d = (a_{0d} - x_d)/a_{0d}$ from the retained fraction of CC $h_{cc} = (a_{0cc} - x_1)/a$, we obtain the fraction of nondiamond modifications $h = h_{cc} - h_d$ retained in the chamber after explosion. As is seen from Fig. 2, the nondiamond carbon modifications (in particular, graphite) accumulate with increasing temperature T_m. The yield of the nondiamond carbon modifications reaches a maximum (~6%) at $T_m \sim 1400$ K and becomes almost zero at $T \sim 3500$ K (Fig. 2, curve cc–udd). This is caused by the fact that the amount of graphite, which is an intermediate product, is determined by two competing processes, namely, graphite inflow due to diamond graphitization and the consumption of graphite upon gasification of

the solid phase. Because of the low activation energy for the first reaction (~11 kJ/mol) and high activation energy for the second reaction (~125 kJ/mol), the graphitization rate is higher than the gasification rate at moderate temperatures ($T < 1000$ K), which results in the accumulation of a carbon nondiamond phase. At high temperatures ($T > 2500$ K), where diamond is virtually absent, the amount of retained graphite decreases and is consumed for the formation of carbon oxide.

8. FINAL ENERGY RELEASE OF EXPLOSIVES WITH A NEGATIVE OXYGEN BALANCE IN AN INERT GAS ATMOSPHERE

Our study of the explosion stages of an explosive charge in a chamber and the consideration of the macrokinetics of the secondary physicochemical processes show that the decrease in the final energy release of an explosive Q_{ex} [3, 19] is a result of the endothermic gasification of CC by the oxygen-containing EPs (CO_2, H_2O), which proceeds against the background of a temperature varying in time, since this gasification absorbs a significant portion of the detonation energy. At small values of m_c/m, a high maximum temperature T_m is reached and the endothermic gasification of CC develops to high degrees, which leads to a decrease in Q_{ex}. With increasing m_c/m, T_m decreases, the amount of retained CC increases, and Q_{ex} increases. When $T_m^* \sim 1550$ K is reached, no gasification occurs and the thermal effect of explosion Q_{ex} is maximum and equal to the heat of detonation Q_{det}. Therefore, calorimetric measurements of the detonation energy release of solid explosives should be performed at $m_c/m > (m_c/m)^* = (Q_{det}/C_v(T)(T_m^* - 300)) - 1 \sim 3.5$ (see also [19]); in this case, $T_m < T_m^*$ and, therefore, CC gasification does not occur and Q_{det} is not changed.

9. CONCLUSIONS

Thus, by considering four separate stages of the explosion of a solid explosive charge in a closed chamber and using the anisothermic periodic reactor of ideal mixing, we have developed a macrokinetic model of retention of CC and its diamond phase that form during detonation and quantitatively described their yields depending on the thermophysical parameters of the medium in an explosion chamber. The maximum yield of detonation diamond synthesized from the trinitrotoluene–hexogen TG50/50 alloy is equal to ~10% and is achieved at a steady-state temperature in the chamber not exceeding $T_m = 550 \pm 50$ K. When this temperature is exceeded, the yield of detonation diamond decreases approximately in inverse proportion to the temperature, and, at $T_m > 2800$ K, there is virtually no diamond phase in the EPs.

Considerable conversion of CC in the presence of the oxygen-containing EP components (CO_2, H_2O) begins at a boundary temperature of the medium exceeding 1550 ± 150 K. The decrease in the final energy release (experimentally detected in calorimetric studies) upon the explosion of solid explosives with a negative oxygen balance placed in an inert gaseous medium or surrounded by massive shells results from the endothermic CC conversion, which absorbs a significant portion of the explosion energy.

The approach described above helped us to choose optimum cooling conditions for producing UDDs.

ACKNOWLEDGMENTS

The author is grateful to B.A. Vyskubenko, V.F. Gerasimenko, V.V. Koksharov, É.É. Lin, A.V. Pevnitskiĭ, V.P. Solov'ev, D.V. Strakhov, and A.P. Tolochko for technical assistance and helpful discussions.

REFERENCES

1. A. I. Lyamkin, E. A. Petrov, A. P. Ershov, *et al.*, Dokl. Akad. Nauk SSSR **302** (3), 611 (1988) [Sov. Phys. Dokl. **33**, 705 (1988)].
2. E. A. Petrov, G. V. Sakovich, and P. M. Brylyakov, Dokl. Akad. Nauk SSSR **313** (4), 862 (1990) [Sov. Phys. Dokl. **35**, 765 (1990)].
3. V. A. Andronov, S. M. Bakhrakh, V. A. Mazanov, *et al.*, Dokl. Akad. Nauk SSSR **314** (6), 1385 (1990) [Sov. Phys. Dokl. **35**, 897 (1990)].
4. B. A. Vyskubenko, V. V. Danilenko, É. É. Lin, *et al.*, Fiz. Goreniya Vzryva **28** (2), 108 (1992).
5. D. Ornellas, D. Karpenter, and S. Gan, Prib. Nauch. Issled. **7**, 92 (1966).
6. Yu. I. Mal'kov, Fiz. Goreniya Vzryva **29** (5), 93 (1993).
7. B. A. Vyskubenko, V. V. Koksharov, V. A. Mazanov, *et al.*, in *Proceedings of the 3rd Khariton Topical Scientific Readings on Extremal State of Substance, Detonation, and Shock Waves* (Vses. Nauchno-Issled. Inst. Éksp. Fiz., Sarov, 2002), p. 333.
8. B. A. Vyskubenko, V. V. Koksharov, V. A. Mazanov, *et al.*, in *Khariton Scientific Readings* (2003) (in press).
9. A. P. Ershov and A. L. Kupershtokh, Fiz. Goreniya Vzryva **23** (3), 118 (1986).
10. V. V. Nikiforov, Vopr. At. Nauki Tekh., Ser.: Teor. Prikl. Fiz., No. 1, 3 (1993).
11. A. L. Kuhl, R. E. Ferguson, and A. K. Oppenheim, Arch. Combust. **19** (1–4), 67 (1999).
12. W. S. Filler, in *Proceedings of 6th International Symposium on Combustion* (Yale Univ., 1956), p. 648.
13. A. Ya. Apin, N. F. Velina, and Yu. A. Lebedev, Prikl. Mekh. Tekh. Fiz. **5**, 96 (1962).
14. F. A. Baum, L. P. Orlenko, K. P. Stanyukovich, and V. P. Chelyshev, *Physics of an Explosion* (Nauka, Moscow, 1975).
15. V. P. Isachenko, V. A. Osipova, and A. S. Sukomel, *Heat Transfer* (Énergiya, Moscow, 1965).
16. B. M. Smirnov, Usp. Fiz. Nauk **164** (7), 665 (1994) [Phys.–Usp. **37**, 621 (1994)].

17. A. M. Kutepov, T. N. Bondareva, and M. G. Berengarten, *General Chemical Technology* (Vysshaya Shkola, Moscow, 1990).

18. E. Yu. Tonkov, *Phase Transformations of Compounds at High Pressure* (Metallurgiya, Moscow, 1988).

19. M. N. Makhov, Khim. Fiz. **19** (6), 52 (2000).

20. A. G. Stromberg and D. P. Semenchenko, *Physical Chemistry* (Vysshaya Shkola, Moscow, 1988).

21. A. S. Predvoditelev, L. N. Khitrin, O. A. Tsukanova, Kh. I. Kolodtsev, and K. Grozdovskiĭ, *Carbon Combustion* (Akad. Nauk SSSR, Moscow, 1949).

22. E. S. Golovina, in *Proceedings of 6th All-Union Symposium on Combustion and Explosion* (Alma-Ata, 1980), p. 106.

23. D. A. Frank-Kamenskiĭ, *Diffusion and Heat Transfer in Chemical Kinetics* (Nauka, Moscow, 1987).

24. A. E. Aleksenskiĭ, M. V. Baĭdakova, A. Ya. Vul', *et al.*, Fiz. Tverd. Tela (St. Petersburg) **39** (6), 1125 (1997) [Phys. Solid State **39**, 1007 (1997)].

25. A. E. Aleksenskiĭ, M. V. Baĭdakova, A. Ya. Vul', and V. I. Siklitskiĭ, Fiz. Tverd. Tela (St. Petersburg) **41** (4), 740 (1999) [Phys. Solid State **41**, 668 (1999)].

26. A. L. Vereshchagin, E. A. Petrov, V. F. Komarov, *et al.*, in *Proceedings of 10th Symposium on Combustion and Explosion* (Chernogolovka, 1992), p. 119.

27. A. I. Lyamkin, Doctoral Dissertation (Krasnoyarsk, 2001).

28. A. L. Vereshchagin, E. A. Petrov, G. V. Sakovich, *et al.*, RF Patent No. 2,051,092 (27 December 1995).

29. A. L. Vereshchagin, *Detonation Nanodiamonds* (Alt. Tekh. Univ., Barnaul, 2001).

Translated by K. Shakhlevich

Physics of the Solid State, Vol. 46, No. 4, 2004, pp. 636–643. Translated from Fizika Tverdogo Tela, Vol. 46, No. 4, 2004, pp. 621–628.

MODIFICATION OF SURFACE AND THE PHYSICOCHEMICAL PROPERTIES OF NANODIAMONDS

Surface Chemistry of Nanodiamonds

I. I. Kulakova

Moscow State University, Vorob'evy gory, Moscow, 119992 Russia

e-mail: kulakova@petrol.chem.msu.ru

Abstract—The experimental data available in the literature and the results obtained by the author in research into the structure of nanodiamonds and the physicochemical and chemical properties of their surface are generalized. An account is given of the problems concerning the chemical state and modification of the nanodiamond surface in gaseous and liquid media and the influence of modification on the sorption and catalytic properties of nanodiamonds, their compactibility, and sintering. The similarity and difference in the behavior of nanodiamonds and diamond macrocrystals in oxidation processes are discussed. The activation energies of oxidation of nanodiamonds by different reagents are determined in the absence and presence of catalysts. © *2004 MAIK "Nauka/Interperiodica".*

1. INTRODUCTION

The particular interest expressed by researchers in nanosized objects stems from the fact that their properties differ significantly from those of bulk materials. Nanoobjects can exhibit radically new effects and phenomena and even a different phase diagram. In particular, Badziag *et al*. [1] showed that nanodiamond (ultradispersed or cluster diamond) is the most stable carbon compound with a particle size of up to 5 nm.

Nanodiamonds synthesized upon explosion of condensed explosives with a negative oxygen balance in a closed volume [2, 3] represent a special type of diamond material. This is a typical nanomaterial whose particles have a mean size of ~4 nm and are predominantly spherical in shape.

According to the core theory [4], each nanodiamond particle, like any solid particle, is a supramolecule with a single-crystal diamond core surrounded by a shell ("coat") consisting of functional groups. These functional groups are chemically bound to the core and determine the chemical state of the nanodiamond surface. Nanodiamond supramolecules can be subdivided into classes according to the nature of the functional groups (Table 1). Judging from the crystallite sizes and the ratio between the number of surface carbon atoms N_{surf} and the total number of carbon atoms N_{total} in a particle, nanodiamonds can be considered a diamond substance in a colloidal state. For a mean diamond particle size of 4.2 nm, the fraction of surface atoms is approximately equal to 15% [5, 6]. This leads to a breaking of

Table 1. Genealogical series of diamond polycondensation products with due regard for changes in the composition and size of macromolecules (according to the data taken from [5])

Size	Hydrocarbons C_nH_x	Alcohols $C_nO_xH_x$	Ketones C_nO_x	N/N_{surf}
		Molecules		
3.5 Å	Adamantane	Tetrahydroxyhexaoxoadamantane		
		Tetrahydroxyadamantane	Hexaoxoadamantane	1
		Condensed polyadamantanes		
<1 nm	with –H groups	with –OH groups	with =O groups	1.3–13
		Colloidal particles		
		Nanodiamonds with shell		
1–10^2 nm	from hydride groups	from hydroxyl groups	from carbonyl groups	13–10^3
		Crystals		
		Diamond microcrystals with shell		
0.1–10^2 μm	from hydride groups	from hydroxyl groups	from carbonyl groups	10^3–10^6
		Diamond macrocrystals with shell		
>0.1 nm	from hydride groups	from hydroxyl groups	from carbonyl groups	>10^6

1063-7834/04/4604-0636$26.00 © 2004 MAIK "Nauka/Interperiodica"

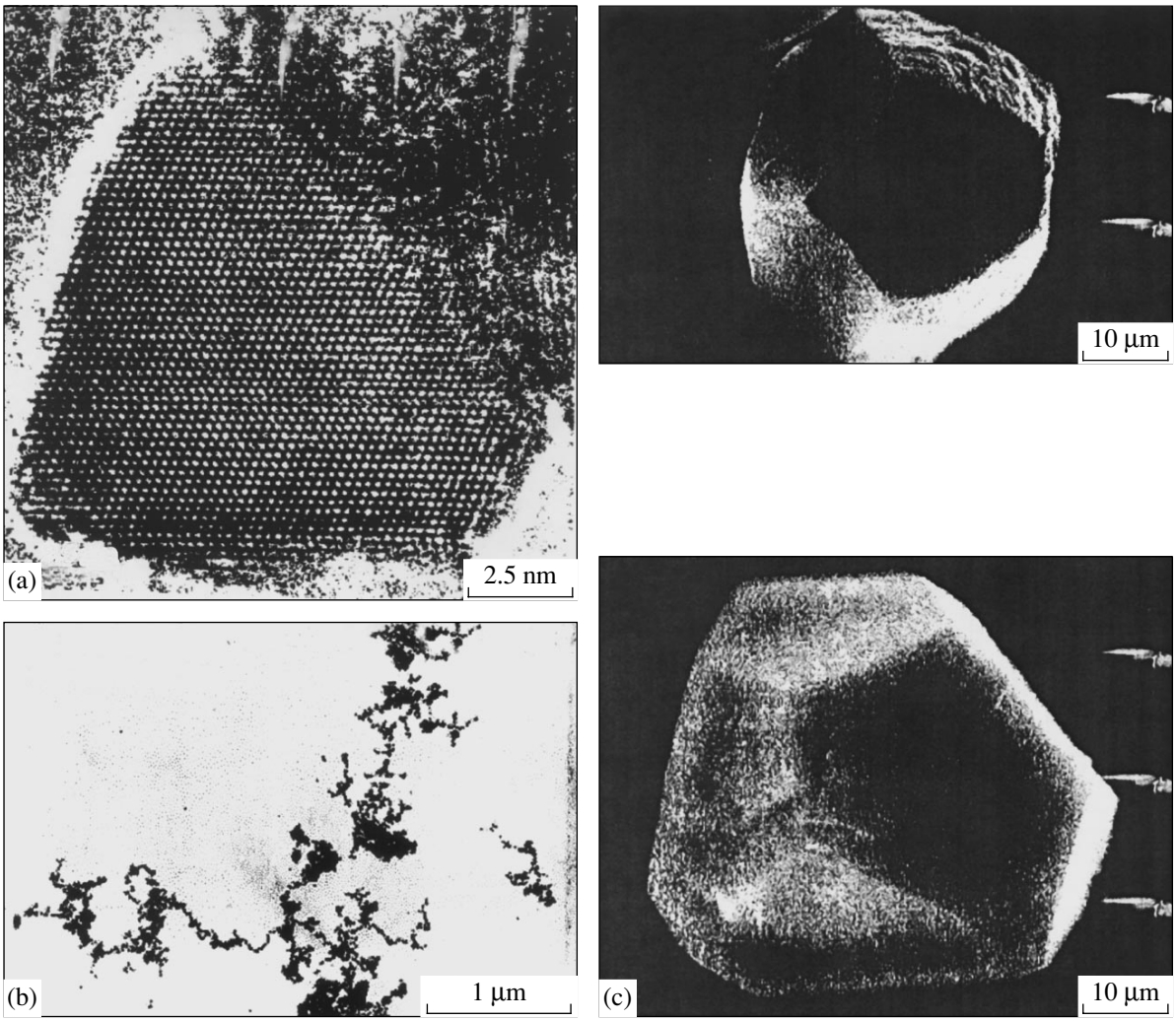

Fig. 1. Electron micrographs of nanodiamonds [14]: (a) arrangement of carbon atoms in a particle, (b) aggregation of nanodiamond particles with the formation of chain structures, and (c) induced self-assembling of nanodiamonds into dodecahedra.

the symmetry in the spatial arrangement of carbon atoms and a decrease in the lattice spacing [3]. Therefore, the properties of nanodiamonds should be governed by the state of their surface to a considerably greater extent as compared to the properties of large-sized diamond crystals, in which the fraction of surface atoms is very small.

It is known that nanodiamonds have a highly defective structure. However, this does not hold true for the nanodiamond particle as a whole. According to high-resolution transmission electron microscopy, carbon atoms are arranged regularly in the particle core (Fig. 1a) and the diamond structure is disordered in peripheral regions of nanodiamond microblocks [3]. In [7–9], it was demonstrated that the single-crystal core of nanodiamond supramolecules is free of defects and only the shell of diamond particles is distorted. The characteristics of the shells of nanodiamonds synthesized by several manufacturers, who used different cooling conditions for explosion products and different procedures of subsequent diamond purification, are compared in Table 2. As is known, these factors affect both the ratio between carbon atoms in the sp^3- and sp^2-hybridized states in the shell and the structure and chemical composition of the shell. Indeed, the data presented in the table indicate that there are differences not only in the chemical composition of the shells but also in their thickness, i.e., in the number of carbon layers and in the interplanar distance l_s in the shell. The presence of nondiamond carbon in nanodiamond particles was experimentally confirmed by Gubarevich *et al*. [10, 11].

2. CHEMICAL COMPOSITION OF NANODIAMONDS

Apart from carbon, detonation nanodiamonds contain a considerable number of heteroatoms, whose content depends on the conditions of synthesis, purification, and subsequent treatment of nanodiamonds [2, 3]. Nanodiamond consists of carbon to the extent of 80–

Table 2. Influence of the cooling conditions for the diamond-containing blend on the composition and structure of the shell of nanodiamond particles (according to the data taken from [9])

No.	Medium of nanodiamond condensation (manufacturer of nanodiamonds)	Characteristics of shells		
		chemical composition	l_s, Å (Δl, %)	number of carbon layers
1	H_2O (Khoros)	Amorphous shell		4
		Adamantane-like clusters (≤50%)	1.88 (9)	
		Structured water on the surface of nanodiamond crystals		
2	CO_2 (Research and Production Association "Altaĭ")	Amorphous shell with a graphite order (85%)	1.88 (9)	>4
		Dangling bonds		
3	CO_2 (ATM "Krasnoyarsk")	Graphite component (50%)		2
		Small-sized graphite clusters	1.96 (5)	
		Amorphous carbon		
		C–H bonds		
4	Ice (ATM "Krasnoyarsk")	Graphite-like component is absent		1
		Crystalline surface of diamond with dangling bonds	1.94 (6)	
		C–H bonds (~5%)		

Note: l_s is the distance between carbon layers in a distorted shell. The fractional decrease in the interplanar distance in the shell as compared to that in the diamond particle core (l_V = 2.06 Å) is given in parentheses.

88%, and this carbon predominantly forms the diamond phase. Moreover, nanodiamond contains oxygen (10% and more), hydrogen (0.5–1.5%), nitrogen (2–3%), and an incombustible residue (0.5–8.0%). In turn, the incombustible residue consists of oxides, carbides, and salts of different elements, such as Fe, Ti, Cr, Cu, K, Ca, Si, Zn, Pb, etc. [12]. These compounds, together with nondiamond carbon, belong to the group of solid-phase impurities that are difficult to remove.

As regards other elements (oxygen, nitrogen, hydrogen), it is believed that they enter into the composition of volatile impurities that are difficult to remove [2]. Actually, part of these elements enter into the composition of molecules (CO, CO_2, N_2, H_2O, etc.) that are sorbed on nanodiamonds and can either form an adsorbed layer on an accessible surface or be incorporated into closed pores. However, the other part of the elements necessarily enter into the composition of functional surface groups. They are not impurities but make up an integral part of the nanodiamond supramolecule, much as oxygen, nitrogen, and other elements enter into the composition of functional derivatives of hydrocarbons. Functional groups can be destroyed and replaced by other groups, but they always persist on the surface of nanodiamonds, as well as on the surface of macrocrystals and powder grains of diamonds of other types.

3. NANODIAMOND AGGREGATION

Nanodiamonds are prone to aggregation with the formation of primary and secondary structures due to the presence of a large number of functional groups on the nanodiamond surface[2, 3, 13–16]. The formation of aggregates depends on the thermal conditions, concentrations, and physicochemical properties of the surface of the particles. Note that the nature of a shell formed by functional groups substantially affects the colloidal properties of nanodiamonds. Nanodiamond particles in dry powders and suspensions can form more stable primary (up to 1–5 μm) and less stable secondary (up to 200 μm) aggregates. After chemical purification of nanodiamonds, particles a few microns in size are formed as a result of agglomeration. Heating in an inert atmosphere at temperatures above 873 K leads to the growth of nanodiamond particles, which take the shape of spherulites (150–200 μm).

Aggregates have a fractal structure. The x-ray diffraction patterns of aggregates after oxidation with hydrogen peroxide always exhibit a reflection from the (002) plane of nondiamond carbon. It seems likely that

soluble aggregates transform into new aggregates with closed pores. These aggregates can be disrupted by ultrasound (for example, in distilled water). Networks, fibers, threads, and chains (Fig. 1b) can be formed in suspensions. Belobrov [14] suggested that diamond nanoparticles have a dipole moment, which vanishes after the formation of supramolecular structures. The spontaneous crystallization from suspensions brings about the formation of soft quasicrystals (up to 50 μm) of different habits. Furthermore, the self-assembling under specific conditions from specially prepared suspensions results in the growth of dodecahedral nanocrystals that possess good faceting (Fig. 1c) and are stable in an electron beam [14].

4. SHELL OF FUNCTIONAL GROUPS ON THE SURFACE OF NANODIAMOND PARTICLES

Since nanodiamonds have a developed surface and a large ratio N_{surf}/N_{total}, the nature of the functional groups forming the shell can be elucidated using IR absorption spectroscopy.

According to IR absorption spectroscopy, the nanodiamond surface treated under different conditions can contain different functional groups, such as oxygen-containing (hydroxyl, carbonyl, ether, anhydride, etc.), nitrogen-containing (amine, amide, cyano, nitro, etc.), sulfone, and other groups [2, 3, 15–19]. Bogatyreva *et al*. [20] revealed that, in addition to carboxyl and carbonyl groups, the nanodiamond surface contains methyl and methylene groups, but in an insignificant amount. Sakovich *et al*. [3] showed that nanodiamonds involve bound and sorbed water. Sorbed water is not removed even during drying of powders at a temperature of 393 K. Apparently, this water is contained in closed pores formed upon aggregation.

The IR spectra of nanodiamonds prior to and after treatments under different conditions are shown in Fig. 2. These spectra were thoroughly interpreted in our earlier work [21]. All the spectra exhibit absorption bands of carbonyl- (1730–1790 cm^{-1}) and hydroxyl-containing (1640, 3400 cm^{-1}) groups. The broad band with a maximum at 1100–1140 cm^{-1} is most likely caused by a superposition of bands associated with impurity nitrogen centers of the *A*, *B*1, *B*2, and *C* types and also with the vibrations of the ≡C–O–C≡ group. (The $–NO_2$ groups at the C_{second} and C_{third} atoms, the $–SO_2OH$ groups, and the –OH groups in –COOH and at the C_{third} atom absorb in the same range, which somewhat reduces the reliability of the interpretation.)

A comparison of the IR spectra depicted in Fig. 2 shows that the location and intensity of the absorption bands attributed to the carbonyl groups depend on the conditions of nanodiamond treatment. Treatment in a nitrogen atmosphere at 973 K leads to decomposition of the carbonyl and carboxyl groups, as can be judged from the decrease in the intensity of the absorption

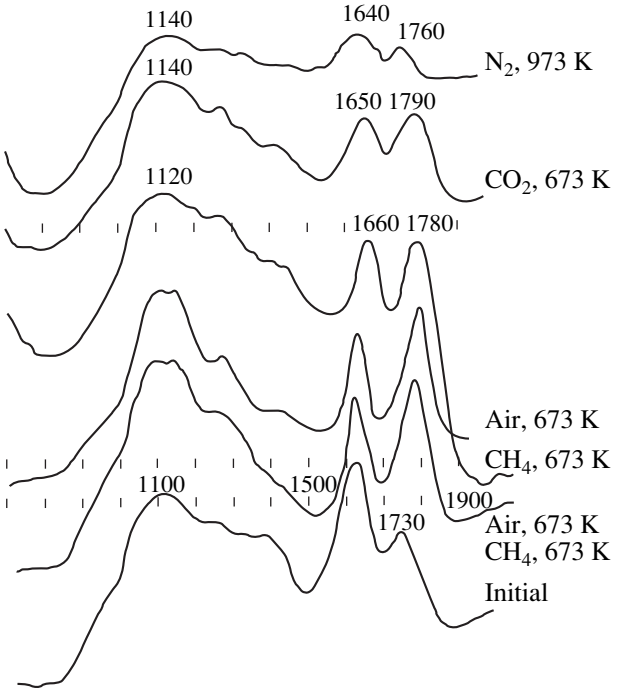

Fig. 2. IR absorption spectra of nanodiamonds treated under different conditions.

bands. After treatment at 673 K, irrespective of the nature of the modifying gas, the maximum of the band at a frequency of 1730 cm^{-1} is shifted to the range 1780–1790 cm^{-1}, which indicates the formation of the groups

$$–C(O)–O–C(O)–, \quad (–O–)_2C=O.$$

According to Sakovich *et al*. [3], it is this latter group that is characteristic of purified nanodiamonds, whereas the large variety of other groupings stem from technological contamination. We cannot agree both with this statement and with the term "impurity functional groups" [2], because nanodiamonds under real conditions are always in contact with a gaseous or liquid medium and interact with it, which necessarily affects the functional groups forming the nanodiamond shell. Indeed, even contact of natural-diamond powders with hydrogen at room temperature brings about the formation of C–H bonds [22].

Judging from the small differences in the IR spectra of nanodiamonds treated under different conditions, we can assume that not all surface groups are accessible even to gaseous reactants. This is confirmed by our experimental data on the concentrations of proton-donor groups on the nanodiamond surface. The contents of proton-donor groups (i.e., acid functional groups) on the nanodiamond surface after treatments under different conditions were calculated from data on the acid–base titration of nanodiamonds with alkali (Table 3). As can be seen from the data presented in Table 3, the number of acid groups increases with an

Table 3. Content of proton-donor groups on the surface of nanodiamond samples treated under different conditions

Treatment conditions	Content of proton-donor groups, 10^{-3} mol/g	
	potentiometric titration	visual titration*
Initial sample	0.548	0.346
Air, 673 K, 2 h	1.006	0.921
Air, 673 K, 5 h	1.467	1.231
Hydrogen, 1073 K, 2 h	0.735	0.570
Hydrogen, 1073 K, 4 h	0.689	0.440

* Visual titration leads to underestimated results due to the difficulties encountered in determining the equivalence points in the presence of colloidal nanodiamond particles in an aliquot.

Table 4. Effect of the chemical modification of nanodiamonds on the limiting pressure P_{lim} and the density ρ of pellets under cold pressing

Parameter	Sample			
	initial	modified		
		H_2	CO_2	HNO_3 (concentrated)
P_{lim}, kg/cm^2	800–900	300–400	1200	1200
ρ, g/cm^3	1.2	1–1.15	1.23–1.3	1.3–1.4

increase in the time of treatment with oxygen and decreases upon treatment with hydrogen. This is in agreement with the general regularity revealed in many works. Actually, the interaction of oxygen with groups located on the nanodiamond surface results in their oxidation and transformation into oxygen-containing groups, which are predominantly acid groups. On the other hand, treatment with hydrogen at high temperatures is attended by the reduction or decomposition of many oxygen-containing groups. However, even after high-temperature treatment with hydrogen for 4 h, a considerable number of acid groups are retained on the nanodiamond surface. Gubarevich *et al*. [23] showed that, depending on the conditions of nanodiamond treatment, the concentration of protogenic groups varies from 0.34 to 2.52 μg-equiv m^{-2}, whereas the concentration of active hydrogen changes from 0.49 to 7.52 μg-equiv m^{-2}.

In many works, it has been noted that the procedure of cooling a diamond-containing blend affects the composition and number of functional groups on the nanodiamond surface. This effect can be explained by the formation of nanodiamond shells with different ratios between carbon atoms in the sp^3 and sp^2 states (Table 2) and, hence, with different abilities to form functional groups.

5. CHEMICAL MODIFICATION OF THE NANODIAMOND SURFACE

It follows from the foregoing that the functional groups always form a shell on the surface of nanodiamond particles. The nature of the functional groups depends on the conditions and methods of synthesis, separation, and purification of the nanodiamonds. With the aim of imparting specific properties to nanodiamond particles, this shell can be modified by chemical reactions, a number of which were noted above. These are gas-phase and liquid-phase oxidation (or reduction) reactions, intermolecular (or intramolecular) decomposition of functional groups upon heating, exchange reactions in groups or replacement of one group by another group, detachment of groups with capture of surface carbon atoms and a change in the surface structure and the degree of hybridization of carbon atoms, and grafting of organic compounds to the surface.

In particular, Voznyakovskiĭ *et al*. [24] showed that the formation of a hydrocarbon shell on the nanodiamond surface by the grafting of organosilyl groups increases the stability of suspensions in nonpolar liquids. The chemical modification of the nanodiamond surface strongly affects the sintering of nanodiamonds. Shul'zhenko and Bochechka [25] found that the chemical modification of initial nanodiamonds, in combination with other factors, leads to a decrease in the degree of graphitization of diamonds upon sintering and, hence, to an increase in the strength and hardness of the polycrystals. The modification of nanodiamonds in an oxidizing or reducing medium [19, 26] affects the optimum conditions of cold pressing (Table 4). Nanodiamonds modified with hydrogen are sintered into compact (vitreous) pellets, whereas nonmodified nanodiamonds under the same conditions are sintered only along the periphery of a pressed pellet.

6. SORPTION PROPERTIES OF NANODIAMONDS

Nanodiamonds possess a high sorption capacity owing to the well-developed surface, which, according to data obtained by different authors, varies from 150 to 450 m^2 g^{-1}. A dry powder adsorbs a large amount of a gas [2, 3]. Bogatyreva *et al*. [20] revealed that, for two batches of nanodiamonds with identical specific surfaces and degrees of purification, the adsorption potentials with respect to nitrogen differ by approximately 40%. It is evident that the adsorption potential is governed by the chemical properties of the surface and the sorbate nature rather than by the aforementioned parameters. Indeed, the same nanodiamond sample interacting with different sorbates possesses different sorption properties [2]. For example, the sorption

Table 5. Transformations of organic solvents upon high-temperature treatment of the diamond-containing blend (N_{nd}/N_d = 1.52)

Solvent	Compounds found in the extract	N_{nd}/N_d (after treatment)
Tetralin	Tetralin (initial)	
	trans-Decalin	
	cis-Decalin	
	Naphthalene	0.79
	Alkylbenzenes (traces)	
trans-Decalin	*trans*-Decalin (initial)	
	cis-Decalin	
	Bicyclo [4.3.0] nonane with a methyl substituent	1.94
	Butylcyclohexane	

Note: Polycyclic aromatic nitrogen-containing compounds are found in the extracts.

capacity of a dry UDD-STP nanodiamond powder is equal to 9 mol kg^{-1} for benzene and 10.5 mol kg^{-1} for chloroform. Moreover, different fractions of the same diamond batch also differ in capacity. Note that nanodiamonds sorb proteins well [27].

The sorption properties of nanodiamonds in suspensions depend on the surface charge of aggregates [28]. This charge is associated with the oxygen-containing groups that are located on the nanodiamond surface and exhibit acid properties. The sign and magnitude of the charge are determined by the concentration and dissociation constant of oxygen-containing groups, the pH of the solution, and the concentration of the supporting electrolyte.

Since nanodiamonds contain surface protogenic groups, they also possess cation-exchange properties. Specifically, the exchange capacity of nanodiamonds with respect to heavy-metal ions (Fe^{2+}, Ni^{2+}, Cr^{6+}) substantially depends on the procedure of their purification or chemical modification, i.e., on the hydrophilic–hydrophobic properties of their surface and also on the cation concentration in the solution [20, 27].

7. THERMAL DESORPTION FROM THE NANODIAMOND SURFACE

The high adsorption capacity of nanodiamonds is responsible for the large amount of physically sorbed and chemisorbed gases and vapors on the surface of nanodiamonds particles. Nozhkina *et al*. [29] demonstrated that nanodiamonds contain up to 10% volatile impurities and that heat treatment under vacuum (0.01 Pa) considerably decreases their content. In this case, the optimum annealing temperature is equal to 673 K. Upon heating of nanodiamonds at temperatures in the range 573–773 K, as much as 1.3 m^3 kg^{-1} of gases, predominantly in the form of carbon dioxide and nitrogen, are removed from the diamond surface [3]. Judging from the activation energies of desorption (48.5, 23.0 kJ mol^{-1}), Sakovich *et al*. [3] made the inference that the physically adsorbed gases are removed. This inference holds true for nitrogen but is invalid for carbon dioxide. It is quite possible that part of the removed carbon dioxide was adsorbed physically. However, first, the activation energy of CO_2 desorption is nearly twice as high as that of nitrogen. This suggests that the CO_2 desorption is a chemical rather than physical process. Second, it is known that carboxyl groups (whose content on the nanodiamond surface is rather high) begin to decompose already at 473 K.

The complex differential thermal analysis of nanodiamonds modified under different conditions revealed that, upon heating of samples in air in the temperature range 300–1250 K, the thermograms exhibit endothermic and exothermic effects and also effects associated with an increase and a decrease in the mass [2, 19]. At temperatures up to 373 K, the mass noticeably

Table 6. Apparent activation energies ε of nanodiamond oxidation in the low-temperature (**I**) and high-temperature (**II**) ranges

No.	Oxidizing agent	Temperature separating ranges **I** and **II**, K	ε, kJ/mol	
			range **I**	range **II**
1	$O_2 + N_2$ (20% O_2)	675	24.7 ± 1.7	96.4 ± 4.2
2	$O_2 + N_2$ (10% O_2)	775	24.7 ± 1.7	96.4 ± 4.2
3	$O_2 + N_2$ (4% O_2)	775	25.6 ± 5.8	91.3 ± 13.0
4	CO_2	900	36.5 ± 7.1	120.4 ± 15.0
5	CO_2, K_2CO_3	840	18.9 ± 5.0	88.8 ± 5.0
6	H_2O	935	22.2 ± 13.4	152.2 ± 7.0
7	H_2O, K_2CO_3	700	20.5 ± 12.1	126.7 ± 10.0

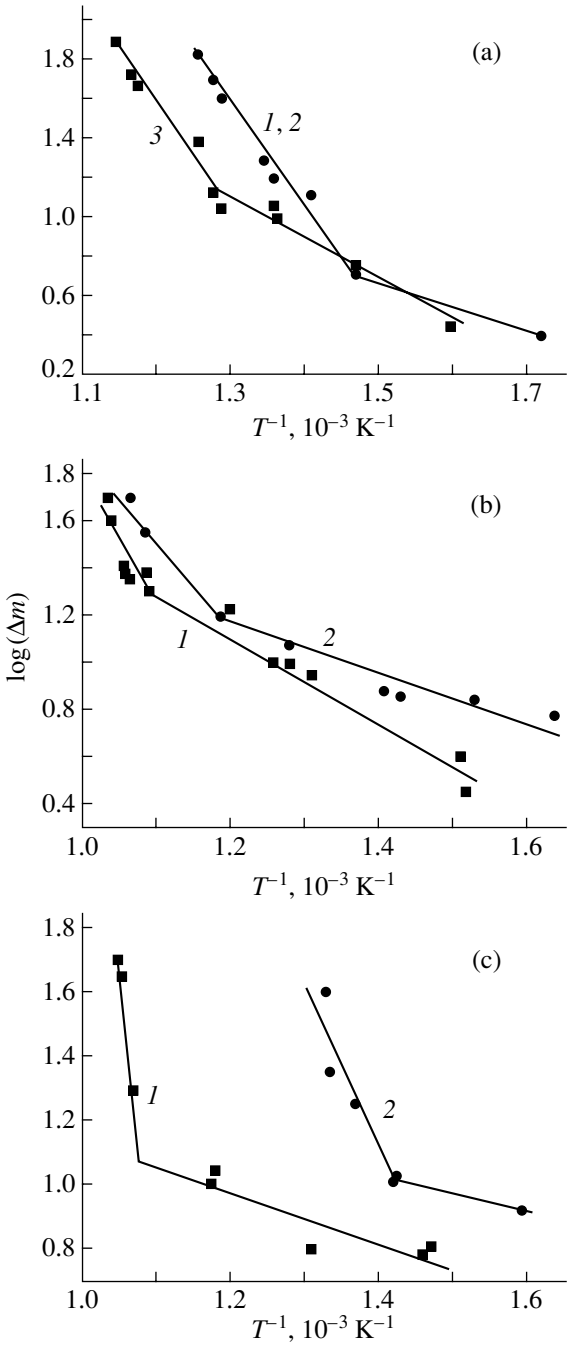

Fig. 3. Temperature dependences of the mass loss during oxidation of nanodiamonds: (a) oxidation with a mixture of oxygen and nitrogen at (*1*) 20% O_2, (*2*) 10% O_2, and (*3*) 4% O_2; (b) oxidation with carbon dioxide (*1*) without a catalyst and (*2*) with K_2CO_3; and (c) oxidation with water vapors (*1*) without a catalyst and (*2*) with K_2CO_3.

increases in the case of diamond samples preliminarily modified with water vapors and methane and remains virtually unchanged for diamond samples modified with carbon dioxide or a mixture of carbon dioxide with methane. In the temperature range 575–725 K, a decrease in the mass is observed for ultradispersed diamonds modified with nitrogen or methane. Note that this effect is more pronounced for diamonds modified with nitrogen. An increase in the temperature above 725 K leads to a decrease in the sample mass. Upon a gradual increase in the temperature, the thermograms exhibit several thermal effects: a broad endothermic peak at temperatures below 773 K, two broad exothermic peaks in the temperature range 773–1120 K, and an endothermic peak at 1130–1225 K. It should be noted that the shape of the peaks and the temperature of their maxima substantially depend on the nature of the modifier gases.

As follows from the results obtained, the preliminary modification of nanodiamonds affects their stability in air. The oxidation of nanodiamonds treated with water vapors begins already at 675 K, whereas nanodiamonds modified with a mixture of CH_4 and CO_2 oxidize at temperatures higher than 775 K. These data also indicate that chemical transformations of surface groups on nanodiamonds and even their oxidation can proceed at temperatures of 573–773 K.

8. CATALYTIC ACTIVITY OF NANODIAMONDS

Finely dispersed nanodiamonds, which possess a high surface energy and a developed specific surface involving proton-donor groups, are catalytically active in different reactions.

For example, investigation into the composition of high-temperature extracts from a diamond-containing blend revealed that these extracts involve products of solvent transformation (Table 5). The most pronounced transformations were observed for tetralin and decalin. It was found that the extracts contain products of isomerization, dehydrogenation, disproportionation, and cracking. Moreover, high-temperature treatment of the diamond-containing blend with decalin leads not to an expected decrease but to an increase in the ratio between the number of nondiamond carbon atoms N_{nd} and the number of diamond carbon atoms N_d in a solid residue (from 1.52 to 1.94). This fact indicates that decalin undergoes polycondensation.

Nanodiamonds are catalytically active in oxidation processes, for example, in the oxidation of CO to CO_2, because the nanodiamond surface is easily saturated with oxygen and activates it [27].

9. NANODIAMOND OXIDATION

Nanodiamonds in oxidizing media exhibit a specific behavior as compared to diamond crystals and even diamond micropowders. This is explained by the high relative content of functional surface groups [2, 19]. The specific features manifest themselves in the fact that the temperature dependences of the mass loss for nanodiamonds in various oxidizing agents exhibit substantially different behaviors in two characteristic temperature ranges (Fig. 3). In the low-temperature range, the change in the nanodiamond mass only weakly depends on the temperature, even though the change in

the mass is already noticeable at 300–350°C. By contrast, in the high-temperature range, the rate of mass loss drastically increases with an increase in the temperature. The oxidative ability of the oxidizing agents studied changes in the following order: air $\gg CO_2 > H_2O$. The addition of potassium ions appreciably promotes nanodiamond oxidation with water vapors and increases the rate of oxidation with carbon dioxide insignificantly, as is the case with diamonds of other types.

The results obtained were used to calculate the apparent activation energies for oxidation of nanodiamonds (Table 6). The temperatures separating the low- and high-temperature ranges for different oxidation conditions are also listed in Table 6. As follows from this table, the activation energies for the same oxidizing agent in the two temperature ranges differ by a factor of 3 to 6. Probably, this can be associated with the competing processes of oxidation and transformation of different functional groups in the low-temperature range. Most likely, the crossover to the high-temperature behavior is due to the formation of a shell composed predominantly of hydroxyl functional groups. The activation energies for oxidation of nanodiamonds in the presence of a catalyst are less than those for the noncatalytic process. On the whole, the activation energies for oxidation of nanodiamonds in the high-temperature range are less than those of kimberlite diamonds by a factor of more than 2.

10. CONCLUSIONS

Thus, the brief overview of the data characterizing the chemical state of the nanodiamond surface clearly demonstrated that the physical and chemical properties of nanodiamonds strongly depend on the nature of the shell of functional groups on the surface of diamond particles. Consequently, the properties of nanodiamonds can be controlled by modifying the shell of functional groups. Moreover, the data presented in this paper indicate that nanodiamond is not a diamond-like material but is a typical diamond whose surface (like the surface of other types of diamond) necessarily contains different functional groups that saturate free valences of surface carbon atoms. The distinguishing feature of ultradispersed diamonds is that, in the series of functional derivatives of diamond cores, they are intermediate in the ratio N_{surf}/N_{total} and the crystallite size between low-molecular species (similar to functional derivatives of adamantane) and high-molecular species (such as diamond macrocrystals with a specific shell of functional groups on the diamond surface).

REFERENCES

1. P. Badziag, W. S. Verwoerd, W. P. Ellis, and N. R. Greiner, Nature **343** (6255), 244 (1990).
2. V. Yu. Dolmatov, Usp. Khim. **70** (7), 687 (2001).
3. G. V. Sakovich, V. F. Komarov, and E. A. Petrov, Sverkhtverd. Mater., No. 3, 3 (2002).
4. B. V. Spitsyn, *Problems and Achievements of the Physicochemical and Engineering Science in the Field of Nanomaterials* (Nauchno-Issled. Fiz.–Khim. Inst., Moscow, 2002), Vol. 2, p. 102.
5. V. B. Aleskovskiĭ, *Chemistry of Supramolecular Compounds* (St. Petersburg Gos. Univ., St. Petersburg, 1996).
6. A. P. Rudenko, I. I. Kulakova, and V. L. Skvortsova, Usp. Khim. **62** (2), 99 (1993).
7. M. B. Guseva, V. G. Babaev, V. V. Khvostov, and Z. Kh. Valliulova, Izv. Ross. Akad. Nauk, Ser. Fiz. **58** (1), 191 (1994).
8. A. Obraztsov, M. Guseva, V. Babaev, *et al.*, Diamond Relat. Mater. **3** (3), 968 (1995).
9. Z. Kh. Valliulova, Candidate's Dissertation (Moscow, 1995).
10. T. M. Gubarevich, N. M. Kostyukova, R. R. Sataev, and L. V. Fomina, Sverkhtverd. Mater., No. 5, 30 (1991).
11. T. M. Gubarevich, Yu. V. Kulagina, and L. I. Poleva, Sverkhtverd. Mater., No. 2, 34 (1993).
12. T. M. Gubarevich, Yu. V. Kulagina, L. I. Poleva, *et al.*, Zh. Prikl. Khim. (St. Petersburg) **66**, 1882 (1993).
13. S. I. Chukhaeva and L. A. Cheburina, Sverkhtverd. Mater., No. 1, 43 (2000).
14. P. I. Belobrov, Doctoral Dissertation (Krasnoyarsk, 1996).
15. G. V. Sakovich, V. D. Gubarevich, F. Z. Badaev, *et al.*, Dokl. Akad. Nauk SSSR **310**, 402 (1990).
16. G. A. Chiganova, Kolloidn. Zh. **56** (2), 266 (1994).
17. L. A. Petrova, A. L. Vereshchagin, V. V. Novoselov, *et al.*, Sverkhtverd. Mater., No. 4, 3 (1989).
18. G. V. Sakovich and V. D. Gubarevich, Zh. Vses. Khim. O-va im. D. I. Mendeleeva **35** (5), 600 (1990).
19. I. I. Kulakova, V. Yu. Dolmatov, T. M. Gubarevich, and A. P. Rudenko, Sverkhtverd. Mater., No. 1, 46 (2000).
20. G. P. Bogatyreva, M. N. Voloshin, M. A. Marinich, *et al.*, Sverkhtverd. Mater., No. 6, 42 (1999).
21. I. I. Kulakova, B. N. Tarasevich, A. P. Rudenko, *et al.*, Vestn. Mosk. Univ., Ser. 2: Khim. **34** (5), 506 (1993).
22. F. M. Tapraeva, A. N. Pushkin, I. I. Kulakova, *et al.*, Zh. Fiz. Khim. **64**, 3135 (1990).
23. T. M. Gubarevich, O. F. Turitsina, L. I. Poleva, and A. V. Tyshetskaya, Zh. Prikl. Khim. (St. Petersburg) **65**, 1269 (1992).
24. A. P. Voznyakovskiĭ, T. Fujimura, V. Yu. Dolmatov, and M. V. Veretennikova, Sverkhtverd. Mater., No. 6, 22 (2002).
25. A. A. Shul'zhenko and A. A. Bochechka, Sverkhtverd. Mater., No. 4, 46 (1988); Sverkhtverd. Mater., No. 6, 50 (2000).
26. I. I. Kulakova and A. P. Rudenko, Sverkhtverd. Mater., No. 1, 40 (2001).
27. G. P. Bogatyreva, M. A. Marinich, E. V. Ishchenko, *et al.*, Sverkhtverd. Mater., No. 6, 10 (2002).
28. N. V. Novikov, V. G. Aleshin, A. A. Smekhnov, *et al.*, Dokl. Akad. Nauk SSSR **300**, 1122 (1988) [Sov. Phys. Dokl. **33**, 461 (1988)].
29. A. V. Nozhkina, N. A. Kolchemanov, A. A. Kardanov, and P. Ya. Detkov, Sverkhtverd. Mater., No. 1, 78 (2000).

Translated by O. Borovik-Romanova

Physics of the Solid State, Vol. 46, No. 4, 2004, pp. 644–648. Translated from Fizika Tverdogo Tela, Vol. 46, No. 4, 2004, pp. 629–632.

MODIFICATION OF SURFACE AND THE PHYSICOCHEMICAL PROPERTIES OF NANODIAMONDS

Self-Organization in Nanocomposites Based on Detonation Nanodiamonds

A. P. Voznyakovskiĭ

Lebedev Research Institute of Synthetic Rubber, Federal State Unitary Enterprise, Gapsal'skaya ul. 1, St. Petersburg, 198035 Russia

e-mail: vniisk@mail.rcom.ru

Abstract—The effect of modifying detonation nanodiamond additives on the stress–strain properties of polymer nanocomposites is investigated using polysiloxane polyblock copolymers as an example. It is shown that the formation of a physical network of supramolecular structures (due to self-organization initiated by force fields of highly active nanoparticles) can lead to an increase in the physicomechanical parameters in the range of small strains (up to 100%) without changing the chain microstructure. The use of composites involving fillers of the *H* type (with a high surface activity) and the *L* type (with a low surface activity) provides a maximum efficiency of interaction of the force fields induced by supramolecular structural units. The force interaction results in a more "efficient" supramolecular organization of the polymer and ensures a synergetic increase in the physicomechanical parameters with the use of *L*–*H* fillers. © *2004 MAIK "Nauka/Interperiodica".*

1. INTRODUCTION

In modern polymer materials science, particular attention has been concentrated on the problem of improving the elastic properties under small strains. It is common practice to use filled composites for this purpose. However, in cases where it is necessary to retain the physicochemical parameters of polymers (for example, gas permeability, strength of adhesion contact), the use of composites with high degrees of filling becomes impossible. This circumstance necessitates modifying polymers with finely dispersed materials (particle size, 10–100 nm), i.e., preparing nanocomposites [1].

Polysiloxane polyblock copolymers of the $(AB)_n$ type, which consist of rigid (with a high vitrifying temperature) (*A*) and flexible (*B*) polysiloxane blocks, exhibit a number of practically valuable properties. These copolymers have been used for synthesizing film-forming materials with a broad spectrum of possible applications (from protective coatings to selectively permeable membranes) [2].

The purpose of this work was to elucidate how the modifying additives of finely dispersed materials affect the physicochemical properties of films formed by polysiloxane polyblock copolymers.

2. SAMPLE PREPARATION AND EXPERIMENTAL TECHNIQUE

2.1. Polymer

A typical example of a polysiloxane block copolymer is provided by the ladder phenylsilsesquioxane–poly(dimethylsiloxane) (LPS–PDMS) polyblock copolymer. For the copolymer used in this work, the ratio between the lengths of the sequences of units of rigid (x) and flexible (y) blocks was $x : y = 25 : 61$. The weight content of flexible PDMS blocks was equal to 42 wt %.

2.2. Finely Dispersed Materials

Detonation nanocarbons, namely, technical-grade diamond-containing nanocarbon (TDNC) and detonation nanodiamonds (DND), were synthesized at the Special Design Bureau "Tekhnolog" (St. Petersburg). Samples of *A*-300 finely dispersed silicon oxide were prepared at the Kalush Chemical Plant. Glass spherules (GS) were supplied by the New Glass Technologies Company (St. Petersburg). The polydispersity of fillers was investigated using dynamic light scattering. The highest degree of dispersion was achieved by ultrasonic treatment of suspensions of finely dispersed particles [3].

Ladder phenylsilsesquioxane–poly(dimethylsiloxane) films were prepared according to the dissolution procedure described earlier in [4].

3. RESULTS AND DISCUSSION

3.1. Individual Fillers

At the preliminary stage of this work, it was necessary to determine the reference dispersity parameters for each filler in a liquid medium. As the reference parameter, we chose the degree of dispersion of fillers in water, because, in this case, it is possible to attain the highest degree of dispersion of hydrophilic nanoparti-

1063-7834/04/4604-0644$26.00 © 2004 MAIK "Nauka/Interperiodica"

cles [5]. The polydispersity distributions constructed from the dynamic light scattering data are depicted in Fig. 1. It can be seen from this figure that the chosen fillers can be actually attributed to nanodispersed materials.

At this stage (in accordance with nanocomposite theory), only individual modifiers were used to fill block copolymers. However, it was found that the physicomechanical characteristics of the prepared films with optimized compositions (filler, 5 wt %) are worse than the parameters of the initial unfilled film. The deterioration of the properties can be associated with the structuring of polymer macrochains in response to force fields of highly active filler particles. The structuring processes correlate with both the aggregation of hydrophilic particles in a nonpolar medium and the related nonuniform distribution of filler particles over the bulk of the polymer matrix. This situation will be considered in the next subsection in greater detail.

3.2. Individual Modified Fillers

The aggregation of particles with hydrophilic surface functional groups (for the most part, groups with labile protons) in nonpolar media can be suppressed through chemical modification of their surface in such a way that these groups will be blocked by nonpolar groups. In this work, the chemical modification of the surface was accomplished according to the silylation reaction [6]. The modified fillers are denoted by the letter "m."

As follows from the results of dynamic light scattering investigations, the structure of suspensions of modified particles in toluene solutions of the LPS–PDMS copolymer remains stable over a period of at least 12 h. This made it possible to use these solutions for preparing films. The physicomechanical parameters of the prepared films with optimized compositions are listed in Table 1. As can be seen, the use of individual modified fillers increases the physicomechanical parameters of the films by 20–30% in the practically important strain range (up to 300%) with retention of satisfactory elastic properties. It should be emphasized that this effect is achieved at a filler content of no more than 5 wt %. Note also that there is no correlation between the stress–strain parameters of the LPS–PDMS films and the type of hydrophobized modifier used. And vice versa, these properties depend on the type of initial modifier. Let us now consider the origin of this difference in greater detail.

Recent investigations in the field of nanosystems have revealed that the physical properties of materials change monotonically with an increase in the degree of dispersion to a threshold value where a number of physical and physicochemical properties undergo a jump-wise change, which is not predicted by the Gibbs thermodynamics [7]. For many materials, such a jump is observed with an increase in the degree of dispersion to particle sizes of less than 10 nm. A rough estimation shows that, at this particle size, the fraction of highly active surface atoms becomes appreciable (2–5%) [8], which is responsible for the substantial change in the surface properties. Therefore, we can assume that the effect of a finely dispersed material used as a filler is determined, to a large extent, by the fraction of particles with sizes of less than 10 nm rather than by the mean diameter calculated for the distribution as a whole.

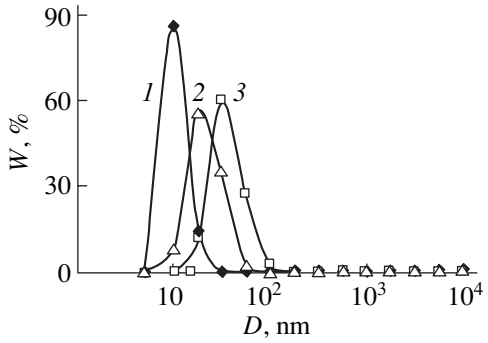

Fig. 1. Polydispersity distributions of initial particles: (*1*) *A*-300 finely dispersed silicon oxide, (*2*) detonation nanodiamonds, and (*3*) glass spherules. The dispersive medium is water.

Under this assumption, we will analyze the physicomechanical parameters of the composite materials synthesized.

First, we consider the nonmodified finely dispersed composites. The fractions of components with particle sizes of less than 10 nm were calculated from the light scattering data (Table 2). It can be seen from Table 2 that, for the studied modifiers, the content of particles with diameters of less than 10 nm varies from 0 for glass spherules to a maximum value of 86% for the *A*-300 finely dispersed silicon oxide. This suggests that there is a clear correlation between the polydispersity

Table 1. Strength parameters of film materials filled with individual modified finely dispersed compounds (T = 20°C)

Sample no.	Filler composition	M_{100}, MPa	M_{300}, MPa	P, MPa	L, %
1	Initial sample	2.6	4.4	6.0	500
2	5% *A*-300m	3.9	5.4	5.9	400
4	5% GSm	3.6	5.5	6.0	390
6	3% DNDm	3.1	4.3	5.2	505

Note: M_{100} is the resistance force at a strain of 100%, M_{300} is the resistance force at a strain of 300%, P is the conventional strength, and L is the elongation.

Table 2. Characteristics of the polydispersity distributions of finely dispersed particles

Parameter of polydispersity distribution	*A*-300	Detonation nanodiamonds	Glass spherules
Mean particle diameter *D*, nm	11.2 (51.8)*	23 (17.9)	39 (20.3)
Content of particles with a size ≤10 nm, %	86 (0)	8 (43.0)	0 (27.0)

* Parameters for particles of modified nanofillers are given in parentheses.

parameter of the fillers and the aforementioned physicomechanical characteristics of the films prepared with these fillers.

Then, we consider the modified fillers. Figure 2 shows the polydispersity distributions of the modified fillers in a nonpolar medium. It can be seen from Fig. 2 that, after the modification, the fillers remain nanodispersed materials. The statistical data obtained from these distributions are presented in Table 2. As follows from this table, the mean particle diameter drastically increases (by a factor of approximately 5) for the modified *A*-300 filler and, in contrast, decreases for the modified detonation nanodiamonds and modified glass spherules. The origin of such a change in the mean diameter of detonation diamond particles can be explained within the model illustrated in Fig. 3.

According to the proposed model (with due regard for the data available in the literature), the detonation nanodiamonds can be regarded as aggregates of fractal nature [9]. Under the assumption that a fractal aggregate can be simulated by a spherical particle, the relationship for the effective radius of such a particle can be written in the following form: $R' = r_0 N^{1/d_f}$, where N is the number of primary particles in the aggregate, d_f is the fractal dimension, and r_0 is the effective cluster radius. The aggregate is stabilized both through the hydrogen bonds formed by different functional groups on the inner surface of particles and through zeolite-type water molecules. The silylation reaction results in the breaking of stabilizing bonds, which leads to a change in the polydispersity parameters. As follows from the fractal model of detonation nanodiamond aggregates, they can break down into N initial particles. However, owing to the steric hindrances to the silylation reaction, only the loosest aggregates can break down, after which the system again transforms into the stable state.

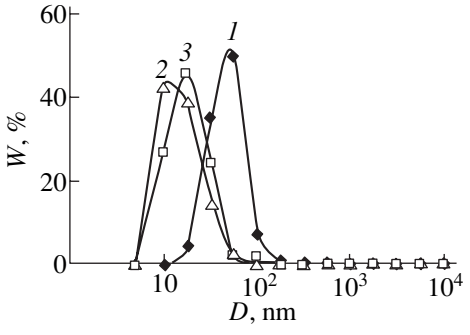

Fig. 2. Polydispersity distributions of modified particles: (*1*) *A*-300 finely dispersed silicon oxide, (*2*) detonation nanodiamonds, and (*3*) glass spherules. The dispersive medium is toluene.

Therefore, the difference between the physicomechanical parameters of the LPS–PDMS composites containing the initial and hydrophobized individual modifiers is a consequence of the change in the size distribution of the modifier particles due to the silylation reaction (a decrease in the fraction of particles less than 10 nm in size). From this inference it immediately follows that the larger the fraction of particles less than 10 nm in size, the stronger the grounds to assign a finely dispersed material to nanofillers.

3.3. Composite Fillers

Following modern concepts, elastomeric materials modified by dispersed fillers are considered to be hierarchic systems with size levels [10, 11]. The polymer volume involving at least one filler particle adjacent to a layer of the matrix is chosen as the lower size level. It can be expected that the higher the surface activity of the particle, the larger the amount of matrix material in a structural unit of the first level and, hence, the larger the volume ratio of the relevant structural units. If the filler is composed of two finely dispersed materials with low (*L* type) and high (*H* type) surface activities, this filler represents a system of two hierarchies corresponding to two types of structural units of particles. In this case, the topological distribution of structural units over the volume is characterized by the formation of ensembles that involve large-sized structural units of *H* particles in the environment of small-sized structural units of *L* particles. It is reasonable to assume that the supramolecular structure thus formed is more isotropic than the structure containing individual fillers of the *H* type. As a result, the physicomechanical characteristics of films modified by a composite filler can turn out to be higher than those obtained with the use of individual fillers; i.e., the synergy effect can manifest itself.

In order to verify the validity of the proposed model of polymer materials with optimum physicomechanical parameters, we prepared a number of films with composite fillers. The modified glass spherules were used as the *L* component, and the technical-grade diamond-containing nanocarbon and modified detonation nanodiamonds served as the *H* component. The use of the

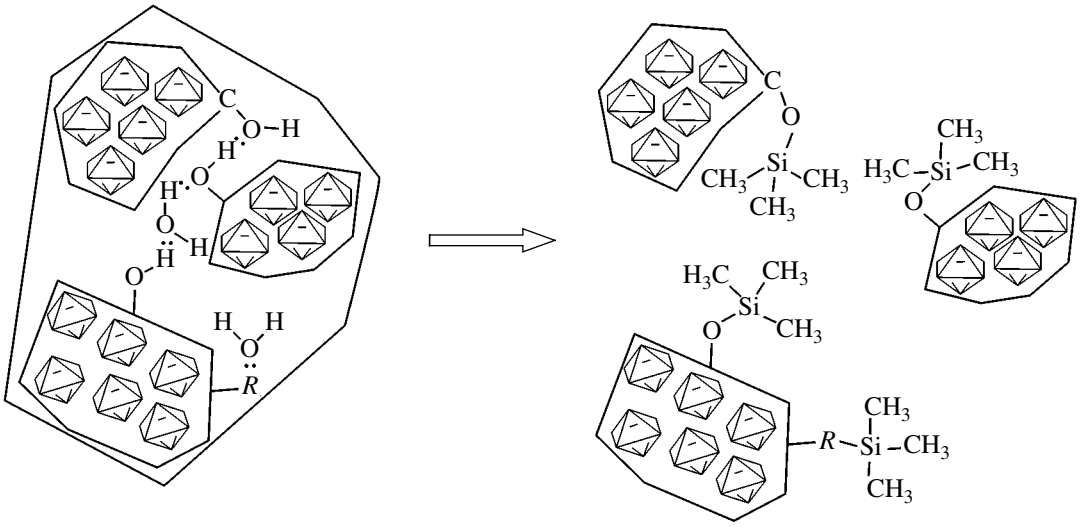

Fig. 3. Schematic drawing of the chemical modification of detonation nanodiamond particles. *R* is a functional group (–OH, $–NH_2$, –COOH, etc.) containing an active proton.

technical-grade diamond-containing nanocarbon among the modified fillers is fairly justified. The detonation nanodiamonds are synthesized in such a way that the technical-grade diamond-containing nanocarbon can be treated as modified detonation nanodiamonds [12]. It should be noted that the modification is accomplished directly in the course of detonation synthesis, and, hence, its efficiency is very high. Therefore, we can assume that particles of diamond allotropy in the technical-grade diamond-containing nanocarbon retain the highest degree of dispersion, which is provided by the synthesis, and, as a consequence, the highest surface activity.

The physicomechanical parameters of the prepared films with optimized compositions are presented in Table 3. The composition was optimized so that, in accordance with the purpose of our investigation, the content of the *H* component would be minimum and the total filler content would be no higher than 5 wt %. A comparison of the data presented in Tables 1 and 3 showed that the use of composite fillers ensures an increase in the physicomechanical parameters in the strain range of interest at the level attained with individual fillers. The sole exception is provided by film 8 (with technical-grade diamond-containing nanocarbon as the *H* component), which is characterized by an appreciable increase in the stress–strain parameters (by a factor of ≈1.7). It should be noted that a comparable increase in these parameters for the films with both composite and individual fillers was achieved at a considerably lower degree of filling with respect to the *H* component in the former case (1 and 5 wt %, respectively). This can be associated with the difference in the supramolecular structures formed by modifiers of these two types. The use of the composites containing the *H*- and *L*-type fillers provides a maximum efficiency of interaction of the force fields induced by supramolecular structural units. In turn, the interaction of the force fields results in a more efficient supramolecular organization of the polymer. Most likely, it is this circumstance that is responsible for the large stress–strain parameters obtained for the composite filler with technical-grade diamond-containing nanocarbon.

Table 3. Effect of composite modifiers on the strength parameters of the ladder phenylsilsesquioxane–poly(dimethylsiloxane) polyblock copolymer (T = 20°C)

Sample no.	Filler composition	M_{100}, MPa	M_{300}, MPa	P, MPa	L, %
1	Initial sample	2.6	4.4	6.0	500
7	1% *A*-300m, 4% GSm	3.4	5.2	5.9	400
8	2.5% TDNC, 2.5% GSm	4.3	6.4	7.0	300
9	1% DNDm, 4% GSm	3.2	5.2	5.8	350

REFERENCES

1. S. N. Chvalun, in *Proceedings of IV Session of International School on Qualification Improvement "Engineering and Chemical Science for Advanced Technologies"* (Nauchno-Issled. Fiz.–Khim. Inst., Moscow, 1998), p. 71.
2. S. Dolgoplosk, V. Savchenko, N. Martyakova, and E. Aleskovskaya, in *Papers of 5th International Conference on Silicone in Coatings* (Brussel, 1996), p. 17.
3. L. V. Agibalova, A. P. Voznyakovskiĭ, V. Yu. Dolmatov, and V. V. Klyubin, Sverkhtverd. Mater., No. 4, 87 (1998).

4. A. P. Voznyakovskiĭ and A. S. Ramsh, Vysokomol. Soedin. **42** (8), 1337 (2000).
5. A. P. Voznyakovskiĭ, V. V. Klyubin, V. Yu. Dolmatov, and L. V. Agibalova, Sverkhtverd. Mater., No. 2, 64 (2000).
6. A. A. Lur'e, *Chromatographic Materials: A Handbook* (Khimiya, Moscow, 1978), p. 179.
7. A. I. Gusev and A. A. Rempel', *Nanocrystalline Materials* (Fizmatlit, Moscow, 2001).
8. N. F. Uvarov and V. V. Boldyrev, Usp. Khim. **70** (4), 307 (2001).
9. V. Yu. Dolmatov, Usp. Khim. **70** (7), 687 (2001).
10. *Structural Mechanisms of Formation of Mechanical Properties of Granular Polymer Composites*, Ed. by V. V. Moshev (Ur. Otd. Ross. Akad. Nauk, Yekaterinburg, 1997).
11. O. K. Garishin, Vysokomol. Soedin. A **44** (4), 666 (2002).
12. A. P. Voznyakovskij, T. Fujimura, A. Yu. Neverovskaya, and V. Yu. Dolmatov, in *Materials of 2nd International Conference on Materials and Coatings for Extreme Environments* (Katsively, Crimea, 2002), p. 201.

Translated by O. Borovik-Romanova

Physics of the Solid State, Vol. 46, No. 4, 2004, pp. 649–650. From Fizika Tverdogo Tela, Vol. 46, No. 4, 2004, pp. 633–634.

MODIFICATION OF SURFACE AND THE PHYSICOCHEMICAL PROPERTIES OF NANODIAMONDS

A New Method for Deaggregation of Nanodiamond from Explosive Detonation: Graphitization–Oxidation Method[1]

Kang Xu and Qunji Xue

State Key Laboratory of Solid Lubrication, Lanzhou Institute of Chemical Physics, Chinese Academy of Sciences, Lanzhou, 730000 China

e-mail: kangxu@lsl.ac.cn

Abstract—In this communication, a new method for the deaggregation of detonation nanodiamond (ND) and some preliminary results using this method are presented. ND is firstly graphitized in nitrogen at 1000°C and then oxidized by air at 450°C to remove the surface graphite layer formed. The sample after such treatment was suspended in water by ultrasonics, and the particle-size distributions were measured. It has been found that the diameters of more than 50% of the ND particles can be reduced to less than 50 nm. © *2004 MAIK "Nauka/Interperiodica".*

Nanodiamond (ND) prepared by explosive detonation is a unique sort of synthetic diamond. The first papers on this type of diamond were published in 1988 [1, 2]. One distinct feature of this kind of diamond is the nanometer-sized particles. As measured by electronic microscopy, the diameters of the fundamental particles are in the range 4–6 nm [3]. But it can also be seen from the TEM image of ND that a large number of nanoparticles aggregate to form fractal clusters with diameters of hundreds of nanometers or even of several micrometers. However, the nature of the aggregation of ND is not very clear. When ND is dispersed in water by ultrasonics, only a small portion of the ND powder can be transferred into particles with diameters less than 100 nm [4].

As accepted by many researches, in nanomaterials, there are two kinds of aggregation: the "soft aggregation" caused by the adsorption of particles and the "hard aggregation" caused by chemical bindings between particles. From the HRTEM images of ND [3], it is evident that each nanosized particle is a diamond single crystallite with a unique lattice image and that there is an unclear boundary between two crystallites. We believe that this is, perhaps, a cocrystalline phase between the two crystallites, which causes the aggregation of the particles. We think this is a special kind of hard aggregation, which may be stronger than the aggregation caused by ordinary chemical bindings. Apparently, it is impossible to deaggregate such bonding between diamond crystallites by ordinary chemical methods.

Kuznetsov *et al*. [5, 6] reported that the HRTEM images of ND heat-treated at temperatures higher than 1000°C in vacuum show that graphitization occurs on the surface of ND crystallite. We deem that, when two diamond crystallites bound together by a cocrystalline are heat-treated, graphite layers could be formed on their surfaces and the boundary regions. If the temperature of heat treatment is not too high and the period of treatment is not too long, it is possible to confine the formation of only a thin layer of graphite on the surface of diamond particles, including their grain boundary. Now, if we can use some suitable method to remove the graphite layer, then the aggregated diamond crystallites can perhaps be deagglomerated. We call this method the graphitization–oxidation method.

ND powders were prepared by the detonation of a 50/50 TNT/RDX charge using water as the cooling and protective medium. The obtained black powder (detonation soot) was treated with a mixture of boiling nitric and sulfuric acid to remove the nondiamond components. For graphitization, the ND was heat-treated in N_2 at 1000°C for 1 h, after which the color of the sample changed completely to dark black, indicating that graphitization occurred. For oxidation, the sample is treated in air at 450°C for several hours. It is worth noting that, only after slight oxidation, i.e., heated in an air flow at 450°C for about 2 h, does the black color of the graphitized diamond particles fade and is the original color of ND completely recovered. So, we can confirm that graphitization of ND at 1000°C for 1 h only produces a thin layer of graphite on the surface of ND crystallites.

The ND sample after the graphitization–oxidation treatment was dispersed in water by ultrasonics. The particle size distributions of ND in the obtained suspensions were measured on a N-4 Plus dynamic laser scattering apparatus (Coutler Co.), and the results are shown in Fig. 1. It can be seen that, in the suspension of the ND after graphitization–oxidation treatment, more than 50% of the particles have diameters less than 50 nm (Fig. 1b), which is much greater than that in the suspension of the untreated ND (Fig. 1a). So, it is believed that the graphitization–oxidation method has some effect on

[1] This article was submitted by the authors in English.

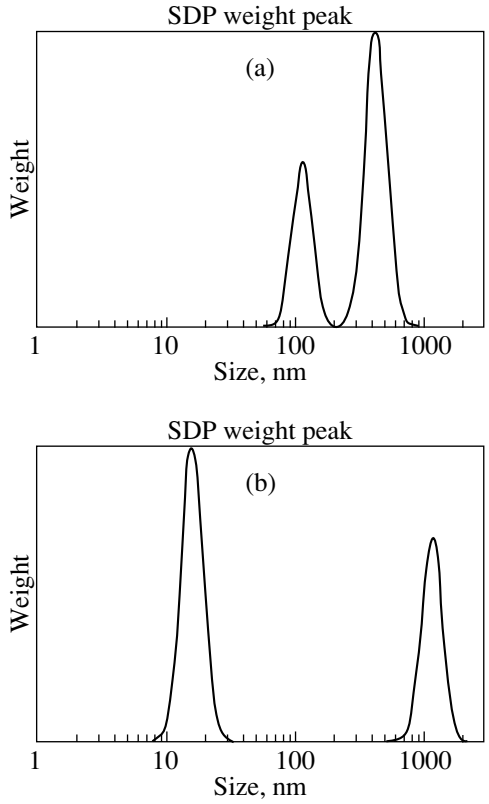

Fig. 1. Particle distribution of aqueous suspensions prepared from (a) original ND and (b) from ND after graphitization–oxidation treatment.

the deaggregation of ND. However, it can also be seen that, after the graphitization–oxidation treatment, some particles with larger diameters (approximately 1000 to 2000 nm) are also formed.

The samples were examined by FTIR spectrometry (on a Bio-Rad FTS-165 IR spectrometer). From the spectra (Fig. 2), we can see that the characteristic band of the carbonyl group (ν = 760 cm^{-1}) disappears after graphitization and reappears after oxidation, while the characteristic band (ν = 1100 cm^{-1}) of the ethereal group (C–O–C) is enhanced after graphitization and oxidation, which means that more bridged oxygen bonds are formed. Whether these bridged oxygen bonds are formed on the surfaces of diamond crystallites or between the crystallites is not clear, but we suppose at least a portion of such bridged oxygen bonds are formed between the diamond crystallites, which results in the formation of agglomerates with larger diameters. If our above suggestion is correct, this means that, during oxidation, more aggregates caused by bridged ethereal bindings are formed. We deem that, in order to deaggregate such a type of bonding, some suitable chemical reactions must be used to cleave the interparticle ethereal bonding. Some preliminary experiments in this aspect were carried out in our laboratory. Several chemical reactions usually used to cleave organic ethers were tested for this purpose, and the samples were examined after treatment by a simple method; that is, the sample was suspended in

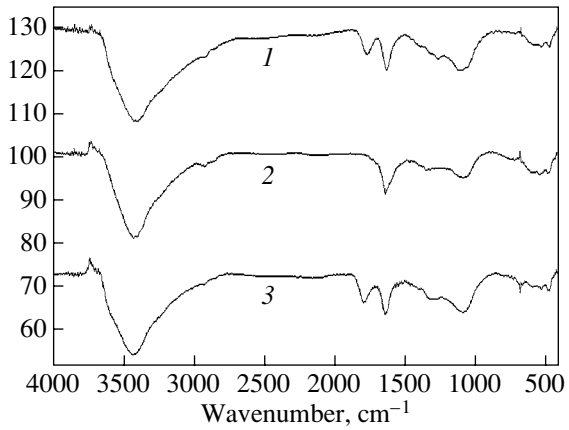

Fig. 2. FTIR spectra of (*1*) original ND, (*2*) ND after graphitization, and (*3*) sample *2* after oxidation.

water by ultrasonics and the amount of the ultrafine particles (with diameters less than 100 nm) in the aqueous suspensions were determined by the centrifugal sedimentation method. The suspension was centrifuged at a speed of 4000 rpm for 30 min, and the amount of particles remaining in the suspension was determined by weighing the residue after drying. The preliminary results indicate that, among the many chemicals used, hydroiodic acid may be the most effective; after reflexing in HI acid solution for 24 h, the amount of ultrafine particles can be remarkably increased. These experiments are still in progress, and the detailed results will be published later.

In summary, a new method for the deaggregation of detonation ND is developed. In this method, the ND is first heat-treated to set off surface graphitization and then air oxidation is used to remove the thin surface graphite layer. So, this method is called the graphitization–oxidation method. The preliminary experimental results of deaggregation of ND using this method indicate that it has some positive effects on the deaggregation of ND. Since the graphitization–oxidation process is rather complicated, further investigation is needed to verify the mechanism and usefulness of this method.

REFERENCES

1. N. R. Gneiner, D. S. Phillips, J. D. Johnson, and F. Volk, Nature **333**, 440 (1988).
2. A. E. Lyamkin, E. A. Petrov, A. P. Ershov, *et al.*, Dokl. Akad. Nauk SSSR **302** (3), 611 (1988) [Sov. Phys. Dokl. **33**, 705 (1988)].
3. T. Xu, K. Xu, and J. Z. Zhao, Mater. Sci. Eng. B **38** (1), L1 (1996).
4. V. L. Agibalov, A. P. Voznyakovskiĭ, V. Yu. Dolmatov, and V. V. Klyubin, Sverkhtverd. Mater., No. 4, 87 (1988).
5. V. L. Kuznetsov, A. L. Chuvilin, Yu. Butenko, *et al.*, Chem. Phys. Lett. **222** (4), 343 (1994).
6. Y. V. Butenko, V. L. Kuznetsov, A. L. Churilin, *et al.*, J. Appl. Phys. **88** (7), 4380 (2000).

Physics of the Solid State, Vol. 46, No. 4, 2004, pp. 651–656. From Fizika Tverdogo Tela, Vol. 46, No. 4, 2004, pp. 635–640.

MODIFICATION OF SURFACE AND THE PHYSICOCHEMICAL PROPERTIES OF NANODIAMONDS

Diamond-to-Graphite Conversion in Nanodiamond and the Electronic Properties of Nanodiamond-Derived Carbon System

T. Enoki

Department of Chemistry, Tokyo Institute of Technology, Tokyo, 152-8551 Japan

e-mail: tenoki@chem.titech.ac.jp

Abstract—Heat-treatment-induced conversion of nanodiamond to nanographite is investigated. Graphitization starts at the surface region around a heat-treatment temperature of 900°C, then it proceeds inward in the particle, and finally it is completed around 1600°C, where nanographite particles form a polyhedron with a hollow inside. The change in the electronic feature is subjected to the structural change induced by the heat treatment. In the intermediate stage of graphitization, where graphene sheets are small and defective, charge transfer takes place from graphitic π-band to nonbonding edge states. Electrophoretic deposition of nanodiamond particles provides a technique for fabricating isolated single nanodiamond particles on a substrate. Successive heat treatment at 1600°C converts a nanodiamond particle to a single nanographene sheet laying flat on a highly oriented pyrolytic graphite substrate. Weak interaction between the nanographene sheet and the substrate is expected to give a model system of nanographene, for which theory predicts the presence of nonbonding π-electron states of the edge origin and its related unconventional nanomagnetism. *© 2004 MAIK "Nauka/Interperiodica".*

1. INTRODUCTION

Nanosized carbon systems, such as fullerenes, carbon nanotubes, and nanographene, are of current interest in supramolecular chemistry, mesoscopic physics, and molecular device applications. Among them, nanodiamond, whose structure is governed by the sp^3 carbon bond network, has unique features different from the other nanosized carbon systems having π-electron networks. In addition, the surface of nanodiamond is subjected to a structural reconstruction or the effect of functional groups attached to the surface. In the case of diamond whose surface carbon atoms are bonded to hydrogen atoms, the electron emission is expected to be associated with negative electron affinity [1]. In the meantime, theoretical works have recently predicted the emergence of unconventional magnetism around the grapheme–diamond interface [2]. In this context, it is interesting to investigate the conversion of nanodiamond to nanographite, where the interface between the graphite and diamond phases is expected to impart structural and electronic features different from both phases. The finiteness in size is also considered to affect the conversion mechanism and resulting structures.

Another challenging issue in nanoscience is the fabrication of a single nanographene sheet, which is ascribed to the nanosized extreme of a condensed polycyclic aromatic molecule in the language of organic chemistry, by using nanodiamond as a starting material. In recent theoretical and experimental works [3–6], it has been revealed that nanographene has a nonbonding π-electron state of edge origin, which gives rise to the appearance of unconventional nanomagnetism.

In the present paper, we have investigated the process of the conversion of nanodiamond to nanographite in the heat-treatment temperature (HTT) range up to 1600°C from structural and electronic aspects by means of x-ray diffraction, high-resolution transmission electron microscope (HRTEM), scanning electron microscopy (SEM), Raman scattering, scanning tunneling microscopy (STM), atomic force microscopy (AFM), magnetic susceptibility, and ESR. Electrophoretic deposition of nanodiamond and subsequent heat treatment was found to produce an isolated single nanographene sheet.

2. HEAT-TREATMENT-INDUCED CONVERSION OF NANODIAMOND TO NANOGRAPHITE

Diamond is converted to graphite thermally by the heat treatment. In such a heat-treatment-induced conversion, nanodiamond behaves differently from bulk diamond due to the smallness of the particles. We have investigated the conversion process induced by heat treatment of nanodiamond particles having a mean size of 5 nm in an argon atmosphere [5, 7]. Raman spectra, which are sensitive to the presence of graphite with the *G* and *D* peaks located in the 1590 and 1350 cm^{-1} regions, respectively, prove the presence of the graphitic ingredient even in the HTT range of 900°C, although no evidence of graphite is indicated in

[1] This article was submitted by the authors in English.

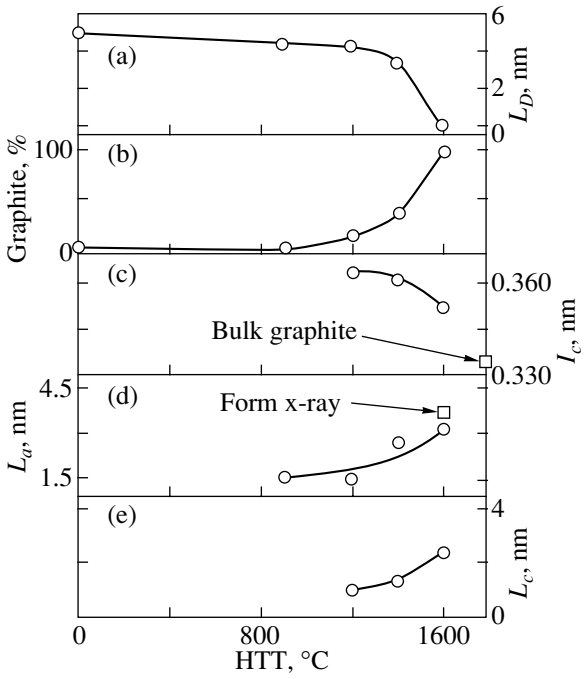

Fig. 1. Variation of the structural parameters with HTT. (a) Diamond size (L_D), (b) conversion ratio of diamond to graphite, (c) observed graphite interlayer distance (I_c), (d) graphite in-plane domain size (L_a), and (e) graphite thickness along the c axis (L_c).

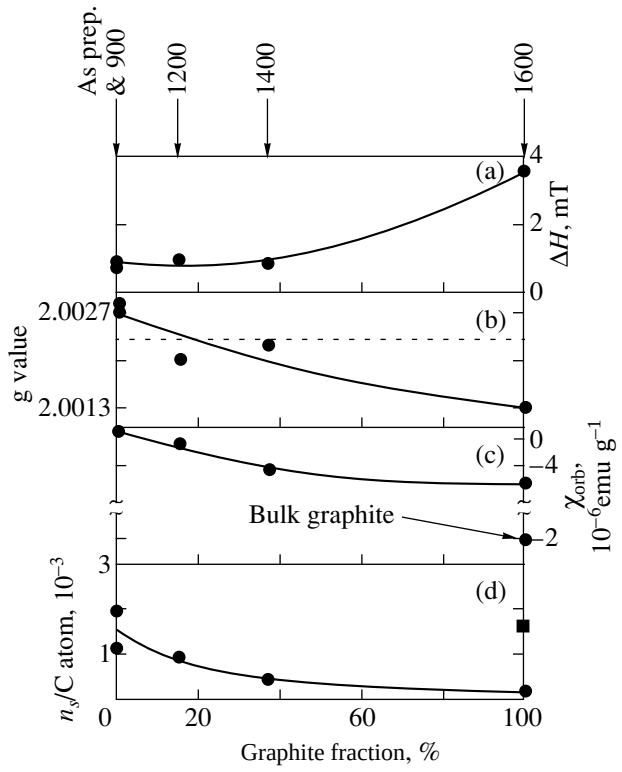

Fig. 2. (a) ESR linewidth H, (b) g value, (c) orbital susceptibility χ_{orb}, and (d) localized spin concentration per carbon atom n_s as a function of the graphite fraction. The dashed line in (b) represents the g value of free-electron spin. The full square at 100% in (d) is the estimate of the π-electron concentration. HTT is also given at the top of the figure.

HRTEM and x-ray diffraction experiments. This suggests that only the surface region of nanodiamond particles is graphitized around that temperature, where nanographene domains are too small to be stacked as in bulk graphite. Graphitization proceeds inward upon further elevation of HTT at the expense of the nanodiamond phase, as proved the appearance of graphitic structures in HRTEM and x-ray diffraction. Figure 1 shows the variation of the structural parameters as a function of HTT. The graphite fraction grows steeply above ~900°C and becomes 100% around HTT = 1600°C. The growth in in-plane size (L_a) is followed by the development of a c-axis stacking structure, as shown in Figs. 1d and 1e. At around HTT = 1600°C, where graphitization is completed, the size of nanographite becomes $L_a \times L_c \approx 3 \times 2.5$ nm, which gives a mean number of stacked graphene sheets of ~7. HRTEM observations visualize the shape of a nanographite particle obtained by heat treatment at 1600°C. The particle forms a polyhedron with a mean size of 7–8 nm and a hollow inside, where each facet consists of a stacking of 3–7 graphene sheets, which is in good agreement with the x-ray diffractions. The interlayer distance I_c, which is a good indication of regularity of the graphitic structure, is considerably larger than that of bulk graphite (I_c = 0.3345 nm) in the beginning of graphitization around HTT = 1200°C, suggesting the presence of remnant corrugated features of the graphene sheets. The value of I_c ~ 0.353 nm at HTT = 1600°C is still larger than that of bulk graphite, though I_c decreases as the HTT is elevated. This is due to the turbostatic nature of the graphene sheets. Interestingly, the interlayer distance tends to be smaller as we go from the surface to the center of the polyhedron [8].

Next, we discuss the change in the electronic structure upon heat treatment. The magnetic properties impart clues for characterizing the electronic properties. Figure 2 presents the ESR linewidth ΔH, g value, orbital susceptibility χ_{orb}, and localized spin concentration n_s as functions of the graphite fraction. The orbital susceptibility is negligibly small ($<10^{-7}$ emu/g) for the samples with HTT < 900°C, suggesting the absence of an extended π-electron network.

The increase in the graphite fraction upon elevating the HTT increases the absolute value of χ_{orb} successively, and above HTT ≥ 1400°C it becomes larger than that expected for the graphene sheet having the in-plane size obtained from the Raman spectra with the assumption that χ_{orb} of the samples can be obtained by extrapolating the values of condensed polycyclic aromatic hydrocarbons consisting of a small number of benzene rings. This means that the samples with HTT ≥ 1400°C have the extended π-electron system, as bulk graphite has. However, the absolute value is still smaller than that of bulk graphite even at HTT = 1600°C. This is considered to be associated partly with the presence of a remnant corrugation of graphene sheets. In addition to this, the anomalous electronic structure generated around the edges of nanographene, which is theoreti-

cally predicted as the nonbonding π-electron state of edge origin, can also be responsible for the modification of the orbital susceptibility. The Raman spectra give a hint in considering this context. Figure 3 presents the positions of the *G* peak, *D* peak, and the peak in the 1620 cm^{-1} region as functions of the graphite fraction, which correspond the E_{2g2} mode, the disorder-induced line, and a shoulder related to the disorderedness of graphite. The *G* peak position is lower than that of bulk graphite in the samples with HTT < 900°C. This downshift is caused by bond angle disorder present in the sp^3-bonded fraction, which forces the graphene sheet to be nonplanar. The increase in the graphite fraction shifts the peak position above the peak position of bulk graphite, resulting in a stiffening of the graphitic lattice. Such stiffening happens in general when charge transfer from acceptor to graphite makes the bonding π band partly vacant. According to previous works [3, 4], nonbonding edge states are present around the peripheries of nanographene sheets. In the present samples, edge states are broadened by the structural disorder in the nanographite particles. Charge transfer from the π band to the edge states generates holes, resulting in an upward shift of the *G* peak, in addition to the reduction in the orbital susceptibility, which demonstrates the importance of the edge states in the electronic structure of the nanographite. In this connection, it should be noted that the presence of holes is confirmed by the thermoelectric power in nanographite [6].

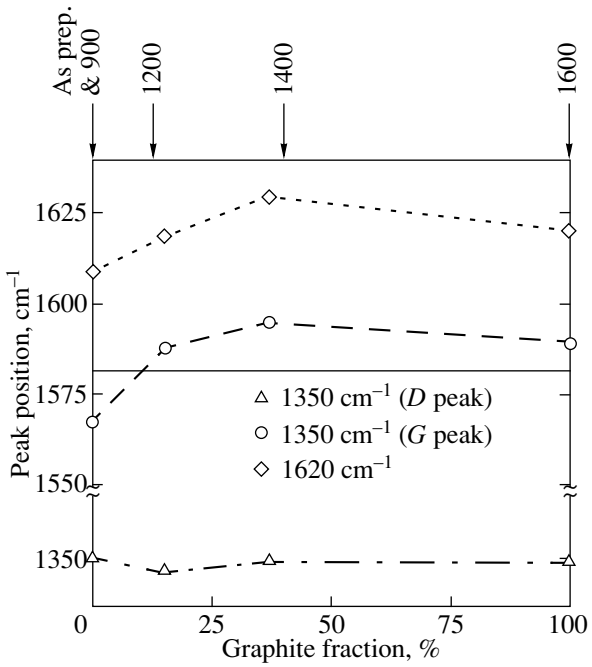

Fig. 3. Peak position in Raman spectra as a function of the graphite fraction for the 1350 cm^{-1} (*D* peak), 1590 cm^{-1} (*G* peak), and 1620 cm^{-1} (diamond) regions. The solid line is the peak position for the bulk graphite *G* peak. HTT is also given at the top of the figure.

Localized spins also reflect the electronic structure modified by the heat treatment. According to the spin concentration plotted as a function of the graphite fraction shown in Fig. 2d, the spin concentration decreases upon an increase in the graphite fraction. The as-prepared nanodiamond particles have many defects, as they are prepared in nonequilibrium conditions produced by explosion-induced transient high pressure. Therefore, a large number of defects are considered to be responsible for the localized spins for HTT < 900°C. This is supported by the fact that the *g* value is quite close to the *g* value of microcrystalline diamond, where the spins are attributed to the paramagnetic centers created by the defects in the sp^3 network [9]. Further heat treatment reduces the spin concentration, with the ESR linewidth broadened and the *g* values shifted downwards to below the *g* value of the free electron spins. In the sample of HTT = 1600°C, where graphitization is completed, the ESR signal is split into sharp and broad signals with different *g* values, which are assigned to the defect spins and π-electron spins, respectively. In the intermediate range with 1200 < HTT < 1400°C, the graphene sheets are strongly corrugated with the presence of defects, in which the defects and π-electron spins are coupled to each other, giving rise to the linewidth broadening. Completion of graphitization wipes defects away from the extended π-electron region, resulting in the splitting of the ESR signal into the two peaks. Interestingly, the spin-lattice relaxation rate is accelerated above HTT = 1400°C. In the sample with HTT = 1600°C, the interaction between edge-state spins and conduction π electrons plays an important role in accelerating the spin-lattice relaxation process. In contract, the presence of defects hinders the interaction, since the relaxation rate has been slowed down.

3. ELECTROPHORETIC DEPOSITION OF NANODIAMOND AND THE FORMATION OF AN ISOLATED SINGLE NANOGRAPHENE LAYER

Nanodiamond particles suspended in a solution can be electrophoretically deposited on a substrate in a controlled way for producing isolated single nanodiamond particles [10]. Successive heat treatment of isolated nanodiamond particles is expected to produce isolated nanographite particles on a substrate. Based on this procedure, we prepared an isolated single nanographene sheet on a highly oriented pyrolytic graphite (HOPG) substrate. As-prepared diamond particles are covered with functional groups containing oxygen, such as carbonyl, carboxylic, lactone, and epoxide. In aqueous and organic suspensions, the dissociation of surface carboxyl groups leads to the formation of negative charges. However, it is found that it is very difficult to isolate single particles due to the trend of particle clusterings.

The improved electrophoretic experiments are carried out with electrodes of HOPG, where nanodiamond

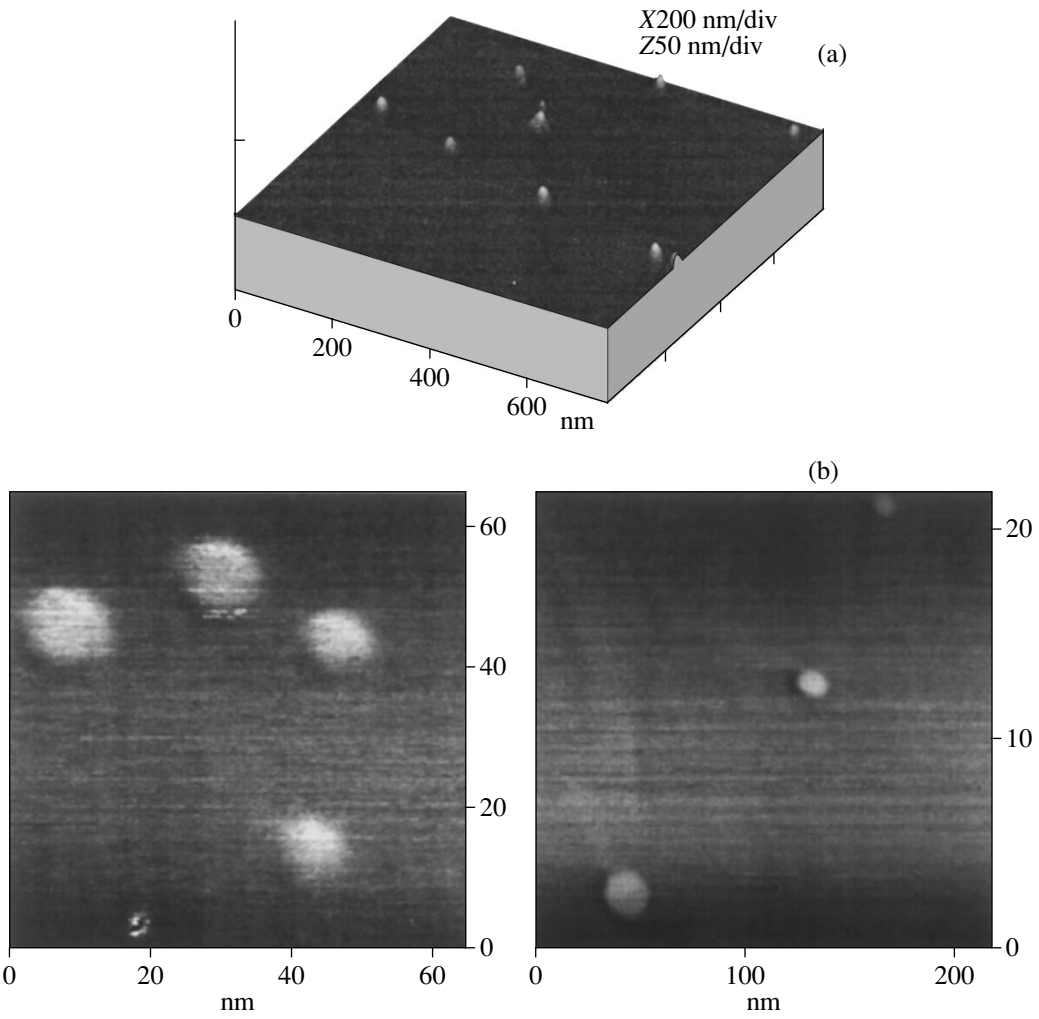

Fig. 4. (a) AFM image of nanodiamond particles dispersed on a HOPG substrate using electrophoretic deposition. (b) STM images of isolated single graphene sheets prepared by heat treatment of nanodiamond particles at 1600°C.

particles are suspended in an isopropyl alcohol solvent mixed with acetone, water, and iodine as additives. Two HOPG electrodes measuring $6 \times 5 \times 0.5$ mm are placed 15 mm apart from each other in the solution. Nanodiamond particles are positively charged in the solution due to free protons, which are produced by the reaction [11]

$$CH_3COCH_3 \rightleftharpoons CH_3C(OH)CH_2,$$

$$CH_3C(OH)CH_2 + I_2 \rightleftharpoons CH_3COCH_2I + H^+ + I^-,$$

and are attached to nanodiamond particles. Judging from SEM observations of the cathode and anode after electrophoretic deposition, we note the presence of nanodiamond particles both on the cathode and anode. However, the density of particles deposited on the anode is very low (~10%) compared with that deposited on the cathode. These findings suggest that the majority of particles are positively charged with their surface adsorbing H^+ ions, though some particles remain with the original negative surface charge that diamond particles take in pure organic solvents without any additives [12]. Thus, the density of deposited nanodiamond particles is subject to the concentration of the additives, the voltage applied, and the deposition time. At low applied voltages (~ –0.07 V/cm), the seeding of nanoparticles takes place, whereas high voltages, such as –67 V/cm, favor an aggregation phenomenon. Interestingly, at a very low concentration of iodine (~ 0.1 mg/l), a simple dipping of electrodes into the suspension without any applied voltage does not result in any deposition. This suggests the feasibility of electrophoretic deposition for seeding nanodiamond particles. It is interesting to note that the density of particles decreases as the deposition time increases. This behavior is attributed to a desorption process that occurs simultaneously with the deposition process. In other words, it seems that nanodiamond particles interact weakly with the surface of the substrate and, consequently, spontaneous separations

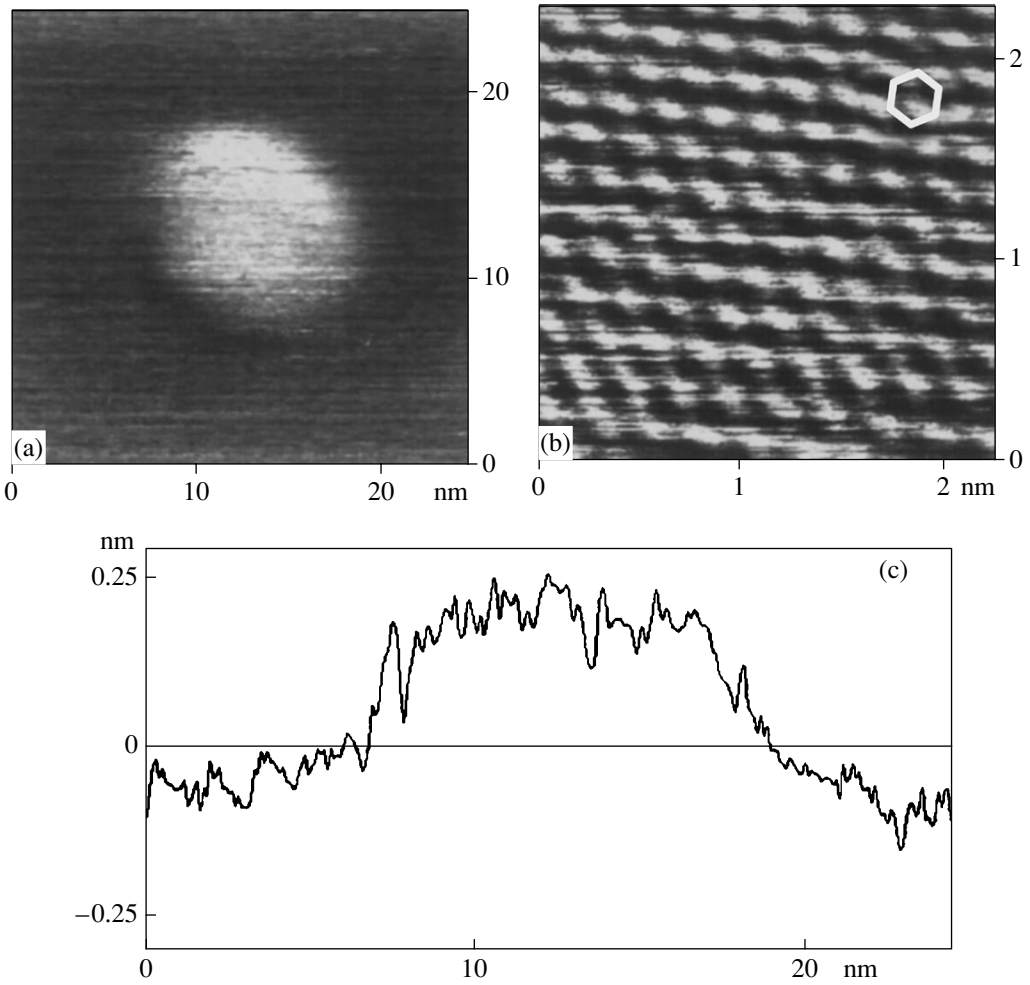

Fig. 5. (a) Image of a single nanographene sheet, (b) lattice image of a single nanographene sheet, and (c) cross-sectional analysis. The hexagon represents a benzene ring. The section profile is in the horizontal direction across the center of the particle.

are possible, leading to the redissolution of particles in the suspension.

The next task is to seed single isolated nanodiamond particles on a substrate from which we obtain isolated single nanographite on the basis of the condition established by the experiments presented above. Isolated nanodiamond particles on a substrate, which are prepared under the conditions of 5 mg/l iodine, an applied voltage of –6.67 V/cm, and a deposition time of 30 s for this purpose, are imaged by AFM as shown in Fig. 4a. From the observed images, it is revealed that the nanodiamond particles are well dispersed, with the interparticle distances large enough to get isolated single particles on the substrate.

The nanodiamond particles are heat treated in an argon atmosphere for 30 min at HTT = 1600°C, which has been suggested to be the appropriate condition for obtaining nanographite particles from the experiments presented in the last section. The obtained particles are imaged by STM as shown in Figs. 4 and 5 [13]. The particles are flat with their planes parallel to the HOPG substrate, where the mean in-plane size of the particles is estimated as ~10 nm. The cross-sectional profile shown in Fig. 5c gives the height of the plane from the substrate to be 0.35–0.37 nm, which is considerably larger than the interlayer distance of bulk graphite (0.3345 nm). Therefore, the obtained particle can be assigned to a single nanographene sheet laying flat on the HOPG substrate. Comparison between the lattice images of the nanographene sheet and the HOPG substrate, which have an in-plane lattice constant of 0.25 nm, suggests that the nanographene sheet is placed epitaxially on the substrate, since the lattice image of the nanographene sheet is well registered to that of the HOPG substrate. This is the first observation of a single nanographene sheet to the best of our knowledge. The number of carbon atoms involved in this nanographene sheet is estimated at roughly $N \sim 3000$.

From the viewpoint of organic chemistry, this is the largest polycyclic condensed aromatic molecule ever observed.

Simply heating nanodiamond particles at 1600°C yields hollow polyhedral nanographite particles, as discussed in the last section. It is surprising to obtain a single nanographene sheet instead of spherical or polyhedral nanographite particles. A trace of oxygen in argon gas in the heat-treatment process might have reacted with the surface of diamond, resulting in part of the particles being oxidized during the heat treatment and thus the observed flat shape. The surface of a nanodiamond particle in contact with the HOPG substrate is more stable to oxidation as compared to the free exposed part. Also, the part that is in contact with the HOPG substrate converts to graphite faster than the free part. The newly converted graphite interacts with the flat HOPG substrate, giving rise to the flat single nanographene sheet.

Finally, we discuss the electronic feature of the nanographene sheet obtained in the experiment. From the observed distance between the nanographene sheet and the substrate, the interlayer interaction (γ_1) becomes reduced by 26–50% when the interlayer distance is elongated from the bulk to 0.35–0.37 nm, where γ_1 = 0.39 eV for the bulk. Therefore, the nanographene sheet obtained in the experiment interacts weakly with the substrate, which is absolutely different form graphene layers produced on metal or carbide surface, as the graphene in the latter is subjected to strong electronic interaction with the substrate through the hybridization of the electronic states [14, 15]. The quantum size effect is also expected to prevail in the electronic structure of the nanographene sheet. The energy discreteness Δ is of the order of W/N, where $W = 6\gamma_0$ is the bandwidth of the π band and the intralayer resonance integral is γ_0 = 3.16 eV. Therefore, the estimated energy discreteness of 75 K is expected to modify the electronic properties at low temperatures through the quantum size effect. More interestingly, in terms of the electronic features, the present nanographene sheet, which is rather independent of the substrate, will be a good target for investigating the nonbonding edge state and its related unconventional nanomagnetism.

4. SUMMARY

Heat-treatment-induced conversion of nanodiamond particles having a mean size of ~5 nm to nanographite in an argon atmosphere is investigated from structural and electronic aspects. Graphitization starts at the surface region around HTT = 900°C, then proceeds inward in the particle, and finally is completed around HTT= 1600°C, where nanographite particles form a polyhedron with a mean size of ~7 nm and a hollow inside. The change in the electronic feature is subjected to the structural change induced by the heat treatment. In the intermediate stage of graphitization, where graphene sheets are small and defective, charge transfer takes place from graphitic π-band to nonbonding edge states. Electrophoretic deposition of nanodiamond particles provides a technique for fabricating single isolated nanodiamond particles on a HOPG substrate. Successive heat treatment at HTT = 1600°C converts a nanodiamond particle to a single nanographene sheet laying flat on a HOPG substrate. The mean size of the nanographene sheets obtained is estimated as ~10 nm, suggesting the presence of ~3000 carbon atoms in a sheet. This is the largest condensed polycyclic aromatic molecule ever reported in organic chemistry. A weak interaction between the nanographene sheet and the substrate, which is reduced by 25–30% as compared to bulk graphite, is expected to give a model system of nanographene, in which theory predicts the presence of nonbonding π-electron states of edge origin and its related unconventional nanomagnetism.

ACKNOWLEDGMENTS

The author expresses his sincere thanks to B.L.V. Prasad, A.M. Affoune, H. Sato, AM. Rao, P.C. Eklund, K. Oshida, M. Endo, Y. Hishiyama, and Y. Kaburagi, on the basis of whose contributions the present work was carried out.

This work was supported by the Grant-in-Aid for "Research for the Future" program, Nanocarbons, and 15105005 from JSPS.

REFERENCES

1. P. K. Baumann and R. J. Nemanich, Surf. Sci. **320**, 409 (1998).
2. K. Kusakabe and M. Maruyama, Phys. Rev. B **67**, 092406 (2003).
3. M. Fujita, K. Wakabayashi, K. Nakada, and K. Kusakabe, J. Phys. Soc. Jpn. **65**, 1920 (1996).
4. K. Wakabayashi, M. Fujita, H. Ajiki, and M. Sigrist, Phys. Rev. B **59**, 8271 (1999).
5. O. E. Andersson, B. L. V. Prasad, H. Sato, *et al.*, Phys. Rev. B **58**, 16387 (1998).
6. Y. Shibayama, H. Sato, T. Enoki, *et al.*, J. Phys. Soc. Jpn. **69**, 734 (2000).
7. B. L. V. Prasad, H. Sato, T. Enoki, *et al.*, Phys. Rev. B **62**, 11209 (2000).
8. V. Yu. Osipov, K. Takai, K. Takahara, *et al.*, private communication.
9. G. K. Walters and T. L. Estle, J. Appl. Phys. **32**, 1854 (1961).
10. A. M. Affoune, B. L. V. Prasad, H. Sato, and T. Enoki, Langmuir **17**, 547 (2001).
11. N. Koura, T. Tsukamoto, H. Shoji, and T. Hotta, Jpn. J. Appl. Phys. **34**, 1643 (1995).
12. J. L. Valdes, J. M. Mitchel, J. A. Mucha, *et al.*, J. Electrochem. Soc. **138**, 635 (1991).
13. A. M. Affoune, B. L. V. Prasad, H. Sato, *et al.*, Chem. Phys. Lett. **348**, 17 (2001).
14. N. R. Gall, E. V. Rut'kov, and A. Y. Tontegote, Int. J. Mod. Phys. **11**, 18 (1997).
15. C. Oshima, H. Itoh, T. Ichinokawa, T. Aizawa, R. Souda, S. Otani, and Y. Ishizawa, *Ordering at Surfaces and Interfaces*, Ed. by A. Yoshimori, T. Shinjo, and H. Watanabe (Springer, Berlin, 1992), Vol. 5, p. 13.

Physics of the Solid State, Vol. 46, No. 4, 2004, pp. 657–661. From Fizika Tverdogo Tela, Vol. 46, No. 4, 2004, pp. 641–645.

MODIFICATION OF SURFACE AND THE PHYSICOCHEMICAL PROPERTIES OF NANODIAMONDS

Electron Emission Properties of Detonation Nanodiamonds[1]

V. V. Zhirnov[1], O. A. Shenderova[1, 2], D. L. Jaeger[1, 2], T. Tyler[1], D. A. Areshkin[1], D. W. Brenner[1], and J. J. Hren[1]

[1] *North Carolina State University, Raleigh, North Carolina, 27695-7907 USA*

[2] *International Technology Center, Research Triangle Park, North Carolina, 27709 USA*

Abstract—This paper summarizes the results of systematic studies of field electron emission from detonation nanodiamond coatings corresponding to nanodiamond powders of different modifications. The role of the chemical composition of the surface of detonation nanodiamond particles in field emission mechanisms is discussed. Field emission–related electronic properties of single diamond nanodots are studied using tight-binding calculations and continuum electrostatic simulations. *© 2004 MAIK "Nauka/Interperiodica".*

1. INTRODUCTION

Extensive studies of field electron emission from diamond have been carried out over the past several years (for a review, see [1]). It was observed experimentally that coating metal field emitters with diamond films (CVD, natural diamond, HPHT, etc.) could significantly enhance electron emission [1]. However, the mechanism of electron emission in such structures is not completely understood because they are complex. The properties of the surface (e.g., electron affinity), new interfaces (e.g., grain boundaries), material inhomogeneities, and/or doping can have dramatic effects on the emission behavior of these composite emitters.

Diamond nanodots (DND) produced by detonation are the smallest (2–5 nm in size) currently observed particles of diamond matter and have many properties that are still unknown. Deposition of the detonation DND on the top of field emission tips allows one to obtain information about the electronic properties of DND from field emission experiments along with information about structure and composition from nondestructive high-resolution transmission electron microscopy.

2. DETONATION NANODIAMOND COATINGS

Detonation DND were deposited onto sharp field emission tips (Si and Mo; curvature radius 10–100 nm) by pulsed electrophoresis in a suspension of diamond nanoparticles in alcohol (for details, see [2–4]). The resulting deposits of diamond nanoparticles were found to depend upon applied voltage, suspension concentration, pulse duration, and tip geometry. This procedure resulted in sufficient control to prepare metal needles with deposits varying from isolated diamond nanodots to continuous nanodiamond films of varying thickness.

Three different types of detonation diamond [5], shown in Table 1, were investigated. Detonation diamond nanoparticles were prepared in the Russian Federal Nuclear Center All-Russian Institute of Technical Physics (VNIITF, Snezhinsk).

Emission *J–F* (current density vs. electric field) characteristics were measured. To compare different coatings of different types of nanodiamond, two parameters were chosen: the emission threshold field (F_{th}) and integral normalized transconductance $\left(g_{\text{n}} = \frac{1}{J}\frac{\Delta J}{\Delta F}\right)$, which is a measure of the steepness of the *J–F* characteristics. As can be seen from Table 1, all three types of nanodiamond coatings showed an improvement in the emission threshold, the smallest threshold being observed for the NdP1 coating. However, the effect of the coatings on the normalized integral transconductance (steepness) was different for different coatings. While the NdO coating resulted in much steeper *J–F* characteristics, as compared to the bare Si emitter, emitters with detonation nanodiamond and NdP1 coatings showed very shallow characteristics in the higher current region (low transconductance). Additional hydrogen-plasma treatment was used to modify surface properties of emitters with NdO and NdP1 coatings (for details, see [2]). Figure 1 shows emission characteristics before and after the plasma treatment. As can be seen, the effects of hydrogen plasma are very different for the two types of nanodiamond.

For the NdO coating, the emission threshold remarkably decreased after hydrogen-plasma treatment and the *J–F* characteristic shifted to the left. The emission threshold improvement was 35% relative to the NdO emitter before hydrogen-plasma treatment and 45% relative to the bare Si field emitter. The hydrogenated NdO coating was found to be the best emissive coating in this series of experiments, having both the

[1] This article was submitted by the authors in English.

Table 1. Properties of three types of detonation nanodiamond particles [5] and field electron emission parameters of corresponding nanodiamond coatings

Nanodiamond type	USDD2	USDD3	USDD4
Alternative name	Nd	NdP1	NdO
Description	Standard	USDD2 with additional acid and high-temperature treatment	USDD3 with additional ozone treatment
Impurities	O, N, H ~ 8–10%	O, N, H ~ 2–4%	N, O ~ 6%
pH of 10% water suspension	5.6–6.2	3.5–4.5	1.6–2.0
Field electron emission parameters			
Change in field emission threshold compared to bare Si field emitter, %	–15	–25	–15
Change in normalized integral transconductance compared to bare Si field emitter, %	–37	–30	+33

lowest emission threshold and highest transconductance.

For the NdP1 coating (Fig. 1b), the emission threshold did not change after treatment in hydrogen plasma. However, the high-current part in the emission characteristics shifted upwards, indicating an increase in transconductance.

The difference in the emission properties of NdO and NdP1 nanodiamond coatings reflects the importance of surface modification. The emission results can be interpreted in terms of the two-barrier metal–diamond–vacuum emission model. In this model, electrons are injected from the conductive electrode (e.g., field emission tip) into diamond through an interface barrier. Then, the electrons move to the diamond–vacuum interface and escape to vacuum through the surface barrier (e.g., the electron affinity). The transparency of both barriers determines the emission threshold. During electron transport in diamond, there are several physical phenomena resulting in the "resistance" of the diamond film, such as negative and positive space charge effects, scattering, hopping conductance, etc. These resistive effects limit the supply of electrons to the surface, which result in shallow or saturated current–voltage characteristics in the higher current region (e.g., lower transconductance).

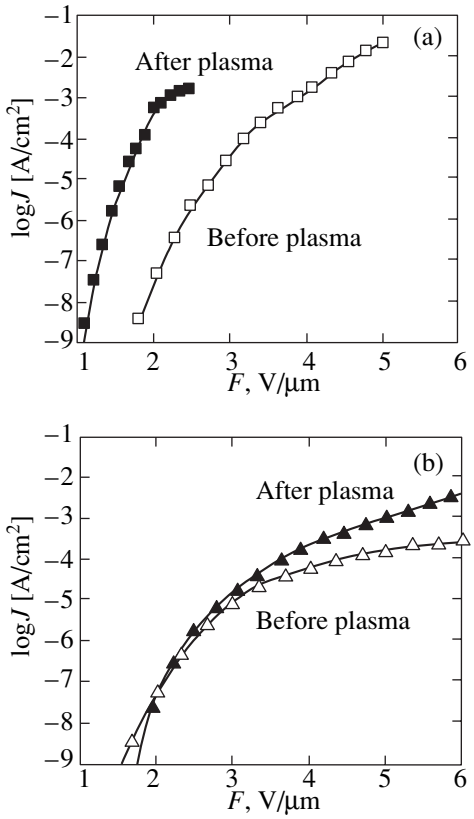

Fig. 1. Hydrogen plasma effect on emission characteristics of detonation nanodiamond coatings: (a) NdO and (b) NdP1.

Nanodiamond of NdO type was treated by ozone, and, correspondingly, it contains larger amounts of oxygen on the surface. Oxygen, being an electronegative element, is known to increase the electron affinity of a diamond surface. Hydrogen-plasma treatment replaces oxygen with hydrogen, which is known to decrease the electron affinity of diamond. Based on the Fowler–Nordheim equation for field emission, the shift of emission characteristics in Fig. 1a corresponds to a decrease in the effective surface barrier of 0.9 eV.

Nanodiamond of NdP1 type (without ozone treatment) apparently contains smaller amounts of oxygen but larger amounts of H and N atoms on the surface. Its emission threshold before H-plasma treatment is lower than NdO; however, the transconductance is lower due to resistive (e.g., negative space charge) effects at higher currents. After H-plasma treatment, the emission threshold did not change; however, the resistance effects became smaller (the transconductance increased). This could indicate the role of nitrogen in the resistance effects, since oxygen-rich samples did not show the resistance effects and the hydrogen content after plasma treatment under the same conditions should be similar in both samples.

3. FIELD EMISSION FROM A SINGLE NANODIAMOND PARTICLE

We attempted to reduce the possible variables by performing experiments with controlled deposits of nanodiamond particles (USDD4—NdO type) with an individual size of about 5 nm. Both the geometry of the underlying metal surface and the diamond particle were observed with atomic resolution using a transmission electron microscope. In the experiments reported here, isolated diamond nanoparticles were deposited onto Mo tips (Fig. 2a) and characterized by field emission, and then the resulting data were compared to that of the bare metal tip before deposition (of the same specimen). Next, a thicker nanodiamond coating was deposited onto the same tip with subsequent field emission measurements. The results of these experiments are summarized in Table 2.

Comparing the *I–V* curves of the bare Mo tip with the same tip with a deposit of one isolated diamond nanoparticle yields a substantial increase (~30%) in the threshold voltage (Fig. 3b, Table 2). However, after the additional deposition of nanodiamond and the formation of a thicker nanodiamond film, a drastic decrease in the threshold voltage (~48%) and increase in the transconductance (~115%) are obvious (Fig. 3b, Table 2).

4. SIMULATION OF FIELD EMISSION–RELATED PROPERTIES

As part of our efforts to develop a reasonable quantitative model of electron emission from diamond nanoparticles, the electronic structure of diamond nanodots containing between 34 and 1600 carbon atoms was calculated using a self-consistent tight-binding Hamiltonian [6, 7]. Analysis of these results indicates that, for cluster sizes larger than approximately 2 nm, quantum confinement effects have relatively little effect and the electrostatic potential distribution is essentially insensitive to cluster size for clusters larger than 1 nm. The calculated electron affinity (EA) of hydrogenated diamond dots with the majority of their surface area corresponding to (111) facets was approximately –1.4 eV. This result is close to the experimental value of –1.27 eV [8] and the theoretical value of –2.0 eV calculated using first-principles density functional theory by Rutter and Robertson [9] for a bulk hydrogenated (111) diamond surface. In the present paper, we address the effect of size on EA in more detail.

It has been demonstrated that the electron affinity of diamond depends on the polar groups on the surface [8]. The sign and magnitude of the surface dipole layer–induced potential drop due to specific polar groups enhances and uniquely determines the electron affinity (Fig. 3a). Figure 3b illustrates continuum electron electrostatic potential distributions within a dielectric sphere with two oppositely charged layers on the surface. The distance between charged layers (0.5 Å) and the related charge density (0.145*e* per carbon atom)

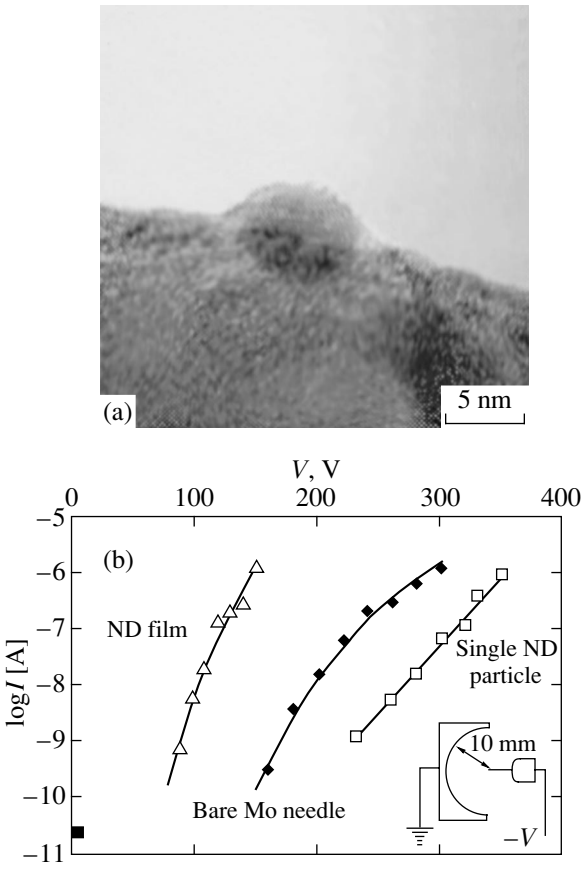

Fig. 2. (a) A single, isolated, tightly bound detonation diamond nanodot on the tip of a needle; field emission characteristics from the isolated nanodiamond particle shown in (a) and (b) a nanodiamond film compared to a bare tip. Inset: schematic of the experimental setup.

corresponds to the C–H dipole strength on a (111) diamond surface obtained from tight-binding simulations. The positive potential drop within the particle shifts the electron energy spectrum upwards and, hence, decreases the EA. Switching the polarity of the charged layers results in an increase in the EA.

For qualitative understanding of the possible effect of size on EA, we assume that introducing a curvature to the initially flat dipole layer corresponding to the macroscopic surface will result in a larger separation of the positively charged H centers for the outer layer (Fig. 3a) and, therefore, inferior conditions for emission. We also assume that the surface area per carbon atom for nanodiamond is similar to that of macroscopic surfaces. Recently, it has been demonstrated that atomic geometrical parameters of hydrogen terminated nanodiamond do not differ appreciably from those for bulk diamond [10]. Given the above assumptions, the effect of size on the potential drop can be evaluated through the equation for the potential distribution inside a spherical capacitor:

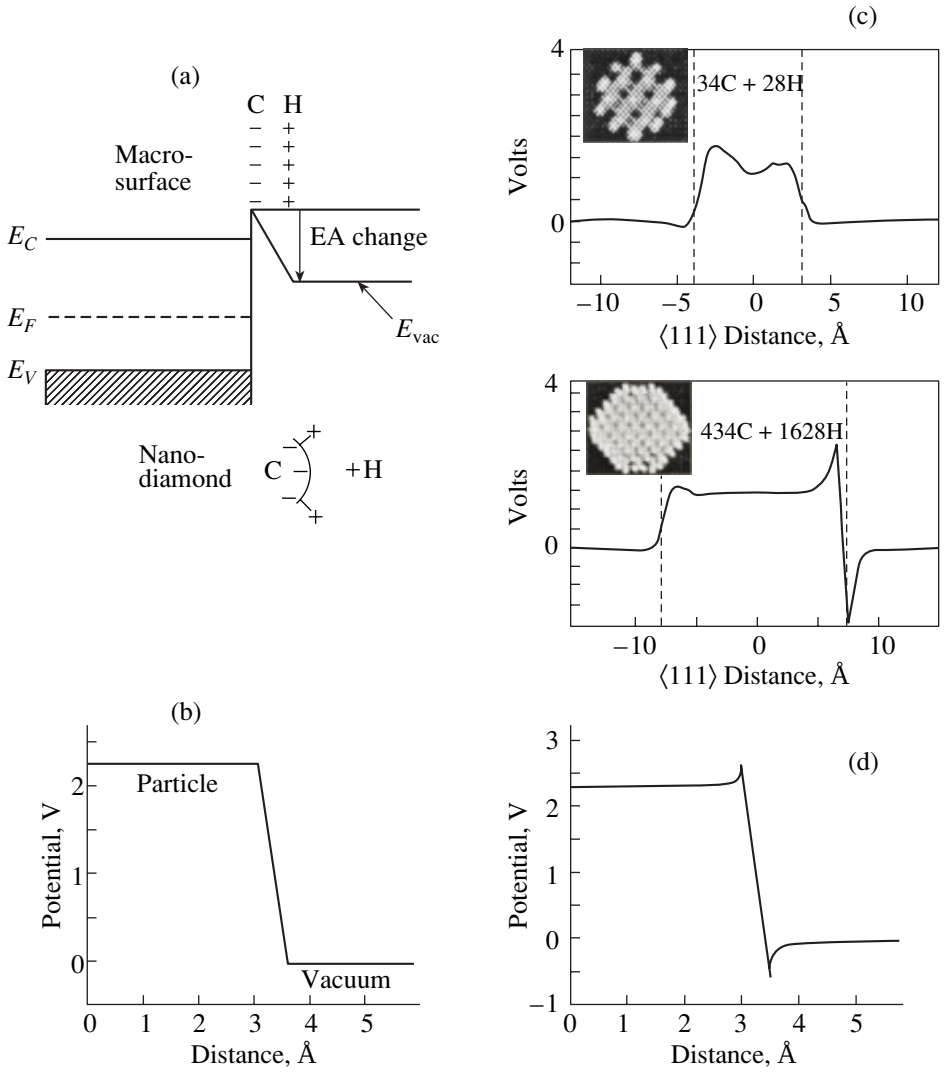

Fig. 3. Illustration of the size effect of electron affinity properties of a nanodiamond particle. (a) Dipole-induced negative electron affinity for a hydrogenated diamond surface. Dipoles are shown for macroscopic flat and "curved" nanoparticle surfaces. Electrostatic potential profile along a radius of a nanodiamond particle calculated for a dielectric sphere with two oppositely charged layers with (b) uniformly distributed charge and with (c) pointed charges on the surfaces. (d) Coulomb potential profile for two diamond clusters calculated with a self-consistent tight-binding Hamiltonian.

$$U = \frac{qd}{A\varepsilon_a}\frac{R}{R+d}.$$

Here, q and d correspond to the charge and length of a dipole, A is the surface area per carbon atom (5.4 Å^2), R is the radius of the inner sphere (carbon atoms), and ε_a is the absolute dielectric permittivity. Figure 4 illustrates the dependence of the voltage drop on the size of the particle using continuum electrostatic simulations. An appreciable effect takes place only for particles with

Table 2. Geometrical and emission parameters of nanodiamond field emitters

	Characteristics	Bare Mo	Single particle	ND film
Geometrical	Metal tip radius, nm	50	50	50
	ND thickness, nm	0	2.3	20
Field emission	Threshold voltage, V	172	222	89
	Transconductance, nA/V	7.63	7.09	16.4
Fowler–Nordheim analysis	Apparent work function, eV	4.05	5.57	2.71

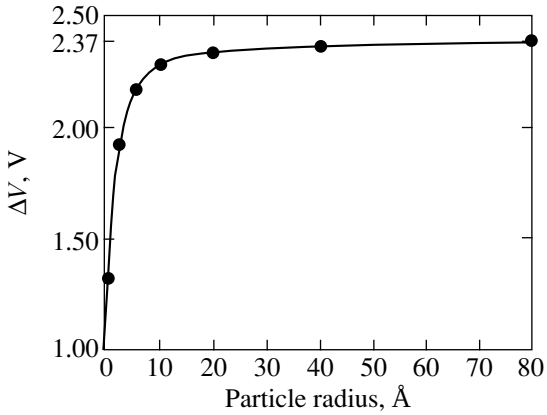

Fig. 4. Illustration of the size dependence of the potential drop within a nanodiamond particle changing the electron affinity. Dipole characteristics are $d = 0.5$ Å and $q = 0.14e$; the area per carbon atom is $A = 5.4$ Å^2.

radii less than ~1 nm. Self-consistent tight-binding simulations indicate a less pronounced size effect for the simulated particles having the shape of truncated octahedrons. A slight decrease (~0.1 V) in the potential can be seen only for a particle less than 1 nm in diameter (Fig. 3d). This can be attributed to the fact that simulated particles are faceted and their surfaces are flat rather than spherical as is assumed in the continuum electrostatic calculations above. Therefore, based on the present results, the effect of size on the EA of a nanoparticle is sensitive to the shape of the particle.

Finally, we point out the presence of small potential spikes in the vicinity of the dipole observed in tight-binding simulations (Fig. 3d). Macroscale descriptions of the negative EA for diamond often neglect these spikes, implying that conduction band electrons experience no barrier to transport into vacuum. These spikes are associated with particular dipoles. Figure 3c shows analogous spikes in the potential profile obtained from continuum electrostatic simulations when continuous charge-layer distribution interface/boundary conditions on surfaces corresponding to dipole layers are substituted by discrete point-charge interface/boundary conditions.

ACKNOWLEDGMENTS

D.W.B., O.A.S., and D.A.A. acknowledge funding by the Office of Naval Research (contract no. 00014-95-1-0279); O.A.S. and D.L.J., the Office of Naval Research (contract no. 00014-02-1-0711).

REFERENCES

1. V. V. Zhirnov and J. J. Hren, MRS Bull. **23**, 42 (1998).
2. V. V. Zhirnov, O. M. Küttel, O. Gröning, *et al.*, J. Vac. Sci. Technol. B **17**, 666 (1999).
3. A. N. Alimova, N. N. Chubun, P. I. Belobrov, *et al.*, J. Vac. Sci. Technol. B **17**, 715 (1999).
4. T. Tyler, V. V. Zhirnov, A. V. Kvit, *et al.*, Appl. Phys. Lett. **82**, 2904 (2003).
5. S. I. Chukhaeva and L. A. Cheburina, Superhard Mater. **2**, 39 (2000).
6. D. W. Brenner, O. A. Shenderova, D. A. Areshkin, *et al.*, Comput. Model. Eng. Sci. **3**, 643 (2002).
7. D. A. Areshkin, O. A. Shenderova, J. D. Schall, and D. W. Brenner, Mol. Simul. **29**, 269 (2003).
8. J. Ristein, Diamond Relat. Mater. **9**, 1129 (2000).
9. M. J. Rutter and J. Robertson, Phys. Rev. B **57**, 9241 (1998).
10. S. P. Russo, A. S. Barnard, and I. K. Snook, Surf. Rev. Lett. (2004) (in press).

Physics of the Solid State, Vol. 46, No. 4, 2004, pp. 662–664. Translated from Fizika Tverdogo Tela, Vol. 46, No. 4, 2004, pp. 646–648.

MODIFICATION OF SURFACE AND THE PHYSICOCHEMICAL PROPERTIES OF NANODIAMONDS

Structure of the Dispersive Medium and Sedimentation Resistance of Suspensions of Detonation Nanodiamonds

A. Yu. Neverovskaya*, A. P. Voznyakovskiĭ*, and V. Yu. Dolmatov**

** Lebedev Research Institute of Synthetic Rubber, Federal State Unitary Enterprise, Gapsal'skaya ul. 1, St. Petersburg, 198035 Russia*

*** Technolog Special Design Bureau, State Technological Institute, St. Petersburg, 192076 Russia*

e-mail: vniisk@mail.rcom.ru

Abstract—The specific features of the stabilization of suspensions formed by detonation nanodiamonds in polar and nonpolar media are investigated. It is demonstrated that the polydispersity of nanodiamond particles in an aqueous medium periodically changes in an ultrasonic field. The conditions are determined under which the optimum dispersity can be maintained for a long time. A technique is devised for chemical modification of the nanodiamond surface through the grafting of organosilyl groups. This technique makes it possible to prepare finely dispersed suspensions of nanodiamonds in nonpolar organic media. A model is proposed for an aggregate that consists of detonation nanodiamond particles and is stabilized through hydrogen bonds formed by functional groups of different types. © *2004 MAIK "Nauka/Interperiodica"*.

1. INTRODUCTION

Detonation nanodiamonds occupy a special place among the known nanocarbons and compare favorably with these nanomaterials owing to the implementation of their pilot production in Russia already in the 1980s (with a total production rate of up to 2 tons per year) [1, 2].

In many fields of their practical application, detonation nanodiamonds are used in the form of suspensions. However, the high surface activity leads to the aggregation of detonation nanodiamond particles even in liquid polar media and, consequently, restricts, to an extent, the possibility of achieving the theoretically predicted properties. Furthermore, in a number of practical situations, it is necessary to use suspensions of detonation nanodiamonds in nonpolar media, even though the nanodiamond surface is hydrophilic [3] and is not solvated by low-molecular liquids. In this respect, an efficient way of stabilizing the degree of dispersion and the structure of suspensions of detonation nanodiamonds in nonpolar media is to modify their surface.

In this work, we investigated the suspensions of detonation nanodiamonds in polar and nonpolar media with the aim of revealing the factors responsible for their stabilization.

2. SAMPLE PREPARATION AND EXPERIMENTAL TECHNIQUE

In our experiments, we used the detonation nanodiamonds synthesized at the Special Design Bureau "Tekhnolog" [4]. The surface of detonation nanodiamonds was modified by chemical grafting with the use of the silylation reaction in an equimolar mixture of Me_3SiCl–$(Me_3Si)_2NH$ and $Me_2ViSiCl$–$(Me_3Si)_2NH$ (where Me = –CH_3, Vi = –CH=CH_2).

In order to choose the optimum conditions for the removal of an adsorption layer from the detonation nanodiamond surface, the kinetics of mass loss in detonation nanodiamonds under high vacuum and elevated temperatures was investigated by mass spectrometry. Examination of detonation nanodiamonds taken from different lots revealed that the composition of the adsorption layer is determined by the chemical composition of the environment at the instant the detonation nanodiamond particles precipitated. From the practical standpoint, a satisfactory degree of surface cleaning is provided by preliminary heating (T = 350°C) under high vacuum for 4 h. In all the experiments performed,

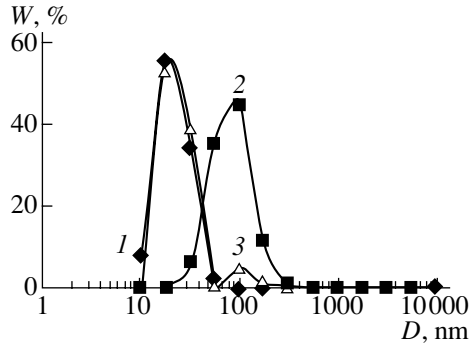

Fig. 1. Relative size distributions of detonation nanodiamond particles in water (*1*) prior to and (*2*, *3*) after ultrasonic treatment for (*2*) 5 and (*3*) 10 min.

1063-7834/04/4604-0662$26.00 © 2004 MAIK "Nauka/Interperiodica"

the detonation nanodiamonds were preliminarily treated under the above conditions.

3. RESULTS AND DISCUSSION

The polydispersity distributions of detonation nanodiamond particles in water are depicted in Fig. 1. Mathematical processing of the data presented in Fig. 1 showed that the detonation nanodiamonds, in terms of their degree of dispersion, belong to nanomaterials: the sizes of ~90% of the particles fall in the range 18–32 nm (Fig. 1, curve *1*). The initial form of the polydispersity distribution persists for 15 min, after which particles with the largest sizes settle out of the suspension. In order to stabilize the initial degree of dispersion, the suspension of detonation nanodiamonds was treated in an ultrasonic field. It was found that the degree of dispersion of the system depends on the time of exposure to an ultrasonic field. The treatment for the first five minutes results in the shift of the polydispersity distribution (Fig. 1, curve *2*) toward the large-size range. Upon exposure to an ultrasonic field for the next five minutes, the polydispersity distribution virtually regains its original form (similar to the initial curve in Fig. 1); however, a number of aggregates are retained (Fig. 1, curve *3*). This degree of dispersion is observed upon treatment in an ultrasonic field for 20 min. Exposure for longer times again leads to aggregation. Such diverse effects of the ultrasonic field on the polydispersity distribution can be associated with the complex processes occurring in the system due to the formation and collapse of cavitation bubbles initiated by the ultrasonic field. Most likely, this can be explained by the surface physicochemical processes resulting in a change in the surface activity of detonation nanodiamonds and also by a structural change in the medium (a change in the fluctuation free volume). Probably, the initial decrease in the degree of dispersion is caused by the removal of solvation shells, which promotes the aggregation. Further exposure to the ultrasonic field leads to dispersion of the newly formed aggregates. Upon ultrasonic treatment for 20 min, the polydispersity distribution is stabilized for approximately 2 h, after which detonation nanodiamonds begin to aggregate. Therefore, in order to ensure an optimum degree of dispersion of detonation nanodiamonds for a long time, the suspension should be periodically rather than permanently exposed to an ultrasonic field. It should be taken into account that, in each cycle, part of the detonation nanodiamond particles (in our experiments, approximately 11 wt %) remain in indestructible aggregates and settle out of the suspension.

Effect of ultrasonic treatment and surface modification on the mean diameter D_n of detonation nanodiamond particles

Parameter	Initial detonation nanodiamonds	Ultrasonic treatment for 5 min	Ultrasonic treatment for 10 min	Modified detonation nanodiamonds
D_n, nm	23.0	95.6	31.2	15.0

The dispersion of detonation nanodiamonds in nonpolar media necessitates chemical modification of the surface. An efficient method of blocking reactive functional groups on the solid surface is based on the silylation reaction. The properties of the surface thus modified are governed by the grafted trimethylsilyl groups. This implies that, after the modification, the surface becomes hydrophobic and free of adsorbed water molecules and hydroxyl functional groups. Moreover, upon the surface modification with trimethylsilyl groups, the degree of dispersion of detonation nanodiamond particles in a nonpolar organic liquid becomes comparable

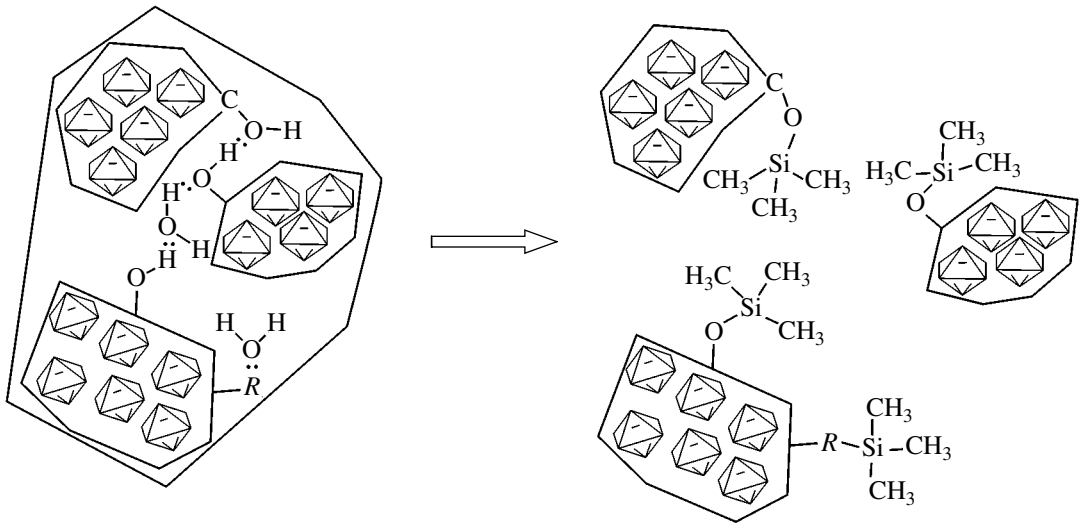

Fig. 2. Schematic drawing of the chemical modification of detonation nanodiamond particles. *R* is a functional group (–OH, $–NH_2$, –COOH, etc.) containing an active proton.

to that in an aqueous medium. In some cases, it is expedient to use the grafting of groups containing double bonds in order to stabilize the surface of detonation nanodiamond particles in nonpolar organic media. This can be accomplished through the replacement of trimethylchlorosilane by dimethylvinylchlorosilane in a silylating mixture. Such a modification of the surface of detonation nanodiamonds results in a paradoxical effect that is difficult to predict, namely, an increase in the degree of dispersion of detonation nanodiamonds in polar media (see table). For the purpose of elucidating this effect, we propose a model of an aggregate that consists of detonation nanodiamond particles and is stabilized through hydrogen bonds formed by functional groups of different types (Fig. 2). According to the proposed model (with due regard for the data available in the literature), the detonation nanodiamond particles can be regarded as aggregates of fractal nature. Under the assumption that a fractal aggregate can be simulated by a spherical particle, the relationship for the effective radius of such a particle can be written in the following form: $R = r_0 N^{1/d_f}$, where N is the number of primary particles in the aggregate, d_f is the fractal dimension, and r_0 is the effective cluster radius. The aggregate is stabilized both through the hydrogen bonds formed by different functional groups on the inner surface of particles and through zeolite-type water molecules. The silylation reaction results in the breaking of stabilizing bonds, which leads to a change in the polydispersity parameters. As follows from the fractal model of detonation nanodiamond aggregates, they can break down into N initial particles. However, owing to the steric hindrances to the silylation reaction, only the loosest aggregates can break down, after which the system again transforms into the stable state.

4. CONCLUSIONS

Thus, it was found that treatment of aqueous suspensions of detonation nanodiamonds in ultrasonic fields diversely affects the polydispersity distribution of nanodiamond particles. In particular, the polydispersity of nanodiamond particles in an aqueous medium periodically changes depending on the time of exposure to an ultrasonic field. The optimum exposure conditions that provide a high degree of dispersion of particles in aqueous suspensions were determined.

A technique was developed for chemical modification of the surface of detonation nanodiamonds through the grafting of organosilyl groups. This technique makes it possible to prepare finely dispersed suspensions of nanodiamonds in nonpolar organic media.

A model was proposed for an aggregate that consists of detonation nanodiamond particles and is stabilized through hydrogen bonds formed by functional groups of different types.

REFERENCES

1. V. Yu. Dolmatov, *Ultradispersed Detonation Diamonds: Production, Properties, and Application* (SPbGPU, St. Petersburg, 2003).
2. V. Yu. Dolmatov, Usp. Khim. **70** (7), 687 (2001).
3. L. V. Agibalova, A. P. Voznyakovskiĭ, V. Yu. Dolmatov, and V. V. Klyubin, Sverkhtverd. Mater., No. 4, 87 (1998).
4. V. Yu. Dolmatov, V. G. Sushchev, V. A. Marchukov, *et al.*, RF Patent No. 2,109,683, Byull. Izobret., No. 12 (1998).

Translated by O. Borovik-Romanova

Physics of the Solid State, Vol. 46, No. 4, 2004, pp. 665–667. Translated from Fizika Tverdogo Tela, Vol. 46, No. 4, 2004, pp. 649–651.

MODIFICATION OF SURFACE AND THE PHYSICOCHEMICAL PROPERTIES OF NANODIAMONDS

Formation of the Energy State and Adsorption Capacity of the Surface of Nanodiamond Powders during Preparation

G. P. Bogatyreva*, M. A. Marinich*, G. A. Bazaliĭ*, N. A. Oleĭnik*, E. V. Ishchenko, and V. L. Gvyazdovskaya***

** Bakul Institute for Superhard Materials, National Academy of Sciences of Ukraine, Avtozavodskaya ul. 2, Kiev, 04074 Ukraine*

*** Shevchenko National University, Vladimirskaya ul. 64, Kiev, 01033 Ukraine*

Abstract—This paper reports on new results of the investigation into the energy state and adsorption capacity of the surface of nanodiamond powders. *© 2004 MAIK "Nauka/Interperiodica".*

1. INTRODUCTION

Considerable progress achieved in the development of technologies for producing powders of ultradispersed diamond (UDD) and the great variety of its practical applications have brought to the fore the necessity of thoroughly investigating the surface properties of this unique material. Of particular interest is the diamond–carbon product obtained at the first stage of the complex technology of nanodiamond powders developed at the Institute for Superhard Materials of the National Academy of Sciences of Ukraine [1].

The present work is a continuation of our investigations into the surface properties of nanodiamond powders at different stages of their synthesis and treatment [2]. For the first time, we have examined the adsorption capacity, the energy state, and the chemical composition of functional groups on the surface of the initial synthesis product, the diamond–carbon material, and the nanodiamond powders. The experiments were performed using the synthesis product prepared by detonation of oxygen-deficient explosives (Alit, Ukraine) [3].

2. SAMPLE PREPARATION AND EXPERIMENTAL TECHNIQUE

Samples were prepared by sequential extraction of UDD from the product of its synthesis. Sample **1** is the initial product of the synthesis. Sample **2** (UDAG) is the diamond–carbon product obtained by treatment of the synthesis product in a hydrochloric solution. Sample **3** (ASUDO) is the UDD powder produced by sequential treatment in a mixture of sulfuric and chromic acids, a sodium hydroxide solution, and a mixture of hydrochloric and nitric acids at the boiling temperatures of the reacting mixtures. Sample **4** (ASUDCh) is the UDD powder after deep electrochemical purification in a 1 *N* HCl solution [4]. After treatment, the precipitates were washed with distilled water at the boiling temperature and dried at 100°C.

In this work, we determined the following physicochemical characteristics of nanodiamond powders: the specific surface *S*, the adsorption potential *A*, and the specific adsorption potential A^1.

The adsorption and structural characteristics and the parameters characterizing the energy state of the surface of the studied sample were calculated by the Brunauer–Emmett–Teller method from the isotherms of low-temperature nitrogen adsorption, which were measured with an Akusorb-2100 instrument [5]. The degree of energy surface inhomogeneity (the adsorption potential distribution) was determined from the absorption isotherms over the entire range of relative pressures. The adsorption potential *A* and the specific adsorption potential A^1 were calculated from the adsorption potential distribution according to the method described in [6].

The chemical composition of the groups adsorbed on the surface of powders was determined by comparing the thermal desorption spectra. The spectra were recorded on an MI 1201 mass spectrometer in the temperature range 20–600°C.

3. RESULTS AND DISCUSSION

The adsorption and structural characteristics of the nanodiamond powders prepared with the use of the above purification techniques are presented in Fig. 1.

As can be seen from Fig. 1, the sequential extraction of the UDD powders is accompanied by a decrease in the specific surface of the samples. The observed decrease in the specific surface occurs primarily as a result of a decrease in the weight fraction of nondiamond carbon species and possible interaction of the particle surface with the reactant. The deep purification slightly increases the specific surface due to the removal of impurities adsorbed on the surface. The adsorption potential for the synthesis product is three times less than that for the UDAG material, which can

1063-7834/04/4604-0665$26.00 © 2004 MAIK "Nauka/Interperiodica"

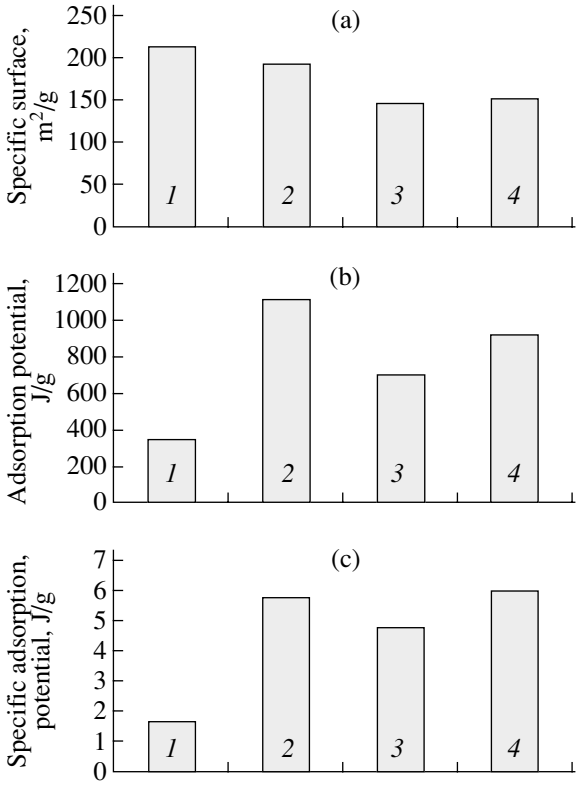

Fig. 1. Adsorption and structural parameters of nanodiamond powders: (a) specific surface, (b) adsorption potential, and (c) specific adsorption potential.

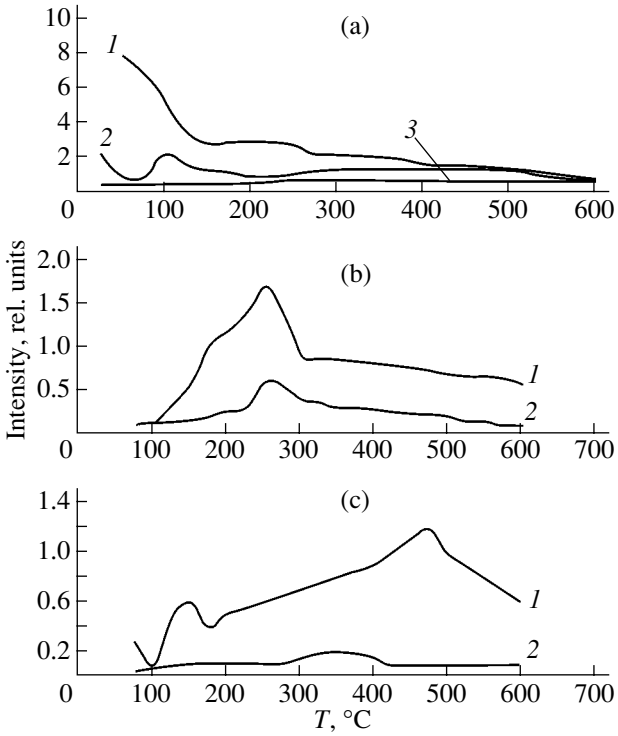

Fig. 2. Thermal desorption spectra of samples on the surface of nanodiamond powders: (a) water vapors on the (*1*) UDAG, (*2*) ASUDCh, and (*3*) ASUDO surfaces; (b) (*1*) hydrochloric acid vapors and (*2*) chlorine on the UDAG surface; and (c) (*1*) atomic and (*2*) molecular oxygen on the UDAG surface.

be associated with the removal of the major portion of metal impurities and the surface activation. The specific surface of the UDAG powder is somewhat less than that of the ASUDO powder. The deep purification of diamond powders leads to an increase in the specific surface of the ASUDCh powder owing to the purification of the surface with reactive atomic oxygen and ClO^- ions. The adsorption potential of the ASUDCh powder is higher than that of the ASUDO powder by a factor of 1.3. Changes in the specific adsorption potential are similar to those in the adsorption potential. The chemical action on the energy state of the surface is reflected in the adsorption potential distribution. After chemical treatment, this distribution covers a wide range of energies. In this case, the energy distribution of active centers on the surface of powders can be treated as homogeneous (if a distribution exhibits one or two maxima, this distribution is considered to be heterogeneous). The energy distribution of active centers on the surface of the ASUDO powder is more homogeneous than that on the surface of the initial synthesis product. The intensity ratio of the maximum and minimum energy peaks is equal to 33 for the synthesis product and 3.2 for the UDAG powder. After removal of nondiamond carbon species, the adsorption potential distribution slightly shifts toward the low-energy range and becomes less homogeneous (the intensity ratio of the maximum and minimum peaks is equal to 8.9). The deep purification results in a similar distribution. It should be noted that, in this case, the adsorption potential distribution becomes more homogeneous and the energy range proves to be wider (the intensity ratio of the maximum and minimum peaks is equal to 5.8).

The chemical composition of the groups adsorbed on the sample surface was determined from a comparison of the intensities of the thermal desorption spectra (Fig. 2).

It was found that water and hydrochloric acid vapors, chlorine, and atomic and molecular oxygen species are desorbed from the UDAG surface. On the other hand, water vapors and atomic and molecular oxygen species are predominantly desorbed from the surface of the ASUDO and ASUDCh powders. Figure 2a shows the thermal desorption spectra of water on the UDAG (curve *1*), ASUDCh (curve *2*), and ASUDO (curve *3*) surfaces. Water vapors whose adsorption proceeds through the physical mechanism are desorbed in the temperature range 25–150°C. After removal of nondiamond carbon species, the desorption intensity of physically adsorbed water decreases by a factor of 9.6. In turn, the deep purification leads to an increase in the intensity of the water desorption peak by a factor of 4.4 as compared to that for the ASUDO powder.

Therefore, an increase in the intensity of the H_2O desorption from the surface of the ASUDCh powder by a factor of 1.6 in the temperature range 50–100°C as compared to that of the ASUDO powder confirms the formation of the hydrophilic surface of the UDD powder upon electrochemical treatment. The thermal desorption spectra of hydrochloric acid vapors and chlorine on the UDAG surface are depicted in Fig. 2b. It can be seen from this figure that the UDAG powder actively adsorbs the hydrochloric acid vapors and chlorine. The maximum of their desorption is observed at a temperature of 250°C. The appearance of the chlorine desorption peak is most likely caused by the dissociation of hydrochloric acid vapors.

The thermal desorption spectra of atomic and molecular oxygen species on the UDAG surface are shown in Fig. 2c. As can be seen, the amount of atomic oxygen is considerably larger than that of molecular oxygen. These data indicate that the diamond–graphite product is an active adsorbent of chlorine and hydrochloric acid vapors and can be used in oxidation catalysis owing to the presence of atomic oxygen on the surface.

The energy characteristics of the surface (adsorption potential, adsorption potential distribution, specific adsorption potential) and the hydrophilic–hydrophobic balance of the surface can serve as criteria for the choice of the field of application of commercial nanodiamond powders [1]. The energy homogeneity of the surface of nanodiamond powders ensures good adhesive properties. These properties make it possible to improve the sintering of polycrystals, to prepare high-quality fine-grained composite electrochemical coatings, etc. In turn, the hydrophily of the nanodiamond surface favors a decrease in the degree of aggregation instability. Consequently, the nanodiamonds can be used in preparing polishing suspensions and electrolytes for producing composite coatings. In this respect, the energy homogeneity in combination with the hydrophoby of the surface of ultradispersed powders are necessary factors for the preparation of polycrystals, composites with organic binders (sealing materials, rubbers, etc.), and pastes. The energy homogeneity in combination with the hydrophily of the surface are required in the production of aqueous nanodiamond suspensions (used for polishing) and electrolytes for composite electrochemical coatings. The energy heterogeneity in combination with the hydrophily of the surface are necessary for the manufacturing of special adsorbents.

The UDAG powder can be used as a technical adsorbent for chlorine production. Moreover, modified derivatives of this powder are promising as catalyst materials.

Depending on the requirements imposed on the manufacturing of particular products, we designed three types of materials:

(1) ultradispersed diamond powders ASUDO and ASUDCh (TU U 28.5-05417377-094-2003),

(2) aqueous diamond suspensions based on ASUDO and ASUDCh (TU U 88.090.052-01), and

(3) ultradispersed diamond–graphite product UDAG (TU U 88.090.051-01).

4. CONCLUSIONS

A flexible technology for synthesizing nanodiamond powders with controlled physicochemical parameters of their surface was developed in Ukraine. The designed powders ASUDO and ASUDCh are intended for the manufacturing of polycrystalline materials, special adsorbents, suspensions, pastes, composites, and coatings.

The possibility of using the UDAG material in oxidation catalysis and as adsorbents for the production of chlorine was justified for the first time.

REFERENCES

1. G. P. Bogatyreva, M. A. Marinich, G. A. Bazaliĭ, *et al.*, Sverkhtverd. Mater., No. 6, 28 (2002).
2. G. P. Bogatyreva, M. N. Voloshin, M. A. Marinich, and V. S. Gavrilova, Sverkhtverd. Mater., No. 6, 42 (1999).
3. V. I. Padalko, G. P. Bogatyreva, and M. N. Voloshin, Instrum. Svit, No. 4/5, 39 (1999).
4. M. V. Novikov, G. P. Bogatir'ova, M. A. Marinich, and G. A. Bazaliĭ, Ukr. Patent No. 36,551A (2001), Byull., No. 3 (2001).
5. G. P. Bogatyreva, Sverkhtverd. Mater., No. 4, 27 (1989).
6. *Methodical Recommendations for Studying the Physicochemical Properties of Superhard Materials*, Ed. by G. P. Bogatyreva (Inst. Sverkhtverd. Mater. Ukr. Akad. Nauk, Kiev, 1992).

Translated by O. Borovik-Romanova

Physics of the Solid State, Vol. 46, No. 4, 2004, pp. 668–671. Translated from Fizika Tverdogo Tela, Vol. 46, No. 4, 2004, pp. 652–655.

MODIFICATION OF SURFACE AND THE PHYSICOCHEMICAL PROPERTIES OF NANODIAMONDS

Effect of Degassing on the Formation of Polycrystals from Diamond Nanopowders Produced by Detonation and Static Syntheses

A. A. Bochechka

Bakul Institute for Superhard Materials, National Academy of Sciences of Ukraine, Avtozavodskaya ul. 2, Kiev, 04074 Ukraine

e-mail: ism1@kibor.kiev.ua

Abstract—The sintering of diamond nanopowders produced by detonation and static synthesis and degassed through vacuum thermal treatment is studied at an initial pressure of 8 GPa in the temperature range 1200–1600°C. Chemical modification of the initial nanopowders, in combination with thermal treatment in vacuum and encapsulation of the working volume, is shown to suppress graphitization of diamond during sintering, thereby increasing the strength and hardness of polycrystals thus obtained. *© 2004 MAIK "Nauka/Interperiodica".*

1. INTRODUCTION

In powder metallurgy, in order to activate sintering, powders are frequently made finer by grinding. According to the Hall–Petch relation, a decrease in the grain size of polycrystals thus obtained results in increased values of the elastic limit, yield strength, and flow stress, which improves the physical-mechanical properties of sintered samples [1].

Experience with diamond micropowder sintering suggests that the finer the powders, the worse the physical-mechanical properties of polycrystals obtained by sintering. The most probable reason for this effect is the interaction between diamond particles and gases in pores that are desorbed from the particle surface during sintering.

It was shown in [2] that the excess pressure produced by desorbed air at a sintering temperature of 1600°C and an external pressure of 8 GPa is significant (>0.5 GPa) in the sintering of diamond powders of ASM 10/7 grade and becomes equal to the external pressure when grains in powders are less than 0.9 μm in size. For this reason, before sintering in a high-pressure apparatus (HPA), diamond powders with particles smaller than 5 μm in size should be degassed and the working volume should be encapsulated. Degassing is of particular importance in sintering powders whose particles are smaller than 100 nm in size, i.e., nanopowders.

In this paper, we present data on the sintering of diamond powders synthesized under detonation or static conditions (SC) and subjected to degassing.

2. EXPERIMENTAL TECHNIQUE

Experiments on sintering are performed on powders of ASM5 0.1/0 grade produced at the Bakul' ISM pilot plant (National Academy of Sciences, Ukraine) and on diamond nanopowders produced under detonation conditions [3] (ultrafine-dispersed diamonds, UDDs).

Physically adsorbed gases on the surface of powders are desorbed through thermal treatment of briquettes in vacuum (residual pressure of 10^{-3} Pa) at 500°C over 2 h [4]. According to [5], water and CO_2 physically adsorbed on the surface of dispersed diamond nanopowders are almost fully removed at this temperature. The working volume is sealed either mechanically or by soldering the metallic container in vacuum [6].

The nature of functional groups adsorbed on the surface of diamonds is established using IR spectroscopy. Absorption spectra are recorded using a Specord IR spectrometer and KBr pellets.

Sintering at high pressures is performed in an HPA of toroid type with a central recess 20 mm in diameter. The heating current and the voltage applied to the heater are measured using a recording meter [7]. The temperature is estimated from the predetermined relation between the power input and the voltage across a Pt 6% Rh–Pt 30% Rh thermocouple (without considering the effect of the pressure). The pressure is determined at room temperature using the known phase transformations in Bi. A briquette of diamond nanopowder (subjected to vacuum thermal treatment and encapsulated) is placed in the central part of the high-pressure chamber, a high pressure of 8.0 ± 0.5 GPa is applied, and the temperature is increased to a given value and is kept constant to within ±30°C. After a designated period of time, the temperature is decreased to room temperature and the pressure is relieved.

1063-7834/04/4604-0668$26.00 © 2004 MAIK "Nauka/Interperiodica"

After sintering, samples are chemically cleaned of the container material and their density is measured by hydrostatic weighing in water [8]. The confidence interval was 0.01 g/cm^3 at a reliability level of 95%.

The crystal structure is studied using transmission electron microscopy and x-ray diffraction.

The hardness and fracture toughness are determined using the indentation method.

3. RESULTS AND DISCUSSION

The dependence of sintering of detonation-produced diamond nanopowders on the degassing method applied is studied as follows. First, powders are compacted. Then, the compacts are annealed in vacuum, which causes gases to desorb from the surface of particles of nanopowders. The working volume is not encapsulated; therefore, the inverse process (sorption of air) proceeds with time. Then, sintering is performed in the HPA.

It is established that, as the amount of gases desorbed from the surface of particles of diamond nanopowders is increased during sintering, the density of the polycrystals thus obtained decreases and their physical-chemical properties deteriorate primarily due to the graphitization of diamond nanoparticles [4].

Physical desorption of gases from the surface of diamond nanoparticles that is provided by thermal treatment and sealing in vacuum suppresses graphitization but does not rule it out entirely. As the sintering temperature is increased, graphitization is enhanced due to chemical bonding of carbonyl and hydroxyl groups chemisorbed on the surface of diamond nanoparticles with the carbon of the diamond cores of the particles.

Chemical modification of the surface of nanoparticles, performed by annealing powders in an atmosphere of inert gas, in combination with thermal treatment in vacuum, removes carbonyl groups and significantly decreases the amount of hydroxyl groups on the surface of nanoparticles, as follows from IR-spectroscopic data (Fig. 1). For this reason, the degree of graphitization of powders in sintering decreases, with the consequence that the density of sintered polycrystals and, therefore, their strength and hardness increase as the sintering temperature is raised (the hardness of a sample is proportional to its density). The maximum hardness of the samples obtained is 28 GPa [4].

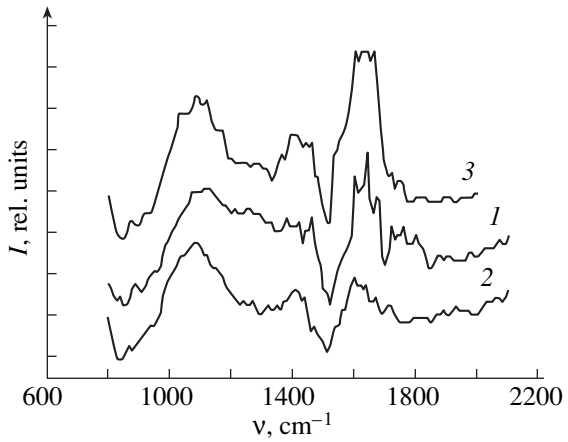

Fig. 1. IR absorption spectra of diamond nanopowders: (*1*) starting UDD powder, (*2*) after modification of the surface and thermal treatment in vacuum, and (*3*) after 12 h of storage in air following modification of the surface and thermal treatment in vacuum.

In [9], in addition to the method in which initial nanopowders are synthesized under detonation conditions, another method was proposed to form a nanostructure in diamond polycrystals. In this method, fine diamond powders synthesized under SC are used in which the particles are strongly deformed and do not form a nanostructure. In the working volume of the HPA, the grain structure is rearranged due to large plastic deformations and strong shear stresses that arise because the load is not hydrostatic. Note that the quantity of surface impurities and structural imperfections in the initial powders

Characteristics of the structure and phase composition of diamond nanopowders and polycrystals produced from them by sintering (obtained from x-ray diffraction data)

Sample	Coherent-scattering region size, Å	Microstresses, GPa	(111) diffraction peak width, deg	I_{003}/I_{111}
Starting SC-synthesized powder ASM5 0.1/0	206	0.82	0.612	–
Starting detonation UDD powder	48	–	1.773	–
Polycrystal obtained by sintering ASM5 0.1/0 (p = 8 GPa, T = 1600°C; m.s.)	42	4.56	4.918	0.185
Polycrystal obtained by sintering ASM5 0.1/0 (p = 8 GPa, T = 1400°C; v.s.)	145	2.74	0.746	–
Polycrystal obtained by sintering UDDs (p = 8 GPa, T = 1600°C; m.s.)	39	3.77	2.023	0.304

Note: I_{003}/I_{111} is the intensity ratio of the (003) rhombohedral graphite peak and (111) diamond peak; m.s. stands for mechanical sealing; and v.s. stands for vacuum soldering.

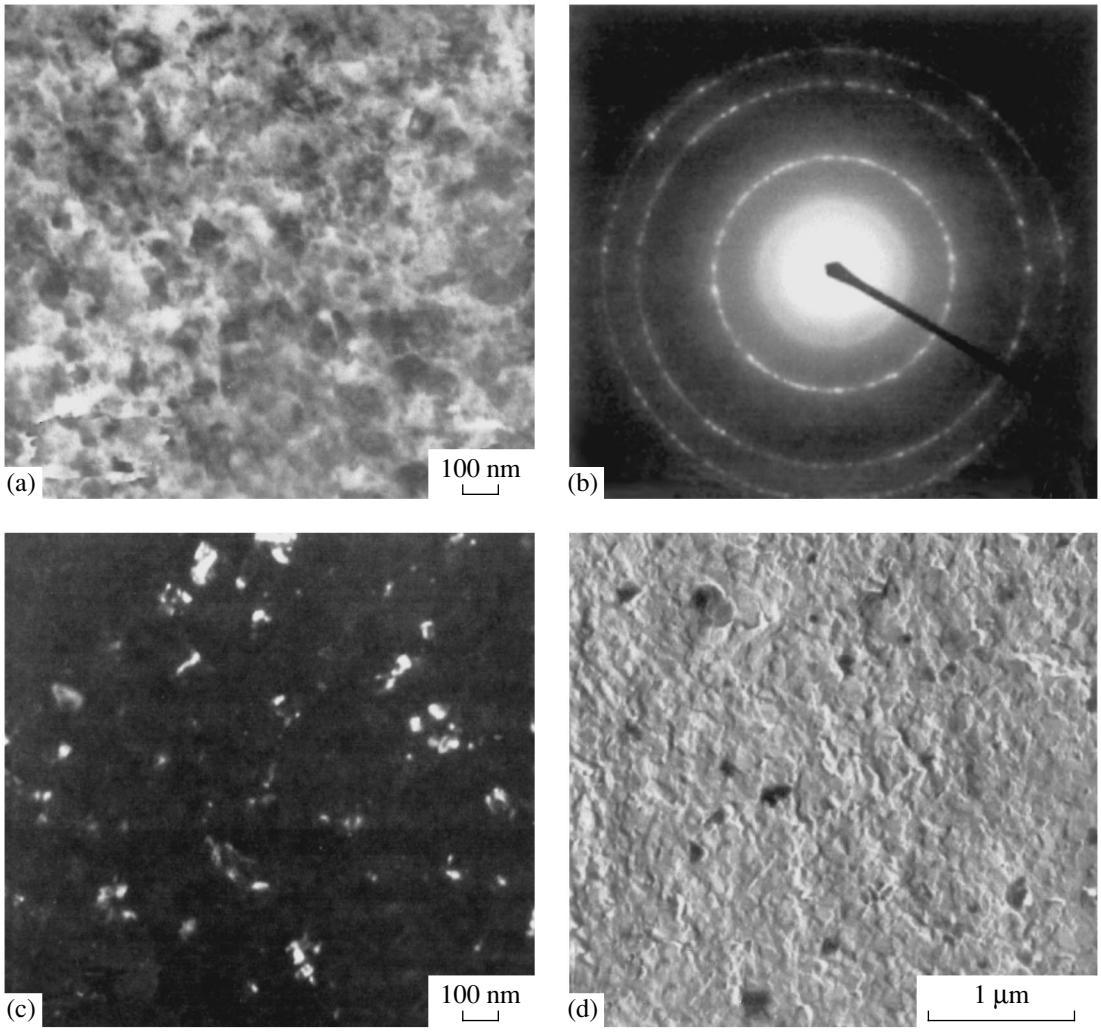

Fig. 2. Structure of a polycrystal obtained by sintering SC-synthesized diamond powder ASM5 0.1/0. (a) Bright-field image, (b) SAD pattern of this area, (c) dark-field image, and (d) microfractograph.

is much less in this case in comparison with that in detonation powders.

The chemical modification of the surface of nanoparticles, in combination with thermal treatment in vacuum, in preparing powders for sintering excludes graphitization of the powders during sintering (when the working volume is sealed by soldering the metallic container in vacuum) or significantly suppresses it (in the case of mechanical sealing), as can be seen from the table.

The application of high pressures (in combination with purification and degassing in vacuum) in sintering diamond nanopowders synthesized under SC with particles approximately 100 nm in size makes it possible to form nanostructural elements 10–50 nm in size in polycrystals, as follows from electron-microscopic examination (Fig. 2). These elements arise from plastic fragmentation of strongly deformed grains during sintering.

The data on the plastic fragmentation of diamond nanoparticles synthesized under SC correlate well with x-ray diffraction data, which indicate that, as the sintering temperature is increased, coherent-scattering regions decrease significantly (by a factor of 5.3 at 1600°C in comparison with the starting powders; see table).

Diamond nanopowders synthesized under SC were used to fabricate cutting plates, and their testing showed that such plates hold great promise for microscale surface machining. For example, in machining an aluminum disk, the final roughness R_a of its surface was 0.012 μm [9].

4. CONCLUSIONS

(1) Chemical modification of initial detonation powders with particles 3–5 nm in size, in combination with thermal treatment in vacuum and encapsulation of the

working volume, brings about the removal of carbonyl groups and a significant decrease in the quantity of hydroxyl groups on the surface of nanoparticles, thereby suppressing diamond graphitization during sintering, which, in turn, results in an increased strength and hardness of the polycrystals thus obtained.

(2) It has been found that polycrystals with grains 10–50 nm in size can be obtained from diamond nanopowders synthesized under SC (with initially highly deformed particles approximately 100 nm in size) and sintered at high pressures after prior purification and degassing in vacuum and encapsulation of the working volume.

(3) A polycrystalline diamond material has been fabricated on the basis of SC-synthesized diamond nanopowders of ASM5 0.1/0 grade. Testing of cutting plates made of this material showed that such plates hold great promise for microscale machining.

REFERENCES

1. V. I. Trefilov, Yu. V. Mil'man, and S. A. Firstov, *Physical Foundations of Strength of Refractory Metals* (Naukova Dumka, Kiev, 1975).
2. A. A. Bochechka, Sverkhtverd. Mater., No. 4, 10 (1998).
3. K. V. Volkov, V. V. Danilenko, and V. I. Elin, Fiz. Goreniya Vzryva, No. 3, 123 (1990).
4. A. A. Shul'zhenko, A. A. Bochechka, L. A. Romanko, *et al.*, Sverkhtverd. Mater., No. 6, 50 (2000).
5. A. V. Nozhkina, N. A. Kolchemanov, A. A. Kardanov, and P. Ya. Detkov, Sverkhtverd. Mater., No. 1, 78 (2000).
6. A. A. Bochechka, Sverkhtverd. Mater., No. 6, 37 (2002).
7. A. A. Shul'zhenko, V. G. Gargin, V. A. Shishkin, and A. A. Bochechka, *Polycrystalline Diamond-Based Materials* (Naukova Dumka, Kiev, 1989).
8. S. S. Kivilis, *Densimeters* (Énergiya, Moscow, 1980).
9. A. A. Shul'zhenko, A. A. Bochechka, G. S. Oleĭnik, *et al.*, Sverkhtverd. Mater., No. 5, 29 (2001).

Translated by Yu. Epifanov

Physics of the Solid State, Vol. 46, No. 4, 2004, pp. 672–674. Translated from Fizika Tverdogo Tela, Vol. 46, No. 4, 2004, pp. 656–658.

MODIFICATION OF SURFACE AND THE PHYSICOCHEMICAL PROPERTIES OF NANODIAMONDS

Magnetic Methods of Purification Control of Nanodiamond Powders

N. V. Novikov, G. P. Bogatyreva, G. F. Nevstruev, G. D. Il'nitskaya, and M. N. Voloshin

Bakul Institute for Superhard Materials, National Academy of Sciences of Ukraine, Avtozavodskaya ul. 2, Kiev, 04074 Ukraine

e-mail: bogatyreva@ism.kiev.ua

Abstract—Magnetic methods of quantitative determination of impurities in nanodiamond powders (NDPs) are discussed. For two types of NDPs, it is shown that the magnetic susceptibility depends on their treatment. © *2004 MAIK "Nauka/Interperiodica".*

Nanodiamond powders (NDPs) are applied in various branches of industry. NDPs are characterized by stable quality, which depends not only on the fabrication conditions but also on the efficiency of removing concomitant products and impurities from NDPs. For this reason, much attention in the technology of NDPs is given to methods of quantitative control of their purity.

The existing methods for checking purity that are applied to diamond-containing materials (x-ray diffraction, IR spectroscopy) are laborious and practically impossible to apply in the case where the impurity content is less than 1%. The application of weight analysis in combination with chemical treatments for purity testing presents severe difficulties.

Magnetic methods find wide use in solid-state chemistry where the effect of chemical bonds on the properties of solids is studied. Obviously, these methods can also be used for solving simpler problems. In this work, we apply methods of magnetochemistry [1] (more specifically, the static magnetic susceptibility method) to determine the amount of impurities in diamond powders (in particular, with the aim of removing undesirable impurities) at different stages of thermal or chemical treatment.

This method for testing is based on the fact that diamonds exhibit stable properties. Diamonds do not form chemical compounds and contain almost no impurities. Due to its crystal structure, pure diamond exhibits stable magnetic properties, which are virtually independent of ambient temperature. Diamond is diamagnetic, and its magnetic susceptibility does not vary [2]. Therefore, the magnetic susceptibility of pure diamond can be used as a standard for comparison in determining the purity of diamond powders and of NDPs in particular.

The magnetic analysis is based on the additivity of the magnetic susceptibilities of the components of real NDPs and of the experimentally measured magnetic susceptibilities of individual impurities and components making up diamond powders [3]. This method makes it possible to determine the impurity content without resorting to a weight analysis by measuring only the magnetic susceptibility of a powder before and after various treatments.

For this purpose, the balance equations are used for the content β of various impurities in a diamond powder, $\sum_{i=1}^{n}\beta_i = 1$, and for the magnetic susceptibility of the powder,

$$\chi_{\text{ini}} = \sum_{i=1}^{n}\beta_i\chi_i, \qquad (1)$$

where β_i and χ_i are the content and magnetic susceptibility of the ith component of the powder, respectively, and χ_{ini} is the magnetic susceptibility of the powder.

The content of the ith impurity β_i in a NDP can be found as

$$\beta_i = \frac{\chi_{i+1} - \chi_{i-1}}{\chi_i - \chi_{i-1}}, \qquad (2)$$

where χ_{i+1} and χ_{i-1} are the magnetic susceptibilities of the powder before and after removal of the ith impurity.

Thus, in order to estimate the content of an individual impurity in a NDP, one needs to measure the magnetic susceptibility of the NDP before and after certain thermal, chemical, and other treatments [4].

The error of the magnetic method is determined by the error in measuring the magnetic susceptibility [5]. A decrease in the mass of a powder due to its purification has almost no effect on the accuracy of the magnetic analysis.

We studied ultrafine-dispersed diamond (UDD) powders with particles less than 20 nm in size. Spectral microanalysis of UDD powders and an IR absorption study of the incombustible remainder of UDD powders showed the presence of a wide variety of impurities that deteriorate UDD powders and affect their magnetic

1063-7834/04/4604-0672$26.00 © 2004 MAIK "Nauka/Interperiodica"

Calculated and experimental values of the magnetic susceptibility of UDD powders

UDD powder	Magnetic susceptibility χ, 10^{-8} m^3/kg		Measurement error of χ, %	Diamond content in UDD powder, %		Accuracy of determination of diamond content, %
	calculation	experiment		calculation	experiment	
1	–0.48	–0.46	4.2	99.5	99.7	0.2
2	–0.59	–0.63	6.8	98.0	97.5	0.5
3	–1.99	–2.12	6.5	80.0	78.4	2.0

susceptibility under physical, thermal, or chemical treatments [4, 6].

Thus, the magnetic susceptibility of an UDD powder χ_n includes the magnetic susceptibilities of pure diamond χ_1, metallic inclusions χ_2, graphite χ_3, carbon material χ_4, and silicon χ_5. The relative contributions from these components are characterized by the quantities β_1, β_2, β_3, β_4, and β_5. The balance equations take the form

$$\beta_{ini} = 1 = \beta_1 + \beta_2 + \beta_3 + \beta_4 + \beta_5,$$

$$\beta_{ini}\chi_{ini} = \beta_1\chi_1 + \beta_2\chi_2 + \beta_3\chi_3 + \beta_4\chi_4 + \beta_5\chi_5.$$

The relative contribution from metallic inclusions (component 1) can be found from

$$\beta_1 = \frac{\chi_{ini} - \chi_{2-5}}{\chi_1 - \chi_{2-5}}, \quad (3)$$

where χ_{2-5} is the magnetic susceptibility of the UDD powder after the removal of metallic inclusions. The relative contributions from the other components or the UDD powder can be determined in a similar way using Eqs. (2) and (3). The determination of the content of carbon impurities in an UDD powder is the most difficult, because these impurities are diamagnetic.

To test the validity of the magnetic method, we performed experiments on mixtures composed of a pure UDD powder and pure graphite. The graphite content in the mixtures was 0.5, 2.0, and 20.0%. Given the magnetic susceptibilities of diamond in the UDD (-0.44×10^{-8} m^3/kg) and of graphite (-8.2×10^{-8} m^3/kg) and the experimentally measured specific magnetic susceptibility of the mixtures, we determined the content of diamond in the mixtures from Eqs. (2) and (3) and compared it with the calculated values (see table). From the table, it can be seen that the error in measuring χ does not exceed 6.8% and that the diamond content in the mixtures is determined to an accuracy better than 2% (0.2–0.5%). Therefore, the magnetic method can be used to determine the contents of individual components in UDD powders.

Thus, based on the fact that the magnetic properties of pure diamond and impurities are stable, we propose the following general scheme of successive treatments of diamonds accompanied by measurement of χ_i and calculation of the content β_i for each impurity using the equations presented above:

$$\chi_{ini} \xrightarrow{1} \chi_1 \xrightarrow{2} \chi_2 \xrightarrow{3} \chi_3 \cdots \xrightarrow{k} \chi_k \cdots \xrightarrow{n} \chi_n. \quad (4)$$

As an example of application of the magnetic method, the figure shows how the magnetic susceptibility of NDPs obtained from two different samples, namely, sample *A* with basically metallic inclusions and sample *B* with basically carbon-containing impurities, is affected by treatments.

As seen from the curve for sample *A*, treatments 1 and 2 reduce the metal content, treatment 3 removes graphitized carbon (thereby increasing χ_3), and treatment 4 causes metallic inclusions to dissolve, with the consequence that a pure diamagnetic diamond powder is obtained, whose magnetic susceptibility χ_4 remains unchanged after check treatment 5.

The χ curve for sample *B* suggests that the amount of metallic inclusions is small (treatments 1, 2) and that the greater part of the impurities is graphitized carbon (treatments 3, 4). The equality of χ_4 and χ_5 after treatment 5 is indicative of the stable quality of the final powder.

The results obtained allow the following conclusions to be drawn.

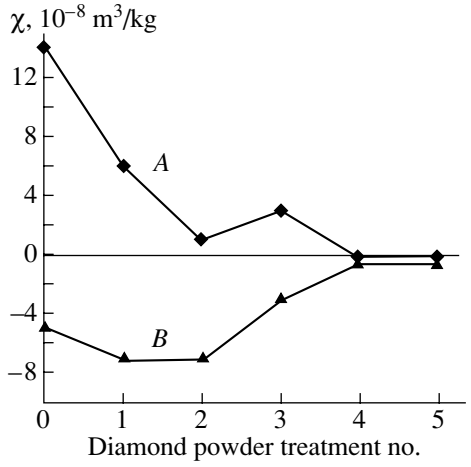

Magnetic susceptibility of nanodiamond powders with basically (*A*) metallic and (*B*) carbon-containing impurities after various treatments. The numerals on the abscissa axis indicate the number of the treatment.

(1) The magnetic susceptibility of pure diamonds, including nanodiamonds, is virtually independent of chemical and physical treatments.

(1) The magnetic properties of real NDPs are dictated by the amount of impurities and their magnetic properties.

(3) Quantitative magnetochemical analysis of impurities in NDPs can be performed by combining measurements of the magnetic susceptibility of NDPs with successive selective treatments.

REFERENCES

1. V. T. Kalinikov and Yu. V. Rakitin, *Introduction to Magnetochemistry* (Nauka, Moscow, 1980).
2. V. S. Veselovskiĭ, *Carbon, Diamonds, Graphite, and Coals* (ONTI, Moscow, 1936).
3. G. P. Bogatyreva, A. S. Vishnevskiĭ, and G. F. Nevstruev, in *Physicochemical Problems in Synthesis of Superhard Materials* (Inst. Sverkhtverd. Mater., Kiev, 1978), p. 134.
4. G. P. Bogatyreva, G. F. Nevstruev, and V. B. Kruk, in *Superhard Materials* (Naukova Dumka, Kiev, 1982), p. 29.
5. V. I. Chechernikov, *Magnetic Measurements* (Mosk. Gos. Univ., Moscow, 1969).
6. T. M. Gubarevich, R. R. Sataev, and V. Yu. Dolmatov, *Chemical Purification of Ultrafine-Dispersed Diamonds* (Krasnoyarsk, 1991), Vol. 1, p. 135.

Translated by Yu. Epifanov

Physics of the Solid State, Vol. 46, No. 4, 2004, pp. 675–677. Translated from Fizika Tverdogo Tela, Vol. 46, No. 4, 2004, pp. 659–661.

MODIFICATION OF SURFACE AND THE PHYSICOCHEMICAL PROPERTIES OF NANODIAMONDS

Carbon Phase Transformations under Electrodynamic Compression

I. P. Makarevich*, A. D. Rakhel, B. V. Rumyantsev***, and B. É. Fridman***

**Institute of Electrophysical Problems, Russian Academy of Sciences, Dvortsovaya nab. 18, St. Petersburg, 191186 Russia*

***Institute for High-Density Energy of the Associated Institute for High Temperatures, Russian Academy of Sciences, ul. Izhorskaya 13/19, Moscow, 125412 Russia*

****Ioffe Physicotechnical Institute, Russian Academy of Sciences, Politekhnicheskaya ul. 26, St. Petersburg, 194021 Russia*

e-mail: alfred/mdlab@mail.ioffe.ru

Abstract—The graphite–diamond phase transition under shock-wave-induced electrodynamic compression has been studied. A sample of a carbon-containing material was loaded by axisymmetric collapse of a copper liner. The liner was acted upon by ponderomotive forces generated by pulsed electric currents with amplitudes of 2–4 MA. The collapse of the cylindrical copper liner with a velocity of ~1 km/s produced stepped loading of the carbon material in an ampoule from 5 to 40 GPa over 4 μs. Purification of the preserved material yielded agglomerates containing polycrystalline diamond. The average size of diamond polycrystals in the agglomerates is 1–2 μm, and the agglomerate yield is ~3%. © *2004 MAIK "Nauka/Interperiodica".*

1. INTRODUCTION

The development of methods for generating high pulsed pressures is of considerable scientific significance and practical importance. Such methods are widely employed in studying the equations of state and phase transformations of substances, as well as in the production of superhard materials. Investigation of the phase state of carbon and the synthesis of diamond are still attracting the interest of researchers dealing with practical applications [1–3]. Currently, high pulsed pressures and shock impact compression are reached primarily with the use of explosives. However, explosive-based technologies suffer a number of shortcomings, the most serious of them being the infrastructure required for them. Therefore, the development of alternative shock-compression methods not based on explosives is an urgent problem of scientific and practical importance. Electrodynamic Z-pinch compression of metal liners is a promising method of obtaining high pulsed pressures [4]. Such experiments on electrodynamic acceleration of massive copper liners and shock impact compression of graphite were carried out at the Institute of Electrophysical Problems, Russian Academy of Sciences.

2. EXPERIMENT

The electrodynamic compression setup consists of a high-voltage capacitive energy storage, which, when shorted to the discharge chamber (Fig. 1) of an electrodynamic test bench, generates pulsed currents of up to 10 MA in amplitude. Test sample *5* in steel ampoule *4* is coaxially aligned inside copper liner *3* by means of steel adapters *2*. Adapters *2* provide continuous electric contact between the copper liner and electrodes *1* during the passage of the current pulse and inward liner collapse. Prior to generation of a current pulse, the discharge chamber is evacuated to a base pressure of 1–5 kPa.

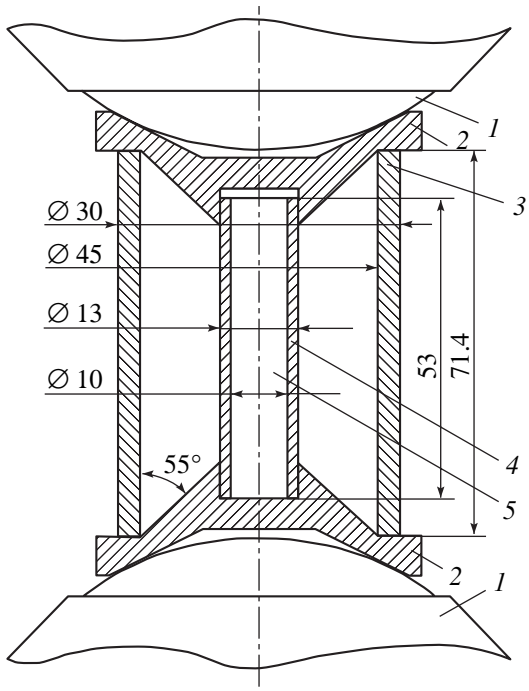

Fig. 1. Discharge chamber of the electrodynamic bench: (*1*) discharge chamber electrodes, (*2*) adapters, (*3*) copper liner, (*4*) steel ampoule, and (*5*) carbon-containing material.

Characteristics of samples, loading parameters, and yield of the diamond phase

Sample composition	Density, kg/m^3	Porosity, %	Pressure, GPa/duration, μs state**				Diamond yield,* in percentage of the carbon phase
			1	2	3	4	
Graphite	1700	25	4.5/1.6	13/1.1	18/0.7	25/0.7	<1
Graphite/copper 1 : 1 mass	3400	6	10/1.2	27/1.0	32/0.6	38/0.6	6

* Residue after oxidizing acidic purification by a solution of potassium bichromate in sulfuric acid.

** Number of state identifies shock impact multiplicity (Fig. 2).

Steel ampoule *4* with the carbon-containing material under study is loaded by a high-velocity axisymmetric collapse of copper liner *3*. The liner is deformed by the ponderomotive forces generated by the pulsed electric current passed through it. As follows from the calculations performed in [4] and experimental findings, the liner acceleration takes up ~60 μs. The velocity of the inner liner surface at collision with the ampoule is 0.95 km/s.

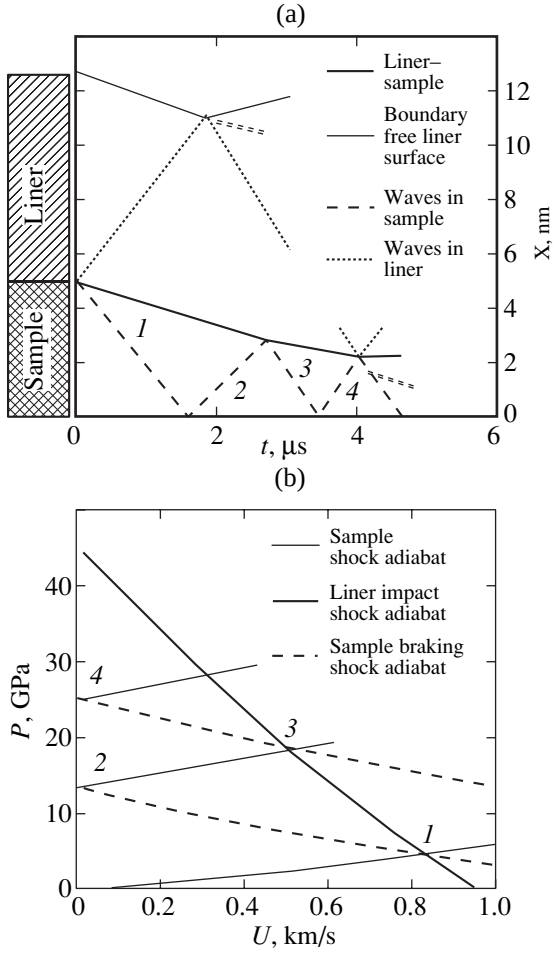

Fig. 2. Diagram of loading of a graphite sample of density 1700 kg/m^3 by a copper liner collapsing with a velocity of 0.95 km/s (the steel shell of an ampoule is considered to be part of the copper liner). (a) Spatial–temporal $X(T)$ shock-wave-loading diagram; the shock-wave-front trajectories correspond to (*1*) compression, (*2*) reflection from the axis, (*3*) secondary compression, and (*4*) secondary reflection from the axis. (b) Shock-wave-loading diagram plotted in the pressure–mass velocity coordinates, $P(U)$; points *1*, *2*, *3*, and *4* are states of the sample on the adiabats of the corresponding shock waves.

The characteristics of the samples studied, the loading parameters, and the content of the diamond phase in the shock-compressed samples are listed in the table.

Figure 2 illustrates the calculation of the shock-wave impacts in a sample resulting from collapse of the liner. The calculation was performed in the plane-wave approximation disregarding dissipative losses [5]. The collapse of cylindrical shock waves generates still higher pressures, which depend on the running radius and dissipative losses.

A spatial and temporal analysis of the loading (Fig. 2a) shows that the given liner dimensions and a collapse velocity of 0.95 km/s provide a loading time of ~4 μs. During this time, the sample is acted upon by four shock impacts. The calculated pressures in the shock waves and the loading times are listed in the table. The maximum pressure reached (Fig. 2b) is not high enough to ensure a complete phase transition in the graphite (25 GPa) but is sufficient for this transition to occur in a graphite/copper mixture (38 GPa) [1, 3], which is borne out by the presence of the diamond phase in the compressed sample material.

After the loading, the material was extracted from the ampoule and chemically oxidized with a sulfuric acid solution of potassium bichromate $K_2Cr_2O_7$ to remove the metal and oxidize the graphite. The residue was dried and analyzed. The estimate of the yield presented in the table is the lower bound because of the nonuniform compression of the ampoule and severe conditions of chemical oxidation, which resulted in a partial oxidation of the diamond phase. Additional glow-discharge plasma-chemical oxidation performed in an air flow produced a dark-gray residue (with a yield of ~50%) consisting of smooth, porous particle aggregates 50–100 μm in size.

The morphology of the particles making up the purified sample material was studied with a scanning electron microscope by measuring the backscattered electron flux, whose intensity is governed by the atomic number of the surface material.

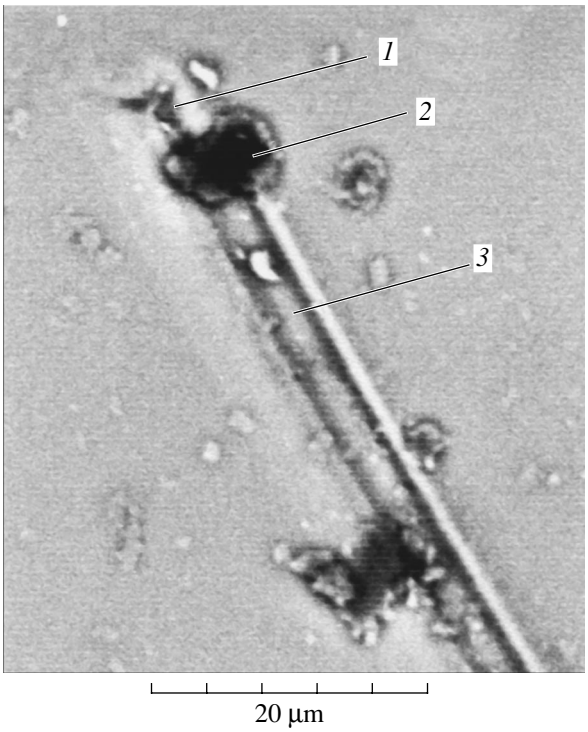

Fig. 3. End of the track on glass produced by an aggregate taken from a purified sample: (*1*) individual diamond polycrystals, (*2*) aggregate, and (*3*) track.

Figure 3 shows an image of the end of the track obtained by shear deformation of a thin layer of the purified material pressed between glass plates. We readily see two crystals of pyramidal shape that braked upon loosing the masking carbon mass and came to a stop. The darker particles with a lower reflection coefficient are carbon grains. The lighter particles are of silicate glass. Additional identification was provided by an x-ray microprobe. The masking carbon mass apparently contains several more crystals, because the track behind it is broader. We estimated the size of the crystals of the diamond phase from the width of extended tracks (whose length was 10^2–10^3 times the grain size) as 1–2 μm.

3. CONCLUSIONS

The electrodynamic compression setup described above provides stepped loading (up to 30–40 GPa in magnitude and up to 4 μs long) of the material under study in a volume of ~4 cm^3. Reactor graphite subjected to these loading conditions was shown to contain a diamond phase with polycrystalline diamond grains up to 1–2 μm in size.

The yield of the diamond phase depends on the graphite density and the graphite/metal mixture composition. Use of a metal/graphite mixture permits one to increase the pressure and provides conditions favorable for the phase transition and preservation of the diamond phase under unloading.

The purification techniques employed in this study permitted isolation of up to 3% of the carbon mass in the form of aggregates consisting of grains of the diamond phase, amorphous carbon, and graphite.

ACKNOWLEDGMENTS

This study was supported by the Russian Foundation for Basic Research, project no. 01-02-17243

REFERENCES

1. M. V. Zhernokletov and G. V. Simakov, in *Proceedings of the Conference of the American Physical Society Topical Group on Shock Compression of Condensed Matter, Seattle* (Washington, 1995), p. 69.
2. V. V. Digonskiĭ and S. V. Digonskiĭ, *Regularities of Diamond Formation* (Nedra, St. Petersburg, 1992).
3. M. Yoshida and N. N. Thadhani, in *Shock Compression of Condensed Matter: Proceedings of the American Physical Society Topical Conference, Williamsburg, Virginia, 1991*, Ed. by S. C. Schmidt (North-Holland, Amsterdam, 1992), p. 585.
4. B. E. Fridman, I. P. Makarevich, A. D. Rakhel, and B. V. Rumyantsev, in *Abstract Book of International Conference on Megagauss Magnetic Field Generation and Related Topics MEGAGAUSS-IX* (Moscow–St. Petersburg, 2002), p. 39.
5. S. G. Andreev, A. V. Babkin, F. A. Baum, *et al.*, in *Physics of an Explosion*, 3rd ed., Ed. by L. P. Orlenko (Fizmatlit, Moscow, 2002), Vol. 1.

Translated by G. Skrebtsov

Physics of the Solid State, Vol. 46, No. 4, 2004, pp. 678–680. Translated from Fizika Tverdogo Tela, Vol. 46, No. 4, 2004, pp. 662–664.

MODIFICATION OF SURFACE AND THE PHYSICOCHEMICAL PROPERTIES OF NANODIAMONDS

Chemical State of Carbon Atoms on the Surface of Nanodiamond Particles

A. P. Dement'ev and K. I. Maslakov

Russian Research Centre Kurchatov Institute, pl. Kurchatova 1, Moscow, 123182 Russia

e-mail: a.dem@ru.net

Abstract—Auger electron spectroscopy study of the chemical state of carbon atoms on the surface of nanodiamond particles is performed. Auger spectra of nanodiamond particles indicate that carbon atoms in nanodiamond are in the same state as those in graphite, i.e., in the $\sigma_s^1\sigma_p^2\pi^1$ state, but the π band is displaced 1 eV in energy below the Fermi level. The surface of nanodiamond particles is inert with respect to the ambient medium. © *2004 MAIK "Nauka/Interperiodica".*

1. INTRODUCTION

The growth of diamond films from the gas phase encounters certain problems. One of these is the uncertainty in the beginning of growth on a silicon substrate. Depositing nanodiamond (ND) particles on a silicon surface makes it possible to reduce the nucleation time appreciably [1, 2]. These results indicate that carbon atoms on the ND particle surface are in a certain chemical state C_d that favors the nucleation and growth of diamond. Identification of this chemical state is of interest for understanding the mechanism of diamond growth from the gas phase. Identification of the chemical state in this case implies the establishment of the bond type in terms of sp^2 or sp^3 hybridization. Naturally, only the topmost layers of ND particles are of importance, since the growth of diamond films is apparently controlled by the interaction of atoms and radicals with the surface. The surface of ND particles was studied in [3] using XPS, PES, and Raman spectroscopy; however, no unambiguous conclusions were drawn in that study as to the hybridization type of carbon in the topmost layer of ND particles.

Auger spectra of carbon atoms (CKVV) exhibit features characteristic of sp^2 and sp^3 hybridized states [4–8]. This is due to the fact that the structure of Auger spectra depends on the energy position of occupied states in the valence band and on the delocalization of holes in the process of Auger relaxation. Moreover, the information provided by these spectra is related to the two-monolayer-thick surface layer [9]. Therefore, this method is most attractive for the study of the chemical state of carbon atoms in the topmost layers of carbon films. However, the Auger spectra of carbon atoms are poorly studied and one should identify not only the chemical state of atoms in each specific case but also the spectral features associated with the structure of the valence band.

Accordingly, the aim of this study is to determine the chemical state of carbon atoms on the surface of ND particles from the Auger spectra.

2. EXPERIMENTAL

The work was carried out using a VG Scientific MK-II electron spectrometer with x-ray excitation of Auger emission. Samples produced at the Kiev Institute for Superhard Materials and in Snezhinsk and Krasnoyarsk were studied. The ND powders were mixed with alcohol using ultrasound, and a silicon plate was placed in the solution at a depth of 1 mm. After drying in air, a continuous coating was formed on the plate containing alcohol, water, and various gases from the air. These adsorbates were removed in the preparation chamber of the spectrometer by pumping down for about 4 h at room temperature or at a temperature of 600 K. A tungsten wire that could be heated to 2300 K was placed in the preparation chamber in order to obtain atomic hydrogen from H_2 or carbon atoms from CH_4. The residual pressure in the analysis chamber and in the preparation chamber was 5×10^{-10} Torr. A sample could be moved between the chambers through a lock. Spectra were recorded in steps of 0.25 eV, and the transmission energy was 50 eV.

The following samples were studied.

(1) ND particles before and after *in situ* treatment by atomic hydrogen and heating to 1100 K.

(2) A natural (110) diamond after *in situ* treatment by atomic hydrogen at 1000 K.

(3) A natural (110) diamond after *ex situ* treatment by atomic hydrogen in an ASTeX-PDS19 growth setup at 1100 K for 8 min under growth conditions but in the absence of CH_4.

(4) A sample obtained after interruption of the diamond growth process in the ASTeX-PDS19 setup.

1063-7834/04/4604-0678$26.00 © 2004 MAIK "Nauka/Interperiodica"

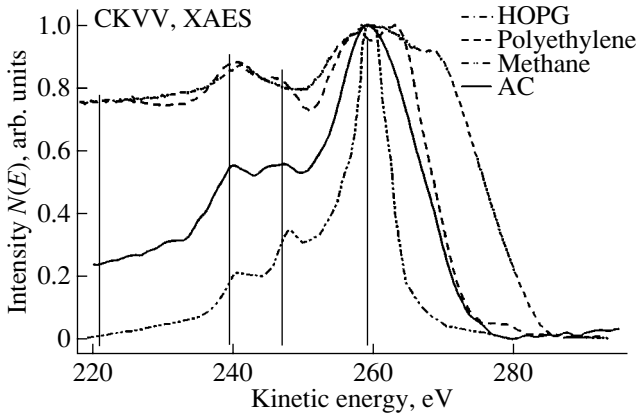

Fig. 1. Comparison of the experimental Auger spectra of HOPG, polyethylene, methane, and carbon adsorbed on a Si substrate.

3. RESULTS AND DISCUSSION

From XPS studies of oxides and metals, it is known that their surfaces always adsorb carbon-containing molecules from the environment (adventitious carbon, AC). It is difficult or even impossible to detect such surface contaminations of carbonic materials by using C1*s* XPS spectra.

Figure 1 compares the Auger spectra of the standards with sp^2 and sp^3 bonds and the spectrum of a carbon-containing contamination on the silicon surface. Samples of highly oriented pyrolytic graphite (HOPG), polyethylene, and fullerenes were prepared in air. The spectra of these samples differ appreciably. The AC spectrum is similar in structure to that of the polyethylene, which indicates that the bonds in AC are of the sp^3 type. The difference in the low-energy features of these spectra can be due to the fact that the AC molecules are not completely bonded to the solid and have dangling bonds. Apparently, if the surfaces of polyethylene, fullerene, and HOPG were to be covered by AC, their spectra would coincide with the AC spectrum.

One should bear in mind that the "information depth" of carbon Auger spectra is 1–2 monolayers. We observed a typical AC spectrum only for samples with sp^2 bonding (melamine $C_3N_6H_6$ and CN_x films), which indicates that AC is present on the surface of carbon–nitrogen compounds.

Figure 2 compares a carbon Auger spectrum of ND particles with the spectra of polyethylene and HOPG. The Auger spectrum of ND particles shown in Fig. 2 was observed in all experiments (curves *1–4*), which indicates that, in all cases, carbon atoms on the surface are in the same chemical state and that this state is inert with respect to AC.

In order to determine the type of chemical bonding of carbon atoms in this state, it is necessary to identify the Auger spectrum. Figure 2 compares the experimental Auger spectra of ND particles and HOPG with the theoretical spectrum obtained by self-convolution of the graphite density of states taken from [10]. Simulation of the experimental spectrum showed that the electronic structure of carbon atoms in ND particles is the same as that in graphite, $\sigma_s^1\sigma_p^2\pi^1$, under the assumption that either the self-convolution $\pi * \pi$ is absent or the π band is displaced downwards of the Fermi level by 1 eV. The latter assumption provides better agreement with the experimental data (Fig. 3).

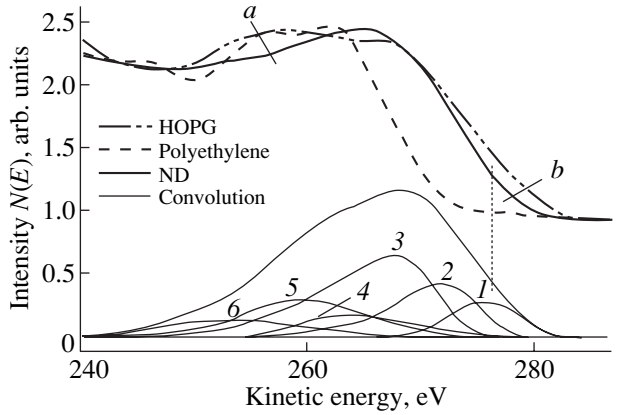

Fig. 2. Comparison of the experimental Auger spectra of HOPG, polyethylene, and ND particles with the self-convolution of the density of states of the graphite valence band: (*1*) $\pi * \pi$, (*2*) $\sigma_p * \pi$, (*3*) $\sigma_p * \sigma_p$, (*4*) $\pi * \sigma_s$, (*5*) $\sigma_p * \sigma_s$, and (*6*) $\sigma_s * \sigma_s$. Labels *a* and *b* indicate the regions of the most characteristic differences between the experimental Auger spectra of nanodiamonds and graphite.

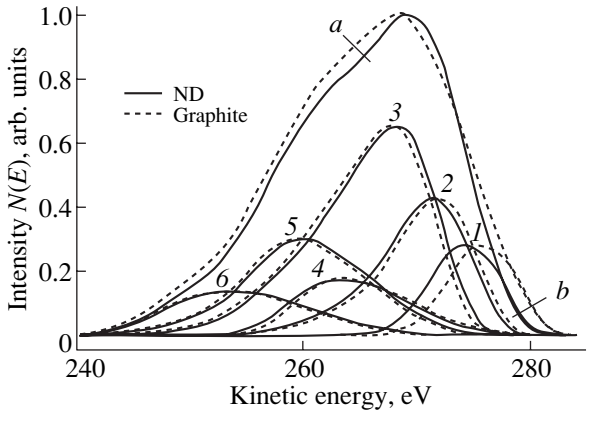

Fig. 3. Comparison of the self-convolution of the density of states of the valence band of graphite and that of ND particles (the π band is shifted downwards of the Fermi level by 1 eV). The curve notation (*1–6*) is the same as that in Fig. 2. Labels *a* and *b* indicate the regions of the most characteristic differences between the calculated spectra of nanodiamonds and graphite.

4. CONCLUSIONS

(1) The $N(E)$ features in the CKVV Auger spectrum of ND particles and of natural (110) diamond after atomic-hydrogen treatment coincide and differ appreciably from those of the spectra of the standards with sp^2 and sp^3 bonds.

(2) According to our interpretation of $N(E)$ of the CKVV Auger spectrum for ND particles, carbon atoms on the surface of ND particles have the same electronic configuration as those in graphite, $\sigma_s^1\sigma_p^2\pi^1$, but with the π level displaced 1 eV below the Fermi level.

(3) The chemical state of carbon atoms on the surface of ND particles is inactive with respect to atmospheric contaminations. As in the case of molecular sieves, considerable gas adsorption by nanodiamond powders is apparently due to their large surface rather than to chemical interactions.

REFERENCES

1. A. A. Smolin, V. G. Ralchenko, S. M. Pimenov, *et al.*, Appl. Phys. Lett. **62**, 3449 (1993).
2. V. I. Konov, A. A. Smolin, V. G. Ralchenko, *et al.*, Diamond Relat. Mater. **4**, 1073 (1995).
3. E. Maillard-Schaller, O. M. Kuettel, L. Diederich, *et al.*, Diamond Relat. Mater. **8**, 805 (1999).
4. T. W. Haas, J. T. Grant, and G. J. Dooley, J. Appl. Phys. **43**, 1853 (1972).
5. P. G. Lurie and J. M. Wilson, Surf. Sci. **65**, 476 (1977).
6. G. Speranza, N. Laidani, L. Galliari, and M. Anderle, Diamond Relat. Mater. **8**, 517 (1999).
7. A. Dementjev, K. I. Maslakov, and O. O. Zabusov, New Diamond Frontier Carbon Technol. **12**, 15 (2002).
8. L. Galliari, G. Speranza, J. C. Lascovitch, and A. Santoni, Surf. Sci. **501**, 253 (2002).
9. C. J. Powell and A. Jablonski, *NIST Electron Inelastic-Mean-Free-Path Database-Version 1.1* (National Inst. of Standards and Technology, Gaithersburg, MD, 2000).
10. J. S. Murday, B. J. Danlap, F. L. Hutson, and P. Oelhafen, Phys. Rev. B **24**, 4764 (1981).

Translated by I. Zvyagin

Physics of the Solid State, Vol. 46, No. 4, 2004, pp. 681–684. From Fizika Tverdogo Tela, Vol. 46, No. 4, 2004, pp. 665–667.

MODIFICATION OF SURFACE AND THE PHYSICOCHEMICAL PROPERTIES OF NANODIAMONDS

Chemical Mechanical Modification of Nanodiamond in an Aqueous System*

Y. W. Zhu[1, 2], X. Q. Shen[2, 3], B. C. Wang[2], X. Y. Xu[2], and Z. J. Feng[1]

[1] *Department of Precision Instruments and Mechanology, Tsinghua University, Beijing, 100084 China*

[2] *China R&D Center, Changsha Research Institute of Mining and Metallurgy, Hunan, 410012 China*

[3] *China Department of Materials Science and Technology, Jiangsu University, Jiangsu, 202013 China*

e-mail: y.w.zhu@63.net

Abstract—The effect of chemical–mechanical modification (CMM) on the ζ potential and size distribution of nanodiamonds was studied. Results show a significant change in the functional groups on its surface after CMM treatment by the anionic surface modifier DN-10. The amount of hydroxyl groups decreases, and two peaks connected with the stretching vibration of carboxylate appear instead of those of carbonyl. The ζ potential goes up significantly, and the size drops to some extent. If treated further with CMM1, a new absorption peak appears at 1382.19 cm^{-1} that is connected with the vibration of some distinctive functional groups that cause an increase in the ζ potential and a decrease in size. © *2004 MAIK "Nauka/Interperiodica".*

1. INTRODUCTION

Owing to its excellent mechanical, medical, and electronic characteristics, nanodiamond has been applied in the fields of run-in engine oil, wear-resistant plating layers of parts, and wear-resistant alloying parts to some extent. It has great application potential in such sectors as the ultrafine polishing of silicon wafers and other manmade crystals and the modification of plastics, rubber magnetic memory devices, and cold cathode displays [1–4]. In these applications, the dispersion and stability of nanodiamond in various suspensions are the decisive preconditions of its application. When used for ultrafine polishing of crystals, aggregates may cause nicks on the surface of a work piece. When used for electroplating or nonelectrolytic plating, aggregates result in an inadequate particle distribution and a decrease in the wear-resistant properties.

In aqueous systems, a particle always carries electric charges due to the ionization, absorption of ions, or preferential substitution of ions [5]. The ζ potential of an ultrafine particle is often used to evaluate the variety and intensity of charge, and it is a very important index reflecting the repulsive force intensity among particles and the dispersion stability. There exist functional groups, such as –COOH, –OH, $–NH_2$,on the surface of nanodiamond [6]. The type and intensity of the functional groups affect its sorption behavior and ionization properties. The status of charge exerts great influence on the stability of nanodiamond suspensions.

It was pointed out in [4] that the ζ potentials for different fractions of ultrafine-dispersed diamond are different.

The chemical–mechanical modification (CMM) treatment is a type of process that simultaneously involves particle fragmentation and surface modification. Good results were achieved by the CMM treatment of calcium carbonate $CaCO_3$ and wollastonite [7, 8].

This paper presents some results on the effect of CMM on the surface functional groups, ζ potential, and size distribution of nanodiamonds.

2. EXPERIMENTAL

A gray powder of the nanodiamond sample *L* (produced by Lingyun Nanomaterials Co., Ltd, China) was investigated. Before measuring the ζ potential, an adequate amount of the nanodiamond powder should be dispersed into deionized water to obtain a suspension. If there is precipitation, the supernatant can be used to measure its ζ potential, as the ζ potential is independent of particle size. All ζ-potential and most size-distribution measurements were conducted using a ZETASIZER3000HS; other size measurements were conducted using small angle x-ray scattering (SAXS) and CILAS 1064 Liquid. The primary size distribution was studied with SAXS, which ran at 35 kV and 30 mA. The x-ray source was generated by CoK_α, and the filter was iron. The size parameters, such as the mean size, the median size, and the distribution, can be obtained from the SAXS results. The CMMs of nanodiamond were carried out in a stirring mill. In the process of stirring, the anionic surfactant DN-10 was added to the mill to modify its surface characteristics. The mass ratio of DN-10 to nanodiamond was 5 : 100, and the peripheral velocity of the stirring vane was about 4.5 m/s. CMM1 is a further treatment after CMM,

* This article was submitted by the authors in English.

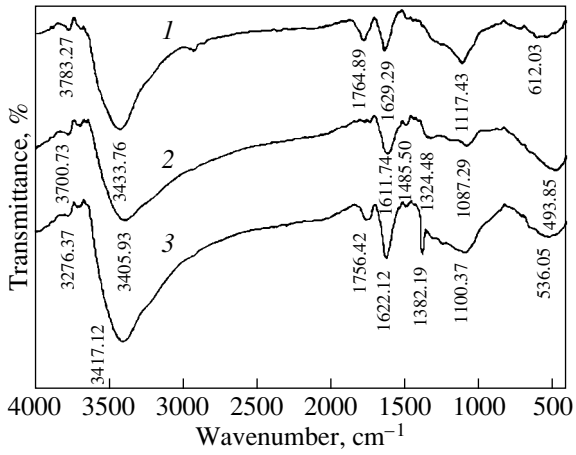

Fig. 1. The ζ potential of nanodiamond before and after treatments: (*1*) sample *L*, (*2*) after CMM treatment, and (*3*) after CMM1 treatment.

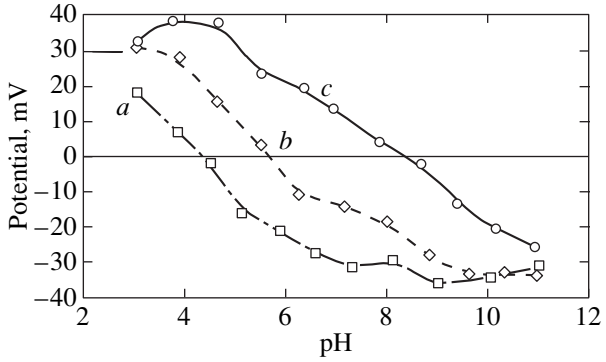

Fig. 2. Infrared spectra before and after treatment: (*1*) sample *L*, (*2*) after CMM treatment, and (*3*) after CMM1 treatment.

which employs the same equipment as CMM but a more acidic environment. The infrared spectral analysis in this work was conducted using Nexus 470.

3. RESULTS AND DISCUSSION

3.1. ζ Potential of Sample L

The ζ potential with the pH curve for sample *L* is presented in Fig. 1 (see curve *1*). Its isoelectric point (IEP) was found at 4.3. The ζ potential is positive in the pH range 3–4.3 and negative in the range 4.3–11. Its absolute value is more than 30 mV in the pH range 7–11, which ensures a stable suspension without coarse particles.

The infrared spectrum of sample *L* (see curve *1*, Fig. 2) reveals a very strong absorption peak located at 1117.43 cm^{-1}. It may be connected with the stretching C–OH vibration of the hydroxyl and/or the C–N vibration of the amine on the nanodiamond surface. It may be reinforced by the absorption of $(SO_4)_2^-$ or $(ClO_4)^-$ during its purification. The absorption peak at 1764.89 cm^{-1} may be connected with a distinctive absorption of carbonyl for carboxyl. There is a very strong absorption peak around 3450 cm^{-1}; it may be induced by the stretching O–H and/or N–H vibration. The absorption peak located at 1629.29 cm^{-1} may be due to the combinational action of I ϑ C=O and II δ N–H + ϑ C–N. It may also be induced by the functional group C–N=O. It can be suggested from the above analysis and a comparison of absorption intensities of the peaks that there are less $–NH_2$ groups and more –COOH groups on the nanodiamond surface. As a result, the particles demonstrated electronegativity in a neutral water system. With an increase in pH, the charge intensity is reinforced because of the absorption of OH^- and the ζ potential becomes more negative. With a decrease in pH, the ζ potential becomes increasingly positive until it demonstrates electropositivity at pH = 4.3 as a result of the absorption of H^+.

3.2. CMMs of Nanodiamond

The ζ potential versus pH curve after the CMM treatment by DN-10 for sample *L* is represented by the curve *2* in Fig. 1. Curve *3* in Fig. 1 represents sample *L* with chemical–mechanical modification through further CMM1 treatment. CMM1 is also a type of CMM, the purpose of which is to change its surface functional groups.

After sample *L* is treated with CMM and CMM1, the ζ potential with the pH curve goes up and the IEP shifts to the right. The ζ potential of nanodiamond increases significantly in the acid range and is greater than 30 mV in the pH range 3–5 for the sample treated with CMM1. As a result, the stability of the nanodiamond suspension in this range improves greatly. Therefore, the suspension in the above pH range could be kept for a long time without obvious precipitation.

After the CMM treatment, the absorption peaks at 1629.29 and 1764.89 cm^{-1} of carbonyl for sample *L* disappear and are substituted by the peaks at 1611.74 and 1324.48 cm^{-1} caused by the stretching vibration of carboxylate. The intensity of the absorption peak located at 1117.43 cm^{-1} decreases significantly, and it shifts 30 cm^{-1} towards the lower wave-number values. This peak is connected with the stretching C–OH and C–N vibrations. The intensity of the absorption peak at 3405.94 cm^{-1} also decreases significantly. The CMM treatment exerted little influence on the C–N groups, but it could make it easily for some functional groups to be linked to the C–OH groups. This suggests that the amount of C–OH bonds on the nanodiamond surface drops. It is the drop in the amount of –OH groups that causes the decrease in the intensity of the absorption peak. The changes mentioned above are the main reasons why the ζ potential for sample CMM shifts upwards in the acid range. The absorption peaks of the stretching vibration of carboxylates for sample CMM1

disappear completely and are substituted by peaks of carbonyl again. Compared with sample *L*, a new absorption peak at 1382.19 cm^{-1} for sample CMM1 appears, in connection with the stretching vibration of some distinctive functional groups, which causes the increase in the ζ potential.

3.3. Effect of CMM on Size Distribution

After CMM and further treatment (CMM1), the size distribution of sample *L* changes markedly (listed in Table 1). Before the CMM treatment, the fraction of particles less than 100 nm in size for sample *L* is only 0.77 wt %, the average size is 2260 nm, and the maximum size is 12 000 nm. Here, the particle size refers to that of the secondary particle, i.e., the aggregate particle size due to various kinds of forces. The results of the SAXS analysis of sample *L* (listed in Table 2) show that the mean size of the primary particles is only 12 nm and all the particles are less than 60 nm in size. Here, we refer to the particle before aggregation (measured using SAXS) as the primary particle. The mean size of the secondary particle measured by ZETASIZER3000HS is 100–200 times coarser than that measured by SAXS; namely, the index of aggregation of the nanodiamond sample *L* is 100–200.

The formation of nanodiamond aggregates and their properties are very complicated. Some are soft aggregates caused by van der Waals forces among particles, and some are hard aggregates caused by chemical bonds among particles. It is very difficult to disperse them, especially the latter. Detonation is a very complicated process of high pressure–high temperature transition involving many chemical reactions. Under those conditions, carbon droplets are easily conglutinated in the cooling and phase transformation process and then hard aggregates form. Nanodiamond has a large specific surface, which results in a huge surface energy. In order to lower the free energy of the system, the fine particles congregate to aggregates with a large size spontaneously. A significant improvement in the nanodiamond size distribution is observed after the CMM treatment: the mean sample size drops from 2260 to 670 nm, and, after further treatment (CMM1), it drops further to 95.6 nm and most of the particles are finer than 100 nm.

Under usual stirring–grinding conditions, smaller particles are formed due to the media grinding and shearing action. However, these smaller particles easily congregate to form larger ones as a result of the demand to reduce the free energy of the system once the stirring stops. So, usual stirring and grinding has little effect on the decrease in size for ultrafine particles. The reason why the nanodiamond aggregates can be effectively crushed during the CMM process may be attributed to the combined action of mechanical grinding and chemical absorption during the stirring and grinding. With the addition of DN-10 to the process of stirring and grinding, smaller aggregates form due to the grinding of media and shearing action and, at the same time, the temperature of the nanodiamond aggregate surface rises and its activity improves, which results in reaction between the DN-10 molecules and active spots on the nanodiamond aggregates. The surface electrical properties change markedly because of the chemical absorption of DN-10. The ζ potential of nanodiamond particles increases sharply in the pH range 3–7, and the enforced repulsive forces among the particles protect them from aggregating. As a result, the mean nanodiamond size drops.

Table 1. Size distribution of nanodiamond before and after treatments

Samples	Mass fraction (<100 nm), %	Mean size, nm	Maximum size, nm
Sample *L*	0.77	2.260	12000
After CMM	7.57	670	3000
After CMM1	81.6	95.6	205.6

Table 2. SAXS results for sample *L*

Size interval, nm	Mass fraction, %	Cumulative, %
1–5	20.1	20.1
5–10	43.0	63.1
10–18	25.2	88.3
18–36	4.7	93.0
36–60	7.0	100

Table 3. Size distributions after the addition of gallic acid

Size range, nm	Volume, %	Number, %
17.8–21.8	0	0
21.8–26.6	3.2	10.5
26.6–32.5	10.6	22.8
32.5–39.7	19.8	28.4
39.7–48.5	24.3	21.0
48.5–59.3	23.0	11.8
59.3–72.5	16.6	5.4
72.5–88.5	2.5	0.1
88.5–108.5	0	0

After treatment of sample *L* with CMM and further treatment with CMM1, its particle size could be further reduced with the addition of 0.5 mg/l gallic acid. Table 3 presents its size distribution. No particles greater than 88.5 nm in size are found. The mean volume size of nanodiamond is 52 nm. The suspension can be used for ultrafine polishing of crystals and composite electrolysis plating and electroplating of parts.

4. CONCLUSIONS

(1) After treatment with CMM, the amount of –OH groups decreases, and if there is further treatment with CMM1, a new absorption peak appears at 1382.19 cm^{-1} that is connected with certain distinctive groups. The ζ potential increases in the acid range, and the stability of its suspension significantly improves.

(2) After treatment with CMM and CMM1, the average volume size drops from 2260 to 95.6 nm. If further dispersed with the addition of 0.5 mg/l gallic acid, the mean volume size reaches 52 nm.

REFERENCES

1. G. Z. Wang, in *Proceedings of the Symposium of Development of Nanodiamond* (Hangzhou, 1999), p. 7.
2. W. Zhu, G. P. Kochanski, and S. Jin, Science **282**, 1471 (1998).
3. N. Kossovsky, A. Gelman, H. J. Huatyszyn, *et al.*, Bioconjug. Chem. **6**, 507 (1995).
4. V. Yu. Dolmatov, Russ. Chem. Rev. **70** (7), 607 (2001).
5. F. S. Li, *Technologies for Ultra-fine Particles* (National Industrial Publ. House, Changsha, 2002), p. 7.
6. E. Mironov, A. Koretz, and E. Petrov, Diamond Relat. Mater. **11**, 872 (2002).
7. H. Ding and Y. S. Han, Non-Metall. Mines, No. 4, 32 (1997).
8. L. Li and X. B. Zheng, Non-Metall. Mines, No. 5, 13 (1993).

Physics of the Solid State, Vol. 46, No. 4, 2004, pp. 685–686. Translated from Fizika Tverdogo Tela, Vol. 46, No. 4, 2004, pp. 668–669.

MODIFICATION OF SURFACE AND THE PHYSICOCHEMICAL PROPERTIES OF NANODIAMONDS

Intercalation of Ultrafine-Dispersed Diamond in Aqueous Suspensions

A. E. Aleksenskiĭ, M. A. Yagovkina, and A. Ya. Vul'

Ioffe Physicotechnical Institute, Russian Academy of Sciences, Politekhnicheskaya ul. 26, St. Petersburg, 194021 Russia

e-mail: blin@mail.ioffe.ru

Abstract—A method for preparing ultrafine-dispersed diamond (UDD) powders with a uniform distribution of metal ion impurity over the bulk of a powder is developed. The uniformity and composition of a UDD sample is demonstrated using x-ray diffraction and chemical analysis. © *2004 MAIK "Nauka/Interperiodica".*

The study of phase transitions between allotropic modifications of carbon has recently become a rapidly developing area of the physics of phase transitions [1–4]. This is due both to the nontrivial properties of carbon itself (it is a chemical element with four strong valences) and to the practical importance of studying the stability of carbon materials for technical applications. Accordingly, study of the transformation of ultrafine-dispersed diamond (UDD) into other modifications of carbon or its compounds [5–7] is of interest. A key problem is the definition of the factors affecting such a transformation.

By studying diamond properties, it was established a long time ago that the presence of certain metals strongly affects phase transitions in carbon. This fact forms the basis of the high-pressure high-temperature (HPHT) technology of industrial production of artificial diamonds [8]. The effect of metals on the graphite–diamond phase transition is still not clearly understood; however, it has been firmly established that this effect is not reduced to simple recrystallization (i.e., to dissolution of the thermodynamically unstable phase and precipitation of the stable phase in the unchanging solvent) [9–11]. In this respect, studies of the effect of carbide-forming elements, such as Fe, Co, and Ni, on phase transitions in UDDs is of special interest, since these elements are widely used as catalysts for UDD production using HPHT technology. The problem is to deposit metal impurities directly on the cluster surface, i.e., to realize the intercalation process.

The distribution of a metal over a UDD powder essentially depends on the method applied to introduce the metal into the UDD; if powders are mixed in the usual way, the impurity distribution over the mixture is highly nonuniform and the metal concentration at the surface of UDD aggregates cannot be controlled. Thus, for further studies, it is important to develop a method of producing dry UDD powders with a uniform and controlled metal distribution over the surface of diamond particles.

We suggest a method for producing a uniform distribution of metal compounds over a UDD. To this aim, a UDD must be transferred to a state with the maximum possible dispersity. It is known that such a state occurs in UDD hydrosols where the dispersed phase consists of strong aggregates 100–200 nm in size. These aggregates contain about 10^4–10^5 UDD clusters with an average size of about 4 nm per unit (micelle) of the dispersed medium [12]. Chemically bonded functional groups (typically, carboxyl group –COOH) were identified at the surface of the aggregates [13]. The presence of such groups can easily be demonstrated by measuring the pH value in high-purity aqueous UDD suspensions. Carboxyl groups and ions of heavy metals form salts. Since the concentration of carboxyl groups at the surface of UDDs is approximately constant, metal ions are uniformly distributed over the surface of UDD conglomerates. Naturally, for multiply charged ions bonded to several carboxyl groups, one can reasonably assume that surface compounds are more stable. When the water is removed from the system, the particles coagulate, forming greater aggregates, as in the case of pure UDD. However, since the metal ions are bonded to the surface of the original UDA aggregates, the salt phase is not separated. After drying, a UDD powder is formed with intercalated metal ions at the UDD surface.

In practice, the doping is performed as follows.

(1) An aqueous solution of a metal salt is prepared (in our case, a 0.1 M solution of iron, cobalt, nickel, or copper acetate or nitrate).

(2) The prepared solutions are mixed with a subacid UDD suspension with a concentration of about 5 wt % and pH = 3–4. It is preferable to use high-purity UDDs, e.g., those prepared by ion-exchange cleaning.

(3) The suspension is rinsed with distilled water, allowed to settle, and dried. After the sediment has deposited, one can qualitatively estimate the degree of transition of the metal to the UDD-bonded form judging from the color of the clarified liquid. If the color

1063-7834/04/4604-0685$26.00 © 2004 MAIK "Nauka/Interperiodica"

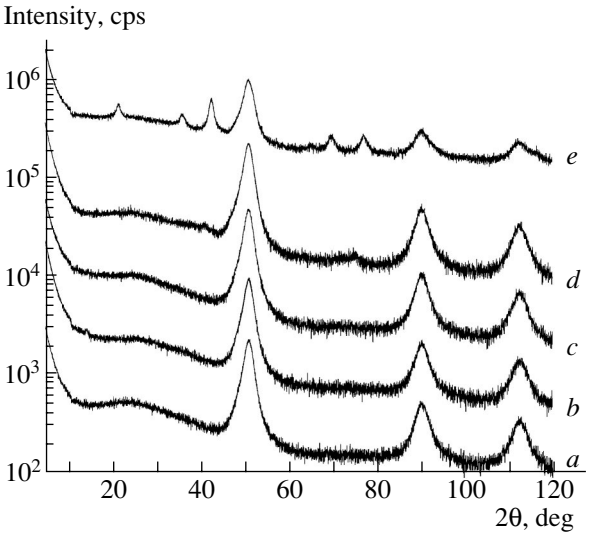

Fig. 1. Diffractograms of (*a*) the original UDD powder and UDD powders intercalated by (*b*) copper, (*c*) nickel, (*d*) iron, and (*e*) cobalt.

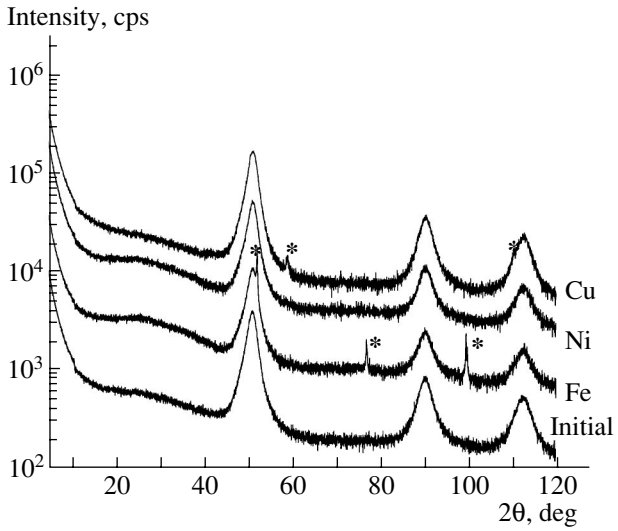

Fig. 2. Diffractograms of UDD powders after annealing in hydrogen at 500°C. The maxima corresponding to metallic phases are marked with asterisks.

that is characteristic of metal ions is absent, one can calculate the amount of absorbed impurity.

Gravimetric and x-ray fluorescence analysis showed that UDD powders prepared in this way can contain up to 10% metal [14]. However, according to x-ray diffractometry, no other crystalline phases other than diamond were detected in the powders.

It is seen in Fig. 1 that the diffraction curves for the powders under study contain only the maxima corresponding to UDD, whereas after thermal treatment (at 500°C) of intercalated UDD powders in a hydrogen atmosphere the diffractograms exhibit only the reflections from metallic phases of intercalated impurities (Fig. 2). This fact can only be interpreted under the assumption that metal impurities are distributed uniformly in the UDD powders but thermal treatment causes impurities to agglomerate into x-ray-detectable metallic phases.

REFERENCES

1. M. S. Dresselhaus, G. Dresselhaus, and P. Eklund, *Science of Fullerenes and Carbon Nanotubes* (Academic, New York, 1996).
2. D. Ugarte, Nature **359** (22), 707 (1992).
3. Y. Shibayama, H. Sato, T. Enoki, *et al.*, J. Phys. Soc. Jpn. **69** (3), 754 (2000).
4. N. R. Greiner, D. S. Phillips, J. D. Johnson, and F. Volk, Nature **333**, 440 (1988).
5. V. L. Kuznetsov, A. L. Chuvilin, Yu. V. Butenko, *et al.*, Chem. Phys. Lett. **222**, 343 (1994).
6. A. E. Aleksenskii, M. V. Baidakova, A. Ya. Vul', *et al.*, Phys. Solid State **39**, 1007 (1997).
7. F. Banhart, J. Appl. Phys. **81** (8), 3440 (1997).
8. P. Wesolowski, Y. Lyutovich, F. Banhart, *et al.*, Appl. Phys. Lett. **71** (14), 1948 (1997).
9. N. Setaka, in *Synthetic Diamond: Emerging CVD Science and Technology*, Ed. by K. E. Spear and J. P. Dismukes (Wiley, New York, 1994), pp. 57–90.
10. G. Bocquillon, C. Bogicevic, C. Fabre, and A. Rassat, J. Phys. Chem. **97**, 12924 (1993).
11. A. Ya. Vul', V. M. Davidenko, S. V. Kidalov, *et al.*, Pis'ma Zh. Tekh. Fiz. **27** (9), 72 (2001) [Tech. Phys. Lett. **27**, 384 (2001)].
12. F. Z. Badaev, O. A. Besedina, P. M. Brylyakov, *et al.*, Dokl. Akad. Nauk SSSR **310**, 402 (1990).
13. L. M. Martinov and Y. I. Nikitin, Colloid J. USSR **52**, 245 (1990).
14. A. E. Aleksenskiĭ, M. V. Baĭdakova, M. A. Yagovkina, and A. Ya. Vul', in *Abstracts of International Symposium on Detonation Nanodiamonds: Production, Properties, and Applications* (St. Petersburg, 2003), p. 75.

Translated by I. Zvyagin

Physics of the Solid State, Vol. 46, No. 4, 2004, pp. 687–695. Translated from Fizika Tverdogo Tela, Vol. 46, No. 4, 2004, pp. 670–678.

APPLICATIONS OF NANODIAMONDS

Polishing Nanodiamonds

A. S. Artemov

Lebedev Physical Institute, Russian Academy of Sciences, Leninskiĭ pr. 53, Moscow, 119991 Russia

e-mail: artpol@mail1.lebedev.ru

Abstract—The results of polishing (using suspensions of nanodiamonds (NDs) produced by detonation synthesis at different plants) of the surfaces of 23 solid materials having different chemical compositions, production processes, structure, electronic properties, hardness, reactivity, and application are described. Atomic force microscopy is used to compare the roughness of these surfaces with the surfaces of such materials subjected to polishing with diamond synthetic micropowders (of grades 1/0, 0.25/0, 0.1/0) and to chemical–mechanical polishing (CMP) with amorphous colloid silica. Stable ND suspensions are shown to cause a number of effects, namely, polishing, scratching, plastic flow of surface layers, and CMP. The aggregative state of solid particles is shown to be of importance. Polishing with NDs is found to be accompanied by mechanical nanoscratching, which can be leveled by the introduction of certain etchants into an ND suspension. The use of amorphous nanoparticles is the only technique that does not induce deformation in the surface layer of a material. © *2004 MAIK "Nauka/Interperiodica"*.

1. INTRODUCTION

The application of ultrafine-dispersed diamonds (UDDs) and nanodiamonds (NDs) in modern electronic engineering is important for the development of both the theory and technology of polishing solid materials and in various fields of electronics.

Although the application of diamonds synthesized by detonation for the polishing of materials [1–4] seems to be obvious, they have not been applied in industry for two reasons. First, in empirical approaches, the physical–mechanical processes that occur in elementary acts of contact between nanocrystalline particles and solid surfaces have not been taken into account. Second, the empirical approaches were based on the principle of mechanical polishing (MP), according to which a solid particle with a small size and high hardness affects a solid material having lower hardness, without regard for colloid-chemical concepts, which serve as the basis for chemical–mechanical polishing (CMP). Therefore, it is still unclear which property of solid particles, namely, the minimum size (colloid size range) or the aggregative state (amorphous or crystalline), is responsible for the quality of a polished surface that is geometrically (minimum roughness) and structurally (without scratches) perfect.

The transition from submicron to nanometer sizes of topological elements in micro- and optoelectronics is a necessary stage in the design of new devices based on surface layers 5–15 nm thick with a minimum geometrical relief varied from a fraction of a nanometer to several nanometers. Moreover, high geometrical and structural uniformity of a surface area of a few tens to several hundreds of centimeters squared is necessary for high-quality dielectric and epitaxial layers, lithography, sputtering, the stabilization of electrophysical surface properties, etc. Therefore, this work fits the sequence of production processes in modern electronics: nanopolishing–nanoepitaxy–nanostructures.

The goal of this work is to obtain experimental data to answer four basic questions: What materials can be promising for polishing with UDDs? What are the physicochemical features and possibilities of UDDs for polishing solid surfaces? Which branches in modern industry call for high-precision surfaces produced with UDDs? What are the economic benefits of UDDs as compared to the existing polishing technologies?

2. EXPERIMENTAL

2.1. Ultrafine-Dispersed Diamonds

We applied UDDs and NDs supplied from manufacturers in the form of powders, suspensions, and pastes. We studied both as-delivered products and suspensions based on them (Table 1).

2.2. Materials

Criteria for choosing the materials and the fields of their application are given in Tables 2 and 3. Apart from polishing with UDD composites, the materials were also subjected, for comparison, to mechanical polishing with synthetic diamond micropowders of grades 1/0, 0.25/0, and 0.1/0 and to CMP with compositions of amorphous colloid silica; these techniques are, as a rule, two stages of the pre-final and/or final polishing, which are well known and widely approved in electronics and optics. The time of polishing with UDDs (NDs) in each stage of sample preparation was 3–12 h. Samples of different

1063-7834/04/4604-0687$26.00 © 2004 MAIK "Nauka/Interperiodica"

Table 1. UDD products for polishing materials

No.	Manufacturer	Product	Solid phase content, wt %	Particle or aggregate size, nm	pH	Sedimentation stability, month	Suspension characteristics
1	Alit, Kiev	pdd	1.8	500–1000	6	12	Powder suspension
2	The same	″	1.0	″	″	″	The same
3	The same	swp 1–3/12	1.8	1000–3000	12	12	Suspension of compacted aggregates
4	The same	″	1.0	″	″	″	The same
5	Sinta, Minsk	Sn-1.4	1.4	4–6	7	3	Neutral aqueous suspension from 8 wt % aqueous suspension
6	The same	Sbas-1.4	1.4	″	12	″	Alkaline aqueous suspension from 8 wt % aqueous suspension
7	The same	Cac-1	1	″	2	″	Acid aqueous suspension from powder
8	SKTB Tekhnolog, St. Petersburg	UDD–CTB	2–4	300–500	7	1	Ultrasound-treated aqueous suspension
9	The same	UDD–TAH	5–10	Up to 100	7	<1	Separating aqueous suspension
10	The same	UDD–CTP	7			<1	Separating aqueous–alcohol suspension
11	SAKID, St. Petersburg	0.25/0		Up to 250	7	–	Aqueous opaque suspension from statically synthesized diamonds
12	The same	0.1/0		Up to 100	7	–	The same

shape and geometrical size were then used in practice or subjected to experimental examinations. The crystallographic orientation was accurate to <1°.

2.3. Equipment

We used machine tools with various kinematics for individual and batch processing: V1M3, SPP-2M, ShP-350, 4PD-200, SD-150, Malvern Multipol, etc.

2.4. Polishers

Polishers of two types were applied: woven polishers based on polyether, polypropylene, polyamide, polyether + polyamide mixture, and some specific polishers and nonwoven polishers, such as polytex, polyvele, artificial leather, etc. They had different mechanical strength, chemical stability, thickness, surface treatment, and fillers.

2.5. Methods of Surface Examination

The surface roughness was studied using optical microscopy (MII-4 and other microscopes), and technological control was performed visually and with an MBS microscope. An atomic force microscopy (AFM) study using a Nanoscope-IIIa microscope was performed in the height and deflection modes to analyze highly smooth surfaces. The smoothness criterion was taken to be the root-mean-square deviation of the asperity heights σ over a certain length of the roughness profile. In each sample, we usually studied from 3 to 12 areas having typical and specific relief features and represented by two- or three-dimensional images taken from regions having area s with sides varying from 0.3 to 13 μm. The images were processed using the FemtoSkan program developed at the Center of Promising Technologies, Moscow.

3. RESULTS AND DISCUSSION

The mechanical energy of abrasive particles interacting with a solid surface in the form of contact pulses causes changes in the surface morphology, crystalline and electronic structure, and chemical composition. When abrasive microparticles are replaced by nanoparticles, the contact zone in which a material is subjected to multiple elastic and plastic deformation decreases. Among the three basic properties (geometrical, structural, mechanical) of a surface, we concentrated on the relief roughness (parameter y), which is one of the numerous standard geometrical parameters, and on certain specific features of surface deformation upon microabrasive action. We found the following features of interaction between ultrafine-dispersed diamonds and a solid surface.

Table 2. Materials for polishing with UDDs (criteria and fields of application)

Chemical composition	Elemental: Si, Ge, W, Mo, Nb, Cu
	Oxides: α-Al_2O_3, SiO_2, $ZrO_2 : Y_2O_3$(ZOY)
	Oxygen-containing: $Gd_3Ga_5O_{12}$(GGG), $Y_3Al_5O_{12}$(YAG), $LiNbO_3$(LNO), $MgO : Al_2O_3(MgAl_2O_4)$, $SrTiO_3$
	Fluorides: CaF_2
	Carbides: SiC
	Nitrides: AlN, Si_3N_4
	Solid solutions: II–VI and III–V compounds
Method of preparation	Czochralski technique: Si, Ge, Nb, $LiNbO_3$, GGG, III–V compounds
	Verneuil technique: $MgAl_2O_4$
	Modified Kyropoulos technique: α-Al_2O_3
	Oriented crystallization: YAG, CaF_2
	Melting in a cold container: ZOY
	Electron-beam floating-zone melting: W, Mo
	Gas-phase sublimation: Cds, ZnSe
	CVD : ZnSe (polycrystal)
	Dry pressing followed by sintering: AlN
Structure	cubic, hexagonal, and trigonal crystals: W (100)(111), Mo (100)(101), Nb (100), Si (100), Ge (111); CdS (0001), ZnSe (100), GaAs (100), GaSb (100), GGG (111), YAG (111), LNO $y + 127°$, $SrTiO_3$ (100) and bicrystals, α-Al_2O_3 (0001), ZOY (100), SiC : 6*H*, CaF_2 (111)
	Polycrystals: Si, Cu, ZnSe CVD
	Amorphous: SiO_2 (KU-1), glass K-8
	Composites: AlN ceramics
Electrical properties	Conductors: W, Mo, Nb, Cu
	Semiconductors: Si, Ge, II–VI and III–V compounds, SiC
	Dielectrics: SiO_2, Si_3N_4, CaF_2, α-Al_2O_3, etc.
Application	Microelectronics
	Optoelectronics
	Acoustoelectronics;
	HTSC electronics
	Optics

3.1. Polishing

For proper treatment conditions and polishers, most machine tools provided surface smoothing for all materials with the formation of a mirrorlike surface without macroscopic defects (chips and cracks). Polishing is accompanied by the removal (loss) of materials. The loss rate depends on the type of machine and polisher used, the conditions employed, the preliminary treatment, and the material hardness; the rate varies over wide limits and is one of the parameters of a polishing process.

When a diamond synthetic powder of grade 1/0 is applied, the surface of a material is covered by numerous, differently oriented continuous straight-line scratches covering the entire surface. When UDD suspensions are used, the character of the scratches changes sharply (Fig. 1), e.g., for W, Ge, α-Al_2O_3, ZOY, etc., and scratches of different types are observed, namely, scratches that are uniform in width, scratches that widen in the middle or narrow toward one of their ends, dot-and-dash or dot (polished) scratches, and short (much less than the sample diameter) and long (straight-line and arched) scratches. Usually, scratches do not occupy the whole surface and there are extended areas that are free of optically resolvable small scratches.

All surfaces have regions with deep scratches [0.68 nm for Ge (Sn-1.4 suspension), up to 6.0 nm for GGG (pdd suspension), 0.8 nm for AlN-3.2 (UDD–CTB suspension), etc.] and large differences in height between valleys and ridges (h_{max}): 19.8 nm for Ge (0.1/0 micropowder), 66 nm for W (1/0 micropowder), 7.7 nm for STO (0.1/0 micropowder), and 0.9 nm for CdS (0.25/0 micropowder). However, in all cases, σ decreases by several times with decreasing diamond-

Table 3. Hardness of materials subjected to polishing with nanodiamond suspensions

No.	Material	Mohs' scratch hardness	Microhardness H, kgf/mm^2
1	CaF_2	4.0	168
2	$LiNbO_3$	5.5	450–500
3	$Cd_3Ga_5O_{12}$	6.5	
4	SiO_2	7.0	770
5	Si	7.0	1100
6	ZrO_2 : Y	8.0	1455, (111)
			1532, (110)
			1694, (100)
7	$Y_3Al_5O_{12}$	8.5	1550, MP (100)
			1770, CP (100)
			1720, MP (111)
			1930, CP (111)
8	α-Al_2O_3	9.0	2200, $\perp C$
			1940, $\parallel C$
9	SiC : 6*H*	9.25–9.5	2350, (0001)

particle size from the micro- to nanoscale and is equal to 10–18 nm for Si (pdd suspension); 0.7 nm for Ge (Sn-1.4); 0.5 nm for W (Sn-1.4); and 0.8–0.7 nm for YAG, ZOY, and LNO (pdd). There are also regions over which the change in height is several tenths of σ (0.3–0.2 nm) or even several hundredths of σ for both rough (with 1/0, 0.25/0, 0.1/0 micropowders) and fine (with UDDs) treatments. The number of such regions in the former case is smaller than in the latter, and the values of σ depend on the direction of the section. Therefore, σ does not reflect the real state of a relief and the specific features of the formation of roughness. To estimate them, it is useful to take into account the width l of large and small scratches, the roughness of their walls, and the roughness of short and relatively long (0.3- to 14-μm) horizontal regions.

3.2. Scratching

Analysis of AFM images (Fig. 2) shows that, irrespective of the hardness and other properties of all materials, their polishing with UDDs (or NDs) occurs with the formation of nanoscratches, whose width, as well as σ, decreases with decreasing diamond particle size: for W, l = 1.7–3 μm for 1/0 micropowder, l = 2.2 μm for UDD–CTB, and l = 0.15 μm for Sn-1.4 and for CaF_2, l = 1.8 μm for 1/0 micropowder, l = 0.5 μm for 0.25/0 micropowder, and l = 0.1 μm for Sn-1.4. The rounded shape of the scratch edges and narrow gaps between them [see Ge (Sn-1.4 suspension); KU-1, LNO, GGG, and ZOY (pdd suspension)] as compared to their shapes after polishing with a diamond micropowder of grade 1/0 indicates that their formation is accompanied by pushing of the material along its surface (tangentially). The fact that l is significantly larger than the particle size for polishing with Sn-1.4 and

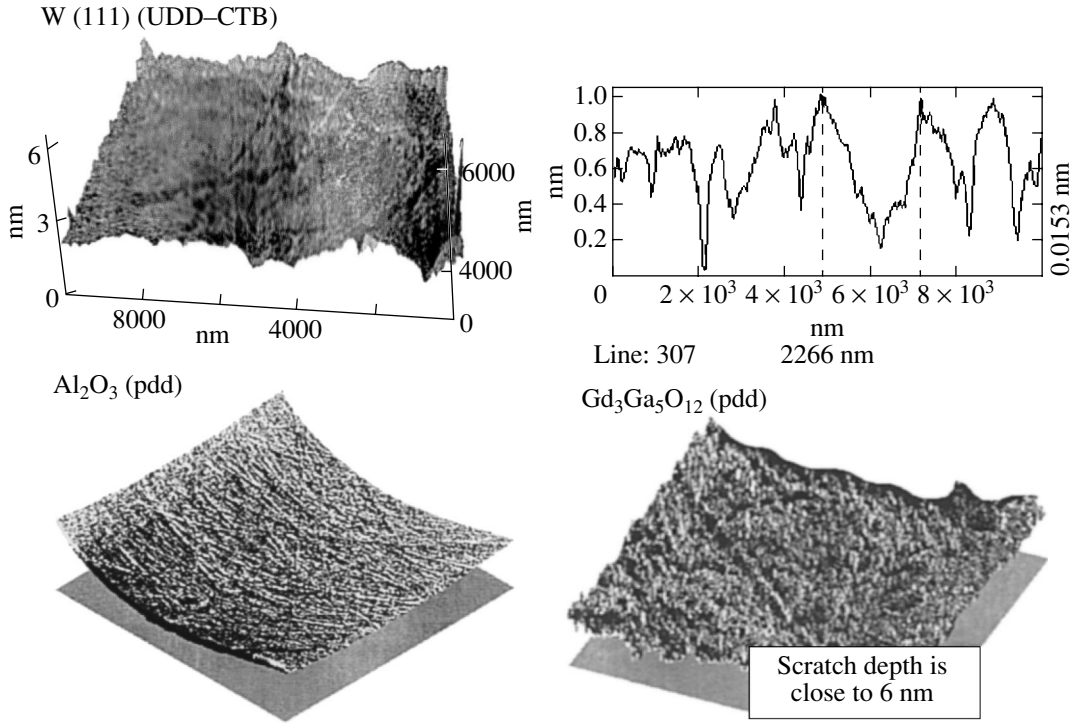

Fig. 1. Polishing of the surfaces of materials with nanodiamond suspensions.

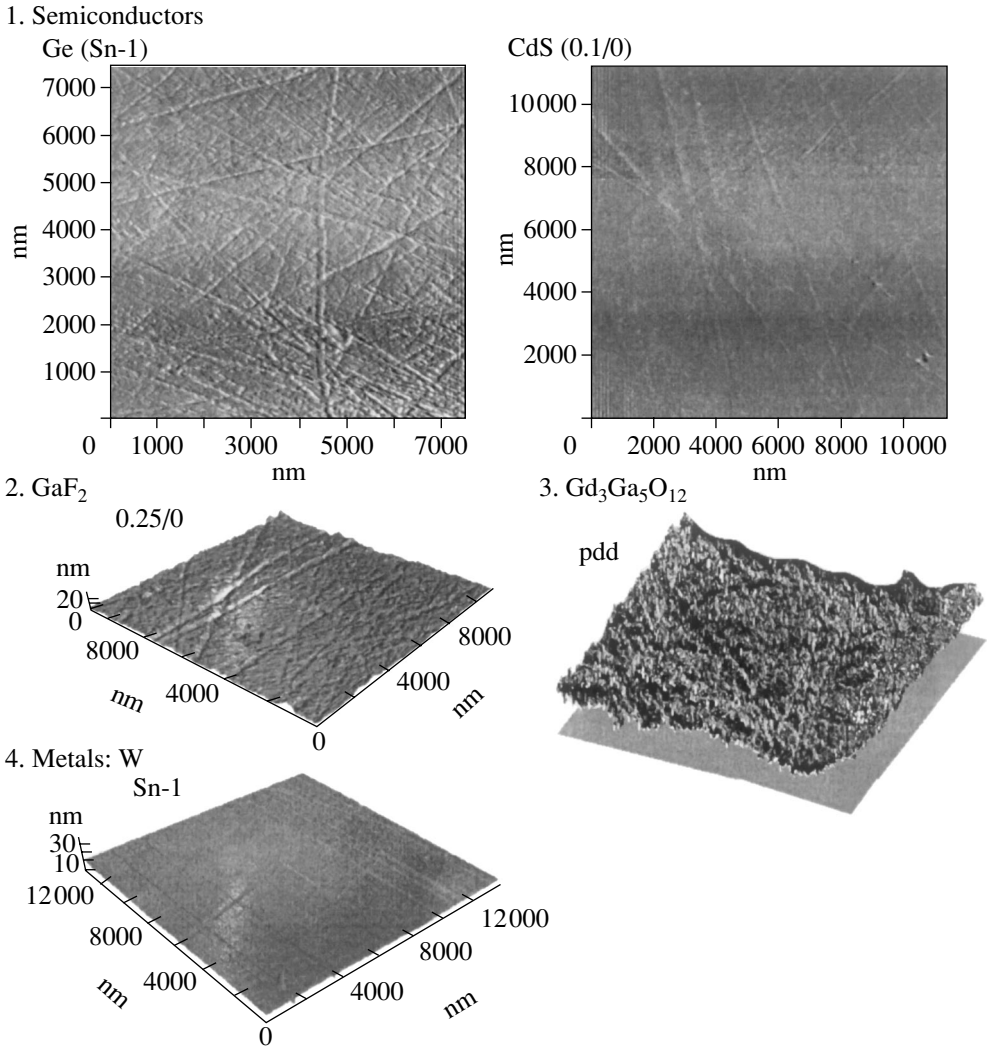

Fig. 2. Surfaces of materials with nanoscratches after polishing with neutral ND suspensions.

UDD–CTB suspensions indicates that the relief (σ, h_{max}) forms under the action of both the primary particles and their aggregates. The ratio of these two parameters is slightly different for different materials and compositions. For the processing of Ge, CdS, STO, and other materials with 0.1/0 suspensions, the values of l correlate with the average sizes of the particles and their aggregates; the values of h_{max} do not exceed 20 nm, and the values of σ are several nanometers. In the case of pdd, where the size of aggregates sintered from initial nanoparticles is 1–3 μm, analogous features are detected: l varies from several tenths of a micrometer to several micrometers and σ varies from several tens of nanometers to several nanometers. Hence, the removal of micro- and nanoscratches produced by polishing with UDDs and the simultaneous formation of nanoroughness occur mainly through the action of primary particles and the decomposition of their aggregates into individual particles. In the dynamic process of failure on this scale, nanoscale wear debris should correspond to nanoroughness [5].

3.3. Plastic Flow

After having been polished with submicron and nanodiamond suspensions [(100) ZnSe (0.25/0 micropowder), CdS and STO (0.1/0 micropowder), ZOY (pdd suspension), Ge (Sn-1.4 suspension)], the surfaces have rounded hillocks and flat regions separated by gentle valleys or curved lines (Fig. 3), whose profiles have no characteristic sharp asperity fluctuations; rather, they are similar to submicron-wavelength waves with h_{max} varying from several nanometers to several tens of nanometers and with σ varying from several tenths of a nanometer to several nanometers (Fig. 3). The scratches retained, e.g., on Ge have rather gentle edges and consist of adjoined hillocks, whose flat regions have $\sigma \ll 1$ nm.

The observed specific features of the relief can be explained by the plastic flow of surface layers in crystals, which is caused by high local temperatures and results, because of poor heat removal from contact zones, in heating of large regions. This hypothesis is

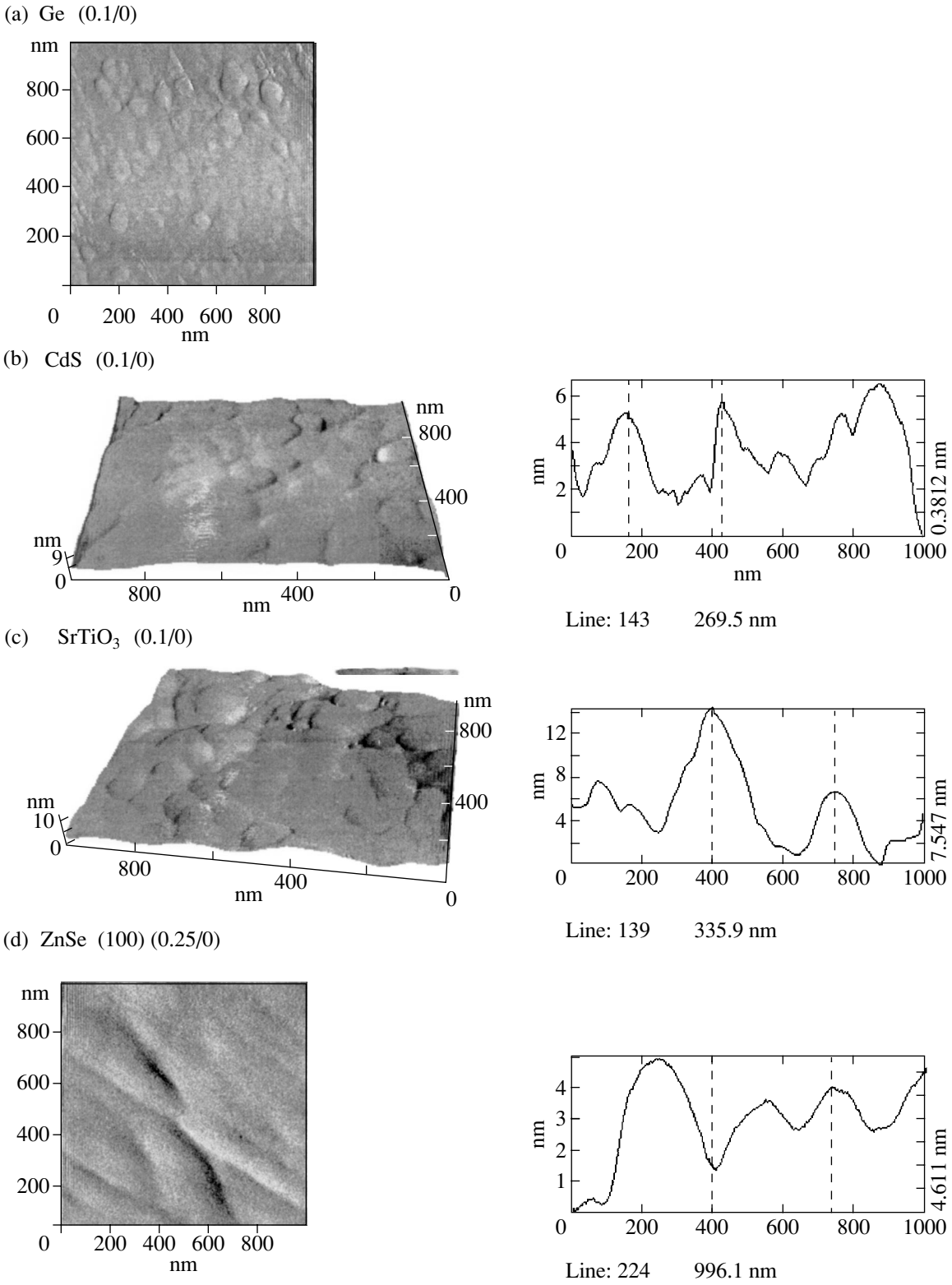

Fig. 3. Plastic flow of the surfaces of materials polished with UDD suspensions.

based on the conclusions drawn in [6], where it was established that dislocations form during microscopic abrasive polishing. In this case, the local temperatures are as high as the threshold value for plasticity, which is about 500°C for Ge and 700°C for Si. According to [7–9], the process of polishing of Si with abrasive particles 0.25–0.8 μm in size or smaller is not accompanied by brittle fracture with allowance for fracture

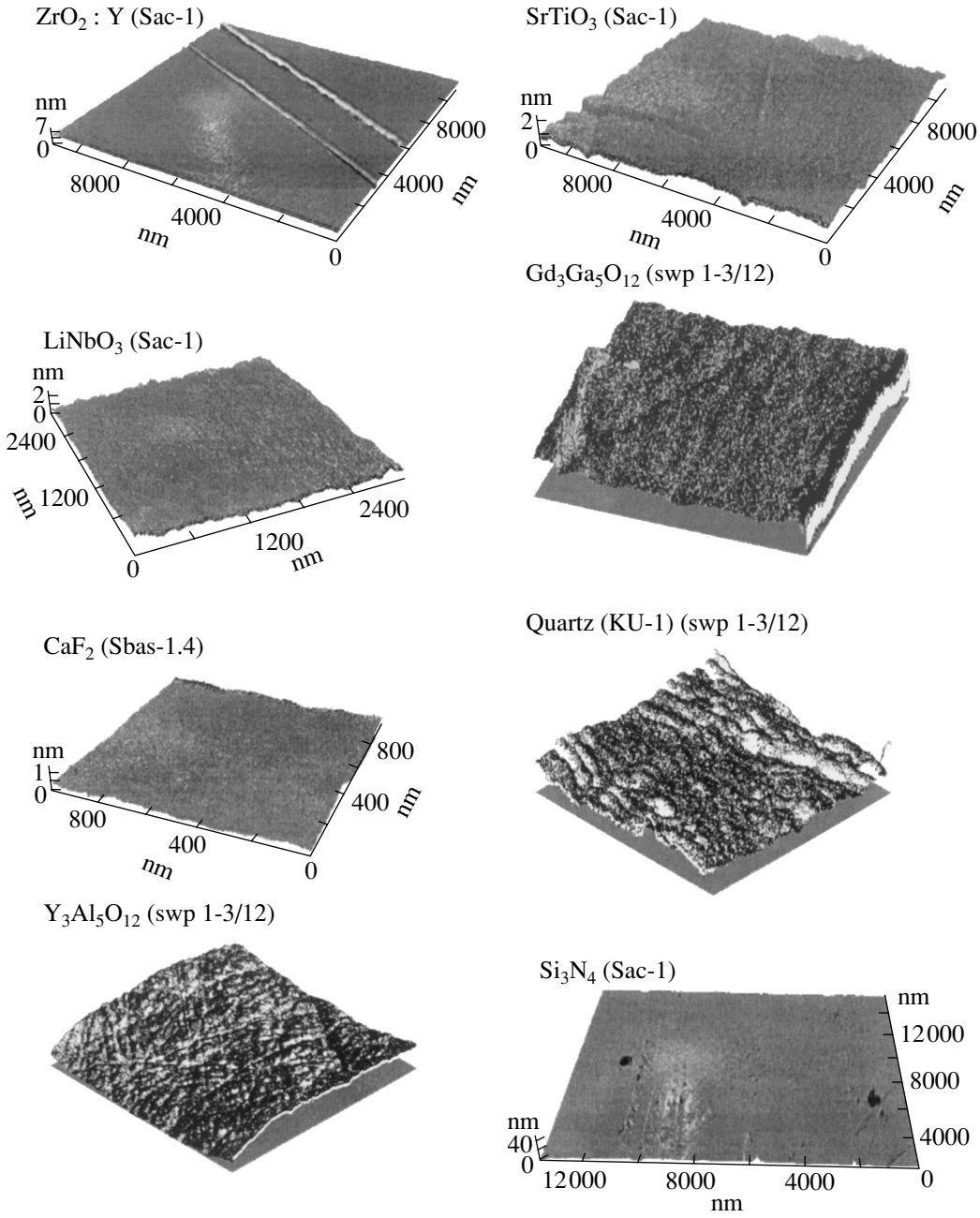

Fig. 4. Chemical–mechanical polishing of materials subjected to polishing with chemically active ND suspensions.

anisotropy. In other words, this processing creates structural (linear) defects in a surface layer and the spherical shape of the particles favors their elastic contact with the surface. Therefore, the factors that can decrease the roughness of treated surfaces and suppress the formation of subsurface structural defects are as follows: appropriate combination of the particle size (nanoparticles) and shape (spherical particles), conditions of particle motion across a surface which control the friction in a contact zone (technological regimes, polisher types), and an increase in the importance of liquid friction and the simultaneous removal of macroscopic and linear defects formed (chemically active aqueous suspensions with a certain ND concentration).

3.4. Chemical–Mechanical Polishing

Figure 4 shows the surfaces of some materials subjected to the action of chemically active ND suspensions. It is seen that, here, σ is significantly smaller than in the case of mechanical polishing with neutral suspensions of the same ND concentration. The effect of polishing depends on the material: it is virtually identical to CMP with amorphous silica for CaF_2, LNO, and

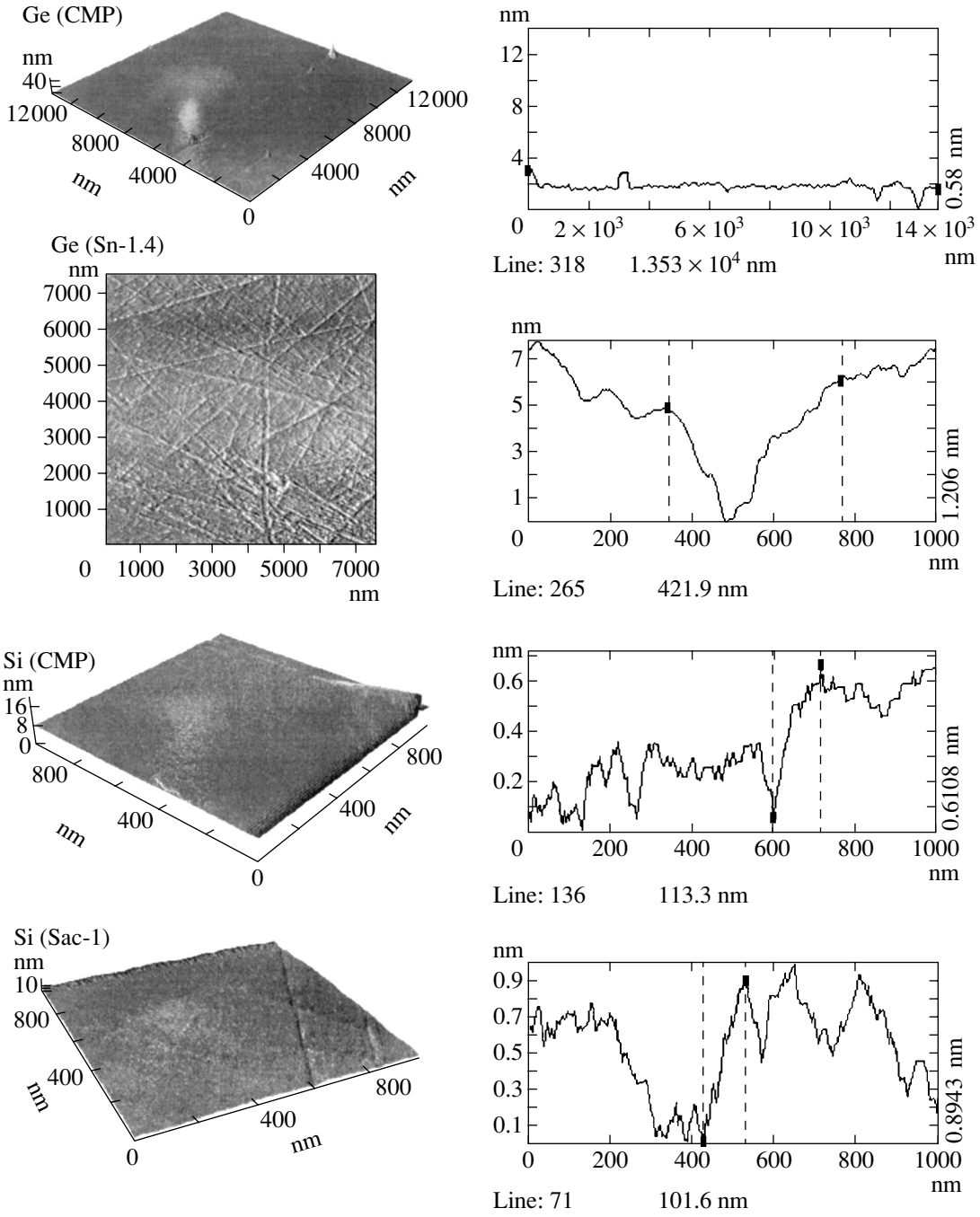

Fig. 5. Effect of the aggregative state of solid nanoparticles on the surface relief and structure of Ge and Si.

Si_3N_4 and is similar to chemical–mechanical polishing with a predominant mechanical component (YAG, GGG, and KU-1). Large scratches produced by ND particles on the surfaces are difficult to remove (STO, ZOY), and their removal is accompanied by the appearance of new scratches. Indeed, the activation of ND (UDD) suspensions with the corresponding chemical etchants changes the character of the effect from mechanical to chemical–mechanical under the MP conditions, i.e., at high flow rates, nonlaminar flows, and fixed or movable solid particles. Naturally, the particles should have the same size (i.e., they should be graded in size) and their concentration in the working zone should be uniform over the entire sample area and be

time-independent at each local point (sedimentation stability of suspensions). In this case, chemical–mechanical processes cause an increase in the specific surface of the material (the average roughness decreases further, and its uniformity over the area increases); a decrease in the surface roughness to nano-sized mechanical and chemical products of wear and an increasing fraction of elastic deformation due to the dissolution of the structural defects formed intensify the process and, what is more important, decrease the temperature required for chemical dissolution (ZOY, LNO, SiC, α-Al_2O_3).

3.5. Effect of the Aggregative State of Solid Particles

The results obtained allow us to answer one of the main questions in modern polishing: What is more important in producing a perfect surface (Fig. 5), the size of the solid particles or their aggregative state (nanocrystalline or amorphous)? From the geometrical standpoint, there is no significant difference in the absolute value of y between the two processes to be compared, although the number of relatively deep nanoscratches and the nonuniformity of y over the area in the case of using even stable ND suspensions are slightly larger than in the case of colloid–chemical polishing with amorphous spherical particles. From the structural standpoint, conclusions are obvious only for the processes of nano- and microscratching (characterized by the values of h_{max} and l); the structure of a thin surface layer after polishing with NDs needs to be studied using modern experimental techniques. However, based on the results of nanoindentation reported in [10], we can assume that the contribution from the dislocation mechanisms to the processes of mass transfer decreases (especially in the early stages of nanoindentation) and the contribution from the vacancy–interstitial mechanism increases as the load applied to an indenter decreases to 10 μN, which corresponds to a decrease in the size of diamond particles to 10 nm (Sn-1.4, Sbas-1.4, Sac-1); such particles create 100-nm indentations in Si. The study of these processes by using a device combining AFM and nanoindentation will allow one to gain a better understanding of the shape formation in the surface layers of various materials upon polishing with nanodiamonds. However, it is certain that, unlike polishing with ND suspensions, CMP with amorphous particles of the same size does not introduce macroscopic defects (scratches) and dislocations into the surface layer.

CONCLUSIONS

Thus, we can formulate requirements for UDDs to be applied in the process of polishing:

(1) UDD particles must be carefully graded in size, e.g., up to 10 nm, 10–50 nm, etc., after an experimental check in the process of polishing;

(2) to create polishing compositions, it is better to store UDDs in the form of aqueous suspensions;

(3) the surface and bulk physicochemical properties of UDDs must be reproducible from batch to batch;

(4) to avoid surface contamination, UDDs must have no chemical impurities according to the technical specifications of microelectronics;

(5) the cost of UDDs must be comparable to that of diamond micropowders and pastes synthesized under static conditions.

Apart from the materials under study, polishing with ND suspensions is promising for other solids, e.g., in silicon microelectronics (for planarization, etc.), optoelectronics, acoustoelectronics, HTSC electronics (preparation of wafers for single- and bicrystals, etc.), laser engineering (fabrication of laser cavities), optics (germanium IR optics, etc.), precision engineering (high-precision metal working), and many other modern industries.

The economic benefits of NDs are based on the lower cost of their production as compared to that of synthetic microdiamonds and on the increase in their output to several tons a year.

REFERENCES

1. T. M. Gubarevich and V. Yu. Dolmatov, Zh. Prikl. Khim. (St. Petersburg) **66** (8), 1878 (1993).
2. V. Yu. Dolmatov, Usp. Khim. **70** (7), 687 (2001).
3. T. M. Gubarevich and V. Yu. Dolmatov, RF Patent No. 2,082,738, Byull. Izobret., No. 18, 141 (1997).
4. A. A. Zakharov, V. A. Yuzova, and N. V. Éristova, *Ultradisperse Materials: Production and Properties* (Krasnoyarsk, 1990).
5. L. S. Tsesnek, Yu. I. Kogan, E. M. Fetisova, and L. A. Bibikova, Opt. Mekh. Prom., No. 12, 32 (1982).
6. J. Jda, Seimitsu Kikai **29** (6), 444 (1963).
7. R. Stickler and Y. R. Booker, Philos. Mag. **8** (89), 859 (1963).
8. R. Stickler and Y. R. Booker, J. Electrochem. Soc. **111** (4), 485 (1964).
9. A. S. Artemov, S. I. Bulychev, V. P. Alekhin, and M. Kh. Shorshorov, in *Proceedings of V All-Union Symposium on Mechanoemission and Mechanochemistry of Solids* (Tallin, 1975).
10. Yu. I. Golovin and A. I. Tyurin, Pis'ma Zh. Éksp. Teor. Fiz. **60** (10), 722 (1994) [JETP Lett. **60**, 742 (1994)].

Translated by K. Shakhlevich

Physics of the Solid State, Vol. 46, No. 4, 2004, pp. 696–702. From Fizika Tverdogo Tela, Vol. 46, No. 4, 2004, pp. 679–684.

APPLICATIONS OF NANODIAMONDS

Nanodiamonds in Magnetic Recording System Technologies[1]

V. I. Kurmashev*, Y. V. Timoshkov, T. I. Orehovskaja**, and V. Y. Timoshkov*****

** Minsk Institute of Management, Minsk, Belarus*

*** Belarus State University of Informatics and Radioelectronics, Minsk, Belarus*

**** PLASMOTEG Engineering Center, National Academy of Sciences of Belarus, Minsk, Belarus*

e-mail: pec@mserv.bas-net.by

Abstract—Features of the codeposition process of Ni, Ni–Fe, Co–P, Co–Fe–P, Ni–P, Ni, and Cu matrices with ultradispersed diamond particles from a sulfate, chloride, acetate, glycine, citrate, and sulfamate baths were investigated in view of applications in magnetic recording systems. The cation and anion surfactants were used to study the liophobic colloid systems and the behavior of ultrafine particles, to prevent agglomeration and sedimentation, and to control particle incorporation into the metal matrix. The mechanical properties of composite films were described from the point of view of applications in high-tech devices. It was determined that wear resistance increased by 2–2.5 times, the microhardness increased by 2 times, and the coefficient of friction and corrosion current decreased by a factor 1.5 and 1.6, respectively. The application of nanodiamond particles in the technology of composite functional layers of hard disks, magnetic heads, micromotors, and micromechanical components makes it possible to considerably increase the reliability of storage information systems.

1. INTRODUCTION

The problems of static and dynamic friction, as well as wear of functional layers, are fundamental for high-tech devices and magnetic recording systems, in particular, for magnetic hard disks, heads, micromotors, and micromechanical systems of positioning. This is connected with the increasing requirements of record density (longitudinal and track), the decrease in bit dimensions, and the minimization of displacements and errors [1].

One of the approaches to solving the problem of friction and wear of mechanically moving elements of micron dimensions for high-tech devices is the use of composite materials, in particular, codeposited metal and alloy with inert hard particles by electrolysis or electrochemical processes [2–5]. The methods of electrochemical synthesis of magnetic films for magnetic recording systems have been well known since 1960s [6]. From this period, the method was considered to be competitive with vacuum methods of film deposition. The same situation took place in the mentioned period related to hybrid and silicon ICs. However, finally, it became obvious for both cases that every method should be considered from the viewpoint of concrete fields of application. At present, electrochemical methods, due to their obvious advantages, allow for fabrication of magnetic films not only in the traditional fields of application (magnetic tapes, disks, heads). One of the most exciting applications of the electrodeposition methods is the microelectromechanical system, which has tremendous future potential. Micromotors have already been created and used in storage devices for precise positioning of magnetic heads. Indeed, the peculiarities of the electrodeposition process make it possible to fabricate high-quality 3D structures (LIGA process) [7].

The aim of the present work is to carry out integrated research into the technology and application of composite soft and hard magnetic films, as well as composite conducting films with inclusion of nanodiamond particles.

2. EXPERIMENTAL DETAILS

The electrodeposition of composite coatings containing ultrafine diamond particles was performed from sulfate, glycine, acetic, and Watts baths. Soft magnetic (NiFe, CoFeP, CoP) and hard magnetic (CoNiP, CoW, CoP) alloys, as well as the conductive matrix of Cu and Ni, were investigated. The influence of the ampholyte (pyridine carboxylic acid, aminoacetic acid), cation-active (monoethanol amide) and anion-active (CTAC, SLS), was estimated. The concentration of ultrafine diamond particles was varied from 0 to 20 g/dm^3 (dry substance). Nanodiamond particles were obtained by a detonation process [8].

The amount of codeposited ultrafine diamond particles was determined both by integral Coulombmetric analysis with the express analyzer AH-7529 (USSR) and by local Auger spectroscopy on a PHI-660 (Perkin Elmer Corp., USA). The Vickers microhardness of coating was measured at a load of 0.5 N with a

[1] This article was submitted by the authors in English.

1063-7834/04/4604-0696$26.00 © 2004 MAIK "Nauka/Interperiodica"

MICROMET-II (Buehler-Met, CH). The structure of the deposits was examined by TEM (EM-125, USSR). The coefficient of friction and the wear were evaluated using a FRETTING II test machine (KU Leuven, BE) [9]. A ball-on-flat geometry was used for the low amplitude oscillating sliding wear tests. Corundum balls 10 nm in diameter (Ceratec, Nl) were loaded on top of the vibrating surface of samples with a constant normal force of 2 N. Displacement strokes of 100 and 500 μm were used at frequencies of 8 and 2 Hz, respectively. The tests were performed in ambient air at 20°C and a relative humidity of 50%. Wear volumes were estimated by RM600 laser profilometry (Rodenstok, D) after 100 000 fretting cycles.

3. RESULTS AND DISCUSSION

In general, during the electrolytic codeposition, the suspended diamond particles interact with the surface of the growing film due to hydrodynamic, molecular, and electrostatic forces [9]. This complex process results in the formation of composite coatings. Auger profiles and local x-ray analysis demonstrate that ultrafine diamond particles are effectively incorporated into the metal matrix (Fig. 1).

Visually, the composite coatings are gray. Pitting was not noticed on the surface. A structural investigation shows (Fig. 2) that pure Ni coatings contain twins, dislocation aggregates inside the grains, and a concentration of solitary dislocations and dislocation walls 20 nm thick along the grain boundaries. The average grain size is about 500 nm. For composite coatings, the grain size reduces up to 30–100 nm. An accumulation of ball-type dislocations along the grain boundaries takes place. Thus, for the first time, it was determined that, during codeposition of matrix and nanodiamond particles, nanocrystalline Ni electrodeposits were formed. The electron diffraction patterns of the coating confirm the presence of cubic carbon according to ASTM 6-675, which indicates the incorporation of diamond particles into the nickel matrix.

Based on the experimental data [5], the qualitative codeposition model of the composite coatings with ultrafine particles is proposed. The specific characteristics of the behavior of the ultrafine particles are considered in the model. The model worked out is based on the assumption that the codeposition of ultrafine particles proceeds through the following stages (Fig. 3):

(1) coagulation of ultrafine particles in the plating solution;

(2) formation of quasistable aggregates and, therefore, a change in the system dispersion constitution;

(3) transport of the aggregates to the cathode surface by convection, migration, and diffusion;

(4) disintegration of the aggregates in the near-cathode surface;

(5) weak adsorption of ultrafine particles and aggregate fragments onto the cathode surface;

(6) strong adsorption of spersion fraction (embedment).

Hydrophobic colloidal systems are thermodynamically unstable due to the surplus surface energy. They exist owing to stabilization by protective ionic and molecular layers. In general, in the bulk suspension, the particles encounter one another due to Brownian motion, gravity, and convection. The forces between them determine whether the encounters result in the particles sticking together or remaining free.

The behavior of dispersed systems is described by the DLVO theory. The stability or coagulation rate of suspensions depends on the sign and magnitude of the overall potential energy of interaction between the particles. The positive electrostatic repulsion energy $U_r(h)$ decreases by an exponential law, whereas negative molecular attraction energy $U_a(h)$ is in inverse proportion to squared distance. As a result, at small distances ($h \longrightarrow 0$, $U_r(h) \longrightarrow$ const, $U_a(h) \longrightarrow -\infty$) and large distances (the exponent diminishes much more rapidly than the power function), the attraction energy between the particles prevails. The electrostatic repulsion energy prevails at intermediate distances. The primary minimum *1* corresponds to direct sticking of particles. In this case, the particles are irreversibly stuck (coalescence). The secondary minimum *2* corresponds to attraction through an interlayer of the environment. In this case, the aggregates may be counteracted relatively easily. The maximum corresponding to intermediate distances characterizes the potential barrier which prevents sticking of the particles. Forces of interaction are extended for hundreds of nanometers.

In the consideration of interaction between the particles, the following conclusions from the DLVO theory should also be mentioned. The height of the energy maximum and the depth of the primary and secondary maxima depend on the parameters of the systems, namely, the zeta potential, particle size, electrolyte concentration (and valence), and the Hamaker constant. At low electrolyte concentrations, the energy maximum may reach high values; this prevents particle aggregation. With an increase in the electrolyte concentration, the height of the energy maximum decreases and disappears at a critical concentration (which depends on the valence of the electrolyte). The coagulation becomes more rapid. Thus, to enhance the stability of the suspension, one needs to reduce the electrolyte concentration and increase the zeta potential.

The transport of the particles toward the cathode surface occurs by convection, migration, diffusion, and Brownian motion.

Migration is the movement of cations, anions, or charged particles through the solution under the influence of an applied potential between the electrodes in the solution. Diffusion is the second process. Electrode reaction depletes the concentration of the oxidant or reluctant at the electrode surface and produces a concentration gradient there. This gives rise to the move-

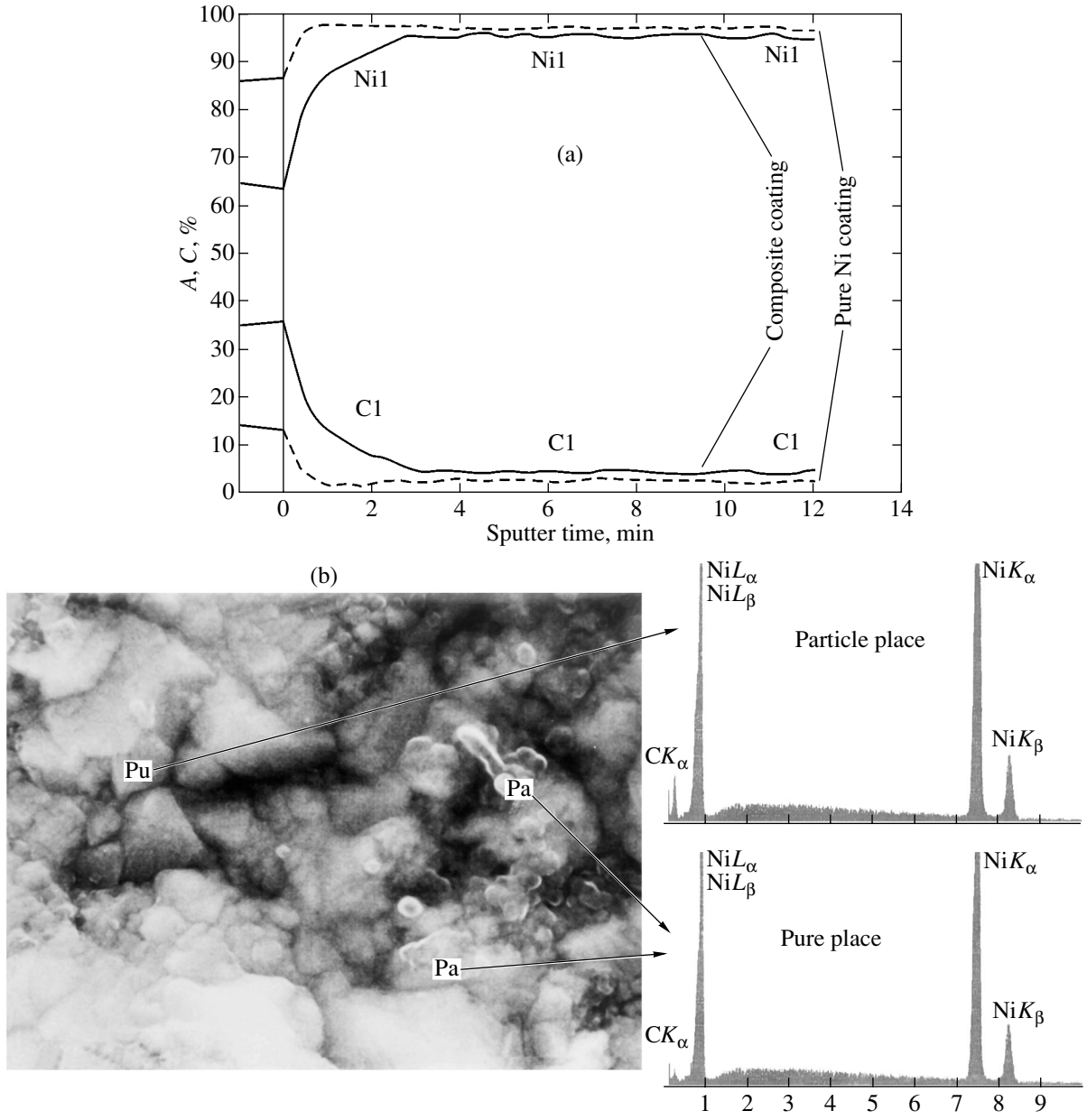

Fig. 1. (a) AES sputter-etch elemental profiles and (b) local x-ray analysis of pure and composite Ni coatings containing nanodiamond particles.

ment of species from the higher to lower concentration. Unlike migration, which only occurs for charged particles, diffusion occurs for both charged and uncharged particles. Convection includes thermal and stirring effects, which can arise extraneously through vibration, shock, and other types of stirring and temperature gradients. At last, Brownian motion, as is known, is strongly affected by the particle size and may be neglected in the case where the particle size is above 1 μm.

The stirring mode is required to be the transition mode between the turbulent flow and the laminar flow in the bulk of the plating bath. Such a mode is of great practical significance, because laminar flow does not provide sufficient stirring of the electrolyte suspension. Alternatively, at a stirring rate corresponding to the turbulent mode, conditions that totally prevent particle embedment appear.

In the near-cathode region, the aggregate is influenced by forces of different nature and direction. The motion of the aggregate is determined by the resultant force, and the integrity of the aggregate, by the sum of the force values. For the investigated system, the following forces are considered:

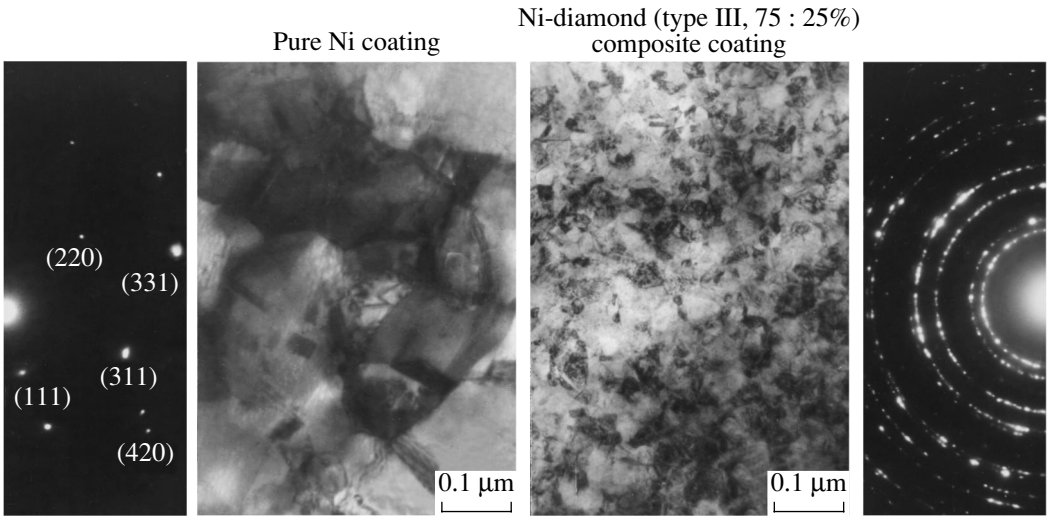

Fig. 2. TEM micrographs of pure and nanocrystalline composite Ni coatings [5].

(1) mechanical forces associated with interaction with the fluid flow and other particles, gravity, and buoyancy;

(2) electrical forces connected with the electric field presents in the plating solution during the electrodeposition process;

(3) molecular forces acting on the particle in the vicinity of the cathode surface.

Mechanical forces. The law of viscous friction is followed in the region of laminar liquid flow in the boundary hydrodynamic layer, and the boundary conditions are $V = 0$ at $y = 0$ and $V = V_0$ at $y = \infty$.

If the particle moves in a flow having a transverse velocity gradient of liquid movement, rotational motion can be imparted to the particle because different velocities of the flow pass the particle from the top and from the bottom. The transverse particle migration appears as the result of the rotational motion. The transverse particle migration results from a pressure drop on the side where the sum of the tangential velocity components of flowing past and rotating the particle reaches a maximum. The transverse particle migration is always directed toward this maximum. In the case under consideration, the particle moves away from the cathode surface.

When the particle is trapped by the cathode, the longitudinal force by the flow of the plating solution affects the particle. If this force exceeds the friction force keeping the particle on the cathode surface, the particle will detach from the growing deposit.

Besides the forces connected to interaction between the particle and hydrodynamic flow, the gravity and buoyancy contribute to the particle motion. The sum of the forces of gravity and buoyancy results in the sedimentation force.

Collisions between the particles in the near-cathode region may change the particle trajectory promoting or preventing movement of the particle to the cathode. Moreover, the particle in the electrolyte may collide with the particle trapped by the cathode and prevent embedment.

Electric forces. The ions in the double layer around the particle interact with the electric field in the plating solution. This results in particle motion along the lines

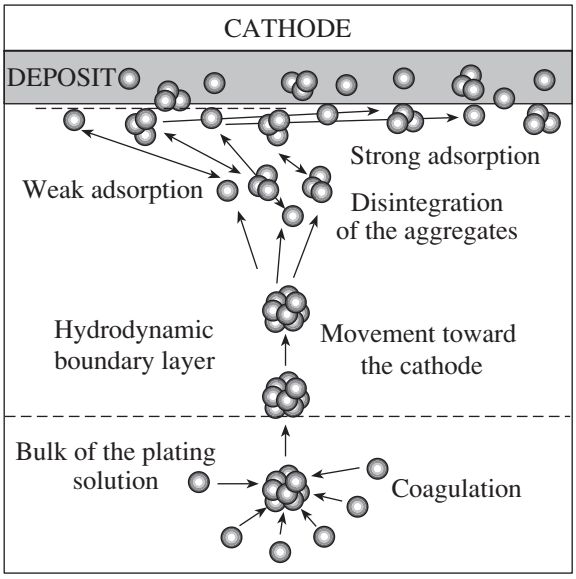

Fig. 3. Mechanism of codeposition of a metal matrix and nanodiamond particles.

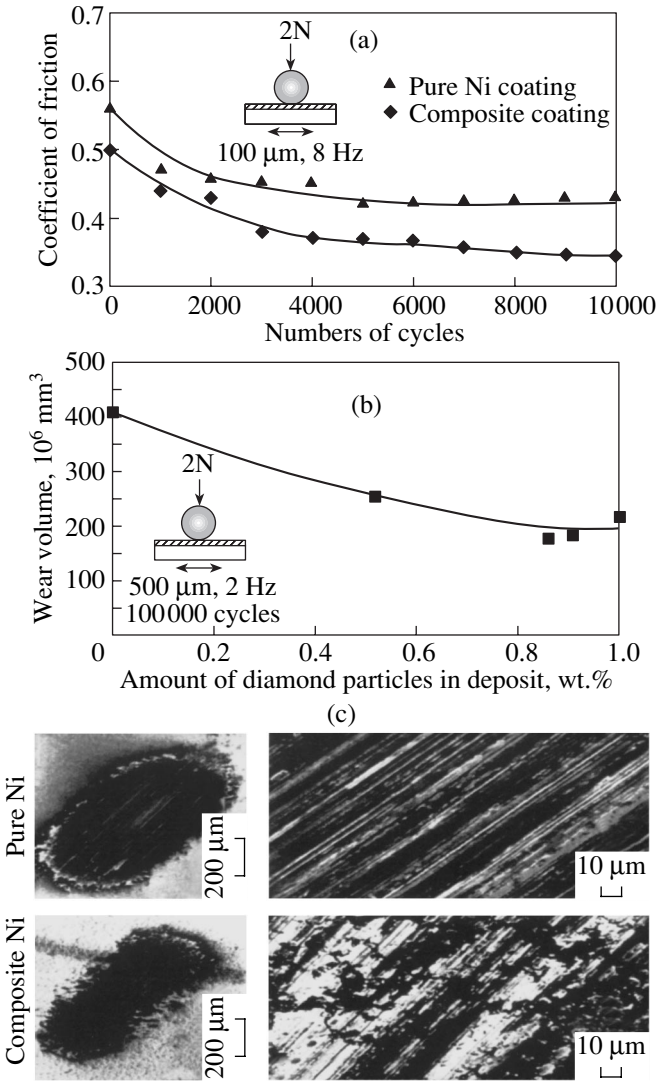

Fig. 4. Physicomechanical properties of the composite coatings: (a) coefficient of friction, (b) wear volume, and (c) SEM images of wear scars after 100 000 fretting cycles.

of the electric field. The motion is affected by the fluid permittivity, particle size, intensity of the electric field in the place where the particle is located, and the zeta potential. The sign and value of the zeta potential are determined by both the particle nature and the constitution of the electrolyte and can be changed through the addition of surfactants to the plating solution. In the near-cathode region, the cathode itself ambiguously affects the electrophoretic particle motion. On the one hand, modification of the electric-field lines in the near-cathode region slows the particle movement, and, on the other hand, the cathode surface itself increases the intensity of the electrophoretic movement. It should be emphasized that this is not a possible measurement of the zeta potential in the near-cathode region because it depends on many factors and can change not only the value but also the sign. Therefore, it is difficult to evaluate the contribution of electrophoretic particle motion to the codeposition process.

In the near-cathode region, the osmotic pressure of the electrolyte affects the particle motion. Electroosmotic motion is the phenomenon of liquid movement through a porous body under the application of an electric field. Assuming the particles in the near-cathode region to be porous bodies, the ionic species moves through this "body" due to the electric field in the plating solution. In turn, the ion flow exerts pressure on the particles and assists particle movement toward the cathode surface. It should be mentioned that the electroosmotic motion of particle is influenced by the same parameters as for electrophoretic motion (see above).

Molecular forces. In the immediate vicinity of the cathode surface, the van der Waals attractive force appears; it occurs with all types atoms or molecules and arises from the charge fluctuations within an atom or molecule associated with the motion of its electrons.

A strong repulsive force appears at short distances, when the electrolyte concentration exceeds a certain value. This force is called the structural or hydration force. It originates from the thin solvent layer being present near the interfaces. This solvent layer is ordered by the hydration of cations adsorbed on the surfaces as the interfaces approach each other. The hydration force results from a change in the structure of the solvent between the interfaces and prevents the interfaces from closely approaching each other.

As the particle aggregate approaches the near-cathode region, the force field increases. If these forces exceed a certain critical value keeping the particles in the aggregated state, the aggregates will disintegrate. Further, single particles and the aggregate chips interact with the cathode and can be adsorbed weakly onto the cathode. The weak adsorption step assumes interaction between the particle and cathode surface through adsorbed layers of ions and solvent molecules. Further, the electric field helps to uncover the particle. The thin interlayer between the cathode surface and particle disappears. This leads to strong field-assisted adsorption, and the particle is overgrown with the deposit.

In terms of functionality, the most important properties are friction and wear resistance. For composite systems, the mechanical properties are determined by the phase composition of the materials, i.e., by the matrix-to-particle ratio. The dependence of the amount of codeposited diamond particles on particle concentration in the plating bath shows that the investigated system may be described by Guglielmi's model [10]. The evolution of the coefficient of friction is shown in Fig. 4. Among the coatings tested, composite nickel coatings containing ultrafine diamond particles show a lower coefficient of friction. The wear volume for pure Ni and composite coatings is shown for fretting tests performed with 100 000 cycles. The amount of particles in the coatings affects the wear rate. The friction behav-

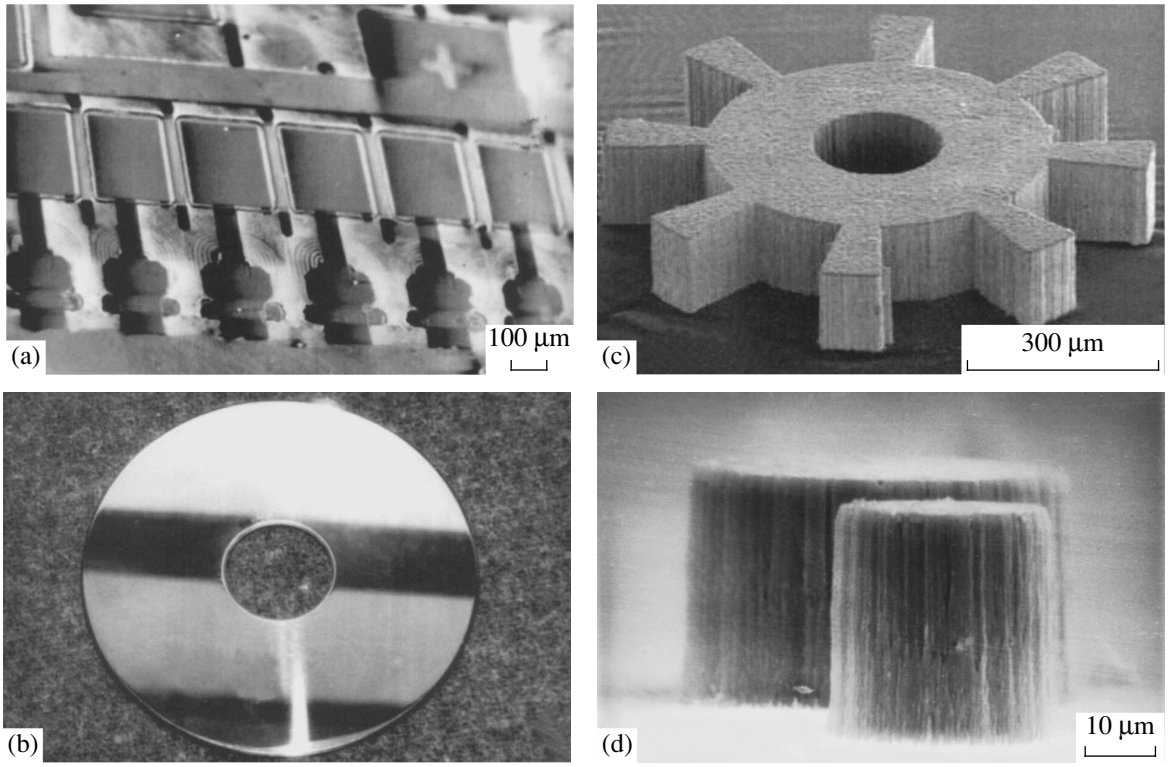

Fig. 5. Some applications of nanodiamonds in magnetic recording systems: (a) thin film magnetic heads, (b) hard disk, and (c, d) MEMS elements [11].

ior of multiphase materials has been described in the literature. The main problem with these approaches is that they are static and apply to ideal surfaces because, during wear of a multiphase material, the topography changes continuously in practice. Localized wear of the matrix takes place in the first phase. After that, the particles become more loaded. This dynamic process may lead to an increased wear resistance of composite materials. Of course, the fretting wear properties of coatings are also influenced by the size, shape, and distribution of the reinforcing phase.

Some composite elements of magnetic recording systems are shown in Fig. 5.

4. CONCLUSIONS

This investigation into composite coatings containing nanodiamond particles has led to the following scientific results and common conclusions.

(1) The grain size of electrolytic nickel coatings is affected by the codeposition of ultrafine diamond particles. Nanocrystalline Ni deposits may be formed by the codeposition of ultrafine diamond particles.

(2) The microhardness of the composite coatings increases up to 420 kg/mm^3 (250 for pure metal).

(3) The embedment of ultrafine diamond particles results in both a decrease in the coefficient of friction from 0.43 to 0.33 and an increase in the wear resistance by a factor of 2.

(4) Composite films with the nanodiamond particles obtained may be applied for components of magnetic recording devices and elements of microelectromechanical systems.

(5) The tribology problem (friction, wear, lubrication) for high-tech devices, in general, and for magnetic recording systems, in particular, is a fundamental problem. In the future, the place of micro- and nanotribology will become more important. The tribology problem for high-tech devices can be solved through joint efforts of scientists working in the field of nanodiamond manufacturing, device designs, and composite-coating technology.

(6) The application of composite electrochemical coatings and layers, in general, and nanodiamonds, in particular, solves the tribology problem. As for microelectromechanical systems, the application of composite coatings and layers is the only way.

(7) Particle incorporation of fine homogeneous sizes, compared with geometric limits, for mechanical high-tech devices is the key task for applying composite coatings in movable micromechanical systems.

REFERENCES

1. *Proceedings of 3rd International Conference on Tribology of Information Storage Devices* (Sendai, Japan, 2001).
2. Yu. V. Timoshkov, A. M. Giro, and V. A. Khomenok, in *Proceedings of Conference on State and Prospective of Microelectronics Development* (Minsk, 1985), p. 218.
3. V. I. Kurmashev, Yu. V. Timoshkov, T. I. Orekhovskaya, and P. M. Brylyakov, J. Magn. Soc. Jpn. **15** (52), 767 (1991).
4. Yu. V. Timoshkov, T. M. Gubarevich, I. S. Molchan, *et al.*, Surf. Mod. Technol. **11**, 991 (1998).
5. Yu. V. Timoshkov, T. M. Gubarevich, T. I. Orekhovskaya, *et al.*, Gal'vanotekh. Obrab. Poverkhn. **7** (2), 20 (1999).
6. Tetsuya Osaka and Takayuki Homma, Electrochem. Soc. Interface **4**, 42 (1995).
7. L. Romankiw, Plating and Surface Finishing (10 January 1997).
8. USSR Patent No. 1,694,710 (1991).
9. J. Fransaer, J.-P. Celis, and J.-R. Roos, J. Electrochem. Soc. **139**, 413 (1992).
10. N. Guglielmi, J. Electrochem. Soc. **119**, 1009 (1972).
11. Yu. V. Timoshkov, O. N. Kudanovich, T. I. Orekhovskaya, *et al.*, in *Proceedings of International Conference on Modern Means of Communication* (2002), News Belarus Eng. Acad. **2** (14/2), 14 (2002).

Physics of the Solid State, Vol. 46, No. 4, 2004, pp. 703–710. Translated from Fizika Tverdogo Tela, Vol. 46, No. 4, 2004, pp. 685–692.

APPLICATIONS OF NANODIAMONDS

Application of Ultrafine-Dispersed Diamonds in Electroplating

G. K. Burkat and V. Yu. Dolmatov

SKTB Tekhnolog, St. Petersburg State Technological Institute, St. Petersburg, 192076 Russia
e-mail: alcen@comset.net

Abstract—The results obtained upon the electrochemical deposition of composite coatings containing ultrafine-dispersed diamonds produced by detonation synthesis are generalized. The main advantages of such coatings over the well-known composite electrochemical coatings are revealed. © *2004 MAIK "Nauka/Interperiodica".*

1. INTRODUCTION

The life of most mechanisms, units, and friction pairs depends substantially on the time of retention of the surface operating properties of a mating pair. One of the well-known methods of improving the physical-mechanical properties of a surface is its galvanic (electrochemical) modification through the deposition of a metallic film having the necessary properties, such as high wear resistance, high corrosion resistance, and a uniform film thickness (which is ensured by the high throwing power of an electrolyte). However, modern engineering imposes more stringent requirements on friction pairs and ordinary metallic films of individual metals or their alloys often cannot satisfy them.

In the past few years, the next generation of electrodeposited coatings, namely, electrochemical composite coatings (ECCs), have aroused considerable interest [1, 2]. The introduction of hard disperse particles (oxides, nitrides, borides, carbides, classic diamonds) into electrochemical coatings is known to increase their microhardness and wear resistance. This effect is caused by a decrease in the crystallite (domain) sizes in a deposited metal and a large number of superhard particles in a coating. Particles deposited along with a metal serve as crystallization centers; therefore, the smaller the particles, the finer the structure of a coating. The microhardness (and the related wear resistance) increases in proportion to $d^{-0.5}$, where d is the crystallite size.

The number of deposited particles that serve as passive fillers reaches 40% of the weight of a deposited metal. Being hard or superhard materials, they increase the hardness and wear resistance of a coating to high levels. However, because of their high content in a coating and their dielectric properties, they strongly affect the electrophysical properties of the coating. Therefore, as a rule, such ECCs cannot be applied in electronics and electrical engineering. In machine building, such particles often cause high brittleness of coatings, thus decreasing their wear resistance. One of the disadvantages of such coatings is possible high wear of the other member of a friction pair, since most fillers are crystals whose cutting edges project from the codeposited metal.

Researchers have aimed at searching for new fillers that could substantially increase the wear resistance, microhardness, adhesion and cohesion, and corrosion resistance of films when their content in the films is low. Moreover, the basic electrophysical properties of these films must remain unchanged.

In the mid 1980s, researchers found that metals could be codeposited with nanodiamonds produced by detonation synthesis (ultrafine-dispersed diamonds (UDDs)) upon their chemical or electrochemical reduction from aqueous solutions [3–5].

Indeed, UDDs have a set of unique properties that distinguish them from both the well-known fillers and carbon materials. UDDs have ultrasmall sizes (4–6 nm), a shape close to ovular or spherical, an extremely large specific surface (up to 450 m^2), and a high surface energy. Moreover, their cutting edges do not project from the surface.

UDD particles have complex structure [6]: a 40-Å core of the classic cubic diamond and a carbon shell 4–10 Å thick around the core, which is made up of transition amorphous (according to x-ray diffraction data) carbon structures. This shell consists of sp^2-hybridized carbon atoms and has a nonuniform ordering of structural fragments. The surface layer, which contains heteroatoms in addition to carbon atoms, is saturated with numerous different functional groups, predominantly oxygen-containing groups. The nondiamond components of pure UDDs are inherent components rather than impurities and substantially determine their specific properties.

Because UDD particles are ultrasmall, the surface interphase interactions considerably increase in importance. The presence of highly polar and reactive groups

1063-7834/04/4604-0703$26.00

Table 1. Properties of chromium coatings

Coating	UDD content in an electrolyte, g/l	Wear resistance		Friction coefficient	Microhardness, kg/mm^2	Temperature in the friction zone, °C
		coating wear, μm	counterface wear, μm			
Chromium without a disperse phase	–	20.2	27.0	0.15	610	185
Chromium with statically synthesized diamonds (less than 0.5 μm)	15	5.6	47.0	0.24	790	170
Chromium with UDDs	2	8.9	29.0	0.14	710	165
	4	4.8	26.5	0.10	920	165
	10	2.9	25.4	0.09	1480	160
	16	2.0	24.0	0.09	2100	155
	20	5.3	30.4	0.13	1900	175
	50	7.7	27.2	0.14	1630	180

concentrated in a small volume at the surface specifies an active effect of UDD particles on the environment.

Contrary to ordinary highly disperse powder fillers, UDD particles are more likely to be a specific structure-forming material rather than a filler. During deposition, suspended UDD particles interact with the surface of a growing coating via hydrodynamic, electrostatic, and molecular forces. Using Auger and infrared spectroscopy, it has been found that UDD particles penetrate a deposited metallic film in the form of individual particles and, most often, as agglomerates.

A special modification of the surface of cleaned UDDs and their introduction into an electrolyte in the form of an aqueous suspension makes it possible to create stable, highly disperse suspensions even in strong electrolytes. UDDs can be in a suspended state due to gas release and thermal convection during the deposition of metal–diamond ECCs.

Since UDD particles are ultrasmall, they are sufficiently densely and uniformly distributed in a coating even when their content is very small (several tenths of a percent [7, 8]), as opposed to all well-known fillers [1, 2].

2. CHROMIUM PLATING

Originally, the electrochemical deposition of chromium with UDDs was developed [3, 4]. This process then provoked considerable interest, since chromium coatings were most often applied to provide high wear resistance for tools and parts. In the studies performed at that time, only the quality of the UDDs differed (as a rule, researchers were not aware of this fact) and, hence, the results varied greatly, ranging from positive to negative [9]. Nevertheless, chromium–diamond coatings have been commercially applied for many years (e.g., at the Élektrokhimpribor integrated industrial plant, Lesnoĭ).

For chromium plating with UDDs, electrolytes that are intended for solid-state chromium plating or self-regulating (buffer) electrolytes are used. The best results (high quality and a simple procedure) have been obtained in a classical electrolyte containing 250, 2.5, and 15–30 g/l of CrO_3, H_2SO_4, and UDDs, respectively. The UDD content in a coating is 0.3–1.0 wt %.

Table 1 gives the properties of chromium coatings having different disperse phases. Wear tests have been performed on a friction machine using the shoe–roller scheme with a drip feed of a low-viscosity oil.

Dolmatov *et al.* [10] studied the electrochemical deposition and quality of chromium–diamond ECCs with nanodiamonds of different nature, namely, UDDs produced at the SKTB Tekhnolog and diamonds of ASM 0.1/0 grade produced by static synthesis and milled to nanoparticles (crystal size of about 100 nm).

Experiments showed that the optimum amount of UDDs required for the maximum wear resistance was 15–20 g/l and that an increase in the UDD concentration to 50 g/l did not change the wear resistance.

A coating prepared from the standard electrolyte without additions loses 15% of its weight in a 20-h wear test on an LTI device; this characteristic for a coating with UDDs is 2–3%, and for a coating with diamonds of ASM 0.1/0 grade, 1–2%. However, the chromium coating containing ASM diamonds abrades the counterface 1.5–3.0 times faster than does the chromium coating with UDDs.

3. COPPER PLATING

The process of copper plating has been studied using a simple acid electrolyte consisting of two components: copper sulfate and sulphuric acid.

Polarization curves measured for an electrolyte containing 0.1–5.0 g/l UDDs showed that UDDs did not change the nature and mechanism of the electrode process. The step-by-step mechanism of copper discharg-

Table 2. Physical–mechanical properties of copper deposits

No.	Electrolyte composition	i, A/dm^2	Current efficiency, %	The number of pores per 1 cm^2	ρ, Ω mm^2/m × 10^3	Microhardness, kg/mm^2	Elasticity, %	Wear, %
1	$CuSO_4$ – 80 g/l	0.5	96.20	–	22.69	–	11.25	42.80
	H_2SO_4 – 100 g/l	0.7	96.60	30	21.89	76.00	10.00	65.80
		1.0	99.07	26	21.06	107.80	7.50	–
		1.2	97.44	24	24.20	110.00	5.00	–
2	In the presence of UDDs 0.1 g/l	0.5	–	–	–	–	–	11.40
		0.7	94.50	28	23.06	76.47	20.00	8.26
		1.0	97.13	18	20.93	79.91	17.50	–
		1.2	98.42	10	23.00	72.00	11.50	–
3	In the presence of UDDs 0.2 g/l	0.5	–	–	–	–	–	6.45
		0.7	98.60	18	20.03	77.70	17.50	7.08
		1.0	99.81	10	21.85	106.49	15.00	–
		1.2	99.07	6	28.83	108.50	7.50	–
4	In the presence of UDDs 0.5 g/l	0.5	–	–	–	–	–	7.50
		0.7	97.51	12	23.62	98.11	15.00	7.72
		1.0	100.51	6	21.39	113.60	14.50	–
		1.2	101.30	5	24.16	104.00	7.50	–
5	In the presence of UDDs 0.7 g/l	0.7	95.71	6	23.70	107.20	15.00	–
		1.0	100.70	5	21.63	124.60	10.00	–
		1.2	99.04	5	25.60	93.44	1.50	–
6	In the presence of UDDs 1.0 g/l	0.7	100.00	28	24.14	97.50	10.00	–
		1.0	101.40	5	22.12	142.30	8.75	–
		1.2	96.26	4	26.95	140.20	2.50	–
7	In the presence of UDDs 2.0 g/l	0.7	99.66	6	28.78	133.27	10.00	–
		1.0	100.00	3	25.73	151.20	7.50	–
		1.2	93.67	3	32.14	150.50	1.50	–
8	In the presence of UDDs 5.0 g/l	0.7	98.00	–	27.81	124.57	4.00	–
		1.0	99.00	–	25.30	153.57	5.00	–
		1.2	100.00	–	39.32	115.21	5.00	–

ing and the nature of the controlling step of polarization also did not change.

The more uniform distribution of a metal over the surface of an electrode characterizes the throwing power of the electrolyte. The throwing power of an electrolyte with UDDs was found to be substantially higher (by a factor of three) than that of the pure electrolyte.

One of the basic properties determining the quality and wear resistance of coatings is their porosity. As the amount of pores increases, the access for an electrolyte or gases to the base metal becomes easier and corrosion becomes more intense.

The application of UDDs significantly affects the porosity of copper coatings, which indicates that UDDs affect the structure and density of deposits adsorbing on the surface of an electrode. The introduction of UDDs into an electrolyte results in a decrease in the amount of pores from 10 cm^{-2} (0.1 g/l UDD) down to their complete disappearance (5.0 g/l UDD). When UDDs were introduced into an electrolyte, all samples were coated with a rainbow corrosion-resistant oxide film. No weight loss in the samples was detected during corrosion tests. The coating had a higher density, finer structure, and higher corrosion resistance as compared to the UDD-free coating.

The effect of the electrolysis conditions (current density) and electrolyte composition on the wear resistance of deposits (a 10-μm-thick copper coating) was studied. When UDDs are introduced into an electrolyte,

Table 3. Corrosion resistance (weight loss, mg/dm^2) of 6-μm coatings measured in a salt spray atmosphere in a climatic chamber (according to GOST (State Standard) 9.308-85); the coatings are deposited from an electrolyte containing 10 g/l ZnO, 100 g/l NaOH, 4 g/l organic additions, and 8 g/l UDDs

Hours	Unprotected steel	Pure Zn 7.5-μm coating (produced in Germany from a chloride electrolyte)	6-μm cadmium coating	Zn–UDD coating	Zn–UDD coating with chromate treatment	Phosphatized Zn–UDD coating
60	127	40	14	24	–	–
150					Corrosion begins at the edges of one of six samples	–
200					No corrosion in five samples	–
350						Corrosion begins at the edges of three of six samples

the wear resistance of deposited copper samples becomes smaller than that of the samples deposited from the pure electrolyte by a factor of 9 to 10.

As the concentration of the UDD addition increases to 5 g/l, the microhardness increases from 108 (deposition from the pure electrolyte) to 154 kg/mm^2.

The introduction of 0.1–1.0 g/l UDD increases the electrical resistivity by 5–10% at current densities of 0.7 and 1.2 A/dm^2; for UDD contents above 2 g/l, this increment is 25–31%.

Table 4. Physicochemical and electrotechnical properties of tin coatings deposited from a sulfuric-acid electrolyte containing 40 g/l $SnSO_4$, 60 g/l H_2SO_4, and 5 g/l OS-20 at 20°C as functions of the UDD content in the electrolyte and the current density

UDD concentration, g/l	Cathode current density, A/dm^2	Solder spreading coefficient	Electrical resistivity, Ω mm^2/m	Porosity, cm^{-2}
0	0.5	2.0	0.172	45
0	1.0	1.8	0.184	17
0	1.5	2.1	0.231	16
0	2.0	2.5	0.304	19
1.0	0.5	2.1	0.166	36
1.0	1.0	1.9	0.168	12
1.0	1.5	1.8	0.231	9
1.0	2.0	2.0	0.192	6
15	0.5	2.1	0.171	5
15	1.0	2.1	0.176	2
15	1.5	1.8	0.222	0
15	2.0	2.0	0.276	1
40	0.5	1.8	0.167	3
40	1.0	2.1	0.180	1
40	1.5	2.1	0.236	2

Table 2 gives the basic physical-mechanical properties of copper deposits.

The data considered indicate that the application of UDDs is a positive factor that increases the throwing power of the electrolyte by a factor of 3, decreases the porosity of a coating to almost zero, increases the corrosion resistance of a coating, and increases its wear resistance by a factor of 9 to 10.

To obtain such high properties, the following electrolyte composition and electrolysis conditions are recommended: 80 g/l $CuSO_4 \cdot 5H_2O$, 100 g/l H_2SO_4, and 2–5 g/l UDD; room temperature (20 ± 2°C); and a cathode current density i_c = 1 A/dm^2.

4. GALVANIZING

Alkaline zincate and weakly acid chloride electrolytes were mainly used in the studies on galvanizing steels [11]. The optimum concentration of UDDs was experimentally found to be 10 g/l (the UDD content in a coating was 0.7 wt %).

Corrosion tests were performed in a climatic chamber at an air temperature of 35°C; for spraying and creating a salt spray atmosphere, a 3% aqueous solution of sodium chloride was used.

The corrosion tests showed that the best Zn–UDD coatings were produced using a zincate electrolyte containing 12 g/l ZnO, 120 g/l NaOH, and 7–10 g/l UDD at a current density of 1–2 A/dm^2. The resistance of such coatings to seawater is 60–62% higher than that of any zinc coating.

Polarization curves in the presence of UDDs in weakly acid electrolytes exhibit a potential shift toward positive values ($\Delta\varphi$ = 5–40 mV), which indicates partial depolarization of the double electrical layer.

As the UDD concentration in the electrolyte increases, the grain size of deposits decreases.

The passivation of Zn–UDD coatings using the standard chromate treatment or passivation radically improves the corrosion resistance (Table 3). Corrosion

is observed only in the zinc coating; no corrosion of the steel substrate is detected.

5. TINNING

Tinning is widely applied in the electronic, electrical manufacturing, and food industries. The existing tin coatings have low wear and corrosion resistance and a low throwing power of the electrolyte. The application of UDDs significantly improves these properties (Table 4); the porosity of a coating sharply decreases and the corrosion resistance increases at virtually the same spreading coefficient of solder and electrical resistivity. The wear resistance of such coating increases by a factor of 3.

6. SILVERING

After testing various silver-containing electrolytes, researchers concentrated their attention on the cyanogen–thiocyanogen silvering electrolyte. Investigations were carried out at various concentrations of UDDs, Ag^+, and additions. The optimum current density depends substantially on the Ag^+ content in the electrolyte.

The wear resistance of silver–diamond coatings was determined by their abrasion upon reciprocating motion of the samples under a load [GOST (State Standard) 16875-71]. The results obtained are given in Table 5. As is seen, the wear resistance of coatings increases with the UDD concentration. Even at a thickness of 1.5–2 μm, a highly wear-resistant silver film can be produced, which allows one to apply thinner silver coatings in many cases and improve the quality of the products.

Testing of samples (electric contacts) that were coated with a 24-μm-thick silver layer using the standard method and a cyanic silvering electrolyte at the Élektroapparat plant (St. Petersburg) showed that the silver weight loss for 24 h was ~22%. Electric contacts with a 5-μm-thick covering, coated using the method proposed by us from a cyanogen–thiocyanogen electrolyte with 0.5 g/l UDD, exhibited a silver mass loss of ~4.5% for 24 h. Testing of the same parts under actual industrial conditions in a VGB-220 high-voltage switch (220 kV, 3200 A) in the course of 6000 switching operations supported the laboratory results and the applicability of this technology for electrical machines.

7. GILDING

In radio electronics, gilding is applied for fabricating various contacts to provide contact resistance under the severest operating conditions.

UDDs in gilding are used to increase the wear resistance and hardness at retained high electrophysical properties. Cyanic acid (citrate), cyanic alkaline, and iron–cyanogen electrolytes were used in gilding [12].

Table 5. Wear resistance of silver–diamond coatings

UDD concentration, g/l	Coating thickness, μm	Wear time, h	Coating weight loss, %
0	5	20	33.3
0.2	1.7	20	6.7
0.5	1.3	20	5
1.0	1.3	40	2.5
2.0	1.5	25	No loss

Table 6. Effect of the UDD concentration in an electrolyte on the wear resistance of gold coatings deposited from a citrate gilding electrolyte that has no organic additions and contains 8 g/l (for metal) $KAu(CN)_2$ and 80 g/l $C_6H_8O_7 \cdot H_2O$ at temperature 20°C, electrolyte pH 4.5, and current density 0.5 A/dm^2

No.	UDD concentration, g/l	Coating weight loss, 10^{-5} g/h (LTI device, 1335-N load)
1	0	93.2
2	0.1	44.0
3	0.5	4.8
4	1	0.4
5	2	2.5
6	5	5.6
7	10	12.3

Table 7. Results of wear tests of samples (1 cm^2, ~2 μm thick, with UDDs) coated with nickel (the UDD content in the electrolyte is 5 g/l)

Current density, A/dm^2	1 (without UDD)	1 (with UDD)	1.5 (with UDD)
Gain in the nickel coating weight after electrolysis (before wear test)	22.7	11.0	16.0
Weight loss (mg) during wear test after			
3 h	15.0	0.35	2.0
4 h	0.2	0.25	0.3
3 h	0.2	0.15	0.1
2 h	1.2	0.2	0.2
Total for 12-h wear test	16.6	0.95	2.6
Weight loss, wt %	73.1	8.6	16.3

The introduction of 0.5–10 g/l UDD into these electrolytes makes it possible to deposit dense, fine-grained, light-colored, half-brilliance golden coatings containing 0.01–1.0 wt % diamond. Such coatings have high wear resistance (Table 6) and high electrophysical and processing characteristics as compared to pure gold coatings.

Table 8. Properties of oxide–diamond films on grade-16082 AlMgSi alloy containing 0.7–1.3% Si, 0.5% Fe, 0.1% Cu, 0.4–1.0% Mn, 0.6–1.2% Mg, 0.25% Cr, 0.2% Zn, and 0.1% Ti; the plate area 1 cm^2

Coating	UDD content in electrolyte	Specific gain in film weight, mg/cm^2	Specific wear resistance (for 10 h), $\Delta m^2/cm^2$
UDD-free oxide film	0	14	11.3
UDD-containing oxide film	0.05	17	9.8
	4.0	32	3.8
	15.0	43	0.9
	30.0	51	No wear

8. NICKEL PLATING

Nickel coatings are widely applied, especially for machine elements and tools. According to the data from [13], the lifetime of nickel–diamond coatings is 20 times that of a pure nickel coating.

Dolmatov *et al.* [14] used a classical nickel-plating electrolyte containing 150–200 g/l $NiSO_4$, 10–15 g/l NaCl, 20–30 g/l $MgSO_4$, and 25–30 g/l H_3BO_3. The deposition conditions were as follows: pH = 4.8–5.2, t = 18–20°C, and a current density of 1–6 A/dm^2. The results of wear tests are given in Table 7. As is seen, the introduction of 5 g/l UDD into the electrolyte leads to an increase in the wear resistance of the coating by a factor of 4.5–8.5.

9. ANODIC OXIDATION

Anodic oxidation is the basic method of protecting from corrosion, increasing strength and wear resistance, and creating dielectric properties on the surfaces of parts made of aluminum and its alloys. Anodic oxidation is widely applied in various fields of machine building and the aircraft industry. An oxide coating is a nonmetallic matrix, namely, a porous film comprising mainly aluminum trioxide. As a rule, aluminum is oxidized in an acid medium and, sometimes, in an alkaline medium.

We found that, when UDDs are introduced into an electrolyte to perform anodic oxidation, they move to an anode (aluminum and its alloys) and penetrate into pores forming during surface oxidation because of their negative charge. They are retained in pores after discharging due to not only mechanical forces but also to van der Waals and other physicochemical forces [15]. The filling is so dense that the gain in the oxide film weight increases by a factor of 2–3.5. The wear resistance of such a film increases by a factor of 10–13, and its corrosion resistance and insulating properties increase substantially.

Thus, the application of UDDs for producing anodic oxide films on aluminum and its alloys results in the films filling with insoluble nanodiamonds during electrolysis and in a substantial improvement in the properties of the deposited nonmetallic inorganic composite coating. The optimum UDD content in an oxidizing electrolyte is 2–15 g/l. The degree of filling oxide films

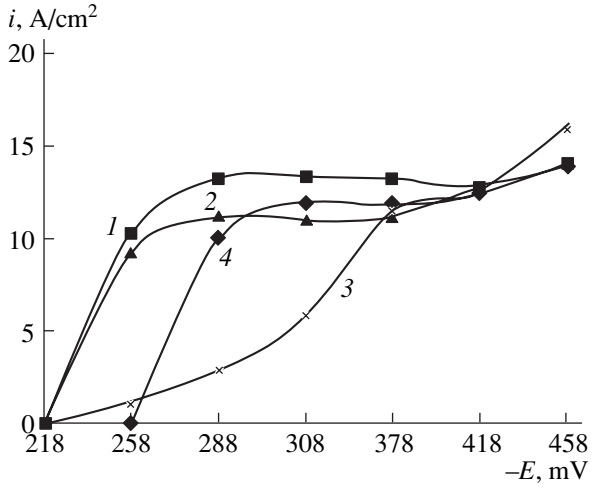

Fig. 1. Polarization of Sn in an acid electrolyte: (*1*) without UDDs, (*2*) 0.5 g/l UDD, (*3*) 1 g/l UDD, and (*4*) 2 g/l UDD.

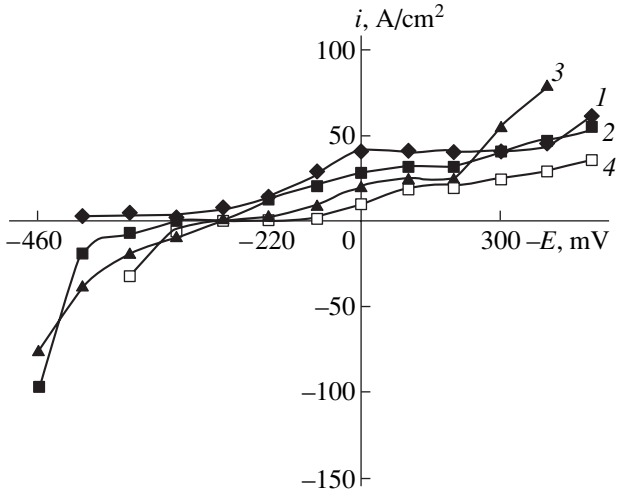

Fig. 2. Polarization of Cu in an acid electrolyte: (*1*) without UDDs, (*2*) 0.5 g/l UDD, (*3*) 1 g/l UDD, and (*4*) 2 g/l UDD.

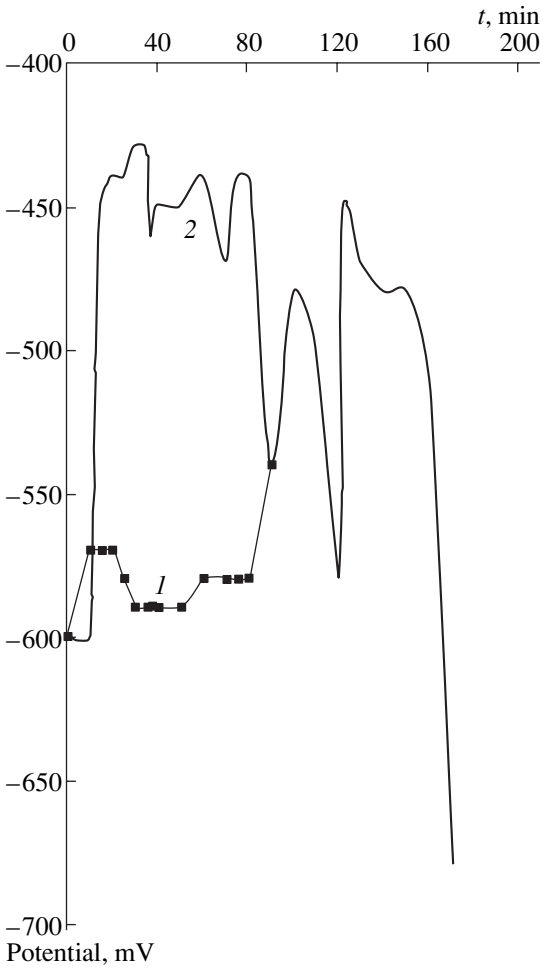

Fig. 3. Measurement of the no-current potential during chemical nickel plating with glycine in solutions (*1*) with and (*2*) without UDDs.

with UDDs depends on the electrolysis temperature and current loads in addition to the diamond concentration in the electrolyte.

The presence of UDDs does not affect the film growth rate; they only fill a film during electrolysis. The enhanced properties of oxide–diamond coatings deposited according to the method proposed and the simplicity of the process make this method competitive among the well-known methods of producing filled oxide films.

Table 8 gives the wear-resistance data for a grade-16082 AlMgSi alloy (Germany) and an electrolyte containing sulfuric acid (200 g/l H_2SO_4). Wear tests were carried out on a friction machine upon reciprocating motion of samples under a load of 200 g/cm^2. The wear resistance was determined as the weight loss of a sample after abrasion for 10 h.

Polarization curves recorded for all processes described above show that the presence of UDDs in an electrolyte facilitates the discharge of metals at a cathode; that is, the curves shift toward positive potentials (see Figs. 1 and 2 for tin and copper, respectively). Moreover, UDDs do not change the kinetics of the process; they mainly affect adsorption phenomena. Although the polarization curves shift toward positive potentials, their slope (polarizability) increases, which indicates that the throwing power of the electrolytes increases. The presence of UDDs, as a rule, strongly facilitates hydrogen release, which is clearly illustrated by the curves recorded during chemical nickel plating with and without UDDs (Fig. 3).

10. CONCLUSIONS

The effect of UDDs produced by detonation synthesis on important commercial galvanic processes, such as chromium plating, copper plating, galvanizing, tinning, gilding, silvering, and anodic coating of aluminum and its alloys, has been studied. For the investigation, we used the traditional, most widely applied electrolytes.

In all processes under study, the service properties of deposited coatings become substantially improved. For example, the introduction of UDDs into an acid copper-plating electrolyte leads to pore-free copper coatings. As compared to the UDD-free coatings, their microhardness is higher by a factor of 1.5, elastic properties are higher by a factor of 2, wear resistance is lower by a factor of 9 to 10, and corrosion resistance is much higher. Moreover, the throwing power of an UDD-containing electrolyte is three times that of the electrolyte without UDDs. The wear resistance of a chromium–diamond coating increases three to ten times. The corrosion resistance of zinc–diamond coatings (zincate electrolyte) increases two to three times, and the throwing power of the electrolyte increases by 33–57%. The application of UDDs for tinning sharply decreases the porosity of a coating (by a factor of 3 to 9), increases the corrosion resistance of the coating, and increases its wear resistance by a factor of 3. The electrophysical properties of such coatings remain virtually unchanged. The wear resistance of silver coatings increases three to ten times, and their microhardness rises up to 180 kg/mm^2. The wear resistance of an anodic film with UDDs increases 10–13 times, and the gain in weight (filling) of such a coating increases by a factor of 2–3.5. Moreover, its corrosion resistance and insulating properties become higher.

REFERENCES

1. R. S. Saĭfullin, *Inorganic Composite Materials* (Khimiya, Moscow, 1983).
2. L. I. Andropov and Yu. N. Lebedinskaya, *Composite Electrochemical Coatings and Materials* (Tekhnika, Kiev, 1986).
3. A. I. Shebalin, V. D. Gubarevich, and P. M. Brylyakov, Patent Application PCT/SU 88/00230 (WO 89/07668), C 25D15/00.

4. A. I. Shebalin, V. D. Gubarevich, P. M. Brylyakov, *et al.*, USSR Inventor's Certificate No. 1,694,710, Byull. Izobret., No. 44, 91 (1991).
5. Jpn. Patent No. 5-10,695 (27 April 1993).
6. A. E. Aleksenskiĭ, M. V. Baĭdakova, A. Ya. Vul', *et al.*, Fiz. Tverd. Tela (St. Petersburg) **39**, 1125 (1997) [Phys. Solid State **39**, 1007 (1997)].
7. V. Yu. Dolmatov and G. K. Burkat, Sverkhtverd. Mater., No. 1, 84 (2000).
8. V. Yu. Dolmatov, G. K. Burkat, V. Yu. Saburbaev, *et al.*, Sverkhtverd. Mater., No. 2, 52 (2002).
9. S. V. Vashchenko and Z. A. Solov'eva, Gal'vanotekh. Obrab. Poverkhn. **1** (5–6), 45 (1992).
10. V. Yu. Dolmatov, T. Fudzhimura, G. K. Burkat, and E. A. Orlova, Sverkhtverd. Mater., No. 6, 16 (2002).
11. B. Lung, G. K. Burkat, V. Yu. Dolmatov, and V. Yu. Saburbaev, RF Patent No. 2,169,798, Byull. Isobret., No. 18(II), 279 (2001).
12. B. Lung, G. K. Burkat, V. Yu. Dolmatov, and V. Yu. Saburbaev, RF Patent No. 2,191,227 (20 October 2002).
13. S. I. Chukhaeva, P. Ya. Detkov, A. P. Tkachenko, and A. D. Toropov, Sverkhtverd. Mater., No. 4, 29 (1998).
14. V. Yu. Dolmatov, B. Lung, and G. K. Burkat, in *Abstracts of International Conference on Materials and Coatings in Extremal Conditions* (Katsiveli, Crimea, 2000), p. 64.
15. F. I. Kukoz, Yu. D. Kudryavtsev, Zh. I. Bespalova, *et al.*, RF Patent No. 2,078,449 (1997), Byull. Izobret., No. 12, 181 (1997).

Translated by K. Shakhlevich

Physics of the Solid State, Vol. 46, No. 4, 2004, pp. 711–715. Translated from Fizika Tverdogo Tela, Vol. 46, No. 4, 2004, pp. 693–697.

APPLICATIONS OF NANODIAMONDS

Shock-Wave Sintering of Nanodiamonds

V. V. Danilenko

ALIT Close Joint Stock Company
Kiev, 03067 Ukraine
e-mail: vvdan@list.ru

Abstract—A two-stage technology of compaction of ultrafine-dispersed diamonds (UDDs) is developed and successfully applied for ampoule-free sintering of dense UDD granules in lead under a pressure of up to 100 GPa. Standard strength tests of polycrystals (fractions 80/63, 125/80) thus obtained showed a wide spread in strength (from grade AS4 to AS80), which is indicative of highly inhomogeneous sintering conditions. A single-crystal diamond is obtained for the first time by using shock-wave compaction; the crystal is a transparent twinned octahedron 0.6 mm in size with an impurity content of less than 0.05%. This result is unexpected and encourages us to believe that this method can be used to manufacture jewellery-grade diamonds (larger than 2 mm in size). The pressure and temperature conditions of sintering are analyzed. © *2004 MAIK "Nauka/Interperiodica".*

Detonation-produced ultrafine-dispersed (nanoscale) diamonds (UDDs) find many applications, in particular, in the fabrication of hard, wear-resistant polycrystals through shock-wave compaction. This extremely complicated method shows considerable promise; indeed, detonation can be used not only for producing UDDs but also for their sintering (during the same explosion); furthermore, shock-wave technology of ampoule-free sintering is profitable in terms of both productivity (amount of UDDs per explosion) and the ratio of the cost of the raw material (UDDs) to the cost of the final product (polycrystalline or single-crystalline diamonds). In contrast to the situation in many other UDD application areas, there is a ready market for polycrystal diamonds with a nanostructure and the area of application of diamond polycrystals is expanding rapidly.

In this paper, we discuss ampoule-free liquid-phase sintering of UDD granules under explosion conditions.

Up to now, attempts to produce strong diamond polycrystals through sintering UDDs under both static [1, 2] and dynamic conditions [3] have not met with success. Clinkers obtained under static conditions exhibit low strength, which can be explained by their high porosity and by graphitization. It was concluded in [1] that the maximum pressure of 10 GPa attainable with conventional compression molds is insufficient for sintering UDDs.

Our first experiments (performed as long ago as 1964) on sintering UDDs in a mixture with lead in cylindrical ampoules showed that UDDs are graphitized [4]. The reasons for the graphitization are the high initial porosity of UDDs, the presence of oxygen adsorbed on the surface of particles (because oxygen is a graphitization catalyst), and the short duration of high pressure, which is insufficient for sintering UDDs and for cooling the sintered UDDs under pressure to prevent graphitization.

The theory of sintering of ultrafine powders (UFPs) with particles less than 1 μm in size has not yet been thoroughly worked out. Certain general features of UFP sintering are considered in [5, 6].

Before sintering, UFPs should be pressed to attain a minimum porosity. Compression of UFPs is hampered by the fact that UFPs contain conglomerates that act as hard frameworks during compaction. In this case, compaction proceeds in steps associated with the successive formation and disintegration of frameworks.

The toughness of conglomerates increases as they decrease in size down to individual particles. The strength of particles is much higher than that of bulk diamond crystals. For example, the strength of ultrafine diamond particles is very high and approaches theoretical estimates (100–200 GPa), because there are no dislocations in them. The high hardness of particles and their clusters is testified to by the fact that cold compacting of UDDs under a static pressure of 8 GPa increases the density of the material only to 60% of the theoretical value [1], which is close to the density of closely packed rigid spheres of the same diameter.

The structure of UDDs can be described in terms of the cluster model (Fig. 1) [1, 5], in which a porous material is divided into microscopic regions of closely packed particles [clusters with a maximum number (8 to 12) of contacts between particles]. It is assumed that the clusters are randomly distributed and that the number of interparticle contacts in the boundary regions is minimum (four or less) [5].

As UDDs (as well as any UFP) are sintered, microscopic regions form in which the Laplace pressure in capillaries far exceeds the average level. Near such regions, tensile stresses arise and cause pores to

1063-7834/04/4604-0711$26.00 © 2004 MAIK "Nauka/Interperiodica"

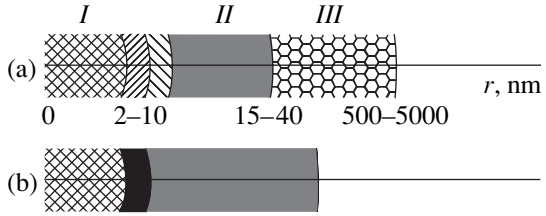

Fig. 1. Models of the UDD structure. (a) Three-level model of the structure of original UDD powders: (*I*) a strong spherical diamond particle with a density of 3.3 to 3.4 g/cm^3 covered with amorphous carbon and adsorbed impurities, (*II*) a cluster of closely packed particles (the number of nearest neighbors is 8 to 12) with a density of 1.8 to 2.2 g/cm^3 (approximately 60% of the particle density), and (*III*) loose conglomerates of clusters with a density of less than 0.4 g/cm^3. (b) Model of the UDD granule structure before sintering; particles are covered with adsorbed hydrogen.

increase in size. If we assume that the Laplace pressure is proportional to the number of contacts, then the pressure in the clusters will differ from that in the regions between the clusters by several orders of magnitude. For example, in a powder with particles 14 nm in size, the pressure is 0.8 GPa in a cluster and 0.08 MPa in the regions between conglomerates of clusters. Due to this difference in pressure, a local compression of clusters arises and the size distribution of pores over the volume of the material changes.

Therefore, there are two types of boundaries in sintered UFPs: one of them (type I) exists in clusters and is analogous to grain boundaries, and the other (type II) occurs between clusters and corresponds to pore boundaries [1]. Thus, compression and sintering are characterized by similar inhomogeneous processes and the structures arising during them.

In UFPs, the recrystallization (in clusters) and sintering of clusters are correlated at low temperatures, $(0.1–0.3)T_m$, whereas in coarse-grained systems collecting recrystallization occurs at $0.7T_m$. These processes are controlled by the generation and migration of nonequilibrium vacancies [6], whose concentration on the boundaries can reach high values corresponding to the state near the melting point.

In solid-state sintering of UFPs, two mass transfer mechanisms are operative, namely, mutual slip of clusters (coagulation) and liquid-phase coalescence. Experiments show that sintering and contraction occur in two steps. In the first step, recrystallization proceeds rapidly through both mechanisms mentioned above or through one of them depending on the temperature. The second step is slow and is similar to collecting recrystallization in character.

Solid-state sintering of UDDs does not proceed very rapidly (for several seconds [1, 2]) and is likely not to go to completion within the duration of shock compression (several microseconds). Even when the impact-molding duration was increased to 425 μs (by increasing the explosive charge), no strong polycrystals were produced through solid-state sintering of diamond powders [7]. Therefore, in sintering UDDs through shock-wave compaction, conditions should be provided for more rapid liquid-phase sintering.

Since a UDD powder has a nonuniform density (Fig. 1), its microscopic regions heat to different temperatures under shock-wave compaction; looser conglomerates heat to a greater extent than more compact clusters of particles, and graphitization after unloading is more probable in the former case. Therefore, the granules to be sintered should have as uniform a structure as possible.

Thus, the high density of particles in a cluster, the small radius of contacting particles, and, as a consequence, the high Laplace pressure favor sintering of the cluster even at low temperatures and pressures. Therefore, preparatory to explosion sintering, it is advantageous to perform slow recrystallization of clusters under static conditions.

We developed and successfully tested a two-step technique for sintering nanoscale diamonds, according to which UDD clusters are first sintered under static conditions (in the course of thermochemical purification and production of high-density granules) and then the clusters in granules are subjected to shock-wave liquid-phase sintering.

High-quality sintering of UDDs can be attained only after prior removal of amorphous carbon and impurities from the surface of particles. The UDD particle surface is cleaned with hydrogen at 850°C for 2 h with subsequent cooling in a hydrogen atmosphere in order for the particle surface to adsorb the hydrogen (Fig. 1). After this cleaning, the x-ray diffraction peaks increase in intensity and electron-microscopic examination shows that selective isolation occurs, with distinctions between clusters and their aggregates becoming more noticeable.

The density of granules of UDDs cleaned with hydrogen is found to be high (up to 2.7 g/cm^3), which indicates that clusters are sintered further during granulation.

Let us consider the conditions under which shock-wave liquid-phase sintering occurs. Shock-wave compaction of a porous material brings about a collapse of pores, which is accompanied by rapid plastic deformation of the substance surrounding the pores and intense local heat generation [8]. In solid ceramic powders characterized by a high limit of elasticity, the heat release is sufficiently intense to cause melting of the substance filling a pore. Then, the molten substance is cooled, because the temperature at different points of the compressed powder levels out. Thus, in shock-wave compressing, the temperature of a filled pore first becomes equal to a high value T_{por} and then decreases to an equilibrium value T_e.

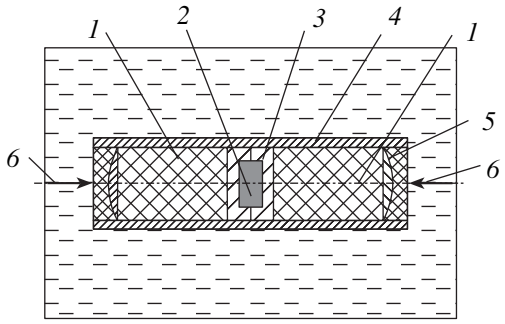

Fig. 2. Setup for ampoule-less sintering of UDD granules in lead. (*1*) TG40 charges, (*2*) mixture of lead and UDD granules, (*3*) lead, (*4*) tube, (*5*) plane lens, and (*6*) synchronous circuit for setting off charges. The setup put in a water jacket.

Since diamond particles are virtually incompressible, we can assume that they are not heated; therefore, heat is released only in the pore volume and the temperatures T_e and T_{por} are given by

$$T_e = p(v_{00} - v)/2c_p, \quad (1)$$

$$T_{por} = T_p/(1 - v_0/v_{00}), \quad (2)$$

where v_{00} and v are the initial and final specific volumes, respectively; p is the pressure; c_p is the average specific heat capacity; and v_0 is the specific volume of the single crystal. If a diamond power is compressed to a pore-free state, we have $v = v_0$.

Due to the high heat conductivity of diamond, the equilibrium temperature is reached very rapidly, in time $t = d^2/D$, where d is the diameter of a particle and $D = 1$ cm^2/s is the thermal diffusivity of diamond.

For diamond powders with particles of diameter $d <$ 26 nm (i.e., for UDDs), according to our calculations [4], thermal equilibrium is established immediately behind the shock wave.

As the porosity and dispersity of a powder are increased, the difference between T_{por} and T_e becomes smaller, because the ratio of the volume of the heated deformed surface layers (filling the pores) to the total volume decreases. If the volumes of pores and UDD particles are assumed to be equal, we obtain $T_{por} = T_e$ for UDDs. Under this assumption, the following two conclusions can be drawn.

(1) In the case of UDDs, diamond particles do not play the role of "internal" heat sinks and the temperature after unloading is virtually equal to the temperature behind the shock wave. Therefore, in order to prevent a compressed UDD granule from graphitization, it should be cooled by an external cooler, e.g., by a colder metal surrounding the granule. Our calculations showed [4] that the time required for UDD granules 0.2, 0.4, and 0.6 mm in diameter to be cooled from 2000 to 1000 K by molten lead at 613 K is 13, 45, and 80 μs, respectively.

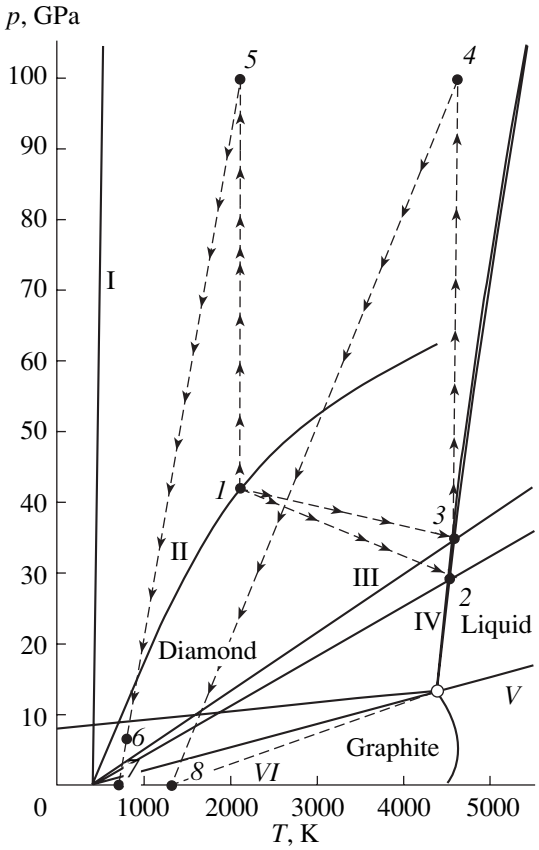

Fig. 3. Phase diagram of carbon, shock adiabats, and processes caused by shock-wave compression of UDD granules embedded in lead in the setup shown in Fig. 2. Shock adiabats: (*I*) diamond single crystal, $p_0 = 3.5$ g/cm^3; (*II*) lead, $p_0 = 11.3$ g/cm^3; (*III*) UDD, $p_{00} = 2.0$ g/cm^3; (*IV*) UDD, $p_{00} = 1.8$ g/cm^3; (*V*) UDD, $p_{00} = 0.6$ g/cm^3; and (*VI*) graphitization curve of diamond. The values of p and T are indicated for (*1*) lead under contact loading with a shock wave produced by setting off TG40 charges, (*2*) UDD with $p_{00} = 1.8$ g/cm^3 in lead at point *1*, (*3*) same but for UDD with $p_{00} = 2.0$ g/cm^3, (*4*) UDD in lead after compression caused by the secondary reflected shock wave, (*5*) same but for lead, (*6*) lead after its unloading in water starting from point *5*, (*7*) same but after full unloading, and (*8*) UDD after unloading (starting from point *4*) and cooling by molten lead.

(2) Equation (2) and the equilibrium temperatures for shock compression found from experimental shock adiabats for diamond powders [4] can be used to estimate the shock compression temperatures of UDDs of the same porosity, because T_{por} for diamond is equal to T_e for UDDs. We used this method to estimate the compression temperatures of UDD granules of density 1.8 and 2.0 g/cm^3 in our experiments on sintering UDDs (the corresponding setup is shown schematically in Fig. 2).

The results of these experiments are presented in Fig. 3. In the p–T plane, shock adiabats of diamond powders and a diamond single crystal in the ranges $p <$ 100 GPa and $T < 5000$ K represent a fan of straight lines whose slope increases with UDD density. UDDs with a density of 0.6 g/cm^3 are strongly heated (to 7200 K under a pressure of 23 GPa [4]); therefore, such highly porous UDDs cannot be compressed to a pore-free state and it is difficult to prevent their graphitization.

The experimental conditions are as follows. The lead is subjected to a plane detonation wave generated by setting off a charge of density 1.67 g/cm^3 and characterized by a pressure of 42 GPa and a temperature of 2100 K [9]. The shock wave compresses UDD granules to pressures of 35 GPa (p_{00} = 2 g/cm^3) and 30 GPa (p_{00} = 1.8 g/cm^3). As a result, the granules are heated to 4600 K and melt.

Due to the cumulative effect of the colliding shock waves, the pressure in the lead and granules increases further to 100 GPa but the temperature remains virtually unchanged. As a result, since the slope of the fusion curve of diamond is positive, the state of the molten UDD falls within the region of solid diamond in the phase diagram and crystallization begins. The crystallization heat is absorbed by the colder lead. The granules continue to cool further in the lead in the course of unloading, which proceeds in two steps. First, the lead is unloaded by water (in 20 μs) and then the water is unloaded (in 80 μs).

The optimum initial UDD porosity for the liquid-phase sintering to occur is likely to correspond to the case where the pressure of the pore-free state is reached at the melting point of UDD particles. Melting of a UDD, as of any UFP, exhibits the following two specific features: it starts from the surface and occurs over a temperature range, where the percentage of melted particles varies from zero to 100% [10]. The melting point of UDDs is 20–30% lower than that of bulk diamond, as is the case with other UFPs [11].

Melting of UDDs under pressure and, in particular, under shock-wave pressure has not yet been studied.

Depending on the specific pressure and initial porosity of a given granule (near their optimum values), the following two scenarios can be proposed for sintering. (1) Only the surface layers of UDD particles, rather than the entire particles, are melted; as a result, a polycrystal with a nanostructure is obtained. (2) The UDD particles in a granule are fully melted; therefore, a single crystal can form in crystallization under pressure.

In both cases, to prevent the graphitization of polycrystals and single crystals and the formation of cracks in them, the duration of cooling by the surrounding metal in the course of relatively slow unloading must be sufficiently long.

After refining the technologies of hydrogen cleaning and granulation of UDDs, we performed experiments on sintering UDDs without using a protecting ampoule. The experimental setup is shown schematically in Fig. 2. The granules ranged in density from 1.8 to 2.7 g/cm^3 and in size from 0 to 600 μm. A certain quantity of granules (approximately 0.4 kg) was mixed with molten lead, and then a block thus obtained was compressed in a chamber (ALIT company) by setting off two 5-kg TG40 charges.

After acid treatment, the mixture of sintered granules and the UDDs synthesized in these experiments were analyzed. The results are as follows.

(1) Isolated transparent diamond single crystals 0.6 mm in size in the form of twinned octahedra were obtained, which is an unexpected result. The crystal composition was investigated at the Institute of Problems of Materials Science (National Academy of Sciences of Ukraine). The crystal was found to consist of 99.9% carbon, 0.1% oxygen, and 0.01% titanium. No other elements were detected. In particular, Fe, Ni, and Mn are absent; i.e., the single crystals are not catalytic diamonds.

A relatively large single crystal was produced through shock-wave compaction for the first time. Therefore, a small part of the compressed UDD granules were under conditions that were optimal for producing and preserving single crystals. Since UDDs are in thermal equilibrium, i.e., any region of a compressed granule is at the same equilibrium temperature, it is likely that a fraction of the granules in our experiments were fully melted and then cooled relatively slowly by the surrounding molten lead.

Earlier, only highly disperse polycrystals had been obtained under explosion conditions. We believe that, in the future, the optimum density of UDD granules will be found, experiments will be performed on a larger scale, and a higher uniformity of compression and unloading will be attained, which will make it possible to produce jewellery-grade diamonds (larger than 2 mm in size).

(2) At the pilot plant of the Institute of Superhard Materials (National Academy of Sciences of Ukraine), grades 80/63 and 125/80 μm were separated and standard strength tests were performed with them (50 grains of each grade). The compression strength was measured using a DA-2M device. Particles were found to vary in strength; for certain grains, the fracture load was as high as 4.7 kg, which corresponds to grinding diamond powers of grade AS80 [4] and suggests that high-quality sintered UDD granules can be produced.

The large scatter in the strengths of the polycrystals can be explained by the fact that the properties of the granules and the compression conditions were nonuniform.

(3) In order to partly separate microscopic polycrystals from fragile UDD aggregates, ultrasonic machining of an aqueous suspension of such a mixture was performed followed by sedimentation. The powdery sediment, as well as sintered granules, was black in color, and its particles could scratch the polished surface of a

corundum single crystal and had clearly defined profiles [4]. A comparison of the grain-size distributions of a UDD and a sediment, performed under identical conditions using a Seisin granulometer (Japan company), showed that these distributions are different; the sediment contains many more particles of a size within the range 1–20 μm [4].

Thus, the results of our preliminary study suggest that it is worthwhile to continue investigations of shock-wave ampoule-less sintering of UDDs with the aim of developing a technology for the industrial production of high-quality diamond single crystals and diamond polycrystals with nanostructure.

REFERENCES

1. V. V. Danilenko, I. A. Petrusha, G. S. Oleĭnik, and N. V. Danilenko, Sverkhtverd. Mater., No. 4, 53 (1988).
2. A. A. Bochechka, Sverkhtverd. Mater., No. 6, 37 (2002).
3. E. E. Lin, V. A. Medvedkin, and S. A. Novikov, in *Proceedings of the EXPLOMET'95 International Conference (1995)*, p. 89.
4. V. V. Danilenko, *Synthesis and Sintering of Diamonds by Explosion* (Énergoatomizdat, Moscow, 2003).
5. V. V. Skorokhod, in *Properties and Application of Dispersed Powders* (Naukova Dumka, Kiev, 1986), p. 91.
6. L. I. Trusov, V. N. Lopovok, V. G. Gryaznov, *et al.*, in *Properties and Application of Dispersed Powders* (Naukova Dumka, Kiev, 1986), p. 98.
7. A. A. Deribas, P. A. Simonov, V. N. Filimonenko, and A. A. Shtertser, Fiz. Goreniya Vzryva **36** (6), 91 (2000).
8. G. V. Belyakov, V. N. Rodionov, and V. P. Samosadnyĭ, Fiz. Goreniya Vzryva, No. 4, 614 (1977).
9. *Physics of Explosion*, Ed. by L. P. Orlenko (Fizmatlit, Moscow, 2002), Vols. 1 and 2.
10. R. S. Berry and B. M. Smirnov, Zh. Éksp. Teor. Fiz. **117** (3), 562 (2000) [JETP **90**, 491 (2000)].
11. I. D. Morokhov, L. I. Trusov, and S. P. Chizhik, *Ultrafine Dispersed Metal Media* (Atomizdat, Moscow, 1977).

Translated by Yu. Epifanov

Physics of the Solid State, Vol. 46, No. 4, 2004, pp. 716–719. Translated from Fizika Tverdogo Tela, Vol. 46, No. 4, 2004, pp. 698–701.

APPLICATIONS OF NANODIAMONDS

Nanodiamonds for Biological Investigations

V. S. Bondar' and A. P. Puzyr'

Institute of Biophysics, Siberian Division, Russian Academy of Sciences, Akademgorodok, Krasnoyarsk, 660036 Russia

e-mail: apuzyr@mail.ru

Abstract—Nanoparticles with a modified surface are prepared from nanodiamonds produced in Russia. The properties of modified nanodiamonds and their hydrosols and organosols are investigated by biophysicists with the aim of preparing nanoparticles with controlled properties for solving biological problems. © *2004 MAIK "Nauka/Interperiodica".*

1. INTRODUCTION

In recent years, we have analyzed the possibility of using nanodiamonds in biological investigations [1–3] and reached the conclusion that, despite undeniable advantages, detonation nanodiamonds have a number of disadvantages from the biological and biochemical standpoints. These are the impossibility of preparing stable hydrosols without ultrasonic treatment, the difficulties encountered in preparing hydrosols with specified concentrations of nanodiamonds, the formation of nanodiamond aggregates upon autoclaving of hydrosols (which is a widely accepted method of sterilization in biology and medicine), and the formation of nanodiamond aggregates in the course of freezing of hydrosols and subsequent thawing of ice (this technique is frequently used for stabilizing the properties of biological materials during long-term storage). In this respect, we attempted to modify the surface of nanoparticles in order to render their properties desirable for biological investigations.

2. SAMPLE PREPARATION AND EXPERIMENTAL TECHNIQUE

The nanodiamonds used in our experiments were synthesized at the Department of Physics of Nanodispersed Materials, Krasnoyarsk Research Center, and the Federal Research and Production Center Altaĭ (Biĭsk). The nanodiamonds were chosen because there are two types of powders that, after addition of water and treatment with an ultrasonic disperser, form or do not form hydrosols that are stable over a long period of time. The nanodiamonds synthesized at the Department of Physics of Nanodispersed Materials (Krasnoyarsk Research Center) according to the procedure described in [4] and chemically purified using the technique proposed in [5] possess the ability to form stable hydrosols. The Federal Research and Production Center Altaĭ has manufactured several types of nanodiamonds with different properties. We performed the experiments with samples **1-3/91** and **30/92**, which are incapable of forming stable hydrosols.

As is known, many physicochemical properties of nanodiamonds substantially depend on the composition and properties of the particle surface formed in the course of synthesis and chemical purification [6]. Apparently, it is almost impossible to affect the physicochemical properties of nanodiamonds through modification of the diamond core. Therefore, the properties of nanodiamonds can be changed only by modifying the nanoparticle surface. We used this approach and succeeded in preparing modified nanodiamonds free of the above disadvantages.

In this work, we compared the characteristics of the initial and modified nanodiamonds and did not dwell on the technique of their modification. It should be noted that all modified nanodiamonds possess similar characteristics that do not depend on the properties of the initial nanodiamonds, which can differ significantly in terms of the colloidal stability of the nanoparticles. For this reason, we do not duplicate results of the same type and present data for only one type of modified nanodiamond sample, with the manufacturer indicated.

An important parameter characterizing the nanoparticle stability in hydrosols is the electrostatic repulsion energy (ξ potential). Depending on the pH of hydrosols and the purification procedure, the ξ potentials for the nanodiamonds synthesized at the Department of Physics of Nanodispersed Materials (Krasnoyarsk Research Center) vary from –30 to –38 mV [6, 7]. The ξ potential for the modified nanodiamonds is shifted to the range from –50 to –52 mV. According to the calculations carried out by Chiganova [7], these changes lead to a considerable increase in the electrostatic repulsion energy of particles. This energy is proportional to the square of the potential of a diffuse layer, which is taken equal to the electrokinetic potential in dilute electrolyte solutions: $U_e \sim \Psi\delta^2$. Probably, the increase in the electrostatic stability of a disperse system provides aggregative stability for hydrosols formed by modified nanodiamonds. It is quite possible that a decrease in the

1063-7834/04/4604-0716$26.00 © 2004 MAIK "Nauka/Interperiodica"

surface impurity concentration, which is characteristic of modified nanodiamonds (Table 1), has a specific effect. Although the factors responsible for the observed changes are as yet not entirely clear, we managed to produce modified nanodiamonds with radically new properties.

3. HYDROSOLS

As a rule, hydrosols of nanodiamonds can be prepared only after ultrasonic treatment of a mixture of a powder with water. In this case, hydrosols that are reliably stable over a long period of time can be produced at a content of no higher than 1 wt % [8]. Despite the "rigid" preparation procedure with the use of ultrasound, part of the nanodiamond particles form a sediment, which leads to a change in their content in the suspension. With the aim of determining the true content of nanodiamonds, it is necessary to dry the hydrosol aliquot and to measure the weight of the particles. As a rule, nanodiamonds can be used only once to prepare a hydrosol. Already after the first removal of the dispersive medium and drying of the sample, in the majority of cases, it is impossible to reproduce the hydrosol without additional mechanical dispersion even with ultrasonic treatment.

The powders of the modified nanodiamonds are characterized by a high colloidal stability of the particles and form stable hydrosols even when water is simply added without ultrasonic dispersion. After repeated removal of the dispersive medium and subsequent addition of water to the dry modified nanodiamond powder, we once again obtain a stable hydrosol (Fig. 1).

Investigations into the properties of nanoparticles revealed that the most significant difference in the stability of hydrosols with time is observed between the initial nanodiamonds manufactured at the Federal Research and Production Center Altaĭ and the modified nanodiamonds. As was noted above, these nanodiamonds do not form stable hydrosols even after ultrasonic dispersion. The modified nanodiamonds prepared from these particles form hydrosols upon simple addition of water. Particles (clusters) in hydrosols formed by the modified nanodiamonds cannot be completely sedimented even through centrifugation at 16000 *g* for 10 min (Fig. 2). This indicates a high colloidal stability of the particles (clusters). It should be noted that the ultrasonic treatment favors a further increase in the colloidal stability of the modified nanodiamonds in hydrosols.

From the biological viewpoint, the advantages of hydrosols formed by modified nanodiamonds are the high colloidal stability in solutions used in biological investigations (buffer solutions, culture media, physiological liquids) and the possibility of achieving a uniform distribution of nanoparticles in an agar gel.

The hydrosols of the initial and modified nanodiamonds substantially differ in behavior in the course of freezing–thawing cycles. During the formation of ice crystals upon freezing of nanodiamond hydrosols, nanoparticles are displaced from the aqueous phase and

Table 1. Percentage of impurities in powders of the initial and modified nanodiamonds (prepared at the Department of Physics of Nanodispersed Materials, Krasnoyarsk Research Center)

Chemical element	Initial nanodiamond powder	Modified nanodiamond powder
Fe	5.7	1.20
B	1	1
Na	0.216	0.417
Ca	0.396	0.291
K	0.076	0.075
Cu	0.1	0.08
Al	0.03	0.02
Sr	0.055	0.02
Ti	0.2	0.1
Mg	0.034	0.002
Ni	0.006	0.004
Cr	0.0046	0.002
Sn	0.0016	0.0014
Pb	0.0015	0.0013
Mo	0.0004	0.0003
Mn	0.00033	0.00025
V	0.00012	0.000044
Ag	0.0000093	0.000003

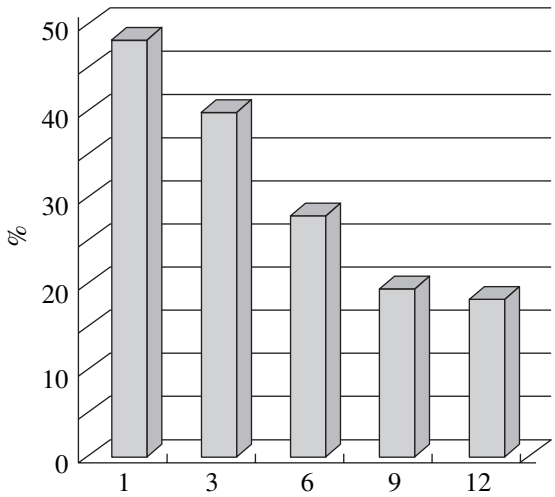

Fig. 1. Variations in the content of modified nanodiamonds in liquid supernatants of hydrosols for 12 cycles of removal and addition of the dispersive medium. The data are calculated from the optical densities of the hydrosols formed by modified nanodiamonds (prepared at the Federal Research and Production Center Altaĭ) after their centrifugation at 16000 *g* for 10 min. The optical density of the initial hydrosol (the first addition of water to the modified nanodiamond powder) without centrifugation is taken as 100%.

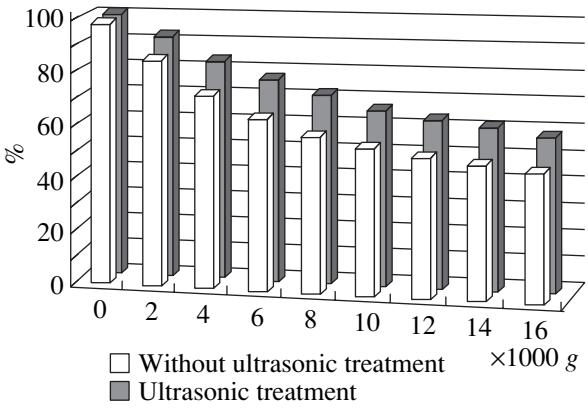

Fig. 2. Contents of modified nanodiamonds (prepared at the Federal Research and Production Center Altaĭ) in ultrasound-treated and untreated hydrosols after centrifugation. The data are calculated from the optical densities of the initial hydrosols and liquid supernatants after centrifugation at different accelerations for 10 min. The optical densities of the initial hydrosols without centrifugation are taken as 100%.

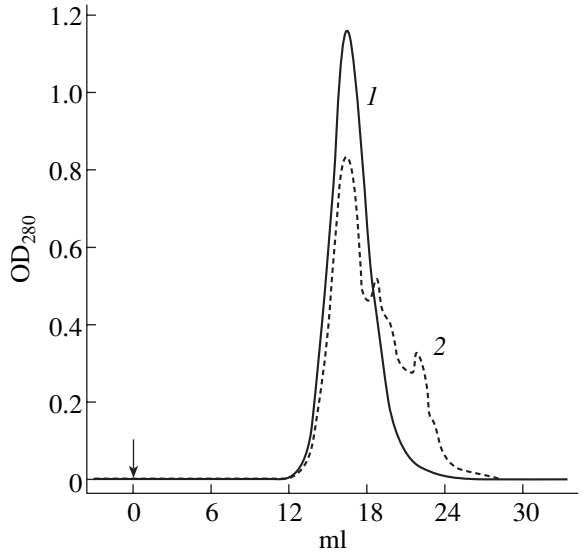

Fig. 3. Chromatograms of samples on the column with an AcA 22 gel: (*1*) the hydrosol of modified nanodiamonds (prepared at the Department of Physics of Nanodispersed Materials, Krasnoyarsk Research Center) and (*2*) ferritin.

form large-sized aggregates. Upon thawing of ice, the nanodiamond aggregates precipitate and their repeated transformation into the colloidal state becomes problematic. The formation of ice in hydrosols of modified nanodiamonds is not accompanied by the precipitation of large-sized nanoparticle aggregates, and, hence, modified nanodiamonds retain the colloidal stability after the thawing of ice.

Column chromatography (gel filtration), without changing the properties of the sorbent matrix, can be performed with hydrosols of modified nanodiamonds. In the chromatogram measured upon gel filtration with a column 1×46.5 cm in size at a flow rate of 5 ml/h, the emergence of particles is characterized by one peak (Fig. 3). We can assume that the modified nanodiamond particles pass through a free volume of columns without penetrating into the pores of gel sorbent particles. The asymmetry of the peak most likely indicates a possible weak interaction of particles with the surface of gel spherules. Chromatography of nanodiamond hydrosols under the same conditions leads to their irreversible location in the upper part of the gel into which the sample is injected.

The use of modified nanodiamonds substantially simplifies the preparation of hydrosols with a specified concentration of nanoparticles. The high colloidal stability of the modified nanodiamonds permits us to remove the restriction on a particle concentration of 1% in stable hydrosols.

4. ORGANOSOLS

Stable colloidal systems of modified nanodiamonds can be prepared not only in water but also with other dispersive media. Table 2 presents the dispersive media (the parameters of solvents were taken from [9]) in which it is possible to obtain colloidal systems of modified nanodiamonds.

Dry powders of the initial and modified nanodiamonds are incapable of forming colloidal solutions (organosols) in pure organic solvents. However, unlike the initial nanodiamonds, the modified nanodiamonds can form organosols in the case when organic solvent–water mixtures are added to a dry powder. For example, the addition of the modified nanodiamond powder to a 35–40% ethanol solution leads to the formation of an organosol without ultrasonic treatment.

The high colloidal stability of the modified nanodiamonds ensures the stability of nanoparticles in mixtures formed upon addition of their hydrosols to organic solvents. In a number of cases, it is possible to produce stable organosols with a high content of organic solvents (for example, a 80% ethanol solution). When the content of an added organic solution exceeds the threshold value, a finely dispersed precipitate is formed in the solution. The precipitate can be transformed into the colloidal state by decreasing the organic solution concentration through the addition of water.

The high stability of modified nanodiamond hydrosols, which is virtually independent of the particle concentration, enables one to prepare organosols with a high content of the dispersed phase.

As a rule, modified nanodiamond organosols possess high colloidal stability over a wide range of temperatures, namely, from the boiling point to the freezing point of the dispersive medium. After the thawing of ice, the organosol retains the colloidal stability. In particular, the modified nanodiamond–ethanol organosol

Table 2. Solvents forming dispersive mixtures used for preparing stable colloidal solutions of modified nanodiamonds (prepared at the Department of Physics of Nanodispersed Materials, Krasnoyarsk Research Center)

Solvent	δ	δ_d	δ_o	δ_a	δ_h	η
Acetone	9.4	6.8	5	2.5	0	
1,2-Dichloroethane	9.7	8.2	4	0	0	0.79
Ethanol	11.2	6.8	4	5	5	1.2
Dimethylformamide	11.5	7.9				
Acetic acid	12.4	7.0				1.26
Dimethyl sulfoxide	12.8	8.4	7.5	5	0	2.2
Water	21	6.3	Large			

Designations: δ is the solubility parameter (calculated from the boiling point), δ_d is the dispersion solubility parameter, δ_o is the orientational (polar) solubility parameter (approximate values), δ_a is the proton-acceptor solubility parameter (approximate values), δ_h is the proton-donor solubility parameter (approximate values), and η is the viscosity at 20°C.

is stable to a temperature of –82.5°C [the temperature was specified with a ScienTemp kelvinator (USA)] and also after the thawing of ice obtained by freezing in liquid nitrogen.

Earlier, we demonstrated that nanodiamonds can be used in biotechnologies, namely, in the rapid separation of a recombinant protein from a crude protein extract [1] and in the creation of planar luminescent biochips [2]. These applications are based on the ability of nanodiamonds to adsorb protein molecules. The results of investigations into the adsorption of marker protein cytochrome C demonstrated that modification of the nanoparticle surface does not result in a change in their sorption properties.

It should be noted that modified nanodiamonds are not ideal objects. This is indicated by the decrease in their colloidal stability upon multiple drying of hydrosols, which is apparently associated with the aggregation of nanoparticles (Fig. 1). However, despite this fact, modified nanodiamonds offer a number of considerable advantages over nanodiamonds in biological investigations. The use of modified nanodiamonds allows one to prepare stable hydrosols with a controlled weight concentration of particles. The autoclaving of modified nanodiamond hydrosols does not lead to precipitation or aggregation, which permits their use in research that requires aseptic (sterile) conditions. The retention of the colloidal stability by modified nanodiamond hydrosols after freezing–thawing cycles, in addition to the aforementioned properties, allows us to consider them to be similar to other reactants used in biological investigations. In some cases, this makes it possible to retain techniques and stereotypes established in biology.

5. CONCLUSIONS

Thus, the results obtained in this work can be summarized as follows.

(1) Modified nanodiamonds with useful properties that are lacking in the initial materials were prepared from nanodiamonds fabricated in Russia.

(2) The modification of the properties of nanodiamonds was aimed at adapting them to biological investigations. Moreover, the modified nanodiamonds can most likely be used in all fields of application of nanodiamond sols with a high colloidal stability, minimum sizes of the nanoparticle clusters, and a specified concentration of nanoparticles.

ACKNOWLEDGMENTS

We would like to thank G.A. Chiganova for measuring the ξ potentials and helpful discussions of the results, I.S. Larionova for supplying the nanodiamond samples used in our experiments, and A.A. Stepen' and G.K. Zinenko for performing the elemental analysis.

REFERENCES

1. V. S. Bondar' and A. P. Puzyr', Dokl. Akad. Nauk **373** (2), 251 (2000).
2. K. V. Purtov, V. S. Bondar', and A. P. Puzyr', Dokl. Akad. Nauk **380** (3), 411 (2001).
3. A. P. Puzyr', S. V. Tarskikh, G. V. Makarskaya, *et al.*, Dokl. Akad. Nauk **385** (4), 561 (2002).
4. A. M. Staver, N. V. Gubareva, A. I. Lyamkin, and E. A. Petrov, Fiz. Goreniya Vzryva **20** (3), 100 (1984).
5. A. S. Chiganov, G. A. Chiganova, Yu. V. Tushko, and A. M. Staver, RF Patent No. 2,004,491, Byull. Izobret., Nos. 45–46, 85 (1993).
6. G. A. Chiganova, Kolloidn. Zh. **56** (2), 266 (1994).
7. G. A. Chiganova, Kolloidn. Zh. **62** (2), 272 (2000).
8. G. A. Chiganova, Kolloidn. Zh. **59** (1), 93 (1997).
9. *Modern Practice of Liquid Chromatography*, Ed. by J. Kirkland (Wiley, New York, 1971; Mir, Moscow, 1974).

Translated by O. Borovik-Romanova

Physics of the Solid State, Vol. 46, No. 4, 2004, pp. 720–725. From Fizika Tverdogo Tela, Vol. 46, No. 4, 2004, pp. 702–706.

APPLICATIONS OF NANODIAMONDS

Precursors for CVD Growth of Nanocrystalline Diamond[1]

T. Soga*, T. Sharda, and T. Jimbo***

** Department of Environmental Technology and Urban Planning, Nagoya Institute of Technology, Nagoya, 466-8555 Japan*

e-mail: soga@elcom.nitech.ac.jp

*** Research and Development, Seki Technotron Corp., Tokyo, 135-0042 Japan*

Abstract—Various routes to grow nanocrystalline diamond films by the chemical vapor deposition technique are reviewed. Among the various routes, NCD films deposited on mirror-polished silicon substrates by biased enhanced growth by microwave plasma chemical vapor deposition are described in detail. The qualitative concentration of NCD was assessed by Raman spectroscopy and x-ray diffraction patterns of the films. The hardness of the films approaches that of natural diamond at optimized conditions while still having a low amount of stress (<1 GPa). © *2004 MAIK "Nauka/Interperiodica".*

1. INTRODUCTION

Conventional polycrystalline diamond films composed of micrometer-sized diamond crystal (microcrystalline diamond, MCD) grown by chemical vapor deposition (CVD) have surface roughness, which limits its uses in many potential areas. For example, the high surface roughness is a major problem for machining and wear applications [1, 2]. Two solutions can be suggested to overcome the problem of high surface roughness: either postpolishing can be adopted or naturally grown smooth films can be developed without significantly compromising their useful properties. However, postpolishing is expensive and time-consuming [3–5], and it may be considered better to concentrate on as-grown smooth and hard films [4–7]. Nanocrystalline diamond (NCD) films, which have superb tribological properties, can be a better alternative of postpolished conventional chemical vapor deposited diamond films. Moreover, smooth NCD films will be used as a DNA chip, electrochemical electrode, heat sink, SAW filter, MEMS, NEMS, etc. Some studies (growth method properties and applications) that have been carried out on NCD in various laboratories all over the world can be found in detail in the most recent review article [8].

A common feature of the majority of the deposition techniques of CVD diamond films is a high concentration of the hydrogen gas (H_2) used as one of the constituents with some hydrocarbon gas, such as CH_4. The high concentration of H_2 results in the generation of a large flux of atomic hydrogen, which is generally believed to play a central role in the various diamond CVD processes. The growth of diamond is described to take place mostly via surface processes of addition and abstraction of radicals from the gas phase [9, 10]. Before realizing the importance of growing a naturally smooth surface, the aim in the area of CVD diamond was to maximize the crystalline quality of CVD diamond. However, diamond grown under nonoptimum conditions, such as with a lower hydrogen concentration or higher carbon activity in the plasma, gives films with small grain size, e.g., several nanometers.

In the already existing ways to grow smooth NCD films, a number of techniques and conditions have been employed. As the need to have as-grown smooth diamond films arose in the last few years, new routes have also emerged that are mostly aimed at growing smooth NCD films. In this paper, based on the literature, some of the growth routes of NCD are briefly discussed followed by a description of some properties of NCD films grown particularly using biased enhanced growth.

2. NANOCRYSTALLINE DIAMOND GROWTH ROUTES

2.1. Hydrogen Deficient Gas Phase

One such process that has been studied in detail was developed at Argonne National Laboratory, USA [11, 12]. In this process, carbon dimer (C_2) is used as a reactive species in hydrogen deficient (CH_4/Ar or C_{60}/Ar) microwave plasma CVD [11]. C_2 is produced by replacing molecular hydrogen by argon and using CH_4 or C_{60} as precursor gases and also by using N_2/CH_4 as the reactant gases in a microwave plasma CVD (MPCVD) system. The NCD films grown on diamond-seeded substrates by this technique are composed of 3-to -15-nm diamond crystallites with up to 1–10% sp^2 carbon residing at the boundaries [10]. Lin *et al.* [13] studied the CH_4/H_2/Ar process in a hot filament CVD (HFCVD) system and proposed a compositional map, which demarcates regions with well-faceted diamond growth, NCD, and nondiamond deposition. Well-faceted MCD (2–10 μm) grow up to 90% Ar. They reported a change in the microstructure from MCD to

[1] This article was submitted by the authors in English.

1063-7834/04/4604-0720$26.00 © 2004 MAIK "Nauka/Interperiodica"

NCD, with a grain size smaller than 50 nm, with the addition of 95.5% Ar.

The effects of adding nitrogen to CH_4/H_2 have also been reported. Wu *et al.* [14, 15] grew NCD films using $N_2/CH_4/H_2$ in an MPCVD system. NCD films with a grain size of 8 nm embedded in the *a*-C matrix were obtained without any hydrogen. The diamond crystallite size in their films increases from 20 to 50 nm as the hydrogen is increased from 5 to 10 sccm, respectively.

Lee *et al.* [16, 17] developed a low-temperatures process ($350 < T < 500$°C) for a low power but high growth rate (up to 2.5 μm/h) NCD film by MPCVD. They used CO-rich CO/H_2 mixtures and obtained smooth NCD films with a grain size of 30–40 nm. The temperature at which the peak growth rate is obtained in this temperature window decreases as the CO/H_2 ratio decreases. Recently, Teii *et al.* [18] also reported the growth of NCD films 20 nm in size at low pressure (80 mTorr) at 700°C by inductively coupled plasma employing $CO/CH_4/H_2$ and $O_2/CH_4/H_2$. In this case, a positive biasing of 20 V was applied to the substrate to reduce the influence of ion bombardment. The films consisted of ball-shaped grains 100 nm in size that are further composed of 20-nm NCD grains.

2.2. Biased Enhanced Nucleation/Growth Using a CH_4/H_2 Gas System

In the case of the growth route for NCD by hydrogen deficient plasmas (Section 2.1), the substrates were mostly pretreated externally before deposition either ultrasonically or mechanically using diamond or other abrasive powders. There is another well-established method to nucleate diamond internally in the conventional growth of MCD films called biased enhanced nucleation (BEN) [19], in which the substrates are a biased, negatively hydrocarbon-rich mixture of hydrocarbon–hydrogen precursor gases. This method, which results in a high density of diamond nucleation (10^{10} cm^{-2} or greater), is the first step and is followed by another one step or two steps to grow heteroepitaxial diamond films. In order to achieve overgrowth of diamond on these nuclei, the BEN process is followed by conventional growth in which the bias is turned off and the growth is continued with a lower percentage of hydrocarbon in the gas phase. It was observed that, in the later stages of growth, when the biasing is turned off and the ratio of hydrocarbon to hydrogen is reduced, only the stable part of the nuclei continue to grow, while remaining get etched off in the process due to the increased concentration of hydrogen in the gas phase [20].

To obtain an NCD film, Sharda *et al.* [21–23] suggested achieving higher densities of diamond nucleation, similar to the BEN process, and, second, in the later stages, maintaining the same high density and continuing their growth throughout the process. In order to materialize this idea, they extended the BEN in an MPCVD system for the whole growth process and termed their process biased enhanced growth (BEG), in which they obtained diamond nucleation and growth on silicon substrates in a single process. The details of the BEG process will be described later.

2.3. Diamond Seeding

Yang *et al.* [24] grew transparent diamond films with a crystallite size below 70 nm in hydrogen and methane microwave plasma CVD on quartz substrates ultrasonically pretreated by 0.5 μm diamond powder for 30 min. Grain size and surface roughness were observed to decrease with increasing methane concentration. A significant reduction in grain size seems to occur at 3% methane, which further reduces at 4% methane even though the nanodiamond concentration in the films also increases. The crystallite size, as estimated by TEM, was 30 nm near the interface and increased to 65 nm near the growth side.

In another method, a diamond layer can be coated on substrates by dielectrophoresis or the spraying method. Zhu *et al.* [25] attached thin nanostructured diamond films to silicon substrates by the spraying or brushing technique using commercially available 10- to 100-nm micropolycrystalline diamond particles (produced by explosives), with each of the particles consisting of 1- to 20-nm crystallites and the associated grain boundaries in an aqueous suspension. Gohl *et al.* [26] deposited a nanodiamond powder coating by the dielectrophoresis technique. They used a nanodiamond powder of size 1–10 nm produced from shock synthesis on a Si tip array, rough Si stumps, and flat standard mirror-polished Si substrates. Xu *et al.* [27] deposited a nanostructured diamond coating on etched silicon substrates by the dielectrophoresis method using ~5-nm nanodiamond powder (produced by explosives) by suspending them in ethanol. Maillard-Schaller *et al.* [28] deposited diamond nanoparticles 4–5 nm in size on flat Si(100) substrates by electrophoresis/dielectrophoresis. Hiraki [29] grew diamond films at 200°C by nanodiamond seeding.

3. BIASED ENHANCED GROWTH OF NCD FILMS

In this section, we will discuss the growth of NCD by the BEG process in detail. The NCD films were grown by the BEG process in a 2.45 GHz device (Seki Technotron Corporation, Japan; formerly, Applied Science and Technology, USA) made in the MPCVD system. The mirror-polished Si(100) substrates were kept on a Mo holder resting on a graphite susceptor. No diamond powder of any other *ex situ* treatment was performed prior to the depositions. The substrate assembly was immersed in 5% methane and hydrogen plasma. In a special arrangement of the substrate assembly, a quartz shield was used to cover the conducting parts of the substrate holder assembly (other than the substrate).

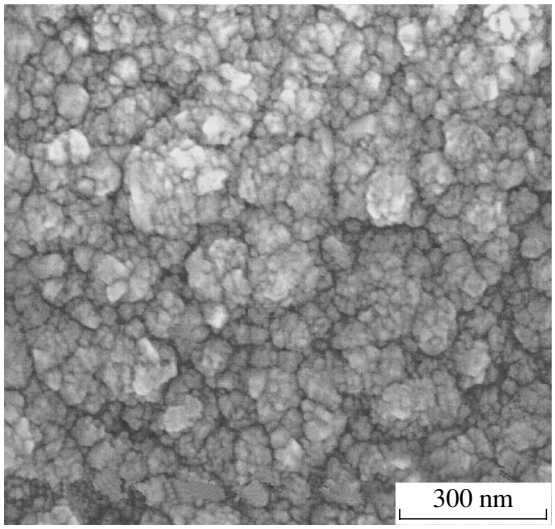

Fig. 1. High-resolution SEM micrograph of an NCD sample.

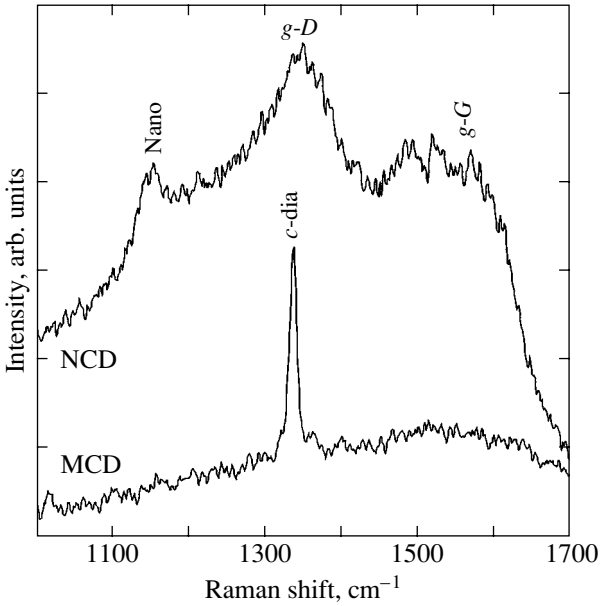

Fig. 2. Typical Raman spectra of an NCD film and MCD film.

This assembly enhances the bias current density when a negative bias is applied to the substrate at low microwave powers without affecting the microwave plasma. The whole growth was performed for 60 min in a single stage run without breaking the bias to the substrate, unlike in the conventional two- or three-stage process for the heteroepitaxial growth of diamond [30, 31]. The applied biasing voltage was varied from 200 to 320 V with all other parameters kept constant. Films were grown at a pressure of 30 Torr (~4000 Pa) with a microwave power of 1000 W at 600°C. The substrate temperature was measured using a thermocouple at the backside of the substrate holder.

Structural characterization of the films was carried out using Raman spectroscopy, x-ray diffraction (XRD), scanning electron microscopy (SEM), and atomic force microscopy (AFM). The laser Raman spectra were obtained in the range 1000–1700 cm^{-1} with a step of 1 cm^{-1}. An Ar^+ laser (λ = 488 nm) with a spot size 200 μm in diameter was used for recording the spectra. The hardness of the films was measured by a nanoindentor (UMIS-2000) using a Berkovich diamond pyramid.

The stress in the films was calculated by measuring the radius of curvature of the substrates before and after the deposition using a modified Stoney equation. The curvature of the films was measured by an Alpha-500 profilometer. The length of a scanned sample segment was 5 mm.

4. PROPERTIES OF NCD FILMS GROWN BY BIASED ENHANCED GROWTH

A high-resolution SEM photograph of the NCD film grown at –200 V is shown in Fig. 1. Careful observation of the micrograph reveals that the film consists of bunches of sharp faceted nanocrystallites less than 30 nm in size. The transmission electron microscopic examination of the same film showed nanocrystallites confined in the form of oriented nanodiamond tubes 10–30 nm in size with a height of a few hundreds of nanometers. Although this structure resembles the columnar or dendritic kind of growth, nanocrystals being confined in nanodiamond tubes is a unique feature of the new approach and method presented in this article. These nanodiamond tubes, having a high packing density of crystallites, appeared to be nearly parallel to the film growth direction. The corresponding electron diffraction patterns were indexed to diamond, with the [111] and [220] diamond textured rings having their texture maxima parallel to the [111] and [220] Si diffraction spots, respectively, when superimposed. This indicates that the majority of the NCD crystallites are preferentially oriented to the Si substrate. On the other hand, the film grown at –320 V, 5% CH_4/H_2, and a substrate temperature of 600°C showed a very different microstructure. This film also had a high packing density but of randomly oriented diamond crystallites 2–5 nm in size. The detailed structure of the NCD film will be published elsewhere [32].

Figure 2 shows the typical Raman spectra of the nanocrystalline films and conventional polycrystalline diamond film. The most significant feature in the Raman spectrum of the NCD film is the intense peak near 1150 cm^{-1} without any feature near 1332 cm^{-1}, an unambiguous signature of cubic crystalline diamond. Although the origin of this peak is assigned to the *trans*-polyacetylene [33], it is widely accepted to be

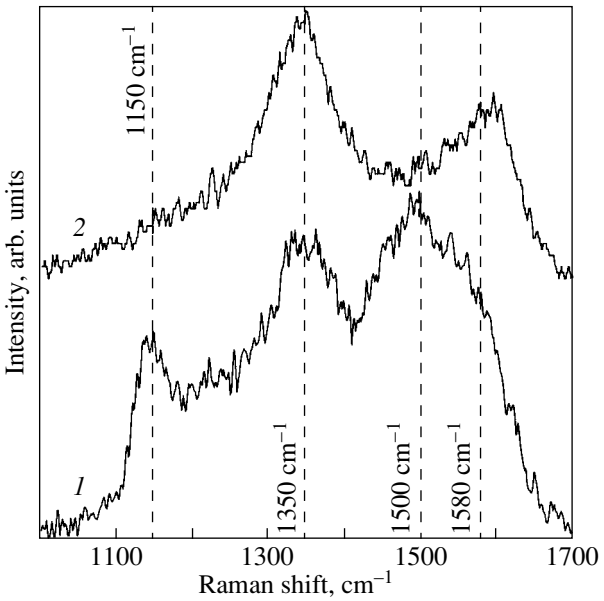

Fig. 3. Raman spectra of NCD films at bias voltages of (*1*) 200 and (*2*) 320 V.

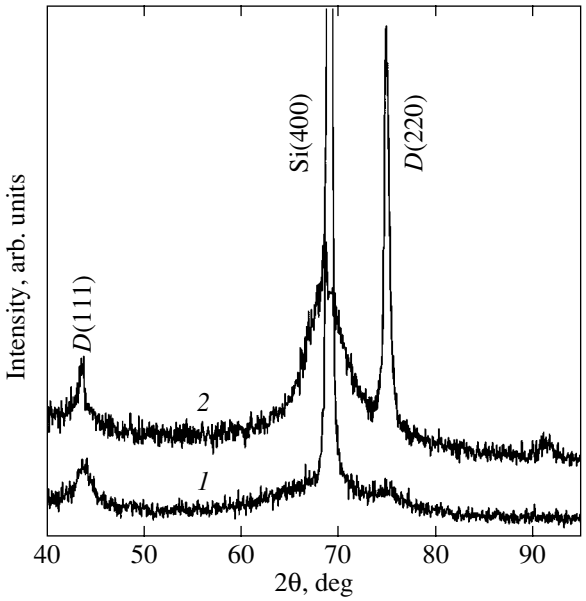

Fig. 4. XRD patterns of the films deposited at a bias voltages of (*1*) 200 and (*2*) 320 V.

related to NCD [34]. The absence of any peak near 1332 cm^{-1}, in spite of having an intense NCD feature, could be due to a high density of defects incorporated in the films but could also be a sign of uniformly distributed short-range sp^3 crystallites in the films [17, 35]. The other significant bands, near 1350 and 1580 cm^{-1}, are well-known graphitic *D* and *G* bands. The Raman feature near 1500 cm^{-1} may be related to the disordered sp^3 carbon in the films [34]. The intensity of this band increases in proportion to the intensity of the NCD feature in the films, as observed by others also [35]. A high density of defects and a significant amount of graphitic carbon are, in fact, expected in the growth of uniformly distributed short-range nanocrystals of diamond because of their large grain boundary area.

Figure 3 shows the Raman spectra of the films deposited on Si(100) at biasing voltages of 200 and 320 V. It should be noted that deposition did not take place when the biasing voltage was lower than 200 V. As can be seen, the intensity of the NCD Raman feature almost vanishes in the films grown at 320 V. Moreover, there is a drastic variation in the position of the graphitic *G* band in the film grown at 320 V. It appears that the relative concentration of sp^3 to sp^2 carbon of the films decreases with biasing voltage in the films. This suggests that the relative intensity of the NCD Raman feature decreases as the biasing voltage increases. In fact, the NCD Raman feature appeared to have almost vanished in the films grown at 320 V. Moreover, there was a drastic variation in the position of the graphitic *G* band in the films grown at 320 V. Overall, it appears that the relative concentration of sp^3 to sp^2 carbon of the films decreases with biasing voltage in the films. However, it should be noted that no peaks associated with graphite could be identified in our films.

The XRD patterns of the films at biasing voltages of 200 and 320 V are shown in Fig. 4. The calculated interplanar spacing corresponding to the peaks at $2\theta \sim 44.05, 75.25 \pm 0.20°$ in the XRD patterns of the films match closely with the interplanar *d* values of the (111) and (220) planes of cubic diamond, respectively. It should be noted that the full width at half maximum (FWHM) of the diamond peaks in the films is in general high as compared to the MCD films. This is well correlated with the fact that diamond nanocrystallites are present in our films. It should be noted that no peaks associated with graphite or features related to amorphous carbon could be identified in our films.

Figure 5 illustrates the summary of the properties grown at different biasing voltages. The hardness of the films decreases with an increase in biasing voltage. Although not shown here, the hardness of NCD films grown by the BEG process at 200 V approaches the hardness of natural diamond when the thickness is increased to 4 μm [22]. The Raman peak ratio I_n/I_g (the ratio of the 1150 cm^{-1} feature to graphite *G* band) varies in the same fashion as the hardness of the films, indicating that the relative concentration of NCD in the films may be responsible for the hardness of the films. The stress in the films increases with increasing bias voltage and increases drastically in the film grown at 320 V. The samples grown at 320 V were visibly bent and accounted for an enormous stress in the films [36]. It should be mentioned that no bending was observed in a sample treated in a separate experiment at a bias voltage of –320 V for an hour using only hydrogen, i.e., without any methane in the gas phase. This means that

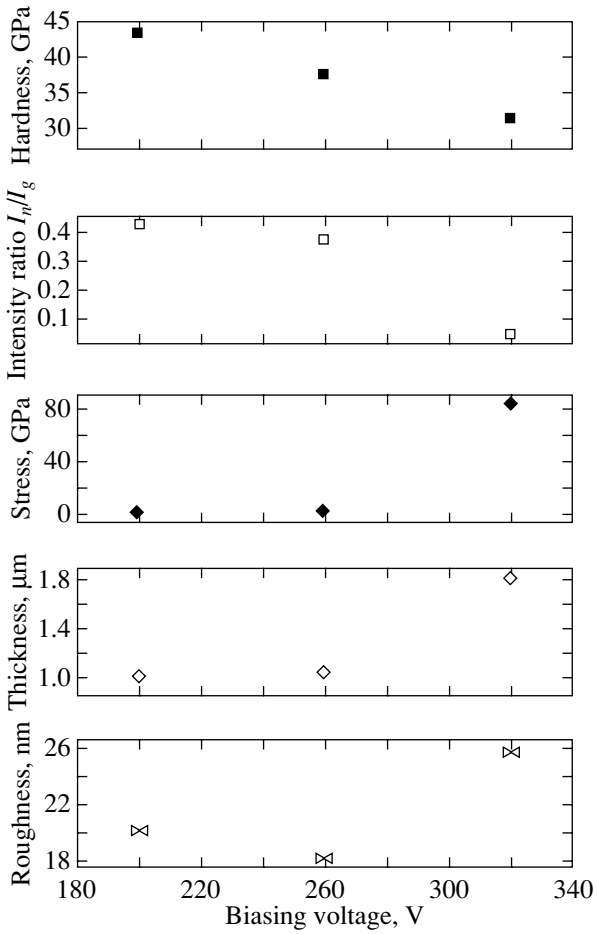

Fig. 5. Plot of hardness, Raman intensity ratio of NCD (I_n) to graphitic *G* band (I_g), compressive stress, layer thickness, and rms surface roughness of the film as a function of the biasing voltage.

the bending occurs solely due to the stress generated in the carbon film deposited on the wafers. To the best of our knowledge, there have not been any reports of such an enormous amount of stress in carbon films. This may be mainly because the films deposited by other groups, if there was a compressive stress greater than 2 GPa, delaminated soon after the deposition due to weak adhesion [37, 38]. However, in our case, a strong adhesion of the films to the substrate is developed, making it possible to observe such a large amount of stress. The strong adhesion in our films may be a result of subplantation of carbon ions with an optimized flux density into the substrate in the initial stages of growth. The layer thickness does not vary much while increasing the biasing voltage from 200 to 260 V but increases drastically at 320 V, almost the same as the stress in the films varied with the biasing voltage. The rms surface roughness of the films first decreases slightly in the film grown at 260 V, followed by a significant increase in the film grown at 320 V.

It should be noticed here that, unlike the case of the growth of ta-C and DLC films by energetic carbon species [38–41], the hardness and stress in the films follow reverse trends with deposition parameters (except in a few cases in temperature series). For example, the hardness in the films decreases with an increase in the biasing voltage and increases with an increase in the methane concentration, whereas the value of the stress in both series follows exactly the reverse trends. Therefore, interestingly, in our case, the NCD film grown under optimum conditions for longer deposition time by the BEG process in the MPCVD system shows the highest hardness with the lowest stress. Another advantage from this new route of growth is that any thickness can be grown because of the strong adhesion of the films to the substrate. The layer thickness first increases gradually up to 35 min of growth, followed by a linear increase with time, as expected. The calculated growth rate under optimum conditions is as high as approximately 1 μm/h.

5. CONCLUSIONS

Nanocrystalline diamond films appear to be quite attractive as smooth diamond films. Several routes for the growth of chemical vapor deposited NCD films were reviewed. Some important results were also highlighted in the growth of NCD films on mirror-polished Si substrates by a particular route in the microwave plasma CVD system termed biased enhanced growth. In a special arrangement made in the microwave plasma CVD system, it was shown that the growth of NCD occurs when a certain negative voltage is applied to the substrate. The NCD characteristics, as assessed by Raman spectroscopy and XRD, decrease, the hardness decreases, and the stress in the films increases as the bias voltage is increased.

REFERENCES

1. D. G. Bhat, D. G. Johnson, A. P. Malshe, *et al.*, Diamond Relat. Mater. **4**, 921 (1995).
2. A. K. Gangopadhyay and M. A. Tamor, Wear **169**, 221 (1993).
3. B. Bhushan, Diamond Relat. Mater. **8**, 1985 (1999).
4. A. Erdemir, G. R. Fenske, A. R. Krauss, *et al.*, Surf. Coat. Technol. **120–121**, 565 (1999).
5. S. K. Choi, D. Y. Jung, S. Y. Kweon, and S. K. Jung, Thin Solid Films **279**, 110 (1996).
6. S. Hogmark, O. Hollman, A. Alahelisten, and O. Hedenqvist, Wear **200**, 225 (1996).
7. D. Zhou, T. G. McCauley, L. C. Qin, *et al.*, J. Appl. Phys. **83**, 540 (1998).
8. T. Sharda and S. Bhattacharyya, in *Encyclopedia of Nanoscience and Nanotechnology*, Ed. by H. S. Nalwa (Am. Sci., California, USA, 2003).
9. L. S. Pan and D. R. Kania, *Diamond: Electronic Properties and Application* (Kluwer Academic, London, 1995).
10. W. Banholzer, Surf. Coat. Technol. **53**, 1 (1992).

11. D. M. Gruen, Annu. Rev. Mater. Sci. **29**, 211 (1999).
12. D. M. Gruen, X. Pan, A. R. Krauss, *et al.*, J. Vac. Sci. Technol. A **12**, 1491 (1994).
13. T. Lin, Y. Yu, T. S. Wee, *et al.*, Appl. Phys. Lett. **77**, 2692 (2000).
14. K. Wu, E. G. Wang, J. Chen, and N. S. Xu, J. Vac. Sci. Technol. B **17**, 1059 (1999).
15. K. Wu, E. G. Wang, Z. X. Cao, *et al.*, J. Appl. Phys. **88**, 2967 (2000).
16. J. Lee, B. Hong, R. Messier, and R. W. Collins, Appl. Phys. Lett. **69**, 1716 (1996).
17. J. Lee, R. W. Collins, R. Messier, and Y. E. Strausser, Appl. Phys. Lett. **70**, 1527 (1997).
18. K. Teii, H. Ito, M. Hori, *et al.*, J. Appl. Phys. **87**, 4572 (2000).
19. S. Yugo, T. Kanai, T. Kimura, and T. Muto, Appl. Phys. Lett. **58**, 1036 (1991).
20. S. T. Lee, H. Y. Peng, X. T. Zhou, *et al.*, Science **287**, 104 (2000).
21. T. Sharda, T. Soga, T. Jimbo, and M. Umeno, Diamond Relat. Mater. **9**, 1331 (2000).
22. T. Sharda, M. Umeno, T. Soga, and T. Jimbo, Appl. Phys. Lett. **77**, 4304 (2000).
23. T. Sharda, T. Soga, T. Jimbo, and M. Umeno, Diamond Relat. Mater. **10**, 1592 (2001).
24. W. B. Yang, F. X. Lu, and Z. X. Cao, J. Appl. Phys. **91**, 10068 (2002).
25. W. Zhu, G. P. Kochanski, and S. Jin, Science **282**, 1471 (1998).
26. A. Gohl, A. N. Alimova, T. Habermann, *et al.*, J. Vac. Sci. Technol. B **17**, 670 (1999).
27. N. S. Xu, J. Chen, Y. T. Feng, and M. J. McNallan, Nature **411**, 283 (2001).
28. E. Maillard-Schaller, O. M. Kuettel, L. Diederich, *et al.*, Diamond Relat. Mater. **8**, 805 (1999).
29. A. Hiraki, Appl. Surf. Sci. **162–163**, 326 (2000).
30. J. Robertson, J. Gerber, S. Sattel, *et al.*, Appl. Phys. Lett. **66**, 3287 (1995).
31. X. Jiang, C.-P. Klages, R. Zachai, *et al.*, Appl. Phys. Lett. **62**, 3438 (1993).
32. T. Sharda and T. Soga (in press).
33. A. C. Ferrari and J. Robertson, Phys. Rev. B **61**, 14095 (2000).
34. R. J. Nemanich, J. T. Glass, G. Lucovsky, and R. E. Shorder, J. Vac. Sci. Technol. A **6**, 1783 (1988).
35. L. C. Nistor, J. V. Landuyt, V. G. Ralchenko, *et al.*, Diamond Relat. Mater. **6**, 159 (1997).
36. T. Sharda, M. Umeno, T. Soga, and T. Jimbo, J. Appl. Phys. **89**, 4874 (2001).
37. F. C. Marques, R. G. Lacerda, G. Y. Odo, and C. M. Lepienski, Thin Solid Films **332**, 113 (1998).
38. R. G. Lacerda and F. C. Marques, Appl. Phys. Lett. **73**, 617 (1998).
39. D. R. McKenzie, D. A. Muller, and B. A. Paithorpe, Phys. Rev. Lett. **67**, 773 (1991).
40. S. Sattel, J. Robertson, M. Scheib, and H. Ehrhardt, Appl. Phys. Lett. **69**, 497 (1996).
41. S. Logothetidis, M. Gioti, P. Patsalas, and C. Charitidis, Carbon **37**, 765 (1999).

Physics of the Solid State, Vol. 46, No. 4, 2004, pp. 726–728. Translated from Fizika Tverdogo Tela, Vol. 46, No. 4, 2004, pp. 707–709.

APPLICATIONS OF NANODIAMONDS

Electrochemical Intercalation of Lithium into Diamond–Pyrocarbon Nanocomposites

T. L. Kulova*, Yu. E. Evstefeeva*, Yu. V. Pleskov*, A. M. Skundin*, V. G. Ral'chenko, S. B. Korchagina***, and S. K. Gordeev*****

** Frumkin Institute of Electrochemistry, Russian Academy of Sciences, Leninskiĭ pr. 31, Moscow, 119071 Russia*

*** Institute of General Physics, Russian Academy of Sciences, ul. Vavilova 38, Moscow, 119991 Russia*

**** Central Research Institute of Materials, St. Petersburg, 193167 Russia*

Abstract—The electrochemical behavior of composite materials based on nanodiamond and carbal is investigated in the course of cathodic intercalation of lithium from an $LiPF_6$ solution in a mixture of propylene carbonate and diethyl carbonate. The amount of lithium intercalated into the composite increases monotonically with an increase in the content of nondiamond carbon. It is concluded that, in the studied composites, the electrochemically active phase is graphite-like carbon distributed over the nano-(micro-)diamond skeleton. The intercalation capacity of carbal is approximately equal to 33 mA-h per gram of graphite-like carbon. © *2004 MAIK "Nauka/Interperiodica".*

1. INTRODUCTION

Nanodiamond–pyrocarbon composite (NDC) materials [1] can serve as model objects for the investigation of various phenomena observed in carbon nanomaterials. In NDC materials, 4- to 5-nm diamond particles are bound through a graphite-like carbon matrix to form a composite. The matrix has the form of a thin layer (less than 1 nm thick) on the surface of the diamond particles. The NDC samples differ in the ratio between the diamond and graphite-like phases, and their specific surface varies from 220 to 350 m^2/g. These materials are characterized by a high open porosity. In recent years, NDC has been investigated as a promising material for field-emission cathodes, sorption, and substrates for the deposition of diamond films [1].

In this work, we investigated the cathodic intercalation of lithium into composite electrodes. Carbon-based electrodes are widely used in lithium-ion accumulators [2]. In these accumulators, the negative electrode is an intercalation compound of lithium with carbon. During charging of the negative electrode, i.e., during cathodic polarization of the electrode in a lithium salt solution in an organic solvent, Li^+ discharges and, then, lithium is incorporated (intercalated) into the carbon crystal lattice:

$$x\mathrm{Li}^+ + xe^- + 6\mathrm{C} \longrightarrow \mathrm{Li}_x\mathrm{C}_6.$$

Upon intercalation of lithium into graphite, the x value changes in the range from 0 to 1. Consequently, the intercalation capacity of graphite amounts to one lithium atom per six carbon atoms or, with allowance made for the Faraday law, 372 mA-h/g. The intercalation capacity is an important characteristic of the accumulator: the greater the intercalation capacity, the better the accumulator. The intercalation and deintercalation should proceed at sufficiently high rates. In this case, the accumulator can be charged and discharged using heavy currents.

The above features of the NDC materials make them interesting for the study of the electrochemical intercalation of lithium. Actually, these materials possess a developed surface of pores, which are covered with a layer of graphite-like carbon; as a result, the entire surface of the pores is accessible for the processes under investigation.

2. EXPERIMENTAL TECHNIQUE

The NDC samples contain particles of detonation nanodiamond (the volume content is 28 vol %) that are bound through a graphite-like (pyrocarbon) matrix. The procedure for synthesizing NDC materials was described earlier in [1]. In the NDC-10, NDC-30, and NDC-40 samples, the contents of graphite-like carbon were equal to 9.1, 23, and 28%, respectively, and the effective thicknesses of the graphite-like layer were 0.2, 0.6, and 0.8 nm, respectively.

Moreover, we studied samples of carbal material. This material is a composite in which diamond particles are also bound through a pyrocarbon matrix [3]. Carbal is an analog of NDC, but its structural units are of a different size. The size of diamond particles is equal to 0.3 μm, the specific surface is 8 m^2/g, the thickness of the graphite-like layer on the surface of diamond grains varies from 10 nm to 1 μm, and the pyrocarbon content is 29%.

The electrodes were examined in model cells containing one working electrode, two lithium counterelec-

1063-7834/04/4604-0726$26.00 © 2004 MAIK "Nauka/Interperiodica"

trodes, and a lithium reference electrode [4]. All the electrodes used were isolated from each other by separators fabricated from a PORP porous polypropylene. The working electrodes were preliminary dried under vacuum at a temperature of 130°C for 8 h.

The model cells were assembled in a glove box in an argon atmosphere. A 1 *M* $LiPF_6$ solution in a 1 : 4 mixture of propylene carbonate and diethyl carbonate was used as an electrolyte. The water content in the electrolyte was measured according to the Fischer method and did not exceed 50 ppm.

The cycling of the composite electrodes (cathodic intercalation and anodic deintercalation of lithium) was performed under galvanostatic conditions at a current density of 0.02–0.12 mA/cm^2 (3 mA per gram of graphite-like carbon). The voltage across the lithium electrode was varied in the range from 2.00 to 0.01 V.

The spectra of the electrochemical impedance in the frequency range from 0.01 Hz to 100 kHz were measured on a Solartron (Model 1250) spectral analyzer equipped with an electrochemical interface (Model 1286).

3. RESULTS AND DISCUSSION

The charge–discharge curves of the NDC-10, NDC-30, NDC-40, and carbal samples are shown in Fig. 1. For all samples, the charge–discharge curves have a shape typical of the curves obtained for nongraphitized carbon. Specifically, the charge–discharge curves have no clearly defined plateaus in the vicinity of the lithium potential (0 V). Cathodic polarization is accompanied not only by lithium intercalation (i.e., the process responsible for the reversible capacity) but also by reduction of the electrolyte (the process responsible for the irreversible capacity). This concurrent process is most pronounced during the first cycle. The reduction of the electrolyte at the electrode surface results in the formation of an inert film. The film prevents further reduction of the electrolyte but does not hinder the intercalation–deintercalation of lithium, because it is conductive with respect to the Li^+ ions. The ratio of the anodic quantity of electricity to the cathodic quantity (the Coulomb efficiency of cycling) for all NDC samples is equal to 1.5–2.0% during the first cycle. Note that the Coulomb efficiency of cycling of the carbal sample during the first cycle is one order of magnitude higher than that for the NDC samples.

The amount of lithium incorporated into the NDC sample increases monotonically as the content of nondiamond carbon increases from the vanishingly small value for the NDC-10 sample to the value corresponding to ~10 mA h per gram of graphite-like carbon for the NDC-40 sample. Therefore, it can be concluded that, in the NDC samples, the electrochemically active phase is graphite-like carbon distributed over the nanodiamond skeleton.

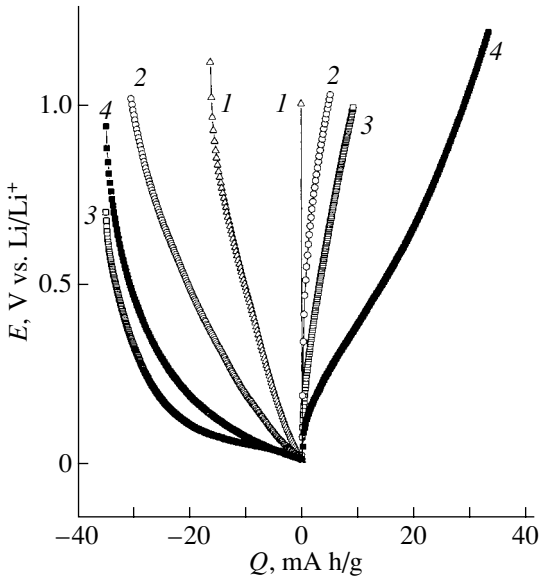

Fig. 1. Charge–discharge curves of negative electrodes in an LP-20 electrolyte: (*1*) NDC-10 (9.1% graphite-like carbon), (*2*) NDC-30 (23% graphite-like carbon), (*3*) NDC-40 (28% graphite-like carbon), and (*4*) carbal. The current densities are 3 and 6 mA per gram of graphite-like carbon for the NDC and carbal samples, respectively.

A similar situation occurs with field electron emission from NDC materials [5] when graphite-like layers serve as emission centers. The presence of diamond nanoparticles determines the geometry of these layers (quasi-two-dimensionality) and its attendant quantum-well effect.

The charge–discharge curves of the carbal sample differ significantly from those of the NDC samples both in the shape and the amount of accumulated electricity. The deintercalation capacity of carbal amounts to approximately 33 mA-h per gram of graphite-like carbon, i.e., approximately 10% of the theoretical limit for the LiC_6 stoichiometry. An increase in the intercalation capacity for the carbal sample can be explained by the greater thickness of the graphite-like carbon film (in the NDC samples, the film is considerably thinner: it can comprise only a few graphite layers, and, therefore, the intercalation possibilities for lithium are reduced to a minimum) and the higher degree of ordering of graphite layers deposited on coarser diamond particles in carbal.

Figure 2 shows the impedance loci measured for the carbal electrode in a working solution before (curve *1*) and after (curve *2*) the intercalation of lithium. Each locus represents a distorted semicircle and corresponds approximately to the equivalent circuit presented in the inset. The elements of this circuit were determined by minimizing the mean-square deviation of the modulus of the measured impedance from the modulus of the impedance calculated with a computer program [6].

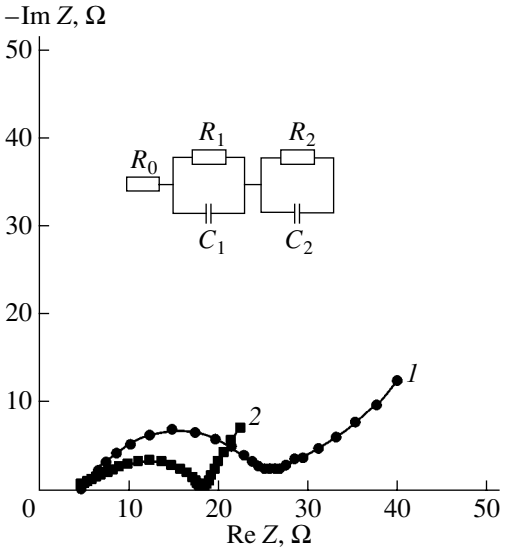

Fig. 2. Impedance loci of the carbal electrode in a working solution (*1*) prior to and (*2*) after intercalation of lithium. The inset shows the equivalent circuit of the electrode.

The physical meaning of the elements constituting the equivalent circuit is not determined completely. It can be assumed that the resistance R_0, which remains unchanged upon the intercalation of lithium, accounts for the bulk resistance of the composite electrode and the electrolyte; the circuit (R_1C_1) corresponds to the electrode–electrolyte interface; and the circuit (R_2C_2) characterizes the intercalation of lithium. After the incorporation of lithium, the differential capacitance C_2 for the carbal electrode increases by one order of magnitude. The variations in the loci for the NDC sample are considerably less pronounced, which can be explained by the smaller amount of intercalated lithium.

At present, it is difficult to evaluate the prospects for using (nano)diamond–pyrocarbon composites in chemical sources of electric energy. However, the first results indicate that investigation of the intercalation of lithium is an informative method for evaluating the electrical and electrochemical characteristics of the composites.

ACKNOWLEDGMENTS

This work was supported by the Russian Foundation for Basic Research, project no. 01-03-32045.

REFERENCES

1. S. K. Gordeev, in *Nanostructured Carbon for Advanced Applications*, Ed. by G. Benedek *et al.* (Kluwer, Dordrecht, 2001), p. 71.
2. A. M. Skundin, O. N. Efimov, and O. V. Yarmolenko, Usp. Khim. **71** (4), 378 (2002).
3. E. P. Smirnov, S. K. Gordeev, Yu. I. Nikitin, *et al.*, Dokl. Akad. Nauk SSSR **274** (4), 887 (1984).
4. O. V. Komarova, T. L. Kulova, and A. M. Skundin, Élektrokhim. Énerg. **2** (3), 121 (2002).
5. A. V. Karabutov, V. D. Frolov, V. I. Konov, *et al.*, J. Vac. Sci. Technol. B **19**, 965 (2001).
6. B. A. Boukamp, Solid State Ionics **20**, 31 (1986).

Translated by N. Korovin

Physics of the Solid State, Vol. 46, No. 4, 2004, pp. 729–732. Translated from Fizika Tverdogo Tela, Vol. 46, No. 4, 2004, pp. 710–713.

APPLICATIONS OF NANODIAMONDS

Use of Ultrafine-Dispersed Nanodiamond for Selective Deposition of Boron-Doped Diamond Films

V. V. Dvorkin*, N. N. Dzbanovskiĭ*, A. F. Pal', N. V. Suetin*, A. Yu. Yur'ev*, and P. Ya. Detkov*****

**Skobel'tsyn Research Institute of Nuclear Physics, Moscow State University, Vorob'evy gory, Moscow, 119992 Russia*

***Troitsk Institute for Innovation and Thermonuclear Research, Troitsk, Moscow oblast, 142190 Russia*

e-mail: afpal@triniti.ru

****All-Russia Zababakhin Research Institute of Technical Physics, Russian Federal Nuclear Center, Snezhinsk, Chelyabinsk oblast, 456770 Russia*

Abstract—A suspension of ultrafine-dispersed nanodiamond was used for introducing (in particular, selectively) high-density centers of diamond nucleation on various substrates. High-quality doped diamond films to be used as electrochemistry electrodes were deposited from the gas phase in a microwave discharge on certain substrates treated using ultrafine-dispersed nanodiamond. A uniform distribution of nucleation centers with concentrations greater than 10^{10} cm^{-2} on silicon substrates was obtained. Electrochemical current–potential curves were measured for continuous films. Diamond meshes of different transparency were grown using selective nucleation. Successful production of high-quality doped diamond meshes gives grounds to consider them the most promising electrodes for use in electrochemistry. © *2004 MAIK "Nauka/Interperiodica".*

1. INTRODUCTION

One of the most promising applications of semiconductor diamond is its use as electrodes for electrochemical processes [1]. The method of realizing hole conduction in diamond is well known and consists in diamond doping with boron, which is quite easily activated even at room temperature [2–5]. In this case, the resistivity is controlled by the density of boron atoms in the diamond crystal lattice, the defect density, the average crystallite size, and the properties of intercrystallite regions, where charge carriers are scattered.

The service life of a diamond film electrode is determined not only by the electrochemical stability of the diamond itself but also by the properties of the intercrystallite regions (the film is polycrystalline). Diamond electrodes are most sensitive to microscopic punctures. Indeed, the thickness of a diamond coating must be as small as possible to reduce costs. However, since the initial nucleation is nonuniform, the density of diamond nucleation centers is also nonuniform; therefore, films that are several microns thick must be grown in order to "heal" all the punctures. Our measurements show that even the presence of submicron punctures in a film can result in degradation of the entire electrode due to the penetration of the electrolyte into the substrate, its etching, and the separation of the diamond film. On the other hand, with increasing film thickness, the problem of film separation arises due to large internal stresses caused by the difference between the coefficients of thermal expansion of the substrate and the film.

Thus, the development of a technique for homogeneous nucleation with a nucleation center density exceeding 10^9 cm^{-2} is of fundamental importance for producing diamond electrodes. The mechanical grinding by diamond powders that is traditionally employed cannot be applied because of the low homogeneity and high defect density. We believe that the introduction of nucleation centers by using detonation nanodiamonds and polymers (photoresists) would be the most appropriate technique for this purpose. In this method, a nanodiamond powder (of ASDU grade) is mixed with a photoresist and then is deposited on a substrate. At the beginning of the deposition, the substrate is treated by a hydrogen plasma, with the result that the polymer is removed and the remaining nanodiamond particles become nucleation centers.

The development of a technique for selective deposition of doped diamond films [6, 7] is an important problem, since in discontinuous films there is practically no internal stress (or it is strongly reduced), the working area is increased, and one can use free meshes as electrodes without substrates susceptible to etching. Experiments on the deposition of boron-doped diamond films or on selective growth of diamond films are well known; however, we are not aware of any studies where the possibility of selective deposition of high-quality conducting submicron diamond films is demonstrated.

The present study deals with the gas-phase deposition (including selective deposition) of high-quality

1063-7834/04/4604-0729$26.00 © 2004 MAIK "Nauka/Interperiodica"

boron-doped diamond films in a resonator-type reactor in which the process is activated by microwave discharge. We also studied the possibility of using the prepared samples as electrodes for electrochemical applications. Diamond films were deposited from a H_2 + C_2H_5OH + $B(CH_3O)_3$ gas mixture in a microwave plasma. The morphology and the crystalline structure of the deposited films were studied. We measured and analyzed the current–potential curves for diamond films deposited on different substrates placed in an inert electrolyte solution.

2. EXPERIMENTAL

2.1. Selective Deposition

The substrates were Si(100) plates with a resistivity of 4.5 Ω cm and linear dimensions of $15 \times 15 \times 0.4$ mm. To obtain a high density of nucleation centers, we used seeds of nanocrystalline ultrafine-dispersed diamond following the method described above. In order to improve the homogeneity of the original distribution of nucleation centers, a nanodiamond suspension in a photoresist was deposited on the surface by centrifuging. The nanodiamond concentration and the deposition modes were chosen so as to produce a homogeneous distribution of nucleation centers with a density of 10^{10}–10^{11} cm^{-2}. For selective deposition of diamond films, the photoresist film containing a diamond nanopowder was selectively removed from specific surface areas by using standard lithographic techniques.

2.2. Mechanical Deposition

A number of metal substrates for the deposition of continuous diamond films were prepared by using the standard procedure of mechanical grinding of the metal surface by a nanodiamond suspension.

2.3. Experimental Setup

The resonator-type microwave setup used in our experiments was constructed according to the classical scheme: an mw waveguide, a gas pipe, and a discharge chamber. In the course of the deposition, the plasma emission spectrum was measured by using a spectroscopic system.

We used a 6-kW magnetron (frequency 2.45 GHz) as a source of mw energy in our setup. The discharge was ignited immediately above the substrate on which a diamond film was deposited.

Films were deposited from H_2 + C_2H_5OH + $B(CH_3O)_3$ mixtures. Boron- and carbon-containing substances were transported to the chamber by passing hydrogen through alcohol with dissolved trimethyl borate. The liquid phase was placed in a special temperature-stabilized evaporator, and the percentage of the vapor in the gas mixture was controlled by the temperature and pressure in the evaporator chamber.

2.4. Diamond-Film Deposition Conditions

The deposition conditions were as follows: the mw power varied from 700 to 1200 W, the H_2 flow rate was 10 l/h, the content of C_2H_5OH + $B(CH_3O)_3$ in the gas mixture varied from 7 to 13.6%, the content of $B(CH_3O)_3$ in the liquid mixture was 3%, the chamber pressure was 80 Torr, and the substrate temperature was ~800°C. To burn the photoresist out, each sample was subjected to prior annealing in a hydrogen atmosphere at a pressure of 45 Torr and a temperature of 600°C for 10 min.

2.5. Sample Properties

The structure and properties of the deposited diamond films were studied. The morphology of the films was monitored by scanning electron microscopy (SEM), and the phase composition, by Raman spectroscopy. The density of nucleation centers was estimated with a tunneling microscope. The electrode characteristics of the films (current–potential curves) were measured in an electrochemical cell in a solution of an inert (0.5 M H_2SO_4) electrolyte.

3. DISCUSSION

Using the deposition method described in the previous section, we were able to achieve densities of the nucleation centers exceeding 10^{10} cm^{-2}, which was demonstrated by scanning electron and tunneling microscopy studies. However, it is seen from Fig. 1a that micropunctures can appear in the film due to inhomogeneity, which can arise during the nanodiamond deposition on the substrate. Although the micropunctures are healed as the film thickness increases, they are potential sites for the appearance of macropunctures, resulting from etching of the intercrystallite nanodiamond (Fig. 1b). The appearance of such macropunctures leads to fast etching of the substrate material and, as a result, to the separation of some parts of the diamond coating of the electrodes and to a change in the properties of the electrochemical cell.

As noted above, an important characteristic of high-quality electrodes is the resistivity, which depends both on the carrier density (i.e., on the boron ion density in the lattice) and on the carrier mobility, which is limited by scattering from intercrystallite boundaries and defects. The same factors determine the important properties of fabricated electrodes, such as the corrosion resistance, stability, background current, and the interval of potentials where the current remains sufficiently low and these characteristics can be measured.

Current–potential curves for inert (0.5 M H_2SO_4) electrolyte solutions are considered a basic characteristic of the behavior of diamond electrodes.

We performed a series of experiments on the growth of polycrystalline diamond films on substrates of a number of metals and alloys. The results from cyclic

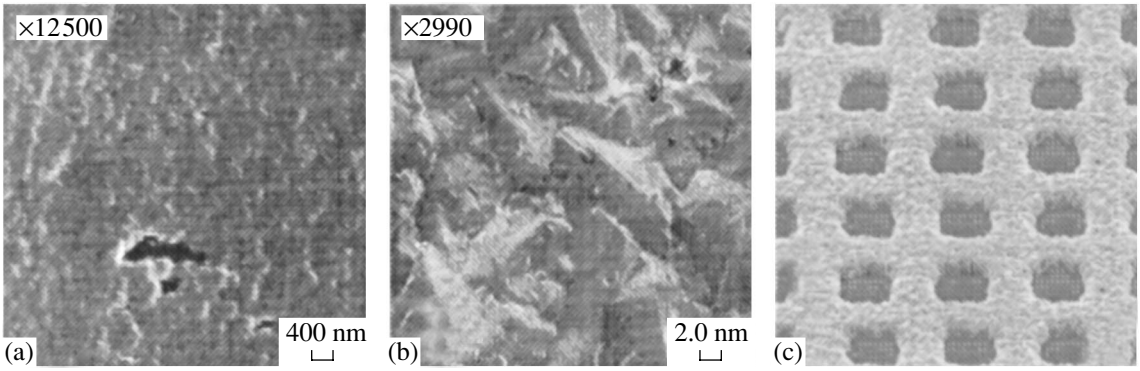

Fig. 1. SEM images of (a) micropunctures on the surface of a continuous diamond film, (b) a macropuncture on the surface of a continuous diamond film, and (c) a selectively deposited doped diamond film.

voltammetry of samples on titanium, tungsten, and molybdenum substrates are shown in Fig. 2; the potential (in volts) with respect to the normal hydrogen electrode is plotted on the *x* axis, and the current (in A cm^{-2}), on the *y* axis.

Micron-thick diamond films were obtained through the deposition on titanium substrates. However, SEM analysis revealed the presence of micro- and macropunctures and microcracks in these films, which are apparently due to the difference in the coefficients of thermal expansion of the contacting materials resulting in the formation of residual stresses in diamond films upon cooling after deposition. When such films were placed in an active medium during electrochemical tests, they degraded quickly (Fig. 2a). The results of the studies reported in [8, 9] show that the deposition of an additional buffer carbide layer for diamond films grown on titanium makes it possible to achieve good adhesion of a film to the substrate and to grow high-quality diamond films with virtually no microdefects. However, the growth of a carbide layer depends on a number of factors (for example, on the titanium quality) and presents a separate complicated problem. Applications of such additional methods of improving the diamond film adhesion to the substrate material are beyond the scope of this work and are not discussed in this study.

Doped diamond films deposited on tungsten showed excellent properties, such as the width of the low-current region (the ideal-polarizability range) and the smoothness of the current–potential curves (Fig. 2b). However, long tests of these electrodes showed slow degradation of the films in an active medium, which is manifested as an increase in the background currents and a narrowing of the ideal-polarizability region with time.

Current–potential curves for doped diamond films on molybdenum substrates (Fig. 2c) are less smooth than those for diamond films on tungsten, but the films on molybdenum do not degrade with time under the same conditions. Therefore, of all the metals under study, molybdenum is the best substrate material for making diamond-film electrodes.

For a further increase in the service life of diamond-film electrodes, it is possible not to put the substrate into an electrolyte solution; e.g., the substrate material can be separated from the diamond film by etching. However, this leads to a considerable decrease in the strength characteristics of the diamond membrane, in particular, due to the presence of internal stresses, which always appear during the growth of polycrystalline films.

One can exclude the factor of internal stresses by depositing diamond films selectively, which simultaneously increases the electrode surface area. Selective deposition can be realized by using our method of introducing nucleation centers; in this case, we can produce practically any film pattern directly during film deposition. The characteristic scale of the pattern is restricted only by the growth of the internal well walls.

The boron density in diamond films affects the film quality and, therefore, its chemical stability. One of our goals was to determine the boron density that provides both a high conductivity and sufficient chemical stability of the films. Hall effect measurements performed by us for a number of diamond films with different doping impurity densities show that the optimal boron density is about 10^{18} cm^{-3}. For greater boron densities in a film, a strong degradation of its structure occurs, resulting in a decrease in the stability of diamond films against the action of an electrolyte. With decreasing boron density accompanied by a decrease in conductivity, no visible improvement in the diamond quality was observed.

The doped films of the highest quality were obtained at a pressure of 80 Torr, a power of 900 W, and a concentration of the liquid mixture in hydrogen of 13.6%. A SEM photograph of one of such samples is shown in Fig. 1c.

Current–potential curves for selectively grown boron-doped diamond films were not measured. This will be the subject of future studies.

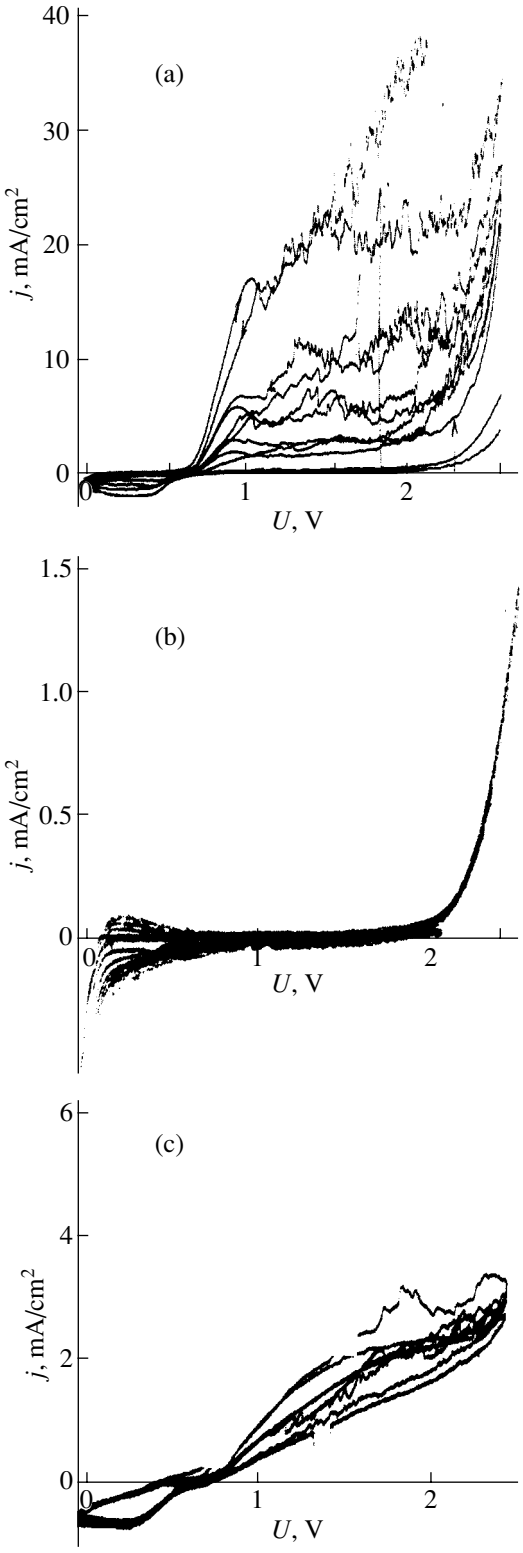

Fig. 2. Current–potential curves for a 0.5-M H_2SO_4 electrolyte solution and films grown on (a) Ti, (b) W, and (c) Mo.

4. CONCLUSIONS

It has been shown that boron-doped high-quality diamond films can be deposited both uniformly and selectively by using nanodiamond powders and the method described above; these films can be used as electrodes in electrochemistry. The optimum growth parameters have been found, and the conditions for stable production of such films have been determined. The application of the seed technique has made it possible to obtain a uniform distribution of nucleation centers with concentrations no less than 10^{10} cm^{-2}.

Our measurements of the current–potential curves for a number of metals have indicated that molybdenum plates were the best for their use as substrates in the production of diamond electrodes for electrochemistry without additional adhesive preparation of the substrate. The possibility of further improvements of the electrode parameters by using free diamond meshes for the same applications has been demonstrated.

ACKNOWLEDGMENTS

The authors thank É.A. Poltoratskiĭ, G.S. Rychkov, and V.G. Pirogov for their assistance in this study.

This study was partially supported by NATO (grant no. SfP-974354), and ISTC-2484.

REFERENCES

1. Yu. V. Pleskov, *Electrochemistry of Diamond* (Editorial URSS, Moscow, 2003).
2. T. Saito, K. Ohtsubo, S. Tsuruga, *et al.*, Electrochem. Soc. Proc. **97-32**, 88 (1988).
3. M. G. Ermakov, A. S. Vedeneev, O. N. Ermakova, *et al.*, Electrochem. Soc. Proc. **97-32**, 658 (1998).
4. C.-F. Chen, S.-H. Chen, T.-M. Hong, and T.-C. Wang, Thin Solid Films **248**, 149 (1994).
5. J. Stiegler, J. Michler, E. Blank, *et al.*, Thin Solid Films **352**, 29 (1999).
6. J. L. Davidson, C. Ellis, and R. Ramesham, J. Electron. Mater. **18** (6), 711 (1989).
7. W. Hänni, C. Muller, M. Binggeli, *et al.*, Thin Solid Films **236** (1–2), 87 (1993).
8. G. Heinrich, T. Grögler, S. M. Rosiwal, *et al.*, Diamond Relat. Mater. **5**, 304 (1996).
9. L. Schäfer, M. Fryda, D. Herrmann, *et al.*, in *Proceedings of the 6th Applied Diamond Conference / Second Frontier Carbon Technology Joint Conference (ADC/FCT 2001)* (Auburn, USA, 2001), p. 158.

Translated by I. Zvyagin

Physics of the Solid State, Vol. 46, No. 4, 2004, pp. 733–737. From Fizika Tverdogo Tela, Vol. 46, No. 4, 2004, pp. 714–717.

APPLICATIONS OF NANODIAMONDS

Modification of the Physical Properties of Chemical Vapor-Deposited Nanostructure Diamond by Argon–Hydrogen Plasma Surface Treatment[1]

Y. Hayashi, D. Mori, T. Soga, and T. Jimbo

Department of Environmental Technology and Urban Planning, Nagoya Institute of Technology, Nagoya, 466-8555 Japan

e-mail: hayashi.yasuhiko@nitech.ac.jp

Abstract—Nanostructure diamond (NSD) film with a hardness as high as 70 GPa and an average surface roughness of 10 nm has been synthesized by the two-step negative substrate bias method combined with post-growth Ar–H_2 plasma irradiation. The Ar–H_2 plasma irradiation has been confirmed to improve the uniformity of grain size and shape and increase the hardness of the NSD film. © *2004 MAIK "Nauka/Interperiodica".*

1. INTRODUCTION

Compared with the polycrystalline diamond film, the nanostructure diamond (NSD) film is very attractive for many industrial applications due to their unique bulk and surface properties, such as a high optical band gap, high hardness, high thermal conductivity, and low electrical conductivity by doping [1–3]. The smoother surface and the wide band gap provide the opportunity to act as ideal transparent protective films on optical components [4]. Polishing of polycrystalline diamond with either chemical or mechanical methods seems to be impractical due to its extreme hardness and chemical inertness. Thus, efficient approaches have to be exploited to grow the transparent diamond film through reducing micrometer-scale diamond grains to nanometer scale [5]. Moreover, the possibilities of microelectromechanical systems (MEMS) and nanoelectromechanical systems (NEMS) devices by using ultrananocrystalline diamond (UNCD) have been explored by Gruen *et al.* [6].

Nanocrystalline diamond has been successfully grown with a microwave plasma-enhanced chemical vapor deposition (MPECVD) using either CH_4–H_2 or Ar–CH_4 gas mixtures and a fullerene–argon mixture as a precursor [1, 7–9]. The morphology of the diamond film depends on the reactant gases, their mixing ratios, negative substrate bias, and the substrate temperature. CVD diamond films are most commonly grown using low partial pressures of CH_4 in H_2. As the partial pressure of CH_4 increases, the crystalline morphology disappears and diamond-like carbon (DLC), which contains a both low quality and graphite-like phase, is formed. In recent years, it has been found that growth under specific conditions between these two extremes can yield high-quality diamond films containing small NSD in disordered graphite.

It is well known that grain size is one the important factors influencing the properties of NSD films. However, the nucleation mechanism and properties of NSD films remain poorly understood because of the difficulty in locating and controlling nucleation sites. In this report, we investigate the properties of an NSD film deposited by a MPECVD with a two-step negative substrate bias and post-growth H_2–Ar plasma irradiation. The two-step substrate bias (SB) process, consisting of a high negative SB at bias-enhanced nucleation (BEN) for a short time followed by a lower negative SB at bias-enhanced growth (BEG), makes it possible to control hydrogen ion energy in the plasma, which is expected to play a dominant role in surface modification and hardness of the NSD film [9, 10]. We will discuss the effect of the substrate temperature at the BEG step and H_2–Ar plasma irradiation after NSD deposition.

2. EXPERIMENTAL

The NSD films were deposited in a 2.45 GHz MPECVD system with a two-step negative substrate bias to reduce the residual stress and the surface roughness. The mirror-polished Si(100) substrates, pretreated in an aqueous solution of HF (HF : H_2O = 1 : 1 by volume) to remove the oxide, were set on a molybdenum (Mo) holder. Then, they were cleaned with H_2 plasma for 20 min at 900°C. The CH_4 concentration, microwave power (MP), and total pressure were maintained at 5%, 1000 W, and 30 Torr, respectively. The growth time at the BEN and BEG steps were 5 and 60 min,

[1] This article was submitted by the authors in English.

1063-7834/04/4604-0733$26.00 © 2004 MAIK "Nauka/Interperiodica"

respectively. The substrate temperature was varied from 400 to 800°C while keeping the substrate bias at BEN of –300V. After deposition, NSD films were treated by the mixture of Ar–H_2 plasma irradiation with different Ar/(H_2+Ar) ratios at MP of 1000 W for 30 min.

The surface morphological features of the nucleation stage in NSD films were examined using a Seiko Instruments SPI-3800N CAFM system with a Pt probe in a vacuum of 10^{-7} Torr. Structural characterizations of the films were carried out with Raman spectra in the back-scattering geometry using the 514.5 nm line of an Ar^+ ion laser at room temperature in the spectral range from 900 to 1800 cm^{-1} with a resolution of 1.0 cm^{-1}. The crystallographic structure and crystallinity of NSD films were investigated by x-ray diffraction (XRD) with a quite shallow incident x-ray angle using Cu K_α radiation. The hardness of the films was measured by a nanoindentor (UMIS-200) using a Berkovich diamond pyramid. The deposition rate was around 600–1800 nm/h, and, in order to minimize the substrate effect on the hardness measurements, maximum loading force did not exceed 10 mN. Therefore, the indentation depth was kept within the critical depth (the maximum penetration depth should not exceed 10% of the film) beyond which there would be severe effects in the hardness measurement of the film from the substrate. Both the UMIS and indenter tip were calibrated using a fused silica standard with known material properties.

3. RESULTS AND DISCUSSION

We first investigated the surface morphology of NSD films in detail. CAFM shows a clear morphological change with variation of the substrate temperature, as shown in Figs. 1a–1d. For a substrate temperature of 600°C, large cauliflower-like clusters 100–130 nm in diameter, composed of many small and uniform grains 30–50 nm in diameter, were obtained, as shown in Fig. 1c. The morphology of the cluster changes from cauliflower-like to columnar above 700°C. The size and shape of the clusters strongly depend on the substrate temperature. We clearly find, as shown in Fig. 1a, a high uniformity of the trapezoidal (columnar) shape clusters composed of small grains, 200 nm square and 100 nm high, which are connected with each other and enhance the alignment of nuclei below 500°C. In other words, a high density (or coverage) of {100}-oriented, textured grains has been obtained. For a substrate temperature above 700°C, some portion of the small grains coalesces together to form crystallites, while the boundary of the crystallite contains individual grains. The current value of the conducting region increased with an increase in the substrate temperature. Comparison of the CAFM current image of NSD films deposited between 400 and 700°C revealed that the conductive difference is at least one order of magnitude. Thus, the surface graphitization of the depositing NSD film might be produced from films deposited above 700°C. The average roughness (Ra) and root mean square (RMS) roughness, as shown in the inset to Fig. 2a, decreased from 9.8 and 12.5 nm to 9.0 and 11.3 nm, respectively, as the substrate temperature was increased from 400 to 500°C. However, both the Ra and RMS again increase as the substrate temperature is increased above 600°C. Figures 1e and 1f show the typical surface morphologies of NSD films deposited at 500°C, as shown in Fig. 1b, and irradiated by Ar–H_2 plasma with Ar concentrations of 50 and 100%, respectively. It is clear that a significant morphological change was observed with Ar–H_2 plasma irradiation as compared to the cauliflower-like surface morphology of the NSD film deposited at 500°C, as shown in Fig. 1b. Moreover, both the Ra and RMS of CAFM, which are shown in the inset to Fig. 2b, remained almost unchanged and the relation between the surface roughness and Ar concentration could not be established. Both the Ra and RMS slightly decrease and the density of small clusters increases with the introduction of the Ar–H_2 plasma irradiation after NSD deposition. The uniformity of the size and shape of the grains is improved by the Ar–H_2 plasma irradiation. Therefore, the surface of NSD film turns out to be smoother. We also observed a significant difference in the grain boundary from the NSD film (not shown here) irradiated by only H_2 plasma (Ar = 0). The surface roughness of CAFM increased with an increase in the H_2 plasma exposure time.

Figure 2a shows the hardness–penetration curves of NSD films with different substrate temperatures indented to a maximum load of 10 mN. The inset to Fig. 2a illustrates the CAFM roughness of NSD films as a function of the substrate temperature. The data show that the hardness of the NSD film is constant over the 35- to 60-nm penetration depth range and that there is almost no influence of the substrate on the measured hardness values. The hardness increases with an increase in the temperature up to around 600°C and decreases with a further increase in temperature. The maximum hardness of 68 GPa was obtained from the NSD film deposited at 500°C. The hardest NSD film was obtained where the CAFM values of Ra and RMS were minimum. Figure 2b shows the hardness–penetration curves of the Ar–H_2 plasma–irradiated NSD films with different Ar concentration. The inset to Fig. 2b illustrates the CAFM roughness of NSD films as a function of the Ar concentration during Ar–H_2 plasma irradiation after NSD deposition. The as-grown NSD film was deposited at a substrate temperature of 600°C, and the initial hardness of NSD film was 60 GPa. It is clear that the film hardness increased from 60 to 70 GPa with an increase in the Ar concentration during Ar–H_2 plasma irradiation. Here, it is worth noting that the hardness of the film irradiated by only H_2 plasma (40 GPa) decreases significantly as compared to that of

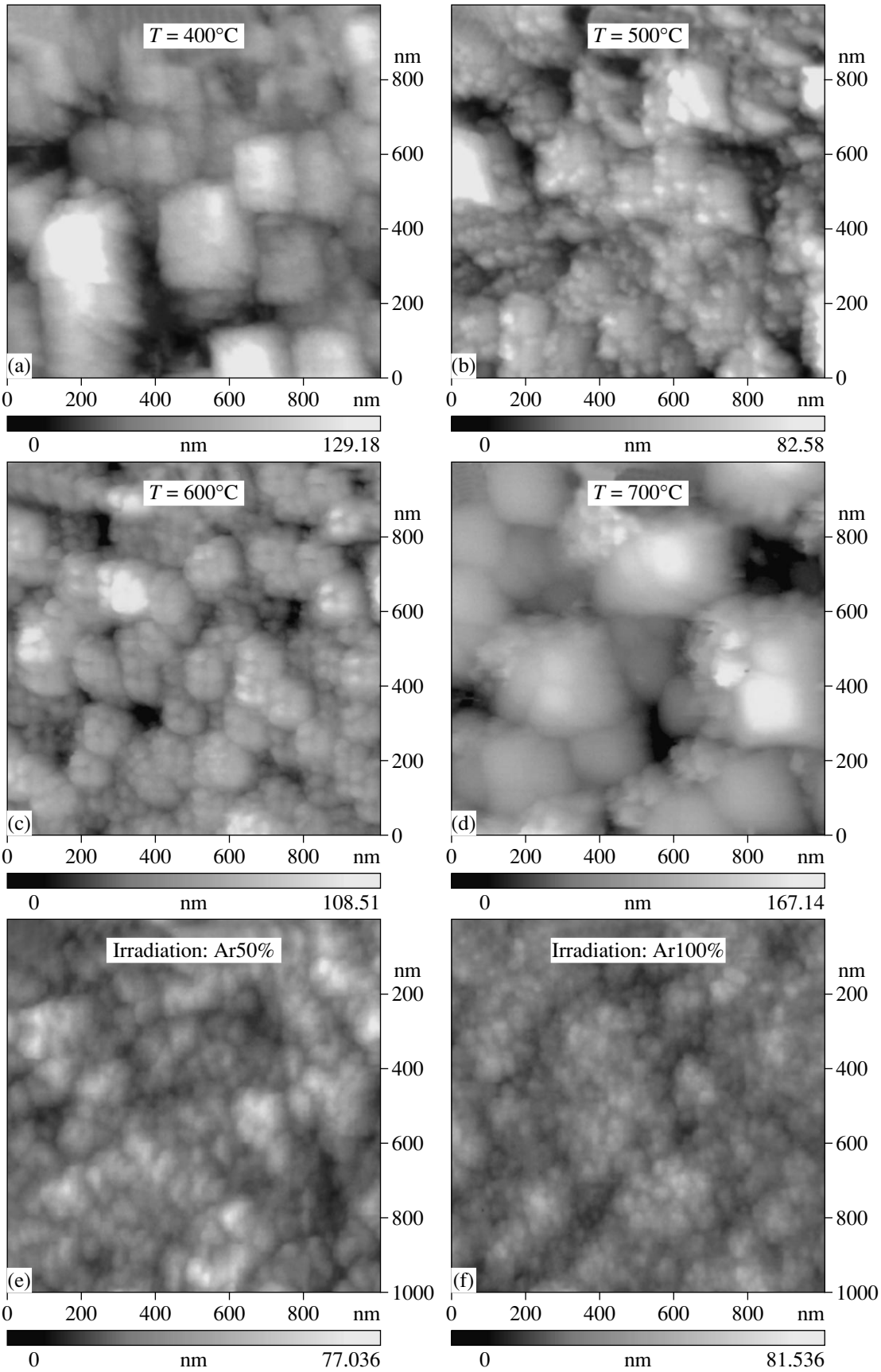

Fig. 1. CAFM surface morphologies of the NSD films deposited at (a) 400, (b) 500, (c) 600, and (d) 700°C and the NSD films irradiated by Ar–H_2 plasma with Ar concentrations of (e) 50 and (f) 100% scanned in 1×1 μm^2.

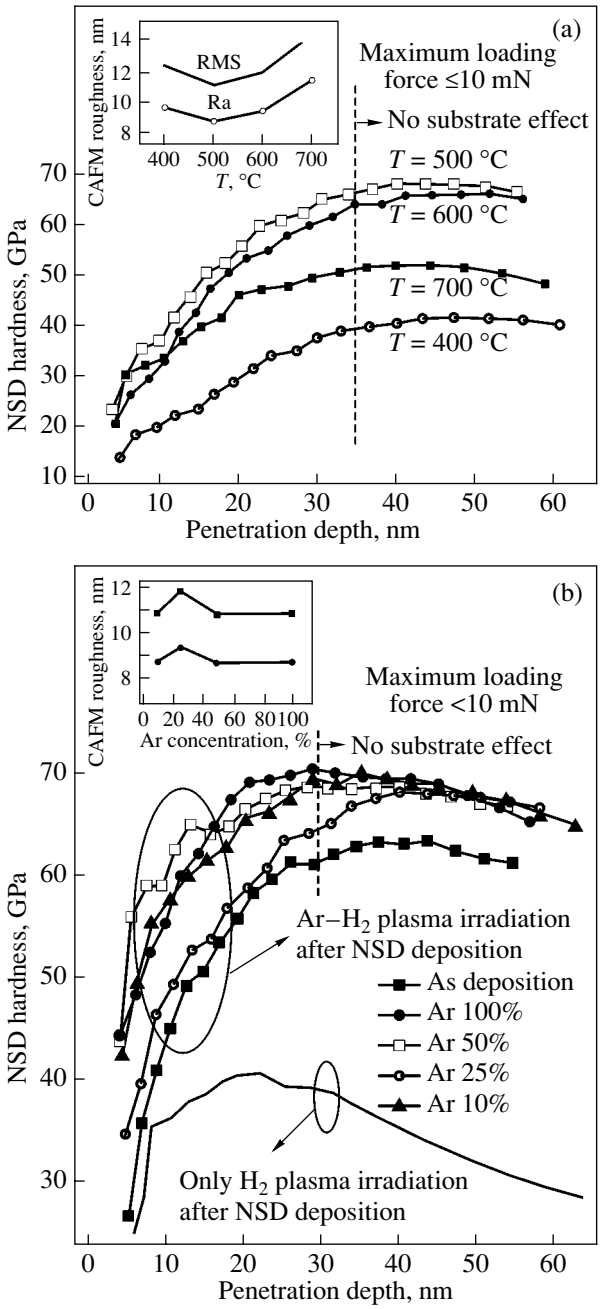

Fig. 2. Hardness–penetration curves of NSD films (a) with different substrate temperature and (b) irradiated by Ar–H_2 plasma with different Ar concentrations indented to a maximum load of 10 mN. The insets to (a) and (b) show the CAFM roughness of NSD films as a function of the substrate temperature and Ar concentration, respectively.

the nonirradiated film (60 GPa). This result indicates the importance of little or no H_2 during Ar–H_2 plasma irradiation.

Visible Raman data obtained for NSD films show similar line shapes composed of four main peaks located at 1140, 1350 (*D* peak), 1460, and 1580 cm^{-1} (*G* peak). Both the *G* and *D* peaks are attributed to sp^2-bonded carbon. The peak at 1140 cm^{-1} has been attributed to nanocrystalline diamond; however, the interpretation of this peak is still not fully confirmed. In comparison with the nonirradiated film, although the peak at 1460 cm^{-1} decreases, the Ar–H_2 plasma irradiation of NSD films does not lead to a significant change in the overall Raman features. On the other hand, both the 1140 and 1460 cm^{-1} peaks disappeared while the *G* and *D* peaks still remained from the NSD film subjected to only hydrogen plasma (Ar = 0).

XRD results reveal that our NSD films mostly consisted of cubic diamond (111). Although, both diamond (111) and diamond (220) were reported from the NSD film deposited by the continuous BEN method, there was no signal at $2\theta = 75°$ of signature of diamond (220) in our films. It should be noted that the NSD film composed of highly (111)-oriented diamond was achieved by using a two-step negative bias method. XRD spectra of films irradiated by Ar–H_2 plasma with different Ar concentrations show that the absolute intensity of diamond (111) is weaker than those of nonirradiated films and diamond (220) is observed in all irradiated films. Thus, the NSD film gradually changes from (111)-oriented diamond to a randomly oriented phase through Ar–H_2 plasma irradiation.

4. CONCLUSIONS

In conclusion, the NSD films composed of (111)-oriented diamond nanocrystals were grown by the two-step negative substrate bias method. A maximum hardness as high as 70 GPa with the smallest Ra and RMS of the CAFM is obtained at a substrate temperature of 500°C. The hardness of the film increased with post-growth Ar–H_2 irradiation due to improvement of the uniformity of smaller grain size and the smooth surface of the NSD film. The hardness and flatness of the film irradiated by only H_2 plasma, however, decreased in comparison with the nonirradiated film. Thus, we confirmed that the introduction of Ar–H_2 plasma after NSD deposition is effective for increasing the hardness of films. Our results demonstrated that hard NSD films can be produced from - Ar–H_2 plasma irradiation after NSD deposition with little or no H_2 using MPECVD.

ACKNOWLEDGMENTS

This work was partly supported by the Research Foundation for the Electrotechnology of Chubu (REFEC), the Daiko Foundation, and the NITECH 21st Century COE Program “World Ceramics Center for Environmental Harmony.”

REFERENCES

1. S. Jiao, A. Sumant, M. A. Kirk, *et al.*, J. Appl. Phys. **90**, 118 (2001).
2. J. Philip, P. Hess, T. Feygelson, *et al.*, J. Appl. Phys. **93**, 2164 (2001).
3. S. Bhattacharyya, O. Auciello, J. Birrell, *et al.*, Appl. Phys. Lett. **79**, 1441 (2001).
4. K. Chakrabarti, R. Chakrabarti, K. K. Chattopadhyay, *et al.*, Diamond Relat. Mater. **7**, 845 (1998).
5. L. C. Chen, P. D. Kichanbare, K. H. Chen, *et al.*, J. Appl. Phys. **89**, 753 (2001).
6. D. Gruen, Annu. Rev. Mater. Sci. **29**, 211 (1999).
7. D. M. Gruen, S. Liu, A. R. Krauss, and X. Pan, J. Appl. Phys. **75**, 1758 (1994).
8. R. Csencsits, D. R. Gruen, A. R. Krauss, and C. Zuiker, Mater. Res. Soc. Symp. Proc. **403**, 291 (1996).
9. C. Z. Gu and X. Jiang, J. Appl. Phys. **88**, 1788 (2000).
10. Y. Hayashi, Y. Matsushita, T. Soga, *et al.*, J. Appl. Phys. **91**, 9752 (2002).

Physics of the Solid State, Vol. 46, No. 4, 2004, pp. 738–741. Translated from Fizika Tverdogo Tela, Vol. 46, No. 4, 2004, pp. 718–721.

APPLICATIONS OF NANODIAMONDS

Application of Modified Nanodiamonds as Catalysts of Heterogeneous and Electrochemical Catalyses

G. P. Bogatyreva*, M. A. Marinich*, E. V. Ishchenko, V. L. Gvyazdovskaya*, G. A. Bazaliĭ*, and N. A. Oleĭnik***

** Bakul Institute for Superhard Materials, National Academy of Sciences of Ukraine, Avtozavodskaya ul. 2, Kiev, 04074 Ukraine*

*** Shevchenko National University, Vladimirskaya ul. 64, Kiev, 01033 Ukraine*

Abstract—The possible use of modified nanodiamond powders in heterogeneous and electrochemical oxidation catalyses is analyzed. It is shown that the efficiency of oxidation catalysis depends on the content of atomic oxygen. The inference is drawn that the electrochemical modification of the surface of nanodiamond powders in a hydrochloric solution and the promotion of the surface with palladium are promising for the preparation of both catalysts of the oxidation of CO to CO_2 and electrodes of low-temperature fuel elements. © *2004 MAIK "Nauka/Interperiodica".*

1. INTRODUCTION

The chemical nature and adsorption properties of the surface of carbon-containing materials are the factors responsible for the mechanism of catalytic processes. In our previous works [1, 2], it was demonstrated for the first time that submicron synthetic diamond powders are catalysts of the oxidation of carbon monoxide to carbon dioxide.

The aim of this work was to analyze the possibility of using modified nanodiamond powders in heterogeneous and electrochemical catalyses. For this purpose, we chose two reactions typical of oxidation catalysis, such as gas-phase oxidation of carbon monoxide CO to carbon dioxide CO_2 and electrochemical oxidation of hydrogen.

2. SAMPLE PREPARATION AND EXPERIMENTAL TECHNIQUE

Samples of ASUDO nanodiamonds prepared by detonation of oxygen-deficient explosives (Alit, Ukraine) served as the object of investigation.

The catalytic activity of nanodiamonds in the reaction of CO oxidation to CO_2 was examined using a continuous-flow setup and chromatographic analysis of the reaction products. The experiments were performed with a gas mixture containing 2 wt % CO, 20 wt % O_2, and 78 wt % He_2. The temperature of complete transformation of CO into CO_2 was used a measure of catalytic activity.

The electrocatalytic activity in the hydrogen oxidation was studied for the initial nanodiamond surface and the surface modified in a 0.1 *N* sulfuric acid solution. The catalytic activity in the electrochemical oxidation of hydrogen was investigated with the use of a P-5848 potentiostate in a hydrogen atmosphere at a film diamond electrode. The electrode was prepared from a mixture of the studied powder and a fluoroplastic lacquer (10 : 1) applied to the end of the pyrographite electrode pressed into a fluoroplastic casing. A disk-shaped floating diffusion electrode 10 mm in diameter was used as a nickel mesh coated with a mixture of the studied powder and the fluoroplastic lacquer.

The exchange current density i_0, which was determined by the extrapolation of the hydrogen overvoltage–current density (η'–i) curve to $\eta = 0$, was used a measure of electrocatalytic activity.

The nanodiamond surface was modified through thermal and electrochemical treatments and through the deposition of metallic palladium in microquantities onto this surface. The two-stage thermal treatment of nanodiamonds was carried out in a hydrogen atmosphere, followed by cooling under special conditions. The electrochemical treatment was performed in a 0.1 *N* hydrochloric acid solution and a 1 *N* potassium hydroxide solution [3, 4]. The nanodiamond surface was promoted with palladium in microquantities through the contact replacement of palladium salts in the solution. The surface state of the initial and modified nanodiamond powders was evaluated using the Brunauer–Emmett–Teller method and mass spectrometry. The mass and thermal desorption spectra were recorded on an MI 1201 mass spectrometer in the temperature range 20–600°C under vacuum at a residual pressure of 10^{-6} Pa [1, 5, 6].

1063-7834/04/4604-0738$26.00 © 2004 MAIK "Nauka/Interperiodica"

3. RESULTS AND DISCUSSION

We investigated the catalytic oxidation of CO to CO_2 on the initial and modified nanodiamond surfaces.

Figure 1a shows the dependences of the degree of transformation of CO into CO_2 on the temperature of the initial surface and the surface electrochemically modified in the hydrochloric acid and potassium hydroxide solutions.

It was found that the oxidation of CO to CO_2 on the initial nanodiamond surface begins at a temperature of 230°C. The maximum degree of transformation of CO into CO_2 is observed at 380°C and amounts to 80%. Upon electrochemical modification of the nanodiamond surface in hydrochloric acid, the onset of CO oxidation to CO_2 is shifted from 230 to 80°C and the degree of transformation is equal to 30–40%. The electrochemical modification in an alkali solution leads to passivation of the nanodiamond surface. As a consequence, no complete transformation of carbon monoxide into carbon dioxide occurs.

The deposition of palladium in amounts no greater than 0.001 wt % onto the nanodiamond surface results in a considerable decrease in the temperature of the complete transformation of CO into CO_2 from 300 to 180°C (Fig. 1b).

The degree of transformation of CO into CO_2 substantially depends on the ratio of the different oxygen species on the nanodiamond surface. The largest contribution is made by atomic oxygen. The thermal desorption spectra of atomic oxygen on the initial and modified surfaces are depicted in Fig. 2a.

It can be seen from Fig. 2a that the thermal desorption spectrum of atomic oxygen on the nanodiamond surface electrochemically treated in the hydrochloric acid solution exhibits a peak in the temperature range 20–100°C. The second peak is observed at approximately 500°C. In the range 150–600°C, the intensities of thermal desorption of atomic oxygen from nanodiamonds treated in the hydrochloric acid and alkali solutions coincide with each other. As is known, the desorption processes observed at temperatures below 150°C occur through the physical mechanism. The desorption processes at temperatures above 150°C predominantly proceed by the chemical mechanism. Therefore, the electrochemical treatment of nanodiamonds in the hydrochloric acid solution leads to saturation of the nanodiamond surface with atomic oxygen. It can be seen from Fig. 2a (curve *2*) that, in this case, the amount of atomic oxygen remains constant over the entire range of temperatures. The amount of atomic oxygen desorbed from the initial surface and the surface electrochemically treated in the alkali solution is substantially smaller.

The thermal desorption spectra of atomic oxygen on the initial and palladium-promoted surfaces of nanodiamond powders are shown in Fig. 2b. As can be seen from this figure, the amount of atomic oxygen desorbed

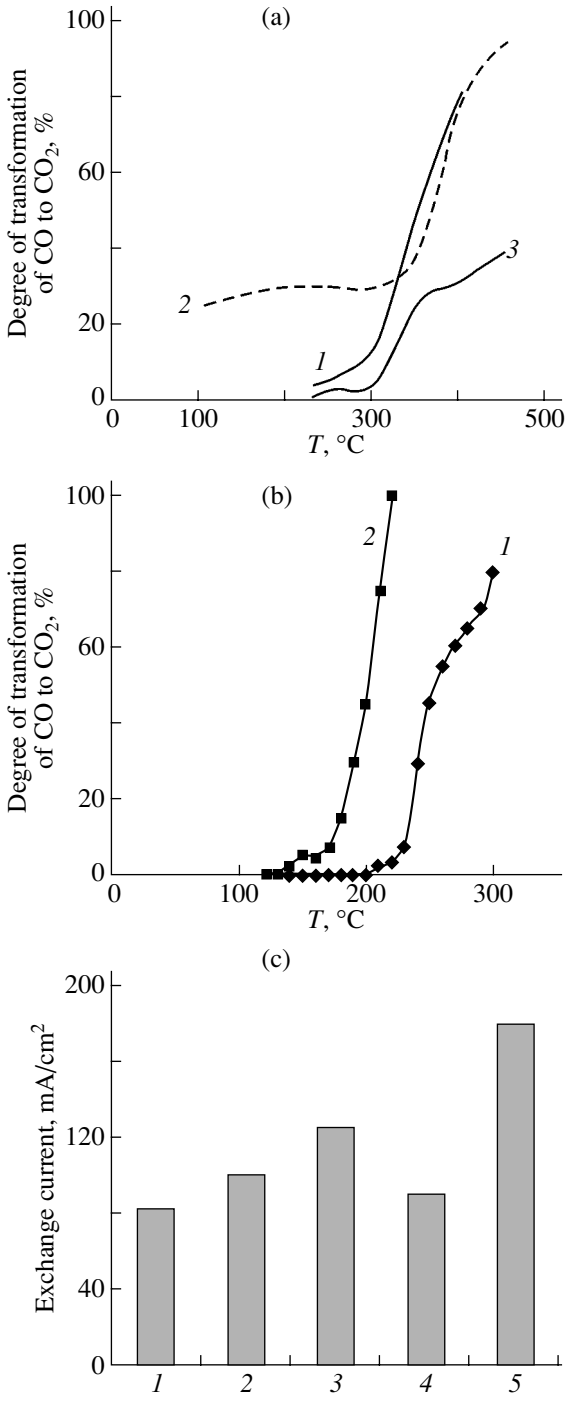

Fig. 1. (a, b) Heterogeneous and (c) electrochemical catalyses of oxidation processes on the surface of nanodispersed powders. (a) Dependences of the degree of transformation of CO into CO_2 on the temperature for (*1*) the initial nanodiamond surface and the surfaces electrochemically treated in (*2*) hydrochloric acid and (*3*) potassium hydroxide solutions. (b) Dependences of the degree of transformation of CO into CO_2 on the temperature for (*1*) the initial nanodiamond surface and (*2*) the surface promoted with palladium. (c) Electrocatalytic activity in the hydrogen oxidation on the surfaces of (*1*) hydrophobic carbon black, (*2*) tungsten carbide, (*3*) vanadium carbide, (*4*) initial nanodiamonds, and (*5*) nanodiamonds modified in a hydrochloric acid solution.

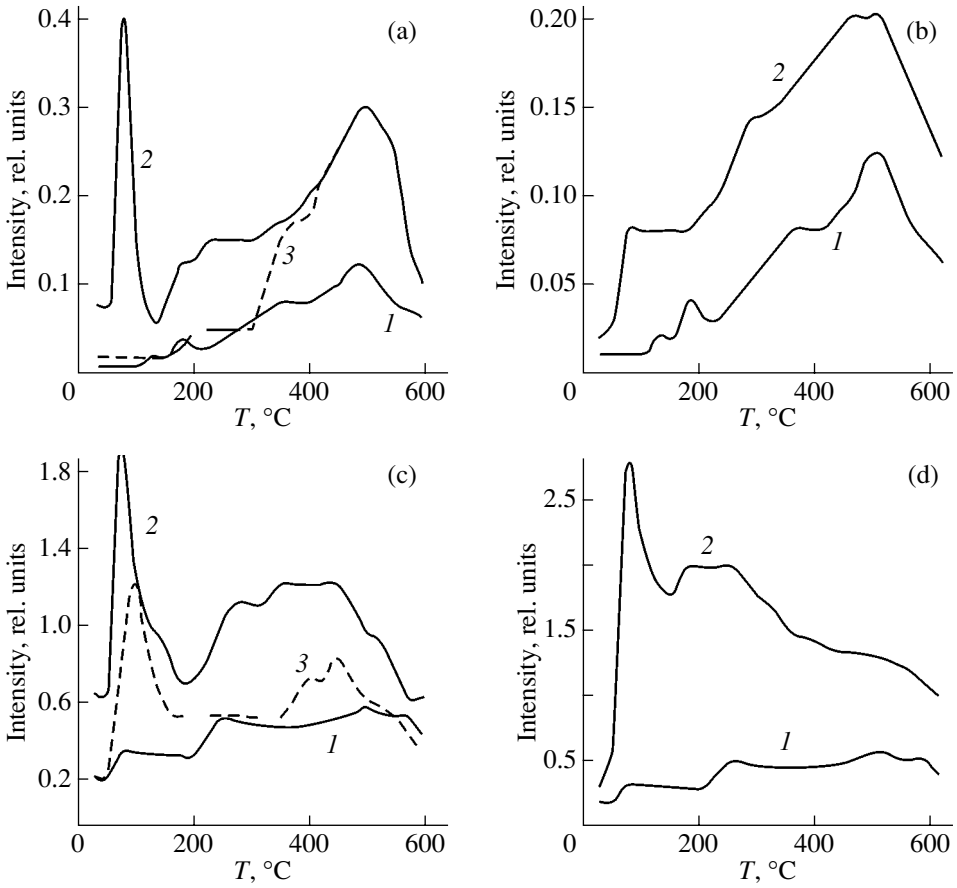

Fig. 2. Thermal desorption spectra of atomic oxygen and water vapors on different nanodiamond surfaces: (a) atomic oxygen on (*1*) the initial surface and the surfaces electrochemically treated in (*2*) hydrochloric acid and (*3*) potassium hydroxide solutions, (b) atomic oxygen on (*1*) the initial surface and (*2*) the surface promoted with palladium, (c) water on (*1*) the initial surface and the surfaces electrochemically treated in (*2*) hydrochloric acid and (*3*) potassium hydroxide solutions, and (d) water on (*1*) the initial surface and (*2*) the surface promoted with palladium.

from the powders promoted with palladium is significantly larger than that from the initial powders.

Thus, promotion of the nanodiamond surface with palladium makes it possible to saturate the surface with atomic oxygen, which, in turn, accelerates the catalytic oxidation of CO to CO_2.

It is of interest to elucidate the mechanism of formation of atomic oxygen on the nanodiamond surface upon modification and promotion. One of the main sources of atomic oxygen can be water vapors. Figures 2c and 2d depict the thermal desorption spectra of water vapors on the surface of the initial, modified, and promoted nanodiamond powders.

As can be seen from Figs. 2c and 2d, the amount of water physically adsorbed on the surface of the powders electrochemically treated in hydrochloric acid is 1.5 times larger than that on the initial surface. The promotion of the nanodiamond surface with palladium in microquantities leads to a sixfold increase in the amount of physically adsorbed water.

The electrochemical oxidation of hydrogen was performed with the initial and modified nanodiamond powders and also with hydrophobic carbon black, tungsten carbide, and vanadium carbide powders. The powders of interest had close specific surfaces (140 m^2/g). It was revealed that the two-stage thermal treatment of nanodiamonds in a hydrogen atmosphere leads to an increase in the exchange current density by a factor of 1.8–2.0 as compared to the initial nanodiamonds [7].

The electrocatalytic activities in the hydrogen oxidation on the surfaces of hydrophobic carbon black, tungsten carbide, vanadium carbide, initial nanodiamonds, and nanodiamonds modified in the hydrochloric acid solution are compared in Fig. 1c. As can be seen, the modified surface of nanodiamonds is characterized by the highest electrocatalytic activity. For identical specific surfaces, the rate of catalytic oxidation of hydrogen with a nanodiamond catalyst is 1.6 times higher than that with vanadium and tungsten carbides.

Let us now analyze the thermal desorption spectra of atomic oxygen on the surface of the initial nanodiamond powders and the powders heat treated in a hydro-

gen atmosphere. It follows from this analysis that thermal treatment of nanodiamonds in a hydrogen atmosphere results in an appreciable decrease in the amount of physically adsorbed atomic oxygen and a substantial increase in the amount of chemisorbed atomic oxygen. At the same time, the two-stage thermal treatment of nanodiamond powders leads to a significant increase in the amount of hydrogen chemisorbed on their surface. It seems likely that chemisorbed species of hydrogen and atomic oxygen contribute to the increase in the rate of electrochemical oxidation of hydrogen.

4. CONCLUSIONS

Thus, it was established that the developed methods for modifying nanodiamond powders provide a means for saturating the nanodiamond surface with atomic oxygen formed upon dissociation of chemisorbed hydroxyl groups.

The results obtained in this work demonstrated that modified and palladium-promoted nanodiamond powders are promising materials for use as both catalysts of the oxidation of carbon monoxide to carbon dioxide and electrodes of low-temperature fuel elements.

REFERENCES

1. G. P. Bogatyreva, E. V. Ishchenko, M. A. Marinich, *et al.*, Sverkhtverd. Mater., No. 2, 65 (2000).
2. G. P. Bogatyreva, M. A. Marinich, E. V. Ishchenko, *et al.*, Sverkhtverd. Mater., No. 6, 10 (2002).
3. M. V. Novikov, G. P. Bogatir'ova, M. A. Marinich, and G. A. Bazaliĭ, Ukr. Patent No. 36,552A (2001), Byull., No. 3 (2001).
4. G. P. Bogatyreva, M. A. Marinich, G. A. Bazaliĭ, and V. L. Gvyazdovskaya, in *Proceedings of II Ukrainian Electrochemical Meeting* (Dnepropetrovsk, 1999), p. 45.
5. V. P. Yatsimirskiĭ, E. A. Ishchenko, N. A. Boldyreva, *et al.*, Teor. Éksp. Khim. **37** (5), 310 (2001).
6. V. P. Yatsimirskiĭ, E. A. Ishchenko, N. A. Boldyreva, *et al.*, Vestn. Donetsk. Univ., Estest. Nauki, No. 1, 217 (2001).
7. M. V. Novikov, G. P. Bogatir'ova, M. A. Marinich, *et al.*, Ukr. Patent No. 50,370 A (2002), Byull., No. 10 (2002).

Translated by O. Borovik-Romanova

Physics of the Solid State, Vol. 46, No. 4, 2004, pp. 742–745. Translated from Fizika Tverdogo Tela, Vol. 46, No. 4, 2004, pp. 722–724.

APPLICATIONS OF NANODIAMONDS

Synthesis of Explosive Decompression-Resistant Rubbers with the Use of Detonation Carbon

L. A. Akopyan*, M. N. Zlotnikov*, B. V. Rumyantsev, N. L. Abramova*, M. V. Zobina*, and T. L. Mordvintseva***

** OAO Research Institute of Rubber Coatings and Products, St. Petersburg, Russia*

*** Ioffe Physicotechnical Institute, Russian Academy of Sciences, Politekhnicheskaya ul. 26, St. Petersburg, 194021 Russia*

Abstract—This paper reports on the results of analyzing the possibility of synthesizing explosive decompression-resistant rubbers based on a Therban hydrogenated acrylonitrile–butadiene rubber containing a mixture of technical-grade detonation carbon (from 0.14 to 27.10 wt %) and fillers with different degrees of dispersion and anisometry. The addition of detonation carbon affects both the α relaxation associated with the segmental mobility and the slow λ relaxation of ordered microblocks. A new class of highly elastic materials that are resistant to explosive decompression is designed and synthesized using technical-grade detonation carbon in a mixture with fillers of different compositions and structures. © *2004 MAIK "Nauka/Interperiodica".*

1. INTRODUCTION

The synthesis of rubbers and industrial rubber products that have to be resistant to explosive decompression in equipment for the oil and gas industry is a complex problem in materials science [1–4]. The mechanical behavior of rubbers under different operating conditions, including the action of explosive decompression, is governed by their relaxation properties [5, 6]. The effect of fillers of different types and degrees of dispersion on the slow λ relaxation associated with the mobility of structural microblocks was revealed by relaxation spectrometry in [7]. Radically new materials can be synthesized with the use of ultradispersed fillers (nanoparticles) [8], specifically of technical-grade detonation carbon consisting of very small carbon and graphitized diamond particles 4–6 nm in size with a specific surface of 173–440 m^2/g.

In this work, we studied composites based on rubbers and fillers of different types, degrees of dispersion, and anisometries (Tables 1–3). The properties of the rubbers were evaluated from the changes in the physicomechanical and relaxation characteristics and from the resistance to explosive decompression.

2. EXPERIMENTAL TECHNIQUE

The relaxation properties were examined by measuring the following dependences and quantities:

(i) the temperature dependences of the mechanical loss tangent $\tan\delta$ in the range from –100 to 200°C (pendulum elastometer; frequency, ~40 Hz; Lebedev Research Institute of Synthetic Rubber, Laboratory of S.K. Kurlyand);

(ii) the stress relaxation σ/σ_0 under uniaxial compression at a temperature of 23 ± 3°C, where σ_0 and σ are the initial (within 5 min) and current stresses, respectively; and

(iii) the elastic modulus E and the gain $K_E = E/E_0$, where E and E_0 are the elastic moduli of the filled and unfilled rubbers, respectively [9].

The physicomechanical properties were evaluated from the ratio A_p/A_{p0}, where A_p and A_{p0} are the specific fracture energies (the area under the stress–strain curve) for the filled and unfilled rubbers, respectively.

In order to estimate the resistance to explosive decompression, the rubbers were treated in carbon dioxide under the following conditions: pressure, 5.8 MPa; temperature, 23 ± 3°C; and depressurization rate, 0.35 MPa/s. The resistance of the rubber to explosive decompression was assessed by the external appearance and from the changes in the weight Δm, the volume ΔV, and the ratio $\Delta m/\Delta V$ for rubber samples subjected to explosive decompression (Table 3).

3. RESULTS AND DISCUSSION

The introduction of technical-grade detonation carbon at low contents (from 0.14 to 1.67 wt %) into commercial rubbers based on polymers of different types with an elastic modulus E ranging from 2.5 to 8.0 MPa (Table 1) leads to a considerable increase in the tear and abrasive resistances for the majority of the studied rubbers. This is associated with the increase in the rate of slow processes of λ relaxation [10]. For high-modulus rubbers ($E \geq 13$ MPa) based on the Therban rubber (Table 2), an increase in the detonation carbon content from 0.26 to 27.10 wt % also results in an increase in the tear resistance, a rise in the rate of processes of λ

1063-7834/04/4604-0742$26.00 © 2004 MAIK "Nauka/Interperiodica"

Table 1. Characteristics of commercial rubbers at low contents of technical-grade detonation carbon

Rubber no.	Polymer and technical carbon types (content, wt %)	Detonation carbon content, wt %	Change in parameters after introduction of detonation carbon, %			
			conventional tensile strength	ultimate elongation	tear resistance	abrasive resistance
1	SKN-18 (49.68)	0.14	21	<10	36	48
	P-234 (28.31)					
2	SKN-18s (37.03)	0.24	<10	<10	31	54
	P-803 (48.15)					
3	SKI-3 (55.63)	0.28	14	22	<10	<10
	P-234 (10.28)	1.67	<10	24	28	<10
4	SKN-26ASM (28.35)	0.26	<10	<10	29	35
	SKN-40ASM (12.15)					
	P-514 (6.32)					
	P-702 (10.73)					
5	SKÉPT (42.51)	0.21	<10	<10	68	33
	P-324 (24.49)					
	P-803 (12.35)					
6	SKÉP-50 (58.37)	0.38	<10	<10	34	38
	P-324 (32.10)	0.58			28	35

Table 2. Characteristics of filled rubbers based on the Therban rubber at different contents of technical-grade detonation carbon

Rubber no.	Detonation carbon content, wt %	Change in parameters (as compared to parameters of unfilled rubber **12**), %				t, h	$K_E = E/E_0$	A_p/A_{p0}
		conventional tensile strength	ultimate elongation	hardness	tear resistance			
12	–	1	1	1	1	~1920	1	1
15	–	87	–33	50	460	6	3.4	3.0
7	0.26	56	–19	38	330	8	2.2	2.8
8	0.53	57	–19	41	350	6	2.7	3.5
9	9.50	56	–31	45	550	5	3.5	2.8
10	17.30	50	–40	53	670	4	3.8	2.4
11	27.10	57	–52	53	780	2	3.9	4.9

Note: t is the time required to reach the ratio $\sigma/\sigma_0 = 0.85$ at $T = 23 \pm 3$°C.

Table 3. Correlation between the relaxation characteristics and the resistance to explosive decompression for Therban-based rubbers

Rubber no.	Content of different fillers, wt %	α transition			Resistance to explosive decompression		t, h	B, N/m
		ΔT, °C	T, °C	tanδ	visual assessment	$\Delta m/\Delta V$, 10^2 g/cm^3		
12	–	28	–10	1.35	Many bubbles	0.4	~1920	10
13	44.6	27	–10	0.82	One bubble	10	7	47
15	43.9	25	–5	0.75	Normal state	80	6	56
14	44.2	22	–5	0.65	″	20	5	67
11	40.6 (including 27.1 wt % detonation carbon)	7	3	0.50	″	22	2	88

Note: ΔT is the transition temperature range at tanδ = 0.5; t is the same as in Table 2.

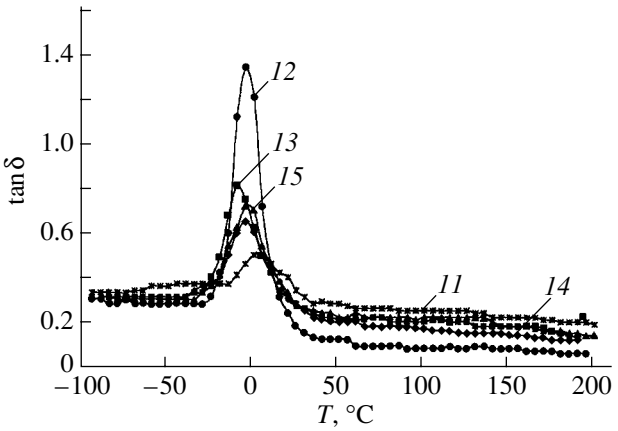

Fig. 1. Temperature dependences of the mechanical loss tangent tanδ for different rubbers. Numbers near the curves correspond to the rubber numbering in Table 3.

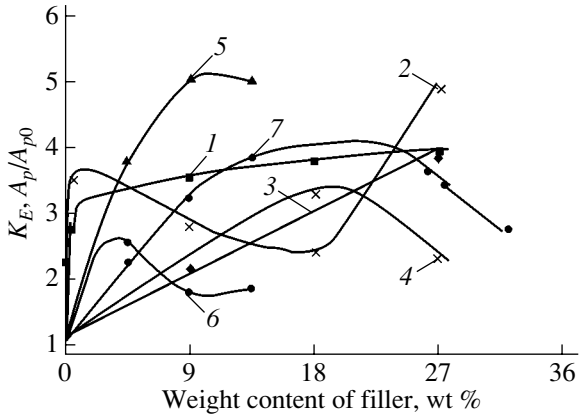

Fig. 2. Dependences of (*1*, *3*, *5*) the gain K_E and (*2*, *4*, *6*, *7*) the fracture energy A_p/A_{p0} on the content of (*1*, *2*) detonation carbon and (*3*–*6*) fillers with different degrees of dispersion and anisometry. Curve *7* is constructed according to the data taken from [9].

relaxation, and a decrease in the time required to reach the ratio $\sigma/\sigma_0 = 0.85$. At a detonation carbon content of 27.10 wt %, the specific fracture energy A_p increases drastically. This is explained by the developed surface of detonation carbon and the formation of a extended network of bonds due to the adsorption interaction of the polymer with functional groups on the filler surface.

The explosive decompression leads to an increase in the rubber volume [4, 11] due to the work done by the sorbed gas after sharp depressurization in the course of the adiabatic process. As a result, the rubber transforms into a three-dimensional strained state [6]. The change in the weight (weight gas swelling) is governed by the sorption properties. In turn, the change in the volume is associated with the sorption, elastic, and strength properties, which depend on the relaxation characteristics and determine the specific fracture energy of rubbers. As was shown in [9], rubbers absorb the energy of the gas upon expansion. Rubbers resistant to explosive decompression should satisfy a number of contradictory requirements and possess a low sorption capacity; sufficiently high elasticity, strength, and elastic modulus; a high resistance to media involved in oil production; etc. In our work, rubbers resistant to explosive decompression were synthesized on the basis of a Therban hydrogenated acrylonitrile–butadiene rubber doped with a mixture of technical-grade detonation carbon and fillers of different types, degrees of dispersion, and anisometries.

It can be seen from Table 3 and Fig. 1 that, for rubbers **11**, **14**, and **15** resistant to explosive decompression, the temperature dependences of the mechanical loss tangent in the α transition range (mechanical vitrification) exhibit peaks with a lower intensity and the temperature range of this transition is narrower as compared to those for rubbers that are not resistant to explosive decompression. Moreover, the so-called free volume of polymers decreases and the ordering of polymer chains becomes more pronounced [8, 12], which leads to a decrease in the segmental mobility. In turn, a shift of the α transition toward the high-temperature range should decrease the gas sorption [11]. The parameter $\Delta m/\Delta V$ (Table 3) can be used to evaluate the fracture strength not only on the surface but also in the bulk of the rubber under explosive decompression. This parameter characterizes the ratio between the contribution of the gas sorption and the contribution of the changes in the elastic and strength properties of the rubber upon gas expansion. An increase in the resistance of rubbers to explosive decompression is accompanied by an increase in the parameter $\Delta m/\Delta V$ and the tear resistance and a decrease in the time required to reach the ratio $\sigma/\sigma_0 = 0.85$.

An increase in the content of fillers of different types and anisometries results in a progressive increase in the gain K_E (Fig. 2). As in [9], the dependence of the ratio A_p/A_{p0} on the filler content exhibits a maximum. The maximum increase in the ratio A_p/A_{p0} (by a factor of ~4.9) and the gain K_E (by a factor of 3.5) is observed at a detonation carbon content of ~27.1 wt %.

4. CONCLUSIONS

Thus, a new class of highly elastic materials that are resistant to explosive decompression was designed and synthesized using technical-grade detonation carbon in a mixture with fillers of different compositions and structures.

REFERENCES

1. G. J. Morgan, in *Proceedings of II International Conference on Oilfield Engineering with Polymers* (London, 1998), p. 159.

2. S. Zakaria and B. Y. Bricoe, Chem. Technol., No. 8, 492 (1990).
3. A. A. Gent, Rubber Chem. Technol. **63** (3), 49 (1990).
4. I. A. Kuznetsova, T. S. Klenova, and S. A. Almaev, in *Heat- and Corrosion-Resistant Rubbers and Industrial Rubber Products* (Moscow, 1979), p. 86.
5. G. M. Bartenev, *Structure and Relaxation Properties of Elastomers* (Khimiya, Moscow, 1979).
6. Yu. S. Zuev, Kauchuk Rezina, No. 4, 36 (2000).
7. L. A. Akopyan, É. V. Gronskaya, M. V. Zobina, *et al.*, Vysokomol. Soedin., Ser. A **27** (2), 399 (1985).
8. Yu. G. Yanovskiĭ, Yu. A. Gamlitskiĭ, V. É. Zgaevskiĭ, and Yu. P. Bass, Kauchuk Rezina, No. 5, 20 (2002).
9. L. A. Peters and J. C. Vicic, in *Proceedings of the International Conference on Rubber Division* (Am. Chem. Soc., Dallas, 1988), p. 813.
10. L. A. Akopyan, M. V. Zobina, B. Kh. Avrushchenko, *et al.*, Trenie Iznos **5** (1), 81 (1984).
11. E. P. Stogova, Candidate's Dissertation (Moscow, 1987).
12. E. A. Sidorovich and A. L. Akopyan, Kauchuk Rezina, No. 3, 17 (2000).

Translated by O. Borovik-Romanova

Physics of the Solid State, Vol. 46, No. 4, 2004, pp. 746–747. Translated from Fizika Tverdogo Tela, Vol. 46, No. 4, 2004, pp. 725–726.

APPLICATIONS OF NANODIAMONDS

Model of Formation of Three-Dimensional Polyurethane Films Modified by Detonation Nanodiamonds

N. V. Sirotinkin, A. P. Voznyakovskiĭ, and A. N. Ershova

St. Petersburg State Technological Institute (Technical University), Moskovskiĭ pr. 26, St. Petersburg, 198013 Russia

e-mail: polymer@post.vnt.ru

Abstract—The possibility of increasing the strain resistance of three-dimensional polyurethane films modified by detonation nanodiamonds is analyzed. It is found that the physicomechanical characteristics of polyurethane foams modified by nanodiamonds at a content of several thousandths of a weight percent change significantly. Models of the hardening of polyurethane films are proposed. © *2004 MAIK "Nauka/Interperiodica".*

1. INTRODUCTION

Polyurethane foam is a polymer material that has found very wide application in various fields of industry and possesses a unique combination of service properties. However, the rigorous criteria used in modern technologies have required that the physicomechanical characteristics of polyurethane foams be changed in a specified manner. In particular, one of the requirements consists in increasing the strain resistance of polyurethane foams. Purposeful changes in the properties of polyurethane through chemical modification have been investigated in sufficient detail. However, it is of interest to modify the physicomechanical properties of polyurethane foams without substantially changing the chemical composition of the material. This can be accomplished using nanotechnologies.

Recent progress achieved in nanotechnologies has made it possible to synthesize a great number of ultradispersed and nanometer-sized systems [1–3]: metallic powders, ceramics, etc. Nanodispersed materials are considered to mean substances that contain more than 20% particles whose size is less than 10 nm. Carbon-containing nanomaterials possess a special phase composition, which, in combination with the specific structure of single particles and cluster aggregates, can provide a significant modifying effect at ultralow degrees of filling of the polymers. Among the nanodispersed materials, we chose nanodiamonds prepared by detonation synthesis.

Commercial production of nanodiamonds through detonation synthesis makes it possible to prepare samples with a specified chemical composition and a stable crystal structure of the nanoparticles. In this respect, study of the ultradispersed products of detonation synthesis is of practical importance.

In this work, we investigated the effect of detonation nanodiamonds on the properties of three-dimensional polyurethane films.

2. EXPERIMENTAL TECHNIQUE

In our experiments, we used nanodiamonds of the following four modifications: (1) nanodiamonds with a particle size ranging from 170 to 200 nm, (2) aminated nanodiamonds with a particle size of 20 nm, (3) silylated nanodiamonds with a particle size of 20 nm, and (4) technical-grade diamond-like carbon (TDC) with a 50% diamond allotropy.

The nanodiamond and technical-grade diamond-like carbon samples used were synthesized at the Special Design Bureau "Tekhnolog" (St. Petersburg). The aminated and silylated nanodiamond samples were prepared at the Federal State Unitary Enterprise "Lebedev Research Institute of Synthetic Rubber" (St. Petersburg).

The polymer matrix (polyurethane foam) was synthesized by the polycondensation reaction of a polyol and isocyanate in an open vessel with a volume of 0.05 m^3. The apparent density and the strain resistance of the polyurethane foam were determined according to standard techniques. Prior to the introduction of the modifiers into the polymer matrix, they were dispersed in the polyol in order to provide a uniform distribution in the matrix.

3. RESULTS AND DISCUSSION

Upon introducing 0.1 wt % nanodiamond with a particle size ranging from 100 to 120 nm, the absorptivity of the polyurethane foam increases by a factor of more than 2.5. This indicates that the number of open pores in the polyurethane foam sample increases. In turn, this leads to a decrease in the strain resistance of the polyurethane foam. With an increase in the content of nanodiamonds to 0.25 wt %, the strain resistance increases to a value characteristic of the initial polyurethane foam (1.3 MPa). In this case, the absorptivity increases by one-third as compared to that of the initial

1063-7834/04/4604-0746$26.00 © 2004 MAIK "Nauka/Interperiodica"

polyurethane foam and, correspondingly, the fraction of surface defects of the film increases.

Detonation nanodiamonds possess a high surface activity [4]. This can lead to the aggregation of particles in nonpolar media and, hence, to a nonuniform distribution of the pores throughout the bulk of the polyurethane foam. In order to suppress the undesirable effect of particle aggregation, we performed amination and silylation of nanodiamonds. These reactions resulted in a decrease in the particle diameter from 170 nm (detonation nanodiamonds) to 20 nm (aminated and silylated nanodiamonds).

The introduction of aminated and silylated nanodiamonds enhances the absorptivity of the polyurethane foam by 42%. This can be explained by the fact that nanodiamonds with 20-nm particles obtained after amination and silylation do not form film defects and do not prevent the formation of a closed surface during foaming. Upon introducing 0.05 wt % aminated nanodiamond, the strain resistance of the polyurethane foam exceeds the durability of the initial sample at the same absorptivity. An increase in the content of silylated nanodiamonds to 0.15 wt % increases the absorptivity of the polyurethane foam and decreases the strain resistance from 1.1 to 0.54 MPa.

The introduction of a more active modifier (TDC) increases the strain resistance of the polyurethane foam from 1.47 MPa (0.05 wt % TDC) to 1.96 MPa (0.15 wt % TDC). With an increase in the TDC content, the absorptivity of the polyurethane foam increases by 48–70% as compared to the absorptivity characteristic of the initial sample of polyurethane foam.

The efficiency of using TDC to modify polyurethane films is associated with the specific features of its synthesis. During detonation synthesis, diamond nanoparticles adsorb finely dispersed carbon from the environment. Therefore, TDC can be regarded as nanodiamond that is modified in the course of synthesis. The content of the active phase (nanodiamonds) in TDC amounts to 50%. Hence, at a TDC content of 0.05 wt %, the content of the active phase in the polyurethane foam sample is equal to 0.025 wt %.

According to the theory developed for composite materials [5], the efficiency of a complex filling agent can exhibit synergetic properties. As a complex filling agent, we used a mixture of TDC with glass spherules.[1] It should be noted that glass spherules can serve as an inactive filling agent [6].

In the case when the process is performed using a mixture of glass spherules with TDC, the absorptivity of the sample decreases to 23% and the strain resistance increases to 1.96 MPa at a TDC content of 0.025 wt %. The observed effect of the modifier at such a low content can be described in the framework of nanocomposite theory based on the concept that particles of the nanostructured material exert a significant influence [2, 7].

Upon introducing TDC into the polyurethane foam sample, the density of the polyurethane foam increases and its absorptivity decreases. This indicates a decrease in the pore size.

Porous systems, in particular, polyurethane foam, are gas-filled polymers in which phase separation occurs at the polymer–air boundary. The appearance of open pores is a result of the formation of defects on the film surface. An increase in the content of nanodiamonds leads to an increase in the number of open pores. In turn, this leads to an increase in the density of film defects, which decreases the strain resistance.

The effect of the modifier introduced in small amounts on the strength characteristics of the polyurethane foam film can be explained in terms of the theory of structural information [8].

4. CONCLUSIONS

Thus, it was demonstrated that the introduction of TDC into the polyurethane foam increases the strain resistance (in contrast to nanodiamonds, whose introduction deteriorates the strength characteristics). The maximum effect was achieved upon introduction of a complex filling agent at a low TDC content.

REFERENCES

1. V. Yu. Dolmatov, Sverkhtverd. Mater., No. 4, 77 (1998).
2. S. S. Ivanchev, A. M. Mesh, N. Reichelt, *et al.*, Vysokomol. Soedin., Ser. A **44** (6), 996 (2002).
3. A. P. Korobko, S. V. Krasheninnikov, I. V. Levakova, *et al.*, Vysokomol. Soedin., Ser. A **43** (11), 1984 (2001).
4. A. A. Skaskevich, Candidate's Dissertation (Minsk, 2002).
5. Yu. S. Lipatov, *Physicochemical Principles of the Filling of Polymers* (Khimiya, Moscow, 1991).
6. I. V. Masik, Candidate's Dissertation (St. Petersburg, 2003).
7. D. V. Ershov, Candidate's Dissertation (Krasnoyarsk, 2003).
8. V. B. Aleskovskiĭ, *Chemistry of Supramolecular Compounds* (St. Petersburg Gos. Univ., St. Petersburg, 1996).

[1] Glass spherules with a mean effective diameter of 10 μm were provided by the Special Design Enterprise STROM (Moscow).

Translated by I. Volkov

Physics of the Solid State, Vol. 46, No. 4, 2004, pp. 748–750. Translated from Fizika Tverdogo Tela, Vol. 46, No. 4, 2004, pp. 727–729.

APPLICATIONS OF NANODIAMONDS

Electrochemical Properties of Compacts of Nano- and Microdisperse Diamond Powders in Aqueous Electrolytes

I. A. Novoselova*, E. N. Fedoryshena*, É. V. Panov*, A. A. Bochechka, and L. A. Romanko****

** Institute of General and Inorganic Chemistry, National Academy of Sciences of Ukraine, pr. Akademika Palladina 32/34, Kiev, 03142 Ukraine*

e-mail: iness@ionc.car.net, fedoryshena@yahoo.com

*** Bakul Institute for Superhard Materials, National Academy of Sciences of Ukraine, Avtozavodskaya ul. 2, Kiev, 04074 Ukraine*

Abstract—The electrochemical behavior of compacts of micro- and nanodisperse diamond powders were studied by using model redox $K_3[Fe(CN)_6]$–$K_4[Fe(CN)_6]$ and $Ce(SO_4)_2$–$Ce_2(SO_4)_3$ systems in aqueous electrolytes. The current–voltage curves for compacts of microdisperse diamonds and the kinetics of reactions on these compacts in a solution of the $[Fe(CN)_6]^{3-/4-}$ system are similar to those obtained by using a metal electrode. For nanodisperse diamonds, the same reactions are essentially irreversible. © *2004 MAIK "Nauka/Interperiodica".*

1. INTRODUCTION

The search for corrosion-resistant and, at the same time, electrochemically active electrode materials stimulates study of new unconventional materials for possible applications in various fields of electrochemistry. Diamonds are materials that possess unique chemical and physical stability. Important progress made in recent years in the field of synthesizing diamonds and controlling changes in their properties, including their electrical properties, has made it possible to use boron-doped semiconductor diamond samples (polycrystalline films, single crystals) as electrode materials for electroanalysis, electrosynthesis, and electrolysis. These materials have an ideal polarizability over a wide range (which is very important for electrode materials), low background currents, and high sensitivity and selectivity to small reagent concentrations [1–3]. However, these materials are expensive and the zonal-sectorial structure of the crystals (nonuniform distribution of acceptor impurities in growth pyramids and face layers) results in poor reproducibility of their electrochemical characteristics. Accordingly, we studied the electrochemical behavior of compacts produced at high pressures and temperatures from diamond powders of different dispersity in aqueous electrolyte solutions to assess the possibilities for their application in electrochemistry.

2. EXPERIMENT

We studied polycrystals obtained by sintering nanodisperse diamond (ND) powders and microdisperse diamonds (MDs) with a particle size of 2–20 nm and 200–250 μm, respectively, at a pressure of 8 GPa and a temperature of 1600°C. The basis for ND production is the detonation of explosives with a negative oxygen balance realized in closed space in a medium inert to carbon. We used ND that was produced by the ALIT company and subjected to additional chemical cleaning and modification of the particle surface. Vacuum degassing of the powders and vacuum sealing of the sintering chamber were performed before sintering. MDs were synthesized under static conditions in the Mg–Zn–C–B system at a pressure of 8 GPa and a temperature of 1700°C. Due to boron doping during synthesis, microfine diamond powders were hole semiconductors.

We estimated the dc resistivity of the materials studied, and its values were found to lie in the range $(1–5) \times 10^3$ Ω cm for different samples. The electrode was a tablet-shaped compact 8 mm in diameter with a thickness of 2 mm for MDs and 5 mm for ND. The Ohmic contact was obtained by depositing silver glue on the reverse side of the tablet. The compact was placed in a Teflon cartridge with a window (to ensure contact between the electrode and an electrolyte) having a silicone gum obturator on its perimeter. Isolation of the tablet from an electrolyte and the current supply was realized by using a pressure screw. All data are normalized to the visible electrode surface. The actual surface area of the electrode exceeds its visible area by a factor of approximately three. All potentials were measured relative to a saturated silver chloride electrode; a platinum foil was used as the counter electrode. Measurements were performed using a standard three-electrode

1063-7834/04/4604-0748$26.00 © 2004 MAIK "Nauka/Interperiodica"

electrochemical cell with separated cathode and anode spaces and a PI-50-1.1 potentiostat with a PR8 programmer. The electrochemical activity of the electrodes under study was estimated from cyclic-voltammetry data in the polarization rate V range 2–100 mV/s for solutions of the $K_3[Fe(CN)_6]$–$K_4[Fe(CN)_6]$ and $Ce(SO_4)_2$–$Ce_2(SO_4)_3$ redox systems in 1 M KCl and 0.5 M H_2SO_4, respectively.

3. RESULTS AND DISCUSSION

Our studies showed that both ND and MD electrodes in the 0.5-M H_2SO_4 background electrolyte have high corrosion stability and the ideal electrode polarizability in a wide range of potentials (from –1.3 to +1.5 V).

We measured cyclic current–voltage curves for ND and MD electrodes in a KCl background electrolyte; the curves exhibit peaks of current at potentials of +0.7 and +0.64 V on the forward and reverse branches, respectively.

The potential difference between the anodic (E_{pa}) and the cathodic (E_{pc}) current peaks for $V \le 10$ mV/s corresponds to reversible one-electron charge transport. The dependence of the magnitude of the current peaks on the polarization rate is linear. The anodic (I_{pa}) and cathodic (I_{pc}) peak currents are equal. Therefore, according to the theory of cyclic voltammetry [4], we can conclude that the electrode reaction is reversible. We could not establish the nature of this reaction. Similar peaks (for currents which were approximately 5 times smaller) were observed on current–voltage curves for a graphite electrode measured simultaneously in the same electrolyte. Observation of this wave on graphite, ND, and MD electrodes indicates that a conducting carbon (probably, graphite-like) phase is present at the boundaries of diamond crystals.

After adding the $[Fe(CN)_6]^{3-/4-}$ depolarizer (10^{-2} M) to the KCl solution, the measured discharge I–E curves for this system with MD electrodes exhibited current peaks (Fig. 1a). From Fig. 1, we see that the potentials of the peaks do not depend on the polarization rate V, the dependence of I_p on $V^{1/2}$ is linear (Fig. 1b), the difference E_{pa}–E_{pc} is equal to 0.06 V (which corresponds to one-electron charge transport), and the anodic and cathodic peak currents are equal. These features indicate that the discharge of the redox system with an MD electrode is reversible. We determined the anodic and cathodic reaction rate constants K_0 and the diffusion coefficient D of the reagents to be $K_0 = 1.6 \times 10^{-3}$ cm/s and $D = 1.2 \times 10^{-5}$ cm^2/s.

The discharge of the redox system with an ND electrode (Fig. 2) occurs at the same potentials as in the case of an MD electrode; the current peaks transform into the limiting currents, which are about 5 times smaller than the peak currents for an MD electrode at the same reagent concentrations. Moreover, the anodic currents are two times smaller than the cathodic currents. These features and the dependence of the half-wave potential on the polarization rate demonstrate the irreversibility of the electrode reaction in the redox system under study.

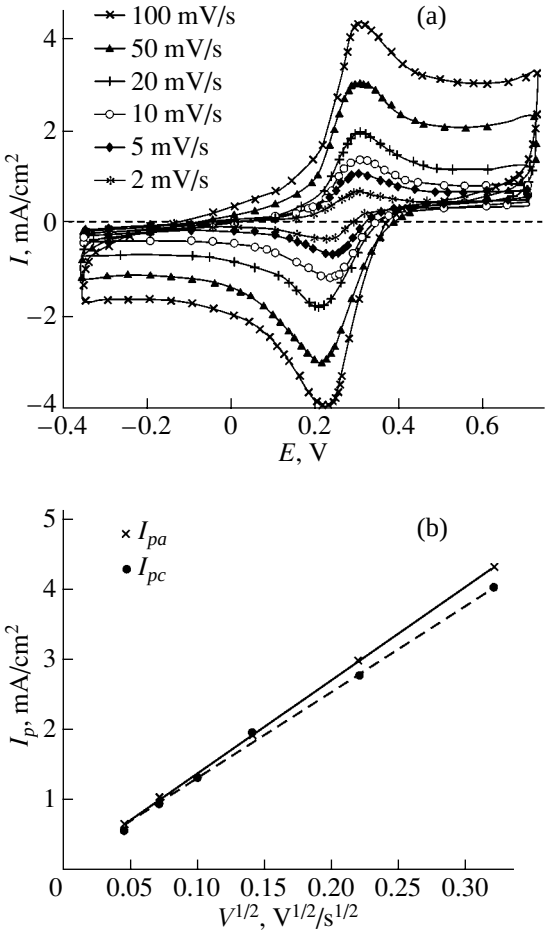

Fig. 1. (a) Cyclic current–voltage curves for the 10^{-2} M $[Fe(CN)_6]^{3-/4-}$ + 1 M KCl system with an MD electrode at different polarization rates. (b) Dependence of the cathodic (I_{pc}) and anodic (I_{pa}) peak currents at the MD electrode on the polarization rate for the 10^{-2} M $[Fe(CN)_6]^{3-/4-}$ + 1 M KCl system.

For the $Ce^{3+/4+}$ redox system, the nature of the MD and ND electrode response is much more complicated and requires further study. We can only note that there are weakly pronounced waves on the cyclic current–voltage curves with the limiting currents at potentials +1.2 V and +1.1 V on the forward and reverse branches, respectively, which corresponds to the discharge of the system. However, in both cases of ND and MD electrodes in an electrolyte, additional waves are observed at more negative potentials; there are no such waves in the background electrolyte without a depolarizer. The behavior of the compacts studied differs from the behavior of larger (3–4 mm) boron-doped diamond sin-

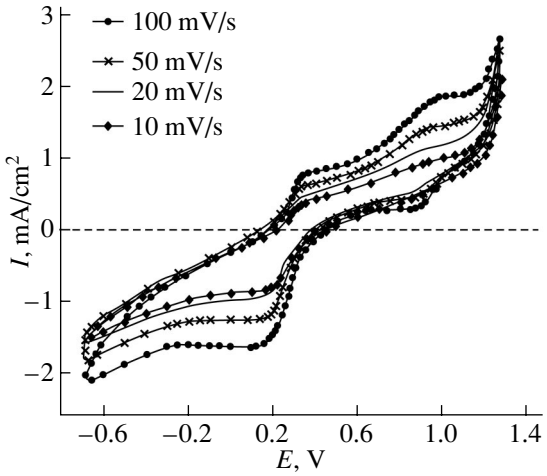

Fig. 2. Cyclic current–voltage curves for the 10^{-2} M $[Fe(CN)_6]^{3-/4-}$ + 1 M KCl solution with an ND electrode at different polarization rates.

gle crystals [3], which exhibit a more pronounced response for this system, though the reaction of Ce^{3+} oxidation occurs at a higher voltage (E_{pa} = +1.7 V).

4. CONCLUSIONS

Thus, pressed compacts of ND and MD powders can be used as indicator electrodes in electrochemical studies. The electrochemical characteristics of MD electrodes in the model $[Fe(CN)_6]^{3-/4-}$ redox system are similar to those of metal electrodes. The advantage of MD electrodes is their stability to corrosion, the availability of the material, the possibility of producing electrodes that are large in size and have a complicated geometry, and the more uniform distribution of an acceptor (boron) impurity in the material. New, but so far unobserved, properties of ND electrodes due to their nanostructure are also quite possible.

A disadvantage of ND and MD electrodes is their low electrocatalytic activity. Therefore, it is expedient to look for new methods of activating the ND surface and to study model reactions at this surface with the aim of using ND and MD electrodes for electrosynthesis and electroanalysis.

REFERENCES

1. Yu. V. Pleskov, Élektrokhimiya **38** (12), 1411 (2002).
2. I. A. Novoselova, É. V. Panov, E. N. Fedoryshena, *et al.*, Sverkhtverd. Mater., No. 1, 27 (2002).
3. I. A. Novoselova, E. N. Fedoryshena, E. V. Panov, *et al.*, in *Abstracts of the 8th International Symposium on Diamond Materials* (Paris, 2003), No. 534.
4. Z. Galus, *Teoretyczne Podstawy Elektroanalizy Chemicznej* (Pa'nstwowe Wydawnictowo Naukowe, Warszawa, 1971; Mir, Moscow, 1974).

Translated by I. Zvyagin

Physics of the Solid State, Vol. 46, No. 4, 2004, pp. 751–754. From Fizika Tverdogo Tela, Vol. 46, No. 4, 2004, pp. 730–733.

APPLICATIONS OF NANODIAMONDS

Nanopolishing of Silicon Wafers Using Ultrafine-Dispersed Diamonds[1]

T. Kurobe*, T. Fujimura*, and H. Ikeda**

** Vision Development Company Limited, Tokyo, 104-0031 Japan*

*** Institute of Development of Raw Materials and Industrial Technologies, Tokyo, 104-0031 Japan*

e-mail: k-vision@rapid.ocn.ne.jp, knakanishi@proof.ocn.ne.jp

Abstract—In the present study, two new methods are proposed for the polishing of silicon wafers using ultrafine-dispersed diamonds (UDDs). The first proposed polishing method uses a polishing tool with an ultrafine abrasive material made through the electrophoretic deposition of UDDs onto a brass rod. Dry polishing tests showed that the surface roughness of the silicon wafer was reduced from R_a = 107 to 4 nm after polishing for 30 min. The second method uses a new polishing pad with self-generating porosity. By polishing with the new pad in combination with the polycrystalline UDD in a water suspension, it is possible to achieve the specified surface roughness of the silicon wafer much faster than when using a conventional pad made of foamed polyurethane. The tests showed that the surface roughness of the silicon wafer was reduced from R_a = 107 to 2 nm after polishing for 90 min. © *2004 MAIK "Nauka/Interperiodica".*

1. INTRODUCTION

To improve the surface roughness and remove residual damages of subsurface layers of silicon wafers after cutting, conventional polishing technologies employ methods of chemical–mechanical polishing (CMP). CMP has comparatively low productivity because it uses abrasive materials with soft grains, such as colloidal silica or oxidized cerium.

To increase the efficiency of polishing of hard materials, several alternative approaches propose to use ultrafine-dispersed diamonds (UDDs) as abrasives. UDDs produced by detonation of explosives with a negative oxygen balance [1] can be obtained after chemical treatment in forms of pastes, powders, and water suspensions with various types and sizes of grains. For example, the typical sizes of the monocrystalline UDD grains in water suspensions lie in the range 4–50 nm and the polycrystalline UDD in water suspensions have grain sizes of several micrometers. The UDD-based slurries have shown superior chemical stability and lubricity; however, these slurries have not been applied widely for precise polishing on the mass-production basis.

In the current study, we propose two new methods for precise polishing using UDDs in water suspensions and investigated its polishing characteristics in a number of experiments.

The first proposed method uses a new grinding wheel with an ultrafine abrasive material made through the electrophoretic deposition of monocrystalline UDDs onto an electrode [2]. In this series of experiments, we tested various types of grinding wheels and evaluated their characteristics for precise polishing of silicon wafers.

The second proposed method uses a new polishing pad, in which the porosity can be generated naturally during polishing. In this series of experiments, we compared the polishing performances using the new polishing pad and a conventional foamed polyurethane pad in combination with the monocrystalline UDD in a water suspension and the polycrystalline UDD in a water suspension for the precise polishing of silicon wafers.

2. EXPERIMENTAL EQUIPMENT

The polishing experiments were conducted using laboratory-scale equipment. The polishing machine consisted of two rotary shafts independently driven by electric motors and a container filled with abrasive materials. The silicon wafer was fixed on the bottom of the container associated with Spindle B. The abrasive grinding wheels and the polishing pads were fixed on Spindle A, where a polishing load of 2 N was applied. The profiles of finished surfaces were measured using a diamond stylus (measuring machine, Taylor Hobson "Talysurf 4").

3. PRECISE POLISHING USING ULTRAFINE ABRASIVE GRINDING WHEELS

3.1. Experimental Conditions

In this series of tests, we evaluated the characteristics of the ultrafine abrasive grinding wheels for dry polishing and wet polishing of the silicon wafers.

[1] This article was submitted by the authors in English.

1063-7834/04/4604-0751$26.00 © 2004 MAIK "Nauka/Interperiodica"

Table 1. Experimental conditions (ultrafine abrasive grinding wheel)

Abrasive grain	UDD (0.5 wt %)
Binder	(a) Sodium alginate (0.25 wt %)
	(b) Sodium alginate (0.2 wt %) + CMC (0.5 wt %)
Work piece	Silicon wafer
Polishing load, N	2
Spindle A, rpm	450
Spindle B, rpm	165
Polishing conditions	(a) Wet polishing
	(b) Dry polishing
Polishing time (max), min	90

Table 2. Experimental conditions (new polishing pad)

Pad	(a) Foamed polyurethane pad
	(b) New pad with self-generating porosity
Work piece	Silicon wafer
Slurry	(a) Monocrystalline UDD in water suspension
	(b) Polycrystalline UDD in water suspension
UDD in slurry, wt %	5
Polishing load, N	2
Spindle A, rpm	250
Spindle B, rpm	50
Polishing time (max), min	180

The grinding wheels were made using the electrophoresis phenomenon. The monocrystalline UDD grains, put into sodium alginate or into a mixture of sodium alginate with carboxymethylcellulose (CMC), were deposited during 60 min on a brass electrode rotating with a speed of 50 rpm. An applied electric potential was varied within the range 10–100 V. The grinding wheel was dried and machined.

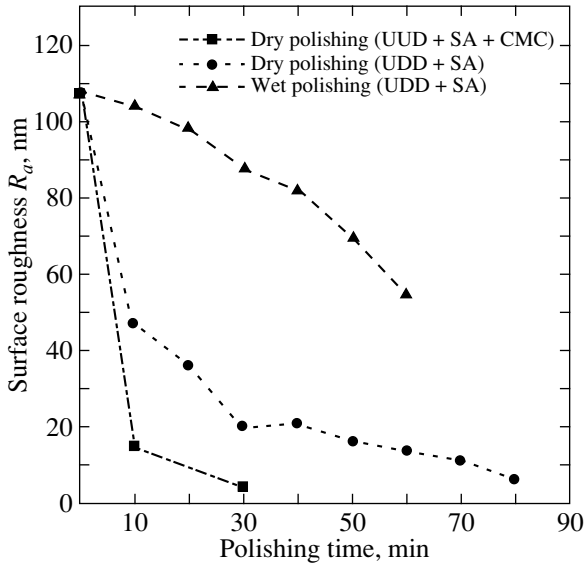

Fig. 1. Results of polishing tests using ultrafine grinding wheels.

Depending on the solution type and the UDD concentration in the solutions, the maximum thickness of an abrasive UDD material reached 1.5 mm. The manufacturing conditions are summarized in Table 1.

3.2. Experimental Results and Discussion

Polishing tests with manufactured ultrafine grinding wheels were conducted in two different environments, wet and dry. It was found that the surface roughness decreased gradually with polishing time for both cases; however, the absolute values of surface roughness were larger in the case of wet polishing than in the case of dry polishing.

In the first series of tests, we used grinding wheels made from a mixture of the monocrystalline UDD and sodium alginate without the addition of CMC. The test results are shown in Fig. 1. The minimum surface roughness achieved after 80 min of dry polishing was R_a = 6 nm. In the case of wet polishing, the grinding wheel broke suddenly after 60 min.

Another series of tests was performed with the grinding wheel made from the monocrystalline UDD grains in a mixture of sodium alginate and CMC. As shown in Fig. 1, the surface roughness of the silicon wafer in this case decreased from R_a = 107 to 4 nm after dry polishing for 30 min.

For small-size silicon wafers, the method showed relatively good polishing performance; however, the overall performance of this method was unsatisfactory due to many uncertain factors, which influenced the manufacturing process of the ultrafine abrasive grinding wheel. It was found that the quality of the grinding wheels was strongly affected by such parameters as the adhesiveness of UDD to the brass electrodes. The wet polishing was not found effective in comparison with the dry polishing. Certainly, this method requires many improvements.

4. PRECISE POLISHING USING PADS WITH SELF-GENERATING POROSITY

4.1. Experimental Conditions

The polishing tests were conducted using the new-type of polishing pad on the equipment described in Section 2. The experimental conditions are listed in Table 2.

Being made from petroleum pitch mixed with halite, the new pad with self-generating porosity has high manufacturability. The molten petroleum pitch was mixed with pulverized halite grains of uniform size and was later solidified and flattened by turning operations in order to create a flat polishing pad. The optical micrographs of the pad are shown in Fig. 2. Self-generation of porosity was achieved in the boundary layer of the pad when the halite grains protruding from the surface of the pitch were dissolved by the UDD slurry during polishing. It was found that the pad with self-generating porosity and the foamed polyurethane pad had similar viscoelastic and mechanical characteristics.

In this series of experiments, we used silicon wafer samples with an initial surface roughness of R_a = 107 nm. The following combinations of polishing materials were tested:

(1) the new pad with self-generating porosity and the slurry of the monocrystalline UDD in a water suspension;

(2) the new pad with self-generating porosity and the slurry of the polycrystalline UDD in a water suspension;

(3) the foamed polyurethane pad and the slurry of the monocrystalline UDD in a water suspension; and

(4) the foamed polyurethane pad and the slurry of the polycrystalline UDD in a water suspension.

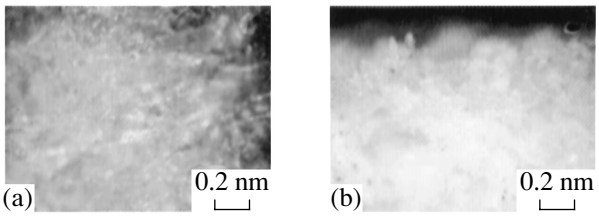

Fig. 2. Optical micrographs of the new pad with self-generating porosity: (a) surface, (b) cross section.

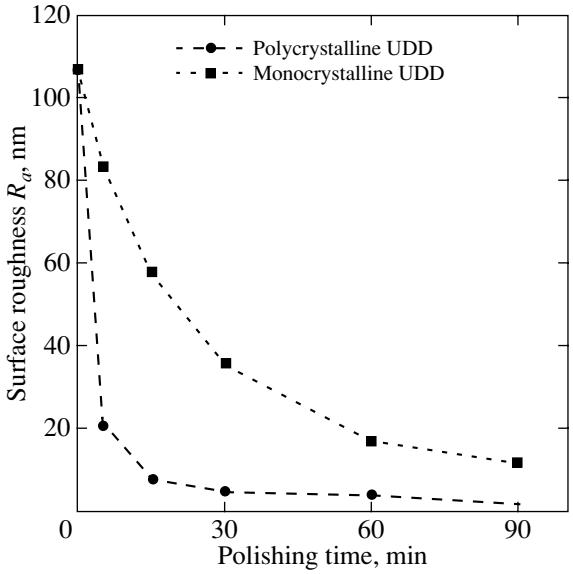

Fig. 3. Surface roughness obtained using the new polishing pad with self-generating porosity.

4.2. Experimental Results and Discussion

The polishing tests showed that, in the case where the UDD in water suspensions with the new self-generating porosity pad is used, the surface roughness of the silicon wafer rapidly decreased at the beginning and slowly decreased during the rest of the polishing process.

The test results for the pad with self-generated porosity are plotted in Fig. 3, and the results for the foamed polyurethane pad are shown in Fig. 4. After polishing for 90 min using the new polishing pad with the polycrystalline UDD in a water suspension, the surface roughness of the silicon wafer decreased from R_a = 107 to 2 nm (Fig. 3). A twofold longer polishing time, about 180 min, was required to achieve the same surface roughness using the foamed polyurethane pad with the polycrystalline UDD in a water suspension. Moreover, the surface was more scratched in this case than it was in the case of the polycrystalline UDD in a water suspension and the pad with self-generating porosity.

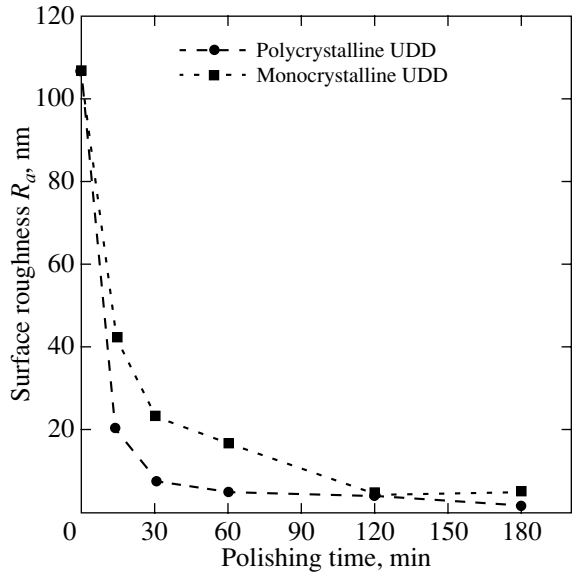

Fig. 4. Surface roughness obtained using the foamed polyurethane pad.

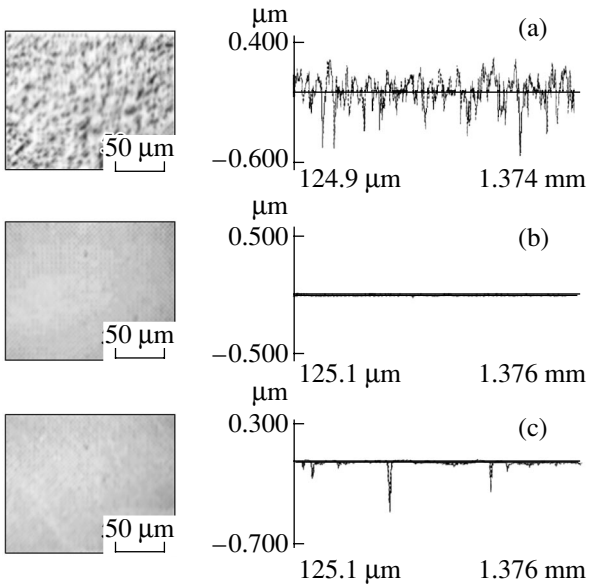

Fig. 5. Optical micrographs of surfaces polished by the new polishing pad with self-generating porosity: (a) prior to polishing, R_a = 107 nm; (b) polycrystalline UDD, t = 90 min, R_a = 2 nm; and (c) monocrystalline UDD, t = 90 min, R_a = 12 nm.

The optical micrographs of the final polished surfaces and the surface profiles are presented in Fig. 5 for the case of the pad with self-generated porosity.

The fast decrease in surface roughness by polishing using the polycrystalline UDD in a water suspension may be explained by the peculiar polishing mechanism, where many new cutting edges could be created after cleaving of the polycrystalline UDD grains during the polishing process.

Thus, using the polycrystalline UDD suspensions in combination with the new polishing pad, it is possible to achieve the specified surface roughness of the silicon wafer much faster than when using the foamed polyurethane pad.

5. CONCLUSIONS

In this study, we proposed two methods for precise polishing of silicon wafers and investigated the effectiveness of the methods using the UDD in water suspensions as abrasives.

The first polishing method uses ultrafine abrasive grinding wheels manufactured with monocrystalline UDDs. The surface roughness of the silicon wafer was reduced from R_a = 107 to 4 nm after 30 min of dry polishing by the ultrafine abrasive grinding wheels. The method showed satisfactory results for dry polishing of silicon wafers, but the overall performance of the method was poor. We concluded that this method still requires improvement and that it cannot be recommended at the current stage of research.

The second method uses a new-type of polishing pad with self-generating porosity. Polishing was done with monocrystalline and polycrystalline UDDs in water suspensions. In addition, we used a conventional foamed polyurethane pad for comparison of the polishing performances. The tests showed that the surface roughness of the silicon wafer was reduced from R_a = 107 to 2 nm after polishing by the new-type of polishing pad and the polycrystalline UDD for 90 min. As compared with polishing by the conventional foamed polyurethane pad, we showed that the same surface roughness of the silicon wafer could be achieved after a twofold shorter polishing time using the pad with self-generating porosity. Although the cutting ability per UDD grain is very small, we considered that many UDD grains per unit of polishing area are responsible for the high polishing performance.

The results of silicon-wafer polishing showed that the pad with self-generating porosity could be effectively used in combination with the polycrystalline UDD in water suspensions.

REFERENCES

1. V. Yu. Dolmatov, Russ. Chem. Rev. **70** (7), 607 (2001).
2. J. Ikeno, Y. Tani, and H. Sato, CIRP Ann. **39** (1), 341 (1990).

Physics of the Solid State, Vol. 46, No. 4, 2004, pp. 755–757. Translated from Fizika Tverdogo Tela, Vol. 46, No. 4, 2004, pp. 734–736.

APPLICATIONS OF NANODIAMONDS

Microstructure and Mechanical Characteristics of Nanodiamond–SiC Compacts

E. A. Ekimov*, E. L. Gromnitskaya*, D. A. Mazalov, A. F. Pal'**, V. V. Pichugin**, S. Gierlotka***, B. Palosz***, and J. A. Kozubowski******

**Institute of High-Pressure Physics, Russian Academy of Sciences, Troitsk, Moscow oblast, 142190 Russia*
***Troitsk Institute for Innovation and Thermonuclear Research, Troitsk, Moscow oblast, 142190 Russia*
e-mail: pichugin@triniti.ru
****Center of High-Pressure Studies, Warsaw, 01-142 Poland*
*****Warsaw Technological University, Warsaw, 00-661 Poland*

Abstract—Superhard nanodiamond–SiC ceramics are prepared by infiltrating liquid Si into porous nanodiamond compacts under pressure. Synthesized samples are 2.2 mm thick and 3–4 mm in diameter. The effect of particle size of dynamically synthesized nanodiamond powders on silicon infiltration and SiC phase formation is studied. It is established that silicon does not penetrate into the pores of nanodiamond powders if the original particle size is smaller than 0.5–1.0 μm. The critical pore size for infiltration is 100–200 nm. A study of the microstructure of the samples showed the presence of the nanometer- and submicron-scale SiC phase. The ultrasound velocities are measured in the prepared compacts, and the elastic moduli are calculated. © *2004 MAIK "Nauka/Interperiodica".*

The mechanical and operating characteristics of diamond-containing compacts can be improved by using nanodiamonds synthesized under dynamic conditions. For example, the nanodiamond hardness (Knoop microhardness, 120–140 GPa) noticeably exceeds the hardness of diamond single crystals (60–120 GPa) [1]. The efficiency of polishing of solid materials by nanodiamond powders is 2–3 times higher than in the case where microcrystalline natural and synthetic diamond powders are used [2]. In contrast to the particles of microcrystalline diamond powders, the particles of polycrystalline nanodiamond powder are strong aggregates with a nanostructure [2]. The size of the crystalline grains forming nanodiamond aggregates is usually about 10 nm. In [3, 4], it was demonstrated that nanodiamond-based bulk materials can be fabricated by infiltrating silicon into nanodiamond polycrystalline powders.

Our aim is to study the infiltration of silicon into nanodiamonds and the sintering of nanodiamond powders differing in particle size. Data on the mechanical characteristics and microstructure of nanodiamond–silicon carbide composites are obtained.

Experiments on the synthesis of bulk nanodiamond-based samples were made at pressures of 8–9 GPa and temperatures of 1800–2100°C using a high-pressure chamber of the "toroid" type [5]. The duration of annealing under pressure was about 20 s. Pellets of a nanodiamond powder of DP grade (Rudolf Spring Ltd; dynamic synthesis from graphite) and silicon (about 18 wt %) were placed one above the other in a graphite crucible (heater). The heater was isolated from the hard-alloy elements of the high-pressure chamber and from the container material by molybdenum screens and boron nitride cartridges, respectively. The density of the samples was determined with a picnometer with an accuracy of ±0.1 g/cm^3. The propagation velocities of longitudinal and transverse waves in the samples were measured with an accuracy of 1.0–1.5% or better. Ultrasonic studies were performed by directly measuring the traveling time of an ultrasonic signal through a sample at a frequency of 10 MHz. To calculate Young's modulus E, the bulk modulus of elasticity K_s, and Poisson's ratio μ, we used the following relations for a homogeneous isotropic medium:

$$K_s = \rho V_l^2 - 1.33\rho V_t^2, \quad E = 3K_s/(A-1),$$

$$\mu = 0.5(A-2)/(A-1),$$

Table 1. Effect of the original nanodiamond powder grain size on silicon infiltration depth

Original powder grain size, μm	Silicon infiltration depth, mm
0–0.05	0
0–0.25	0
0.5–1.0	1.2
1–2	2.2*
2.2–3.5	2.2*
4–6	2.2*

* The thickness of the diamond compact is 2.2 mm.

1063-7834/04/4604-0755$26.00 © 2004 MAIK "Nauka/Interperiodica"

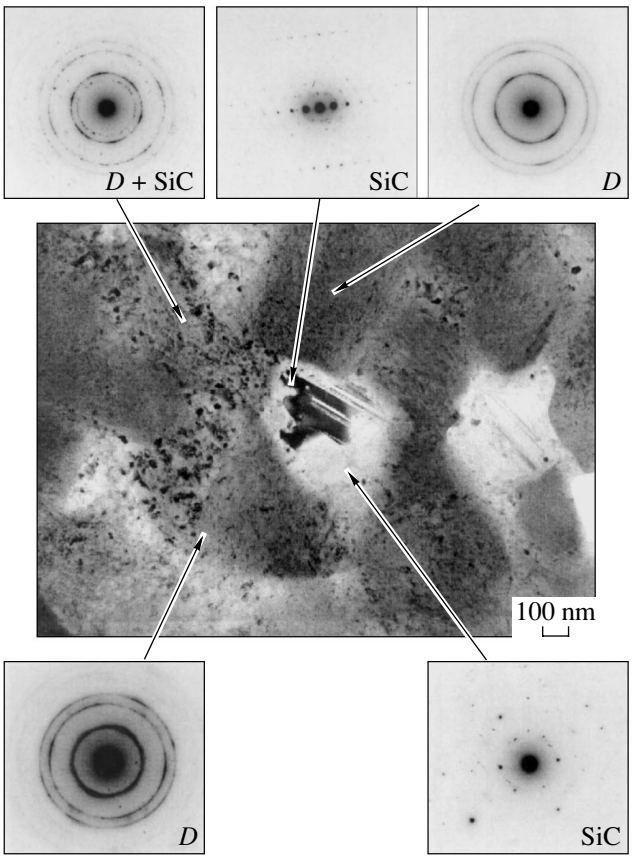

Fig. 1. Microstructure of the nanodiamond–SiC composite material. Diffraction patterns are obtained for the regions indicated by arrows; *D* stands for nanodiamond.

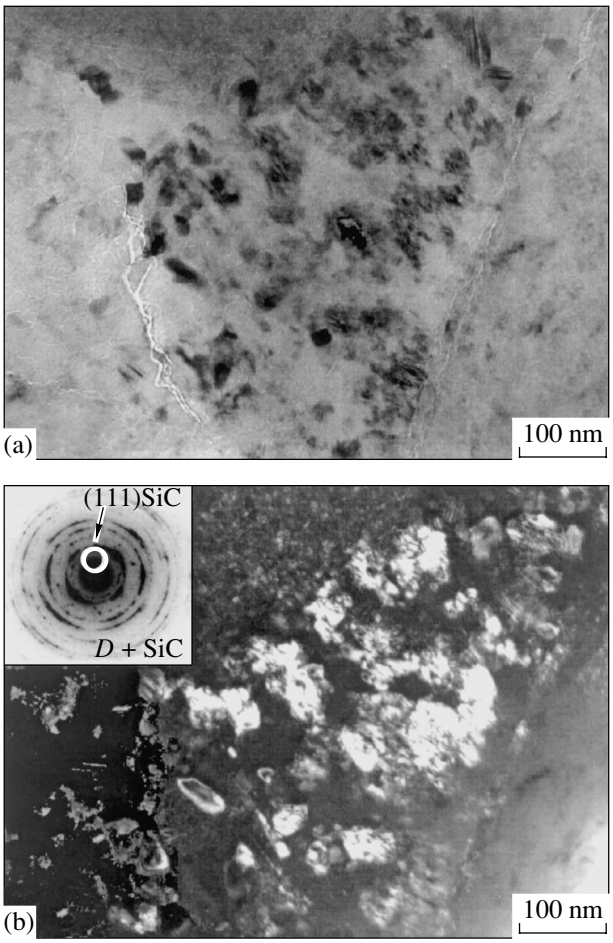

Fig. 2. Microstructure of nanocrystalline SiC interlayers in the composite. (a) Bright-field image and (b) dark-field image for the (111) SiC reflection (see inset).

where ρ is the density and $A = V_l^2/V_t^2$, with V_l and V_t being the velocities of longitudinal and transverse acoustic waves, respectively. Microhardness H_v was measured by using a Vickers pyramid with an indenter load of 4.9 N. The microhardness of the (111) face of natural light-brown diamond single crystals was found to be 90–150 GPa.

Nanodiamond powders differing in particle size were infiltrated by silicon and sintered in the form of cylinders 2.2 mm high and 3.0–3.5 mm in diameter. The samples consisting of diamond and SiC (Si) were prepared in the dynamic regime: infiltration of silicon into the nanodiamond material began near the silicon melting temperature (about 900°C at a pressure of 8 GPa) when the temperature was increased to the required value. The amount of silicon placed in the reaction chamber was chosen so as to fill all pores of the diamond compact and to avoid the formation of graphite-like carbon. The sintering process was terminated with annealing at a temperature of 1800–2100°C for 20 s. Table 1 lists data on the infiltration of silicon into porous diamond compacts. From these data, it follows that infiltration of silicon into nanodiamond porous compacts did not occur if diamond powders with particle sizes smaller than 0.5–1.0 μm were used. The graphitization of diamond and the formation of SiC prevent the penetration of silicon into small pores. Studies of the sample microstructure (Figs. 1, 2) show the presence of the SiC phase on two scales, namely, on a nanometer (near the nanodiamond grain surface) and submicron scale (inside the pores). The critical pore size for infiltration was estimated from the SiC-phase interlayer thickness using scanning and transmission electron microscopy to give 100–200 nm. The thickness of the SiC-phase interlayers was determined at the boundary between the impregnated and nonimpregnated parts of a compact. X-ray phase analysis showed that all prepared samples consisted of two phases: the nanodiamond phase and the SiC phase; no substantial recrystallization of nanodiamonds was observed. The presence of submicron SiC crystals inside large pores can result from recrystallization of nanometer-sized silicon carbide grains in the carbon solution in liquid silicon. Table 2 lists the measured mechanical characteris-

Table 2. Physical properties of diamond compacts

Original diamond powder grain size, μm	ρ, g/cm^3	Vickers microhardness H_v, GPa	V_l, km/s	V_t, km/s	E, GPa	K_s, GPa	μ
0.5–1	3.4	60 ± 5	14.546	9.406	690	320	0.14
1–2	3.4	69 ± 7	15.310	9.793	754	363	0.15
2.2–3.5	3.45	66 ± 10	15.705	8.153	604	546	0.32
4–6	3.45	70 ± 10	14.571	10.070	720	260	0.041
Diamond + Co	4.0 [7]	63.7–78.4 [6]*	13.0–16.5 [8]		890 [7]		

* Knoop microhardness.

tics of the prepared compacts. It follows that the microhardness of compacts decreases as the particle size of the original powders is decreased, which is probably due to the fact that the size of imprints in the indentation was close to the particle size for coarser grained fractions of nanodiamond powders. The sample microhardness is comparable to the hardness of diamond compacts prepared using traditional methods. The velocity of longitudinal ultrasonic waves in compacts (15.3–15.7 km/s) appeared to be maximal for the samples prepared by infiltrating silicon into nanodiamond powders with a particle size of 1.0–3.5 μm. For comparison, Table 2 lists data on the microhardness and ultrasound velocity for a polycrystalline diamond that was sintered with cobalt additives [6–8]. The values of Poisson's ratio and of the bulk modulus calculated for a sample with a particle size of 2.2–3.5 μm (Table 2) appear to be anomalously high for covalent structures (diamond) and seem to indicate elastic anisotropy of the synthesized samples [9]. Anisotropy of the sample properties can be due, e.g., to the anisotropy of pressure in the toroid-type chamber with one loading axis.

ACKNOWLEDGMENTS

This study was supported in part by the Russian Foundation for Basic Research, project no. 02-03-33166.

REFERENCES

1. T. Irifune, A. Kurio, S. Sakamoto, *et al.*, Nature **421**, 599 (2003).
2. O. R. Bergman and N. F. Bailey, *High Pressure Explosive Processing of Ceramics*, Ed. by R. Graham and A. B. Sawaoka (Trans. Tech., Switzeland, 1987), p. 67.
3. E. A. Ekimov, A. G. Gavriliuk, B. Palosz, *et al.*, Appl. Phys. Lett. **77** (7), 954 (2000).
4. E. A. Ekimov, E. L. Gromnitskaya, S. Gierlotka, *et al.*, J. Mater. Sci. Lett. **21** (21), 1699 (2002).
5. L. G. Khvostantsev, High Temp.–High Pressures **16** (2), 165 (1984).
6. R. N. Wentorf, R. C. De-Vries, and F. P. Bundy, Science **208**, 873 (1980).
7. P. D. Gigle, in *Proceedings of the 6th AIRAPT International High Pressure Conference, Boulder, 1977*, Ed. by K. D. Timmerhause and M. S. Barder (Plenum, New York, 1979), Vol. 1, p. 914.
8. P. A. Bex and D. C. Roberts, Ind. Diamond Rev. **1** (1), 1 (1979).
9. A. G. Glazov, V. V. Muzamad'yarov, V. V. Brazhkin, *et al.*, Pis'ma Zh. Éksp. Teor. Fiz. **73** (10), 621 (2001) [JETP Lett. **73**, 552 (2001)].

Translated by I. Zvyagin

Physics of the Solid State, Vol. 46, No. 4, 2004, pp. 758–760. Translated from Fizika Tverdogo Tela, Vol. 46, No. 4, 2004, pp. 737–739.

APPLICATIONS OF NANODIAMONDS

Applications of Nanodiamonds for Separation and Purification of Proteins

V. S. Bondar', I. O. Pozdnyakova, and A. P. Puzyr'

Institute of Biophysics, Siberian Division, Russian Academy of Sciences, Akademgorodok, Krasnoyarsk, 660036 Russia

e-mail: bondvs@mail.ru

Abstract—Recombinant apoobelin and recombinant luciferase are separated from bacterial cells of *Escherichia coli* with the use of detonation nanodiamonds. The application of nanodiamonds has a number of points in its favor, namely, (i) simplifies the procedures for purifying the proteins, (ii) decreases the time of their separation to 30–40 min, (iii) eliminates the necessity of using special chromatographic equipment, and (iv) makes it possible to prepare high-purity apoobelin and luciferase materials with protein yields of 35–45 and 45–60%, respectively. The possible mechanisms of interaction of protein molecules and nanodiamond particles are analyzed. © *2004 MAIK "Nauka/Interperiodica".*

1. INTRODUCTION

Detonation nanodiamonds [1] are of particular interest to biochemists, because these materials exhibit unique physicochemical properties, such as a highly developed surface of particles (270–280 m^2/g) with a large number of surface ionogenic (carboxyl, carbonyl, hydroxyl, ether) groups, hydrocarbon fragments, and metal microimpurities [2, 3]. Taken together, these factors allow one to treat nanodiamonds as new sorbents suitable for the separation and purification of proteins.

In this work, we used nanodiamonds to separate recombinant Ca^{2+}-activated photoprotein apoobelin and recombinant luciferase from bacterial cells of *Escherichia coli*.

2. SAMPLE PREPARATION AND EXPERIMENTAL TECHNIQUE

The nanodiamonds used in our experiments were synthesized at the Department of Physics of Finely Dispersed Materials, Krasnoyarsk Research Center [3].

The choice of the proteins under investigation was motivated by the fact that they belong to luminescent systems of different types, substantially differ in functional molecular structure, and can be separated by different methods. The Ca^{2+}-activated photoproteins are light-emitting EF proteins that occur in marine Coelenterata organisms and generate photons in the visible spectral region upon interaction with calcium ions [4]. These proteins are stable enzyme–substrate complexes that consist of a small single-subunit apoprotein molecule (nearly 20 kDa), a substrate (coelenterazine) molecule, and oxygen. Luciferases are light-emitting proteins contained in marine luminous bacteria. These proteins are heterodimers (consist of α and β subunits), have a molecular mass of approximately 80 kDa, and involve flavin as a cofactor in the structure [5]. The apoobelin and luciferase genes were cloned and expressed in *Escherichia coli* cells, which permitted us to separate the producer strains of these proteins [6, 7]. Photoproteins and luciferases have been widely used as light-emitting indicators in bioluminescent analysis [5, 8].

Upon expression of particular genes in *Escherichia coli* cells, recombinant proteins synthesized by the cells are accumulated in the form of insoluble aggregates, so-called inclusion bodies [9]. This property underlies the method of separating these proteins, including apophotoproteins [10, 11]. The universally accepted technique of purification involves separation of the inclusion body fraction after cell disruption (for example, by ultrasound or a French press), extraction of the recombinant protein from this fraction by a highly concentrated denaturing chaotropic agent (urea, guanidine–HCl), chromatographic purification, and protein refolding after removal of the chaotropic agent. The purification of recombinant apoobelin according to such a procedure takes at least two days [6, 11]. On the other hand, many recombinant proteins, such as luciferases, can be accumulated in a cytosol fraction of synthesizing cells without the formation of inclusion bodies [7]. Compared to proteins, luciferases have a more complex structure and are more sensitive to disrupting factors, for example, to chaotropic agents and heavy metal ions. Therefore, these features should be taken into account in the purification of luciferases. These proteins have been purified without denaturing agents by using a procedure that includes several chromatographic stages and takes at least two or three days [5].

1063-7834/04/4604-0758$26.00 © 2004 MAIK "Nauka/Interperiodica"

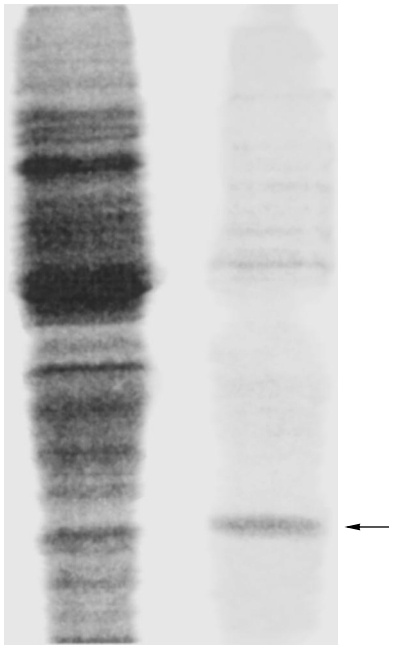

Fig. 1. Electrophoresis images of the recombination apoobelin samples at the stages of separation from bacterial cells of *Escherichia coli* with the use of nanodiamond particles: (*1*) the initial extract and (*2*) the final product. The arrow indicates the position of the apoobelin.

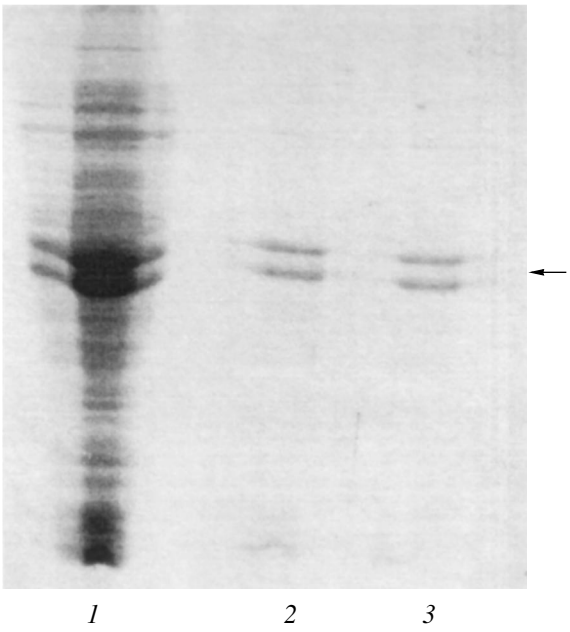

Fig. 2. Electrophoresis images of the recombination luciferase samples at the stages of purification from a biomass of bacterial cells of *Escherichia coli* with the use of nanodiamond particles: (*1*) the initial extract and (*2*, *3*) the final luciferase products prepared upon sequential desorption of the enzyme from the nanoparticle surface with an eluating buffer. The arrow indicates the positions of the α and β luciferase subunits.

3. RESULTS AND DISCUSSION

The apoobelin protein was separated with the use of nanodiamonds according to the following procedure. Cell proteins were extracted from a biomass with a chaotropic agent (6 M urea) for 1 h. The cell debris was removed by centrifugation. The nanodiamond particles were resuspended in a supernatant and then sedimented through centrifugation. The sediment of particles with adsorbed proteins, including apoobelin, was washed twice with a buffer in order to remove unadsorbed inert proteins. The apoobelin protein was desorbed from the particle surface with a buffer containing SH reagent (dithiothreitol) at a concentration of 10 mM. The apoobelin product prepared according to the above procedure has a high degree of purity (Fig. 1), and the apoobelin yield is no less than 35–45%.

The technique of purifying the luciferase protein involved the following stages. The biomass was disrupted in water by ultrasound, and the cell debris was removed through centrifugation. The nanodiamond particles were added to the supernatant, stirred, and sedimented through centrifugation. The sediment was washed twice in order to remove unadsorbed inert proteins. The luciferase protein was desorbed from the particle surface with a 20-mM desorbing buffer. According to the electrophoretic data (Fig. 2), the final product has a high degree of purity and the luciferase yield is 45–60%.

It should be noted that the technique of protein purification with the use of nanodiamonds is characterized by high rapidity. After preparing the initial extracts, the separation procedure takes no more than 30–40 min. It seems likely that this technique can be more correctly regarded as adsorption–desorption chromatography in the bulk. The technique enables one to simplify the separation of proteins substantially, to decrease the time consumption, and to eliminate the necessity of using special chromatographic equipment. The advantage of nanodiamond application is that, in addition to efficient protein separation, the protein can be concentrated, because it can be desorbed using very small amounts of an eluent. For example, from cells with a very low apoobelin concentration (30–300 μg per 1 g of biomass), it is possible to extract a concentrated, virtually homogeneous apoobelin material with a yield of 40–50% for 30–40 min. This cannot be achieved in the case of column chromatography, because compounds are washed out with an eluent whose volume is determined by the retention parameters of the column and the mass transfer. It should also be noted that the use of nanodiamonds ensures the complete separation of luciferase from endogennic NADH : FMN oxidoreductase. This fact is very important, because contamination with oxidoreductase, which contributes to the operation of a luminescence bienzyme system [5], reduces the quality of luciferase in analytical applications.

The data obtained in purifying the apoobelin and luciferase proteins with the use of nanodiamonds allow us to propose possible mechanisms of the interaction of protein molecules with the particle surface. An analysis of the data on the elution of apoobelin with the SH reagent and investigations into the treatment of the nanoparticle surface with a selective blocker of SH groups, namely, 5,5'-dithiobis(2-nitrobenzoic acid), and a chelator (EDTA) of bivalent ions demonstrate that protein molecules can interact with nanodiamonds through the formation of S–S bridges (approximately 10% of molecules) and coordination bonds (approximately 40% of molecules). The remaining protein molecules (50%) most likely interact with nanodiamond particles through other mechanisms. For example, multipoint interaction of protein molecules with different functional groups on the particle surface is a very possible mechanism. Apparently, the interaction can occur through the formation of ionic, hydrophobic, and covalent bonds (except for S–S bonds) or their possible combinations. This is confirmed by the fact that repeated treatment or an increase in the SH reagent concentration do not lead to an increase in the apoobelin yield at the elution stage, and the luciferase desorption efficiently proceeds with an increase in the buffer molarity. The occurrence of the interaction between proteins and particles through different mechanisms should be recognized more as an advantage, as it allows us to treat nanodiamonds as universal sorbents capable of providing different chromatographic operations.

In the above cases, protein purification with nanodiamonds was performed in the bulk. The use of nanodiamonds as a new material for column chromatography also seems to hold considerable promise. Actually, we prepared a nanodiamond-based sorbent that makes it possible to carry out the column chromatographic analysis at normal pressures. The applicability of this sorbent to the adsorption–desorption of protein molecules was demonstrated using the cytochrome C protein as an example.

REFERENCES

1. A. M. Staver, N. V. Gubareva, A. I. Lyamkin, and E. A. Petrov, Fiz. Goreniya Vzryva **20** (3), 100 (1984).
2. G. A. Chiganova, Kolloidn. Zh. **56** (2), 266 (1994).
3. G. A. Chiganova and S. A. Chiganov, Neorg. Mater. **35** (5), 581 (1999).
4. J. R. Blinks, F. G. Prendergast, and D. G. Allen, Pharmacol. Rev. **28**, 1 (1976).
5. I. I. Gitel'zon, É. K. Rodicheva, S. I. Medvedeva, G. A. Primakova, S. I. Bartsev, G. A. Kratasyuk, V. N. Petushkov, V. V. Mezhevikin, E. S. Vysotskiĭ, V. V. Zavoruev, and V. A. Kratasyuk, *Luminous Bacteria* (Nauka, Novosibirsk, 1984).
6. B. A. Illarionov, L. A. Frank, V. A. Illarionova, *et al.*, Methods Enzymol. **305**, 223 (2000).
7. B. A. Illarionov and N. A. Tyul'kova, RF Patent No. 2,073,714 (1997).
8. J. R. Blinks, W. G. Wier, P. Hess, and F. G. Prendergast, Prog. Biophys. Mol. Biol. **40**, 1 (1982).
9. R. C. Hockney, Trends Biotechnol. **12**, 456 (1994).
10. N. L. Stults, N. F. Stocks, H. Rivera, *et al.*, Biochemistry **31**, 1433 (1992).
11. V. S. Bondar, A. G. Sergeev, B. A. Illarionov, *et al.*, Biochim. Biophys. Acta **1231**, 29 (1995).

Translated by O. Borovik-Romanova

Physics of the Solid State, Vol. 46, No. 4, 2004, pp. 761–763. Translated from Fizika Tverdogo Tela, Vol. 46, No. 4, 2004, pp. 740–742.

APPLICATIONS OF NANODIAMONDS

Design of a Luminescent Biochip with Nanodiamonds and Bacterial Luciferase

A. P. Puzyr', I. O. Pozdnyakova, and V. S. Bondar'

Institute of Biophysics, Siberian Division, Russian Academy of Sciences, Akademgorodok, Krasnoyarsk, 660036 Russia

e-mail: apuzyr@mail.ru

Abstract—An "aluminum oxide film–adhesive layer–nanodiamond–luciferase" supramolecular structure is prepared on a flat plate. It is demonstrated that, in this structure, the enzyme retains the catalytic activity. The structure prepared can be treated as a luminescent biochip prototype for use in bioluminescent analysis. © *2004 MAIK "Nauka/Interperiodica".*

1. INTRODUCTION

In recent years, considerable attention has been focused on the development of new techniques for solving applied problems in biology, protein chemistry, biophysics, molecular biology, ecology, etc. In particular, the design of various indicator recording systems based on the use of protein molecules with marker properties holds much promise. Among marker proteins are light-emitting proteins, which are capable of generating photons in the visible spectral region. The attractiveness of these testing methods is related to their high sensitivity, rapidity of analysis, simplicity of recording a light signal, broad potential application, etc. [1–4].

Earlier [5], we developed a luminescent biochip prototype based on detonation nanodiamond particles and light-emitting protein obelin. When interacting with Ca^{2+} ions, this protein generates visible-light photons and, hence, the biochip can be used for their recording in different-type liquids, including biological liquids [5]. At the same time, it is of interest to create similar indicator test systems on the basis of other light-emitting proteins. This will permit one to develop the concept regarding the mechanisms of interaction of protein molecules with the surface of nanodiamond particles, on the one hand, and to expand the field of possible applications of such bioluminescent sensor, on the other. In particular, for this purpose, it is possible to use luciferases of marine bacteria, which have found wide application in bioluminescent analysis as monoenzymes in bienzyme [luciferase–nicotinamide adenine dinucleotide (NADH) : flavin mononucleotide (FMN) oxidoreductase] and related systems [6]. Proteins of this group have a molecular mass of approximately 80 kDa, are heterodimers (consist of α and β subunits), and involve flavin as a cofactor in the structure.

In the present work, we designed a luminescent biochip prototype based on detonation nanodiamond particles and bacterial luciferase.

2. SAMPLE PREPARATION AND EXPERIMENTAL TECHNIQUE

The nanodiamonds used in the experiments were synthesized at the Department of Physics of Finely Dispersed Materials (Krasnoyarsk Research Center) and were purified by the gas-phase method in the presence of boron oxide [7]. Hydrosols from nanodiamond particles were prepared according to the procedure proposed in our earlier work [5]. Luciferase and NADH : FMN oxidoreductase samples were produced using the procedures described in [8, 9]. The luciferase activity was measured with a bienzyme reaction and photoreduced FMN [9]. The measurements were performed on a BLM 8801 bioluminometer (Special Design Bureau "Nauka," Krasnoyarsk) calibrated against the Hastings–Weber radioactive reference sample [10]. One luminescence unit corresponded to 10^7 photons/s. When determining the luciferase activity according to the bienzyme reaction, the reaction mixture in the measuring cell contained 4 mM Tris-HCl buffer (450 μl, pH 7.0), 4.7×10^{-6} M C_{14} aldehyde (10 μl), 7.8×10^{-5} M FMN (10 μl), NADH : FMN oxidoreductase (1–3 μl; enzyme activity, 1 E/ml), and the sample to be studied (5–50 μl). The reaction was initiated by the addition of 10^{-2} M NADH (5 μl). In the case when the luciferase activity was determined with photoreduced FMN, the reaction mixture contained the aforementioned buffer (450 μl), 4.7×10^{-6} M C_{14} aldehyde (50 μl), and the sample to be studied (5–50 μl). The reaction was initiated by the introduction of reduced FMN (7.8×10^{-5} M, 500 μl).

1063-7834/04/4604-0761$26.00 © 2004 MAIK "Nauka/Interperiodica"

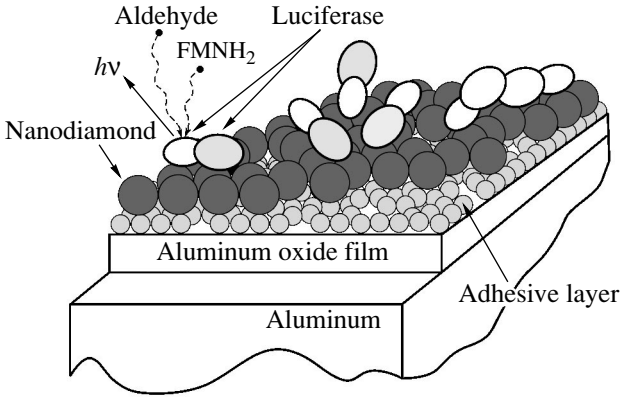

Fig. 1. A hypothetical "aluminum oxide film–adhesive layer–nanodiamond–luciferase" supramolecular structure of the biochip for the components arranged in monolayers.

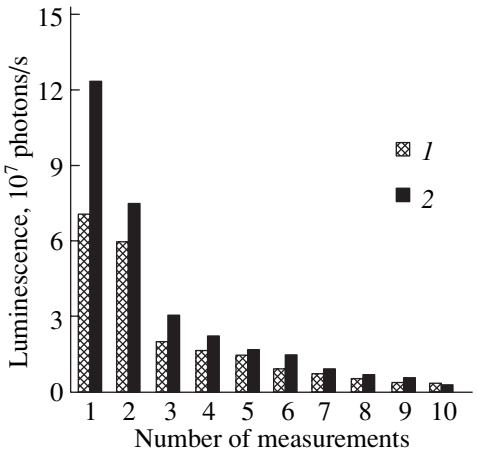

Fig. 2. Variations in the luminescence signal intensity upon multiple measurements with the use of a flat plate involving the supramolecular structure in which a nanodiamond–luciferase complex acts as an indicator element: (*1*) the plate in the reaction mixture in a measuring cell and (*2*) the reaction mixture after removing the plate.

3. RESULTS AND DISCUSSION

At the first stage of our investigations, we demonstrated that the addition of an aqueous solution of luciferase to a suspension of nanodiamond particles and subsequent stirring of the mixture leads to fast and complete adsorption of the enzyme on the particle surface. After sedimenting nanodiamonds by centrifugation at 16000 *g* for 1–3 min, no luciferase activity is observed in a supernatant. The protein-to-nanodiamond ratio necessary for complete adsorption of the enzyme from the solution can be calculated from the adsorption capacity of nanoparticles. With the use of marker proteins (bovine serum albumin, cytochrome C), we found that 1 mg of nanodiamond particles can adsorb 0.3–0.5 mg of the protein on the surface. After adsorption, luciferase molecules are firmly retained on the nanodiamond surface and are not washed off upon multiple washing of the particle sediment with water and the 20 mM Tris-HCl buffer (pH 7.0). The enzyme adsorbed on nanodiamond particles can exhibit catalytic activity both in the bienzyme reaction and with photoreduced FMN. However, in both cases, luciferase molecules are partially desorbed from the surface of nanodiamond particles. After the reaction is performed and particles are removed from the reaction mixture, this mixture is characterized by a luciferase activity. At the same time, the particles hold a considerable number of enzyme molecules on their surface. When nanodiamond particles are washed free of the reaction mixture components and reaction products, they can be used again in luminescence measurements. It was experimentally found that one sample of nanodiamond particles can be used to carry out ten or more measurements. Note that part of the enzyme molecules are desorbed in each experiment. Most likely, this is associated with the conformational transformations of enzyme molecules, which occur at the instant they are involved in the catalytic reaction. This assumption is confirmed by the fact that the individual components of the bioluminescent reaction (C_{14} aldehyde, FMN, NADH), their combinations, and the addition of oxidoreductase do not result in the desorption of luciferase from the nanodiamond surface.

At the next stage, we analyzed the possibility of fabricating a luminescent biochip prototype in which a nanodiamond–luciferase complex acts as an indicator element. An aluminum plate was used in the biochip design. It was revealed that aluminum oxide films do not adsorb luciferase molecules from protein solutions and nanodiamond particles with adsorbed enzyme molecules from suspensions. Therefore, as in the biochip based on nanodiamond particles and obelin [5], the nanodiamond–luciferase complex was attached to the plate by an adhesive layer, which was preliminary applied to the aluminum oxide film. A hypothetical "aluminum oxide film–adhesive layer–nanodiamond–luciferase" supramolecular structure of the biochip is shown in Fig. 1. This structure with the nanodiamond–luciferase complex as an indicator element is not washed out from the plate by water and the 20 mM Tris-HCl buffer (pH 7.0). This suggests a sufficiently high stability of the structure and a strong adhesion to the plate surface. The luciferase activity on the plate prepared was also examined by two techniques (in the bienzyme reaction and with photoreduced FMN). For this purpose, the plate was placed in the measuring cell with the buffer and the reaction was initiated by adding the required components. In both cases, the luminescence signal was observed in the system. Thereafter, the plate was removed from the measuring cell and the luminescence signal was recorded once again. Despite the absence of the plate, the luciferase activity was observed in the reaction mixture. This indicates that, as in the experiments with suspensions, part of the enzyme

molecules are desorbed from the chip surface in the course of the reaction. The plate was washed with a stream of distilled water in order to remove the reaction products and the remaining desorbed protein. Then, the plate was placed in a pure measuring cell with the buffer and the luminescence was measured in the system. It was found that the intensity of the luminescence signal from the plate decreases with each subsequent measurement (Fig. 2). However, this decrease is not a serious obstacle to the use of the proposed test systems in the bioluminescent analysis. Actually, the intensity of the luminescence signals from the plate is sufficiently high and can be recorded despite the decrease in the amount of enzyme on the chip surface.

4. CONCLUSIONS

Thus, the results obtained in this work demonstrated the possibility of fabricating a luminescence biochip whose main element consists of detonation nanodiamond particles with a light-emitting luciferase protein on the surface. The test system proposed can be used in bioluminescent analysis. Stronger fixation of enzyme molecules to the surface can be achieved using chemical (covalent bonding with chemical reactants) and biological (protein–protein interactions with additional molecules) methods. Verification of the aforementioned potentialities of these methods is a subject for further investigation.

REFERENCES

1. J. R. Blinks, W. G. Wier, P. Hess, and F. G. Prendergast, Prog. Biophys. Mol. Biol. **40**, 1 (1982).
2. V. A. Kratasyuk and I. I. Gitel'zon, Usp. Mikrobiol. **21**, 3 (1987).
3. V. S. Bondar', E. S. Vysotskiĭ, O. M. Rozhmanova, and S. G. Voronina, Biokhimiia **56**, 806 (1991).
4. B. A. Illarionov, L. A. Frank, V. A. Illarionova, *et al.*, Methods Enzymol. **305**, 223 (2000).
5. K. V. Purtov, V. S. Bondar', and A. P. Puzyr', Dokl. Akad. Nauk **380** (3), 411 (2001).
6. I. I. Gitel'zon, É. K. Rodicheva, S. I. Medvedeva, G. A. Primakova, S. I. Bartsev, G. A. Kratasyuk, V. N. Petushkov, V. V. Mezhevikin, E. S. Vysotskiĭ, V. V. Zavoruev, and V. A. Kratasyuk, *Luminous Bacteria* (Nauka, Novosibirsk, 1984).
7. G. A. Chiganova and S. A. Chiganov, Neorg. Mater. **35** (5), 581 (1999).
8. V. S. Bondar', E. S. Vysotskiĭ, V. V. Zavoruev, *et al.*, Prikl. Biokhim. Mikrobiol. **24** (6), 745 (1988).
9. V. N. Petushkov, G. A. Kratasyuk, N. S. Rodionova, *et al.*, Biokhimiia **49** (4), 692 (1984).
10. J. W. Hastings and G. Weber, J. Opt. Soc. Am. **53**, 1410 (1963).

Translated by O. Borovik-Romanova

Physics of the Solid State, Vol. 46, No. 4, 2004, pp. 764–766. Translated from Fizika Tverdogo Tela, Vol. 46, No. 4, 2004, pp. 743–745.

APPLICATIONS OF NANODIAMONDS

Compaction of Nanodiamonds Produced under Detonation Conditions and Properties of Composite and Polycrystalline Materials Made on Their Basis

P. A. Vityaz* and V. T. Senyut**

**National Academy of Sciences of Belarus, Minsk, Belarus*

e-mail: vitiaz@presidium.bas-net.by

***Institute of Mechanics and Reliability of Machines, National Academy of Sciences of Belarus, Minsk, 220072 Belarus*

e-mail: vsenyut@tut.by

Abstract—It is believed that materials based on ultrafine (nanoscale) diamond powders can possess high-level physical-mechanical and performance parameters characteristic of a nanocrystalline state. In certain cases, however, conventional methods for compacting ultrafine-dispersed diamonds (UDDs) fail and cannot be used to fabricate materials with desired properties. The difficulties associated with the ultrafine-dispersed state of the initial diamond powders can be surmounted by modifying the chemical and phase composition of the UDD surface. The possible use of UDDs as a catalyst that is conductive to the occurrence of chemical and phase transformations in certain substances at high pressures is analyzed. Sintering UDDs in the region of metastability of diamond makes it possible to produce porous polycrystalline aggregates with large specific surface area and very hard transparent particles. © *2004 MAIK "Nauka/Interperiodica".*

The synthesis of composites and polycrystals based on ultrafine-dispersed diamonds (UDDs) is currently one of the promising technologies in the science of diamond materials. This conclusion is derived from the following facts.

(1) Highly efficient technologies of fabrication and purification of diamonds have been developed [1].

(2) Structural and phase transformations in ultrafine-dispersed media occur at lower values of the external factors than in the case of "bulk" powders.

(3) It is believed that nanocrystalline materials based on ultrafine (nanoscale) diamond powders can possess high-level physical-mechanical and performance parameters [2].

(4) The area of use of such materials expands as more disperse initial raw materials are employed.

However, in producing nanostructural materials, conventional methods for compacting and sintering UDDs fail in certain cases. The main reasons for low physical and mechanical parameters of UDD-based compacts are as follows: high dispersion of UDDs, their polycrystalline structure, large specific surface area, high impurity content, low compressibility and high porosity of samples, and the tendency of powders toward graphitization at moderate sintering temperatures [3]. The compressibility and density of initial compacts can be increased using modified UDDs or by centrifuging powders in various media [4].

In a number of papers, it was reported that the inverse transformation of diamond into graphite is observed when UDDs are sintered in the region of thermodynamic stability of diamond. Graphitization can be significantly suppressed by introducing B_2O_3, SiO_2, or B in the working mixture, which is favorable for the formation of glasses with oxygen-containing compounds located on the UDD surface.

The glassy phase promotes sintering, decreases porosity, and increases the mechanical strength of compacts as compared with samples sintered without admixtures.

Sintering of UDDs with copper, aluminum, and phenolformaldehyde resin has been investigated at high pressures and moderate temperatures [5]. The samples obtained by sintering with various binders were used to polish optical glass (K-8) that was preliminarily polished with a diamond paste of grade 3/2. An instrument was developed that made it possible to attain a roughness R_Z of 5–6 nm by polishing the glass surface for 5–10 min [6].

Modification of the surface of UDD powders by changing its chemical composition can improve the physical and mechanical properties of compacts. For example, CH_4, C_2H_5OH, and H_2 promote sintering at high pressures and high temperatures and thereby significantly increase the microhardness of samples [7]. The mechanical strength of a sample is determined by its residual porosity and the spatial distribution of stresses in the sinter, which, in turn, depends on the geometric parameters of the initial compact and the form of the high-pressure press mold.

1063-7834/04/4604-0764$26.00 © 2004 MAIK "Nauka/Interperiodica"

We studied compacted UDDs modified by adding B, Ti, and Si. These admixtures bind oxygen (which promotes graphitization of diamond) and, at the same time, favor the formation of carbides during heat treatment. The hardness of such samples is 25–30 GPa, and their sintering pressure and temperature are lower than those of samples obtained from unmodified powders [7].

It is found that, in the case where UDDs modified with non-diamond carbon are compacted under static high-pressure conditions, the structure and properties of compacts depend on the structure and dispersion of the non-diamond carbon. For example, in the case of sintering of UDDs modified with graphite that resulted from surface graphitization of UDDs and is bound to the surface of nanodiamonds, micrometer-sized diamond particles are produced and arranged predominantly in the pores of compacts. When powders mixed with disordered non-diamond carbon are subjected to thermal treatment under the same conditions, a compact material with a microhardness of the order of 55–65 GPa and a density of 2.5–2.7 g/cm^3 is formed on the basis of the UDD charge. The structure of this material is shown in Fig. 1. Studies of UDDs sintered (under static high-pressure conditions) with various grades of graphite used in fabricating diamond powders showed that, in this case, UDDs can catalyze the graphite–diamond phase transformation. This transformation is preceded by amorphization of the graphite and a subsequent formation of intermediate diamond-structure polytypes and cubic diamond. Similar processes are observed in thermobaric treatment of UDDs mixed with a powder of hexagonal boron nitride *h*-BN [8, 9]. In the initial stage of the transformation, amorphization of the initial *h*-BN occurs. As the treatment temperature is increased, first wurtzite-structure boron nitride *W*-BN and then cubic boron nitride *c*-BN arise. The transformation of graphite-like boron nitride into the cubic modification occurs within a wide temperature range (600–1600°C) at a pressure of 7 GPa. The distinctive feature of the graphite–diamond polymorphic transformation and the *h*-BN–*c*-BN transformation in the presence of UDDs is that these transformations are characterized by lower temperatures of formation of dense (diamond-like) phases and occur without conventional catalysts.

The effect of nanodiamonds on the physicochemical transformations that occur during ceramic sintering has been investigated. In particular, it was reported in [8] that a number of structural and phase transformations dependent on the temperature of charge sintering were observed to occur when UDDs and AlN were sintered at high static pressures. X-ray diffraction data indicate that, in addition to the initial powders, corundum Al_2O_3 forms in the sintered material at a moderate temperature of treatment (1000–1400°C). Graphitization is insignificant, and the (111) diffraction peak of diamond narrows and increases in intensity. The density of samples in this case is 3.0–3.1 g/cm^3. As the treatment temperature is increased to 1450–1500°C, the UDD and AlN interact strongly with oxygen and the corundum content in samples increases. Starting with 1800°C, a new phase, aluminum oxynitride Al–O–N, appears in addition to the initial components (UDD, AlN, Al_2O_3); the corundum content decreases sharply and vanishes as the temperature is increased. The maximum density of samples is 3.1–3.25 g/cm^3, and the hardness is 13–20 GPa for an indenter load of 200 g.

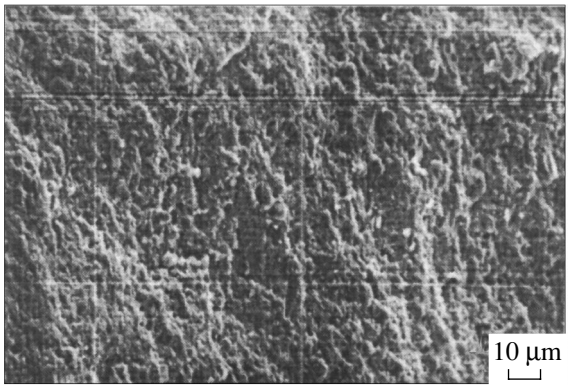

Fig. 1. Microstructure of a polycrystal produced under static compression over 15 s (pressure 7 GPa, temperature 2300°C).

UDDs can also be used to fabricate nanostructural polycrystalline powders. Both purified UDD powders and those modified with non-diamond carbon can be employed for this purpose. They are sintered at a high pressure in the region of stability of diamond or graphite depending on the prior treatment. Then, clinkers are dispersed and subjected to chemical purification. In this way, individual granules ranging in size from fractions of a micrometer to tens of micrometers can be obtained, with their specific surface area being smaller than that of the initial UDD [10].

By performing thermal treatment of UDDs at low pressures ($p \sim 1.33 \times 10^{-1}$ Pa) in the temperature range 1000–1200°C, variously shaped particles transparent to visible light can be obtained that range in size from 100 to 750 μm (Fig. 2). In this case, the treatment of the charge should be performed under conditions that obstruct recrystallization of the graphite, which can also occur at high sintering temperatures and low pressures. X-ray diffraction analysis of particles obtained at moderate sintering temperatures showed reflections corresponding to graphite-like phases; an increase in the charge sintering temperature gives rise to an annealing of metastable structures. The phase composition of the products of vacuum treatment of UDDs depends on the initial charge, its preliminary processing, and the mode of the subsequent thermal treatment. The largest particles are faceted and do not differ in appearance from diamond crystals synthesized under static conditions. For the most part, the microhardness varies from

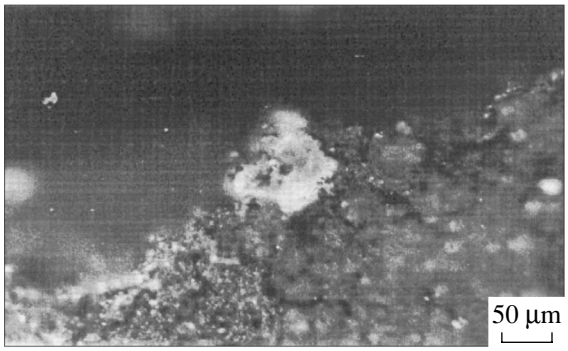

Fig. 2. UDD-based large particle on the surface of a compact after sintering in vacuum.

10 to 40–50 GPa; the maximum values (100 GPa) are obtained in indenting the largest, most perfect particle (the diameters of the long and short diagonals are 750 and 300 μm, respectively) [10].

Thus, a number of new effects inherent in the ultradisperse state of the substance have been detected. In particular, it has been found that thermobaric treatment of UDDs, graphite, and boron nitride powders can bring about the formation of diamond and cubic boron nitride, respectively, in the region of catalytic synthesis of superhard materials. Sintering of variously modified UDDs under analogous conditions brings about the formation of compact materials with a relatively high microhardness, which is determined by the disperse nanostructure. Sintering at low pressures makes it possible to fabricate composites that are suitable for final polishing of various materials and to produce compacts from which one can obtain (after dispersion and subsequent chemical purification) fairly strong porous polycrystalline particles with a disperse nanostructure. The thermobaric treatment of a UDD-based charge in the region of stability of graphite brings about the formation of filaments and transparent particles up to several hundred micrometers in size, with the microhardness of such particles reaching the value characteristic of diamond single crystals. Nanoscale diamonds allow one to extend the range of diamond and diamond-containing composites and to improve the efficiency of the existing technology of superhard materials.

ACKNOWLEDGMENTS

This study was supported by the state scientific and technical program “Diamonds” (project nos. 1.04, 2.32, 3.23).

REFERENCES

1. V. V. Danilenko, I. A. Petrusha, G. S. Oleĭnik, and N. V. Danilenko, Sverkhtverd. Mater., No. 4, 53 (1998).
2. R. A. Andrievskiĭ, Poroshk. Metall. (Minsk) **22**, 119 (1999).
3. V. V. Danilenko, *Synthesis and Sintering of Diamonds by Explosion* (Énergoatomizdat, Moscow, 2003).
4. V. T. Senyut and O. A. Prokhorov, in *Abstracts of Conference on Materials and Technologies* (Gomel, 2000), p. 73.
5. V. B. Shipilo, I. M. Starchenko, E. V. Zvonarev, and V. T. Senyut, *Diamond-Based Composites and Related Materials* (Kluwer Academic, Dordrecht, 1997), p. 349.
6. G. R. Gorodkin, L. K. Gleb, I. M. Starchenko, and V. T. Senyut, in *Abstracts of Conference on New Materials and Technologies* (Minsk, 1998), p. 109.
7. P. A. Vityaz, V. T. Senyut, and S. V. Gladkikh, in *Proceedings of International Conference on Hard Materials and Diamond Tooling* (Lausanne, 2002), p. 177.
8. E. V. Zvonarev, V. T. Senyut, I. M. Starchenko, and V. M. Finskaya, Sverkhtverd. Mater., No. 4, 41 (1998).
9. I. M. Starchenko and A. M. Tolkachev, in *Proceedings of International Conference on Materials and Coatings for Extreme Performances* (Katsiveli, Crimea, 2002), p. 236.
10. V. T. Senyut, Sverkhtverd. Mater., No. 6, 68 (2002).

Translated by Yu. Epifanov

Physics of the Solid State, Vol. 46, No. 4, 2004, pp. 767–769. Translated from Fizika Tverdogo Tela, Vol. 46, No. 4, 2004, pp. 746–748.

APPLICATIONS OF NANODIAMONDS

Physical-Mechanical Properties of Nanocrystalline Materials Based on Ultrafine-Dispersed Diamonds

V. T. Senyut and E. I. Mosunov

Institute of Mechanics and Reliability of Machines, National Academy of Sciences of Belarus, Minsk, 220072 Belarus

e-mail: vsenyut.@tut.by, nanotech@inmash.bas-net.by

Abstract—The physical-mechanical properties of polycrystals produced on the basis of ultrafine-dispersed diamonds (UDDs) at high static pressures with the use of thermal treatment in vacuum are investigated. The properties of the polycrystals are shown to depend on the sintering conditions and sintering technique, as well as on the modification of the starting powders. With the addition of metals (Co, Ti) to UDD powders, the mechanical strength of compacts increases, their structure improves, and their parameters can be optimized at lower thermobaric treatment temperatures. By studying the products of thermal treatment of UDDs in vacuum, it is established that the compacts and individual particles that form during thermal treatment differ significantly in microhardness. © *2004 MAIK "Nauka/Interperiodica".*

To date, highly efficient methods have been developed for the large-scale manufacture of ultrafine-dispersed diamonds (UDDs) under detonation of explosive materials [1]. Furthermore, diamond thus obtained is more finely dispersed than diamond powders produced using other methods. For this reason, the fabrication of polycrystals from such UDDs is of considerable interest [2]. Studies dedicated to this subject show that, in sintering UDD powders, the particle packing is different from that in coarse-grained powders and diffusion is important. Therefore, sintering should be performed at the maximum possible pressures and temperatures. However, even in this case, the formation of grain boundaries is retarded by surface impurities [3]. Consolidation of diamond nanoparticles at high temperatures is accompanied by the transformation of diamond into graphite. Graphitization occurs in the thermodynamic region of stability of diamond and begins at a temperature (1000°C) that is too low for diamond powders to sinter [4]. The formation of high-density compacts from unmodified UDDs is likely to start at significantly higher pressures and temperatures, which cannot be reached with the high-pressure apparatus commonly used to synthesize and sinter superhard materials [1].

The sintering of nanopowders is significantly affected by impurities present on the UDD surface. Variations in the chemical and phase composition of the UDD surface and in the amount of impurities on it can affect both the physical-mechanical properties of sintered materials and the regime of sintering. It was shown in [5, 6] that the addition of 1–3 wt % boron and certain glass-forming oxides to a UDD-based charge mixture increases the temperature of the onset of graphitization and the duration of UDD exposure at high temperatures without increasing the density and strength of compacts. It is expected that the addition of components active with respect to carbon to a UDD-based charge mixture will decrease the sintering parameters and improve the properties of the sintered materials.

The objective of this work is to study the effect of variations in the regime of thermobaric compaction on the properties of unmodified UDD samples and samples modified with metals (Co, Ti). An attempt is also made to produce nanocrystalline materials at low pressures, in particular, under vacuum conditions.

We took as dopants cobalt (because it is a catalyst for carbon) and titanium (because it shows an affinity for carbon and adsorbs oxygen in the course of thermal treatment). Furthermore, modified UDDs are used to attain a uniform distribution of additives over the charge mixture.

The UDD powders modified with Co and Ti (up to 10 wt %) and the deep-cleaned unmodified UDD powders used by us were prepared at the Sinta NP ZAO (Minsk). Original samples 3–5 mm in diameter and 2–4 mm high are compacted at a pressure of 0.1–0.3 GPa. Experiments are performed either under a static pressure of 7 GPa on a high-pressure apparatus of the "anvil with a hollow" type at temperatures of 1000–2300°C or in vacuum (1.33×10^{-1} Pa) at a temperature of 1100°C.

The microhardness of samples is measured on a PMT-3 device under a load of 2 N, and the density is determined using hydrostatic weighing in CCl_4. The microstructure is examined on unetched microsections and cleaved faces of samples using a Mikro-200 metallographic microscope and a CamScan scanning microscope analyzer. X-ray structural analysis is carried out on a DRON-3 diffractometer.

In the first stage of the work, we studied the compaction of deep-cleaned unmodified UDD powders at high

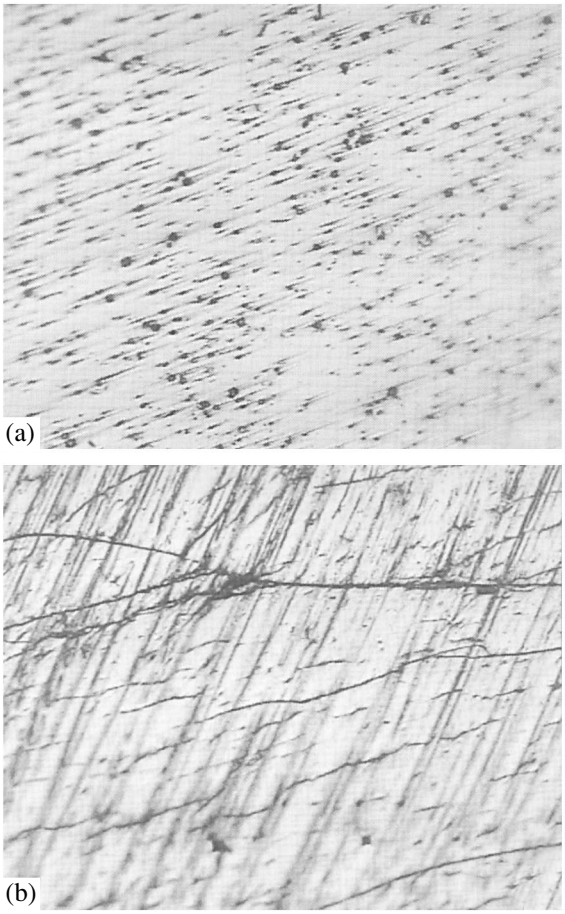

Fig. 1. Microstructure (200×) of a sample produced from a UDD powder modified with cobalt. Sintering is performed under a pressure of 7 GPa over 15 s at a temperature of (a) 1300 and (b) 2300°C.

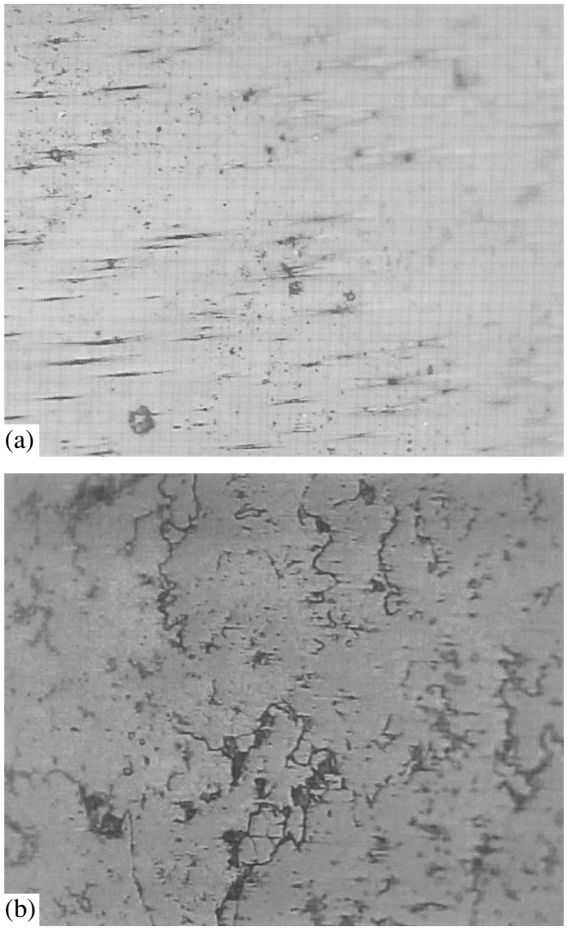

Fig. 2. Microstructure (200×) of a sample produced from a UDD powder modified with titanium. Sintering is performed under a pressure of 7 GPa over 15 s at a temperature of (a) 1300 and (b) 2300°C.

pressures. It is established that, at a sintering temperature of 1300°C, the microhardness of a sample is 20 GPa at a density of 2.73 g/cm^3. The maximum microhardness (30–35 GPa) at a density of 2.85–2.90 g/cm^3 is reached at sintering temperatures of 1600–1800°C, and the microstructure of a sample in this case contains micropores 2 to 5 μm in size accounting for up to 5% of the microsection area and pores 10 to 18 μm in size accounting for up to 15%. Thermobaric treatment at temperatures above 1800°C activates graphitization, which decreases the density and microhardness of samples.

In the second stage, we studied the sintering of UDDs modified with Co and Ti. For samples modified with Co, the density and microhardness of sinters increase as the sintering temperature is increased to 1300°C. At a pressure of 7 GPa and a temperature of 1300°C, the microstructure of a sample exhibits pin holes 2.5 to 5 μm in size accounting for up to 30% of the entire area and the maximum microhardness is 25 to 31 GPa at a density of 2.83 g/cm^3 (Fig. 1a). An x-ray diffraction study revealed a small quantity of graphite. As the sintering temperature is increased further, the density and microhardness decrease. For example, the microstructure of a sample sintered at a pressure of 7 GPa and a temperature of 2300°C (Fig. 1b) contains a developed network of microcracks and has no pin holes; the microhardness is 14–16 GPa, and the density is 2.7 g/cm^3. An x-ray diffraction study showed the presence of graphite in the sample.

For UDD-based samples modified with Ti, the density and microhardness also increase as the sintering temperature is increased to 1300°C. The microstructure of a sample sintered at a pressure of 7 GPa and a temperature of 1300°C exhibits pin holes 1 to 2 μm in size accounting for up to 10% of the entire area (Fig. 2a). The maximum microhardness of the sample is 28–31 GPa at a density of 2.74 g/cm^3. The x-ray diffraction data show that the intensity of the (002) reflection of graphite is higher than that in the case of a UDD-based sample modified with Co and sintered under the same

conditions and that the sample modified with Ti contains titanium carbide.

A scanning microscopy study revealed that the cleaved faces of samples are covered with thin films 10- to 30-μm long. According to microanalysis data, the titanium content is maximum in the films (3.5 wt %); near the film–matrix interface, the titanium content decreases to 2 wt % and then again increases up to 2.5–3.0 wt % with distance away from the interface into the matrix. The microstructure of a sample sintered at a pressure of 7 GPa and a temperature of 2300°C exhibits micropores 1 to 2 μm in size and pores 10 to 25 μm in size (up to 20%), as well as microcracks (Fig. 2b). The microhardness of the sample is 26–29 GPa. On the whole, the UDD-based samples modified with Ti are more fragile, as indicated by chips and microcracks that arose around the periphery of indentations in measuring the microhardness. No chips and microcracks are observed in measuring the microhardness of the UDD-based samples modified with Co.

Thus, the samples produced from modified UDD powders at a sintering temperature of 1300°C exhibit higher values of microhardness and density than those produced from unmodified UDD powders. These parameters decrease as the sintering temperature is raised.

In the third stage of the work, we studied the properties of the products of UDD sintering in vacuum. For this purpose, we used samples produced from deep-cleaned UDD powders not modified with metals. The samples thus obtained have a microhardness of 0.8–1.0 GPa and a density of 1.1–1.2 g/cm^3 and contain graphite. Certain samples contain transparent particles, filaments, and scales 100 to 750 μm in size with a microhardness of 10–50 GPa. The microhardness of a particle 700 to 750 μm in size with a habit characteristic of diamond is measured to be 100 GPa. X-ray structural analysis did not reveal graphite in these particles.

Thus, we have established in this work that prior modification of UDDs with Co and Ti affects the microstructure and properties of the polycrystals obtained from them. The addition of Co favors graphitization of UDDs at high sintering temperatures but does not affect it at sufficiently low sintering temperatures. The addition of Ti favors the formation of graphite at low temperatures; however, at higher temperatures, the hardness of samples changes only insignificantly, which can be due to the formation of titanium carbide. The regimes of thermobaric treatment for which optimum properties of samples are attained also depend on the modifying additive. For UDD powders modified with Co and Ti and sintered at 1300°C, the density of the samples increases from 2.73 to 2.83 g/cm^3 and their microhardness increases from 20 to 31 GPa in comparison with the respective characteristics of unmodified UDD powders. In the case of thermobaric sintering at temperatures above 1800°C, samples with reduced density and microhardness are obtained, due to graphitization, for all kinds of powders used in this work.

In the case where samples are produced from unmodified UDD powders by sintering in vacuum, the microhardness of the samples is of the order of 1.0 GPa and the density is 1.1–1.2 g/cm^3. The sintering products contain particles that are aggregates of UDDs. The microhardness of such particles is 10–100 GPa, which is one to two orders of magnitude higher than that of the matrix without UDD aggregates.

ACKNOWLEDGMENTS

This study was supported by the state scientific and technical program “Diamond” (project no. 2.32).

REFERENCES

1. V. Yu. Dolmatov, *Ultrafine-Dispersed Diamonds of Detonation Synthesis: Production, Properties, and Application* (SPbGPU, St. Petersburg, 2003).
2. V. V. Danilenko, I. A. Petrusha, G. S. Oleĭnik, and N. V. Danilenko, Sverkhtverd. Mater., No. 4, 53 (1998).
3. V. F. Britun and A. V. Kurdyumov, Sverkhtverd. Mater., No. 4, 36 (1998).
4. A. A. Shul’zhenko, A. A. Bochechka, L. A. Romanko, *et al.*, Sverkhtverd. Mater., No. 6, 50 (2000).
5. E. V. Zvonarev, V. T. Senyut, V. B. Shipilo, and I. M. Starchenko, in *Abstracts of Conference on New Materials and Technologies* (Minsk, 1996), p. 25.
6. V. B. Shipilo, I. M. Starchenko, E. V. Zvonarev, and V. T. Senyut, Mater. Technol. Instrum. (Minsk) **2** (4), 61 (1997).

Translated by Yu. Epifanov

Physics of the Solid State, Vol. 46, No. 4, 2004, pp. 770–774. Translated from Fizika Tverdogo Tela, Vol. 46, No. 4, 2004, pp. 749–753.

SEMICONDUCTORS AND DIELECTRICS

Electroluminescence in SiO_2 Layers in Various Structures

A. P. Baraban, P. P. Konorov, L. V. Miloglyadova, and A. G. Troshikhin

Fock Institute of Physics, St. Petersburg State University, ul. Ul'yanovskaya 1, Petrodvorets, St. Petersburg, 198504 Russia
e-mail: laramil@rabler.ru

Received June 30, 2003; in final form, September 4, 2003

Abstract—Electroluminescence (EL) in an electrolyte–insulator–semiconductor system is used to study oxide layers in Si–SiO_2–Si_3N_4 and Si–SiO_2 structures prepared using various techniques. The EL spectra of all the structures contained the 2.7-eV emission band characteristic of the radiative relaxation of excited sililene centers. A comparative study of the conditions conducive to the formation of such luminescence centers in various structures containing SiO_2 layers was made, and their nature was refined. © *2004 MAIK "Nauka/Interperiodica".*

1. INTRODUCTION

Investigation of the electroluminescence (EL) in layers of SiO_2, whose spectrum contains a number of bands in the region 250–800 nm [1–10], is of fundamental interest both in terms of the electronic processes taking place in such layers and their application potential. The latter aspect gains particular significance in view of the intense developments in the field of flat solid-state screens. Viewed from this standpoint, the use of EL in SiO_2 layers integrated in Si–SiO_2 or associated systems appears particularly promising, because this would make it possible to combine the achievements reached in solid-state screen fabrication with planar silicon technology and, thus, promote progress in the visual presentation of information.

This communication reports on a comparative study of the spectral response of the EL in SiO_2 layers deposited on silicon. Attention was focused on the 2.7-eV emission band and the nature of centers responsible for this band, which is typical of SiO_2 layers. This band is seen in a variety of structures containing such layers and is one of the strongest in the emission spectrum. A comparison of the conditions conducive to the appearance of this band in various structures with SiO_2 layers may help to better understand the character of the electronic processes occurring in these layers in strong electric fields and to define the nature of the corresponding luminescence centers more precisely.

2. CHARACTERIZATION OF THE STRUCTURES AND EXPERIMENTAL TECHNIQUE

We studied Si–SiO_2 structures prepared using the following methods:

(1) thermal oxidation of KDB-10 single-crystal silicon by standard technologies (d_{ox} = 110 nm);

(2) SIMOX technology based on implanting 190-keV oxygen ions (to a dose of 1.8×10^{18} cm^{-2}) into the silicon bulk at a temperature of 650°C, followed by annealing at 1320°C for 6 h and etching off of the outer silicon layer (d_{ox} = 400 nm);

(3) thermal oxidation of KÉF-5 (100) silicon in humid oxygen at 950°C (d_{ox} = 250 nm) with subsequent implantation of argon ions into the bulk of the oxide layer; the dose of implanted ions was 10^{13}–3.2×10^{17} cm^{-2}, and their energy (130 keV) was chosen such that the maximum of the implanted ion distribution was at the center of the oxide layer;

(4) galvanostatic anode oxidation (AO) of KDB-10 single-crystal silicon (d_{ox} = 100 nm);

(5) deposition of a silicon nitride layer 80 and 100 nm thick (in a low-pressure reactor) from a silane plus ammonia mixture on Si–SiO_2 structures thermally prepared in dry oxygen at a temperature of 1100°C on KDB-10 (100) substrates (Si–SiO_2–Si_3N_4 structures with oxide thicknesses of 40, 77, and 100 nm).

The EL spectra were measured in the region 250–800 nm in the electrolyte–insulator–semiconductor system following the technique described in considerable detail in [1]. This system is advantageous in that it permits the injection of electrons and their heating in SiO_2 layers within a broad range of fields, which is a necessary condition for the excitation of EL centers [1–3]. Also, the possibility of controlled etching-off of the oxide layer while simultaneously measuring the EL spectral response makes it possible to determine the spatial distribution of EL centers in SiO_2 layers.

3. EXPERIMENTAL RESULTS

Figure 1 presents EL spectra of the Si–SiO_2 structures prepared by thermal oxidation of silicon measured at various electric fields in the oxide layer. The EL in the 2.7-eV band was observed under application to the oxide layer of an electric field E_{ox} above a certain threshold level E^*, which gave rise to collision ionization (CI) in the bulk of the oxide layer. The strength of this field is related to the oxide layer thickness d_{ox}

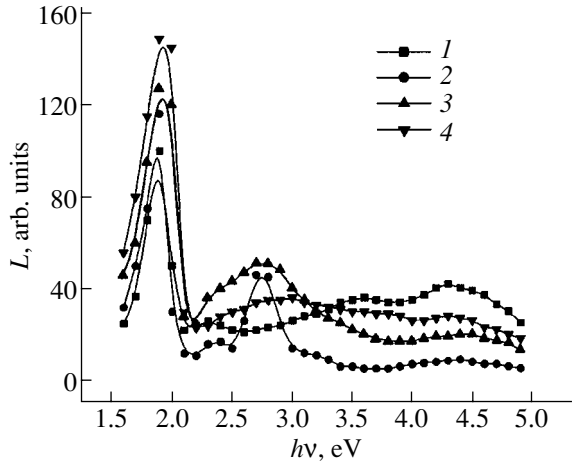

Fig. 1. EL spectra of Si–SiO_2 structures obtained by thermal oxidation of silicon in "dry" oxygen at 1100°C and plotted for various values of the electric field in the oxide layer E_{ox}: (*1*) 13.0, (*2*) 13.95, (*3*) 14.1, and (*4*) 14.9 MV/cm. The oxide layer thickness is 110 nm. The calculated value of E^* is 13.9 MV/cm.

through $E^* = C_1 + C_2/d_{ox}$ [3]. The appearance of the EL in the 2.7-eV band was shown in [3] to be due to the presence in the oxide layer of hot electrons with an excess energy of over 9 eV, which are necessary to initiate CI in the SiO_2 matrix. The region of localization of the EL and, hence, of the luminescence centers (LC) in this band coincided with that of the maximum probability of the CI process and shifted with increasing electric field from the Si/SiO_2 interface toward the outer boundary of the oxide layer. The termination of CI (due to a decrease in the electric field strength in the oxide layer or field-induced degradation of the Si–SiO_2 structure) was accompanied by EL quenching. Preliminary application of a field $E_{ox} > E^*$ to the Si–SiO_2 structures did not initiate subsequent EL formation in the 2.7-eV band for fields $E_{ox} < E^*$, which do not cause CI. This means that it is the CI process that accounts for the formation of 2.7-eV LCs in the bulk of the oxide layer and their subsequent excitation by hot electrons, whose energy can be lower than 9 eV. Also, the LCs formed were found to be short lived, because the termination of CI in the SiO_2 layer was accompanied by a practically complete disappearance of these centers.

The EL spectra of the Si–SiO_2 structures prepared using the SIMOX technology exhibited a number of essential differences (Fig. 2). The 2.7-eV EL band in these structures was the strongest in the spectrum, and its intensity was about 400 times higher than that of the analogous band in the spectra of thermally prepared Si–SiO_2 structures. Note that this emission band was observed in electric fields substantially lower than those needed for the CI process in the bulk of the oxide layer to set in. This implies the formation of 2.7-eV LCs directly in the course of the preparation of the structures. The EL spectra measured in parallel with the etching-off of the oxide layer indicated the 2.7-eV LCs to be localized primarily near the Si–SiO_2 interface. Note that the EL spectrum also contained an emission band of energy (4.4 ± 0.1) eV, which could be fitted well by a Gaussian with an FWHM of (0.4 ± 0.1) eV. No other emission bands were observed to exist.

Figure 3 presents EL spectra of Si–SiO_2 structures subjected to argon ion implantation into the oxide layer. These EL spectra contained three emission bands at 1.9, 2.7, and 4.4 eV. The EL bands at 2.7 and 4.4 eV were present in the EL spectra starting from an implantation dose of 10^{13} cm^{-2} and were observed in electric fields that did not cause CI in the oxide layer. A further increase in the implantation dose up to 10^{17} cm^{-2} reduced the intensities of these emission bands, which was replaced by a strong increase as the 3.2×10^{17} cm^{-2} dose was reached. Note that the intensity ratio of the

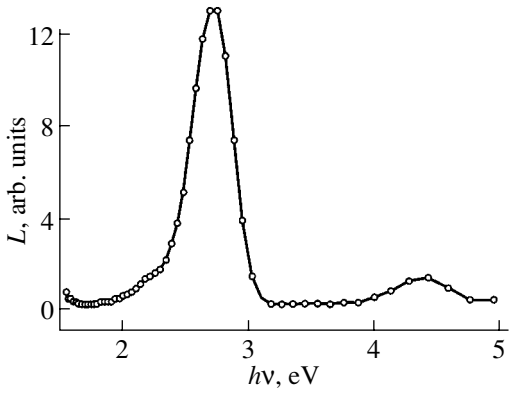

Fig. 2. EL spectrum of Si–SiO_2 structures prepared by SIMOX technology.

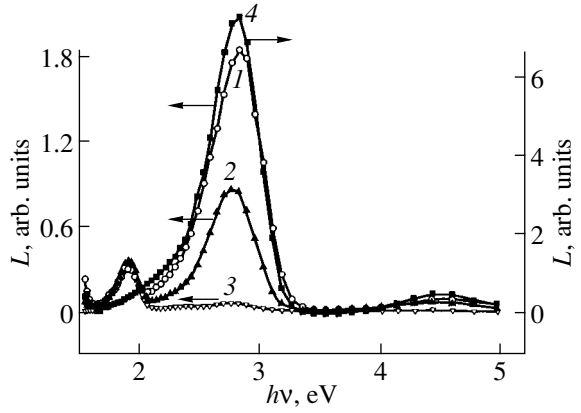

Fig. 3. EL spectra of Si–SiO_2 EL structures after argon ion implantation to dose D equal to (*1*) 10^{13}, (*2*) 10^{14}, (*3*) 10^{16}, and (*4*) 3.2×10^{17} cm^{-2}.

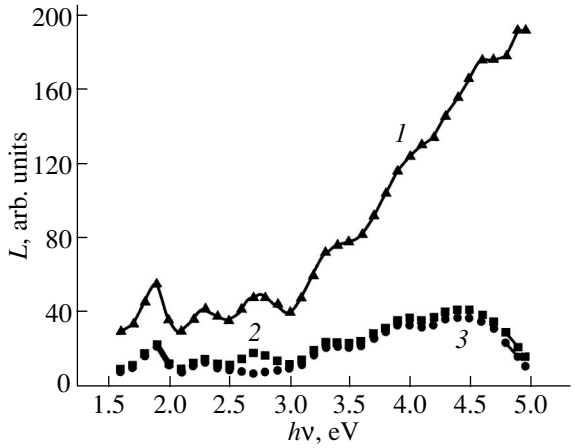

Fig. 4. Effect of anodic oxidation on the EL spectrum of a Si–SiO_2–electrolyte system. The oxide growth rate is (*1*) 1.5 and (*2*) 0.01 nm/min, and (*3*) is the EL spectrum of a Si–SiO_2 structure prepared by the anodic process in a nonoxidizing electrolyte.

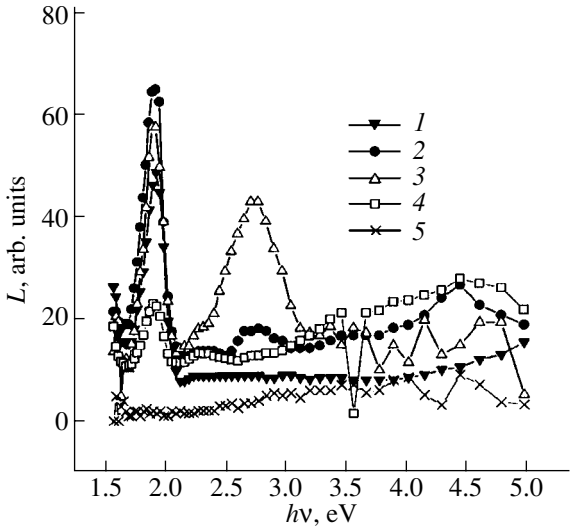

Fig. 5. EL spectra of (*1*) Si–SiO_2(400 Å)–Si_3N_4(800 Å), (*2*) Si–SiO_2(770 Å)–Si_3N_4(800 Å), (*3*) Si–SiO_2(1000 Å)–Si_3N_4(1000 Å), (*4*) Si–SiO_2(1000 Å)–Si_3N_4(1000 Å) after etching the Si_3N_4 layer off with hydrofluoric acid, and (*5*) Si–Si_3N_4.

emission bands at 2.7 and 4.4 eV remained the same in all cases. It was established that the LCs responsible for the 2.7- and 4.4-eV bands are located 30–100 nm away from the Si–SiO_2 boundary [4], i.e., that the maximum of their distribution is closer to the boundary with silicon than the maximum of the implanted argon. A higher implant dose brought about a broadening of the LC distribution and a shift of its maximum towards the boundary with silicon [4]. Annealing (500–1100°C, 10 s) of the Si–SiO_2 structures after the implantation (except for the implantation to a dose of 3.2×10^{17} cm^{-2}) resulted in a decrease in the intensity of both EL bands.

The silicon AO process used to prepare Si–SiO_2 structures was accompanied by luminescence [11, 12] whose spectrum contained a clearly resolved emission band at 2.7 eV (Fig. 4). In silicon produced by galvanostatic AO, this band appeared in the course of formation of the oxide layer starting with a thickness of ~40 nm [1]. Termination of the AO by replacing the oxidizing electrolyte (ethylene glycol with KNO_3) with an aqueous solution of a neutral electrolyte (1-*N* solution of Na_2SO_4) brought about almost complete quenching of this band (Fig. 4). Replacing this solution with the starting electrolyte resulted in recovery of the band. The EL spectrum (recorded in the neutral electrolyte) of the Si–SiO_2 structures prepared by AO was similar to that of thermally formed structures. The 2.7-eV band was observed in this case only in electric fields exceeding a certain critical level and initiating CI in the bulk of the oxide layer. However, here, the critical field was again about half that observed in the case of thermally prepared Si–SiO_2 structures. Preliminary application of a field to AO-produced Si–SiO_2 structures at levels high enough to initiate CI in the oxide layer did not generate EL in the 2.7-eV band in weaker electric fields.

Figure 5 displays EL spectra of the Si–SiO_2–Si_3N_4 structures. The EL spectrum obtained in the conditions excluding the possibility of the onset of CI in a SiO_2 layer ($E_{ox} < E^*$) contained in this case a clearly pronounced band at ~2.7 eV, whose intensity increased with the thickness of both the SiO_2 and the Si_3N_4 layer and depended superlinearly on the density of the current flowing through the structure [5]. The latter observation indicates that the excitation mechanism of this band is related to the electron heating processes taking place in the oxide layer. The EL spectrum obtained after the silicon nitride layer had been etched off did not contain the 2.7-eV EL band, which gives one grounds to connect its appearance to the formation of the layered insulator, because the EL intensity of the silicon nitride layer itself was an order of magnitude lower (Fig. 5).

4. DISCUSSION OF THE RESULTS

A common feature of the above EL spectra of the various structures containing SiO_2 layers is the presence of the 2.7-eV emission band, which can be approximated by a Gaussian with an FWHM of (0.35 ± 0.05) eV. This suggests that the LCs responsible for this band are related to defects that have the same nature in all cases considered. Such defects are most likely the so-called sililene centers (O_2=Si:), which actually represent doubly oxygen-coordinated silicon atoms. As follows from the literature, defects of this type feature two radiative transitions, at ~ 2.7 and ~4.4 eV, whose

excitation energy is ~5 eV [13]. Note that the room-temperature intensity of the radiative transitions of energy 2.7 eV exceeds that of the 4.4-eV transition. These centers may form in various structures through a variety of mechanisms, whereas their excitation in all the above cases occurs through interaction with hot electrons that are created in insulating layers in strong electric fields and possess an excess energy above 5 eV.

The formation of sililene centers in thermally produced $Si–SiO_2$ structures is apparently directly connected with the CI process. The generation of electron–hole pairs in the bulk of the oxide layer brings about the rupture of two Si–O bonds in one silicon–oxygen tetrahedron with the formation of short-lived O_2=Si: defects. The termination of CI is accompanied by restoration of the broken bonds (which is stimulated by their spatial proximity) and, hence, by LC destruction. The threshold character of the dependence of the 2.7-eV EL band intensity on electric field in the oxide layer (Fig. 6) should be assigned to specific features of electron transport in strong electric fields, which originate from the CI-induced electron multiplication and creation of an additional hot-electron excess-energy dissipation channel connected with the appearance of the 2.7-eV EL band. The numerical modeling of electron transport in SiO_2 including the above features was performed in the Boltzmann kinetic approximation using the Monte Carlo macroparticle approach [14, 15] to derive the dependence of the 2.7-eV EL band intensity on the electric field in the oxide layer. The qualitative agreement between the numerical calculations and our experimental data (Fig. 6) supports the assumption that the EL in the 2.7-eV band is connected with CI processes occurring in the bulk of the oxide layer. The 4.4-eV band, which is likewise characteristic of the sililene centers, cannot be clearly identified in this case because of its substantially lower intensity.

The formation of sililene centers in SIMOX-grown structures can be associated with aggregation of silicon clusters near the Si/SiO_2 interface in the course of fabrication of the structures [16]. The high concentration of doubly oxygen-coordinated silicon defects permits reliable observation of the 4.4-eV band, the second characteristic feature of these defects. This observation is an additional argument for the validity of our ideas concerning the nature of the centers responsible for the EL at 2.7 eV.

To explain the mechanisms of formation of the sililene centers in argon-implanted structures, we have to take into account that the energy of implanted ions can dissipate through interaction with the atomic and electron subsystems of the oxide layer. The interaction with the electron subsystem is accompanied by electron–hole pair generation, and the interaction with the atomic subsystem causes structural distortions of the SiO_2 matrix. Energy dissipation in the outer part of the oxide layer is channeled equally through interaction with the electron and atomic subsystems. In the bulk of the oxide layer, the most probable mechanism of energy dissipation of the implanted argon involves coupling to the atomic subsystem, which brings about intense rupture of Si–O bonds near the maximum of the implanted-argon distribution and a displacement of Si and O atoms into the oxide layer (to a distance of 80–170 nm for the O atoms and of 30–70 nm for the Si atoms away from the maximum of the argon distribution, as estimated in [4]). This process forms two off-stoichiometric SiO_x regions, with $x > 2$ and $x < 2$, in the bulk of the oxide layer [17]. The sililene centers form in the oxygen-depleted SiO_2 region through the rupture of two Si–O bonds in the same silicon–oxygen tetrahedron and the displacement of oxygen atoms into the bulk of the oxide layer, and this is what accounts for the stability of the defects thus produced. The decrease in the EL band intensity at 2.7 and 4.4 eV brought about by annealing can be assigned to a partial recovery of the broken silicon–oxygen bonds in the bulk of the oxide layer, which entails a decrease in the concentration of the doubly oxygen-coordinated silicon atoms.

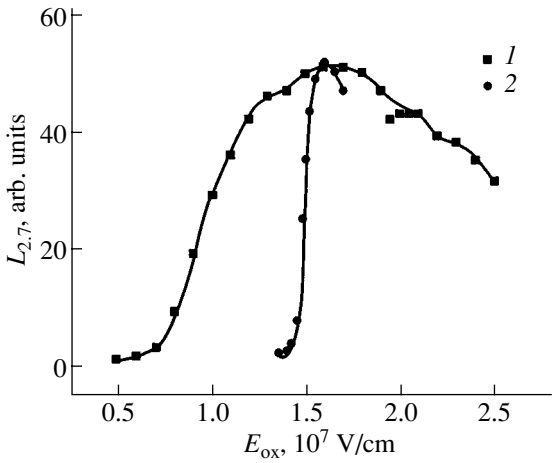

Fig. 6. Intensity of the 2.7-eV EL band as a function of the electric field in the oxide layer (*1*) obtained by numerical modeling [14, 15] and (*2*) measured experimentally.

The assumption that the 2.7-eV EL band is associated with the sililene centers is supported in studies of the silicon AO processes. The AO of silicon displays a linear section in the kinetics of the oxide layer formation [1], which is accompanied by luminescence at 2.7 eV. The defects responsible for the 2.7-eV EL band are created directly in the region of formation of the oxide layer, where the probability for the sililene centers to arise is high. Because the electron energy required to excite sililene centers exceeds 5 eV, the radiation observed by us should be localized within the oxide layer at a certain distance from the interface injecting the electrons, i.e., from the electrolyte. The minimum distance is actually the sum of two components, more specifically, of the electron tunneling length from the electrolyte to the oxide layer and of the

distance required to heat the electrons to an excess energy of ~5 eV. Silicon AO in this stage of kinetics occurs under a constant electric field strength of ~20 MV/cm in the oxide layer [1]. The tunneling length, determined by the height of the potential barrier for electrons (~4.4 eV) and by the electric field at the SiO_2–electrolyte interface, is ~2 nm. The distance required for electron heating to occur, as obtained by numerical modeling of the electron transport in SiO_2 [18], is ~8 nm. Thus, within the linear section of the kinetics (starting from a layer thickness of ~40 nm), the oxide layer forms in the bulk of SiO_2 ~10 nm away from the outer boundary, which agrees with the available literature data [19].

The occurrence of EL in the 2.7-eV band in Si–SiO_2–Si_3N_4 structures in electric fields not high enough for the onset of CI in the bulk of the oxide layer originates from the process employed to deposit a silicon nitride layer on the Si–SiO_2 structures. This process is accompanied by the formation of a transition layer containing sililene centers. The thickness of the transition layer (and, hence, the concentration of sililene centers) increases with the thickness of the oxide and silicon nitride layers. In its chemical composition, the transition layer actually represents a layer of silicon oxynitride (SiN_xO_y), which is characterized by a high concentration of sililene centers and the 2.7-eV luminescence [20]. The LCs in the transition layer are excited in this case by the hot electrons forming in the silicon nitride layer. Under typical conditions of EL excitation, the electric fields produced in the silicon nitride layers are 6–9 MV/cm; these fields heat electrons to an energy exceeding 5 eV [21], which is sufficient to excite the sililene centers at the SiO_2/Si_3N_4 interface.

5. CONCLUSIONS

Identification of the sililene centers (O_2=Si:) with the LCs responsible for the 2.7- and 4.4-eV luminescence permits one to describe, from a common standpoint, the totality of the experimental data on the luminescence observed in this spectral region in silicon–insulator structures containing SiO_2 layers. Furthermore, our study of the luminescence yielded additional information on the growth of the silicon–insulator structures and on the electronic processes occurring in them in strong electric fields. Viewed as candidates for the development of flat solid-state electroluminescent screens operating in the 2.7-eV EL band, the best promise is held by SIMOX-grown structures and Si–SiO_2 structures obtained by thermal oxidation of silicon with subsequent argon implantation into the oxide layer; thus far, these structures exhibit the highest emission intensity in this band.

ACKNOWLEDGMENTS

This study was supported by the GRACENAS Center of the Ministry of Education of the Russian Federation, project no. PD02-1.2-356.

REFERENCES

1. A. P. Baraban, V. V. Bulavinov, and P. P. Konorov, *Electronics of SiO_2 Layers on Silicon* (Leningr. Gos. Univ., Leningrad, 1988).
2. A. P. Baraban, P. P. Konorov, A. A. Kruchinin, and Yu. A. Tarantov, Élektrokhimiya **20** (4), 539 (1984).
3. A. P. Baraban, I. V. Klimov, N. I. Tenoshvili, *et al.*, Pis'ma Zh. Tekh. Fiz. **15** (17), 44 (1989) [Sov. Tech. Phys. Lett. **15**, 680 (1989)].
4. A. P. Baraban and L. V. Miloglyadova, Zh. Tekh. Fiz. **72** (5), 56 (2002) [Tech. Phys. **47**, 708 (2002)].
5. A. P. Baraban, D. V. Egorov, A. Yu. Askinazi, and L. V. Miloglyadova, Pis'ma Zh. Tekh. Fiz. **28** (23), 14 (2002) [Tech. Phys. Lett. **28**, 978 (2002)].
6. A. P. Baraban, P. P. Konorov, L. V. Malyavka, and A. G. Troshikhin, Zh. Tekh. Fiz. **70** (8), 87 (2000) [Tech. Phys. **45**, 1042 (2000)].
7. P. Solomon and N. Klein, J. Appl. Phys. **47** (3), 1023 (1976).
8. D. J. Di Maria, J. R. Kirtley, and E. J. Pakulis, J. Appl. Phys. **56** (2), 401 (1984).
9. T. N. Theis, J. R. Kirtley, and D. J. Di Maria, Phys. Rev. Lett. **50** (10), 750 (1983).
10. A. J. Pepe, W. Chen, and M. Oyler, J. Electrochem. Soc. **140** (4), 1090 (1993).
11. A. Gee, J. Electrochem. Soc. **107** (9), 787 (1960).
12. S. P. Maminova and L. L. Odynets, Élektrokhimiya **1** (3), 365 (1965).
13. L. N. Skuya, A. N. Streletskiĭ, and A. B. Pakovich, Fiz. Khim. Stekla **14**, 481 (1988).
14. A. P. Baraban, E. A. Semykina, and M. B. Vaniouchov, Semicond. Sci. Technol. **15**, 546 (2000).
15. A. P. Baraban, E. A. Semykina, and M. B. Vaniouchov, Phys. Low-Dimens. Semicond. Struct., No. 3/4, 27 (2000).
16. V. V. Afanas'ev, A. Stesmans, and A. G. Revesz, J. Appl. Phys. **82** (5), 2184 (1997).
17. B. Garido, J. Samitier, and S. Bota, J. Non-Cryst. Solids **187**, 101 (1995).
18. E. A. Semykina and T. E. Nikulina, in *Abstracts of International Conference Dielectrics-97* (St. Petersburg, 1997), Part 2, p. 70.
19. A. P. Baraban, I. V. Klimov, and P. P. Konorov, Vestn. Leningr. Univ., Ser. 4: Fiz. Khim. **4** (25), 71 (1988).
20. V. A. Gritsenko, *Atomic and Electronic Structure of Amorphous Insulators in Silicon MIS Devices* (Nauka, Novosibirsk, 1993).
21. D. J. Di Maria and Y. R. Abernathey, J. Appl. Phys. **60** (5), 1727 (1985).

Translated by G. Skrebtsov

Physics of the Solid State, Vol. 46, No. 4, 2004, pp. 775–779. Translated from Fizika Tverdogo Tela, Vol. 46, No. 4, 2004, pp. 754–758.

LATTICE DYNAMICS AND PHASE TRANSITIONS

Ferroelastic Phase Transition in Crystalline $K_3Na(CrO_4)_2$: Acoustic Studies

A. K. Radzhabov*, E. V. Charnaya*, B. Mroz, C. Tien***, Z. Tylczynski**, and C.-S. Wur*****

**Fock Institute of Physics, St. Petersburg State University, ul. Ul'yanovskaya 1, Petrodvorets, St. Petersburg, 198504 Russia*

e-mail: charnaya@paloma.spbu.ru

***Institute of Physics, A. Mickiewicz University, Poznan, 60-780 Poland*

****Department of Physics, Cheng Kung University, Tainan, 10701 Taiwan*

Received July 28, 2003

Abstract—Ultrasonic studies of the temperature behavior of the velocity and damping of sound for the *xx* and *zz* longitudinal and *yx* and *zx* transverse waves in $K_3Na(CrO_4)_2$ have been carried out in the temperature interval 185–295 K, which includes the region of the ferroelastic phase transition. The acoustic parameters for both shear and longitudinal waves were found to have anomalies in the region of the phase transition with a Curie temperature of 235.5 K. A theoretical analysis of the softening of the elastic moduli c_{44} and c_{66} was performed on the basis of the Landau expansion in terms of the strain tensor components ε_4 and $(\varepsilon_2 - \varepsilon_1)/2$ considered as the linearly coupled primary and secondary order parameter, respectively. The absolute values of the elastic moduli c_{11}, c_{33}, c_{44}, c_{66}, c_{12}, and c_{14} at 295 K were calculated. © *2004 MAIK "Nauka/Interperiodica".*

1. INTRODUCTION

$K_3Na(CrO_4)_2$ belongs to crystals with the structural formula $A_3B(CO_4)_2$, where *A* and *B* are Li, K, Na, Rb, Cs, or NH_4 and CO_4 stands for the SO_4, CrO_4, or SeO_4 tetrahedra. Many members of this family undergo ferroelastic phase transitions. $K_3Na(CrO_4)_2$ passes through two structural phase transitions at 239 and 853 K [1]. On the basis of x-ray diffraction measurements [2, 3], it was suggested in [1] that the low-temperature transition can be represented by the scheme $\bar{3}m \longrightarrow 2/m$ and that the observation of ferroelastic domains below 239 K indicates the transition to be of ferroelastic nature. This stimulated a study of the temperature variation of the dynamic elastic moduli of the crystal in the vicinity of T_c. However, earlier ultrasonic measurements were performed only for the elastic modulus c_{44} [2], as the strong ultrasound scattering from the domain structure permitted study above the phase transition only. Nevertheless, the noticeable softening of this modulus observed to occur as one approached the Curie point was attributed to the ferroelastic character of the transition. The temperature behavior of the elastic moduli for the $K_3Na(CrO_4)_2$ crystal was studied in [4] by Mandelshtam–Brillouin scattering of light in the interval 140–300 K. In the vicinity of T_c, one observed a noticeable softening (which was similar in magnitude) of the moduli c_{44} and c_{66} and a break in the temperature dependences of c_{11} and c_{33}. As in the ultrasonic experiments, light scattering from the domain structure confined the studies of c_{66} and c_{44} to the region below the Curie point. Based on the change in the crystal symmetry, the phase transition was interpreted in [4] as first order, although no temperature hysteresis of the velocity was observed. It was suggested in [4] to describe the phase transition in terms of Landau theory with a mixed order parameter introduced in [5]. This interpretation does not, however, fit well with the group-theoretical description of ferroelastic phase transitions proposed later in [6].

We present here the results of ultrasonic studies of the $K_3Na(CrO_4)_2$ crystal carried out in the interval 185–295 K, which includes the Curie point. We measured the temperature variations in the velocity and damping coefficient (with respect to their room-temperature values) for longitudinal acoustic waves propagating along the *x* and *z* crystallographic axes of the trigonal system and *x*-polarized transverse waves moving along the *y* and *z* axes. The interpretation of the experimental data obtained was based on the phenomenological model [6] involving two linearly coupled order parameters. Our acoustic studies identified one of these parameters as primary, (i.e., responsible for the phase transition) and the other as secondary. These studies were complemented by room-temperature measurements of the absolute velocities of a number of acoustic modes, which permitted calculation of six elastic moduli of the $K_3Na(CrO_4)_2$ crystal.

2. THEORETICAL MODEL

According to the group-theoretical analysis performed in [6], the ferroelastic phase transition from point group $\bar{3}m$ to group $2/m$ is a first-order transition described by two order parameters, one of which is primary, i.e., responsible for the phase transition itself, and the other is secondary, i.e., linearly coupled with the primary parameter. Depending on the actual properties of a crystal, the primary, η_1, and secondary, η_2, order parameters can be the strain tensor components ε_4 and $(\varepsilon_2 - \varepsilon_1)/2$, respectively, or vice versa. Because of the symmetry being $\bar{3}m$ and of the transition being first-order [6], the Landau expansion should contain an invariant of third order in η_1. Thus, the Landau expansion for the $\bar{3}m \longrightarrow 2/m$ ferroelastic phase transition can be written as

$$\Phi = \Phi_0 + \frac{1}{2}c_{\eta 1}\eta_1^2 + \frac{1}{3}c_{\eta 1}^{(3)}\eta_1^3 + \frac{1}{4}c_{\eta 1}^{(4)}\eta_1^4 + \frac{1}{2}c_{\eta 2}\eta_2^2 + c_{\eta 1\eta 2}\eta_1\eta_2, \quad (1)$$

where $c_{\eta 1}$, $c_{\eta 2}$, and $c_{\eta 1\eta 2}$ are elastic moduli of the second order and $c_{\eta 1}^{(3)}$ and $c_{\eta 2}^{(4)}$ are elastic moduli of the third and fourth order, respectively. The modulus $c_{\eta 1}$ scales with temperature as $c_{\eta 1} = c_0(T - T_0)$, where T_0 is a characteristic temperature. Using Eq. (1), one can readily verify that the effective elastic moduli associated with the primary and secondary order parameters, respectively, and acting here as the inverse susceptibilities behave differently with temperature above T_c. To derive an expression for the elastic modulus $\tilde{c}_{\eta 1}$ related to the primary order parameter, one has to add the term $-\eta_1 H_1$, accounting for the interaction of η_1 with the corresponding field H_1, to expansion (1). Furthermore, limiting ourselves to the case of $T > T_c$, we drop in Eq. (1) the terms that involve the third and fourth powers of the primary order parameter. Thus, in the presence of a field, the equilibrium equations can be cast as

$$c_{\eta 1}\eta_1 + c_{\eta 1\eta 2}\eta_2 - H_1 = 0, \quad (2)$$

$$c_{\eta 2}\eta_2 + c_{\eta 1\eta 2}\eta_1 = 0. \quad (3)$$

Deriving the inverse susceptibility from Eq. (2)

$$\frac{\partial H_1}{\partial \eta_1} = c_{\eta 1} + c_{\eta 1\eta 2}\frac{\partial \eta_2}{\partial \eta_1} \quad (4)$$

and substituting $\partial\eta_2/\partial\eta_1$ into Eq. (4) with the use of Eq. (3), one readily obtains an expression for $\tilde{c}_{\eta 1}$

$$\tilde{c}_{\eta 1} = c_0(T - T_0'), \quad (5)$$

where

$$T_0' = T_0 + \frac{c_{\eta 1\eta 2}^2}{c_0 c_{\eta 2}}. \quad (6)$$

In a similar way, one can derive an expression for the temperature behavior of the modulus $\tilde{c}_{\eta 2}$ related to the secondary order parameter:

$$\tilde{c}_{\eta 2} = c_0(T - T_0')/(T - T_0). \quad (7)$$

Note that the corresponding expressions for a second-order phase transition were derived in a general form, for instance, in [7, 8].

As follows from Eqs. (5) and (7), the effective modulus related to the primary order parameter depends linearly on temperature above the phase transition point, whereas the dependence of $\tilde{c}_{\eta 2}$ on T deviates from a straight line. The difference in the theoretical temperature dependences between the effective elastic moduli related to the primary and secondary order parameters makes it possible to experimentally determine which of the two coupled order parameters, ε_4 or $(\varepsilon_2 - \varepsilon_1)/2$, is primary for $K_3Na(CrO_4)_2$.

3. EXPERIMENT AND RESULTS

Transparent, yellowish crystals of $K_3Na(CrO_4)_2$ were grown in an aqueous solution at a constant temperature of 315 K. The crystal composition was monitored by chemical and x-ray diffraction analysis. The $6 \times 5 \times 5$-mm sample chosen for measurements was parallelepiped-shaped, with the edges parallel to the trigonal crystallographic axes. The crystal orientation was set to no worse than 1°.

The measurements were performed using two modifications of the pulse echo method at a frequency of 4 MHz. The technique of Williams–Lamb [9] was used to measure the absolute velocities of sound at room temperature and the temperature behavior of the parameters of longitudinal acoustic waves (damping was insignificant in these cases). The temperature behavior of the parameters of transverse waves was investigated by studying the interference of a pulse that has passed through the sample with that reflected from its front face. This technique was developed for acoustic measurements in strongly absorbing media [10]. All measurements were carried out under slow cooling and heating of the sample. Below 245 K, the rate of temperature variation did not exceed 0.05 K min^{-1}. The temperature gradient in the sample was not over 0.02 K cm^{-1}. The relative error was 0.01% for the velocity and 6% for the damping. The error of room-temperature measurements of absolute velocities was 0.4 and 0.7% for the longitudinal and transverse waves, respectively.

The experimental data obtained for the absolute velocities at room temperature permitted calculation of the six elastic moduli of $K_3Na(CrO_4)_2$, which are listed

Elastic moduli of $K_3Na(CrO_4)_2$ (in units of 10^{10} N m^{-2}) at 295 K

c_{11}	c_{33}	c_{44}	c_{66}	c_{12}	c_{14}
6.04 ± 0.05	6.44 ± 0.05	1.51 ± 0.04	3.11 ± 0.06	−0.18 ± 0.15	0.29 ± 0.04

Note: The relations used for the calculations are $c_{11} = \rho v_{xx}^2$, $c_{33} = \rho v_{zz}^2$, $c_{44} = \rho v_{zx}^2$, $c_{66} = \rho v_{yx}^2$, $c_{12} = c_{11} - 2c_{66}$, and $2\rho v_{yy}^2 = (c_{11} + c_{44}) + \sqrt{(c_{11} - c_{44})^2 + 4c_{14}^2}$, where $\rho = 2772$ kg/m^3 [5] is the specific weight of the crystal.

in the table. All the moduli, except c_{33}, are in good agreement with the data [4] obtained using the Mandelshtam–Brillouin light scattering technique. However, the ultrasonic method provides a higher accuracy than the optical one.

Figures 1–4 graphically display the temperature behavior of the velocity and damping of sound for the transverse *zx* and *yx* modes and longitudinal *xx* and *yy* modes obtained under cooling and heating of the sample. One sees clearly pronounced anomalies in the velocities of all waves below 240 K. For longitudinal waves, however, the changes were considerably weaker than those for transverse waves. The velocity anomalies were accompanied by a growth of the damping coefficient, which was likewise noticeably larger for the transverse modes. No temperature hysteresis was observed within the experimental accuracy either for the velocity or for the damping coefficient (Figs. 1–4), just as in studies of the low-temperature phase transition in $K_3Na(CrO_4)_2$ using other methods.

The changes in the transverse-wave velocities displayed in Figs. 1 and 2 agree both in character and magnitude with the anomalies in the moduli c_{66} and c_{44} reported in [2, 4]. However, the observed decrease in the longitudinal-wave velocity (Figs. 3, 4) is at odds with the data from [4], where only a change in the slope of the temperature dependences of c_{11} and c_{33} at T_c was revealed.

4. DISCUSSION OF THE RESULTS

The experimentally observed decrease in the transverse-wave velocity (Figs. 1, 2) corresponding to a softening of the c_{44} and c_{66} elastic moduli [$c_{66} = (c_{11} - c_{12})/2$ above the phase transition point] is in agreement with the theoretical predictions outlined in Section 2. A relatively weak softening of c_{44} and c_{66} in $K_3Na(CrO_4)_2$ compared to other proper ferroelastics (see, e.g., [7]) should most likely be attributed to this phase transition being first-order. However, this transition should be classed among weak first-order transitions, because no noticeable temperature hysteresis was observed in the elastic properties of the crystal under heating and cooling.

To properly identify the primary and secondary order parameters with strain tensor components, we used ultrasonic measurements to calculate the temperature dependences of the elastic moduli c_{44} and c_{66} presented in Fig. 5. We readily see that, within the experimental accuracy, the modulus c_{44} linearly depends on temperature in the interval from 235.5 to 238 K, whereas the temperature dependence of the elastic modulus c_{66} exhibits a clearly pronounced nonlinear

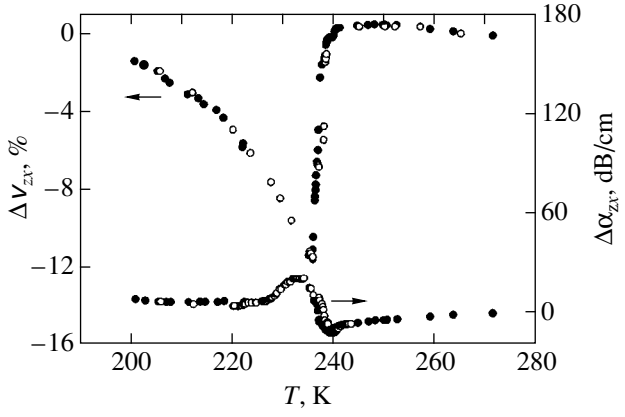

Fig. 1. Relative temperature variations in the velocity Δv_{zx} and in the damping coefficient $\Delta\alpha_{zx}$ for a transverse *x*-polarized ultrasonic wave propagating along the *z* axis. Filled symbols correspond to cooling, and open symbols, to heating.

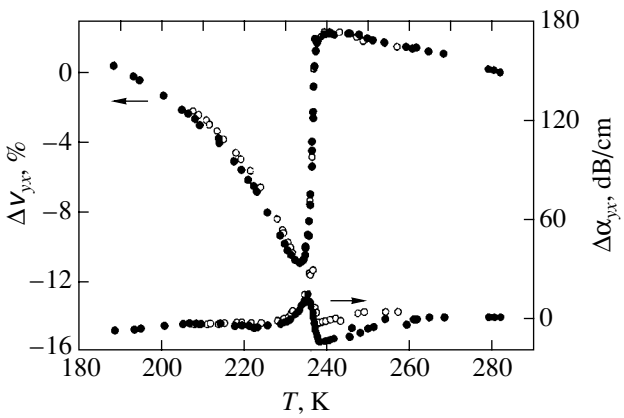

Fig. 2. Relative temperature variations in the velocity Δv_{yx} and in the damping coefficient $\Delta\alpha_{yx}$ for a transverse *x*-polarized ultrasonic wave propagating along the *y* axis. Filled symbols correspond to cooling, and open symbols, to heating.

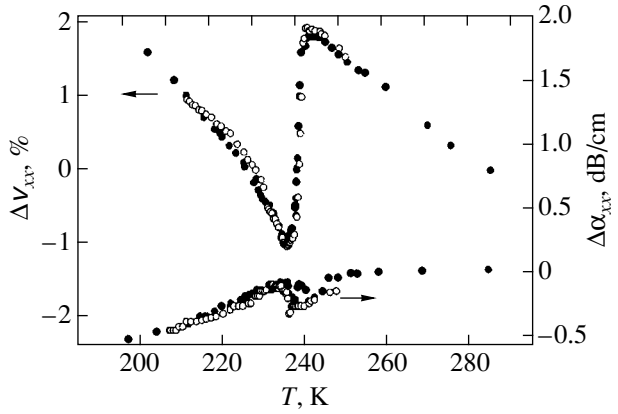

Fig. 3. Relative temperature variations in the velocity Δv_{xx} and in the damping coefficient $\Delta\alpha_{xx}$ for a longitudinal ultrasonic wave propagating along the x axis. Filled symbols correspond to cooling, and open symbols, to heating.

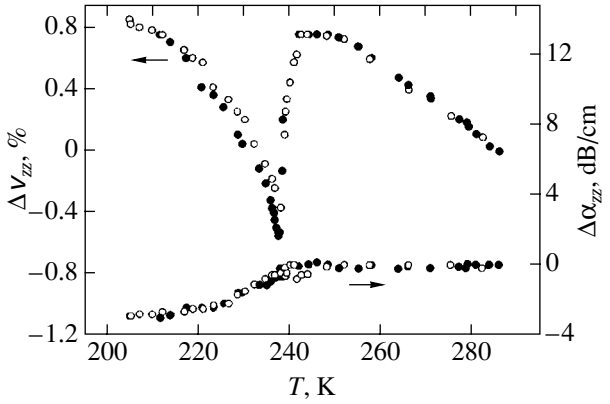

Fig. 4. Relative temperature variations in the velocity Δv_{zz} and in the damping coefficient $\Delta\alpha_{zz}$ for a longitudinal ultrasonic wave propagating along the z axis. Filled symbols correspond to cooling, and open symbols, to heating.

character. Thus, in accordance with Eqs. (5) and (7), one should accept that ε_4 is the primary parameter η_1, with the related effective modulus $\tilde{c}_{\eta 1} = c_{44}$, and that $(\varepsilon_2 - \varepsilon_1)/2$ is the secondary order parameter, with the corresponding modulus $\tilde{c}_{\eta 2} = c_{66}$. Also, $c_{\eta 1 \eta 2}$ should obviously be equal to c_{14}. By extrapolating the $c_{44}(T)$ straight line to the intercept with the temperature axis, one can find the temperature T_0' entering Eq. (5). We find from Fig. 5 that $T_0' = 228 \pm 0.5$ K and $c_0 = 0.155$. Using the value of T_0' thus found, one obtains good agreement between the experimental temperature dependence $c_{66}(T)$ and theoretical relation (7) by setting the temperature T_0 equal to 214 K. The comparatively large difference between T_0 and T_0' ($\Delta T = 14$ K) indicates a fairly strong coupling between the primary and secondary order parameters. Note, however, that the value of ΔT thus found is considerably larger than the value following from Eq. (6), 0.2 K.

Another Landau expansion was employed in [4] to describe the low-temperature $\bar{3}m \longrightarrow 2/m$ transition in $K_3Na(CrO_4)_2$. The combination $\varepsilon_s = a(\varepsilon_1 - \varepsilon_2) + b\varepsilon_4$, where a and b are numerical coefficients, was used as the only order parameter [5]. The elastic modulus related to this order parameter has the form $c_{2s} = (c_{44} + 2c_{66} - \sqrt{(2c_{66} - c_{44})^2 + 8c_{14}^2})/2$ [5]. The temperature dependence of the modulus c_{2s}, which was calculated from ultrasonic measurements, is also displayed in Fig. 5 for comparison. The modulus c_{14} was derived from the expression $2\rho v_{yy}^2 = (c_{11} + c_{44}) + \sqrt{(c_{11} - c_{44})^2 + 4c_{14}^2}$, where ρ is the specific weight of the crystal and v_{yy} is the velocity of the yy mode. As seen from Fig. 5, the $c_{2s}(T)$ curve approaches a linear dependence $c_{2s} \sim (T - \tilde{T})$ corresponding to the Landau expansion used in [4]. Note that the temperature $\tilde{T}_0 \cong 228$ K coincides with the above temperature T_0'. Thus, a comparison of the theoretical approaches employed in the present study and in [4] suggests that, while both versions of the Landau expansion are valid for description of the ferroelastic phase transition in $K_3Na(CrO_4)_2$, expansion (1) is better substantiated from the group-theoretical standpoint.

As follows from the expressions for the second-order elastic-modulus tensor of a crystal of symmetry $\bar{3}m$, the strains ε_1 and ε_3 are not related linearly with

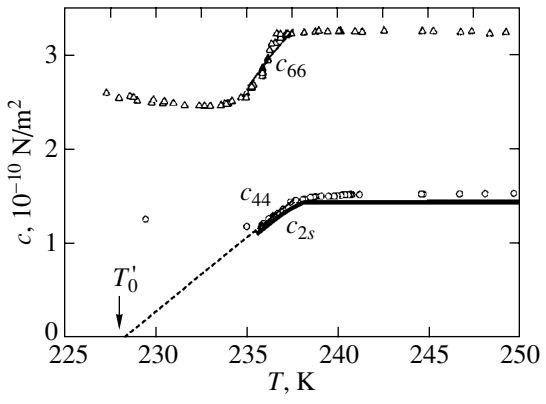

Fig. 5. Temperature dependences of the elastic moduli c_{66} (triangles), c_{44} (circles), and c_{2s} (bold solid line) derived from ultrasonic measurements. The thin solid lines plot theoretical relations calculated from Eqs. (5) and (7). The dashed line is an extrapolation of the $c_{44}(T)$ dependence to the intercept with the temperature axis made to determine T_0'.

the primary order parameter and, hence, near the phase transition, the *xx* and *zz* acoustic modes should not undergo noticeable anomalies comparable in magnitude to those of the *zx* and *yx* modes. Our measurements support this conclusion (Figs. 3, 4). Nevertheless, the graphs presented in Figs. 3 and 4 differ from the results obtained in [4] using Mandelshtam–Brillouin scattering, where only breaks in the $c_{11}(T)$ and $c_{22}(T)$ curves were revealed. This difference could be assigned to a slow relaxation of the order parameter with a time τ satisfying the conditions $\omega\tau \ll 1$ for ultrasonic frequencies and $\omega\tau \gg 1$ for thermal phonons, as was proposed in [11] for the $(NH_4)LiH_3(SO_4)_4$ crystal.

Interestingly, the observed anomalies in the temperature dependences of the shear elastic moduli in $K_3Na(CrO_4)_2$ appear to be more characteristic of improper ferroelastic transitions. The reason for this remains unclear, because the proper character of the transition in $K_3Na(CrO_4)_2$ follows directly from the symmetry change $\bar{3}m \longrightarrow 2/m$.

5. CONCLUSIONS

Thus, we have presented the results of an acoustic study of crystalline $K_3Na(CrO_4)_2$ performed in the interval 185–295 K. The velocity and damping of longitudinal and transverse sound waves propagating along the crystallographic axes of the crystal were found to have anomalies near the ferroelastic phase transition. The phase transition temperature derived from the ultrasonic measurements is 235.5 K. The Landau expansion with two linearly coupled order parameters, ε_4 and $(\varepsilon_2 - \varepsilon_1)/2$, was analyzed for the phase transition under study. Acoustic measurements showed ε_4 to be the primary order parameter responsible for the phase transition.

REFERENCES

1. T. Krajewski, B. Mroz, P. Piskunowicz, and T. Breczewski, Ferroelectrics **106**, 225 (1990).
2. G. Madariaga and T. Breczewski, Acta Crystallogr. C **46**, 2019 (1990).
3. J. Fabry, T. Breczewski, and G. Madariaga, Acta Crystallogr. B **50**, 13 (1994).
4. B. Mroz, H. Kiefte, M. J. Clouter, and J. A. Tuszynski, Phys. Rev. B **43**, 641 (1991).
5. N. Boccara, Ann. Phys. (N.Y.) **47**, 40 (1968).
6. P. Toledano, M. M. Fejer, and B. A. Auld, Phys. Rev. B **27**, 5717 (1983).
7. A. K. Radzhabov and E. V. Charnaya, Fiz. Tverd. Tela (St. Petersburg) **43**, 701 (2001) [Phys. Solid State **43**, 732 (2001)].
8. E. K. H. Salje, *Phase Transitions is Ferroelastic and Coelastic Crystals* (Cambridge Univ. Press, Cambridge, 1993).
9. J. Williams and J. Lamb, J. Acoust. Soc. Am. **30**, 308 (1958).
10. B. F. Borisov, E. V. Charnaya, and A. K. Radzhabov, Phys. Status Solidi B **181**, 337 (1994).
11. Z. Tylczynski and B. Mroz, Solid State Commun. **101**, 653 (1997).

Translated by G. Skrebtsov

Physics of the Solid State, Vol. 46, No. 4, 2004, pp. 780–787. Translated from Fizika Tverdogo Tela, Vol. 46, No. 4, 2004, pp. 759–766.

LOW-DIMENSIONAL SYSTEMS AND SURFACE PHYSICS

Anisotropy of Optical Constants of ZnSe/BeTe Heterostructures with No Common Atoms at the Interfaces

A. S. Gurevich*, V. P. Kochereshko*, A. V. Platonov*, A. Baar, D. R. Yakovlev***, and G. Landwehr*****

**Ioffe Physicotechnical Institute, Russian Academy of Sciences, Politekhnicheskaya ul. 26, St. Petersburg, 194021 Russia*

***Universität of Ulm, Ulm, 89091 Germany*

****Physikalisches Institut der Universität Würzburg, Würzburg, 97074 Germany*

Received August 28, 2003

Abstract—The in-plane anisotropy of the refractive index and absorption coefficient in the blue–green spectral region in ZnSe/BeTe type-II heterostructures with no common atoms at the interface has been studied by ellipsometry in reflection. It was established that the relative difference (anisotropy) in the refractive index and absorption coefficient remains nonzero throughout the range covered and reaches 0.6% for the refractive index and 85% for the absorption coefficient. It was found that, in contrast to excitonic transitions involving a heavy hole, the anisotropy in absorption for the light-hole exciton is larger in magnitude and is of the opposite sign.

1. INTRODUCTION

Recent studies of the ZnSe/BeTe type-II periodic heterostructures have revealed that the photoluminescence (PL) signal of the spatially indirect exciton is linearly polarized in the plane of the structure [1, 2], with the degree of polarization being about 80% along the [110] and $[1\bar{1}0]$ crystallographic axes. This effect is due to the local symmetry of the interface separating the two zinc-blende substances being lower than the symmetries of the original semiconductors.

In contrast to the original, bulk semiconductor with zinc-blende structure and T_d point symmetry, an ideal interface and, hence, a single heterojunction has C_{2v} symmetry. This lowered point symmetry of the heterojunction allows manifestations of an in-plane anisotropy in the optical properties, and this is what was seen in [3] in the linear polarization of in-plane PL of the indirect exciton localized near the interface.

The PL spectra of the indirect exciton relate only to the local properties of a given interface and do not yield any information on the optical properties of a sample as a whole. The optical constants of semiconductor heterostructures are measured, as a rule, using reflection and transmission spectroscopy. However, reflectance spectra alone do not provide an independent measurement of the real and imaginary parts of the refractive index of light. To determine both of them, one needs to obtain two spectra of the same sample measured in reflection and transmission.

This communication reports on studies of ZnSe/BeTe superlattices (SL) grown on GaAs substrates. Because these substrates exhibit strong light absorption in the spectral region of interest to us here, it was impossible to measure transmittance spectra. Therefore, we studied the optical anisotropy of our samples using ellipsometry in reflection. The period of the heterostructures studied was considerably smaller than the wavelength in the spectral region used; therefore, the optical properties of such structures can be described by the effective refractive and absorption indices or by the effective permittivity tensor [4].

The reflection ellipsometry was employed to measure the spectral response of the effective refractive and absorption indices of ZnSe/BeTe superlattices in the blue–green spectral region. It was found that the effective refractive and absorption indices in the [110] and $[1\bar{1}0]$ crystallographic directions differ throughout the spectral range covered.

2. EXPERIMENTAL

We studied ZnSe/BeTe SLs with a type-II band offset that were MBE-grown on semi-insulating GaAs substrates in the [001] direction. The thickness of the ZnSe layers in an SL was 100 Å, that of the BeTe layers was 50 Å, and the total SL thickness was 3000 Å, which adds up to 20 ZnSe/BeTe periods. Because the lattice misfit between the ZnSe, BeTe, and GaAs compounds does not exceed 0.4%, these heterostructures are practically unstrained. No purposeful doping of the samples studied was undertaken. Figure 1 shows the band diagram of the type-II SLs of interest. In these SLs, the electrons are localized in the ZnSe layers and the holes, in the BeTe layers. We studied ZnSe/BeTe SLs with inequivalent interfaces (Zn–Te, Be–Se). Such an inter-

face has point symmetry C_{2v} and lowers the symmetry of the sample as a whole to C_{2v} [3].

Figure 2 presents reflectance spectra of linearly polarized light from a ZnSe/BeTe SL obtained in the region of spatially direct exciton transitions, i.e., transitions in the ZnSe layers, and normalized against the light source intensity and spectral response of the detector. The reflectance spectra were measured for nearly normal incidence of light on the sample (the angle of incidence did not exceed 12°). The sample temperature was 77 K; the sample was mounted in a cryostat on a copper finger immersed in liquid nitrogen, thus providing heat exchange between the liquid nitrogen and the sample. To exclude the effect of light refraction at the interface between the liquid nitrogen and the cryostat windows, the sample itself was not immersed in liquid nitrogen. The light beams striking the sample and reflected from it were passed through linear polarizers with parallel axes. The measurements were conducted for two different orientations of the polarizer axes relative to the sample crystallographic axes. In one case, the light was linearly polarized in the [110] direction; i.e., the light polarization plane was parallel to the [110] crystallographic axis of the sample (Fig. 2a). In the other case, the light was linearly polarized in the $[1\bar{1}0]$ direction (Fig. 2b).

The reflectance spectra are seen to contain the line of the spatially direct exciton localized in the ZnSe layers ($e1$–$hh1$). A comparison of the reflectance spectra measured for the different light polarizations reveals a difference in the amplitude of the exciton resonance line for the two polarizations. The amplitude of the resonance obtained with light polarized along the [110] axis (Fig. 2a) is larger than that for the $[1\bar{1}0]$-polarized light. Furthermore, the spectrum obtained with the $[1\bar{1}0]$ polarization (Fig. 2b) exhibits a feature associated with a light-hole spatially direct exciton ($e1$–$lh1$), which is not seen with the [110] polarization. This difference between the reflectance spectra suggests that the refractive index of light near the excitonic resonance depends on the mutual orientation of the sample and the plane of polarization of light, a feature indicating anisotropy in the optical properties in the plane of the structure.

Analysis of the reflectance spectra alone does not permit one to independently measure the coefficients of refraction and absorption of light (or the real and imaginary parts of the permittivity). To establish which of these two parts behaves anisotropically and to measure their spectral response, we made use of ellipsometry in reflection.

This method is based on deriving the optical properties of solids from the changes that the polarization of a plane light wave undergoes in reflection from the surface of a sample under study. We used reflection ellipsometry in a setup with a rotating compensator (phase shifting plate) [5]. This setup of the ellipsometer makes

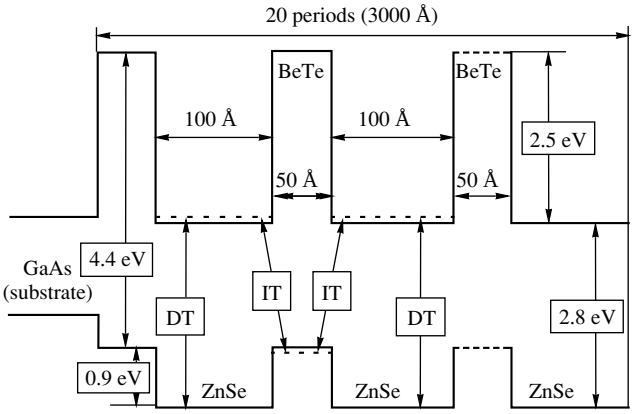

Fig. 1. Band diagram of the ZnSe/BeTe periodic heterostructure (superlattice) with a type-II band offset. The structure contains 20 periods. DT is a spatially direct optical transition in ZnSe layers of energy $E \sim 2.8$ eV, and IT is a spatially indirect optical transition of energy $E \sim 1.9$ eV.

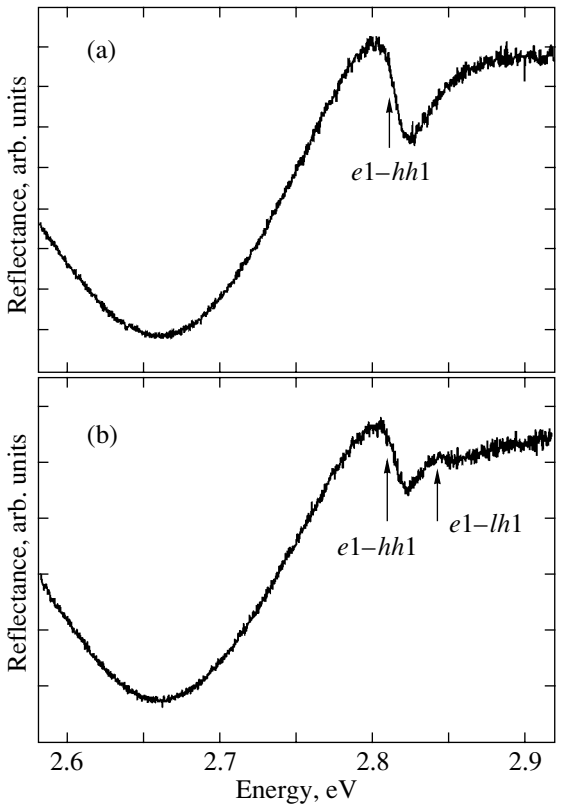

Fig. 2. Reflectance spectra of linearly polarized light from a ZnSe/BeTe superlattice obtained in the spectral region corresponding to spatially direct optical transitions in ZnSe layers: (a) reflectance spectrum of light linearly polarized along the [110] crystallographic direction of the sample and (b) same with light linearly polarized along $[1\bar{1}0]$. Angle of incidence $\theta_0 = 12°$, and sample temperature $T = 77$ K.

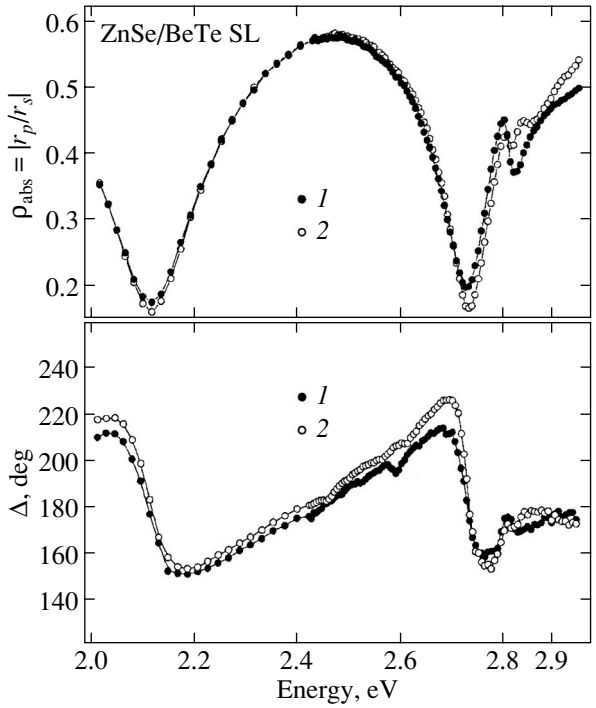

Fig. 3. Spectral responses of ρ_{abs} and Δ measured at an angle of incidence $\theta_0 = 53.64°$ for the case where the $[1\bar{1}0]$ crystallographic axis of the sample is (*1*) parallel or (*2*) perpendicular to the plane of incidence. Sample temperature $T = 77$ K.

it possible to perform a full measurement of the polarization state of light (the azimuthal angle of the polarization ellipse, the length ratio of its axes, the sign of this ratio), which is necessary for determining the optical constants of thin films with thicknesses comparable to the wavelength of light in the spectral range covered.

According to the accepted terminology (see, e.g., [6]), the linearly polarized monochromatic plane wave is called the *s* (*p*) wave if its electric vector is perpendicular (parallel) to the plane of light incidence on the sample. The plane of light incidence is defined by the rays striking and reflected from the sample. In our ellipsometric measurements, linearly polarized light impinged on the sample at a given angle and the polarization of the light reflected from the sample was measured. The known states of polarization of the light wave before and after reflection from the sample could then be used to find the ratio of the complex amplitude Fresnel reflection coefficients [6]:

$$\rho_{exp}(\hbar\omega) = \frac{r_p}{r_s} \equiv \rho_{abs}(\hbar\omega)\exp[i\Delta(\hbar\omega)]. \qquad (1)$$

Here, r_p and r_s are the complex amplitude Fresnel reflection coefficients for the *p* and *s* waves, respectively; ρ_{abs} is the modulus of the Fresnel coefficient ratio (the angle ψ related to ρ_{abs} through $\tan\psi = \rho_{abs}$ is frequently considered in place of ρ_{abs}); and Δ is the argument of the Fresnel coefficient ratio. The modulus of the Fresnel coefficient ratio, ρ_{abs}, shows the extent to which the reflection of the *p* wave is weaker than that of the *s* wave for a given energy of the photons striking the sample. The argument Δ of the Fresnel coefficient ratio is the phase difference between the *p* and *s* waves upon reflection from the sample. Thus, ellipsometry measurements performed at a given wavelength of light and for the given angle of light incidence on the sample with the orientation of the sample crystallographic axes relative to the incidence plane yielded two independent real quantities characterizing the optical properties of the heterostructure under study. The measured complex quantity ρ_{exp} for the given wavelength of light permits one to find the optical constants of the sample (the refractive index, the absorption coefficient) at the same spectral point.

3. EXPERIMENTAL RESULTS

We carried out ellipsometric measurements in the range $50° < \theta_0 < 65°$ of angles of light incidence on the sample. The angles of incidence were set to within $\pm 0.02°$ and monitored continually in the course of the experiments. Two measurements were performed for a given angle of incidence, with the $[1\bar{1}0]$ crystallographic axis of the sample oriented parallel and perpendicular to the incidence plane. The ellipsometric measurements were carried out at the sample temperature, 77 K. To monitor the angle of light incidence carefully, the sample, rather than being immersed in liquid nitrogen, was fixed to a copper finger placed in liquid nitrogen.

Figure 3 plots the dependences of ρ_{abs} and Δ on the incident frequency measured ellipsometrically for the incidence angle $\theta_0 = 53.64°$ with the $[1\bar{1}0]$ crystallographic axis of the sample oriented parallel and perpendicular to the plane of incidence. The graphs clearly indicate there is optical anisotropy in the plane of the structure, because, all other conditions being equal, the measured values of ρ_{abs} and Δ depend on the mutual orientation of the plane of light incidence and of the crystallographic axes of the sample. Note the characteristic feature that the observed optical anisotropy reaches a maximum at energies close to that of the spatially direct exciton in the ZnSe layers ($E \approx 2.8$ eV) and remains nonzero practically throughout the spectral range covered. The periodic pattern of the quantities plotted in Fig. 3 over a broad spectral range can be identified with the interference of light in the ZnSe/BeTe SL under study, because its thickness, 3000 Å, is comparable to the wavelength of light in the spectral range used ($\lambda = 4200$–6200 Å).

4. TREATMENT OF EXPERIMENTAL DATA

Because the SL period is much less than the wavelength of light in the spectral range studied ($Kd_0 \ll 1$, where K is the wave vector of light, d_0 is the ZnSe/BeTe SL period), we can consider this SL in the approximation of an optically anisotropic, uniform effective medium [4] and describe its coupling with light through the effective permittivity tensor. The semiconductor compounds making up the SL under study crystallize in the zinc-blende structure having T_d symmetry.

As already mentioned, the existence of inequivalent interfaces in the ZnSe/BeTe SL, with each of them having C_{2v} point symmetry, lowers the symmetry of the sample as a whole to C_{2v} [3]. Hence, the permittivity tensor of the SL under study becomes diagonal when referred to the C_2 twofold symmetry axes, i.e., to the [110], [$1\bar{1}0$], and [001] crystallographic directions. To find the principal values of the permittivity tensor of the SL from experimental ellipsometric data, we express the ratio of the complex Fresnel amplitude reflection coefficients for the *p* and *s* waves through the angle of incidence of light on the sample, the SL thickness, the principal values of the permittivity tensor of the SL, and the permittivity of the substrate.

The problem of the reflection of polarized light from a sample consisting of a uniform isotropic layer of a given thickness deposited on a uniform isotropic substrate can be solved using the transfer matrix formalism described, for instance, in [6]. This problem can be generalized to the case of the reflection of polarized light from an anisotropic uniform layer–isotropic substrate system. Note that because the surface of the ZnSe/BeTe SL under study is (001) oriented, one of the principal axes of the permittivity tensor coincides in direction with the normal to the sample surface, with the other two axes of the tensor lying in the sample plane. In the case where one of the two in-plane principal axes of the permittivity tensor is perpendicular to the plane of incidence and the other is parallel to it, the *p* and *s* components of the polarized light are reflected by an anisotropic sample independently of each other. For this orientation of the permittivity tensor axes of the ZnSe/BeTe SL with respect to the plane of incidence, the Fresnel reflection coefficients of the sample under study acquire a simple analytical form.

Introducing an orthogonal reference frame such that the plane of incidence coincides with the *yz* plane and the *xy* plane is parallel to the sample surface (with the *z* axis being perpendicular to the sample surface), we obtain the following expressions for the complex Fresnel amplitude reflection coefficients r_p and r_s:

$$\rho_{\text{theory}} = \frac{r_p}{r_s},$$

$$r_p = \frac{r_{01p} + r_{12p}\exp(2i\beta_p)}{1 + r_{01p}r_{12p}\exp(2i\beta_p)}, \qquad (2)$$

$$r_s = \frac{r_{01s} + r_{12s}\exp(2i\beta_s)}{1 + r_{01s}r_{12s}\exp(2i\beta_s)}.$$

Here, r_{01p} and r_{12p} are the *p*-wave complex amplitude reflection coefficients of the outer medium–anisotropic layer interface and of the anisotropic layer–substrate interface, respectively; β_p is the phase incursion of the *p* wave acquired in transit through the anisotropic layer; and r_{01s}, r_{12s}, and β_s are the analogous quantities for the *s* wave. Expressing these quantities through the principal values of the permittivity tensor of the SL under study, we come to

$$\begin{cases} r_{01s} = \dfrac{\sqrt{\varepsilon_0 - \varepsilon_0\sin^2\theta_0} - \sqrt{\varepsilon_{xx} - \varepsilon_0\sin^2\theta_0}}{\sqrt{\varepsilon_0 - \varepsilon_0\sin^2\theta_0} + \sqrt{\varepsilon_{xx} - \varepsilon_0\sin^2\theta_0}} \\ r_{12s} = \dfrac{\sqrt{\varepsilon_{xx} - \varepsilon_0\sin^2\theta_0} - \sqrt{\varepsilon_{\text{sub}} - \varepsilon_0\sin^2\theta_0}}{\sqrt{\varepsilon_{xx} - \varepsilon_0\sin^2\theta_0} + \sqrt{\varepsilon_{\text{sub}} - \varepsilon_0\sin^2\theta_0}} \\ \beta_s = 2\pi\dfrac{d}{\lambda_0}\sqrt{\varepsilon_{xx} - \varepsilon_0\sin^2\theta_0}, \end{cases} \qquad (3)$$

$$\begin{cases} r_{01p} = \dfrac{\varepsilon_{yy}\sqrt{\varepsilon_0 - \varepsilon_0\sin^2\theta_0} - \varepsilon_0\sqrt{\varepsilon_{yy} - \varepsilon_0\sin^2\theta_0}}{\varepsilon_{yy}\sqrt{\varepsilon_0 - \varepsilon_0\sin^2\theta_0} + \varepsilon_0\sqrt{\varepsilon_{yy} - \varepsilon_0\sin^2\theta_0}} \\ r_{12p} = \dfrac{\varepsilon_{\text{sub}}\sqrt{\varepsilon_{yy} - \varepsilon_0\sin^2\theta_0} - \varepsilon_{yy}\sqrt{\varepsilon_{\text{sub}} - \varepsilon_0\sin^2\theta_0}}{\varepsilon_{\text{sub}}\sqrt{\varepsilon_{yy} - \varepsilon_0\sin^2\theta_0} + \varepsilon_{yy}\sqrt{\varepsilon_{\text{sub}} - \varepsilon_0\sin^2\theta_0}} \\ \beta_p = 2\pi\dfrac{d}{\lambda_0}\sqrt{\varepsilon_{yy} - \varepsilon_0\sin^2\theta_0}. \end{cases} \qquad (4)$$

In Eqs. (3) and (4), θ_0 is the angle of light incidence on the sample, ε_0 is the permittivity of the outer medium, ε_{xx} and ε_{yy} are the principal values of the permittivity tensor of the ZnSe/BeTe SL, d is the total thickness of the SL, ε_{sub} is the substrate permittivity, and λ_0 is the wavelength of light in vacuum.

Thus, Eqs. (2)–(4) relate the unknown components of the permittivity tensor of the ZnSe/BeTe SL to the experimentally measured ratio ρ_{exp} of the complex Fresnel amplitude reflection coefficients for the structure under study. The fact that the thickness of the ZnSe/BeTe system is of the same order of magnitude as the wavelength of light in the spectral range of interest makes expansion of the exponential in Eq. (2) in the

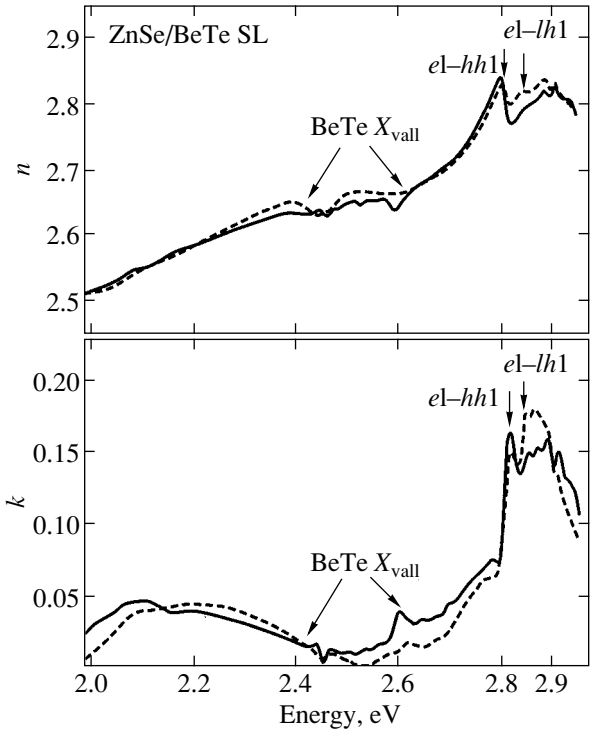

Fig. 4. Dependences of the refractive index n and absorption coefficient k of the ZnSe/BeTe superlattice on light frequency. Solid lines refer to the optical constants obtained for the [110] crystallographic direction of the structure. Dashed lines relate to the optical constants in the $[1\bar{1}0]$ direction. Sample temperature $T = 77$ K.

small parameter d/λ_0 impossible. Therefore, analytic representation of the principal values of the permittivity tensor of the ZnSe/BeTe SL through the experimentally measured quantity ρ_{exp} appears to be an intractable problem, because the quantities involved are related by a transcendental equation. For this reason, the principal values $\varepsilon_{[110]}$ and $\varepsilon_{[1\bar{1}0]}$ of the permittivity tensor of the SL under study were found numerically in the following way.

We introduce the following notation for the measured values of the complex Fresnel amplitude reflection coefficients. Let $\rho_{exp}^{(1)}$ and $\rho_{exp}^{(2)}$ be the values found at the angle of incidence $\theta_0 = 53.64°$ in the case where the $[1\bar{1}0]$ crystallographic axis of the sample under study is perpendicular and parallel to the plane of incidence, respectively. In measurements of $\rho_{exp}^{(1)}$, the [110] direction corresponds to the permittivity ε_{xx} in Eq. (3), and, in measurements of $\rho_{exp}^{(2)}$, this direction is associated with ε_{yy} in Eq. (4). For all the wavelengths for which $\rho_{exp}^{(1)}$ and $\rho_{exp}^{(2)}$ were measured, the unknown complex permittivities $\varepsilon_{[110]}$ and $\varepsilon_{[1\bar{1}0]}$ corresponding to the [110] and $[1\bar{1}0]$ directions of the structure were varied until the error function F defined as

$$F(\varepsilon_{[110]}, \varepsilon_{[1\bar{1}0]}) = \sum_{i=1}^{2} \left|\rho_{exp}^{(i)} - \rho_{theory}\right|^2, \qquad (5)$$

reached a minimum. Here, $\rho_{exp}^{(1)}$ and $\rho_{exp}^{(2)}$ are the measured values of the ratio of the complex Fresnel amplitude reflection coefficients for the two sample orientations relative to the light incidence plane and ρ_{theory} are the analogous values calculated from Eqs. (2)–(4). For the permittivity of the substrate, we used the values for undoped GaAs taken from [7]. The total SL thickness was 3000 Å. For each wavelength of light of the spectral range under study, the minimum of the error function F in Eq. (5) was found using the steepest descent method under simultaneous variation of the real and imaginary parts of the permittivities of the ZnSe/BeTe SL that correspond to the [110] and [[$1\bar{1}0$]crystallographic directions.

In what follows, we consider not the principal values of the permittivity tensor but rather the corresponding refractive index and absorption coefficient defined as

$$\begin{aligned}(n_{[110]} + ik_{[110]})^2 &= \varepsilon_{[110]},\\ (n_{[1\bar{1}0]} + ik_{[1\bar{1}0]})^2 &= \varepsilon_{[1\bar{1}0]}.\end{aligned} \qquad (6)$$

Here, $n_{[110]}$ and $n_{[1\bar{1}0]}$ are the refractive indices of the ZnSe/BeTe SL in the [110] and $[1\bar{1}0]$ crystallographic directions and $k_{[110]}$ and $k_{[1\bar{1}0]}$ are the absorption coefficients for these crystallographic directions.

5. REFRACTIVE INDEX AND ABSORPTION COEFFICIENT

Figure 4 presents the spectral responses of the refractive index and the absorption coefficient of the ZnSe/BeTe SL extracted from experimental data. One clearly sees the following features. Both for the [110] (solid lines) and $[1\bar{1}0]$ (dashed lines) crystallographic directions, a strong line of the heavy-hole exciton transition ($e1$–$hh1$) in the first quantum confined subband stands out. The feature associated with the $e1$–$lh1$ light-hole exciton transition is also observed in the responses of the optical constants along [110] and $[1\bar{1}0]$, but in the latter direction the $e1$–$lh1$ feature is substantially smaller in amplitude. The spectral responses of the refractive index and of the absorption coefficient obtained for the ZnSe/BeTe SL were used to determine the resonance energies of spatially direct excitonic transitions. The transition energy is $E_{hh} = 2.818$ eV for the

heavy-hole exciton and E_{lh} = 2.850 eV for the light-hole exciton.

In the interval from 2.45 to 2.65 eV, the spectral responses of the refractive index and of the absorption coefficient exhibit a feature (BeTe X_{vall}) that is apparently due to electron transitions from the valence band of BeTe to its conduction-band X valley [8]. The BeTe compound is an indirect-gap semiconductor [9], but because the electrons with wave vectors along the growth axis of the structure are quantum confined to the BeTe layers, these transitions should be direct in the wave-vector space.

To get a better idea of the character and extent of the in-plane optical anisotropy in the ZnSe/BeTe SL, we consider the spectral responses of the difference between the optical constants corresponding to the [110] and $[1\bar{1}0]$ crystallographic directions of the heterostructure under study. The anisotropy of the refractive indices, which is defined as $\delta n = n_{[1\bar{1}0]} - n_{[110]}$, remains nonzero practically throughout the spectral range covered and reaches its maximum $\delta n^{\max} \approx 0.035$ at an energy E = 2.838 eV. Note that the anisotropy of the refractive index passes through zero at the energy of the $e1$–$hh1$ heavy-hole exciton resonance, which correlates with the absence of noticeable splitting between the $e1$–$hh1$ heavy-hole exciton resonances for light polarized along the [110] and $[1\bar{1}0]$ directions (Fig. 5). The anisotropy of the absorption coefficient $\delta k = k_{[1\bar{1}0]} - k_{[110]}$ attains its maximum, $\delta k^{\max} \approx 0.03$, at a photon energy E = 2.861 eV (Fig. 5). The absorption coefficient anisotropy is seen to have opposite signs for transitions involving the heavy ($e1$–$hh1$) and the light ($e1$–$lh1$) holes. As with the anisotropy of the refractive index, the anisotropy of the absorption coefficient remains nonzero practically throughout the spectral range under study.

The responses plotted in Fig. 5 clearly exhibit features apparently associated with spatially direct transitions in the BeTe layers, more specifically, from the valence band to the X valley (BeTe X_{vall}). At lower energies (in the interval 2.0–2.4 eV), the optical constant anisotropy originates from the spatially indirect transitions in the ZnSe/BeTe SL involving an electron localized in the ZnSe layer and a hole localized in the BeTe layer. Furthermore, at a photon energy of 2.13 eV, the anisotropy in the absorption coefficient passes through zero and the anisotropy in the refractive index is close to zero (Fig. 5). Thus, within the spectral range covered, the ZnSe/BeTe SL has an "isotropic" point (IP), which is in agreement with calculations of the matrix elements of spatially indirect optical transitions in type-II heterostructures [10].

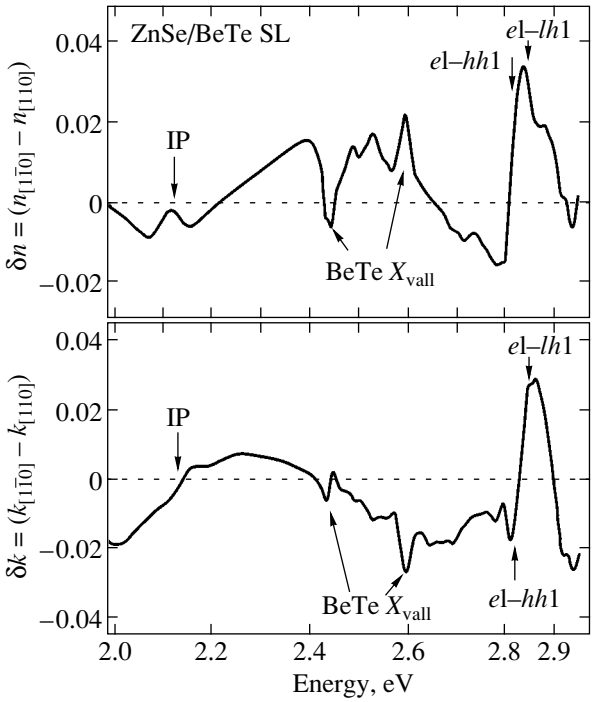

Fig. 5. Spectral response of the difference between the optical constants along the $[1\bar{1}0]$ and [110] crystallographic directions of the ZnSe/BeTe superlattice (δn is the difference between the refractive indices, δk is the difference between the absorption coefficients). Sample temperature T = 77 K.

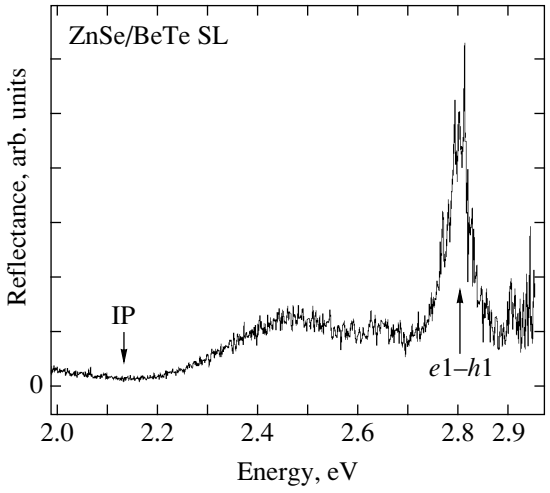

Fig. 6. Reflectance spectrum of polarized light from a ZnSe/BeTe superlattice. The light incident on the sample is *s* polarized. The [110] crystallographic axis of the sample makes an angle of 45° with the plane of incidence. The reflected light is measured in *p* polarization. Sample temperature T = 77 K.

The relative magnitude of the refraction anisotropy, which is defined as $\Delta n = (n_{[1\bar{1}0]} - n_{[110]})/(n_{[1\bar{1}0]} + n_{[110]})$, reaches a maximum of 0.6% at an energy E = 2.836 eV. The relative anisotropy in the absorption coefficient $\Delta k = (k_{[1\bar{1}0]} - k_{[110]})/(k_{[1\bar{1}0]} + k_{[110]})$ reaches 85% in the spectral region corresponding to spatially

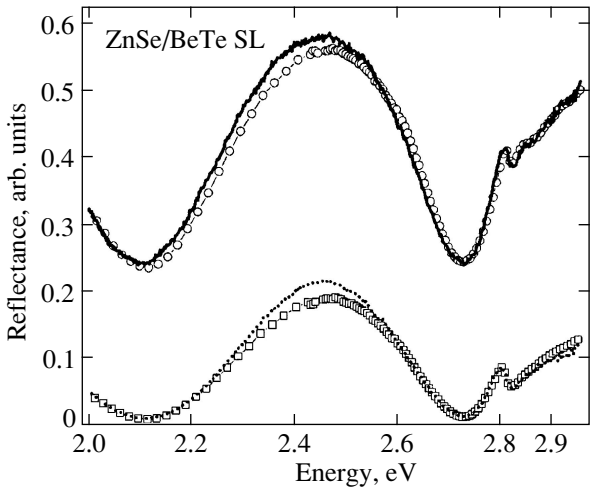

Fig. 7. Reflectance spectra of linearly polarized light from a ZnSe/BeTe superlattice. Circles and squares refer to the reflectance spectra of *s*- and *p*-polarized light, respectively, calculated from measured spectral responses of the optical constants of the ZnSe/BeTe superlattice. The calculation was performed for an angle of incidence $\theta_0 = 53.57°$. Solid and dashed lines are reflectance spectra of *s*- and *p*-polarized light obtained at the same angle of incidence. Sample temperature $T = 77$ K.

direct transitions in the BeTe layers. Such a large difference between Δn and Δk stems from the smallness of the light absorption coefficient in the ZnSe/BeTe SL in the spectral range under study.

Figure 6 displays the reflectance spectrum of polarized light from a ZnSe/BeTe SL measured in the following way. The light was passed through a linear polarizer with the axis perpendicular to the plane of incidence, reflected from the sample at an angle $\theta_0 = 53.57°$, and, on passing through one more linear polarizer whose axis was parallel to the plane of incidence, impinged on a detector. The sample was oriented such that its [110] crystallographic axis made an angle of 45° with the plane of light incidence on the sample. The reflectance spectrum shown is normalized against the spectral responses of the light source and the detector for the corresponding directions of polarization. With the sample oriented in this way relative to the polarizer axes, the nonzero amplitude of the reflected light can be due only to optical anisotropy, which transfers part of the radiation from the *s* to *p* polarization. The reflectance spectrum shown in Fig. 6 is the total (absorption plus refraction) sign-independent characteristic of the optical anisotropy of the sample and demonstrates the birefringence effect in the ZnSe/BeTe SL. The graph is dominated by the feature due to *e*1–*h*1 exciton transitions in the ZnSe layers. This is in agreement with the spectral responses of the anisotropy in the optical constants of the ZnSe/BeTe SL (Fig. 5), which imply that it is in the spectral region of spatially direct transitions in the ZnSe layers that the optical anisotropy reaches a maximum in absolute value. The reflectance spectrum of Fig. 6 reveals a minimum of the signal (anisotropy) at a photon energy of 2.13 eV, which corresponds to the isotropic point derived earlier from the spectral responses of the anisotropy in the refractive index and the absorption coefficient of the ZnSe/BeTe SL (Fig. 5).

The spectral responses of the optical constants of the ZnSe/BeTe type-II SL measured in this study permit one to calculate the absolute values of the reflectance of polarized light using Eqs. (2)–(4). Figure 7 compares reflectance spectra of polarized light from the ZnSe/BeTe SL, which were calculated and measured for the angle of incidence $\theta_0 = 53.57°$ with the [110] crystallographic axis of the sample oriented parallel to the plane of incidence. We readily see that the calculated and measured spectral responses of the reflectance of linearly polarized light from the ZnSe/BeTe SL agree satisfactorily throughout the spectral range covered. The agreement between the calculated and measured reflectance spectra becomes very good in the spectral region where the optical anisotropy of the heterostructures under study is maximal, i.e., in the region of the excitonic resonances ($E \approx 2.8$ eV, see Figs. 5, 6).

6. CONCLUSIONS

We reported on the first measurement of the refractive index and absorption coefficient of light on ZnSe/BeTe type-II periodic heterostructures with inequivalent interfaces by using ellipsometry in reflection. It has been found that the lowering of the symmetry of heterostructures with different anion and cation compositions caused by inequivalent interfaces gives rise to the appearance of a lateral optical anisotropy, which manifests itself in the refractive index and the absorption coefficient along the [110] and $[1\bar{1}0]$ crystallographic directions in the ZnSe/BeTe SL being different. The magnitude of the optical anisotropy remains nonzero throughout the spectral range covered and reaches its maximum near the excitonic resonances. The observed optical anisotropy in the refraction and absorption of light is assigned [3] to the mixing of light- and heavy-hole states at the interfaces, which gives rise to a difference between the matrix elements of the optical transition for two different sample orientations relative to the plane of polarization of incident light.

ACKNOWLEDGMENTS

This study was supported by the Russian Foundation for Basic Research (project no. 01-02-17758a) and the Ministry of Industry, Science, and Technology.

REFERENCES

1. A. V. Platonov, V. P. Kochereshko, E. L. Ivchenko, *et al.*, in *Proceedings of 6th International Symposium on Nanostructures: Physics and Technology* (St. Petersburg, 1998), p. 28.

2. A. V. Platonov, V. P. Kochereshko, E. L. Ivchenko, *et al.*, Phys. Rev. Lett. **83** (17), 3546 (1999).
3. E. L. Ivchenko, A. A. Toropov, and P. Voisin, Fiz. Tverd. Tela (St. Petersburg) **40** (10), 1925 (1998) [Phys. Solid State **40**, 1748 (1998)].
4. E. L. Ivchenko and G. E. Pikus, *Superlattices and Other Heterostructures. Symmetry and Optical Phenomena*, 2nd ed. (Springer, Berlin, 1997).
5. P. S. Hauge, Surf. Sci. **96** (1), 108 (1980).
6. M. Born and E. Wolf, *Principles of Optics*, 4th ed. (Pergamon, Oxford, 1969; Nauka, Moscow, 1970).
7. P. Lautenschlanger, M. Garriga, S. Logothetidis, and M. Cardona, Phys. Rev. B **35** (17), 9174 (1987).
8. A. A. Toropov, O. V. Nekrurkina, M. O. Nestoklon, *et al.*, Phys. Rev. B **67**, 113307 (2003).
9. M. Nagelstraβer, H. Dröge, H.-P. Steinrück, *et al.*, Phys. Rev. B **58** (16), 10394 (1998).
10. E. L. Ivchenko and M. O. Nestoklon, Zh. Éksp. Teor. Fiz. **121** (3), 747 (2002) [JETP **94**, 644 (2002)].

Translated by G. Skrebtsov